Cracow University of Technology

Constitutive Model Of Graded Micro-Structure Obtained Via Strain Induced Phase Transformation

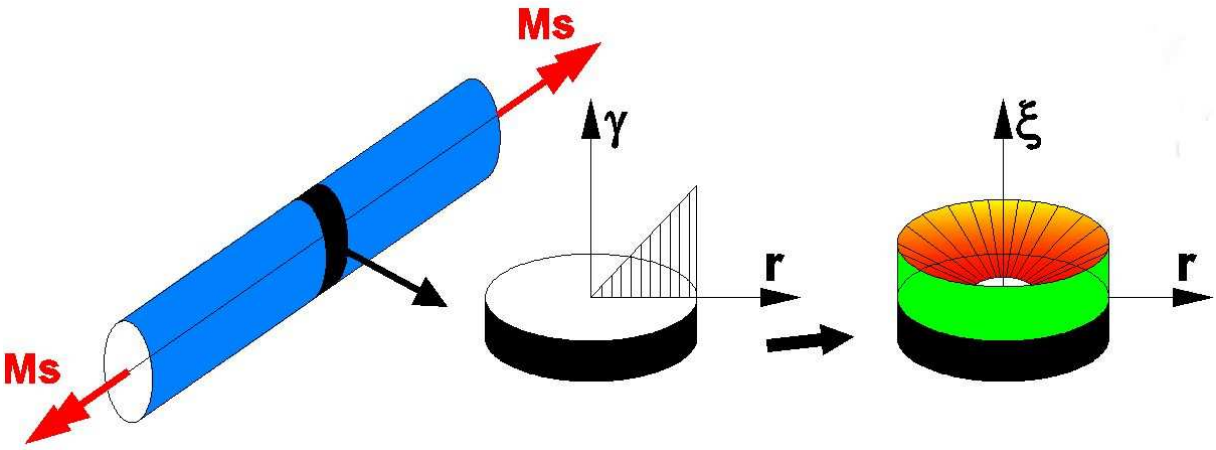

Model struktury gradientowej otrzymanej w wyniku przemiany fazowej sterowanej odkształceniem

Rafał Ortwein

Supervisor: Prof. dr hab. inż. Błażej Skoczeń

Cracow
January 2015

Acknowledgements

First of all I would like to thank to my colleagues from CERN where I spent 2,5 years during the Doctoral Student Programme. Many thanks to Jean-Philippe Tock, my CERN supervisor, who supported me during my 2,5 year stay in financing many experimental set-ups. Thanks to him the experimental material was very rich. Many thanks to Alain Bastard, who helped me a lot in preparation of the experimental set-up, performing first experiments with liquid nitrogen. He provided me with all the necessary tools, and helped in solving the problems that came on the way. It allowed development from relatively simple, monotonic torsion tests at room temperature to cyclic torsion tests at liquid nitrogen temperature, with martensite content measurements during the loading.

Next I would like to thank all the team from the MME-MM section (Mechanical & Materials Engineering – Materials & Metrology): Alexandre Gerardin, Dawid Marcinek, Philippe Deweulf, Floriane Leaux. They all helped me with the material tests that were carried out, including: microscopic observations, X-ray technique, preparation of the samples, martensite content measurements, micro-hardness measurements, tensile tests. All these colleagues were very kind to devote part of their time and to help me with my research. Without that help it would not be done.

Marco Buzio from the MSC-MM section (Magnets, Superconductors & Cryostats – Magnetic Measurements) helped me with the measurement of the martensite content via magnetic methods.

Many thanks to Arnaud Pierre Bouzoud for designing the first experimental set-up for the torsion tests and designing the geometry of the sample. The set-up fulfilled very well its requirements.

I would like to thank as well Pierre Tibaron for helping me with the design of the set-up for the buckling test. The assembly satisfied perfectly the design conditions.

Andre Jacquemod from MSC-SCD (Magnets, Superconductors & Cryostats - Superconductors and Devices) helped me with the first conception of the set-up for the torsion.

I appreciate the help of my colleagues from my own section MSC-CI (Magnets, Superconductors & Cryostats – Cryostats & machine Integration): Yann Leclercq, Delio Duarte Ramos, Vittorio Parma, Arnaud Vande-Craen and I thank them for useful comments and suggestions.

I appreciate all the comments, suggestions and many long discussions with Monika Sitko on the experimental and theoretical results. Many thanks for motivation as well.

Many thanks to Daniel Ziemiański from the MME-EDM section (Mechanical & Materials Engineering - Engineering Design & Measurements) for his help in the preparation of the buckling test. Big thanks to Michael Guinchard who agreed to schedule the buckling test, and handled the tensile machine during the test.

All these colleagues contributed somehow to the research, so in the end I could gather very rich material with sound experimental evidence, not only theoretical predictions.

Of course I want to thank my university supervisor, prof. dr hab. inż. Błażej Skoczeń, for very good ideas and a lot of positive motivation. As well as for setting very high expectations.

All this was a very big challenge in my life. The project took 4 full years both of my work and private time. I have spent more than thousand hours on the experimental research, studying the literature, writing publications and writing the final thesis. It was certainly the biggest and most difficult work that I've ever done.

Table of contents

1. Literature survey 11
1.1. General information about stainless steels 11
1.2. Theoretical and experimental results describing the phenomenon of phase transformation in stainless steels 15
1.3. Functionally graded structures obtained via martensitic transformation 24
2. The aim and the scope of Thesis 27
2.1. Introduction 27
2.2. Objectives of the Thesis 32
3. 3D constitutive model of continuum undergoing phase transformation at cryogenic temperatures 33
3.1. Introduction 33
3.2. The general constitutive model 33
3.3. Mathematical modeling of the plastic strain induced phase transformation 34
3.4. Derivation of the Bain strain tensor 38
3.5. Calculations of the plastic strain tensor 40
3.5.1. J2 yield surface 40
3.5.2. Hardening variables 42
3.5.3. Kinematic hardening variable 42
3.5.4. Derivations of terms dX_{a0} and $dX_{a\xi}$ 43
3.5.5. Derivation of term dX_{a+m} 45
3.5.6. Summary of the kinematic hardening 55
3.5.7. Isotropic hardening 55
3.5.8. Mixed hardening 56
3.5.9. Summary of the plastic strain tensor derivation 57
3.5.10. Calculation of the plastic multiplier λ 58
3.6. Summary of the constitutive model 61
4. Uniaxial constitutive model of continuum undergoing shear strain induced phase transformation 63
4.1. Introduction 63
4.2. Kinetics of the shear strain induced phase transformation 63
4.3. Derivation of the stress versus strain relationship 64
4.3.1. Difference between the Cauchy and the Hencky strain measures 66
4.3.2. General equations describing the constitutive model 67

4.3.3. Simplifications of the modulus C_{a+m} 68
4.3.4. Simplification of the shear stress versus shear strain relations 71
4.4. Torque versus the angle of twist 72
4.4.1. Closed-form analytical solutions for the torque versus the unit angle of twist 74
4.4.2. Exact formulae and error estimation 76
4.5. Identification of parameters of the model 78
5. Circular rods subjected to monotonic torsion at 77K - experiments 81
5.1. Description of experimental set-up 81
5.2. Geometry and material of the sample 84
5.3. Procedure of the test 85
5.4. Results of torsion test for 304 stainless steel samples 87
5.5. Performance of the FGSM made of 304 stainless steel 89
5.6. Deformation of twisted samples 91
5.7. Summary of torsion experiments for 304 stainless steel 95
5.8. Conclusions 96
6. Microscopic analysis of FGSMs 97
6.1. Microscopic observations 97
6.1.1. Extracting material samples 97
6.1.2. Ferrite content measurements 98
6.1.3. Microstructure observations of martensite 99
6.1.4. Sample 1 - loaded at 293K until rupture 99
6.1.5. Sample 2, loaded at 77K and twisted to 870° 104
6.1.6. Sample 3, loaded at 293K and twisted to 870° 107
6.1.7. Sample in raw state 111
6.1.8. Conclusions from the microscopic observations 115
6.2. Micro-hardness measurements 116
6.2.1. Experimental method 116
6.2.2. Results for Sample 1, loaded at 293K until rupture 118
6.2.3. Results for sample 2, twisted at 77K to 870° 121
6.2.4. Sample 3, twisted at 293K to 870° 124
6.2.5. Sample 4, twisted at 77K until rupture 126
6.2.6. Raw sample from 304 stainless steel 128
6.2.7. Raw sample of 304L austenitic stainless steel 130

6.2.8. Summary and conclusions of the micro-hardness measurements 132
6.2.9. Conclusions 134
6.3. Martensite content measurements 135
6.3.1. Martensite content measurement based on magnetic permeability. Set-up 1 136
6.3.2. Martensite content measurement based on magnetic permeability. Set-up 2 140
6.3.3. Measurements via the EBSD technique (Electron Backscatter Diffraction) 145
6.3.4. Martensite content measurements by means of X-ray technique 146
6.3.5. Measurements by using Feritscope 147
6.3.6. Results of ferrite content measurements by means of Feritscope 155
6.3.7. Summary of the martensite content measurements by means of Feritscope 165
6.3.8. Conclusions from the martensite content measurements 169
7. Torsion tests: round bars made of 304L, 316L and 316LN stainless steel 170
7.1. The measurement method 170
7.2. Torsion test at 77K of sample made of 316L stainless steel 174
7.2.1. Martensite content evolution on the surface, for sample C1 174
7.2.2. Deformation of sample C1 176
7.3. Torsion test at 77K of sample made of 304L stainless steel 177
7.3.1. Martensite content evolution on the surface, for sample D1 178
7.3.2. Deformation of sample D1 (304L) 179
7.4. Torsion test at 77K of sample made of 316LN stainless steel 180
7.4.1. Martensite content evolution on the surface, for sample E1 181
7.4.2. Deformation of sample E1 (316LN) 182
7.5. Torsion test at 77K of sample made of 304 stainless steel 183
7.5.1. Sample 6.1 (304 ss) 183
7.5.2. Sample 6.2 (304 ss) 184
7.5.3. Sample 7.1 (304 ss) 186
7.5.4. Sample 7.2 (304 ss) 189
7.6. The summary of results for stainless steels: 304, 304L, 316L, 316LN 191
7.7. Conclusions 194
8. Comparison between the theory and the experiment 195

8.1. Introduction 195
8.2. Calibration of the model based on the kinetics of phase transformation 195
8.2.1. Calibration for 304 stainless steel 195
8.2.2. Samples made of grades: 304L, 316L, and 316LN 198
8.3. Torque versus the angle of twist, theory and experiment 199
8.3.1. Identification for grade 304 stainless steel 199
8.3.2. Identification for grades 304L, 316L, and 316LN ss 201
8.4. Prediction of stress versus strain based on the constitutive model 203
8.4.1. Prediction for grade 304 ss 203
8.4.2. Prediction for grades 304L, 316L, and 316LN 204
8.5. Error estimation for the exact and simplified formulae C_{a+m} 205
8.6. Error estimation for the exact formulae of the torque versus the angle of twist 207
8.6.1. Error estimation for grade 304 stainless steel 207
8.6.2. Error estimation for grades 304L, 316L, and 316LN 208
8.6. Conclusions 208
9. Cyclic torsion of round bars at 77K and 293K 209
9.1. Introduction 209
9.2. Plan of the measurements 209
9.3 Experimental results 210
9.3.1. Data for 304 stainless steel 210
9.3.2 Data for 316L stainless steel 220
9.3.3 Data for 304L stainless steel 223
9.3.4. Data for 316LN stainless steel 227
9.4. Discussion of results of the cyclic torsion 230
9.4.1. Results for torque ±70 Nm (A1, C4, D4, E4) 230
9.4.2. Results for torque ±80 Nm (A2, C3, D3, E3) 231
9.4.3. Results for torque ±100 Nm (A4, C2, D2, E2) 232
9.4.4. Results for all the load controlled tests (±70 Nm, ±80 Nm, ±100 Nm) 233
9.5. Deformation of the samples 234
9.6. Summary and conclusions 239
10. Plastic shakedown 240
10.1. Introduction 240
10.2. Mechanism of structural shakedown 240

10.3. Boundedness of energy dissipation during structural shakedown 242
10.4. Experimental results: energy dissipation during elastic-plastic torsion 245
10.5 Energy dissipated in subsequent cycles 251
10.4. Conclusions 254
11. Tensile tests at room temperature 255
11.1. Samples for the tensile test 255
11.2. Martensite content measurements before tensile test 256
11.2.1. Sample 1 (grade 304 ss) 256
11.2.2. Sample 2 (grade 304 ss) 257
11.2.3. Sample 3 (grade 304 ss) 258
11.2.4. Sample 4 (grade 304 ss) 258
11.2.5. Sample A9 (grade 304 ss) 259
11.2.6. Sample A10 (grade 304 ss) 260
11.2.7. Summary of the martensite content measurements 260
11.3. Martensite content measurements after tensile test 261
11.4. The experimental method 261
11.5. Results of tensile test 262
11.5.1. Tensile test results for sample 1 263
11.5.2. Tensile test results for sample 2 264
11.5.3. Tensile test results for sample 3 265
11.5.4. Tensile test results for sample 4 266
11.5.5. Tensile test results for sample A9 267
11.5.6. Tensile test results for sample A10 269
11.5.7. Tensile test results for sample 62 271
11.5.8. Tensile test results for the raw sample (grade 304 ss) 272
11.5.9. Summary of tensile tests 273
11.6. Stress - strain curves 274
11.7. Summary and conclusions 277
12. Buckling of FGSMs - experiments 278
12.1. Description of the experiment 278
12.2. The procedure of test 285
12.3. Measuring transverse deflection of sample by using recorded videos 287
12.4. Experimental results 288

12.4.1. Results for the raw sample 288
12.4.2. Results for sample A1 289
12.4.3. Results for sample A2 290
12.4.4. Results for sample A3 292
12.4.5. Results for sample A4 293
12.4.6. Results for sample A5 294
12.4.7. Results for sample A6 296
12.4.8. Results for sample A7 297
12.4.9. Results for sample A8 299
12.4.10. Comparison of the results 299
12.5. Deformation of the samples 304
12.6. Summary and conclusions 305
13. Stability of functionally graded bars - modeling 306
13.1. Finite element model of functionally graded column based on bilinear elastic-plastic material 306
13.1.1. Parameters of the material model 306
13.1.2. Building the finite element model 307
13.1.3. FEM model versus experimental results 317
13.1.4. Detailed results of numerical simulations for sample A2 318
13.1.5. Numerical simulations versus experiment for sample A2 320
13.2. Finite element model with microstructure 323
13.2.1. Description of the problem 323
13.2.2. Tensile properties of samples with variable martensite content 323
13.2.3. Approximation of the martensite content distribution 325
13.2.4. Calculating the average martensite content 327
13.2.5. Finite element model in Ansys 328
13.2.6. Discussion and conclusions 332
13.3. Conclusions 332
14. Summary and conclusions of the Thesis 333
1. Przegląd literatury 338
2. Cel i zakres pracy 338
3. Wieloosiowy model konstytutywny kontinuum podlegającego przemianie fazowej w temperaturach kriogenicznych 340

4. Jednoosiowy model konstytutywny kontinuum podlegającego przemianie fazowej indukowanej odkształceniem plastycznym 342
5. Zestaw eksperymentalny do testów skręcania w temperaturach 77K i 293K 343
6.1. Analiza mikroskopowa elementów FGSM 344
6.2. Badania mikrotwardości..... 345
6.3. Pomiary zawartości martenzytu 345
7. Testy skręcania: pręty o przekroju kołowym ze stali austenitycznych 304L, 316L and 316LN 346
8. Porównanie wyników eksperymentalnych i teoretycznych..... 347
9. Cykliczne skręcanie prętów w temperaturach 77K i 293K 347
10. Przystosowanie plastyczne do obciążeń cyklicznych 348
11. Test rozciągania w temperaturze pokojowej..... 349
12. Wyboczenie kolumn o strukturze gradientowej - eksperyment 350
13. Wyboczenie kolumn o strukturze gradientowej - modelowanie 350
14. Podsumowanie i wnioski..... 351
15. References 352

NOTATION

SCALARS

T	temperature
V	volume
V_α	volume of the unit cell of martensite (α' phase)
V_γ	volume of the unit cell of austenite (γ phase).
Δv	relative volume change during martensitic transformation
M	torque
t	time
t_ξ	time corresponding to phase transformation threshold
t_L	time corresponding to saturation of martensite content
$\mathrm{J_{IC}}$	fracture toughness
p	pressure or accumulated plastic strain
p_ξ	accumulated plastic strain transformation threshold
Σ	triaxiality parameter
$\bar{\tau}$	equivalent shear stress
τ_0	shear yield stress
τ_ξ	shear stress corresponding to phase transformation threshold
σ_y	normal yield stress
M_s	martensite start temperature
M_s^σ	temperature upon which phase transformation spontaneously occurs in a sample loaded with yield stress
M_d	temperature above which phase transformation does not occur
A	slope of phase transformation kinetics
ξ_L	saturation value of martensite content
$\bar{\theta}$	Lode angle
ξ, $f^{\alpha\prime}$, f_m	volume fraction of martensite
f_a	volume fraction of austenite
ε_ξ^p	threshold value of plastic strain upon which phase transformation starts to occur
ε_C	Cauchy strain
ε_H	Hencky strain
ε_0	elastic strain upon yielding
ε_{eq}^p	equivalent plastic strain
γ	shear strain
γ_ξ^p	shear strain transformation threshold
γ_{max}	maximum shear strain in the constitutive model
J_2	second invariant of stress deviator
R	isotropic hardening variable, radius of samples cross-section
C_{a0}	tangential modulus of pure austenite
C_{a+m}	homogenized tangential stiffness modulus of two phase continuum (austenite + martensite)
$\mathrm{C}_{(a+m)Ex}$	exact expression of the tangential modulus of two phase continuum
b	length of the Burgers vector
l	mean distance between inclusions
d	diameter of martensite inclusion
h	material dependent parameter related to "Orowan mechanism"

μ, G	shear modulus
μ_a, G_a	Shear modulus of austenite
μ_{ta}	tangential shear modulus of austenite
μ_m	shear modulus of martensite
μ_{MT}	shear modulus of two-phase continuum
μ^*	shear modulus of the Hill influence tensor
k	bulk modulus
k_{ta}	tangential bulk modulus of austenite
k_m	bulk modulus of martensite
k_{MT}	bulk modulus of two-phase continuum
k^*	bulk modulus of the Hill influence tensor
ν_a	Poisson's ratio of austenite
ν_m	Poisson's ratio of martensite
E_{ta}	tangential stiffness modulus of austenite
E_a	Young modulus of austenite
E_m	Young modulus of martensite
$\dot{\lambda}$	plastic multiplier
f_y	yield function
H	hardening modulus
φ	angle of twist
φ_ξ	angle of twist corresponding to phase transformation threshold
φ_L^p	angle of twist corresponding to saturation of martensitic phase
φ_0	angle of twist corresponding to yield stress
θ	unit angle of twist
θ_0	unit angle of twist corresponding to yield point
θ_ξ	unit angle of twist corresponding to phase transformation threshold
L	length of the sample, inductance
Fr	true ferrite content
Fm	measured ferrite content
CF_T	correction factor to cover the thickness of the sample
CF_D	correction factor to cover the distance from the edge
CF_C	correction factor involving curvature of the sample
μ_r	relative magnetic permeability
P^{diss}	dissipated power
W^{diss}	dissipated energy
β	Bauschinger parameter
A_0	area of samples cross-section

2nd order tensors

$\underline{\underline{\sigma}}$	stress tensor
$\underline{\underline{s}}$	stress deviator
$\underline{\underline{\varepsilon}}$	total strain tensor
$\underline{\underline{\varepsilon}}^{p}$	plastic strain tensor
$\underline{\underline{\varepsilon}}^{th}$	thermal strain tensor
$\underline{\underline{\varepsilon}}^{bs}$	"Bain strain" tensor
$\underline{\underline{\varepsilon}}_{\mu}^{bs}$	microscopic eigen-strain tensor
$\underline{\underline{\mathrm{I}}}$	second rank identity tensor
$\underline{\underline{X}}$	back-stress tensor
$\Delta\underline{\underline{\sigma}}_{a+m}$	stress increment in two phase continuum (austenite and martensite)
$\Delta\underline{\underline{\sigma}}_{a}$	stress increment in austenitic phase
$\Delta\underline{\underline{\sigma}}_{m}$	stress increment in martensitic phase
$\underline{\underline{n}}$	vector normal to the yield surface

4nd order tensors

$\underline{\underline{\underline{\underline{E}}}}$	4th order elasticity tensor
$\underline{\underline{\underline{\underline{E}}}}_{a}$	4th order elasticity tensor of austenite
$\underline{\underline{\underline{\underline{E}}}}_{m}$	4th order elasticity tensor of martensite
$\underline{\underline{\underline{\underline{J}}}}$	volumetric 4th rank projector
$\underline{\underline{\underline{\underline{K}}}}$	deviatoric 4th rank projector
$\underline{\underline{\underline{\underline{I}}}}$	4th rank identity tensor
$\underline{\underline{\underline{\underline{E}}}}_{ta}$	linearized tangential stiffness operator of austenite
$\underline{\underline{\underline{\underline{\mathrm{E}}}}}^{*}$	Hill influence tensor

1. Literature survey

The literature review has been divided into three main sub-chapters. The first one is concentrated on the general information about stainless steels and their applications. It is important to perform a general overview and get an idea where the results of the present thesis could be applied. Description of all the brands of stainless steels, their microstructures and properties are important, as similar characteristics can be found in the newly created functionally graded structures.
The second sub-chapter is an overview of the most important constitutive models and the experimental results for materials that undergo plastic strain induced phase transformation.
Finally, the last one is devoted to functionally graded microstructures obtained via strain induced martensitic transformation – the subject of particular importance for the present thesis.
As a general note, the literature review is organized mainly in a chronological order. In some cases similar publications or publications of the same Authors were mentioned together.

1.1. General information about stainless steels

World production of crude steel amounts to approximately 1.6 billion tones, and about 2% of this production is reserved for stainless steel. The demand for stainless steel is ever increasing (Fig. 1.1a), according to Zaera et al. (2012) by roughly 6% a year.
The most widely used stainless steel grades are the austenitic 18/9 steels, also denoted by AISI 304 or 304L, which form more than 50% of the global production of stainless steel. Together with AISI 410 and AISI 316/316L these three grades make over 80% of the total tonnage of stainless steel.

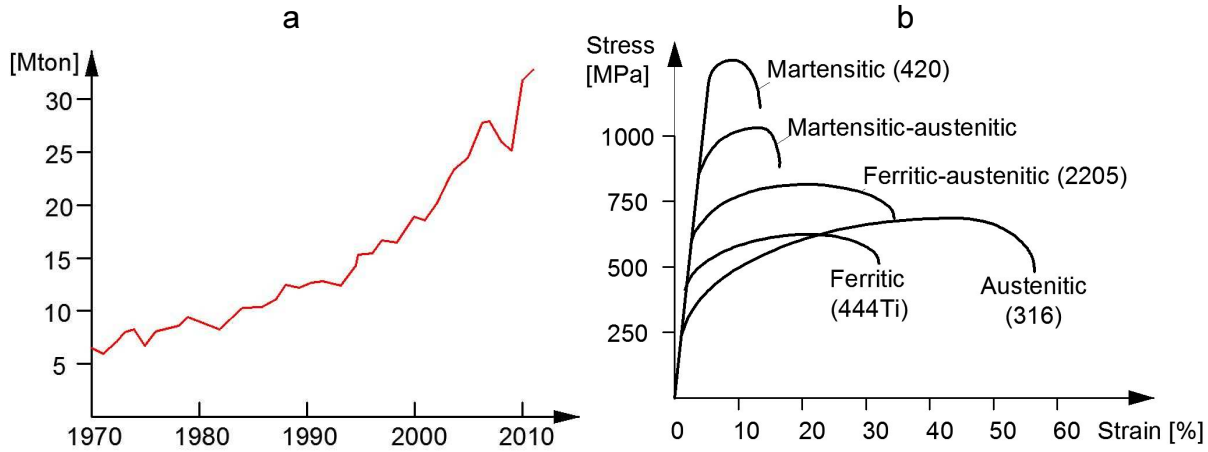

Figure 1.1. a) World stainless steel production [124], b) Stress versus strain curves for several types of stainless steel [125] at 293K

Stainless steels can be subdivided into the following grades:

- Austenitic
- Martensitic
- Ferritic
- Duplex
- Precipitation hardening
- Dual phase (DP)

General information about all these kinds of steel are presented in the following paragraphs.

Austenitic stainless steels have good to excellent corrosion resistance, good formability and weldability. Their good impact strength at low temperatures is often exploited in cryogenic applications.

Martensitic stainless steels form the smallest group of all stainless steels. They have higher carbon content compared to the other grades, to improve their strength and hardenability. They have the highest yield strength from all the grades (Fig. 1.1b). However, ductility of the martensitic steels is relatively low.

Ferritic stainless steels generally have better engineering properties than austenitic grades, but have reduced corrosion resistance, because of lower chromium and nickel content. They are usually less expensive.

Duplex stainless steels have mixed microstructure of austenite and ferrite, the aim being to produce a 50/50 mix, although in commercial alloys the ratio may reach some 40/60. Duplex stainless steels have roughly twice the strength compared to austenitic stainless steels and improved resistance to localized corrosion, particularly pitting, crevice corrosion and stress corrosion cracking.

The properties of duplex stainless steels are achieved with an overall lower alloy content making their use cost-effective for many applications.

The precipitation hardening (PH) grades form highly specialized family of stainless steels, satisfying the need for very high-strength materials with good corrosion resistance. In terms of corrosion, they have the same resistance levels as austenitic steels. The advantage of the PH alloys over the strictly martensitic stainless steels is that they attain great strength with higher toughness and corrosion resistance. In addition, they can be fabricated in a relatively soft state and then hardened with very little dimensional change.

The term “dual-phase” firstly reported by Hayami and Furukawa, refers to the presence of essentially two phases in the microstructure: ferrite and martensite, although small amounts of bainite, pearlite and retained austenite may also be present.

Dual-phase steels exhibit a number of superior mechanical properties, such as continuous yielding behavior, low 0,2% offset yield strength, high work hardening rate, high tensile strength and remarkably high uniform and tensile elongations. The mechanical properties of dual-phase steels arise from structural features, that is the fine dispersion of hard martensite particles in a ductile ferritic matrix (cf. Tsipouridis, 2006). The performance of DP steels is almost as good as of TRIP steels (Fig. 1.6). Dual phase steels perform similarly in terms of strength, only the total and the uniform elongations are slightly smaller than for the TRIP steels. A comparative study has been done by Curtze et al. (2009), where the Authors measured tensile behavior at different temperatures and strain rates for TRIP and DP steels. The Authors explained the reason for high strength of DP steels, that it comes from hard martensite islands dispersed in the ferrite matrix.

For example, two microstructures of DP steels: with about 50% and with 34% of martensite, respectively, are presented in Fig. 1.2 a, b.

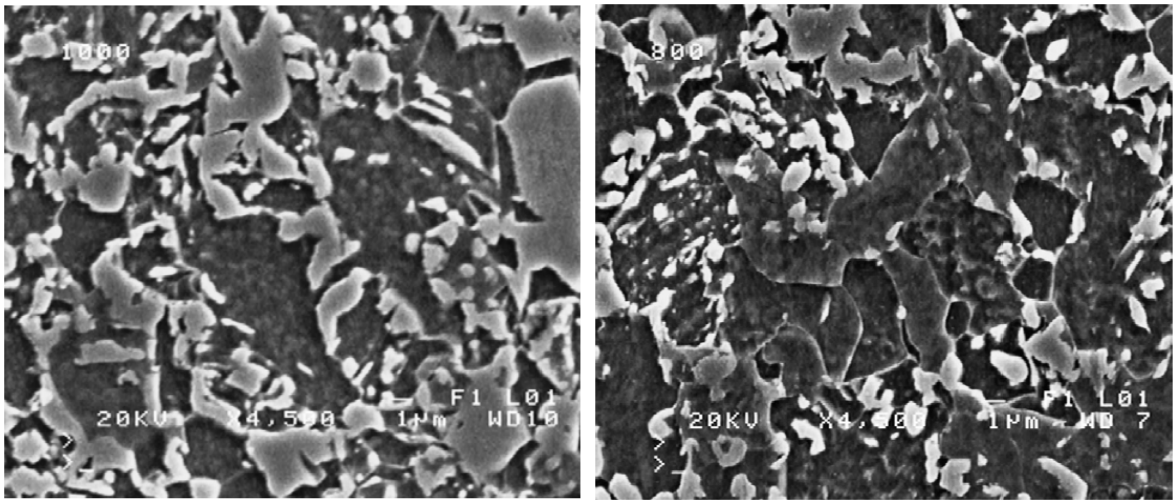

Figure 1.2. a) Image of the microstructure of steel DP1000 with ~49% of ferrite and ~50% of martensite(ferrite – dark grains, martensite – bright grains), b) ~65% of ferrite and ~34% of martensite (cf. Krajewski and Nowacki, 2014)

Stainless steel products come in the following forms: cold rolled sheets (60% of the total production), bars and wires (20%), hot rolled plates (10%), tubes (6%), castings and other (4%).

Industrial applications consume about 75% of the total production, and the rest are consumer items (washing machines, pans, cutlery, sinks, etc.).

For the industrial applications the biggest consumer is the food brewery industry (25%), the chemical, oil and gas industry (20%), transport (8%), energy production (7%), textile industry (6%), buildings and general constructions (5%).

In the paper by Zaera et al. (2012) the Authors stated that it was expected that the demand for stainless steel would be increasing by the same rate (about 6%) over the next decades. According to the Authors the properties of austenitic stainless steels foster their industrial applications in: surgical instruments, houseware, containers, piping, vessels, power plants, pharmaceutical industry, petrochemical industry, food-processing equipment, architecture and construction structures.

Several grades out of the standard wrought austenitic stainless steels have been extensively used for equipment operating at cryogenic temperatures, almost up to the absolute zero. As the temperature decreases the strength of these steels increases rapidly. At the same time ductility and impact toughness are maintained at a high level. The steels are used for handling liquid gases and for other liquids where corrosion resistance is also required, e.g. the low-temperature processing of foods and other products where product contamination must be held to a minimum [126]. The most widely used wrought stainless steels for cryogenic service are the AISI Types 304 and 304L. Types 316, 316L, 321 and 347 are also used, depending upon the availability of the particular form or size required.

Wrought stainless steels with controlled additions of nitrogen (with improved proof stress and tensile strength in comparison with the traditional grades) are also used for service at cryogenic temperatures. These steels can be used the construction of pipes, pumps, valves, pressure vessels and containers [127].

Austenitic stainless steels, because of their excellent combination of mechanical and physical properties are being considered for load-bearing structures of large superconducting magnets. For example used for the construction of the Large Hadron Collider at CERN. Austenitic stainless steels are as well used for plasma containment structures in magnetic fusion experiments (e.g. ITER).

The cross-section of a standard Dipole magnet for the LHC was presented in Fig. 1.3. There are more than 1200 such dipole magnets around circumference of 27km ring of the LHC accelerator. Each of these magnets measures 15 meters. The superconducting coils are held by austenitic stainless steel collars presented in Fig. 1.4. Both the coils and the collars are cooled to the temperature of 1.9K using large quantities of superfluid liquid helium.

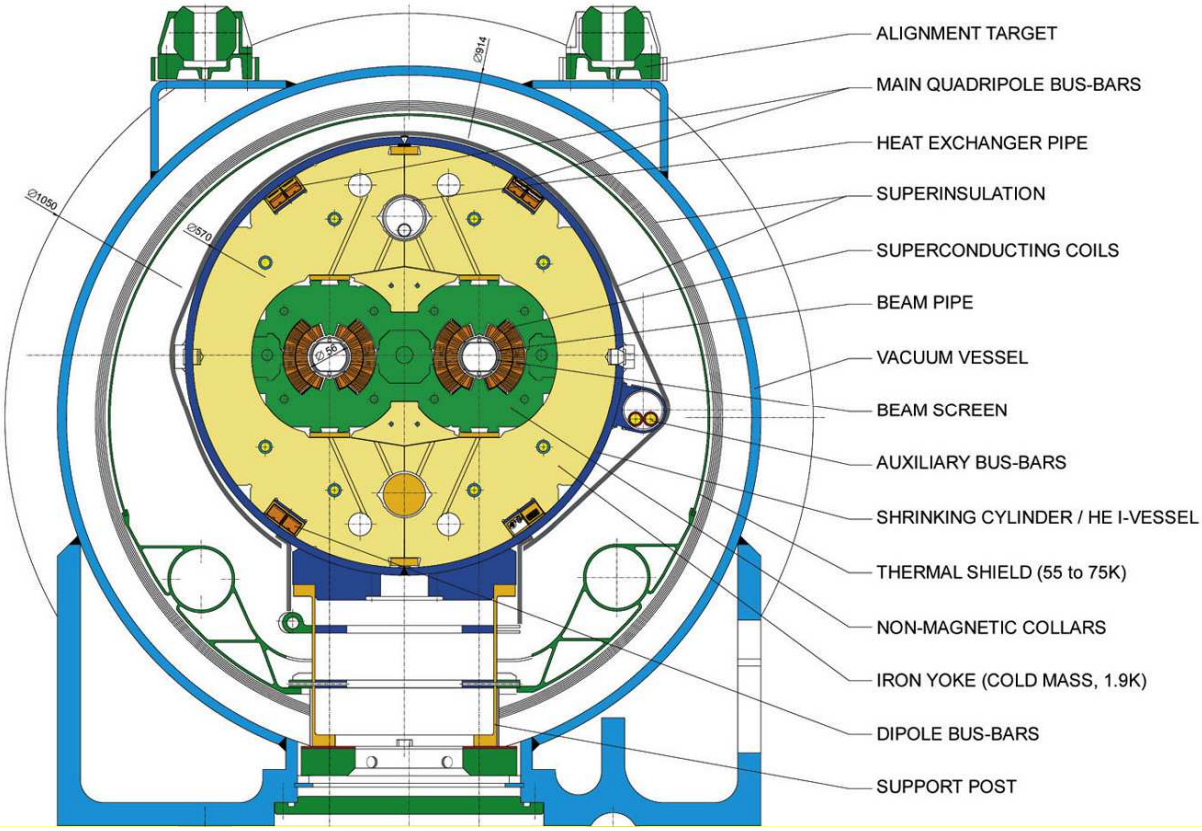

Figure 1.3. LHC Dipole – standard cross-section. CERN AC/DI/MM – HE107 – 30 04 1999

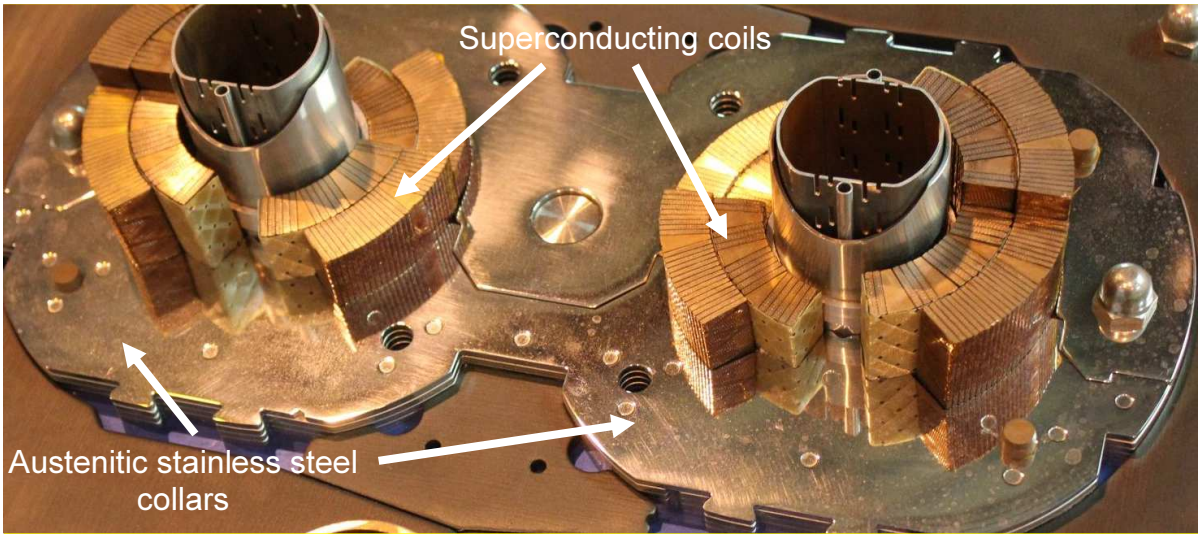

Figure 1.4. Stainless steel collars around superconducting coils in the LHC Dipole electromagnet.

1.2. Theoretical and experimental results describing the phenomenon of phase transformation in stainless steels

In the first few paragraphs general description of the phenomenon is outlined. Later on, detailed literature survey is presented, where the most important features of the publications are mentioned. For outstanding papers, more detailed description is given.

The phenomenon of plastic strain induced phase transformation results in the evolution of phases from the metastable austenite to martensite. In this particular type of transformation, the process is driven by the plastic strains. From the thermodynamical point of view, the Gibbs free energy corresponding to the transformation is smaller for the martensite than for the austenite. Thus, naturally, micro-structural change is invoked. This process occurs for a given range of temperatures, namely between the M_s and the M_d, which will be discussed later. Above the temperature M_d (which is usually in the order of several hundreds of degrees) the austenitic phase is completely stable. Thus, no plastic strain can trigger the phase transformation.

The plastic strain driven martensitic transformation causes the so called TRIP effect, which stands for “Transformation Induced Plasticity”. This effect refers to the increased capacity of the material to undergo plastic deformation, compared to the untransformed material.

TRIP phenomenon has been studied for decades. Based on this phenomenon, the so called TRIP steels have been developed. Their microstructure is composed of retained austenite (min. 5%), embedded in a primary matrix of ferrite. In addition, hard phases such as martensite and bainite are present in varying amounts (Fig. 1.5).

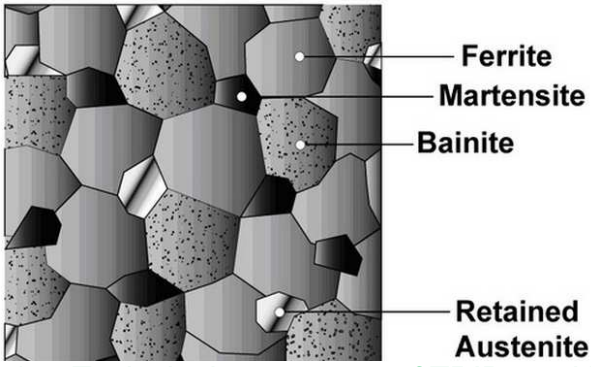

Figure 1.5. Typical microstructure of TRIP steel [128]

TRIP steels are characterized by high strength and relatively high ductility. Both result from transformation of austenite to martensite, and the martensite has much higher strength and hardness than the austenite. Substantial hardening resulting from the martensitic transformation can delay the onset of necking, and lead to higher uniform and total elongations. In Fig. 1.6 a comparison of the stress-strain curves is shown for three types of steels: Dual phase steel (DP), High strength low alloy steel (HSLA), and TRIP steel. TRIP steel performs best in terms of strength and ductility. This effect is very interesting and can improve manufacturability, safety and reduce weight of structures.

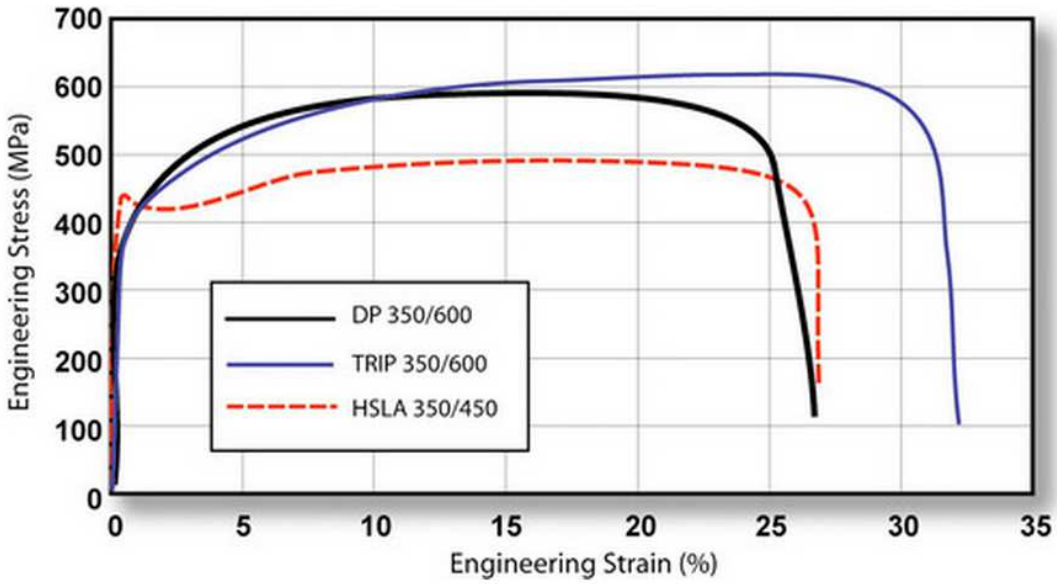

Figure 1.6. Stress-strain behavior of 3 steels: TRIP, DP (dual phase), HSLA (high strength low alloy steel) [120]

First important work on TRIP effect was done by Greenwood and Johnson (1965). The Authors developed a phenomenological model for the TRIP effect. To clarify, TRIP effect is understood as generation of irreversible strain, which accompanies the phase transformation, even when the outside stress is below the yield point of the weaker phase (austenite). Greenwood and Johnson (1965) explained TRIP phenomenon as corresponding to plastic accommodation of internal stresses emerging from martensitic phase transformation. This effect is also known as the "accommodation effect".

Another very important work was carried out by Magee (1966), where the so called "orientation effect" was investigated. According to Magee 24 crystallographically possible martensitic variants may be formed during the transformation.

The most important role in explaining which variant of 24 is going to be formed, according to Magee, was played by internal and applied stresses.

The model of Greenwood and Johnson (1965) was later on extended by Leblond et al. (1989a) to take into account the multiaxial stress states.

One of the most important contributions to the subject of the strain induced phase transformation was made by Olson and Cohen (1975). The Authors have developed a phenomenological model where the intersections of shear bands have been shown to be effective sites for the strain-induced martensitic nucleation. The Authors derived the expression for the volume fraction of martensite versus plastic strain, where two parameters were temperature dependent. Good agreement with the available data for 304 stainless steel was obtained.

Following the results of Olson and Cohen (1975), Olson and Azrin (1978) conducted experimental research to better understand transformation kinetics and its relation to flow properties in high-strength TRIP steels. True-stress, true-strain and volume fraction of martensite were identified during both uniform and localized flow as a function of temperature.

Later on Stringfellow and Parks (1991) developed a constitutive model and examined the effect of the transformation on the state of stress and strain near a tip of a stationary crack.

Experiments conducted on 31Ni-5Cr high strength (tensile yield stress of 1300 MPa) precipitation hardened austenitic stainless steel by Leal (1984) have shown very high fracture toughness (the ability of a material to absorb energy and plastically deform without fracturing) of $J_{IC} = 300\ [\mathrm{MPa \cdot m}]$. Data from experiments by Stevehaung (1990) have shown even higher values of $J_{IC} = 590\ [\mathrm{MPa \cdot m}]$. Stringfellow and Parks wanted to explain the remarkable fracture toughness reported by Leal (1984) and Stevehaung (1990) of certain TRIP steels.

Generally, inverse relationship between strength and toughness is observed. However, the 31Ni-5Cr stainless steel is characterized by high strength and toughness, which is remarkable. The Authors have shown that significant amounts of martensite can form even at the temperatures that are well above M_d for uniaxial tension, when triaxiality is higher than 2 ($\Sigma > 2$). Here, the triaxiality parameter was defined as $\Sigma = -p/(\sqrt{3}\bar{\tau})$, where p denotes pressure and $\bar{\tau}$ is equivalent shear stress. Such conditions occur near a crack tip. The Authors considered blunting of an initially sharp crack. Due to the triaxial nature of the stress-state ahead of the crack tip, a considerable amount of martensite was formed in this region. An area of increased hardness formed directly ahead of the crack tip due to the evolution of much harder martensite phase. The Authors conclude that “the dramatic strain-hardening caused by the transformation process delays the final loss of stability to much higher strain levels”. Stevehaug (1990) supported this notion in his experiments. He observed the classical zig-zag pattern of crack propagation in the non-transforming materials, however, in the transforming ones, he observed that the crack often branched leading to significant blunting. This deflection of the crack front appeared to be a major factor contributing to the observed high toughness. Later on, Olson (1996) applied numerical modeling of ductile fracture and made metallographic study of near-crack-tip transformation and localization processes. He identified that, the transformation toughening mechanism is ”associated with the flow stabilizing influence of pressure-sensitive strain hardening provided by strain-induced transformation”.

Stringfellow et al. (1992) generalized the Olson and Cohen model and used the self-consistent approach assuming that the martensite inclusions are spherical in shape.

The kinetics of Olson and Cohen was extended to take into account not only the plastic strain and the temperature, but also the stress state. Good agreement was achieved with the experimental data available for austenitic steels.

A different approach based on energy was proposed by Bhattacharyya and Weng (1994). The Authors have calculated the stress-strain behavior of a ductile system with martensitic transformation under the action of stress. Martensite grains were assumed as thin spheroidal platelets randomly oriented in the matrix. No “a priori” law for the transformation kinetics was assumed. Martensite fraction was calculated incrementally based on the change of Gibbs free energy during the transformation.

In the papers by Diani et. al. (1995a, 1995b, 1996) a micromechanical model that describes the TRIP phenomenon in steels was proposed. The Authors developed a model which can describe the irreversible transformation strain as a function of the martensite fraction and the stress level. The orientation variants of the martensite have been taken into account.

Another approach was formulated by Levitas (1998) who developed the conditions for the transformation of elementary volume inside an elastoplastic material through the extremum dissipation principle. Later on, Levitas et al. (1998) performed finite element calculations based on the proposed model.

A lot of work was put into theoretical and numerical study of the plastic behavior of steels during phase transformation by Leblond et al. (1986a, 1986b), and Leblond (1989b).
In the paper by Cherkaoui et al. (1998), the Authors derived the behavior of an austenitic single crystal, from which the overall behavior of TRIP steels could be obtained. Volume fractions of each martensite variant and plastic strains related to product and parent phases were taken into account as internal variables. With their help the microstructure evolution of a single crystal was formulated.
Tomita and Shibutani (2000) performed very detailed and interesting study on the deformation behavior of TRIP steels under monotonic and cyclic loading. Uniaxial tension tests were performed under constant strain rate at various temperatures: 77K, 113K, 153K, 213K, 233K, 253K, 273K, 293K, 373K. In order to elucidate the dependence of the martensitic transformation on the non-uniform deformation, the volume fraction was predicted and measured for the uniaxial tension of bars with a ringed notch. Good correspondence between the local volume fraction of the martensitic phase around the notch and simulations validated the proposed constitutive model for non-uniform deformation behavior. Additional computational simulations were performed on smooth/ringed-notched bars under cyclic loading.
Lebedev and Kosarchuk (2000) performed a study of the martensitic transformation in type 18-10 austenitic stainless steel both at room and at low temperatures (down to 77K). The influence of temperature and stress state on the kinetics of martensitic transformation was investigated. The Authors measured the evolution of both α' and ε martensite variants. They concluded that the deformation by tension caused more intense formation of both α' and ε martensite variants than by torsion and compression. Second conclusion was the intensification of the γ→α' transformation with increasing stress triaxiality and reduction of the Lode parameter.
Cherkaoui et al. (2000) developed a micro-mechanical model to predict the conditions of nucleation and growth of a martensitic micro-domain inside an inhomogeneous plastic strain field. The overall behavior of a polycrystalline steel was deduced using the self-consistent scale transition method. The model reproduced both Magee and Greenwood-Johnson effects. Good agreement with the experimental data was obtained.
The Authors describe the role of the temperature, stress and plastic strain in the progress of the martensitic transformation (Fig. 1.7).

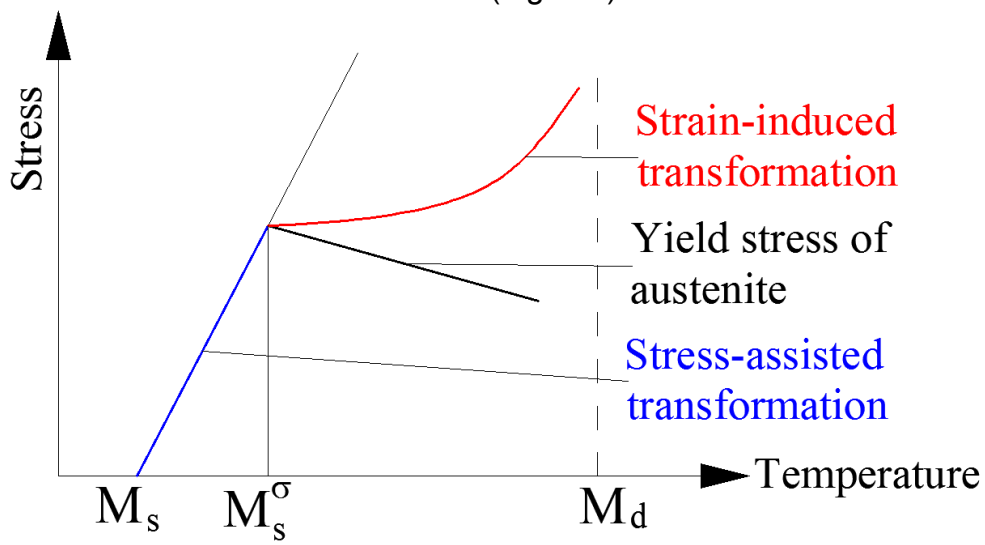

Figure 1.7. Schematic representation of critical stress for martensitic transformation as a function of temperature (Cherkaoui et al. 2000)

At the temperatures below M_s, martensitic phase transformation occurs on cooling without applied stress. Above M_s up to M_s^σ the transformation occurs by "elastic" stress, and the critical stress necessary to undergo martensitic phase transformation increases linearly with temperature. In the temperature range $M_s \div M_s^\sigma$ the transformation is defined as the "stress-assisted" one. At the temperatures above M_s^σ significant plastic flow precedes the transformation. In the temperature range $M_s^\sigma \div M_d$ the phase transformation is defined as "plastic strain induced". Above M_d the austenitic phase is thermodynamically stable, thus, no martensitic phase transformation occurs.

The Authors explained the source of remarkable properties of ductility and toughness of TRIP steels. They "result on one hand from the inelastic strain accompanying martensitic transformation, and on the other hand from the internal stress field emerging from this phase change leading to additional plastic flow known as the TRIP effect". The Authors stated, that the TRIP phenomenon allows development of steel with good compromise between ductility and toughness.

In the papers by Fischer (1990, 1992) and Fischer et al. (1995, 1996, 2000), rigorous micromechanical investigations lead to quantification of both the Greenwood-Johnson and the Magee effects. A proposal of a modified constitutive law for elasto-plastic material with phase change was made.

Jacques et al. (2001) investigated the damage resistance and the fracture toughness in TRIP-assisted multiphase steel sheets. They found that fracture toughness at the cracking initiation was lower for steels with higher tensile strength and ductility. So the TRIP effect improves formability by delaying plastic localization but reduces fracture toughness at crack initiation. This results proved that not for all TRIP steels the toughness increases (as shown by Leal (1984) and Stevehaug (1990)), but it could decrease as well. It was shown, that cracking initiates in the zones containing only martensite and no more retained austenite. The Authors conclude that enhancement of the balance between resistance to plastic instabilities and resistance to cracking requires a limitation of the amount of retained austenite.

Taleb and Sidoroff (2003) proposed a more complete formulation of the model by Leblond to account for the results from Taleb et al. (2001).

Very different approach was presented in the work by Oberste-Brandenburg and Bruhns (2004). The Authors proposed a tensorial description of the transformation kinetics of the martensitic phase transformation. A macroscopic second order tensor describing the thermodynamic force for the phase transformation was proposed. The ability of the model to calculate large structures has been demonstrated.

Papatriantafillou et al. (2004, 2006) developed a constitutive model for mechanical behavior of steels exhibiting TRIP effect. The model has been implemented into a finite element code. Forming limit diagrams for sheets made of TRIP steels have been calculated.

In the paper by Lichtenfeld et al. (2006), the Authors performed tensile test on two steels: 304L and 309. No martensitic transformation was observed in 309 steel, as the temperature of the test was greater than M_d (stable austenite).

Garion et al. (2006) developed a constitutive model to describe the FCC→BCC (face center cubic to body center cubic) phase transformation in austenitic stainless steels. In order to identify the parameters of the model, AISI 316L stainless steel samples were used. The Authors measured martensite fraction at cryogenic conditions, down to 4.2K temperature obtained with liquid helium cooling. The kinetics of phase transformation was described by three parameters: transformation threshold (p_ξ), slope (A) and saturation level (ξ_L).

It was assumed that the phase transformation is driven by the accumulated plastic strain (p). An assumption of linearization of the transformation kinetics was used. The magnetic permeability of fine gauge stainless steel sheets subjected to monotonic straining was measured as a function of strain. The model has been applied in the design of thin-walled bellows expansion joints for the Large Hadron Collider (LHC).

Dan et. al. (2007) developed a constitutive model describing TRIP effect in steels with strain rate dependence. Four phases: ferrite, bainite, austenite and martensite were modeled. Martensite volume fraction was tested by means of X-rays, in order to compare the results with the simulations. Volume fraction of martensite as a function of the strain rate, the effective plastic strain and the temperature from 77K to 298K agreed very well with the experimental data. The fact that the model accounts for large strains, temperature and agrees very well with the experimental data dependent on strain, strain rate and temperature, makes this model worth further insight.

Another constitutive model describing formation of martensite in the austenitic steels under large strains was developed by Hallberg et. al. (2007). The model was formulated within the macroscopic continuous framework with the thermodynamic formalism. Two, yield and transformation potentials were used. The results agreed well with the experimental findings. Two simulations: necking of a bar and deep drawing have been performed. The Authors conclude that the necking is delayed due to the influence of the martensitic transformation. Thus, martensitic transformation increases the formability of the sheet metal in the temperature range of 233K to 293K. The authors conclude as well that “the transformation from austenite to martensite has appealing traits, such as the high rate at which the transformation occurs and the possibility to obtain a material with inhomogeneous ductility, making these steels interesting in practical applications”. As the yield stress of martensite surpasses that of the austenite, the Authors concluded that “this makes it possible to influence the localization of plastic deformation for example in forming operations, e.g. by controlling the temperature of the tooling”.

Petit et al. (2007) performed experimental tensile study at -60ºC on AISI 304 stainless steel to produce strain induced α’ martensite. The authors used EBSD (Electron Beam Scatter Diffraction) and X-ray methods to study the microstructure evolution and the γ→α’ transformation mechanism. In addition, a micromechanical model was applied to simulate the deformation behavior, the transformation kinetics and the microstructure evolution. The Authors discuss in details the martensitic transformation mechanism and the role of ε-martensite on the formation of α’ martensite. It is worth mentioning, that the Authors assumed 20% strain limit in the model, as it was formulated within the small strains framework. Actually the same assumption was used in the present Thesis. Even if this assumption is worth discussing, it is often seen in the literature and leads to good agreement between the theoretical and the experimental results.

Another approach in modeling of the strain-induced martensitic transformation consists in the so called crystal plasticity. Essentially, the crystal plasticity models are formulated at the level of a single crystal.

Many such models have been developed, among them Tjahjanto et al. (2006, 2007a,b, 2008) and Turteltaub and Suiker (2005, 2006), which were based on the transformation kinetics proposed by Suiker and Turteltaub (2005a,b). These models could predict the mechanical behavior of TRIP steels and provide useful insight when optimizing mechanical parameters of steels.

Some other interesting papers dealing with the micromechanical modeling and multi-scale simulations w.r.t. the martensitic phase transformation were recently published by Delannay et a. (2008), Meftah et al. (2007) and Lee et al. (2010). In the paper by Lee et al. (2010), temperature increase was calculated as a function of the plastic strain and the strain rate. The Authors calculated martensite fraction as a function of the plastic strain and the strain rate as well as true stress versus true strain. All these results agree very well with the experimental data obtained by Han et al. (2004).
Mróz and Ziętek (2007) investigated cyclic hardening of steels subjected to martensitic transformation. Mixed type of hardening was used. The Authors postulated relating back stress to the fraction of martensite by a nonlinear function.
Lacroix et al. (2008) investigated the relationship between microstructure and fracture resistance of TRIP-assisted multiphase steels. Eight samples with various microstructures and different volume fractions of the constitutive phases (ferrite, bainite, retained austenite and martensite) were prepared. The Authors concluded that the ductile tearing resistance of TRIP-aided steels increased significantly with the retained austenite stability.
According to McGuire (2008), in lean austenitic stainless steels (201, 301, 304), martensite formed during the phase transformation remains quite stable, and does not revert until heated well above the temperature at which it was formed (Fig. 1.8). To fully reverse the transformation in 304 stainless steel the temperature of 800°C is needed. McGuire further states that “the carbon levels of austenitic stainless steels are relatively low, so strain-induced martensite is self-tempering and not brittle”, which is a very positive characteristics.

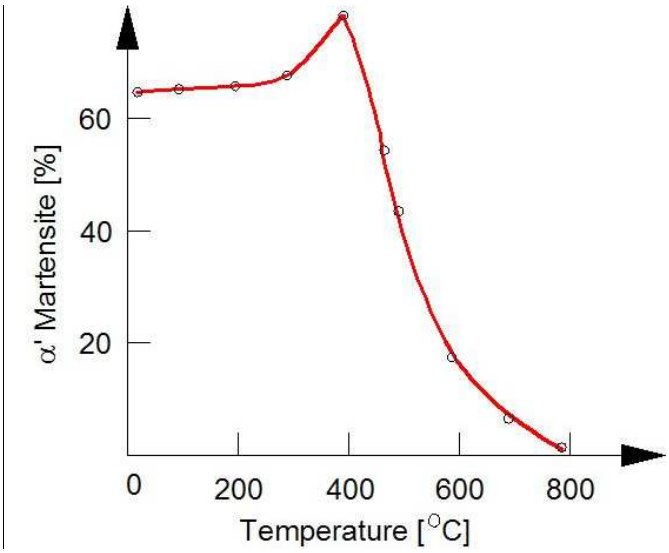

Figure 1.8. Martensite content versus temperature for 304 stainless steel (McGuire 2008)

Choi et al. (2009) developed a microstructure based finite element model to predict the complex behavior of TRIP steels, including ductile failure modes under different loading conditions. The input mechanical properties (microstress-strain curves) of the constituent phases for the RVE were obtained from the HEXRD experiment (high energy X-ray diffraction) with the assistance of a self-consistent model.
In the work by Das and Tarafder (2009) the Authors investigated fracture morphologies in the austenitic stainless steels as well as the martensitic transformation.

Multiple martensitic transformation mechanisms were observed during deformation of AISI 304LN steel at room temperature: γ (fcc) → ε (hcp), γ (fcc) → α' (bcc), γ (fcc) →mechanical twins→ α' (bcc) and γ (fcc)→ε(hcp)→ α' (bcc).
Mahnken et al. (2009) formulated a constitutive model of transformation induced plasticity for a low-alloy steel and used homogenization to obtain data not available in the literature. The material model was applied to investigate phase transformation in a shaft subjected to temperature loading by means of the finite element method.
Later on Mahnken et al. (2012) developed a multi-phase model at large strains using a thermodynamic framework. Two phase transformations have been described, transformation of the ferritic-pearlitic initial state into austenite and formation of bainite and martensite.
A study of the deformation induced martensitic transformation in cold-rolled and cold-drawn 316 stainless steel has been carried out by Nakada et al. (2010). Volume fraction of martensite has been measured both for cold-rolled and cold-drawn samples as a function of the equivalent strain. It is worth pointing out that the equivalent strain in such processes achieves almost 4.0 (logarithmic strain). Martensite fractions up to 100% were reached during cold drawing, 80% during cold rolling. Optical micrographs showing microstructure development were taken at the strains: 0.3, 0.6 and 1.6. The Authors concluded that in the cold-drawn specimen deformation-induced martensite is formed at the intersections of two kinds of deformation twins showing different directions.
However in the cold-rolling process the twin boundary near the austenite grain tends to be a preferential nucleation site. For this reason, martensitic transformation is more enhanced in cold drawing, since the intersection of twin boundaries yields a larger number of nucleation sites.
Beese and Mohr (2011) investigated the effect of stress triaxiality and Lode angle on the kinetics of strain-induced austenite-to-martensite transformation. 301LN stainless steel sheets were used for experimental testing at room temperature. Simple shear and large strain in-plane compression tests were carried out as well as uniaxial and equi-biaxial tests. In situ martensite content measurement was performed with Feritscope. The Authors concluded that a monotonically increasing function of stress triaxiality was insufficient to describe the transformation curve. They proposed a stress-state-dependent transformation kinetics incorporating the effect of the Lode angle parameter in addition to the stress triaxiality. Here, the dimensionless Lode angle parameter was defined as

$$\bar{\theta} = 1 - \frac{2}{\pi} arccos\left(\frac{3\sqrt{3}}{2}\frac{J_3}{\sqrt{J_3^2}}\right) \; with \; J_3 = det(\boldsymbol{s}) \tag{2.1}$$

For equi-biaxial tension or uniaxial compression $\bar{\theta} = -1$, for pure shear $\bar{\theta} = 0$ and for uniaxial tension $\bar{\theta} = 1$. Accurate predictions were obtained for 301LN stainless steel over a wide range of stress states.
Later on Beese and Mohr (2012) proposed a phenomenological macroscopic model for steels exhibiting strain-induced austenite-to-martenstie transformation. The kinetics developed in the previous work (Beese and Mohr, (2011)) was incorporated. Both kinematic and isotropic hardening were used. Isotropic hardening was assumed to depend on dislocation density and martensite volume fraction. The framework of finite strain isothermal rate-independent anisotropic plasticity was used. Excellent agreement was obtained during numerical simulations and experiments for uniaxial tension, uniaxial compression, transverse plane strain tension and pure shear.

In addition, the Authors performed punch and notch tension tests and compared the experimental results with their constitutive model. Again, very good agreement was obtained.
Kubler et al. (2011) proposed a semi phenomenological model of the behavior of TRIP steels. The model was intended to reduce typical number of internal variables of crystalline models. The Authors used mean-field approach at the phase level with the concept of Mean Instantaneous Transformation Strain (MITS). A number of internal variables were reduced to the global volume fraction, the elasto-plastic strain in each phase and the MITS.
Zaera et al. (2012) developed a constitutive model for steels exhibiting SIMT (stress induced martensitic transformation) based on the previous works of Olson and Cohen (1975), Stringfellow et al. (1992) and Papatriantafillou et al. (2004, 2006).
Fischlschweiger et al. (2012) developed a mean-filed model for transformation induced plasticity including back-stress effects for non-proportional loadings. The Authors achieved good agreement with the results on a maraging steel (by Nagayama et al. (2001, 2002) and Tanaka et al. (2003)).
Cakmak et al. (2012) studied the phase transformation kinetics and texture evolution of a TRIP steel subjected to torsional loadings. The Authors used a short sample to obtain high strains. The strain of 2.55 obtained at room temperature resulted in 63.5% martensite fraction.
Perdahcıoğlu and Geijselaers (2012) developed a macroscopic model to simulate the mechanically induced martensitic transformation in metastable austenitic stainless steels. The model was verified by mechanical tests under biaxial loading (tension and shear simultaneously) and bending test (van Beeck et al. (2011)), with good agreement achieved.
An interesting study was performed by Malik et al. (2013), where the Authors investigated the effect of external loading on the martensitic transformation. The elasto-plastic phase field model was used. Crystallographic orientation of the grains in the polycrystal was randomly chosen. Volume fraction of martensite was obtained for all kinds of external loadings, namely: hydrostatic compressive stress, hydrostatic tensile stress, shear stress, tensile stress, compressive stress. Good agreement with the empirical observations found in the literature was obtained.
Prüger et al. (2014) developed a thermo-mechanical coupled model for TRIP steels. The model takes into account temperature dependent constitutive law for TRIP steel, if high strain rates are expected. The Authors provide a thermodynamically consistent model, opposed to the models developed by Olson and Cohen (1975), Stringfellow et al. (1992), Tomita and Iwamoto (1995).
Martensitic transformation was extensively studied in cryogenic conditions, where a simplified linearized kinetics was proposed (Skoczeń (2007), Sitko et al. (2010), Sitko and Skoczeń (2012), Ortwein et al. (2014)). Further insight into mentioned papers is provided in the next sub-chapter.
To summarize, one can notice that many different approaches to model the plastic strain induced phase transformation exist in the literature. In general, they can be divided into four kinds of models: macroscopic phenomenological ones, microscopic or crystal plasticity models, mean-field models and semi phenomenological ones. All of them present some positive and some negative features. The phenomenological models are the simplest ones formulated in global variables, the easiest to calibrate and use, but they do not explain effects at micro-scale. In this case, the Magee effect is not considered.

The microscopic and crystal plasticity model explain physics at the micro-level, but often don't allow to simulate larger structures, as the computational cost is too high. Another problem is the calibration of material parameters, which is often hardly possible because of lack of experimental data. For this reason the scale transition methods like homogenization are often used, to average properties at the micro-scale and allow more global simulations. Semi phenomenological models are the ones in which some parts are expressed locally and some in the global way.
Such variety in the modeling philosophy proves that all the techniques are valuable, and provide different perspective w.r.t. to the phenomenon. Depending on the application, one always has the possibility to choose the best tool.

1.3. Functionally graded structures obtained via martensitic transformation

In the paper by Skoczeń (2007) the Author introduced for the first time the concept of "functionally graded structural members" obtained via the low temperature strain induced phase transformation. The idea consisted in twisting stainless steel bars in liquid nitrogen temperature (Fig. 1.9a). The microstructure obtained via this process, predicted by Skoczeń (2007), is presented in Fig. 1.9b. It contains elastic core (pure austenite), plastic zone (deformed austenite) in the middle layer, and mixture of austenite and martensite (resulting from transformation) in the outside layer. Because of microstructure variation in the cross-section of the bar, the name "functionally graded structure" was attributed. The microstructure depends on the amount of plastic strain. Thus, for the case of torsion, linear distribution of martensite is expected as shear strain is linear function of radius, as well. The plastic strain can be controlled by the angle of twist. Thus, higher martensite fractions can be obtained by applying higher angles of twist. Low temperature was applied, as the rate of the phase transformation is much higher compared to the room temperature conditions.
Actually, this concept was experimentally verified in the present Thesis.

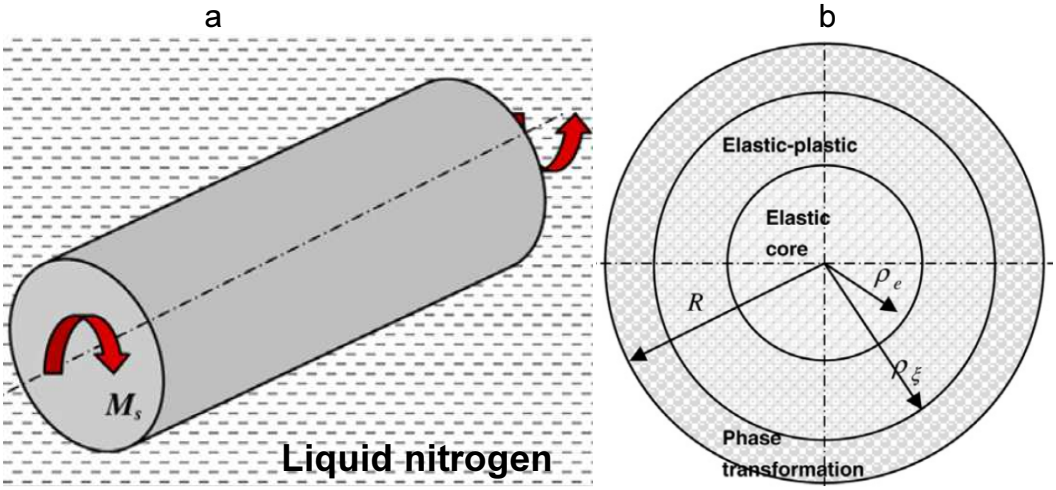

Figure 1.9. a) Structural member subjected to torsion at 77K, b) Functionally graded microstructure (cf. Skoczeń (2007))

Sitko et al. (2010) studied functionally graded structural members obtained via bending at cryogenic temperatures. The Authors simulated bending of cantilever beam with rectangular cross-section made of metastable austenitic stainless steel. Linear distribution of strain in the cross-section drives the martensitic transformation, leading to the microstructure presented in the Fig. 1.10.

It contains austenite in the inner layers, and inhomogeneous mixture of austenite and martensite in the outer layers, with martensite fraction linearly increasing towards the surface.
Such a functionally graded structural member is expected to carry higher load (bending moment), to have much higher hardness of the outside layer and still to be ductile because of the austenitic core.

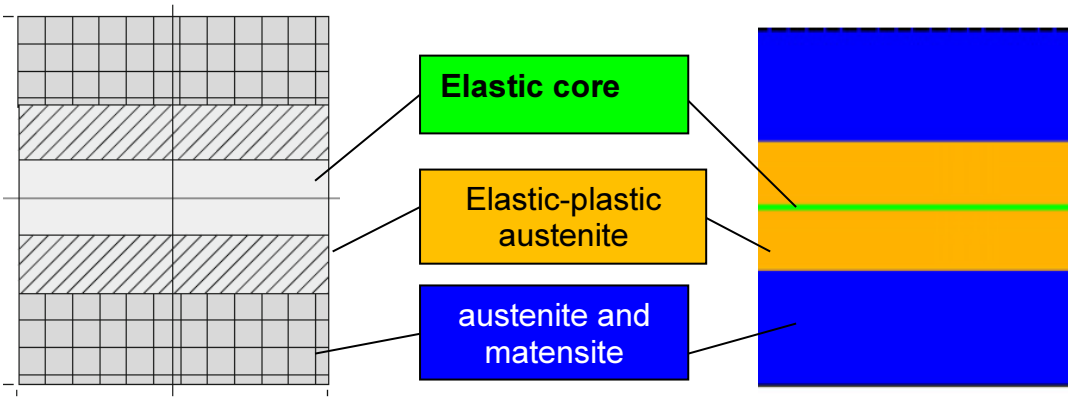

Figure 1.10. Cross-section of functionally graded structural member obtained by bending (cf. Sitko et al. (2010)).

Sitko and Skoczeń (2012) investigated the effect of the martensitic transformation on plastic adaptation to cyclic loads at cryogenic temperatures. The Authors simulated mechanical behavior of bellows expansion joints, commonly applied in the compensation systems, under cyclic loads. The structure was made of 316L stainless steel and was loaded at 77K. The geometry of bellows convolution and the distribution of stress is presented in Fig. 1.11a, whereas, the volume fraction of martensite through the thickness is illustrated in Fig. 1.11b. Compared to the previous examples, cyclic loading leads to progressive transformation in the course of loading and to progressively increasing martensite fraction. For 316L stainless steel the martensite content becomes saturated at 30% (material parameter), which is illustrated in the results of the numerical simulation (Fig. 1.11b).
Again, inhomogeneous martensite distribution was obtained like in the previous functionally graded structural members obtained via torsion and bending.

a b

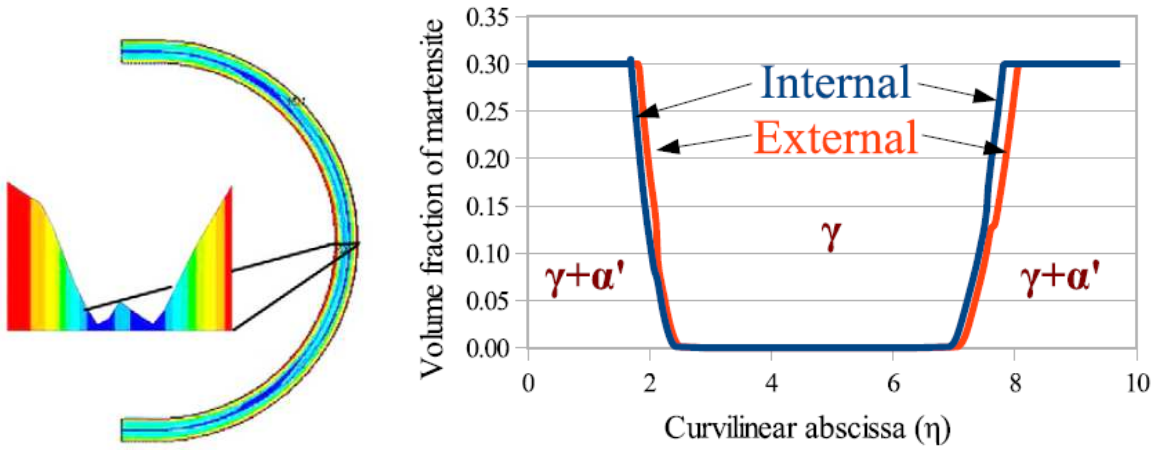

Figure 1.11. a) Geometry of bellows convolution and the stress distribution, b) distribution of martensite along the half-wave of convolution (cf. Sitko and Skoczeń, (2012))

Van Beeck et al. (2011) carried out an interesting research. The mechanical behavior of beams made of metastable austenitic steels subjected to pure bending has been studied. The Authors used a newly developed machine (Boers et al. (2010)) in which no contact forces were applied to the sample in the bending zone. This is not the case for other bending techniques, e.g. three-point bending test. The Authors measured the evolution of the martensitic phase via microscopic methods and in-situ, by means of Ferritescope. Microscopic samples were extracted for several bending angles. It turned out that there was asymmetry in the martensite fraction in the compressive and tensile zones (Fig. 1.12). More martensite was formed on the tensile side. The Authors measured the spring back angle and reported that for the sample with metastable austenite the elastic spring-back is increasing as the phase transformation is progressing, whereas the inelastic one decreases. This clearly shows that martensitic phase responds elastically, and while its content is increasing more volume of the material becomes elastic.
This study represents an experimental proof for the simulations done by Sitko et al. (2010), where bending was analyzed. It is possible to create a functionally graded structural member by means of bending. However, the work by Van Beeck et al. (2011) showed that the transformation kinetics has to account for the difference between the compression and the tension, to reproduce well the experiment.

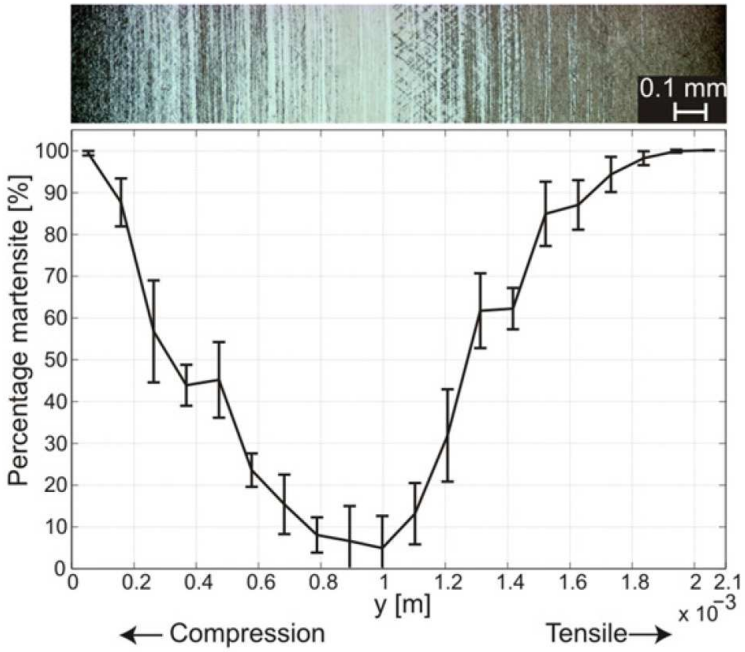

Figure 1.12. Distribution of martensite measured by using Feritscope and illustrated in the microscopic picture (cf. van Beeck et al. (2011))

In the paper by Ortwein et al. (2014) some of the results presented in the Thesis have been published, namely the 3D constitutive model and analytical formulas derived for pure torsion. As also, some experimental results from torsion experiments at room and at cryogenic temperatures as well as the measurements of martensite content and micro-hardness in the cross-section have been published. The parameters of the constitutive model were identified. Simulations of martensite content and torque versus the angle of twist were compared with the experimental data. It has been proven that it is possible to control the microstructure (martensite fraction) in the course of torsion by means of angle of twist, both at 77K and at 293K. The idea of functionally graded structural members obtained by torsion was experimentally realized.

2. The aim and the scope of Thesis

2.1. Introduction

The subject of the present Thesis consists in the theoretical and experimental study of structural members (elements, components) with functionally graded microstructure obtained by means of the plastic strain induced phase transformation (PSIPT). The plastic strain induced phase transformation is commonly observed in austenitic stainless steels, extensively used in structural applications (304, 301, 316, etc.) within a wide range of temperatures. The phase transformation usually involves a transition from initial homogeneous continuum to a multi-phase heterogeneous continuum caused by external loading, often beyond the yield stress. One of possible examples consists in the evolution from the initial austenitic structure to the martensitic one, that has significantly higher mechanical properties (strength, hardness). Thus, as a result of this phase transformation, the microstructure of the material becomes heterogeneous and contains a mixture of the austenite and the martensite. In general, the proportion between these phases can vary within the volume of the member. Thus, suitable functionally graded microstructure can be obtained.

The idea of an element with functionally graded microstructure was introduced by Skoczeń (2007). Skoczeń came up with the idea to twist a bar made of metastable austenitic stainless steel at cryogenic temperature, which would drive the martensitic transformation in a controlled way. As the strain - in the case of torsion - is a linear function of the radius, one would obtain an axisymmetric linear distribution of the martensitic phase in the cross-section of the bar. Such a structure would be substantially stronger, because of drastically higher mechanical properties of the martensitic phase compared to the austenitic one.

In his work Skoczeń developed a 3D constitutive model for a material which undergoes the plastic strain induced phase transformation, and he derived the formulas both for the stress versus strain and for the torque versus the unit angle of twist. These formulas allow prediction of the distribution of martensite as a function of the angle of twist as well as the global response of the bar - torque versus the angle of twist.

Based on the concept introduced by Skoczeń (2007), it is possible to optimize mechanical properties of the structure made of austenitic stainless steel, by means of the plastic strain induced martensitic transformation. This idea is outlined in Fig. 2.1.

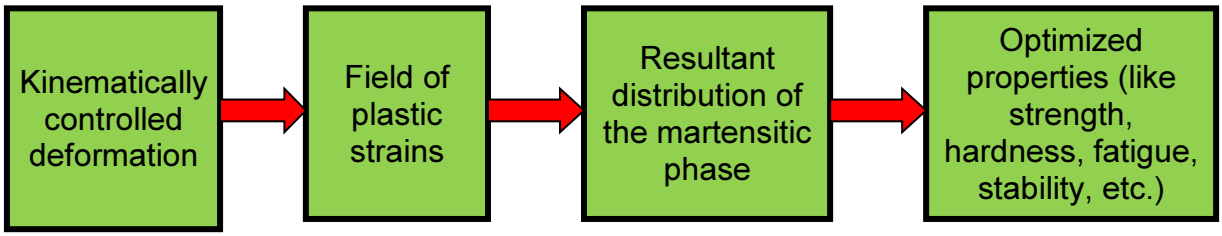

Figure 2.1. The idea of structural optimization by means of the plastic strain induced phase transformation

Kinematic control leads to a predefined field of plastic strains in the volume of the structure, which drives the phase transformation. Thus, a controlled distribution of the martensitic phase is obtained inside the volume of the element.

Such a distribution of secondary phase, characterized by different mechanical properties than the primary one, leads to enhanced mechanical properties.

The resulting mixture of phases, thanks to the presence of martensite, has much higher mechanical properties compared to the previous austenitic structure.
To better understand the idea presented in Fig. 2.1 and its applications, one has to answer the following questions:

- what is the correlation between the deformation (block 1, Fig. 2.1) and the resulting distribution of secondary (martensite) phase (block 3, Fig. 2.1)?
- how the mechanical properties depend on the proportion and distribution of the phases?
- what are possible types of deformation that can be used to drive and control the transformation?

Last question can be fairly easily answered, by indicating the following types of loading:

- tension or compression,
- twisting,
- bending,
- any complex loading composed of the above mentioned cases (like: bending and torsion or tension and torsion, etc.).

Of course, some of the loading types are easier to realize, like the tension or compression, thanks to the common tensile machines. The other loading types (like torsion with tension) are rather difficult to realize, and specially designed equipment is required.
The answer to the first question requires defining the field of plastic strains as a function of the type of loading. Secondly, it is crucial to compute the distribution of martensite based on the previously obtained plastic strains field. Obtaining the plastic strains field is fairly straightforward. One can use the Cauchy equations that connect the displacement field with the components of the strain tensor. In particular, for torsion the relationships between the shear strains and the unit angle of twist can be easily obtained through commonly known formulas. For complex types of loading, the general theory of plasticity can be used. For some cases analytical expressions are available, for other cases the finite element models are readily available (e.g. Ansys, Abaqus).
Knowing the field of plastic strains, the question remains how to obtain the distribution of secondary phase. To answer this question one needs to know the kinetics of the phase transformation, which relates the production rate of secondary phase and its driving force - the plastic strain rate. Transformation kinetics is described in details in Chapter 3. For now, just to explain the concept, one assumes for simplicity that the martensite fraction at any given material point is a linear function of the local plastic strain. Thus, the volume fraction of martensite can be calculated by multiplying the plastic strain by a constant, material dependent parameter, with one reservation however, that the plastic strain has to exceed some threshold value for the transformation to occur.
Now, knowing how to obtain the field of plastic strains, and then the resulting martensite distribution, let's look into a simple example. Consider a bar of rectangular cross-section under tensile loading (Fig. 2.2). For tensile loading, a homogeneous state of stress and strain occurs. Within a given cross-section, any point undergoes the same displacement, which leads to a constant plastic strain distribution on the whole cross-section.
The volume fraction of martensite is proportional to the plastic strain, thus, one obtains constant martensite distribution within the whole cross-section as well (Fig. 2.2). Similar situation would occur for compression.

The plastic strain would be exactly the same as to the value, but with an opposite sign. Yet, the same martensite distribution would be obtained.

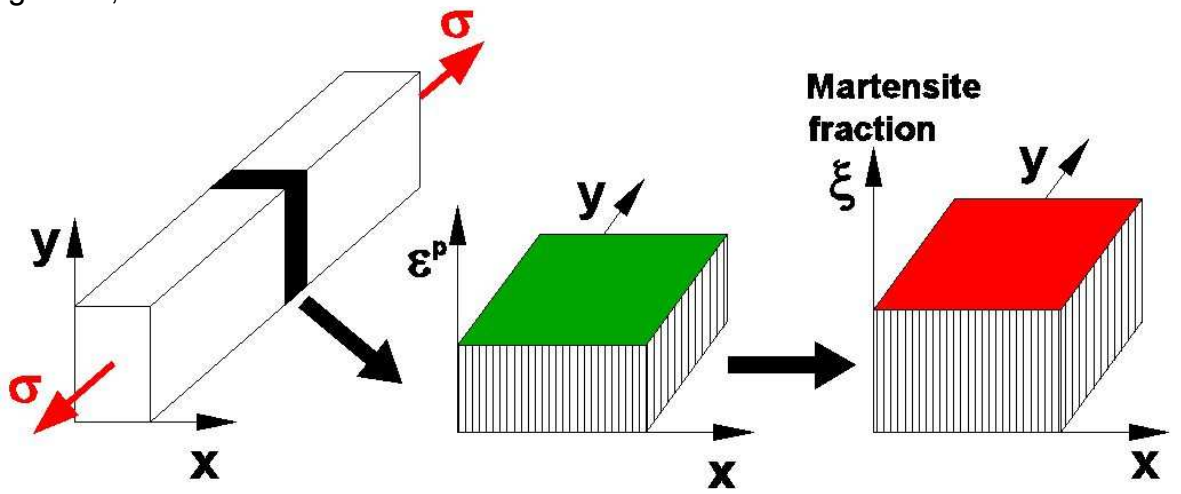

Figure 2.2. Tension of a bar, plastic strain distribution within the cross section and the resulting martensite content distribution (ξ)

According to the scheme shown in Fig. 2.1, for given tensile loading one would obtain a homogeneous structure with constant volume fraction of martensite, thus, constant volume fraction of austenite as well. The question of how this microstructure may affect the final properties has already been studied. Many tests have been performed under tensile loading on the austenitic stainless steels. The results indicate the increasing yield and ultimate strength with increasing martensite content, as well as increased ductility (uniform and total elongation, as in TRIP steels) (Weidner et al. (2013), Ma and Hartmaier (2015), Pruger et al. (2014), Wang et al. (2014), Dan et al. (2008)).

Tensile loading was the simplest example. Now, let us consider pure bending. According to the Bernoulli hypothesis, bending causes inhomogeneous distribution of stresses and strains within the cross-section of a beam. Under the action of pure bending moment, the stresses and the strains are linear functions of the distance from the neutral axis (Fig. 2.3). In such a case, around the center of the cross-section, for very small plastic strains, no martensite is formed. Beyond this region linearly increasing martensite content is obtained, with its maximum at the surface – there, where the plastic strains reach maximum.

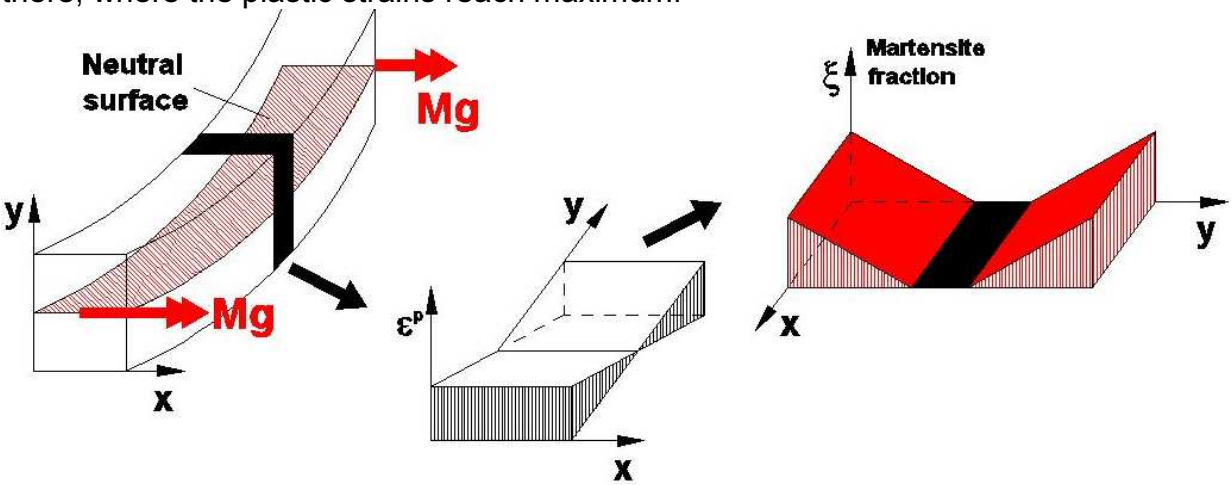

Figure 2.3. Bending of rectangular beam, strain distribution and the resulting martensite fraction distribution

The idea of obtaining functionally graded structural members by means of bending has been theoretically studied by Sitko et al. (2010), and verified experimentally by van Beeck et al. (2011). Van Beeck proved the possibility of obtaining such a functionally graded microstructure at room temperature conditions.
However, within the scope of the present Thesis the tests at cryogenic conditions are the most important ones. As performing precise bending tests at the liquid nitrogen temperature is very difficult and expensive, this type of loading is not very convenient. On the other hand, as torsion tests are easier to realize at cryogenic temperatures, torsional loading has been selected for further analysis. It is a subject of extensive study throughout this Thesis, including monotonic and cyclic torsion experiments.
A circular bar loaded by twisting moment *Ms* has been drawn in Fig. 2.4. For simple torsion, shear strain is proportional to the radial coordinate. Martensite fraction distribution becomes an axisymmetric function with respect to the radius of the cross-section. For strains smaller than the transformation threshold no transformation is induced, thus zero martensite fraction is obtained in the center.

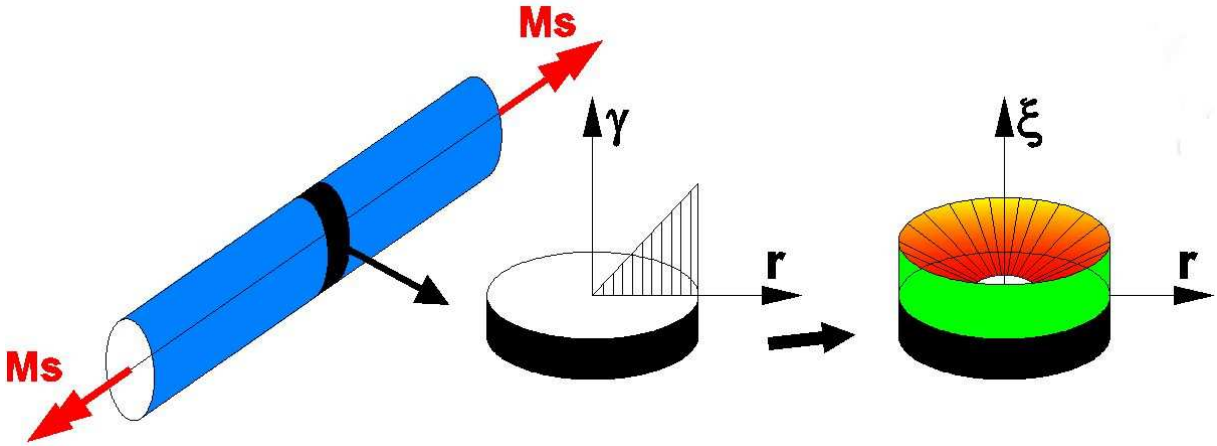

Figure 2.4. Variable martensite content obtained via plastic strain induced phase transformation driven by torsional loading

Such a structure is characterized by several positive features compared to untransformed austenitic structure. These are:
1. Higher yield strength and the limit carrying capacity, which comes from much higher mechanical properties of the martensite compared to austenite. As the content of martensite is equal to zero in the center (or very small), the sample remains ductile in the core.
2. The possibility to carry higher loads (twisting moments), thanks to the presence of martensite.
3. Better wear-resistance of the outside layer, because of the presence of martensite near the surface. The hardness of martensite is about 3 times higher than of the austenite.
4. Higher critical load and higher load in the post-buckling range. As the martensitic transformation is driven by the plastic strains, in the post-critical range the deformation causes progressive plastic yielding which in turn drives the PSIPT caused substantial hardening, that increases the load carrying capacity of the structure.
5. Higher fatigue-strength, as the coherent martensitic phase stops micro-cracks growth.

The above positive features constitute motivation for the research. The first objective was to create, for the first time, a functionally graded structure by means of torsional loading. This aim required designing and manufacturing a cryostat suitable to perform torsion tests at liquid nitrogen and room temperature. Next step was to carefully check all the positive properties (the list above), and verify if they really hold.
Assuming that these properties are validated, one can think of many applications of such structures. One of possible applications leads to manufacturing specific parts and components of particle accelerators.
Modern high energy particle accelerators operate usually at cryogenic conditions, where not only the mechanical but also the thermal properties are very important. For larger cross-sections of components the heat in-leaks occur, thus, more cooling power is required to maintain suitable cryogenic conditions. This increases the cost of cryogenic equipment and of the accelerators maintenance. Having smaller cross-section is beneficial as the integrated heat flux is proportional to the area of the cross-section. The increased strength would allow smaller dimensions and would result in better thermal performance of the component. Sometimes the strength requirement can be so severe and the geometrical constrains so strict, that using functionally graded structure can provide the only solution.

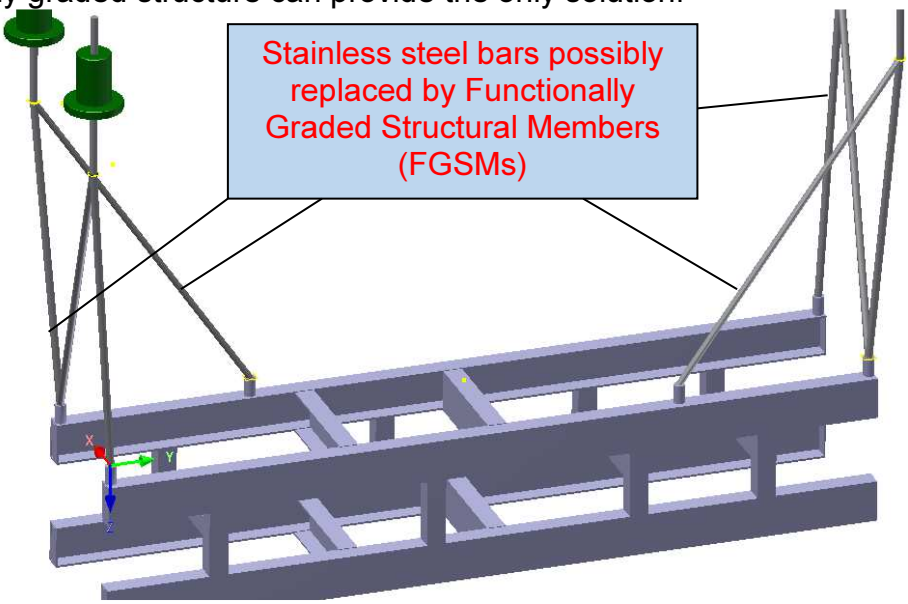

Figure 2.5. Supporting frame for the HIE-ISOLDE cryomodule

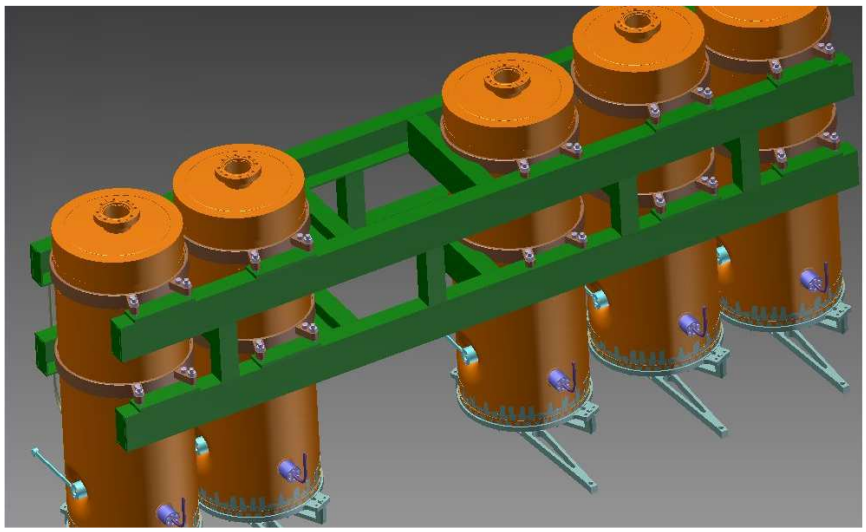

Figure 2.6. The HIE-ISOLDE cryomodule frame with superconducting cavities

As one of many possible examples, the supporting bars of the HIE-ISOLDE (High Intensity Isotope Separator On Line Device) could be replaced by a set of functionally graded structural members, in the form of two-phase bars (Fig. 2.5).
The HIE-ISOLDE cryomodule was designed at CERN during 2011-2013, and its development will continue for several years. The frame of this cryomodule has to support the weight of five super-conduction cavities, as presented in Fig. 2.6.
This structure has to be very reliable, and has to fulfill very strict alignment conditions for the beam of ions to be correctly accelerated. In order to prove that the use of functionally graded structures (FGSMs) is beneficial, thorough experimental investigations will have to be carried out. Their results will show if FGSMs are suitable for such demanding applications.

2.2. Objectives of the Thesis

The aim of the Thesis consists in the experimental and theoretical study of functionally graded structural members obtained by means of the plastic strain induced phase transformation that occurs during kinematically controlled torsion of round bars at cryogenic temperatures. The study consists of microscopic observations, martensite content measurements, micro-hardness measurements, tensile tests, torsional loading tests and stability (buckling) tests. First of all, however, a theoretical formulation of the appropriate constitutive model of FGSMs is postulated in order to match the obtained experimental results.
The scope of the Thesis has been summarized below in two categories: the experimental and the theoretical research.

The scope of the Thesis:
1. Experimental research:
1.1. Developing a Functionally Graded Structural Member (FGSM) by means of torsion at cryogenic (77K) and room temperatures.
1.2. Comparing performance of FGSMs subjected to torsion with the response of a fully austenitic structure.
1.3. Performing a series of material tests on the newly created FGSMs: microscopic observations, micro-hardness and martensite content measurements within the cross-section.
1.4. Creating FGSMs by cyclic torsion at 77K and at room temperature, measuring the torque versus the angle of twist and evolution of the martensitic phase due to loading.
1.5. Performing a series of cyclic torsion tests to evaluate the phenomenon of plastic shakedown for various stainless steels.
1.6. Performing tensile tests on the newly created FGSM bars with variable martensite content distributions.
1.7. Performing axial compression tests on the FGSMs and comparing their behavior with the fully austenitic structure.

2. Theoretical research:
2.1. Developing and calibrating a multiscale and multiaxial constitutive model of a continuum that undergoes the plastic strain induced fcc-bcc phase transformation.
2.2. Obtaining closed-form analytical solutions for one-dimensional case of torsion of round bars made of metastable materials.
2.3. Developing a model that can describe the response under compressive loads and loss of stability in the presence of phase transformation.

3. 3D constitutive model of continuum undergoing phase transformation at cryogenic temperatures

This chapter is devoted to presentation of the constitutive model. The model is similar like in the papers by Garion et al. (2006), Skoczeń (2007), Sitko et al. (2010), Sitko and Skoczeń (2012), Ortwein et al. (2014). The strength of the model lies in its relative simplicity and in a specific linearized form of transformation kinetics, which allows obtaining closed analytical solutions. The model will be described in details, contrary to these publications, where only the most important derivations were shown. In the present chapter almost all the derivations are made explicitly to facilitate the understanding as well for the less advanced readers. In the authors experience, such derivations are not easy to find and difficult to understand, thus in his opinion they present additional value for the Thesis.

3.1. Introduction

The constitutive model represents the basic relationships between the state of stress and the state of strain. In Euclidean 3D space the constitutive equation relates the stress tensor with the strain tensor. Moreover, the model has to be able to capture all the relevant physical phenomena. In the present work the most important one is the plastic strain induced phase transformation, which leads to evolution in the mechanical properties. The phase transformation is characterized by a scalar parameter ξ. How the material parameters, such as the hardening modulus, depend on this parameter is described in details in the course of this chapter.
Section 3.2 introduces the general 3D constitutive equation. Next one is devoted to the kinetics of the plastic strain induced phase transformation. Subsequently, the following chapters are devoted to derivations of the successive elements of the constitutive model.

3.2. The general constitutive model

The constitutive model is described by the following equation:

$$\underline{\underline{\sigma}} = \underline{\underline{\underline{\underline{E}}}} : \left(\underline{\underline{\varepsilon}} - \underline{\underline{\varepsilon}}^{p} - \underline{\underline{\varepsilon}}^{th} - \underline{\underline{\varepsilon}}^{bs} \right) \tag{3.1}$$

where:

- $\underline{\underline{\sigma}}$ denotes the stress tensor
- $\underline{\underline{\underline{\underline{E}}}}$ denotes the 4th order elasticity tensor
- $\underline{\underline{\varepsilon}}$ denotes the total strain tensor
- $\underline{\underline{\varepsilon}}^{p}$ denotes the plastic strain tensor
- $\underline{\underline{\varepsilon}}^{th}$ denotes the thermal strain tensor
- $\underline{\underline{\varepsilon}}^{bs}$ denotes the, so called, “Bain strain” tensor

The thermal strain tensor $\underline{\underline{\varepsilon}}^{th}$ will be ignored in the present work. All the experimental tests were performed in the constant temperature conditions, and the temperature variation was minor. Thus, the thermal strains were practically of no account.

The independent variable is the constitutive equation is the strain tensor $\underline{\underline{\varepsilon}}$ and the dependent one is the stress tensor $\underline{\underline{\sigma}}$ (or possibly the inverse). Definitions of the remaining tensors ($\underline{\underline{\varepsilon}}^{bs}$, $\underline{\underline{\varepsilon}}^{p}$, $\underline{\underline{\underline{E}}}$) are presented in the following chapters.

One can expect various couplings between the phase transformation variable (ξ) and the variables of the constitutive model ($\underline{\underline{\varepsilon}}^{bs}$, $\underline{\underline{\varepsilon}}^{p}$) (Eq. 3.1).

Mathematical description of the phase transformation is presented in the following section.

3.3. Mathematical modeling of the plastic strain induced phase transformation.

The plastic strain induced phase transformation appears in several structural materials, most commonly in austenitic stainless steels, but also in titanium alloys or other materials. In the present work one concentrates on the austenitic stainless steels, which are commonly used in structures operating in a wide range of temperatures, from very high (e.g. 800 ºC) to extremely low, almost down to absolute zero (for example at 1.8K in the superconducting magnets at CERN).

The phenomenon of the plastic strain induced phase transformation causes change from austenitic (FCC – face centered cubic) to martensitic (BCC – body centered cubic) material structure. Both are characterized by very different material properties. Martensite is known to be hard and brittle, whereas austenite is soft and ductile. Actually, the hardness and the brittleness of martensite depend on the content of carbon in the alloy. The hardness is proportional to its content (cf. Pierman et al. (2014)).

The martensite has much higher yield and tensile strength, but fails at smaller strains, whereas the austenite has lower yield strength, but fails at much higher strains (usually higher than 0.5).

In order to model the strain induced phase transformation a scalar variable is introduced: ξ – the volume fraction of martensite. It is defined in the RVE (Representative Volume Element) as the ratio between the volume of the martensitic phase and the total volume of the RVE element (Fig. 3.1). Thus the parameter ξ can change from 0 (pure austenite) to 1 (pure martensite).

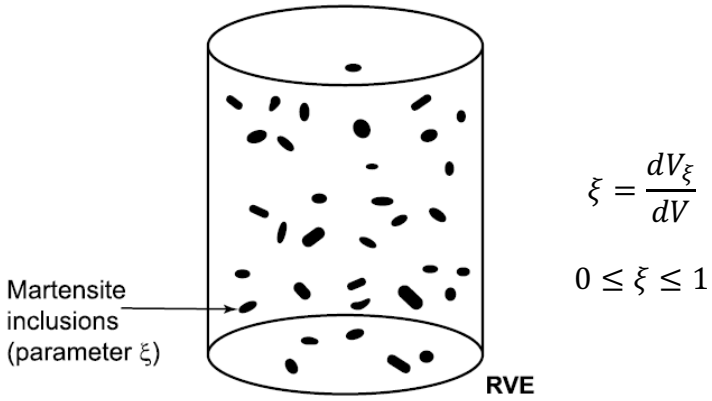

Figure 3.1. Representative volume element with martensite inclusions

In order to further model the phase transformation one has to identify parameters, that the volume fraction of martensite ξ depends on.

Many experimental and theoretical works have been devoted to this subject (see Olson and Cohen (1975), Heckler et al. (1982), Shin et al. (2001), Iwamoto et al. (1998), Yan et al. (2006), Perdahcioglu et al. (2008), Beese and Mohr (2011)).
The general conclusion form these papers was that the volume fraction of martensite depends on:

- temperature,
- plastic strain,
- stress state,
- strain rate.

In the present model, the strain rate has very little importance, as all the experiments have been carried out in quasi-static conditions. Thus strain rate dependence can be omitted. The evolution of the martensite content has been investigated in the present work only under the action of torsional loading (shear stress). The transformation kinetics devoted to the torsion case is presented in chapter 4.
The remaining parameters the kinetics depends on are the temperature and the plastic strain. Many experimental works have been carried out in order to measure the volume fraction of martensite as a function of temperature and inelastic strain.
Both parameters were taken into account in the kinetics proposed by Olson and Cohen (1975). The Authors proposed, for the first time successfully, description of the strain induced martensitic nucleation. According to the Authors the volume fraction of martensite as a function of plastic strain is:

$$f^{\alpha'} = 1 - exp\{-\beta[1 - exp(-\alpha\varepsilon)]^n\} \tag{3.2}$$

$$\beta = \frac{\bar{v}^{\alpha'}K}{(\bar{v}^{sb})^n}p \tag{3.3}$$

where:

- $f^{\alpha'}$ denotes the volume fraction of martensite
- ε denotes the plastic strain
- α denotes parameter which defines the course of shear-band formation, its temperature sensitive through its dependence on stacking-fault energy
- β denotes parameter proportional to the probability that an intersection will form an embryo, it is temperature dependent through its relation to the chemical driving force
- n denotes a fixed exponent, used in the law that expresses the relation between the number of shear-band interactions per unit austenite volume to the number of shear bands
- $\bar{v}^{\alpha'}$ denotes the average volume per martensite unit
- $\bar{v}^{sb}$ denotes the average volume of shear bands
- K denotes a constant equal to $K = \pi d^2/16$ where d is approximately the austenitic grain size
- p denotes the probability that a shear-band intersection will generate a martensite embryo

Eq. 3.2 was fitted to the data obtained by Angel (1954) for 304 stainless steel. An exponent of $n = 4.5$ was found to give the best overall agreement between the experimental results and the proposed model. The temperature dependence of parameters α and β was showed in Fig. 3.2.
The kinetics proposed by Olson and Cohen (1975) was able to fit very well to the experimental results obtained by Angel (1954) for 7 different temperatures.

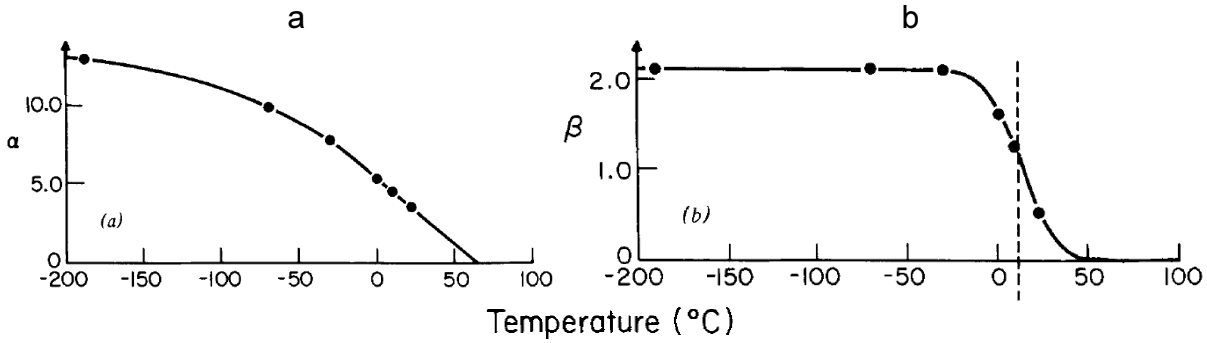

Figure 3.2. Temperature dependence of the parameters of Eq. 3.2 from Olson and Cohen (1975), a) α representing the rate of shear-band formation, b) β representing the probability of an intersection forming a martensitic embryo

Another approach to model the martensitic transformation was proposed by Koistinen and Marburger (1959). The Authors developed an equation for the diffusionless transformation from austenite to martensite, where martensite content can be calculated as

$$f_{\alpha'} = 1 - exp[-a(M_s - T)] \quad for \quad T < M_s \tag{3.4}$$

where a is an adjustable parameter, M_s is the martensitic start temperature and T is the temperature in Kelvin. The equation was developed for pure iron carbon alloys during the austenite to martensite transformation, e.g. for quenching. Formula proposed by Koistinen and Marburger (3.4) works well for processes controlled only by temperature.

Further after many other researchers studied the subject of phase transformation. For example Shin et al. (2001) performed tensile tests on 304 stainless steel at various temperatures (Fig. 3.3a). Generally, the martensite fraction increases with decreasing temperature. The highest amount was achieved at -196°C and the smallest at 40°C. The rate of the transformation is much higher at lower temperatures as well.

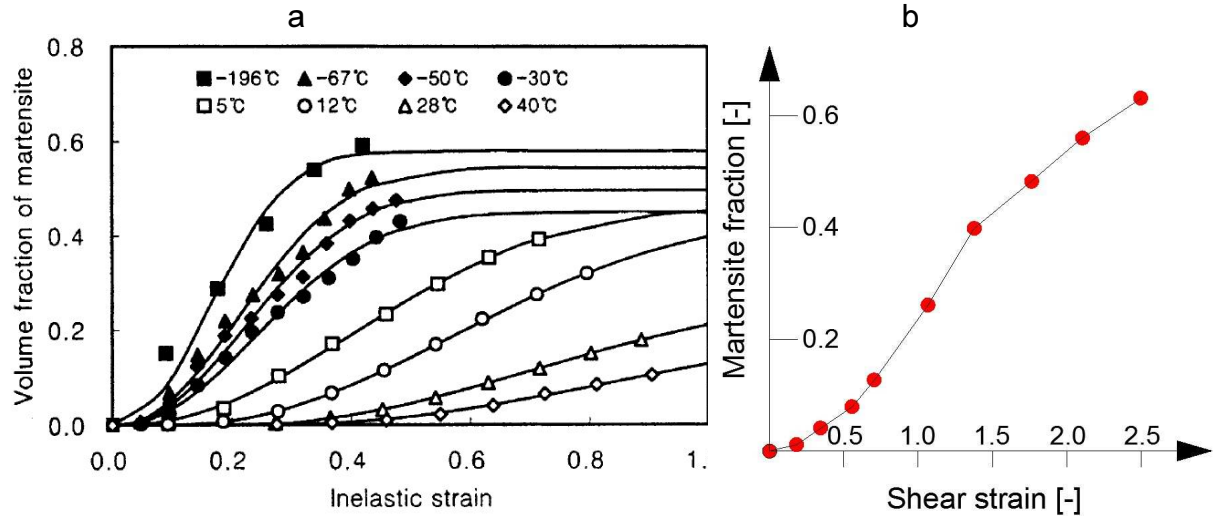

Figure 3.3. a) Volume fraction of martensite versus inelastic strain for 304 stainless steel measured during tensile tests (cf. Shin et al. (2001)), b) Results from Cakmak et al. (2012)

The kinetics proposed by Shin et al. (2001) was described by the following equation:

$$\xi = f_s \cdot [1 - exp(-\beta(\varepsilon - \varepsilon_0)^n)] \tag{3.5}$$

where: f_s was the saturation value for martensite, β was the stability of retained austenite, n was the stress-mode dependent parameter, ε_0 was the inelastic strain threshold for martensite nucleation.
This model requires 4 material constants and its represented by a complex function, difficult to use in further calculations (e.g. integration).
Similar transformation behavior to the one reported by Shin et al. (2001) is observed under torsion. However, very few experimental data are available. Recently Cakmak et al. (2012) measured the evolution of martensite fraction as a function of shear strain under torsion at room temperature (Fig. 3.3b). The character of the resulting curve is similar to these observed in tensile experiments.
In the present study two temperature levels have been used: the liquid nitrogen temperature (77K) and the room temperature (293K). The kinetics at 20ºC has not been registered by Shin et al. (2011), yet the result should fall between the two registered ones, for 12ºC and 28ºC (Fig. 3.3a).
Based on the results presented in Fig. 3.3a, the rate of the phase transformation increased with decreasing temperature. The central part of the kinetics for -196ºC is almost linear (Fig. 3.3a), whereas in the initial range very small volume fraction of martensite is obtained. For higher inelastic strains a saturation is reached as no more martensite can be induced in the material.
Thus for both temperatures: -196ºC (77K) and 20ºC (293K) transformation kinetics can be linearized (Fig. 3.4a). The linearization helps to simplify the constitutive model and it allows to develop closed-form analytical solution for the torsion of a circular bar that undergoes the phase transformation.

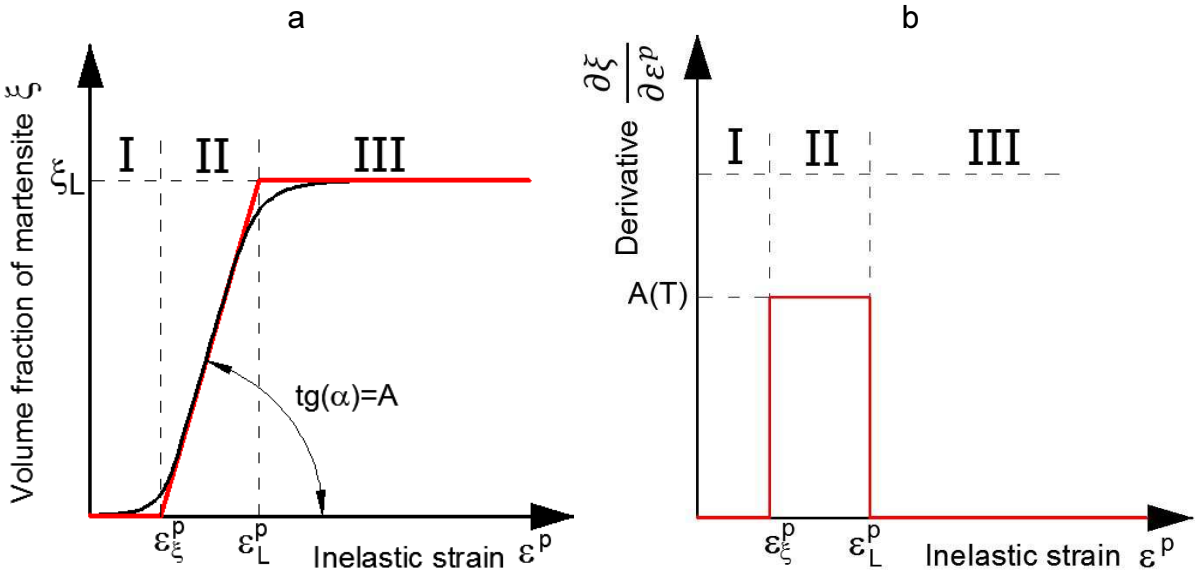

Figure 3.4. a) Linearized kinetics of the phase transformation, b) Transformation rate versus inelastic strain

The linearized kinetics is suitable not only for cryogenic temperatures. Actually all the curves obtained by Shin et al. (2001) can be described by means of this simplified model with good precision.
The linearized kinetics (Fig. 3.4a) can be divided into 3 regions (I, II, III). In the first region (I) martensitic transformation does not occur, in the second one (II) the rate of transformation is constant (Fig. 3.4b) and equal to A(T), and in the 3rd one (III) the fraction of martensite saturates to ξ_L.
The simplified, linearized kinetics is described by the following function with three parameters: ε_ξ^p, $A(T)$, ξ_L:

$$\xi = \begin{cases} 0, & 0 < \varepsilon^p \leq \varepsilon_\xi^p \\ A(T) \cdot \left(\varepsilon^p - \varepsilon_\xi^p\right) & \varepsilon_\xi^p < \varepsilon^p \leq \varepsilon_L^p \\ \xi_L & \varepsilon^p > \varepsilon_L^p \end{cases} \tag{3.6}$$

where:

- ε_ξ^p is the threshold value of the plastic strain, at which the phase transformation starts to occur,
- $A(T)$ is a temperature dependent material function, which describes the slope of the transformation kinetics (Fig. 3.4b),
- ξ_L is the maximum volume fraction of martensite possible to obtain, a material dependent parameter.

The parameter ε_L^p, indicated in Fig. 3.4a, can be calculated based on the other parameters, as $\varepsilon_L^p = \varepsilon_\xi^p + \xi_L / A(T)$.

Equation (3.6) can be described by using double Heaviside function as well:

$$\xi = A(T) \cdot \varepsilon^p \cdot H\left[\left(\varepsilon^p - \varepsilon_\xi^p\right)(\xi_L - \xi)\right] \tag{3.7}$$

For the double Heaviside function equal to 1, the volume fraction of martensite is equal to $A(T) \cdot \varepsilon^p$.

The proposed kinetics can be used only for one dimensional loading. For complex loadings the kinetics has to be generalized. After Garion et al. (2006), the volume fraction of martensite equals:

$$\xi = A(T) \cdot p \cdot H\left[\left(\mathrm{p} - \mathrm{p}_\xi\right)(\xi_L - \xi)\right] \tag{3.8}$$

And in the rate form:

$$\dot{\xi} = A(T) \cdot \dot{p} \cdot H\left[\left(\mathrm{p} - \mathrm{p}_\xi\right)(\xi_L - \xi)\right] \tag{3.9}$$

Where $\dot{p}$ is the accumulated plastic strain rate, defined as:

$$\dot{p} = \sqrt{\frac{2}{3} \cdot \underline{\underline{\dot{\varepsilon}}}^p : \underline{\underline{\dot{\varepsilon}}}^p} \tag{3.10}$$

and p_ξ stands for the accumulated plastic strain threshold.

The generalized kinetics (3.9) allows calculation of the martensite content under any complex state of loading, including cyclic loads.

3.4. Derivation of the Bain strain tensor

The “Bain strain” denotes the strain which is associated with the phase transformation from the FCC (Face Centered Cubic) austenite structure to the BCC (Body Centered Cubic) martensitic one. The “Bain strain” is caused by difference in the unit cell volume of austenite and martensite (martensitic cell has bigger volume). The relative volume change which influences the “Bain strain” can be calculated as:

$$\Delta v = \frac{V_\alpha - V_\gamma}{V_\gamma} \tag{3.11}$$

where:

- V_α is the volume of the unit cell of martensite (often called α’ phase) (Fig. 3.5),
- V_γ is the volume of the unit cell of austenite (often denoted as γ phase).

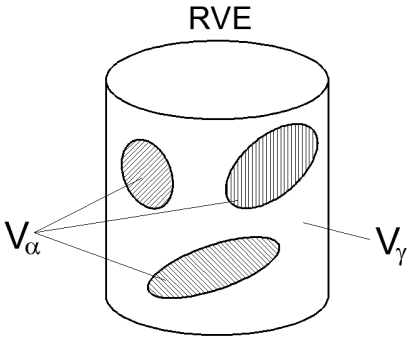

Figure 3.5. Volumes V_α and V_γ inside the RVE

The mesoscopic strain tensor $\underline{\underline{\varepsilon}}^{bs}$ is obtained by integrating the microscopic eigen-strain tensor $\underline{\underline{\varepsilon}}_{\mu}^{bs}$ over the RVE:

$$\underline{\underline{\varepsilon}}^{bs} = \frac{1}{V}\int_{V} \underline{\underline{\varepsilon}}_{\mu}^{bs} dV \tag{3.12}$$

The above integral can be rewritten in the following way:

$$\underline{\underline{\varepsilon}}^{bs} = \frac{V_\gamma}{V}\frac{1}{V_\gamma}\int_{V_\gamma} \underline{\underline{\varepsilon}}_{\mu}^{bs} dV + \frac{V_\alpha}{V}\frac{1}{V_\alpha}\int_{V_\alpha} \underline{\underline{\varepsilon}}_{\mu}^{bs} dV \tag{3.13}$$

Assuming that the microscopic eigen-strain in the austenitic phase is equal to zero, one obtains the following equation:

$$\underline{\underline{\varepsilon}}^{bs} = \frac{V_\gamma}{V}\frac{1}{V_\gamma}\int_{V_\gamma} \underline{\underline{0}} dV + \frac{V_\alpha}{V}\frac{1}{V_\alpha}\int_{V_\alpha} \underline{\underline{\varepsilon}}_{\mu}^{bs} dV = \frac{V_\alpha}{V}\frac{1}{V_\alpha}\int_{V_\alpha} \underline{\underline{\varepsilon}}_{\mu}^{bs} dV \tag{3.14}$$

where:

$$\frac{V_\alpha}{V} = \xi \tag{3.15}$$

$$\frac{1}{V_\alpha}\int_{V_\alpha} \underline{\underline{\varepsilon}}_{\mu}^{bs} dV = \langle \underline{\underline{\varepsilon}}_{\mu}^{bs} \rangle \tag{3.16}$$

Inserting Eq. 3.15 and 3.16 into Eq. 3.14 gives:

$$\underline{\underline{\varepsilon}}^{bs} = \xi \langle \underline{\underline{\varepsilon}}_{\mu}^{bs} \rangle \tag{3.17}$$

In the case of displacive transformation the eigen-strain tensor takes the following form (Wechsler et al. (1953), Fisher (1997)).

$$\underline{\underline{\varepsilon}}_{\mu}^{bs} = \begin{pmatrix} 0 & 0 & \frac{\gamma}{2} \\ 0 & 0 & 0 \\ \frac{\gamma}{2} & 0 & \Delta v \end{pmatrix}_{(\vec{x},\vec{y},\vec{z})} \tag{3.18}$$

Where $\vec{x}$, $\vec{y}$, $\vec{z}$ stands for the local coordinate system. The habit plane of the martensite variant is represented by ($\vec{x}$, $\vec{y}$), whereas $\vec{z}$ is the normal vector. The transformation shear is denoted by γ and the volume change by Δv. Martensite platelets are assumed to be randomly oriented in the initial austenitic structure (Skoczeń (2007), Sitko and Skoczeń (2012), Garion et al. (2006)). Thus one can expect a random orientation of martensite inclusions in the RVE. Therefore, integration of randomly oriented eigen-strains over the RVE gives a purely isotropic tensor:

$$\langle \underline{\underline{\varepsilon}}_{\mu}^{bs} \rangle = \frac{1}{3}\Delta v \underline{\underline{I}} \tag{3.19}$$

Finally, the mesoscopic “Bain strain” tensor, from Eq. 3.17, is equal to:

$$\underline{\underline{\varepsilon}}^{bs} = \frac{1}{3}\xi\Delta v\underline{\underline{I}} \tag{3.20}$$

The "Bain strain" tensor is proportional to the local volume fraction of martensite (ξ) and to the relative volume change between phases (Δv). According to Garion et al. (2006) the relative volume change for 304L stainless steel amounts to some $\Delta v = 0.05$.

3.5. Calculations of the plastic strain tensor

In order to derive the plastic strain tensor $\underline{\underline{\varepsilon}}^{p}$ one has to assume a function describing the yield surface. In the present Thesis the Huber-Mises-Hencky yield surface has been used. This yield function depends exclusively on the second invariant of the stress deviator and is often called "J2 plastic surface".

The so called associated flow rule has been adopted, meaning that in the stress space the plastic strain tensor is normal to the yield surface. According to the associated flow rule, the plastic strain can be calculated by differentiating the yield function with respect to the stress tensor.

Yield surface changes during the process of plastic flow. This change is controlled by the hardening variables of two types: kinematic and isotropic. Both variables are addressed in the next sections.

After defining all the necessary quantities, the plastic strain tensor will be finally derived in the section 3.5.9.

3.5.1. J2 yield surface

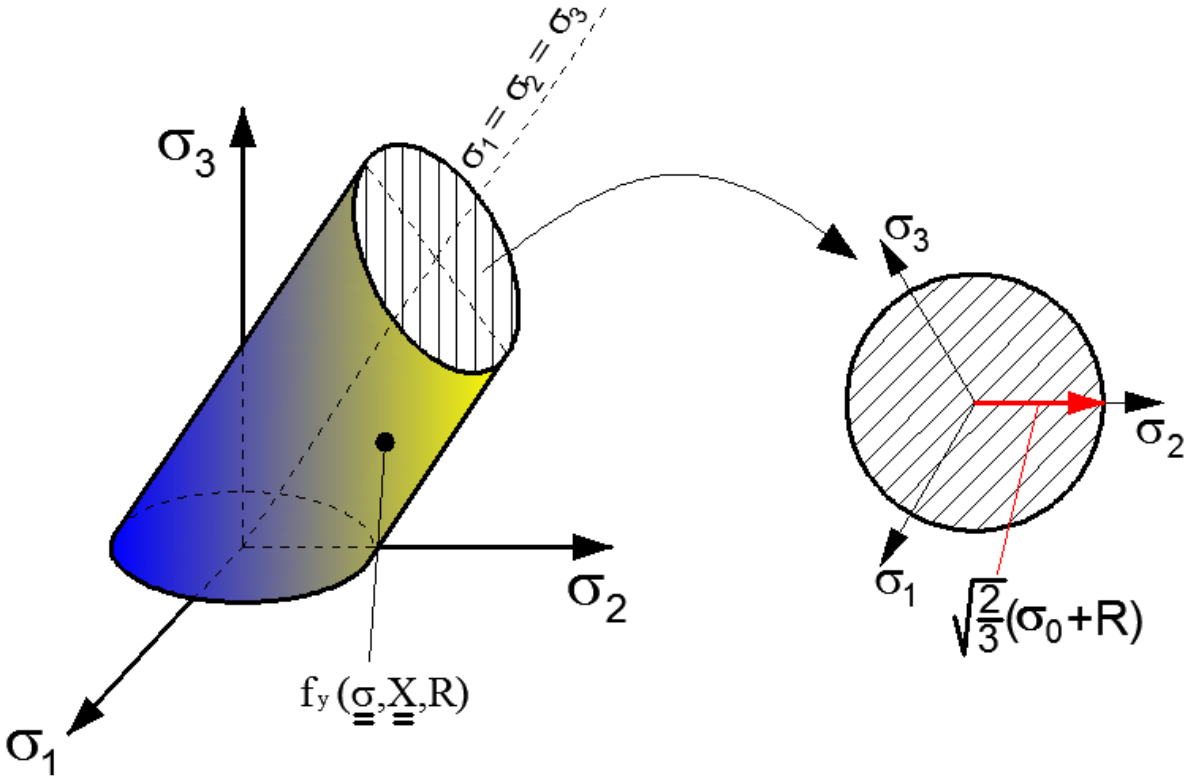

Figure 3.6. The yield surface in the coordinate system of principal stresses.

The yield surface is based on the second invariant of the stress deviator, and it is described by the equation:

$$f_y\left(\underline{\underline{\sigma}}, \underline{\underline{X}}, R\right) = J_2\left(\underline{\underline{\sigma}} - \underline{\underline{X}}\right) - \sigma_y - R \tag{3.21}$$

Where:

- $J_2\left(\underline{\sigma}-\underline{\underline{X}}\right)$ is the second invariant of the difference between the stress deviator and the kinematic hardening variable (back stress),
- $\underline{\underline{X}}$ is the so called "back stress" tensor, the tensor pointing the center of the yield surface,
- σ_y is the current yield stress (scalar),
- R is the isotropic hardening variable (scalar).

The J2 yield surface represents a cylinder in the coordinate system of the principal stresses $\sigma_1, \sigma_2, \sigma_3$ (Fig. 3.6). The axis of the cylinder is described by the equations $\sigma_1 = \sigma_2 = \sigma_3$. The isotropic hardening causes the radius of the cylinder to increase (Fig. 3.6). The radius of the cylinder depends on the initial yield stress (σ_0) and the isotropic hardening scalar variable (R), and it is equal to $\sqrt{\frac{2}{3}}(\sigma_0 + R)$ [129].

The kinematic hardening represents the rigid translation of the yield surface. Kinematic hardening is described by a tensor $\underline{\underline{X}}$, called "back stress", which indicates the position of the center of the yield surface. The yield surface with illustration of the kinematic hardening, presented in the coordinate system of principal stresses σ_1, σ_2, is shown in Fig. 3.7.

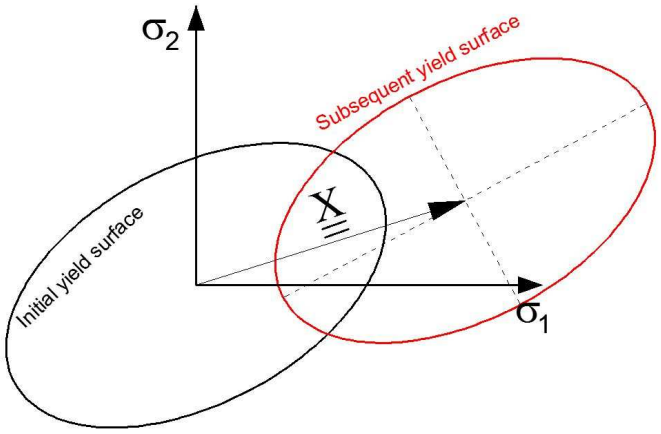

Figure 3.7. Yield surface and its translation caused by kinematic hardening

The function $J_2\left(\underline{\sigma}-\underline{\underline{X}}\right)$ equals:

$$J_2\left(\underline{\sigma}-\underline{\underline{X}}\right) = \sqrt{\frac{3}{2}\left(\underline{s}-\underline{\underline{X}}\right):\left(\underline{s}-\underline{\underline{X}}\right)} \tag{3.22}$$

where $\underline{s}$ is the stress deviator, which is equal to:

$$\underline{s} = \underline{\sigma} - \frac{1}{3}Tr\left(\underline{\sigma}\right)\underline{\underline{I}} \qquad Tr\left(\underline{\sigma}\right) = \sigma_{11} + \sigma_{22} + \sigma_{33} \tag{3.23}$$

The identity tensor $\underline{\underline{I}}$ can be represented in the matrix form by:

$$\underline{\underline{I}} = \begin{pmatrix} 1 & 0 & 0 \\ 0 & 1 & 0 \\ 0 & 0 & 1 \end{pmatrix} \tag{3.24}$$

So the stress deviator (3.23) in the matrix notation equals:

$$\underline{\underline{s}} = \begin{pmatrix} \frac{2}{3}\sigma_{11} - \frac{1}{3}(\sigma_{22}+\sigma_{33}) & \sigma_{12} & \sigma_{13} \\ \sigma_{21} & \frac{2}{3}\sigma_{22} - \frac{1}{3}(\sigma_{11}+\sigma_{33}) & \sigma_{23} \\ \sigma_{31} & \sigma_{32} & \frac{2}{3}\sigma_{33} - \frac{1}{3}(\sigma_{11}+\sigma_{22}) \end{pmatrix} \tag{3.25}$$

3.5.2. Hardening variables

As already mentioned (see the description of the yield surface) there are two hardening variables:

- The center of the yield surface, represented by tensor $\underline{\underline{X}}$,
- The radius of the yield surface, represented by scalar R.

Detailed description of both variables, including coupling with the phase transformation (parameter ξ), is presented in the next two sections.

3.5.3. Kinematic hardening variable

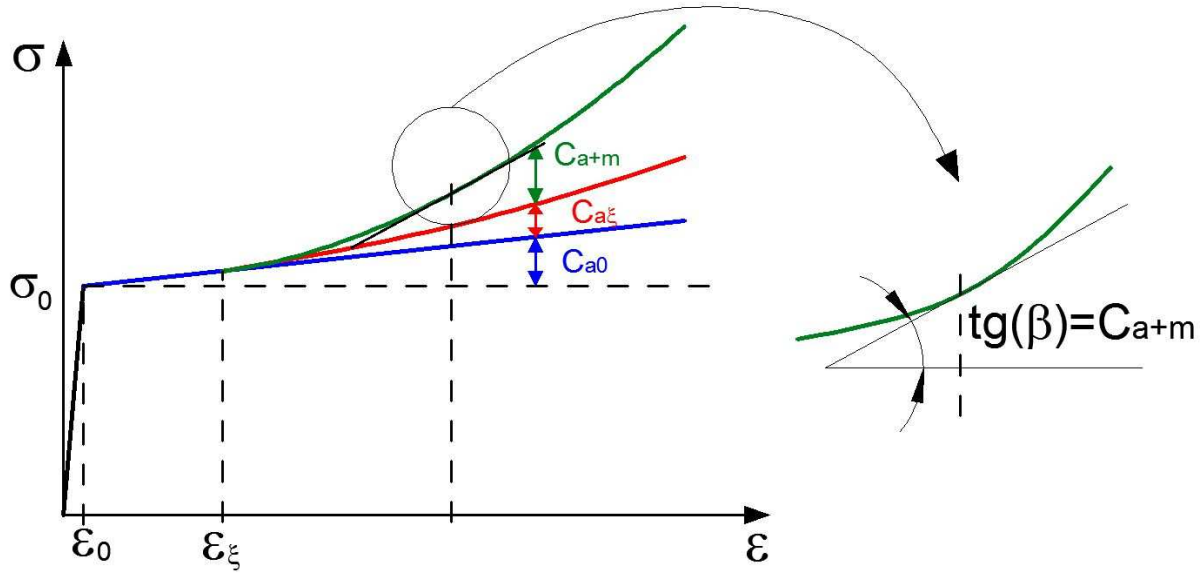

Figure 3.8. The principle of homogenization, linearized tangent stiffness moduli

The stress increment within the phase transformation range (for strains higher than the threshold value ε_{ξ}^{p}) has three contributions:

- Increment caused by hardening of pure austenite, represented by the tangential modulus C_{a0},
- Increment caused by hardening related to the Orowan mechanism (interactions between martensite inclusions and dislocations in the austenitic matrix), represented by the tangential modulus $C_{a\xi}$,
- Increment caused by hardening associated with the properties of mixture of austenite and martensite, resulting from the homogenization principle, represented by the modulus C_{a+m}.

According to Fig. 3.8, the kinematic hardening variable is affected by the presence of martensite. The corresponding evolution law was postulated in the following incremental form (Garion et al. 2006, Skoczeń 2007, Sitko et al. 2010, Sitko and Skoczeń 2012, Ortwein et al. 2014):

$$d\underline{\underline{X}} = d\underline{\underline{X}}_{a0} + d\underline{\underline{X}}_{a\xi} + d\underline{\underline{X}}_{a+m} \tag{3.26}$$

Where:

- $d\underline{\underline{X}}_{a0}$ is the kinematic hardening of pure austenite,
- $d\underline{\underline{X}}_{a\xi}$ represents the kinematic hardening caused by the interaction of dislocations in the austenitic matrix with martensitic inclusions (Orowan mechanism),
- $d\underline{\underline{X}}_{a+m}$ represents the kinematic hardening caused by the homogenized properties of the mixture of austenite and martensite.

Two first terms: $d\underline{\underline{X}}_{a0}$ and $d\underline{\underline{X}}_{a\xi}$ are treated in the next section. The third term $d\underline{\underline{X}}_{a+m}$ is derived using the homogenization principle and it will be treated separately in the following sections.

3.5.4. Derivations of terms dX_{a0} and $dX_{a\xi}$

First term in Eq. 3.26 is proportional to the increment of the plastic strain tensor, namely:

$$d\underline{\underline{X}}_{a0} = \frac{2}{3} C_{a0} d\underline{\underline{\varepsilon}}^{p} \tag{3.27}$$

where C_{a0} is the hardening modulus of pure austenite.

The second term $d\underline{\underline{X}}_{a\xi}$ represents the hardening caused by the so called Orowan mechanism. This term results from the interaction between the newly created martensite inclusions and the moving dislocations. The movement of dislocations is hindered by the presence of martensite, thus, hardening occurs.

When a dislocation passes through an obstacle (e.g. an inclusion of martensite), in order to move through, shear stress is required (Orowan mechanism, Fig. 3.9).

On the basis of the micromechanical analysis, the general formula for the shear stress relates the shear modulus μ, the length of the Burgers vector b and the mean distance between inclusions l.

$$\tau_p = \mu \frac{b}{l} \tag{3.28}$$

The total volume of the considered RVE equals (Fig. 3.10):

$$V = (l + d)^3 \tag{3.29}$$

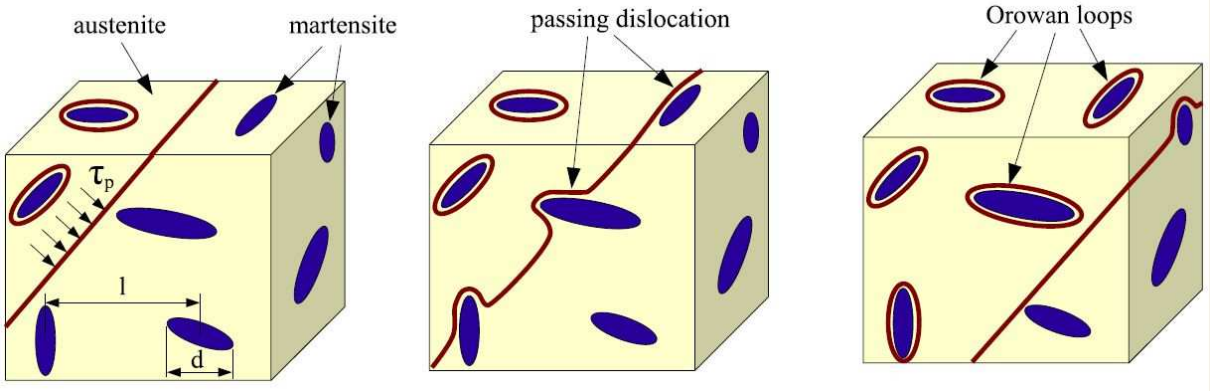

Figure 3.9. RVE with passing dislocation and the mechanism of Orowan loops (cf. Sitko and Skoczeń (2012))

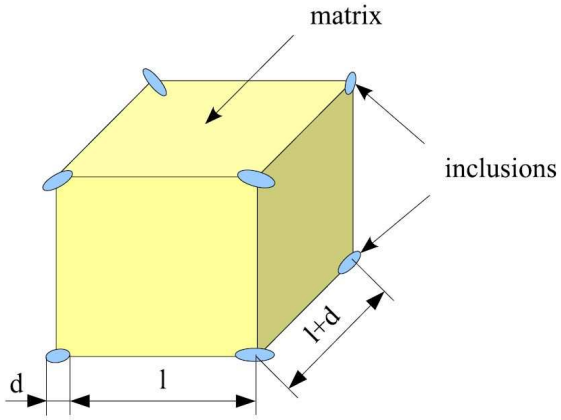

Figure 3.10. Unit cell RVE containing inclusions (cf. Sitko and Skoczeń (2012))

Since the size of inclusions is small when compared to the distance between them, Eq. 3.29 can be simplified:

$$V \cong l^3 \tag{3.30}$$

For the sake of simplicity, it is assumed that the inclusions have spherical shape. The volume of martensite inclusion equals:

$$V_\xi = \frac{4}{3}\pi\left(\frac{d}{2}\right)^3 = \pi\frac{d^3}{6} \tag{3.31}$$

Thus, the volume fraction of martensite reads (Fig. 3.1):

$$\xi = \frac{V_\xi}{V} = \frac{\pi d^3}{6l^3} = \frac{\pi}{6}\left(\frac{d}{l}\right)^3 \tag{3.32}$$

From Eq. 3.32 the distance l between inclusions, as a function of the size of inclusion and the volume fraction of martensite, equals:

$$\frac{1}{l} = \frac{1}{d}\sqrt[3]{\frac{6\xi}{\pi}} \tag{3.33}$$

Substituting Eq. 3.33 into Eq. 3.28, one obtains the shear stress needed for a dislocation to pass across the inclusion as a function of the volume fraction of martensite:

$$\tau_p = \frac{\mu b}{d}\sqrt[3]{\frac{6\xi}{\pi}} \tag{3.34}$$

The volume fraction of martensite can be expressed as a sum of the initial volume fraction of inclusions ξ_0 and the increment $\Delta\xi$ caused by the phase transformation:

$$\xi = \xi_0 + \Delta\xi \tag{3.35}$$

In the view of Eq. 3.35, the shear stress (Eq. 3.34) is equal to:

$$\tau_p = \frac{\mu b}{d}\left[\frac{6(\xi_0 + \Delta\xi)}{\pi}\right]^{\frac{1}{3}} \tag{3.36}$$

And further:

$$\tau_p = \frac{\mu b}{d}\left(\frac{6}{\pi}\xi_0\right)^{\frac{1}{3}}\left[1 + \frac{\Delta\xi}{\xi_0}\right]^{\frac{1}{3}} \tag{3.37}$$

By expanding the expression in brackets into the Tyler series, one arrives at:

$$\left[1 + \frac{\Delta\xi}{\xi_0}\right]^{\frac{1}{3}} \cong 1 + \frac{\Delta\xi}{3\xi_0} - \frac{1}{9\xi_0^2}(\Delta\xi)^2 + O(\Delta\xi^3) \tag{3.38}$$

Neglecting the second order terms and above, the final expression for the shear stress reads:

$$\tau_p = \frac{\mu b}{d}\left(\frac{6}{\pi}\xi_0\right)^{\frac{1}{3}}\left(1 + \frac{\xi - \xi_0}{3\xi_0}\right) \tag{3.39}$$

The shear stress in the case of two-phase material becomes approximately linear function of the volume fraction of martensite (Skoczeń (2007)). In the light of Eq. 3.39, the function $\phi(\xi)$, takes the linear form:

$$\phi(\xi) = 1 + h\xi \tag{3.40}$$

where *h* is a material dependent parameter, reflecting the interactions between the dislocations and the martensite inclusions. This parameter can be obtained experimentally.

The function $\phi(\xi)$ can be interpreted as part of the hardening process that corresponds to the increase in the volume fraction of martensite. The higher the volume fraction of martensite the more hardening occurs, as the probablility that a dislocation will stack on an inclusion increases.

The back stress increment $d\underline{\underline{X}}_{a\xi}$, in the light of Eq. 3.40, equals:

$$d\underline{\underline{X}}_{a\xi} = \frac{2}{3}C_{a0}h\xi d\underline{\underline{\varepsilon}}^p \tag{3.41}$$

The hardening modulus $d\underline{\underline{X}}_{a\xi}$ is a linear function with respect to the volume fraction of martensite and the plastic strain increment.

The combined effect of both terms $d\underline{\underline{X}}_{a0}$ and $d\underline{\underline{X}}_{a\xi}$ reflects total hardening in the elasto-plastic austenitic phase:

$$d\underline{\underline{X}}_a = d\underline{\underline{X}}_{a0} + d\underline{\underline{X}}_{a\xi} = \frac{2}{3}C_{a0}d\underline{\underline{\varepsilon}}^p + \frac{2}{3}C_{a0}h\xi d\underline{\underline{\varepsilon}}^p = \frac{2}{3}C_{a0}(1 + \mathrm{h}\xi)d\underline{\underline{\varepsilon}}^p \tag{3.42}$$

Where the term $C_{a0}(1 + \mathrm{h}\xi)$ is denoted as:

$$C_a(\xi) = C_{a\xi} = C_{a0}(1 + \mathrm{h}\xi) \tag{3.43}$$

3.5.5. Derivation of term dX_{a+m}

In order to derive the term $d\underline{\underline{X}}_{a+m}$ (see equation 3.26), homogenization technique has been used. According to the homogenization principle two phase mixture of austenite and martensite is replaced by homogenized pseudo isotropic continuum. Its properties depend on the properties of both constituents - homogenized phases.

The homogenized hardening modulus is defined via the term $d\underline{\underline{X}}_{a+m}$. It is proposed in the following form (Skoczen 2007, Sitko et al. 2010):

$$d\underline{\underline{X}}_{a+m} = \frac{2}{3}\mathrm{C}_{a+m}d\underline{\underline{\varepsilon}}^p \tag{3.44}$$

Originally the homogenization method has been developed in order to compute average stiffness of two or more elastic phases. For example, it has been developed for composites with matrix and fibers of different mechanical properties. In this particular case, the homogenization method was applied to elastic-plastic material (elastic martensite and plastic austenite). So, actually, the homogenization was applied on the step-by-step basis to the current linearized tangent stiffness moduli of austenite and martensite (Fig. 3.8). The linearized moduli are built in a similar way, like for an elastic material.

Derivation of the unknown modulus C_{a+m} is rather complex. Even though C_{a+m} is a scalar function of the parameter ξ, the homogenization principle has to be applied to the 4th order stiffness tensors. The stiffness tensors (operators) have to be defined for pure martensite and for the linearized elasto-plastic austenite. Thus the derivation consists of the following steps:

1. Introducing isotropic representation of the 4th order elasticity tensor
2. Defining 4th order stiffness tensors :
   2.1. For the elastic-plastic austenite (additional derivation of the tangent modulus E_{ta} is necessary)
   2.2. For the martensite fraction
   2.3. For the homogenized material
3. Introducing the principle of Mori-Tanaka homogenization
4. Calculating the unknown C_{a+m} modulus

All these steps are treated separately, in the above mentioned order, in the subsequent sections.

3.5.5.1. Representation of 4th order stiffness tensor

The behavior of the material is assumed to be isotropic, thus only two mechanical parameters are necessary, for example the bulk modulus k and the shear modulus μ. The isotropic stiffness tensor can be expressed as:

$$\underline{\underline{\underline{\underline{E}}}} = 3k\underline{\underline{\underline{\underline{J}}}} + 2\mu\underline{\underline{\underline{\underline{K}}}} \tag{3.45}$$

where:

- k is the bulk modulus
- μ is the shear modulus
- $\underline{\underline{\underline{\underline{J}}}}$ is the volumetric 4th rank projector
- $\underline{\underline{\underline{\underline{K}}}}$ is the deviatoric 4th rank projector

Parameters k and μ can be expressed in terms of the Poisson's ratio (ν), and the Young modulus (E) by the following well known formulas:

$$k = \frac{E}{3 \cdot (1 - 2\nu)} \tag{3.46}$$

$$\mu = \frac{E}{2 \cdot (1 + \nu)} \tag{3.47}$$

and the projectors $\underline{\underline{\underline{\underline{J}}}}$ and $\underline{\underline{\underline{\underline{K}}}}$ as:

$$\underline{\underline{\underline{\underline{J}}}} = \frac{1}{3}\underline{\underline{\mathrm{I}}} \otimes \underline{\underline{\mathrm{I}}} \qquad \underline{\underline{\underline{\underline{K}}}} = \underline{\underline{\underline{\underline{I}}}} - \underline{\underline{\underline{\underline{J}}}} \tag{3.48}$$

Where:

- $\underline{\underline{\mathrm{I}}}$ is the second rank identity tensor,
- $\underline{\underline{\underline{\underline{I}}}}$ is 4th rank identity tensor,
- $\otimes$ denotes dyadic product

Tensors $\underline{\underline{\underline{\underline{I}}}}$ and $\underline{\underline{\underline{\underline{J}}}}$ can be rewritten in the index notation as follows:

$$J_{ijkl} = \frac{1}{3}\delta_{ij}\delta_{kl}\,; \quad I_{ijkl} = \left(\frac{1}{2}\delta_{ik}\delta_{jl} + \delta_{il}\delta_{jk}\right) \tag{3.49}$$

Inserting the definitions from Eq. 3.48 into the definition of the isotropic elasticity tensor (eq. 3.45) one obtains:

$$\underline{\underline{\underline{\underline{E}}}} = k\underline{\underline{\mathrm{I}}} \otimes \underline{\underline{\mathrm{I}}} + 2\mu\left(\underline{\underline{\underline{\underline{I}}}} - \frac{1}{3}\underline{\underline{\mathrm{I}}} \otimes \underline{\underline{\mathrm{I}}}\right) \tag{3.50}$$

and after some rearrangements, finally:

$$\underline{\underline{\underline{\underline{E}}}} = \left(k - \frac{2}{3}\mu\right)\left(\underline{\underline{\mathrm{I}}} \otimes \underline{\underline{\mathrm{I}}}\right) + 2\mu\underline{\underline{\underline{\underline{I}}}} \tag{3.51}$$

It is worth pointing out, that the term $\left(k - \frac{2}{3}\mu\right)$ is the Lame first parameter called λ. Equation 3.51 allows to calculate the full 4th rank elasticity tensor knowing the two material parameters: k and μ.

3.5.5.2. 4th order stiffness tensors for elastic-plastic austenite

For the austenitic phase, linearization of the stress strain relationship in the plastic range can be expressed as:

$$\Delta\underline{\underline{\sigma_a}} = \underline{\underline{\underline{\underline{E_{ta}}}}} : \Delta\underline{\underline{\varepsilon}} \tag{3.52}$$

where $\underline{\underline{\underline{\underline{E_{ta}}}}}$ is a linearized tangential stiffness operator.

The tangential stiffness operator can be further expressed in terms of the tangential bulk modulus k_{ta} and tangential shear modulus μ_{ta} (cf. Sitko and Skoczeń (2012)) as:

$$\underline{\underline{\underline{\underline{E_{ta}}}}} = 3k_{ta}\underline{\underline{\underline{\underline{J}}}} + 2\mu_{ta}\left(\underline{\underline{\underline{\underline{K}}}} - \frac{\underline{\underline{n}} \otimes \underline{\underline{n}}}{1 + \frac{C}{3\mu}}\right) \tag{3.53}$$

where:

- $\underline{\underline{\underline{\underline{J}}}}$ and $\underline{\underline{\underline{\underline{K}}}}$ are 4th rank projectors, defined through Eq. 3.48
- $\underline{\underline{n}}$ is the vector normal to the yield surface
- C is the hardening modulus of the austenitic phase
- μ is the shear modulus of austenite

The vector normal to the yield surface $\underline{\underline{n}}$ equals:

$$\underline{\underline{n}} = \sqrt{\frac{3}{2}}\frac{\underline{\underline{s}} - \underline{\underline{X}}}{J_2\left(\underline{\underline{s}} - \underline{\underline{X}}\right)} \tag{3.54}$$

Where:

- $\underline{\underline{s}}$ is the stress deviator
- $\underline{\underline{X}}$ is the back stress tensor
- $J_2\left(\underline{\underline{s}} - \underline{\underline{X}}\right)$ is the second invariant of the difference between the stress deviator and the back stress tensor (3.22).

As shown by Doghri and Ouaar (2003) or Doghri and Tinel (2005), it is more convenient to apply the elastic–plastic tangent stiffness operator reduced to its isotropic form, without losing the precision of computations. Thus, the nonlinear term in the Eq. 3.53 has been ignored. Finally, $\underline{\underline{\underline{\underline{E}}}}_{ta}$ equals:

$$\underline{\underline{\underline{\underline{E}}}}_{ta} = 3k_{ta}\underline{\underline{\underline{\underline{J}}}} + 2\mu_{ta}\underline{\underline{\underline{\underline{K}}}} \tag{3.55}$$

where the tangential shear μ_{ta} and bulk k_{ta} modules are expressed as (cf. Skoczeń (2007)):

$$\mu_{ta} = \frac{E_{ta}}{2(1+\nu_a)} \tag{3.56}$$

$$k_{ta} = \frac{E_{ta}}{3(1-2\nu_a)} \tag{3.57}$$

where:

- ν_a is Poisson's ratio of austenite,
- E_{ta} is one dimensional tangential stiffness of austenite.

The derivation of the unknown operator E_{ta} is presented in the following section.

3.5.5.3. Derivation of tangential modulus $\boldsymbol{E_{ta}}$

Similar derivation can be found in Souza Neto et al. (2008).

The stress rate in the plastic range is proportional to the strain rate and the proportionality coefficient which is the tangential modulus E_{ta}:

$$\dot{\sigma} = E_{ta}\dot{\varepsilon} \tag{3.58}$$

According to the Hooke law the stress rate equals to:

$$\dot{\sigma} = E(\dot{\varepsilon} - \dot{\varepsilon}^p) \tag{3.59}$$

The plastic strain rate $\dot{\varepsilon}^p$ can be calculated as:

$$\dot{\varepsilon}^p = \dot{\lambda}\frac{\partial \mathrm{f_y}}{\partial \sigma} \tag{3.60}$$

Where $\dot{\lambda}$ is the plastic strain multiplier, and $\mathrm{f_y}$ is the yield function. Assuming the yield function in the simplest form, with no hardening one has:

$$\mathrm{f_y} = \sigma - \sigma_y \tag{3.61}$$

Thus the plastic strain rate $\dot{\varepsilon}^p$ equals:

$$\dot{\varepsilon}^p = \dot{\lambda}\frac{\partial(\sigma - \sigma_y)}{\partial \sigma} = \dot{\lambda} \tag{3.62}$$

Further on, to calculate the plastic strain rate $\dot{\varepsilon}^p$ one has to specify the plastic multiplier $\dot{\lambda}$. It can be calculated from the consistency condition, which requires differentiation of the yield function.

The consistency condition requires that:

$$\frac{df_y}{dt} = \dot{f}_y = 0 \tag{3.63}$$

The differentiation of the yield function $\mathrm{f_y}(\sigma, \sigma_y)$ gives:

$$\frac{\mathrm{df_y}(\sigma, \sigma_y)}{dt} = \frac{d\sigma}{dt} - \frac{d\sigma_y(\varepsilon^p)}{dt} = \dot{\sigma} - \frac{\partial \sigma_y}{\partial \varepsilon^p}\frac{\partial \varepsilon^p}{\partial t} = \dot{\sigma} - \frac{\partial \sigma_y}{\partial \varepsilon^p}\dot{\varepsilon}^p \tag{3.64}$$

where:

$$\frac{\partial \sigma_y}{\partial \varepsilon^p} = \mathrm{H} \tag{3.65}$$

H is the hardening modulus, which is the derivative of the yield stress with respect to the plastic strain. Inserting Eq. 3.65 into 3.64 one gets:

$$\dot{\mathrm{f}_\mathrm{y}} = \dot{\sigma} - \mathrm{H}\dot{\varepsilon^p} \tag{3.66}$$

Taking into account the consistency condition 3.63 one has:

$$\dot{\sigma} = \mathrm{H}\dot{\varepsilon^p} \tag{3.67}$$

Inserting Eqs 3.59 and 3.62 into Eq. 3.67 one obtains:

$$E\left[\dot{\varepsilon} - \dot{\lambda}\right] = \mathrm{H}\dot{\lambda} \tag{3.68}$$

Thus:

$$\dot{\lambda} = \frac{E\dot{\varepsilon}}{H + E} \tag{3.69}$$

Having derived the plastic multiplier $\dot{\lambda}$, the tangential modulus E_{ta} is now derived. Taking equations 3.58, 3.59, 3.62 and 3.69 one obtains:

$$E\left(\dot{\varepsilon} - \frac{E}{H + E}\dot{\varepsilon}\right) = E_{ta}\dot{\varepsilon} \tag{3.70}$$

Finally:

$$E_{ta} = \frac{EH}{E + H} \tag{3.71}$$

where in our particular case the hardening modulus $H = \partial\sigma_y/\partial\varepsilon^p$ is equal to the hardening modulus of austenite, defined by Eq. 3.43.

$$H = C_a(\xi) = C_{a0}(1 + h\xi) \tag{3.72}$$

Finally, the tangential modulus E_{ta} (after inserting equation 3.72 into 3.71) equals:

$$E_{ta} = \frac{E_a \cdot C_a(\xi)}{E_a + C_a(\xi)} = \frac{E_a \cdot C_{a0}(1 + h\xi)}{E_a + C_{a0}(1 + h\xi)} \tag{3.73}$$

3.5.5.4. 4th order stiffness tensor for martensite

Elastic stiffness tensor of martensite is expressed in the isotropic form, as defined by Eq. 3.24:

$$\underline{\underline{\underline{\underline{E_m}}}} = 3k_m \underline{\underline{\underline{\underline{J}}}} + 2\mu_m \underline{\underline{\underline{\underline{K}}}} \tag{3.74}$$

with:

$$\mu_m = \frac{E_m}{2(1 + \nu_m)} \tag{3.75}$$

$$k_m = \frac{E_m}{3(1 - 2\nu_m)} \tag{3.76}$$

where the martensitic phase is characterized by:

- μ_m - the shear modulus
- k_m - the bulk modulus

- E_m - the Young modulus
- ν_m - the Poisson ratio.

3.5.5.5. 4th order stiffness tensor for the homogenized material

The stiffness tensor representing two-phase continuum, resulting from the Mori-Tanaka homogenization, is postulated in exactly the same isotropic form:

$$\underline{\underline{\underline{\underline{E}}}}_H = \underline{\underline{\underline{\underline{E}}}}_{MT} = 3k_{MT}\underline{\underline{\underline{J}}} + 2\mu_{MT}\underline{\underline{\underline{\underline{K}}}} \tag{3.77}$$

where:

- μ_{MT} is the shear modulus of two-phase continuum
- k_{MT} stands for the bulk modulus of two-phase continuum.

3.5.5.6. The principle of Mori-Tanaka homogenization

Eshelby (1957) solved the problem of single ellipsoidal inclusion embedded in an infinite homogeneous matrix and subjected to uniform transformation strain. He showed that the stresses and the strains within the inclusion can be derived. This solution became a basis of numerous homogenization algorithms, such as the self-consistent (R. Hill, 1965) or the Mori–Tanaka (M-T) algorithm (Mori and Tanaka (1973)). From the M-T algorithm the effective stiffness modulus can be obtained by means of the following formula:

$$\left[\underline{\underline{\underline{\underline{E}}}}_{MT} + \underline{\underline{\underline{\underline{\mathrm{E}}}}}^*\right]^{-1} = \sum f_i \left[\underline{\underline{\underline{\underline{E}}}}_i + \underline{\underline{\underline{\underline{\mathrm{E}}}}}^*\right]^{-1} \tag{3.78}$$

where f_i are the volume fractions of the constituents (austenite and martensite), and $\underline{\underline{\underline{\underline{\mathrm{E}}}}}^*$ stands for the Hill influence tensor. Expanding Eqs 3.78 one obtains:

$$\left[\underline{\underline{\underline{\underline{E}}}}_{MT} + \underline{\underline{\underline{\underline{\mathrm{E}}}}}^*\right]^{-1} = f_a \left[\underline{\underline{\underline{\underline{E}}}}_{ta} + \underline{\underline{\underline{\underline{\mathrm{E}}}}}^*\right]^{-1} + f_m \left[\underline{\underline{\underline{\underline{E}}}}_m + \underline{\underline{\underline{\underline{\mathrm{E}}}}}^*\right]^{-1} \tag{3.79}$$

where f_m is the volume fraction of martensite ($f_m = \xi$), and f_a is the volume fraction of austenite ($f_a = 1 - \xi$). Inserting these definitions into 3.79 one has:

$$\left[\underline{\underline{\underline{\underline{E}}}}_{MT} + \underline{\underline{\underline{\underline{\mathrm{E}}}}}^*\right]^{-1} = (1-\xi)\left[\underline{\underline{\underline{\underline{E}}}}_{ta} + \underline{\underline{\underline{\underline{\mathrm{E}}}}}^*\right]^{-1} + \xi\left[\underline{\underline{\underline{\underline{E}}}}_m + \underline{\underline{\underline{\underline{\mathrm{E}}}}}^*\right]^{-1} \tag{3.80}$$

The Hill influence tensor has similar isotropic structure:

$$\underline{\underline{\underline{\underline{\mathrm{E}}}}}^* = 3k^*\underline{\underline{\underline{J}}} + 2\mu^*\underline{\underline{\underline{\underline{K}}}} \tag{3.81}$$

where the bulk modulus k^* and the shear modulus μ^* are equal to:

$$k^* = \frac{4}{3}\mu_{ta} \tag{3.82}$$

$$\mu^* = \frac{\mu_{ta}(9k_{ta} + 8\mu_{ta})}{6(k_{ta} + 2\mu_{ta})} \tag{3.83}$$

Having defined the equivalent stiffness of the mixture of austenite and martensite $\underline{\underline{\underline{\underline{E}}}}_{MT}$, one can calculate the surplus stress increment resulting from the evolution of proportions between austenite and martensite:

$$\Delta\underline{\underline{\sigma}}_m = \Delta\underline{\underline{\sigma}}_{a+m} - \Delta\underline{\underline{\sigma}}_a \tag{3.84}$$

It is equal to the difference between the increment caused by the combined effect of the mixture of both phases (homogenization), and the increment resulting from the response of the austenitic phase. The Eq. 3.84 can be further written as:

$$\Delta\underline{\underline{\sigma}}_m = \left(\underline{\underline{\underline{\underline{E}}}}_{MT} - \underline{\underline{\underline{\underline{E}}}}_{ta}\right) : \Delta\underline{\underline{\varepsilon}} \tag{3.85}$$

It is assumed here, that the strain increment is mainly due to the plastic strains: $\Delta\underline{\underline{\varepsilon}} \cong \Delta\underline{\underline{\varepsilon}}^p$, therefore, the surplus stress increment reads:

$$\Delta\underline{\underline{\sigma}}_m = \left(\underline{\underline{\underline{\underline{E}}}}_{MT} - \underline{\underline{\underline{\underline{E}}}}_{ta}\right) : \Delta\underline{\underline{\varepsilon}}^p \tag{3.86}$$

Inserting expressions for $\underline{\underline{\underline{\underline{E}}}}_{MT}$ (Eq. 3.77) and $\underline{\underline{\underline{\underline{E}}}}_{ta}$ (Eq. 3.55) into 3.86 reads:

$$\Delta\underline{\underline{\sigma}}_m = \left(3(k_{MT} - k_{ta})\underline{\underline{\underline{\underline{J}}}} + 2(\mu_{MT} - \mu_{ta})\underline{\underline{\underline{\underline{K}}}}\right) : \Delta\underline{\underline{\varepsilon}}^p \tag{3.87}$$

Because the tensor of plastic strains $\Delta\underline{\underline{\varepsilon}}^p$ has deviatoric character, the projector $\underline{\underline{\underline{\underline{J}}}}$ has volumetric character and the projector $\underline{\underline{\underline{\underline{K}}}}$ has again deviatoric character, the following equations are true:

$$\underline{\underline{\underline{\underline{J}}}} : \Delta\underline{\underline{\varepsilon}}^p = \underline{\underline{0}} \tag{3.88}$$

$$\underline{\underline{\underline{\underline{K}}}} : \Delta\underline{\underline{\varepsilon}}^p = \Delta\underline{\underline{\varepsilon}}^p \tag{3.89}$$

Finally, the surplus stress increment due to the presence of martensite in the austenitic matrix is equal to:

$$\Delta\underline{\underline{\sigma}}_m = 2(\mu_{MT} - \mu_{ta})\Delta\underline{\underline{\varepsilon}}^p = \mathrm{C}_{a+m}\Delta\underline{\underline{\varepsilon}}^p \tag{3.90}$$

where C_{a+m} stands for the surplus tangent stiffness modulus:

$$\mathrm{C}_{a+m} = 2(\mu_{MT} - \mu_{ta}) \tag{3.91}$$

Thus, the modulus C_{a+m} depends on the shear modulus μ_{ta}, defined by Eq. 3.56, and the homogenized modulus μ_{MT}. The derivation of μ_{MT} is described in the subsequent section.

3.5.5.7. Derivation of the surplus tangent stiffness modulus C_{a+m}

Taking into account Eq. 3.80, and inserting the stiffness tensors $\underline{\underline{\underline{\underline{E}}}}_m$ (Eq. 3.74), $\underline{\underline{\underline{\underline{\mathrm{E}}}}}^*$ (Eq. 3.81), $\underline{\underline{\underline{\underline{E}}}}_{ta}$ (Eq. 3.55), $\underline{\underline{\underline{\underline{E}}}}_{MT}$ (Eq. 3.77) one obtains:

$$\left[3k_{MT}\underline{\underline{\underline{\underline{J}}}} + 2\mu_{MT}\underline{\underline{\underline{\underline{K}}}} + 3k^*\underline{\underline{\underline{\underline{J}}}} + 2\mu^*\underline{\underline{\underline{\underline{K}}}}\right]^{-1} = (1-\xi)\left[3k_{ta}\underline{\underline{\underline{\underline{J}}}} + 2\mu_{ta}\underline{\underline{\underline{\underline{K}}}} + 3k^*\underline{\underline{\underline{\underline{J}}}} + 2\mu^*\underline{\underline{\underline{\underline{K}}}}\right]^{-1} + \xi\left[3k_m\underline{\underline{\underline{\underline{J}}}} + 2\mu_m\underline{\underline{\underline{\underline{K}}}} + 3k^*\underline{\underline{\underline{\underline{J}}}} + 2\mu^*\underline{\underline{\underline{\underline{K}}}}^*\right]^{-1} \tag{3.92}$$

Multiplying the above equation by $\left[\underline{\underline{\underline{\underline{J}}}}\right]^{-1}$, and knowing that $\underline{\underline{\underline{\underline{J}}}}:\underline{\underline{\underline{\underline{J}}}} = 1$ and $\underline{\underline{\underline{\underline{J}}}}:\underline{\underline{\underline{\underline{K}}}} = 0$ one obtains:

$$[3k_{MT} + 3k^*]^{-1} = (1-\xi)[3k_{ta} + 3k^*]^{-1} + \xi[3k_m + 3k^*]^{-1} \tag{3.93}$$

Multiplying the same Eq. 3.92 by $\left[\underline{\underline{\underline{\underline{K}}}}\right]^{-1}$, and using $\underline{\underline{\underline{\underline{K}}}}:\underline{\underline{\underline{\underline{K}}}} = 1$ one obtains:

$$[2\mu_{MT} + 2\mu^*]^{-1} = (1-\xi)[2\mu_{ta} + 2\mu^*]^{-1} + \xi[2\mu_m + 2\mu^*]^{-1} \tag{3.94}$$

Rearranging Eqs 3.93 and 3.94, one obtains the formulas allowing to calculate the homogenized bulk and shear modules k_{MT} and μ_{MT}:

$$3k_{MT} + 3k^* = \left[\frac{(1-\xi)}{3k_{ta} + 3k^*} + \frac{\xi}{3k_m + 3k^*}\right]^{-1} \tag{3.95}$$

$$2\mu_{MT} + 2\mu^* = \left[\frac{(1-\xi)}{2\mu_{ta} + 2\mu^*} + \frac{\xi}{2\mu_m + 2\mu^*}\right]^{-1} \tag{3.96}$$

After simple rearrangements one obtains suitable formulas for μ_{MT} and k_{MT}:

$$\mu_{MT} = \frac{1}{2}\left[\frac{(1-\xi)}{2\mu_{ta} + 2\mu^*} + \frac{\xi}{2\mu_m + 2\mu^*}\right]^{-1} - \mu^* \tag{3.97}$$

$$k_{MT} = \frac{1}{3}\left[\frac{(1-\xi)}{3k_{ta} + 3k^*} + \frac{\xi}{3k_m + 3k^*}\right]^{-1} - k^* \tag{3.98}$$

In order to calculate the modulus C_{a+m} (Eq. 3.91), the μ_{MT} modulus is necessary, thus the Eq. 3.97 will be taken into account in what follows. In the formula 3.97, μ_m has been defined by Eq. (3.75), μ_{ta} by Eq. (3.56) and μ^* by Eq. (3.83).

Taking into account the expression for μ^* (Eq. 3.83), and inserting μ_{ta} (Eq. 3.56) and k_{ta} (Eq. 3.57) one gets:

$$\mu^* = \frac{E_{ta}}{2(1+\nu_a)} \frac{\left(9\frac{E_{ta}}{3(1-2\nu_a)} + 8\frac{E_{ta}}{2(1+\nu_a)}\right)}{6\left(\frac{E_{ta}}{3(1-2\nu_a)} + 2\frac{E_{ta}}{2(1+\nu_a)}\right)} \tag{3.99}$$

After dividing the numerator and the denominator of Eq. 3.99 by E_{ta}, and reducing to the common denominator one obtains:

$$\mu^* = \frac{E_{ta}}{2(1+\nu_a)} \frac{\left(\frac{9\cdot 2(1+\nu_a) + 24(1-2\nu_a)}{6(1-2\nu_a)(1+\nu_a)}\right)}{6\left(\frac{2(1+\nu_a) + 6(1-2\nu_a)}{6(1-2\nu_a)(1+\nu_a)}\right)} \tag{3.100}$$

Reducing further the above fraction leads to:

$$\mu^* = \frac{E_{ta}}{2(1+\nu_a)} \frac{(42-30\nu_a)}{6(8-10\nu_a)} \tag{3.101}$$

Finally:

$$\mu^* = \frac{E_{ta}}{4(1+\nu_a)} \frac{(7-5\nu_a)}{(4-5\nu_a)} \tag{3.102}$$

Inserting equations for μ^* (Eq. 3.102), μ_{ta} (Eq. 3.56) and μ_m (Eq. 3.75) into the expression for μ_{MT} (Eq. 3.97) reads:

$$\mu_{MT} = \frac{1}{2}\left[\frac{(1-\xi)}{\frac{E_{ta}}{(1+\nu_a)}+\frac{E_{ta}}{2(1+\nu_a)}\frac{(7-5\nu_a)}{(4-5\nu_a)}}+\frac{\xi}{\frac{E_m}{(1+\nu_m)}+\frac{E_{ta}}{2(1+\nu_a)}\frac{(7-5\nu_a)}{(4-5\nu_a)}}\right]^{-1} - \frac{E_{ta}}{4(1+\nu_a)}\frac{(7-5\nu_a)}{(4-5\nu_a)} \tag{3.103}$$

As the above expression is rather complex, it is convenient to divide it and work with its less complex parts. Namely:

$$\mu_{MT} = \frac{1}{2}[F1+F2]^{-1} - \mathrm{F3} \tag{3.104}$$

Where:

$$F1 = \frac{(1-\xi)}{\frac{E_{ta}}{(1+\nu_a)}+\frac{E_{ta}}{2(1+\nu_a)}\frac{(7-5\nu_a)}{(4-5\nu_a)}} \tag{3.105}$$

$$F2 = \frac{\xi}{\frac{E_m}{(1+\nu_m)}+\frac{E_{ta}}{2(1+\nu_a)}\frac{(7-5\nu_a)}{(4-5\nu_a)}} \qquad F3 = \mu^* = \frac{E_{ta}}{4(1+\nu_a)}\frac{(7-5\nu_a)}{(4-5\nu_a)} \tag{3.106}$$

Taking into account expression $F1$ and simplifying its denominator one obtains:

$$F1 = \frac{(1-\xi)}{\frac{E_{ta}}{(1+\nu_a)}\left[1+\frac{(7-5\nu_a)}{2(4-5\nu_a)}\right]} = \frac{(1-\xi)}{\frac{E_{ta}}{(1+\nu_a)}\frac{15}{2}\left(\frac{1-\nu_a}{4-5\nu_a}\right)} \tag{3.107}$$

Adding the terms $F1$ and $F2$ gives:

$$F1+F2 = \frac{(1-\xi)}{\frac{E_{ta}}{(1+\nu_a)}\frac{15}{2}\left(\frac{1-\nu_a}{4-5\nu_a}\right)}+\frac{\xi}{\frac{E_m}{(1+\nu_m)}+\frac{E_{ta}}{2(1+\nu_a)}\frac{(7-5\nu_a)}{(4-5\nu_a)}} \tag{3.108}$$

and further:

$$\frac{(1-\xi)\left[\frac{E_m}{(1+\nu_m)}+\frac{E_{ta}}{2(1+\nu_a)}\frac{(7-5\nu_a)}{(4-5\nu_a)}\right]+\xi\frac{E_{ta}}{(1+\nu_a)}\frac{15}{2}\left(\frac{1-\nu_a}{4-5\nu_a}\right)}{\frac{E_{ta}}{(1+\nu_a)}\frac{15}{2}\left(\frac{1-\nu_a}{4-5\nu_a}\right)\left[\frac{E_m}{(1+\nu_m)}+\frac{E_{ta}}{2(1+\nu_a)}\frac{(7-5\nu_a)}{(4-5\nu_a)}\right]} \tag{3.109}$$

which equals:

$$\frac{\left[\frac{E_m}{(1+\nu_m)}+\frac{E_{ta}}{2(1+\nu_a)}\frac{(7-5\nu_a)}{(4-5\nu_a)}\right]+\xi\left[\frac{E_{ta}[15(1-\nu_a)-(7-5\nu_a)]}{(1+\nu_a)2(4-5\nu_a)}-\frac{E_m}{(1+\nu_m)}\right]}{\frac{E_{ta}}{(1+\nu_a)}\frac{15}{2}\left(\frac{1-\nu_a}{4-5\nu_a}\right)\left[\frac{E_m}{(1+\nu_m)}+\frac{E_{ta}}{2(1+\nu_a)}\frac{(7-5\nu_a)}{(4-5\nu_a)}\right]} \tag{3.110}$$

Finally:

$$F1+F2 = \frac{\left[\frac{E_m}{(1+\nu_m)}+\frac{E_{ta}}{2(1+\nu_a)}\frac{(7-5\nu_a)}{(4-5\nu_a)}\right]+\xi\left[\frac{E_{ta}}{(1+\nu_a)}-\frac{E_m}{(1+\nu_m)}\right]}{\frac{E_{ta}}{(1+\nu_a)}\frac{15}{2}\left(\frac{1-\nu_a}{4-5\nu_a}\right)\left[\frac{E_m}{(1+\nu_m)}+\frac{E_{ta}}{2(1+\nu_a)}\frac{(7-5\nu_a)}{(4-5\nu_a)}\right]} \tag{3.111}$$

Coming back to Eq. 3.104 one obtains:

$$\frac{1}{2}[F1+F2]^{-1} = \frac{\frac{E_{ta}}{(1+\nu_a)}\frac{15}{2}\left(\frac{1-\nu_a}{4-5\nu_a}\right)\left[\frac{E_m}{(1+\nu_m)}+\frac{E_{ta}}{2(1+\nu_a)}\frac{(7-5\nu_a)}{(4-5\nu_a)}\right]}{2\left[\frac{E_m}{(1+\nu_m)}+\frac{E_{ta}}{2(1+\nu_a)}\frac{(7-5\nu_a)}{(4-5\nu_a)}\right]+\xi\left[\frac{E_{ta}}{(1+\nu_a)}-\frac{E_m}{(1+\nu_m)}\right]} \tag{3.112}$$

and μ_{MT} from Eq. 3.104 equals:

$$\mu_{MT} = \frac{\frac{15}{4}\frac{E_{ta}}{(1+\nu_a)}\left(\frac{1-\nu_a}{4-5\nu_a}\right)\left[\frac{E_m}{(1+\nu_m)} + \frac{E_{ta}}{2(1+\nu_a)}\frac{(7-5\nu_a)}{(4-5\nu_a)}\right]}{\left[\frac{E_m}{(1+\nu_m)} + \frac{E_{ta}}{2(1+\nu_a)}\frac{(7-5\nu_a)}{(4-5\nu_a)}\right] + \xi\left[\frac{E_{ta}}{(1+\nu_a)} - \frac{E_m}{(1+\nu_m)}\right]} - \frac{E_{ta}}{4(1+\nu_a)}\frac{(7-5\nu_a)}{(4-5\nu_a)} \tag{3.113}$$

At this point it is convenient to insert the expression for μ_{MT} (Eq. 3.113) into the formula for the modulus C_{a+m} (Eq. 3.91). Thus, C_{a+m} equals:

$$\mathrm{C}_{a+m} = \frac{\frac{15}{2}\frac{E_{ta}}{(1+\nu_a)}\left(\frac{1-\nu_a}{4-5\nu_a}\right)\left[\frac{E_m}{(1+\nu_m)} + \frac{E_{ta}}{2(1+\nu_a)}\frac{(7-5\nu_a)}{(4-5\nu_a)}\right]}{\left[\frac{E_m}{(1+\nu_m)} + \frac{E_{ta}}{2(1+\nu_a)}\frac{(7-5\nu_a)}{(4-5\nu_a)}\right] + \xi\left[\frac{E_{ta}}{(1+\nu_a)} - \frac{E_m}{(1+\nu_m)}\right]} - \frac{E_{ta}}{2(1+\nu_a)}\frac{(7-5\nu_a)}{(4-5\nu_a)} - \frac{E_{ta}}{(1+\nu_a)} \tag{3.114}$$

Combining the last two terms one obtains:

$$\mathrm{C}_{a+m} = \frac{\frac{15}{2}\frac{E_{ta}}{(1+\nu_a)}\left(\frac{1-\nu_a}{4-5\nu_a}\right)\left[\frac{E_m}{(1+\nu_m)} + \frac{E_{ta}}{2(1+\nu_a)}\frac{(7-5\nu_a)}{(4-5\nu_a)}\right]}{\left[\frac{E_m}{(1+\nu_m)} + \frac{E_{ta}}{2(1+\nu_a)}\frac{(7-5\nu_a)}{(4-5\nu_a)}\right] + \xi\left[\frac{E_{ta}}{(1+\nu_a)} - \frac{E_m}{(1+\nu_m)}\right]} - \frac{E_{ta}}{(1+\nu_a)}\left[\frac{(7-5\nu_a)}{2(4-5\nu_a)} + 1\right] \tag{3.115}$$

and

$$\mathrm{C}_{a+m} = \frac{\frac{15}{2}\frac{E_{ta}}{(1+\nu_a)}\left(\frac{1-\nu_a}{4-5\nu_a}\right)\left[\frac{E_m}{(1+\nu_m)} + \frac{E_{ta}}{2(1+\nu_a)}\frac{(7-5\nu_a)}{(4-5\nu_a)}\right]}{\left[\frac{E_m}{(1+\nu_m)} + \frac{E_{ta}}{2(1+\nu_a)}\frac{(7-5\nu_a)}{(4-5\nu_a)}\right] + \xi\left[\frac{E_{ta}}{(1+\nu_a)} - \frac{E_m}{(1+\nu_m)}\right]} - \frac{15E_{ta}}{2(1+\nu_a)}\frac{(1-\nu_a)}{(4-5\nu_a)} \tag{3.116}$$

After extracting a common term one gets:

$$\mathrm{C}_{a+m} = \frac{15}{2}\frac{E_{ta}}{(1+\nu_a)}\left(\frac{1-\nu_a}{4-5\nu_a}\right)\left(\frac{\left[\frac{E_m}{(1+\nu_m)} + \frac{E_{ta}}{2(1+\nu_a)}\frac{(7-5\nu_a)}{(4-5\nu_a)}\right]}{\left[\frac{E_m}{(1+\nu_m)} + \frac{E_{ta}}{2(1+\nu_a)}\frac{(7-5\nu_a)}{(4-5\nu_a)}\right] + \xi\left[\frac{E_{ta}}{(1+\nu_a)} - \frac{E_m}{(1+\nu_m)}\right]} - 1\right) \tag{3.117}$$

and

$$\mathrm{C}_{a+m} = \frac{15}{2}\frac{E_{ta}}{(1+\nu_a)}\left(\frac{1-\nu_a}{4-5\nu_a}\right)\left(\frac{-\xi\left[\frac{E_{ta}}{(1+\nu_a)} - \frac{E_m}{(1+\nu_m)}\right]}{\left[\frac{E_m}{(1+\nu_m)} + \frac{E_{ta}}{2(1+\nu_a)}\frac{(7-5\nu_a)}{(4-5\nu_a)}\right] + \xi\left[\frac{E_{ta}}{(1+\nu_a)} - \frac{E_m}{(1+\nu_m)}\right]}\right) \tag{3.118}$$

Thus, finally C_{a+m} equals:

$$\mathrm{C}_{a+m} = \frac{15}{2}\frac{E_{ta}}{(1+\nu_a)}\frac{\left(\frac{1-\nu_a}{4-5\nu_a}\right)\xi\left[\frac{E_m}{(1+\nu_m)} - \frac{E_{ta}}{(1+\nu_a)}\right]}{\left[\frac{E_m}{(1+\nu_m)}(1-\xi) + \frac{E_{ta}}{(1+\nu_a)}\left[\xi + \frac{(7-5\nu_a)}{2(4-5\nu_a)}\right]\right]} \tag{3.119}$$

Inserting the expression for modulus E_{ta} (Eq. 3.56) into Eq. 3.119 one obtains:

$$\mathrm{C}_{a+m} = \frac{E_a \cdot C_{a0}(1+h\xi)}{[E_a + C_{a0}(1+h\xi)]}\frac{\xi\frac{15}{2}\frac{(1-\nu_\mathrm{a})}{(4-5\nu_\mathrm{a})(1+\nu_\mathrm{a})}\left[\frac{\mathrm{E_m}}{(1+\nu_\mathrm{m})} - \frac{E_a \cdot C_{a0}(1+h\xi)}{[E_a + C_{a0}(1+h\xi)](1+\nu_\mathrm{a})}\right]}{\left[\frac{\mathrm{E_m}(1-\xi)}{(1+\nu_\mathrm{m})} + \frac{E_a \cdot C_{a0}(1+h\xi)}{[E_a + C_{a0}(1+h\xi)](1+\nu_\mathrm{a})}\left(\xi + \frac{(7-5\nu_\mathrm{a})}{2(4-5\nu_\mathrm{a})}\right)\right]} \tag{3.120}$$

The final expression for the homogenized tangent stiffness modulus C_{a+m} is a function of the volume fraction of martensite (ξ) and the parameters of the constitutive model: E_a, $\mathrm{E_m}$, C_{a0}, ν_a, ν_m, h.

3.5.6. Summary of the kinematic hardening

The kinematic hardening causes the yield surface to translate. The center of the yield surface, which is described by the back stress tensor $\underline{\underline{X}}$, was defined in the incremental form by Eq. 3.26. The first term $d\underline{\underline{X}}_{a0}$ was defined by Eq. 3.16, the second one $d\underline{\underline{X}}_{a\xi}$ by Eq. 3.41 and the third one $d\underline{\underline{X}}_{a+m}$ by Eq. 3.44. The back stress increment equals:

$$d\underline{\underline{X}} = \frac{2}{3}C_{a0}d\underline{\underline{\varepsilon}}^{p} + \frac{2}{3}C_{a0}h\xi d\underline{\underline{\varepsilon}}^{p} + \frac{2}{3}\mathrm{C}_{a+m}d\underline{\underline{\varepsilon}}^{p} \tag{3.121}$$

Which can be simplified to:

$$d\underline{\underline{X}} = \frac{2}{3}(C_{a0} + C_{a0}h\xi + \mathrm{C}_{a+m})d\underline{\underline{\varepsilon}}^{p} = \frac{2}{3}C_{X}(\xi)d\underline{\underline{\varepsilon}}^{p} \tag{3.122}$$

where $C_X(\xi)$ is the kinematic hardening modulus. The modulus $C_X(\xi)$ is a function of the volume fraction of martensite and the parameters of the constitutive model.

$$C_{X}(\xi) = C_{a0} + C_{a0}h\xi + \mathrm{C}_{a+m} \tag{3.123}$$

3.5.7. Isotropic hardening

The isotropic hardening is described by a scalar parameter R, which causes the yield surface to grow (increase its size). The physical meaning of the isotropic hardening is related to the fact that the yield stress increases. If only kinematic hardening was present, the yield stress would not change. The isotropic hardening phenomenon is also coupled with the phase transformation. While the microstructure changes from the austenite to the stronger martensite one may expect the yield stress to increase. Thus, the isotropic hardening should depend on the volume fraction of martensite.
The isotropic hardening variable is defined via its incremental form. The increment of the scalar R is equal to the stress increment, caused by the presence of martensie. As the stress increment has tensorial representation, a norm has been applied to obtain a scalar variable. According to Skoczeń (2007), the isotropic hardening increment takes the form:

$$\Delta R = \Delta R_{m} = \|\Delta\sigma_{m}\| = \sqrt{\frac{2}{3}\Delta\sigma_{m}:\Delta\sigma_{m}} \tag{3.124}$$

Inserting the increment of stress $\Delta\sigma_m$ from Eq. 3.90 into Eq. 3.124 gives:

$$\Delta R = \sqrt{[2(\mu_{MT} - \mu_{ta})]^{2}\cdot\frac{2}{3}\Delta\underline{\underline{\varepsilon}}^{p}:\Delta\underline{\underline{\varepsilon}}^{p}} = 2(\mu_{MT} - \mu_{ta})\Delta p \tag{3.125}$$

In the incremental form, the evolution of the isotropic hardening parameter reads:

$$\mathrm{d}R = dR_{a+m} = 2(\mu_{MT} - \mu_{ta})\mathrm{d}p = \mathrm{C}_{a+m}\mathrm{d}p \tag{3.126}$$

Where the accumulated plastic strain increment is computed as:

$$\mathrm{d}p = \sqrt{\frac{2}{3}\mathrm{d}\underline{\underline{\varepsilon}}^{p}:\mathrm{d}\underline{\underline{\varepsilon}}^{p}} \tag{3.127}$$

Thus, the increment of the isotropic hardening variable (Eq. 3.126) is proportional to the increment of the accumulated plastic strain $\mathrm{d}p$ and to the homogenized tangent stiffness modulus C_{a+m}.

3.5.8. Mixed hardening

Usually, both types of hardening (isotropic and kinematic) are simultaneously observed in the structural materials. In order to account for mixed (kinematic-isotropic) hardening, the Bauschinger parameter β has been introduced according to the parameterization by Zyczkowski (1981). The Bauschinger parameter allows to calculate the yield stress for the reverse loading (Fig. 3.11):

$$\beta = \frac{\sigma' + \sigma'^{-}}{2(\sigma' - \sigma_0)} \tag{3.128}$$

where:

- σ' is the stress level at which the unloading starts
- σ'^{-} is the yield stress at the reverse active process
- σ_0 is the initial yield stress

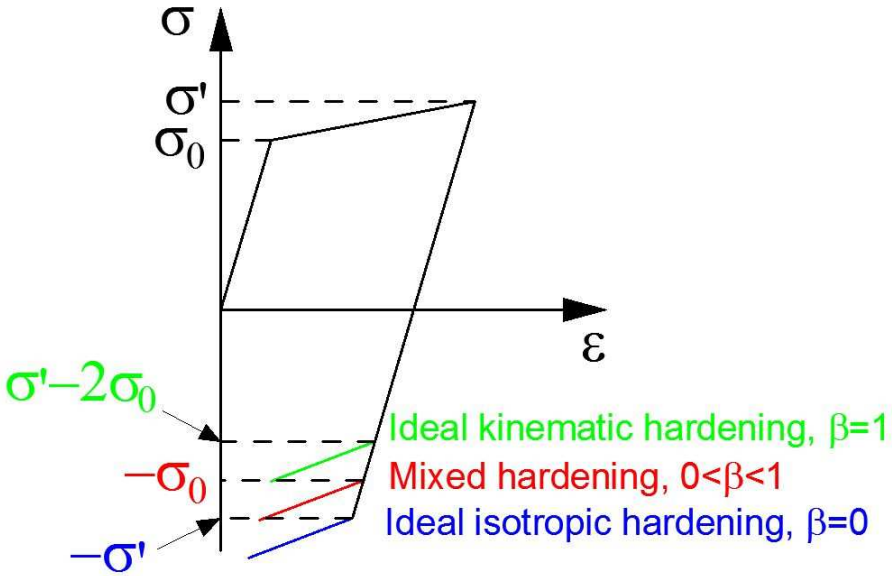

Figure. 3.11. Bauschinger parameter, and types of hardening

Parameter β is used to determine the ratio between the isotropic hardening (no Bauschinger effect, $\beta = 0$) and the kinematic hardening (ideal Bauschinger effect $\beta = 1$). It can be identified based on tests of cyclic loads (tension-compression or torsion). Finally, the evolution of the isotropic hardening depends also on the Bauschinger parameter (Sitko 2010, Sitko and Skoczeń 2012) and is equal to:

$$\mathrm{d}R = (1 - \beta)\mathrm{C}_{a+m}\mathrm{d}p \tag{3.129}$$

and in the rate form:

$$\dot{R} = (1 - \beta)\mathrm{C}_{a+m}\dot{p} \tag{3.130}$$

By integration with respect to the accumulated plastic strain, the isotropic hardening variable equals:

$$R = \int_0^{\mathrm{p}*} (1-\beta)\mathrm{C}_{a+m}\mathrm{d}p \tag{3.131}$$

where $\mathrm{p}*$ denotes final value of the accumulated plastic strain.
The integration of Eq. 3.131 is not possible analytically, since the modulus C_{a+m} depends in a complicated way on the volume fraction of martensite (ξ), which in turn is a function of the accumulated plastic strain (Eq. 3.8). Thus, the integration has to be carried out numerically.
Similarly, the Bauschinger parameter is added to the evolution law of the kinematic hardening (Skoczeń, 2007):

$$d\underline{\underline{X}} = \frac{2}{3}[C_{a0} + C_{a0}h\xi + (1-\beta)\mathrm{C}_{a+m}]d\underline{\underline{\varepsilon}}^p \tag{3.132}$$

Thus, in the rate form one obtains:

$$\dot{\underline{\underline{X}}} = \frac{2}{3}[C_{a0} + C_{a0}h\xi + (1-\beta)\mathrm{C}_{a+m}]\dot{\underline{\underline{\varepsilon}}}^p = \frac{2}{3}C_X(\xi)\dot{\underline{\underline{\varepsilon}}}^p \tag{3.133}$$

where $C_X(\xi)$ has been updated from Eq. (3.123) to the one below, incorporating the Bauschinger parameter:

$$C_X(\xi) = C_{a0} + C_{a0}h\xi + (1-\beta)\mathrm{C}_{a+m} \tag{3.134}$$

Inserting into the above equation the expression for the C_{a+m} (Eq. 3.120) one has:

$$C_X(\xi) = C_{a0}(1+h\xi) + \frac{(1-\beta)E_aC_{a0}(1+h\xi)}{2[E_a + C_{a0}(1+h\xi)]} \frac{\frac{15\xi\cdot(1-\nu_\mathrm{a})}{(4-5\nu_\mathrm{a})(1+\nu_\mathrm{a})}\left[\frac{\mathrm{E_m}}{(1+\nu_\mathrm{m})} - \frac{E_a\cdot C_{a0}(1+h\xi)}{[E_a + C_{a0}(1+h\xi)](1+\nu_\mathrm{a})}\right]}{\left[\frac{\mathrm{E_m}(1-\xi)}{(1+\nu_\mathrm{m})} + \frac{E_a\cdot C_{a0}(1+h\xi)}{[E_a + C_{a0}(1+h\xi)](1+\nu_\mathrm{a})}\left(\xi + \frac{(7-5\nu_\mathrm{a})}{2(4-5\nu_\mathrm{a})}\right)\right]} \tag{3.135}$$

Finally, the kinematic hardening variable can be obtained by integration of the Eq. 3.132 with respect to the increment of the plastic strain tensor $d\underline{\underline{\varepsilon}}^p$:

$$\underline{\underline{X}} = \int_0^{\underline{\underline{\varepsilon}}^{p*}} \frac{2}{3}C_X(\xi)d\underline{\underline{\varepsilon}}^p \tag{3.136}$$

where $\underline{\underline{\varepsilon}}^{p*}$ denotes the final value of the plastic strain tensor on the loading path.
Again, the integration is not possible in the analytical way, since $C_X(\xi)$ is a complicated function of the martensite volume fraction (ξ), which in turn is a function of the plastic strain (Eq. 3.8).

3.5.9. Summary of the plastic strain tensor derivation

The plastic strain tensor can be calculated according to the associated flow rule. Thus, differentiating the yield function with respect to the stress tensor, namely:

$$\dot{\underline{\underline{\varepsilon}}}^p = \dot{\lambda}\frac{\partial f_y}{\partial \underline{\underline{\sigma}}} \tag{3.137}$$

and further:

$$\frac{\partial f_y}{\partial \underline{\underline{\sigma}}} = \frac{\partial J_2\left(\underline{\underline{\sigma}} - \underline{\underline{X}}\right)}{\partial \underline{\underline{\sigma}}} - \frac{\partial \sigma_y}{\partial \underline{\underline{\sigma}}} - \frac{\partial \mathrm{R}}{\partial \underline{\underline{\sigma}}} \tag{3.138}$$

The yield stress σ_y is constant, thus:

$$\frac{\partial \sigma_y}{\partial \underline{\underline{\sigma}}} = \underline{\underline{0}} \tag{3.139}$$

The isotropic hardening variable R (Eq. 3.131) does not depend on the stress $\underline{\underline{\sigma}}$, thus:

$$\frac{\partial \mathrm{R}}{\partial \underline{\underline{\sigma}}} = \underline{\underline{0}} \tag{3.140}$$

The second invariant J_2 was defined by Eq. (3.22). Its derivative $\partial J_2\left(\underline{\underline{\sigma}} - \underline{\underline{X}}\right)/\partial \underline{\underline{\sigma}}$ equals:

$$\frac{\partial f_y}{\partial \underline{\underline{\sigma}}} = \frac{\partial J_2\left(\underline{\underline{\sigma}} - \underline{\underline{X}}\right)}{\partial \underline{\underline{\sigma}}} = \frac{\frac{3}{2}\cdot 2\cdot\left(\underline{\underline{s}} - \underline{\underline{X}}\right)\cdot\frac{\partial\left(\underline{\underline{s}} - \underline{\underline{X}}\right)}{\partial \underline{\underline{\sigma}}}}{2\sqrt{\frac{3}{2}\left(\underline{\underline{s}} - \underline{\underline{X}}\right):\left(\underline{\underline{s}} - \underline{\underline{X}}\right)}} = \frac{\frac{3}{2}\cdot\left(\underline{\underline{s}} - \underline{\underline{X}}\right)\cdot\frac{\partial\left(\underline{\underline{s}} - \underline{\underline{X}}\right)}{\partial \underline{\underline{\sigma}}}}{\sqrt{\frac{3}{2}\left(\underline{\underline{s}} - \underline{\underline{X}}\right):\left(\underline{\underline{s}} - \underline{\underline{X}}\right)}} \tag{3.141}$$

Where $\partial\left(\underline{\underline{s}} - \underline{\underline{X}}\right)/\partial \underline{\underline{\sigma}}$ ($\underline{\underline{s}}$ defined by Eq. 3.23) equals:

$$\frac{\partial\left(\underline{\underline{s}} - \underline{\underline{X}}\right)}{\partial \underline{\underline{\sigma}}} = \frac{\partial\left(\underline{\underline{\sigma}} - \frac{1}{3}Tr\left(\underline{\underline{\sigma}}\right)\underline{\underline{I}} - \underline{\underline{X}}\right)}{\partial \underline{\underline{\sigma}}} = 1 \tag{3.142}$$

Inserting Eq. 3.142 into Eq. 3.141, and the results to Eq. 3.138 gives:

$$\frac{\partial f_y}{\partial \underline{\underline{\sigma}}} = \frac{\partial J_2\left(\underline{\underline{\sigma}} - \underline{\underline{X}}\right)}{\partial \underline{\underline{\sigma}}} = \frac{3}{2}\frac{\left(\underline{\underline{s}} - \underline{\underline{X}}\right)}{\sqrt{\frac{3}{2}\left(\underline{\underline{s}} - \underline{\underline{X}}\right):\left(\underline{\underline{s}} - \underline{\underline{X}}\right)}} \tag{3.143}$$

Thus, the plastic strain rate tensor (Eq. 3.137), after inserting Eq. 3.143, takes the form:

$$\underline{\underline{\dot{\varepsilon}}}^p = \dot{\lambda}\frac{3}{2}\frac{\left(\underline{\underline{s}} - \underline{\underline{X}}\right)}{\sqrt{\frac{3}{2}\left(\underline{\underline{s}} - \underline{\underline{X}}\right):\left(\underline{\underline{s}} - \underline{\underline{X}}\right)}} \tag{3.144}$$

The plastic multiplier $\dot{\lambda}$ will be addressed in the subsequent section.

3.5.10. Calculation of the plastic multiplier $\dot{\lambda}$

The plastic multiplier $\dot{\lambda}$ can be calculated from the consistency condition:

$$\dot{f}_y\left(\underline{\underline{\sigma}}, \underline{\underline{X}}, R\right) = 0 \tag{3.145}$$

which is expanded to:

$$\dot{f}_y\left(\underline{\underline{\sigma}}, \underline{\underline{X}}, R\right) = \frac{\partial f_y}{\partial \underline{\underline{\sigma}}}:\underline{\underline{\dot{\sigma}}} + \frac{\partial f_y}{\partial \underline{\underline{X}}}:\underline{\underline{\dot{X}}} + \frac{\partial f_y}{\partial \mathrm{R}}\dot{R} = 0 \tag{3.146}$$

One has to calculate 3 derivatives: $\partial f_y/\partial \underline{\underline{\sigma}}$, $\partial f_y/\partial \underline{\underline{X}}$, $\partial f_y/\partial \mathrm{R}$. The first one has been already calculated (Eq. 3.143). The second one ($\partial f_y/\partial \underline{\underline{X}}$) equals ($f_y$ defined by Eq. 3.21):

$$\frac{\partial f_y}{\partial \underline{\underline{X}}} = \frac{\partial\left[J_2\left(\underline{\underline{\sigma}} - \underline{\underline{X}}\right) - \sigma_y - \mathrm{R}\right]}{\partial \underline{\underline{X}}} = \frac{\partial J_2\left(\underline{\underline{\sigma}} - \underline{\underline{X}}\right)}{\partial \underline{\underline{X}}} - \frac{\partial \sigma_y}{\partial \underline{\underline{X}}} - \frac{\partial \mathrm{R}}{\partial \underline{\underline{X}}} \tag{3.147}$$

The three resulting derivatives were treated separately. Starting from the simple ones: $\partial\sigma_y/\partial \underline{\underline{X}}$ and $\partial \mathrm{R}/\partial \underline{\underline{X}}$.

The yield stress (σ_y) is constant, thus:

$$\frac{\partial \sigma_y}{\partial \underline{\underline{X}}} = \underline{\underline{0}} \tag{3.148}$$

The isotropic hardening variable (Eq. 3.131) does not depend on $\underline{\underline{X}}$, thus:

$$\frac{\partial \mathrm{R}}{\partial \underline{\underline{X}}} = \underline{\underline{0}} \tag{3.149}$$

The derivative of the second invariant $J_2\left(\underline{\underline{\sigma}} - \underline{\underline{X}}\right)$ (Eq. 3.22) equals:

$$\frac{\partial J_2\left(\underline{\underline{\sigma}} - \underline{\underline{X}}\right)}{\partial \underline{\underline{X}}} = \frac{\frac{3}{2} \cdot 2 \cdot \left(\underline{\underline{s}} - \underline{\underline{X}}\right) \cdot \frac{\partial\left(\underline{\underline{s}} - \underline{\underline{X}}\right)}{\partial \underline{\underline{X}}}}{2\sqrt{\frac{3}{2}\left(\underline{\underline{s}} - \underline{\underline{X}}\right) : \left(\underline{\underline{s}} - \underline{\underline{X}}\right)}} = \frac{\frac{3}{2} \cdot \left(\underline{\underline{s}} - \underline{\underline{X}}\right) \cdot \frac{\partial\left(\underline{\underline{s}} - \underline{\underline{X}}\right)}{\partial \underline{\underline{X}}}}{\sqrt{\frac{3}{2}\left(\underline{\underline{s}} - \underline{\underline{X}}\right) : \left(\underline{\underline{s}} - \underline{\underline{X}}\right)}} \tag{3.150}$$

with:

$$\frac{\partial\left(\underline{\underline{s}} - \underline{\underline{X}}\right)}{\partial \underline{\underline{X}}} = \frac{\partial\left(\underline{\underline{\sigma}} - \frac{1}{3} Tr\left(\underline{\underline{\sigma}}\right) \underline{\underline{I}} - \underline{\underline{X}}\right)}{\partial \underline{\underline{X}}} = -1 \tag{3.151}$$

Inserting Eq. 3.151 into Eq. 3.150 gives:

$$\frac{\partial J_2\left(\underline{\underline{\sigma}} - \underline{\underline{X}}\right)}{\partial \underline{\underline{X}}} = -\frac{\frac{3}{2} \cdot \left(\underline{\underline{s}} - \underline{\underline{X}}\right)}{\sqrt{\frac{3}{2}\left(\underline{\underline{s}} - \underline{\underline{X}}\right) : \left(\underline{\underline{s}} - \underline{\underline{X}}\right)}} \tag{3.152}$$

Now inserting Eq. 3.152, Eq. 3.148 and Eq. 3.149 into Eq. 3.147 one obtains:

$$\frac{\partial f_y}{\partial \underline{\underline{X}}} = -\frac{3}{2} \frac{\left(\underline{\underline{s}} - \underline{\underline{X}}\right)}{\sqrt{\frac{3}{2}\left(\underline{\underline{s}} - \underline{\underline{X}}\right) : \left(\underline{\underline{s}} - \underline{\underline{X}}\right)}} = -\frac{\partial f_y}{\partial \underline{\underline{\sigma}}} \tag{3.153}$$

It is worth noticing that the derivative $\partial f_y / \partial \underline{\underline{X}}$ has opposite sign w.r.t. the derivative $\partial f_y / \partial \underline{\underline{\sigma}}$ (Eq. 3.143).

The third derivative $\partial f_y / \partial \mathrm{R}$ from 3.146 equals:

$$\frac{\partial f_y}{\partial \mathrm{R}} = \frac{\partial\left[J_2\left(\underline{\underline{\sigma}} - \underline{\underline{X}}\right) - \sigma_y - \mathrm{R}\right]}{\partial \mathrm{R}} = \frac{\partial J_2\left(\underline{\underline{\sigma}} - \underline{\underline{X}}\right)}{\partial \mathrm{R}} - \frac{\partial \sigma_y}{\partial \mathrm{R}} - \frac{\partial \mathrm{R}}{\partial \mathrm{R}} = 0 - 0 - 1 \tag{3.154}$$

Inserting the formulae for the derivatives: $\partial f_y / \partial \mathrm{R}$ (Eq. 3.154), $\partial f_y / \partial \underline{\underline{X}}$ (Eq. 3.153), $\partial f_y / \partial \underline{\underline{\sigma}}$ (Eq. 3.143) into the consistency condition (Eq. 3.146) reads:

$$\frac{3}{2} \frac{\left(\underline{\underline{s}} - \underline{\underline{X}}\right)}{\sqrt{\frac{3}{2}\left(\underline{\underline{s}} - \underline{\underline{X}}\right) : \left(\underline{\underline{s}} - \underline{\underline{X}}\right)}} : \dot{\underline{\underline{\sigma}}} - \frac{3}{2} \frac{\left(\underline{\underline{s}} - \underline{\underline{X}}\right)}{\sqrt{\frac{3}{2}\left(\underline{\underline{s}} - \underline{\underline{X}}\right) : \left(\underline{\underline{s}} - \underline{\underline{X}}\right)}} : \dot{\underline{\underline{X}}} - \dot{R} = 0 \tag{3.155}$$

which can be simplified to:

$$\frac{3}{2} \frac{\left(\underline{\underline{s}} - \underline{\underline{X}}\right)}{\sqrt{\frac{3}{2}\left(\underline{\underline{s}} - \underline{\underline{X}}\right) : \left(\underline{\underline{s}} - \underline{\underline{X}}\right)}} : \left[\dot{\underline{\underline{\sigma}}} - \dot{\underline{\underline{X}}}\right] - \dot{R} = 0 \tag{3.156}$$

In the above formula there are still three unknown time derivatives: $\dot{\underline{\underline{\sigma}}}$, $\dot{\underline{\underline{X}}}$, $\dot{R}$, which have to be specified. Taking into account Eq. 3.1 for $\underline{\underline{\sigma}}$, and applying time derivative gives ($\underline{\underline{\varepsilon}}^{th} = \underline{\underline{0}}$):

$$\dot{\underline{\underline{\sigma}}} = \underline{\underline{\underline{\underline{E}}}} : \left(\dot{\underline{\underline{\varepsilon}}} - \dot{\underline{\underline{\varepsilon}}}^{p} - \dot{\underline{\underline{\varepsilon}}}^{bs}\right) \tag{3.157}$$

The strain tensor $\underline{\underline{\varepsilon}}$ is the free variable. The rate of the plastic strain tensor $\dot{\underline{\underline{\varepsilon}}}^{p}$ has been derived (Eq. 3.144). The derivative of the Bain strain tensor $\dot{\underline{\underline{\varepsilon}}}^{bs}$ has still to be calculated. From the definition of $\underline{\underline{\varepsilon}}^{bs}$ (Eq. 3.20) one obtains:

$$\dot{\underline{\underline{\varepsilon}}}^{bs} = \frac{d\underline{\underline{\varepsilon}}^{bs}}{dt} = \frac{d}{dt}\left[\xi \cdot \frac{1}{3}\Delta v \underline{\underline{I}}\right] = \frac{1}{3}\dot{\xi}\Delta v \underline{\underline{I}} \tag{3.158}$$

Thus inserting Eq. 3.144 and Eq. 3.158 into Eq. 3.157 one finally gets $\dot{\underline{\underline{\sigma}}}$ as:

$$\dot{\underline{\underline{\sigma}}} = \underline{\underline{\underline{\underline{E}}}} : \left(\dot{\underline{\underline{\varepsilon}}} - \dot{\lambda}\frac{3}{2}\frac{\left(\underline{\underline{s}} - \underline{\underline{X}}\right)}{\sqrt{\frac{3}{2}\left(\underline{\underline{s}} - \underline{\underline{X}}\right) : \left(\underline{\underline{s}} - \underline{\underline{X}}\right)}} - \frac{1}{3}\dot{\xi}\Delta v \underline{\underline{I}} \right) \tag{3.159}$$

The second time derivative from Eq. 3.155 was the rate of the kinematic hardening variable $\dot{\underline{\underline{X}}}$, which was defined in the Eq. 3.122. After inserting the expression for $\dot{\underline{\underline{\varepsilon}}}^{p}$ from Eq. 3.144 one gets:

$$\dot{\underline{\underline{X}}} = \frac{2}{3}C_X(\xi)\dot{\underline{\underline{\varepsilon}}}^{p} = \frac{2}{3}C_X(\xi)\left[\dot{\lambda}\frac{3}{2}\frac{\left(\underline{\underline{s}} - \underline{\underline{X}}\right)}{\sqrt{\frac{3}{2}\left(\underline{\underline{s}} - \underline{\underline{X}}\right) : \left(\underline{\underline{s}} - \underline{\underline{X}}\right)}}\right] = \dot{\lambda}\frac{C_X(\xi)\left(\underline{\underline{s}} - \underline{\underline{X}}\right)}{\sqrt{\frac{3}{2}\left(\underline{\underline{s}} - \underline{\underline{X}}\right) : \left(\underline{\underline{s}} - \underline{\underline{X}}\right)}} \tag{3.160}$$

The last missing time derivative from the consistency condition (Eq. 3.155) is the rate of the isotropic hardening $\dot{R}$ (Eq. 3.130). It is proportional to the rate of the accumulated plastic strain $\dot{p}$ (Eq. 3.10).
After inserting the expression for $\dot{\underline{\underline{\varepsilon}}}^{p}$ (Eq. 3.144) one obtains:

$$\dot{p} = \sqrt{\frac{2}{3}\dot{\lambda}\frac{3}{2}\frac{\left(\underline{\underline{s}} - \underline{\underline{X}}\right)}{\sqrt{\frac{3}{2}\left(\underline{\underline{s}} - \underline{\underline{X}}\right) : \left(\underline{\underline{s}} - \underline{\underline{X}}\right)}} : \dot{\lambda}\frac{3}{2}\frac{\left(\underline{\underline{s}} - \underline{\underline{X}}\right)}{\sqrt{\frac{3}{2}\left(\underline{\underline{s}} - \underline{\underline{X}}\right) : \left(\underline{\underline{s}} - \underline{\underline{X}}\right)}}} = \sqrt{\left(\dot{\lambda}\right)^2 \frac{\frac{3}{2}\left(\underline{\underline{s}} - \underline{\underline{X}}\right) : \left(\underline{\underline{s}} - \underline{\underline{X}}\right)}{\frac{3}{2}\left(\underline{\underline{s}} - \underline{\underline{X}}\right) : \left(\underline{\underline{s}} - \underline{\underline{X}}\right)}}$$

$$= \sqrt{\left(\dot{\lambda}\right)^2} = \dot{\lambda} \tag{3.161}$$

Thus the rate of the accumulated plastic strain $\dot{p}$ is equal to the plastic multiplier $\dot{\lambda}$. Lastly, the derivative $\dot{R}$ is equal:

$$\dot{R} = (1-\beta)\mathrm{C}_{a+m}\dot{p} = (1-\beta)\mathrm{C}_{a+m}\dot{\lambda} \tag{3.162}$$

Inserting the calculated time derivatives: $\dot{\underline{\underline{\sigma}}}$ from Eq. 3.159, $\dot{\underline{\underline{X}}}$ from Eq. 3.160 and $\dot{R}$ from Eq. 3.162 into the consistency condition (Eq. 3.155) one obtains:

$$\frac{\frac{3}{2}\left(\underline{\underline{s}} - \underline{\underline{X}}\right)}{\sqrt{\frac{3}{2}\left(\underline{\underline{s}} - \underline{\underline{X}}\right) : \left(\underline{\underline{s}} - \underline{\underline{X}}\right)}} : \left[\underline{\underline{\underline{\underline{E}}}} : \left(\dot{\underline{\underline{\varepsilon}}} - \frac{\dot{\lambda}\frac{3}{2}\left(\underline{\underline{s}} - \underline{\underline{X}}\right)}{\sqrt{\frac{3}{2}\left(\underline{\underline{s}} - \underline{\underline{X}}\right) : \left(\underline{\underline{s}} - \underline{\underline{X}}\right)}} - \frac{\dot{\xi}\Delta v \underline{\underline{I}}}{3} \right) - \frac{\dot{\lambda}[C_X(\xi)]\left(\underline{\underline{s}} - \underline{\underline{X}}\right)}{\sqrt{\frac{3}{2}\left(\underline{\underline{s}} - \underline{\underline{X}}\right) : \left(\underline{\underline{s}} - \underline{\underline{X}}\right)}}\right] - (1-\beta)\mathrm{C}_{a+m}\dot{\lambda} = 0 \tag{3.163}$$

After further simplifications:

$$\frac{\frac{3}{2}\left(\underline{\underline{s}} - \underline{\underline{X}}\right)}{\sqrt{\frac{3}{2}\left(\underline{\underline{s}} - \underline{\underline{X}}\right) : \left(\underline{\underline{s}} - \underline{\underline{X}}\right)}} : \left[\underline{\underline{\underline{\underline{E}}}} : \left(\dot{\underline{\underline{\varepsilon}}} - \frac{\dot{\xi}\Delta v \underline{\underline{I}}}{3} \right)\right] - \frac{\frac{3}{2}\left(\underline{\underline{s}} - \underline{\underline{X}}\right)}{\sqrt{\frac{3}{2}\left(\underline{\underline{s}} - \underline{\underline{X}}\right) : \left(\underline{\underline{s}} - \underline{\underline{X}}\right)}} : \underline{\underline{\underline{\underline{E}}}} : \frac{\dot{\lambda}\frac{3}{2}\left(\underline{\underline{s}} - \underline{\underline{X}}\right)}{\sqrt{\frac{3}{2}\left(\underline{\underline{s}} - \underline{\underline{X}}\right) : \left(\underline{\underline{s}} - \underline{\underline{X}}\right)}} - \dot{\lambda}[C_X(\xi)]$$

$$- (1-\beta)\mathrm{C}_{a+m}\dot{\lambda} = 0 \tag{3.164}$$

Finally the following formula is derived:

$$\dot{\lambda} = \frac{\frac{\frac{3}{2}\left(\underline{\underline{s}} - \underline{\underline{X}}\right)}{\sqrt{\frac{3}{2}\left(\underline{\underline{s}} - \underline{\underline{X}}\right) : \left(\underline{\underline{s}} - \underline{\underline{X}}\right)}} : \left[\underline{\underline{\underline{\underline{E}}}} : \left(\dot{\underline{\underline{\varepsilon}}} - \frac{\dot{\xi}\Delta v \underline{\underline{I}}}{3}\right)\right]}{\left[\frac{\frac{3}{2}\left(\underline{\underline{s}} - \underline{\underline{X}}\right)}{\sqrt{\frac{3}{2}\left(\underline{\underline{s}} - \underline{\underline{X}}\right) : \left(\underline{\underline{s}} - \underline{\underline{X}}\right)}} : \underline{\underline{\underline{\underline{E}}}} : \frac{\frac{3}{2}\left(\underline{\underline{s}} - \underline{\underline{X}}\right)}{\sqrt{\frac{3}{2}\left(\underline{\underline{s}} - \underline{\underline{X}}\right) : \left(\underline{\underline{s}} - \underline{\underline{X}}\right)}} - C_X(\xi) - (1-\beta)\mathrm{C}_{a+m}\right]} \tag{3.165}$$

Where the stress deviator $\underline{\underline{s}}$ was defined by Eq. 3.23. Inserting the constitutive law (Eq. 3.1) into Eq. 3.23 one obtains $\underline{\underline{s}}$ in the following form:

$$\underline{\underline{s}} = \underline{\underline{\underline{\underline{E}}}} : \left(\underline{\underline{\varepsilon}} - \underline{\underline{\varepsilon}}^{p} - \underline{\underline{\varepsilon}}^{bs}\right) - \frac{1}{3} Tr\left(\underline{\underline{\underline{\underline{E}}}} : \left(\underline{\underline{\varepsilon}} - \underline{\underline{\varepsilon}}^{p} - \underline{\underline{\varepsilon}}^{bs}\right)\right) \underline{\underline{I}} \tag{3.166}$$

As the plastic strain tensor $\underline{\underline{\varepsilon}}^{p}$ is present in the expression for the stress deviator $\underline{\underline{s}}$, which constitutes the final formula for the plastic multiplier $\dot{\lambda}$, no explicit calculation of $\dot{\lambda}$ is possible. Because of the entangled definition (Eq. 3.165), it has to be evaluated numerically by an iterative process.

The plastic multiplier $\dot{\lambda}$ (Eq. 3.165) depends on:

- the elastic stiffness tensor $\underline{\underline{\underline{\underline{E}}}}$,
- the volume fraction of martensite and its rate (ξ, $\dot{\xi}$) which are functions of the plastic strain (Eq. 3.8) and plastic strain rate (Eq. 3.9),
- homogenized modulus C_{a+m} (Eq. 3.120), which is a function of the parameters of the model and the martensite content (ξ),
- modulus $C_X(\xi)$ defined by Eq. 3.123, which is a function of model parameters and ξ,
- the kinematic hardening variable $\underline{\underline{X}}$ (Eq. 3.136), which depends on the modulus $C_X(\xi)$ and the plastic strain tensor $\underline{\underline{\varepsilon}}^{p}$.

3.6. Summary of the constitutive model

In the present section, the results of all the derivations are summed up. The final formulas are repeated for clarity.

The constitutive model consists of the following equations:

1. The relationship between the stress and the strain (Eq. 3.1), while the thermal strain is ignored $\underline{\underline{\varepsilon}}^{th} = \underline{\underline{0}}$. Thus:

$$\underline{\underline{\sigma}} = \underline{\underline{\underline{\underline{E}}}} : \left(\underline{\underline{\varepsilon}} - \underline{\underline{\varepsilon}}^{p} - \underline{\underline{\varepsilon}}^{bs}\right) \tag{3.167}$$

2. The definition of the “Bain strain” tensor (Eq. 3.20):

$$\underline{\underline{\varepsilon}}^{bs} = \xi \cdot \frac{1}{3} \Delta v \underline{\underline{I}} \tag{3.168}$$

3. The kinetics of the plastic strain induced phase transformation (Eq. 3.9):

$$\dot{\xi} = A(T) \cdot \dot{p} \cdot H\left[\left(\mathrm{p} - \mathrm{p}_{\xi}\right)\left(\xi_L - \xi\right)\right] \tag{3.169}$$

4. The definition of the plastic strain rate tensor (Eq. 3.144):

$$\underline{\underline{\dot{\varepsilon}}}^{p} = \dot{\lambda}\frac{3}{2}\frac{\left(\underline{\underline{s}}-\underline{\underline{X}}\right)}{\sqrt{\frac{3}{2}\left(\underline{\underline{s}}-\underline{\underline{X}}\right):\left(\underline{\underline{s}}-\underline{\underline{X}}\right)}} \tag{3.170}$$

5. The plastic multiplier (Eq. 3.165):

$$\dot{\lambda} = \frac{\frac{\frac{3}{2}\left(\underline{\underline{s}}-\underline{\underline{X}}\right)}{\sqrt{\frac{3}{2}\left(\underline{\underline{s}}-\underline{\underline{X}}\right):\left(\underline{\underline{s}}-\underline{\underline{X}}\right)}}:\left[\underline{\underline{\underline{\underline{E}}}}:\left(\underline{\underline{\dot{\varepsilon}}}-\frac{\dot{\xi}\Delta v\underline{\underline{I}}}{3}\right)\right]}{\left[\frac{\frac{3}{2}\left(\underline{\underline{s}}-\underline{\underline{X}}\right)}{\sqrt{\frac{3}{2}\left(\underline{\underline{s}}-\underline{\underline{X}}\right):\left(\underline{\underline{s}}-\underline{\underline{X}}\right)}}:\underline{\underline{\underline{\underline{E}}}}:\frac{\frac{3}{2}\left(\underline{\underline{s}}-\underline{\underline{X}}\right)}{\sqrt{\frac{3}{2}\left(\underline{\underline{s}}-\underline{\underline{X}}\right):\left(\underline{\underline{s}}-\underline{\underline{X}}\right)}}-C_X(\xi)-(1-\beta)\mathrm{C}_{a+m}\right]} \tag{3.171}$$

6. The evolution of the kinematic hardening variable $\underline{\underline{\dot{X}}}$ (Eq. 3.122):

$$\underline{\underline{\dot{X}}} = \frac{2}{3}[C_{a0}+C_{a0}h\xi+(1-\beta)\mathrm{C}_{a+m}]\underline{\underline{\dot{\varepsilon}}}^{p} = \frac{2}{3}C_X(\xi)\underline{\underline{\dot{\varepsilon}}}^{p} \tag{3.172}$$

7. The evolution of the isotropic hardening variable $\dot{R}$ (Eq. 3.130):

$$\dot{R} = (1-\beta)\mathrm{C}_{a+m}\dot{p} \tag{3.173}$$

8. The accumulated plastic strain rate $\dot{p}$ (Eq. 3.10):

$$\dot{p} = \sqrt{\frac{2}{3}\underline{\underline{\dot{\varepsilon}}}^{p}:\underline{\underline{\dot{\varepsilon}}}^{p}} \tag{3.174}$$

9. The expression for the homogenized modulus C_{a+m} (Eq. 3.120):

$$\mathrm{C}_{a+m} = \frac{E_a\cdot C_{a0}(1+h\xi)}{[E_a+C_{a0}(1+h\xi)]}\frac{\xi\frac{15}{2}\frac{(1-\nu_\mathrm{a})}{(4-5\nu_\mathrm{a})(1+\nu_\mathrm{a})}\left[\frac{\mathrm{E_m}}{(1+\nu_\mathrm{m})}-\frac{E_a\cdot C_{a0}(1+h\xi)}{[E_a+C_{a0}(1+h\xi)](1+\nu_\mathrm{a})}\right]}{\left[\frac{\mathrm{E_m}(1-\xi)}{(1+\nu_\mathrm{m})}+\frac{E_a\cdot C_{a0}(1+h\xi)}{[E_a+C_{a0}(1+h\xi)](1+\nu_\mathrm{a})}\left(\xi+\frac{(7-5\nu_\mathrm{a})}{2(4-5\nu_\mathrm{a})}\right)\right]} \tag{3.175}$$

10. The expression for the modulus $C_X(\xi)$ (Eq. 3.135):

$$C_X(\xi) = C_{a0}(1+h\xi)+\frac{(1-\beta)E_aC_{a0}(1+h\xi)}{2[E_a+C_{a0}(1+h\xi)]}\frac{15\xi\cdot(1-\nu_\mathrm{a})}{(4-5\nu_\mathrm{a})(1+\nu_\mathrm{a})}\left[\frac{\mathrm{E_m}}{(1+\nu_\mathrm{m})}-\frac{E_a\cdot C_{a0}(1+h\xi)}{[E_a+C_{a0}(1+h\xi)](1+\nu_\mathrm{a})}\right]\left[\frac{\mathrm{E_m}(1-\xi)}{(1+\nu_\mathrm{m})}+\frac{E_a\cdot C_{a0}(1+h\xi)}{[E_a+C_{a0}(1+h\xi)](1+\nu_\mathrm{a})}\left(\xi+\frac{(7-5\nu_\mathrm{a})}{2(4-5\nu_\mathrm{a})}\right)\right] \tag{3.176}$$

The above presented constitutive model has the following material dependent parameters (12):

1. Parameters related to the phase transformation:

$A(T)$	ε_ξ^p	ξ_L	Δv

Table 3.1. Parameters related to the kinetics of the phase transformation

2. Parameters related to the continuum model:

E_a	C_{a0}	ν_a	$\mathrm{E_m}$	ν_m	h	β	ε_0

Table 3.2. Parameters related to the continuum model

Calibration of the above parameters is addressed in the next chapter.

4. Uniaxial constitutive model of continuum undergoing shear strain induced phase transformation

4.1. Introduction

Describing the evolution of the phase transformation, in a circular bar subjected to torsion, is of particular importance for the present work. Closed-form analytical solutions are sought in order to avoid time consuming and complex FEM simulations, which requires writing user defined routines, debugging and testing.
The most important aspect of the 3D model that allows obtaining closed-form analytical solutions is the simplified description of the transformation kinetics. Having described the evolution of martensite as a piecewise linear function (instead of double exponent one) drastically reduced the complexity of the hardening modulus C_{a+m}.
In order to make the analytical integration of C_{a+m} with respect to shear strain possible, the function C_{a+m} was simplified. Some terms have been omitted as they were insignificant compared to the others. Yet, it turned out that the results obtained from the simplified analytical formula and obtained numerically from the exact representation of C_{a+m} are in very good agreement, which validates the approach (see Chapter 8).
In the first section the kinetics of the plastic strain induced phase transformation is described for the case of torsion. Later on, the relationship between the stress and the strain is derived. Finally, the stress distribution is integrated over the cross-section of the bar and the global relationship between the torque and the angle of twist is obtained.
The relationship between the torque and the angle of twist is very important as it allows comparison with the experimentally measured values. By fitting the theoretical curve to the experimental results one can identify the parameters of the constitutive model.
The experiments have been carried out at two temperature levels: at 77K, the temperature of liquid nitrogen bath, and at ambient temperature (293K). The experimental set-up and the results are described in Chapter 5 and, later on, in Chapter 8 a comparison between the theoretical and the experimental results is presented.

4.2. Kinetics of the shear strain induced phase transformation

As indicated in section 3.3, the phase transformation is driven by the plastic strains or, in the general case, by the accumulated plastic strain. The same holds for pure torsion, where only the shear component of the strain occurs. Thus, under torsion the phase transformation is driven by the plastic shear strain γ^p. Referring to Eq. 3.7, the transformation kinetics can be written as:

$$\dot{\xi} = A(T) \cdot \dot{\gamma}^p \cdot H\left[\left(\gamma^p - \gamma_\xi^p\right)(\xi_L - \xi)\right] \tag{4.1}$$

or in the incremental form:

$$\mathrm{d}\xi = A(T) \cdot \mathrm{d}\gamma^{\mathrm{p}} \cdot H\left[\left(\gamma^p - \gamma_\xi^p\right)(\xi_L - \xi)\right] \tag{4.2}$$

Again, double Heaviside function $H\left[\left(\gamma^p - \gamma_\xi^p\right)(\xi_L - \xi)\right]$ has been used. This function takes the value of 1 if the argument is greater of equal to 0, and 0 otherwise.

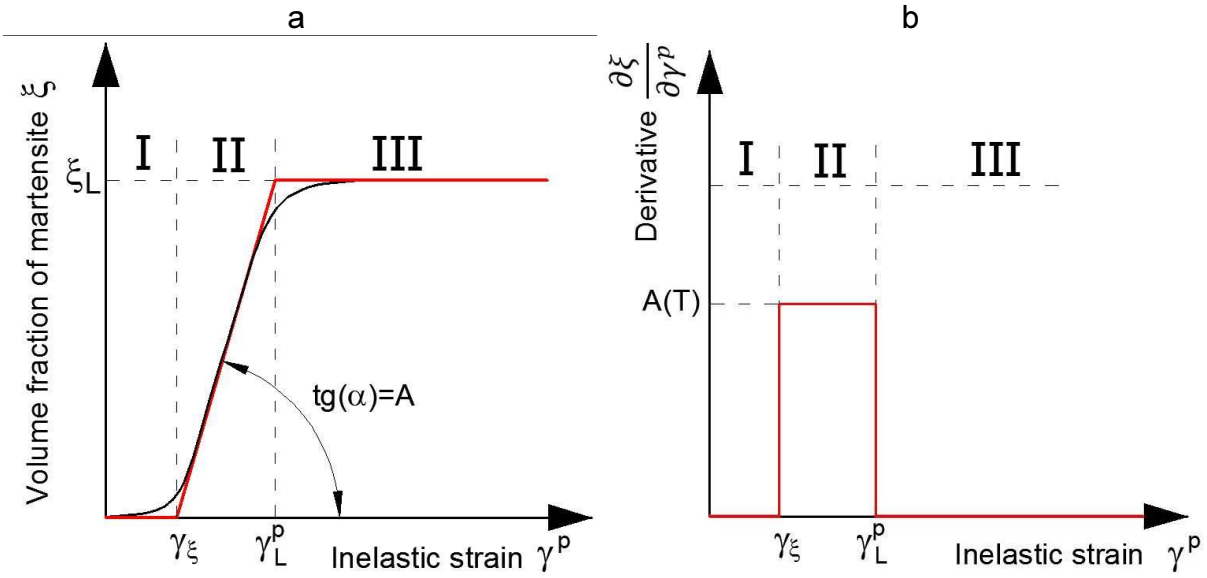

Figure 4.1. a) Volume fraction of martensite versus plastic shear strain, b) the derivative $\partial\xi/\partial\gamma^p$

Eq. 4.2 can be integrated explicitly over the plastic shear strain $\mathrm{d}\gamma^{\mathrm{p}}$:

$$\xi = \int_0^{\gamma^p} A(T) \cdot H\left[\left(\gamma^p - \gamma_\xi^p\right)\left(\xi_L - \xi\right)\right] d\gamma \tag{4.3}$$

Depending on the value of the integral limit γ^p, this integral can take three values:

$$\xi = \begin{cases} 0, & \gamma^p \le \gamma_\xi^p \\ A(T) \cdot \left(\gamma^p - \gamma_\xi^p\right) & \gamma_\xi^p < \gamma^p \le \gamma_L^p \\ \xi_L & \gamma^p > \gamma_L^p \end{cases} \tag{4.4}$$

So, for shear strains smaller than the threshold γ_ξ^p, no phase transformation occurs (Fig. 4.1a). For shear strain greater than γ_ξ^p and smaller than γ_L^p, the martensite content is a linear function of the shear strain. Lastly, for shear strains greater than γ_L^p saturation occurs and the limit of martensite content has been achieved. It is worth pointing out, that the evolution of martensite content can happen only for $\gamma_\xi^p < \gamma^p \le \gamma_L^p$ (Fig. 4.1b). The rate $(\partial\xi/\partial\gamma^p)$ is then equal to $A(T)$, which is a temperature dependent material function.

4.3. Derivation of the stress versus strain relationship

In the present section the stress-strain relations for a round bar undergoing plastic strain induced phase transformation will be derived. Torsional deformation, including the main parameters such as the angle of twist φ and the shear strain γ, is illustrated in Fig 4.2. It is assumed that generatrix (line on the surface parallel to the axis of the bar) remains straight after twisting (Fig. 4.2).

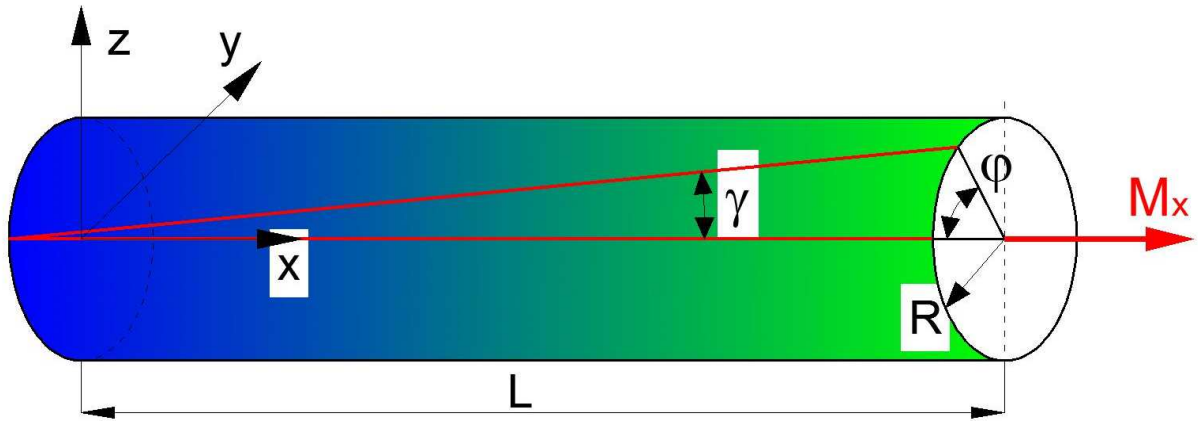

Figure 4.2. Kinetics of deformation in simple torsion; γ is the shear strain, φ denotes the angle of twist

The shear stress τ and the shear strain γ within the *yz* plane are the only non-zero components of the stress and the strain tensors:

$$\underline{\underline{\varepsilon}} = \begin{pmatrix} 0 & 0 & 0 \\ 0 & 0 & \varepsilon_{yz} \\ 0 & \varepsilon_{zy} & 0 \end{pmatrix} = \begin{pmatrix} 0 & 0 & 0 \\ 0 & 0 & \gamma/2 \\ 0 & \gamma/2 & 0 \end{pmatrix} \tag{4.5}$$

$$\underline{\underline{\sigma}} = \begin{pmatrix} 0 & 0 & 0 \\ 0 & 0 & \tau_{yz} \\ 0 & \tau_{zy} & 0 \end{pmatrix} = \begin{pmatrix} 0 & 0 & 0 \\ 0 & 0 & \tau \\ 0 & \tau & 0 \end{pmatrix} \tag{4.6}$$

The constitutive model has been reduced to one-dimensional relationships between the shear stress τ and the shear strain γ. The model is presented in Fig. 4.3. It is described by three separate functions in the regions I (elastic), II (elastic-plastic) and III (phase transformation).

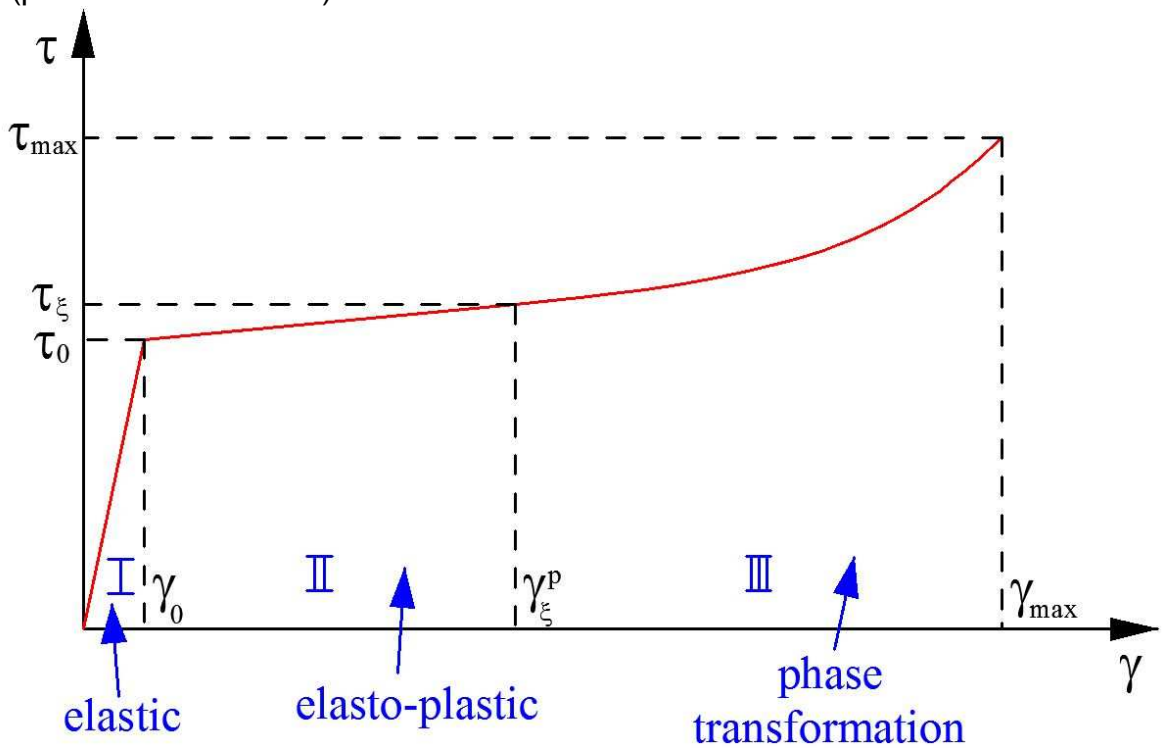

Figure 4.3. One-dimensional constitutive model of shear strain induced phase transformation

The first portion of the stress-strain curve refers to the elastic range (part I), the second portion refers to the elastic-plastic range (part II) including linear hardening, and the third portion refers to nonlinear hardening (part III) caused by the plastic strain induced phase transformation.
The nonlinear hardening in the 3rd portion may be decomposed into 3 elements:

- classical linear hardening,
- hardening due to interactions between dislocations and inclusions,
- increase of tangent stiffness due to evolution of proportion between two constituents (austenite and martensite).

In the description of one dimensional model, the following symbols are used:

- γ_0 is the elastic shear strain limit,
- γ_ξ^p denotes the phase transformation threshold,
- γ_{max} is the shear strain limit related to the small strains assumption,
- τ_0 denotes the yield shear stress,
- τ_ξ stands for the shear stress corresponding to the beginning of the phase transformation,
- τ_{max} is the maximum shear stress corresponding to γ_{max}.

4.3.1. Difference between the Cauchy and the Hencky strain measures

In order to define the shear strain limit γ_{max} in the framework of small-strains theory, a comparison of the Cauchy and the Hencky strain measures has been carried out. Using the well-known formulas for small (Cauchy) and true (Hencky) strains, one can compute the relative difference between them, Fig. 4.4:

$$\varepsilon_C = \frac{\Delta l}{l_0} \qquad \varepsilon_H = ln(1+\varepsilon_C) \qquad Difference[\%] = \frac{\varepsilon_C - \varepsilon_H}{\varepsilon_C} \cdot 100\% \tag{4.7}$$

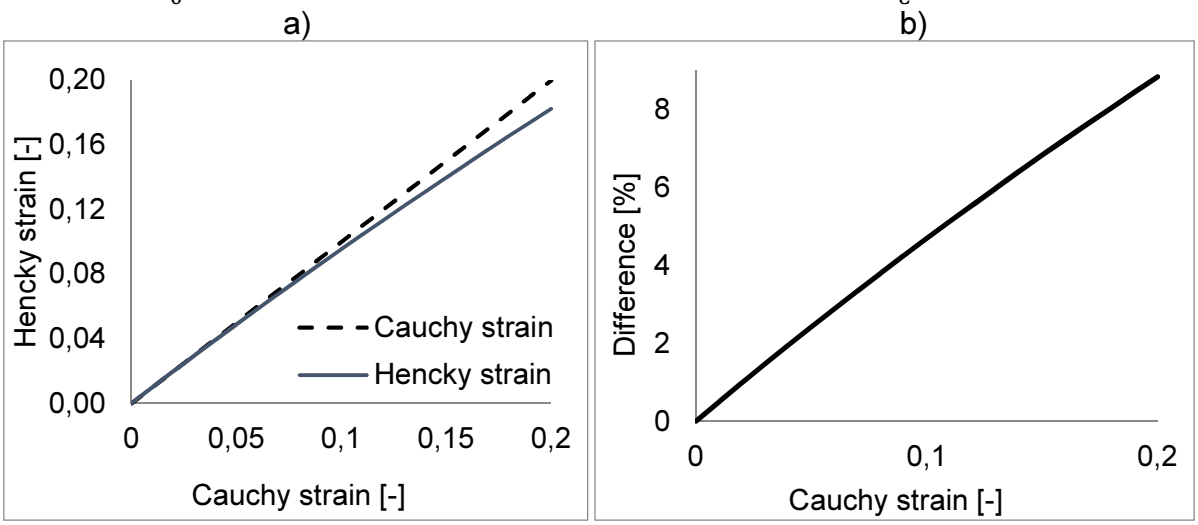

Figure 4.4. a) Hencky strain as a function of Cauchy strain, b) The relative difference between both strain measures

By limiting the normal strain to ε_C=0.2 one commits an error smaller than 9% (Fig. 4.4b). The normal strain can be converted to shear strain by using the equivalence of strain intensities:

$$\varepsilon_{eq}^p = \sqrt{\frac{2}{3}\left[\left(\varepsilon_{11}^p\right)^2 + \left(\varepsilon_{22}^p\right)^2 + \left(\varepsilon_{33}^p\right)^2 + 2\cdot\left[\left(\varepsilon_{12}^p\right)^2 + \left(\varepsilon_{13}^p\right)^2 + \left(\varepsilon_{23}^p\right)^2\right]\right]} \tag{4.8}$$

Inserting the components of the strain tensor (Eq. 4.5) into the definition of ε_{eq}^{p} (4.8) one obtains:

$$\varepsilon_{eq}^{p} = \sqrt{\frac{2}{3}\left[0+0+0+2\cdot\left[0^2+0^2+\left(\frac{\gamma}{2}\right)^2\right]\right]} = \sqrt{\frac{2}{3}\cdot 2\left[\frac{\gamma}{2}\right]^2} = \frac{\gamma}{\sqrt{3}} \tag{4.9}$$

Thus, assuming the maximum axial strain of $\varepsilon_{max} = 0.2$, one gets:

$$\gamma_{max} = \sqrt{3}\cdot\varepsilon_C = \sqrt{3}\cdot 0.2 = 0.346 \tag{4.10}$$

Thus within the framework of small strains, the limit of the normal strain ($\varepsilon_{max} = 0.2$) yields for the case of torsional loading: $\gamma_{max} = 0.346$.

4.3.2. General equations describing the constitutive model

Having defined general limit of the model in terms of shear strain γ_{max}, the stress-strain relations are derived by contracting 3D model presented in Chapter 3 to one-dimensional case. Keeping in mind Fig. 4.3, the elastic part (I) follows the linear elasticity law, therefore:

$$\tau_I = G\cdot\gamma \tag{4.11}$$

where $G = \mu_a$ denotes the shear modulus of pure austenite.
The elastic-plastic part (II) with linear hardening can be described by:

$$\tau_{II} = \tau_0 + C_{a0}\cdot(\gamma - \gamma_0) \tag{4.12}$$

where C_{a0} is the basic linear hardening modulus of pure austenite. Finally, within the phase transformation part (III), the shear stress is defined as:

$$\tau_{III} = \tau_\xi + \Delta\tau_3 \tag{4.13}$$

where the stress increment $\Delta\tau_3$ consists of three terms corresponding to: linear hardening, interaction between dislocations and inclusions and homogenization (Fig. 4.5):

$$\Delta\tau_3 = \Delta\tau_{\text{lin}} + \Delta\tau_{\text{int}} + \Delta\tau_{\text{MT}} \tag{4.14}$$

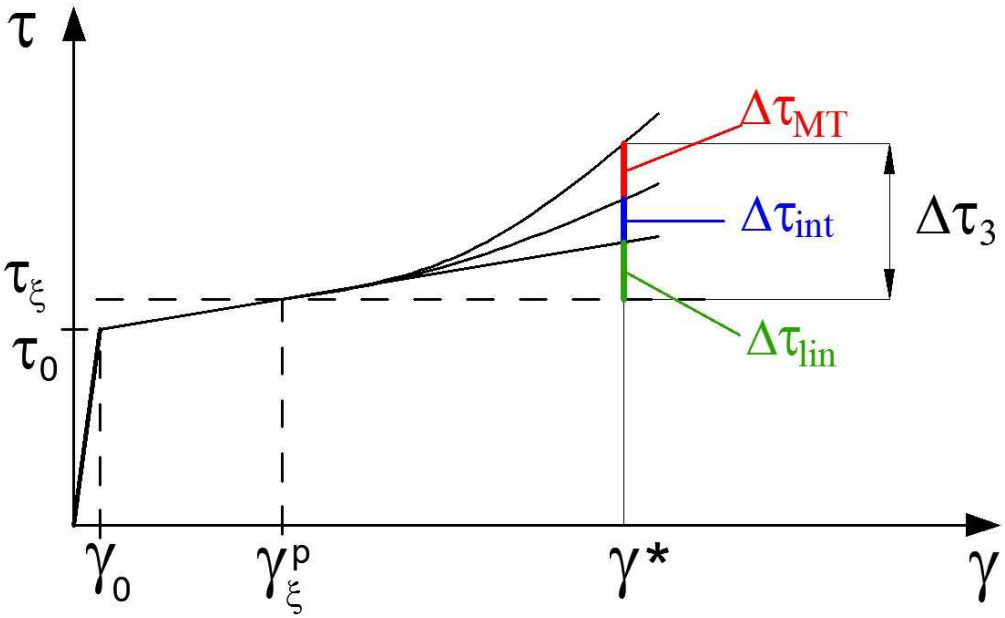

Figure 4.5. Stress increments within the phase transformation range

The infinitesimal representation of the first increment $d\tau_{\mathrm{lin}}$ equals:

$$d\tau_{\mathrm{lin}} = C_{a0} \cdot \mathrm{d}\gamma^p \tag{4.15}$$

It describes the hardening of purely austenitic phase. The second increment $d\tau_{\mathrm{int}}$ reads:

$$d\tau_{\mathrm{int}} = C_{a0} \cdot \mathrm{h} \cdot \xi \cdot \mathrm{d}\gamma^p \tag{4.16}$$

This term has been derived based on the Orowan mechanism (Eq. 3.41) and is proportional to the volume fraction of martensite (ξ). The parameter h can be identified from the torsion experiments, as the best fit w.r.t. the experimental data.

The third increment $d\tau_{\mathrm{MT}}$ can be derived based on the general formula for the stress increment, caused by the presence of martensite (Eq. 3.90). Reducing Eq. 3.90 to one dimensional case of torsion gives:

$$\Delta\tau_{MT} = 2(\mu_{MT} - \mu_{ta})\Delta\varepsilon^p \tag{4.17}$$

Taking into account the fact that $\Delta\varepsilon^p = \Delta\gamma^p/2$ one obtains:

$$\Delta\tau_{MT} = 2(\mu_{MT} - \mu_{ta})\frac{\Delta\gamma^p}{2} = \frac{1}{2}\mathrm{C}_{a+m}\Delta\gamma^p \tag{4.18}$$

Thus, the increment $d\tau_{\mathrm{MT}}$ equals:

$$d\tau_{\mathrm{MT}} = \frac{1}{2}\mathrm{C}_{a+m}\mathrm{d}\gamma^p \tag{4.19}$$

It is quite important to keep in mind that the increment $d\tau_{\mathrm{MT}}$ is proportional to the increment of plastic shear strain $\mathrm{d}\gamma^p$ and the modulus C_{a+m}, and there is a factor of "1/2" there.

Inserting into the expression for τ_{III} (Eq. 4.13) the increments $d\tau_{\mathrm{lin}}$ (Eq. 4.15), $d\tau_{\mathrm{int}}$ (Eq. 4.16) and $d\tau_{\mathrm{MT}}$ (Eq. 4.19) gives:

$$\tau_{III} = \tau_\xi + \int_{\gamma_\xi}^{\gamma} \left[C_{a0} \cdot \left(1 + h\xi(\gamma)\right) + \frac{1}{2}C_{a+m}\right]\mathrm{d}\gamma^p \qquad \gamma_\xi < \gamma < \gamma_{max} \tag{4.20}$$

where the modulus C_{a+m} was derived in Chapter 3 (Eq. 3.120). The final formula for C_{a+m} is repeated here for convenience:

$$\mathrm{C}_{a+m} = \frac{E_a \cdot C_{a0}(1+h\xi)}{[E_a + C_{a0}(1+h\xi)]} \frac{\xi\frac{15}{2}\frac{(1-\nu_\mathrm{a})}{(4-5\nu_\mathrm{a})(1+\nu_\mathrm{a})}\left[\frac{\mathrm{E_m}}{(1+\nu_\mathrm{m})} - \frac{E_a \cdot C_{a0}(1+h\xi)}{[E_a + C_{a0}(1+h\xi)](1+\nu_\mathrm{a})}\right]}{\left[\frac{\mathrm{E_m}(1-\xi)}{(1+\nu_\mathrm{m})} + \frac{E_a \cdot C_{a0}(1+h\xi)}{[E_a + C_{a0}(1+h\xi)](1+\nu_\mathrm{a})}\left(\xi + \frac{(7-5\nu_\mathrm{a})}{2(4-5\nu_\mathrm{a})}\right)\right]} \tag{4.21}$$

The integral (4.20) cannot be calculated analytically. In order to obtain a closed-form solution, some simplifications have to be introduced into C_{a+m} (Eq. 4.21). Nevertheless, Eq. 4.21 will be integrated numerically in order to evaluate the error induced by the postulated simplifications.

All the introduced simplifications are addressed in the following section.

4.3.3. Simplifications of the modulus C_{a+m}

The first postulate consists in equality of the Young moduli of pure austenite and of pure martensite $E_a = E_m$, which is actually true for the austenitic stainless steels. This leads to the following formula for C_{a+m}:

$$\mathrm{C}_{a+m} = \frac{E_a \cdot C_{a0}(1+h\xi)}{[E_a + C_{a0}(1+h\xi)]} \frac{\xi\frac{15}{2}\frac{(1-\nu_\mathrm{a})}{(4-5\nu_\mathrm{a})(1+\nu_\mathrm{a})}\left[\frac{\mathrm{E_a}}{(1+\nu_\mathrm{m})} - \frac{E_a \cdot C_{a0}(1+h\xi)}{[E_a + C_{a0}(1+h\xi)](1+\nu_\mathrm{a})}\right]}{\left[\frac{\mathrm{E_a}(1-\xi)}{(1+\nu_\mathrm{m})} + \frac{E_a \cdot C_{a0}(1+h\xi)}{[E_a + C_{a0}(1+h\xi)](1+\nu_\mathrm{a})}\left(\xi + \frac{(7-5\nu_\mathrm{a})}{2(4-5\nu_\mathrm{a})}\right)\right]}$$

(4.22)

After dividing the numerator and the denominator of Eq. 4.22 by E_a one gets:

$$C_{a+m} = \frac{E_a \cdot C_{a0}(1+h\xi)}{[E_a + C_{a0}(1+h\xi)]} \frac{\xi \frac{15}{2} \frac{(1-\nu_a)}{(4-5\nu_a)(1+\nu_a)} \left[\frac{1}{(1+\nu_m)} - \frac{C_{a0}(1+h\xi)}{[E_a + C_{a0}(1+h\xi)](1+\nu_a)}\right]}{\left[\frac{(1-\xi)}{(1+\nu_m)} + \frac{C_{a0}(1+h\xi)}{[E_a + C_{a0}(1+h\xi)](1+\nu_a)}\left(\xi + \frac{(7-5\nu_a)}{2(4-5\nu_a)}\right)\right]} \tag{4.23}$$

Extracting the term E_a in the fractions leads to:

$$C_{a+m} = \frac{C_{a0}(1+h\xi)}{\left[1 + \frac{C_{a0}}{E_a}(1+h\xi)\right]} \frac{\xi \frac{15}{2} \frac{(1-\nu_a)}{(4-5\nu_a)(1+\nu_a)} \left[\frac{1}{(1+\nu_m)} - \frac{\frac{C_{a0}}{E_a}(1+h\xi)}{\left[1 + \frac{C_{a0}}{E_a}(1+h\xi)\right](1+\nu_a)}\right]}{\left[\frac{(1-\xi)}{(1+\nu_m)} + \frac{\frac{C_{a0}}{E_a}(1+h\xi)}{\left[1 + \frac{C_{a0}}{E_a}(1+h\xi)\right](1+\nu_a)}\left(\xi + \frac{(7-5\nu_a)}{2(4-5\nu_a)}\right)\right]} \tag{4.24}$$

The modulus C_{a0} is of the order of $2 \cdot 10^9$ *Pa*, the constant *h* is of the order of $h \approx 1$, and the Young modulus E_a is of the order of $2 \cdot 10^{11}$ *Pa*, whereas the martensite content ξ ranges from 0 to 1. So for $h=1$ and $\xi = 1$ the term $\frac{C_{a0}}{E_a}(1+h\xi)$ is approximately equal to:

$$\frac{C_{a0}}{E_a}(1+h\xi) \cong \frac{2 \cdot 10^9}{2 \cdot 10^{11}}(1+1) = 0.02 \tag{4.25}$$

Thus, the above result is fairly small when compared to unity, therefore, this term may be neglected.

After neglecting the term $\frac{C_{a0}}{E_a}(1+h\xi)$ (compared to 1) in Eq. 4.24, one obtains:

$$C_{a+m} = \frac{C_{a0}(1+h\xi)}{1} \frac{\xi \frac{15}{2} \frac{(1-\nu_a)}{(4-5\nu_a)(1+\nu_a)} \left[\frac{1}{(1+\nu_m)} - \frac{\frac{C_{a0}}{E_a}(1+h\xi)}{(1+\nu_a)}\right]}{\left[\frac{(1-\xi)}{(1+\nu_m)} + \frac{\frac{C_{a0}}{E_a}(1+h\xi)}{(1+\nu_a)}\left(\xi + \frac{(7-5\nu_a)}{2(4-5\nu_a)}\right)\right]} \tag{4.26}$$

In the numerator the term:

$$\frac{C_{a0}(1+h\xi)}{E_a(1+\nu_a)} \tag{4.27}$$

is small when compared to:

$$\frac{1}{(1+\nu_m)} \tag{4.28}$$

Inserting the numbers, the following estimation is made (for $\xi = 1$ the first term reaches its maximum):

$$\frac{C_{a0}(1+h\xi)}{E_a(1+\nu_a)} = \frac{2 \cdot 10^9 \cdot (1+1)}{2 \cdot 10^{11} \cdot (1+0.5)} = \frac{2}{150} = 0.01(3) \tag{4.29}$$

$$\frac{1}{(1+\nu_m)} = \frac{1}{(1+0.3)} \cong 0.769 \tag{4.30}$$

Thus, the ratio of the terms (4.30) and (4.29) equals: $0.769/0.01(3) = 57.7$. Again, the term $C_{a0}(1+h\xi)/E_a(1+\nu_a)$ turns out to be small when compared to the term $1/(1+\nu_m)$, and can be omitted.

As a result, Eq. 4.26 reduces to:

$$C_{a+m} = \frac{C_{a0}(1+h\xi)}{1} \frac{\xi \frac{15}{2} \frac{(1-\nu_a)}{(4-5\nu_a)(1+\nu_a)} \left[\frac{1}{(1+\nu_m)}\right]}{\left[\frac{(1-\xi)}{(1+\nu_m)} + \frac{C_{a0}(1+h\xi)}{E_a(1+\nu_a)}\left(\xi + \frac{(7-5\nu_a)}{2(4-5\nu_a)}\right)\right]} \tag{4.31}$$

Additionally, the following term in the denominator:

$$\frac{C_{a0}(1+h\xi)}{E_a(1+\nu_a)}\left(\xi + \frac{(7-5\nu_a)}{2(4-5\nu_a)}\right) \tag{4.32}$$

may be neglected when compared to:

$$\frac{(1-\xi)}{(1+\nu_m)} \tag{4.33}$$

To prove this, two expressions from the denominator are estimated for extreme values of the parameter ξ, $\xi = 0$ and $\xi = 1$. For $\xi = 0$ one has:

$$\xi = 0, \quad \frac{C_{a0}(1+h\xi)}{E_a(1+\nu_a)}\left(\xi + \frac{(7-5\nu_a)}{2(4-5\nu_a)}\right) = \frac{2\cdot 10^9}{2\cdot 10^{11}(1+0.5)}\left(\frac{(7-5\cdot 0.5)}{2(4-5\cdot 0.5)}\right)$$
$$= \frac{1}{100\cdot(1+0.5)}\left(\frac{4.5}{3}\right) = 0.01 \tag{4.34}$$

$$\xi = 0, \quad \frac{(1-\xi)}{(1+\nu_m)} = \frac{1}{(1+0.3)} = 0.769 \tag{4.35}$$

Thus for $\xi = 0$ the ratio of terms: $(1-\xi)/(1+\nu_m)$ to $\frac{C_{a0}(1+h\xi)}{E_a(1+\nu_a)}\left(\xi + \frac{(7-5\nu_a)}{2(4-5\nu_a)}\right)$ equals $0.769/0.01 = 76.9$. Thus the second term is small in comparison to the first one, and can further be ignored.

For $\xi = 1$ one obtains:

$$\xi = 1, \quad \frac{C_{a0}(1+h\xi)}{E_a(1+\nu_a)}\left(\xi + \frac{(7-5\nu_a)}{2(4-5\nu_a)}\right) = \frac{2\cdot 10^9\cdot 2}{2\cdot 10^{11}(1+0.5)}\left(1 + \frac{(7-5\cdot 0.5)}{2(4-5\cdot 0.5)}\right)$$
$$= \frac{2}{100\cdot 1.5}\left(\frac{7.5}{3}\right) = \frac{1}{30} = 0.0(3) \tag{4.36}$$

$$\xi = 1, \quad \frac{(1-\xi)}{(1+\nu_m)} = \frac{0}{(1+0.3)} = 0 \tag{4.37}$$

In this case the second term is equal to 0, and the first term is non-zero, which is contradictory w.r.t. initial assumption. However, the extreme case of $\xi = 1$ will in reality never appear, since the phase transformation is usually limited to $\xi = \xi_L \cong 0.5$. For which the second term equals

$$\xi = 0.5, \quad \frac{(1-0.5)}{(1+\nu_m)} = \frac{0.5}{(1+0.3)} = 0.385 \tag{4.38}$$

Now, the ratio of the terms $(1-\xi)/(1+\nu_m)$ to $\frac{C_{a0}(1+h\xi)}{E_a(1+\nu_a)}\left(\xi + \frac{(7-5\nu_a)}{2(4-5\nu_a)}\right)$ equals $0.385/0.0(3) = 11.6$. Thus, the second term is relatively small and might also be neglected.

Eq. 4.31 now reads:

$$\mathrm{C}_{a+m} = \frac{C_{a0}(1+h\xi)}{1}\,\frac{\xi\dfrac{15}{2}\dfrac{(1-\nu_a)}{(4-5\nu_a)(1+\nu_a)}\left[\dfrac{1}{(1+\nu_m)}\right]}{\left[\dfrac{(1-\xi)}{(1+\nu_m)}\right]} \tag{4.39}$$

Eventually, a simplified formula for C_{a+m} is postulated in the form:

$$\mathrm{C}_{a+m} = \frac{15}{2}\frac{(1-\nu_a)\cdot C_{a0}}{(4-5\nu_a)(1+\nu_a)}\frac{\xi(1+h\xi)}{(1-\xi)} \tag{4.40}$$

The final expression for the homogenized modulus C_{a+m} has been drastically simplified compared to Eq. 4.21. The volume fraction of martensite is a function of the plastic shear strain (Eq. 4.4). Inserting the active part of Eq. 4.4 (for $\gamma > \gamma_\xi^p$) into Eq. 4.40 gives:

$$\mathrm{C}_{a+m}(\gamma) = \frac{15}{2}\frac{(1-\nu_a)\cdot C_{a0}}{(4-5\nu_a)(1+\nu_a)}\frac{A(T)\cdot\left(\gamma^p-\gamma_\xi^p\right)\left(1+hA(T)\cdot\left(\gamma^p-\gamma_\xi^p\right)\right)}{\left(1-A(T)\cdot\left(\gamma^p-\gamma_\xi^p\right)\right)} \tag{4.41}$$

In what follows, it is assumed that the plastic strain is equal to the total strain: $\gamma^p \approx \gamma$. This is justified by the fact, that the elastic shear strain amounts to $\gamma_0 \approx 0.007$, which is very small when compared to $\gamma_{max} \approx 0.34$. Therefore, the following assumption is made:

$$\gamma^p = \gamma \tag{4.42}$$

Thus, from Eq. 4.41 one obtains:

$$\mathrm{C}_{a+m}(\gamma) = \frac{15}{2}\frac{(1-\nu_a)\cdot C_{a0}}{(4-5\nu_a)(1+\nu_a)}\frac{A(T)\cdot\left(\gamma-\gamma_\xi^p\right)\left(1+hA(T)\cdot\left[\gamma-\gamma_\xi^p\right]\right)}{\left(1-A(T)\cdot\left[\gamma-\gamma_\xi^p\right]\right)} \tag{4.43}$$

The simplified (Eq. 4.43) and exact (Eq. 4.21) formulas for the modulus C_{a+m} are compared in the chapter 8, after the identification of the parameters of the model.

4.3.4. Simplification of the shear stress versus shear strain relations

Inserting the previously derived modulus $\mathrm{C}_{a+m}(\gamma)$ (Eq. 4.43) into the equation for stress τ_{III} (Eq. 4.20), one arrives at:

$$\tau_{III} = \tau_\xi + \int_{\gamma_\xi}^{\gamma}\left[C_{a0}\cdot\left(1+hA\cdot\left(\gamma-\gamma_\xi^p\right)\right)+\frac{15}{4}\frac{(1-\nu_a)\cdot C_{a0}}{(4-5\nu_a)(1+\nu_a)}\frac{A\cdot\left(\gamma-\gamma_\xi^p\right)\left(1+hA\left[\gamma-\gamma_\xi^p\right]\right)}{\left(1-A\cdot\left[\gamma-\gamma_\xi^p\right]\right)}\right]\mathrm{d}\gamma \tag{4.44}$$

After performing the integration one obtains:

$$\tau_{III} = \tau_\xi + \frac{1}{2}C_{a0}\left(\gamma-\gamma_\xi^p\right)\left[2+Ah\left(\gamma-\gamma_\xi^p\right)\right] + \frac{15C_{a0}(\nu_a-1)}{4A(-4+\nu_a+5\nu_a^2)}\left[A\left(\gamma-\gamma_\xi^p\right)\left(2+Ah\left(\gamma-\gamma_\xi^p\right)\right)+2(1+h)ln\left(1-A\left(\gamma-\gamma_\xi^p\right)\right)\right] \tag{4.45}$$

The final formula has been verified using the symbolic integration in the Mathematica software. Summing up, the shear stresses are defined as follows:

$$\tau_I = G \cdot \gamma \qquad \boldsymbol{\gamma < \gamma_0} \tag{4.46}$$

$$\tau_{II} = \tau_0 + C_{a0} \cdot (\gamma - \gamma_0) \qquad \boldsymbol{\gamma_0 < \gamma < \gamma_\xi^p} \tag{4.47}$$

$$\tau_{III} = \tau_\xi + \frac{1}{2} C_{a0}\left(\gamma - \gamma_\xi^p\right)\left[2 + Ah\left(\gamma - \gamma_\xi^p\right)\right] + \\ + \frac{15 C_{a0}(1-\nu_a)}{8A(-4+\nu_a+5\nu_a^2)}\left[A\left(\gamma - \gamma_\xi^p\right)\left(2 + \left(2 + A\left(\gamma - \gamma_\xi^p\right)\right)h\right) + 2(1+h)ln\left(1 - A\left(\gamma - \gamma_\xi^p\right)\right)\right]$$

$$\boldsymbol{\gamma_\xi^p < \gamma < \gamma_{max}} \tag{4.48}$$

The expressions describing the elastic (Eq. 4.46) and the elasto-plastic regions (Eq. 4.47) are quite simple. The expression for $\tau_{III}(\gamma)$, for the shear strains $\gamma > \gamma_\xi^p$ (Eq. 4.48), becomes rather complicated. Yet, its analytical form makes it still much easier to use when compared to numerical simulations, necessary otherwise.

4.4. Torque versus the angle of twist

The torque is derived by integrating the stresses over the cross-section, according to the well-known formula (Fig. 4.6a):

$$M = \int \tau \cdot r dA \tag{4.49}$$

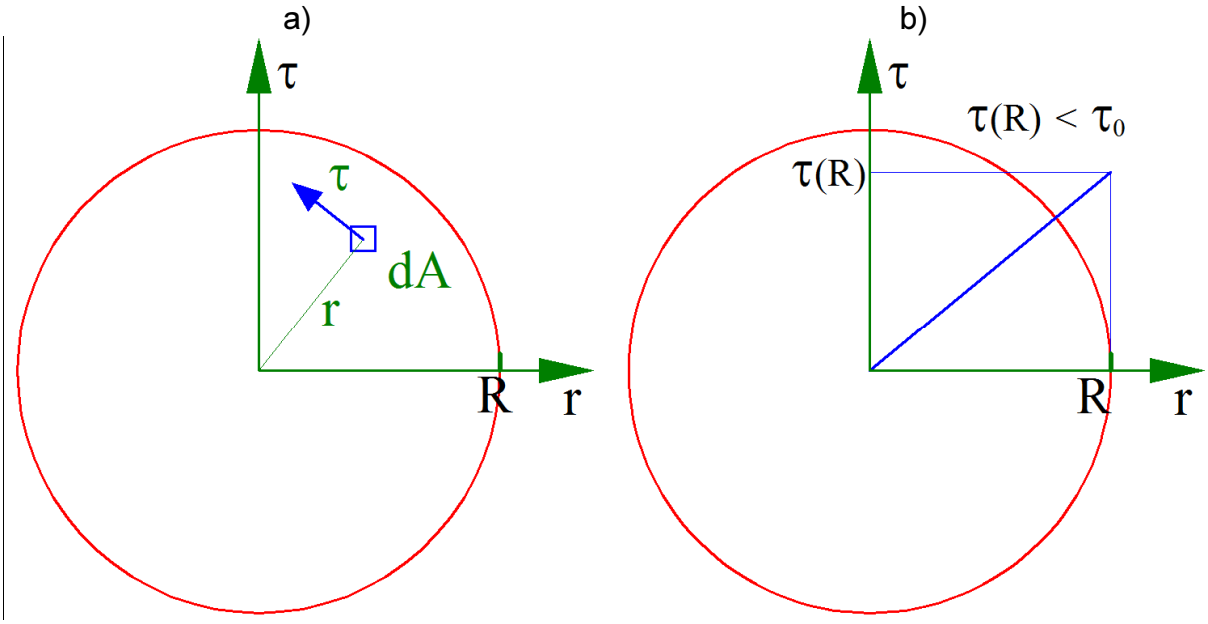

Figure 4.6. a) Shear stress acting on infinitesimally small area dA, b) Shear stress distribution in the first range (elastic)

Generally, there are three different cases depending on the value of shear strain *γ*:

- purely elastic response (Fig. 4.6b),
- the elastic-plastic response (Fig. 4.7a)
- the elastic-plastic response with phase-transformation (Fig. 4.7b)

Thus, the distribution of the stresses along the radius of the sample may take three different forms, as presented in Figs 4.6b and 4.7a, b.

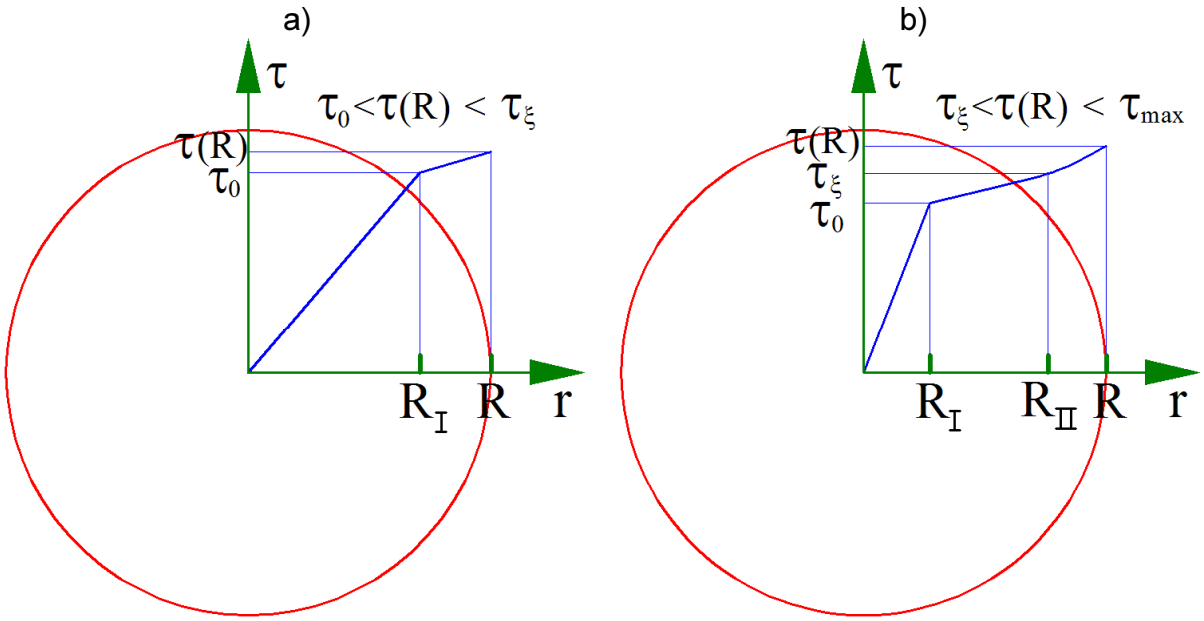

Figure 4.7. Shear stress distribution: a) for the elastic-plastic case, b) for the phase transformation case.

Using Eq. 4.49, the value of the torque may be determined for all three above mentioned cases. For the elastic case one obtains:

$$M_I = \int \tau_I \cdot r dA = \int_0^R \tau_I \cdot 2\pi r^2 \, dr \tag{4.50}$$

For the elasto-plastic case (Fig. 4.7a):

$$M_{II} = \int \tau_I \cdot r dA_I + \int \tau_{II} \cdot r dA_{II} = \int_0^{R_I} \tau_I \cdot 2\pi r^2 \, dr + \int_{R_I}^R \tau_{II} \cdot 2\pi r^2 \, dr \tag{4.51}$$

And for the case with the phase transformation (4.7b):

$$M_{III} = \int \tau_I \cdot r dA_I + \int \tau_{II} \cdot r dA_{II} + \int \tau_{III} \cdot r dA_{III} =$$
$$\int_0^{R_I} \tau_I \cdot 2\pi r^2 \, dr + \int_{R_I}^{R_{II}} \tau_{II} \cdot 2\pi r^2 \, dr + \int_{R_{II}}^R \tau_{III} \cdot 2\pi r^2 \, dr \tag{4.52}$$

Where:

- τ_I denotes the shear stress distribution in the elastic range
- τ_{II} is the shear stress function in the elastic-plastic range
- τ_{III} is the shear stress function in the phase transformation range
- R_I is the radial coordinate for which the elastic shear strain γ_0 is reached: $\gamma(R_I) = \gamma_0$
- R_{II} is the radial coordinate for which the shear strain transformation threshold γ_ξ^p is reached: $\gamma(R_{II}) = \gamma_\xi^p$

In order to calculate the integrals of the shear stress over the area of the cross-section (4.50, 4.51, 4.52), the shear stress has to be expressed as a function of the radial coordinate $\tau(r)$, instead of the previously obtained function of strain $\tau(\gamma)$. According to the linear kinematic hypothesis, commonly used for torsion, the shear strain is proportional to the radius and the unit angle of twist θ:

$$\gamma = \theta \cdot r \tag{4.53}$$

where the unit angle of twist θ is defined as:

$$\theta = \frac{d\varphi}{dx} \tag{4.54}$$

and φ is the global angle of twist (see Fig. 4.2). Assuming that the deformation is homogeneous, meaning that the angle of twist is constant per unit of length, the unit angle of twist becomes constant $\theta = const$. Thus, the angle of twist can be obtained from Eq. (4.54) by integration:

$$\varphi = \int_0^L \theta dx = \theta \cdot L \tag{4.55}$$

Finally, the unit angle of twist θ can be easily calculated from simple formula:

$$\theta = \frac{\varphi}{L} \tag{4.56}$$

Afterwards, the torque will be expressed as the function of the unit angle of twist θ, but it can be easily expressed as a function of the global angle φ, by using the above simple formula (Eq. 4.56).

4.4.1. Closed-form analytical solutions for the torque versus the unit angle of twist

Introducing the definition of strain γ (Eq. 4.53) into the definitions of shear stress (Eqs 4.46÷4.48), one obtains:

$$\tau_I = G \cdot \theta \cdot r, \qquad \theta < \theta_0 \tag{4.57}$$

$$\tau_{II} = \tau_0 + C_{a0} \cdot (\theta \cdot r - \gamma_0), \qquad \theta_0 < \theta < \theta_\xi \tag{4.58}$$

$$\tau_{III} = \tau_\xi + \frac{1}{2} C_{a0} \left(\theta r - \gamma_\xi^p\right) \left[2 + Ah\left(\theta r - \gamma_\xi^p\right)\right] + \frac{15 C_{a0}(1-\nu_a)}{8A(-4+\nu_a+5\nu_a^2)} \left[A\left(\theta r - \gamma_\xi^p\right)\left(2 + \left(2 + A\left(\theta r - \gamma_\xi^p\right)\right)h\right) + 2(1+h) ln\left(1 - A\left(\theta r - \gamma_\xi^p\right)\right)\right]$$

$$\theta_\xi < \theta < \theta_{max} \tag{4.59}$$

where the unit angle of twist θ_0 corresponds to the elastic shear strain γ_0 that is reached on the surface of the bar (for $r = R$). Thus, from Eq. 4.53 one derives:

$$\theta_0 = \frac{\gamma_0}{R} \tag{4.60}$$

Analogously, one can define θ_ξ and θ_{max}:

$$\theta_\xi = \frac{\gamma_\xi}{R} \tag{4.61}$$

$$\theta_{max} = \frac{\gamma_{\max}}{R} \tag{4.62}$$

After inserting definition of τ_I (Eq. 4.57) into the expression for the torque M_I (Eq. 4.50) one obtains:

$$M_I = \int_0^R G\theta r \cdot 2\pi r^2 \, dr \tag{4.63}$$

After simple integration one gets:

$$M_I(\theta) = \frac{\pi R^4 G}{2}\theta \tag{4.64}$$

The final formula in the elastic range $M_I(\theta)$ is linear with respect to the unit angle of twist. Similarly, inserting the definition of stresses τ_I (Eq. 4.57) and τ_{II} (Eq. 4.58) into the definition of M_{II} (4.51), one obtains:

$$M_{II} = \int_0^{R_I} G \cdot \theta \cdot 2\pi r^3 \, dr + \int_{R_I}^{R} [\tau_0 + C_{a0} \cdot (\theta \cdot r - \gamma_0)] \cdot 2\pi r^2 \, dr \tag{4.65}$$

where the first integral is performed over the limits $0 \div R_I$, and the second one over the limits $R_I \div R$. R_I denotes the radius for which the elastic strain γ_0 is reached $\gamma(R_I) = \gamma_0$. Thus, from Eq. 4.53 one obtains:

$$\gamma_0 = \theta R_I \rightarrow R_I = \frac{\gamma_0}{\theta} \tag{4.66}$$

Integrating Eq. (4.65), leads the following formula:

$$M_{II}(\theta) = A_1 + A_2 \cdot \theta + A_3 \cdot \frac{1}{\theta^3} \tag{4.67}$$

where the functions A_1, A_2, A_3 are equal:

$$A_1 = \frac{2\pi R^3}{3}[\tau_0 - C_{a0} \cdot \gamma_0] \tag{4.68}$$

$$A_2 = \frac{C_{a0}\pi R^4}{2} \tag{4.69}$$

$$A_3 = \pi\gamma_0^3\left[\frac{-2\tau_0}{3} + \frac{C_{a0} \cdot \gamma_0}{6} + \frac{G \cdot \gamma_0}{2}\right] \tag{4.70}$$

M_{III} is derived in a similar manner, by inserting definitions of stresses τ_I (Eq. 4.57), τ_{II} (Eq. 4.58) and τ_{III} (Eq. 4.59) into the formula for M_{III} (Eq. 4.52):

$$M_{III} = \int_0^{R_I} G \cdot \theta \cdot 2\pi r^3 \, dr + \int_{R_I}^{R_{II}} [\tau_0 + C_{a0} \cdot (\theta \cdot r - \gamma_0)] \cdot \pi r^2 \, dr$$

$$+ \int_{R_{II}}^{R} \left[\tau_\xi + \frac{1}{2} C_{a0}\left(\theta r - \gamma_\xi^p\right)\left[2 + Ah\left(\theta r - \gamma_\xi^p\right)\right]\right] 2\pi r^2 \, dr +$$

$$\int_{R_{II}}^{R} \frac{15C_{a0}(1-\nu_a)}{8A(-4+\nu_a+5\nu_a^2)}\left[A\left(\theta r - \gamma_\xi^p\right)\left(2 + \left(2 + A\left(\theta r - \gamma_\xi^p\right)\right)h\right) + 2(1+h)ln\left(1 - A\left(\theta r - \gamma_\xi^p\right)\right)\right] 2\pi r^2 \, dr \tag{4.71}$$

where R_{II} is the radius for which the shear strain equals $\gamma(R_{II}) = \gamma_\xi^p$. From Eq. 4.53 one obtains:

$$R_{II} = \frac{\gamma_\xi}{\theta} \tag{4.72}$$

Finally, one derives:

$$M_{III}(\theta) = B_1\theta^{-3} + B_2\theta^{-2} + B_3\theta^{-1} + B_4 + B_5\theta + B_6\theta^2 + B_7\theta^{-3}ln\left[1 - A\left(\theta R - \gamma_\xi^p\right)\right]$$
$$+ B_8 ln\left[1 - A\left(\theta R - \gamma_\xi^p\right)\right] \tag{4.73}$$

where the terms B_1 through B_8 take the following form:

$$B_1 = \pi\left[C_{a0}\left(\frac{\gamma_0^4}{6} - \frac{2\gamma_0\gamma_\xi^3}{3} + \frac{\gamma_\xi^4}{2}\right) + \frac{G\gamma_0^4}{2}\right] + \frac{\pi C_{a0}\gamma_\xi(1+\mathrm{h})(1-\nu_a)}{(-4+\nu_a+5\nu_a^2)\mathrm{A}}\left[\frac{5}{2A^2} + \frac{25\gamma_\xi}{4\mathrm{A}} + \frac{55\gamma_\xi^2}{12}\right] +$$

$$\frac{\pi C_{a0}\gamma_\xi^4}{(-4+\nu_a+5\nu_a^2)}\left[\frac{-1}{24} + \frac{5h}{8} + \frac{A\gamma_\xi h}{120} - \frac{11\nu_a}{24} - \frac{5h\nu_a}{8} + \frac{11A\gamma_\xi h\nu_a}{120} + \frac{5\nu_a^2}{6} - \frac{A\gamma_\xi\nu_a^2 h}{6}\right]$$
$$+ \pi\left[\frac{2\tau_0}{3}\left(-\gamma_0^3 + \gamma_\xi^3\right) + \frac{\tau_\xi\gamma_\xi^3}{(-4+\nu_a+5\nu_a^2)}\left(\frac{8}{3} - \frac{2\nu_a}{3} - \frac{10\nu_a^2}{3}\right)\right] \tag{4.74}$$

$$B_2 = \frac{5C_{a0}\left(1+A\gamma_\xi\right)^2(1+h)(\nu_a-1)\pi R}{2A^3(-4+\nu_a+5\nu_a^2)} \tag{4.75}$$

$$B_3 = \frac{5C_{a0}\left(1+A\gamma_\xi\right)(1+h)(\nu_a-1)\pi R^2}{4A^2(-4+\nu_a+5\nu_a^2)} = B2\frac{RA}{2\left(1+A\gamma_\xi\right)} \tag{4.76}$$

$$B_4 = \frac{C_{a0}\pi R^3}{(-4+\nu_a+5\nu_a^2)}\left[\frac{5}{6A}(1+h)(\nu_a-1)+\frac{\gamma_\xi}{6}-\frac{5\gamma_\xi h}{2}-\frac{A\gamma_\xi^2 h}{12}+\frac{11\gamma_\xi\nu_a}{6}+\frac{5\gamma_\xi\nu_a h}{2}\right.$$
$$\left.-\frac{11A\gamma_\xi^2 h\nu_a}{12}-\frac{10\gamma_\xi\nu_a^2}{3}+\frac{5A\gamma_\xi^2 h\nu_a^2}{3}\right]+\frac{\pi R^3\tau_\xi}{(-4+\nu_a+5\nu_a^2)}\left[-\frac{8}{3}+\frac{2\nu_a}{3}+\frac{10\nu_a^2}{3}\right] \tag{4.77}$$

$$B_5 = \frac{C_{a0}\pi R^4}{8(-4+\nu_a+5\nu_a^2)}\left[\nu_a(20\nu_a-11)-1+h\left(-15(\nu_a-1)+A\gamma_\xi\left(1+\nu_a(11-20\nu_a)\right)\right)\right] \tag{4.78}$$

$$B_6 = \frac{C_{a0}\pi R^5 Ah\cdot\left(-1+\nu_a(20\nu_a-11)\right)}{20(-4+\nu_a+5\nu_a^2)} \tag{4.79}$$

$$B_7 = \frac{5C_{a0}\pi\left(1+A\gamma_\xi\right)^3(1+h)(\nu_a-1)}{2A^4(-4+\nu_a+5\nu_a^2)} \tag{4.80}$$

$$B_8 = -\frac{5C_{a0}\pi R^3(1+h)(\nu_a-1)}{2A(-4+\nu_a+5\nu_a^2)} \tag{4.81}$$

4.4.2. Exact formulae and error estimation

The first source of error was introduced when the modulus C_{a+m} was simplified. The expressions for the stress and the torque in the regions I and II (Fig. 4.3) are the same, no simplifications were needed there. Only in the 3rd region, where the phase transformation occurs, the exact formulae are different compared to the simplified ones. Exact solutions can be obtained by using complete expression for C_{a+m}, and after introducing the parameters of the model and performing numerical integration. This was done afterwards in the chapter 8.

The error estimation for $M_{III}(\theta)$ is obtained by using the exact definition of the modulus C_{a+m} (Eq. 3.119). Repeating Eq. 3.119 gives:

$$C_{(a+m)Ex} = \frac{15}{2}\frac{E_{ta}}{(1+\nu_a)}\frac{\left(\frac{1-\nu_a}{4-5\nu_a}\right)\xi\left[\frac{E_m}{(1+\nu_m)}-\frac{E_{ta}}{(1+\nu_a)}\right]}{\left[\frac{E_m}{(1+\nu_m)}(1-\xi)+\frac{E_{ta}}{(1+\nu_a)}\left[\xi+\frac{(7-5\nu_a)}{2(4-5\nu_a)}\right]\right]} \tag{4.82}$$

Where the modulus E_{ta}, derived in Eq. (3.73), is repeated here for convenience:

$$E_{ta} = \frac{E_a\cdot C_a(\xi)}{E_a+C_a(\xi)} = \frac{E_a\cdot C_{a0}(1+h\xi)}{E_a+C_{a0}(1+h\xi)} \tag{4.83}$$

Now, inserting the expression for ξ (Eq. 4.4) into Eqs 4.82 and 4.83 one obtains $C_{(a+m)Ex}$ as a function of shear strain. With the assumption $\gamma = \gamma^p$ one has:

$$\mathrm{C}_{(a+m)Ex} = \frac{15}{2}\frac{\frac{E_{ta}}{(1+\nu_a)}\left(\frac{1-\nu_a}{4-5\nu_a}\right)A\left(\gamma-\gamma_\xi^p\right)\left[\frac{E_m}{(1+\nu_m)}-\frac{E_{ta}}{(1+\nu_a)}\right]}{\left[\frac{E_m}{(1+\nu_m)}\left(1-A\left(\gamma-\gamma_\xi^p\right)\right)+\frac{E_{ta}}{(1+\nu_a)}\left[A\left(\gamma-\gamma_\xi^p\right)+\frac{(7-5\nu_a)}{2(4-5\nu_a)}\right]\right]} \quad (4.84)$$

$$E_{ta} = \frac{E_a \cdot C_{a0}\left(1+hA\left(\gamma-\gamma_\xi^p\right)\right)}{E_a + C_{a0}\left(1+hA\left(\gamma-\gamma_\xi^p\right)\right)} \quad (4.85)$$

The shear stress - shear strain function is derived by means of Eq. 4.20, after replacing C_{a+m} with $\mathrm{C}_{(a+m)Ex}$:

$$\tau_{IIIEx}(\gamma) = \tau_\xi + \int_{\gamma_\xi}^{\gamma}\left[C_{a0}\cdot\left(1+hA\left(\gamma-\gamma_\xi^p\right)\right)+\frac{1}{2}\mathrm{C}_{(a+m)Ex}\right]\mathrm{d}\gamma^p \qquad \gamma_\xi < \gamma < \gamma_{max} \quad (4.86)$$

Thus:

$$\tau_{IIIEx}(\gamma) = \tau_\xi + \int_{\gamma_\xi}^{\gamma} C_{a0}\cdot\left(1+hA\left(\gamma-\gamma_\xi^p\right)\right)\mathrm{d}\gamma^p +$$

$$+\int_{\gamma_\xi}^{\gamma}\frac{15}{4}\frac{\frac{E_{ta}}{(1+\nu_a)}\left(\frac{1-\nu_a}{4-5\nu_a}\right)A\left(\gamma-\gamma_\xi^p\right)\left[\frac{E_m}{(1+\nu_m)}-\frac{E_{ta}}{(1+\nu_a)}\right]}{\left[\frac{E_m}{(1+\nu_m)}\left(1-A\left(\gamma-\gamma_\xi^p\right)\right)+\frac{E_{ta}}{(1+\nu_a)}\left[A\left(\gamma-\gamma_\xi^p\right)+\frac{(7-5\nu_a)}{2(4-5\nu_a)}\right]\right]}\mathrm{d}\gamma^p \quad (4.87)$$

Further integration has been carried out numerically, by using Maple software after introducing the numerical values of the parameters of the model.
Similar procedure has been applied in order to derive the exact expression for the torque. The stress as a function of the current radius is used to obtain torque, based on definition 4.52. The shear stress as a function of the radius reads:

$$\tau_{IIIEx}(\mathrm{r}) = \tau_\xi + \int_{\gamma_\xi}^{\theta r}\left[C_{a0}\cdot\left(1+hA\left(\gamma-\gamma_\xi^p\right)\right)+\frac{1}{2}\mathrm{C}_{(a+m)Ex}\right]\mathrm{d}\gamma^p \qquad \gamma_\xi < \gamma < \gamma_{max} \quad (4.88)$$

and the exact formula for the torque is as follows:

$$M_{III}(\theta) = \int_0^{R_I} G\cdot\theta\cdot 2\pi r^3\,dr + \int_{R_I}^{R_{II}}[\tau_0 + C_{a0}\cdot(\theta\cdot r-\gamma_0)]2\pi r^2\,dr + \int_{R_{II}}^{R}\tau_{IIIEx}(\mathrm{r})\cdot 2\pi r^2\,dr \quad (4.89)$$

The radius R_I was previously defined by Eq. 4.66, and R_{II} by Eq. 4.72. Again, Eq. 4.89 was integrated numerically by means of Maple software.
Simplified (Eq. 4.73) and exact (Eq. 4.89) formulas for the torque versus the unit angle of twist in the phase transformation range were compared in the chapter 8, after identifying the parameters of the model from the experimental data.

4.5. Identification of parameters of the model

The list of the parameters of the model was presented at the end of Chapter 3. In view of the torsion related problems, the parameters listed in the previous chapter: ε_ξ^p and ε_0 (related to tensile strain) are now replaced by their equivalents related to shear strains, namely: γ_ξ^p and γ_0. The identification of all the relevant parameters was addressed in the following paragraphs:

1. Three parameters A, γ_ξ^p, ξ_L are obtained from experimental identification of the kinetics of phase transformation. The kinetics relates the martensite content to inelastic strain. In the present work, the martensite content has been measured within the cross-section of twisted bar, along four diagonal lines. Thus, relation $\xi(r)$ has been effectively obtained. From this relation one can directly identify three sought parameters.

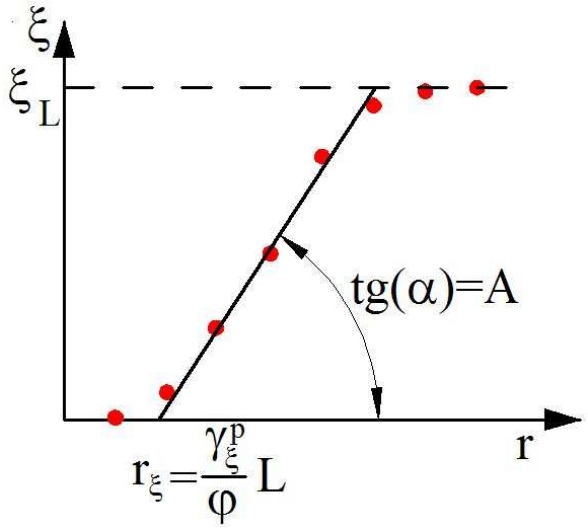

Figure 4.8. Identification of the parameters A, γ_ξ^p, ξ_L describing the kinetics of the phase transformation

After inserting the expression for shear strain γ (Eq. 4.53) and for the unit angle of twist (Eq. 4.56) into the kinetics of phase transformation (Eq. 4.4), one gets in the transformation range:

$$\xi = A(T) \cdot \left(\frac{\varphi}{\mathrm{L}}\mathrm{r} - \gamma_\xi^p\right) \tag{4.90}$$

This equation describes the line approximating the experimental results (red dots in Fig. 4.8). L is the known length of the bar, and φ is the angle of twist to which the sample was deformed. Of course, one needs to cut the sample to be able to measure martensite content within its cross-section. So, eventually, only two unknown parameters are present in the formula (4.90). Thus, one can identify them to best fit the experimental results. The third parameter, the saturation value of martensite content ξ_L, can be directly extracted from the experimental results (Fig. 4.8).

2. The relative volume change Δv is generally known from literature. After Garion et al. 2006 this constant is equal to: $\Delta v = 0.05$. The same value of this parameter was used by Sitko et al. (2010), and Sitko and Skoczeń (2012).

3. The Poisson ratios: ν_a, ν_m. The Poisson ratio for martensite has been assumed equal to $\nu_m = 0.3$, the same as for the stainless and the carbon steels. The Poisson ratio for the austenitic phase has been assumed equal to $\nu_a = 0.5$, according to the incompressibility condition.

4. The Young modulus of martensite E_m has been assumed equal to the Young modulus of austenite: $E_m = E_a$.

5. The parameters: E_a, γ_0, have been effectively obtained from the experimental results of the torque versus the angle of twist (Fig. 4.10).
In the course of experiment, the torque has been measured as a function of the angle of twist. Theoretical formulas were derived as a function of the unit angle of twist. Yet, it is rather straightforward to obtain the torque as a function of the angle of twist. It is sufficient to insert the formula $\theta = \varphi/L$ (Eq. 4.56) into the final formulas for $M(\theta)$ (Eqs 4.73, 4.67, 4.64).
For clarity, the theoretical stress strain curve has been repeated, and important parameters have been labeled (Fig. 4.9). Three ranges: I (elastic), II (elastic-plastic), III (phase transformation) can be easily identified in the stress-strain plot (Fig. 4.9) and in the torque versus the angle of twist plot (Fig. 4.10).

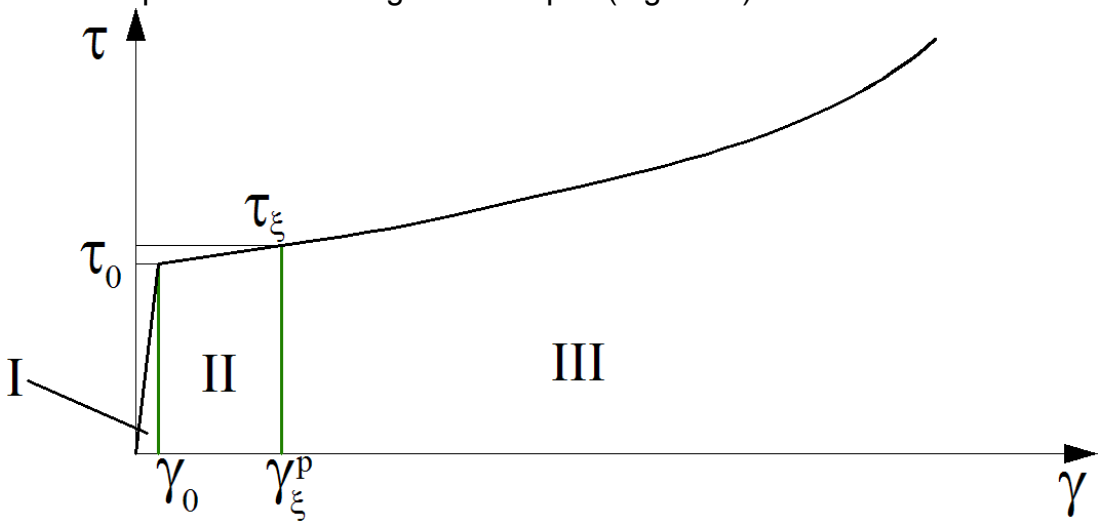

Figure 4.9. Theoretical function of shear stress versus shear strain.

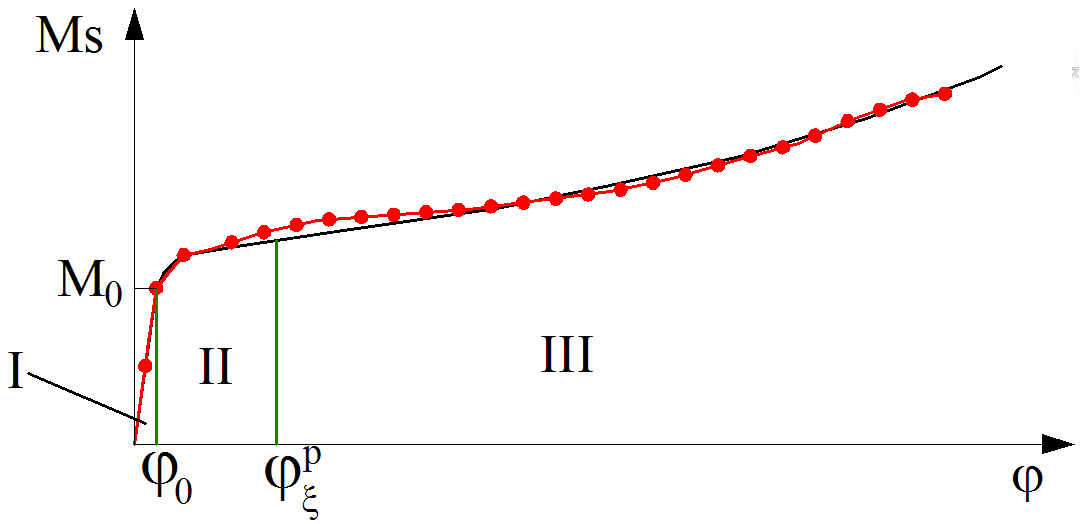

Figure 4.10. Torque versus the angle of twist; experimental results (red dots), and theoretical curve

The elastic range is described by linear formula (Eq. 4.64), relating the torque to the angle of twist. Inserting Eq. 4.56 into Eq. 4.64, one obtains:

$$M_I(\varphi) = \frac{\pi R^4 G}{2}\frac{\varphi}{L} \tag{4.91}$$

Furthermore, inserting the formula for the shear modulus G (of austenite) into Eq. (4.91), one gets:

$$M_I(\varphi) = \frac{\pi R^4}{2}\frac{E_a}{2(1+\nu_a)}\frac{\varphi}{L} \tag{4.92}$$

The above equation (Eq. 4.92) describes the linear elastic part in Fig. 4.10. From this formula one can identify the Young modulus E_a and the angle φ_0. From φ_0 one can easily calculate the shear strain γ_0. To do so, one has to combine the formulas 4.53 with 4.56 and insert $r = R$. This gives:

$$\gamma_0 = \frac{\varphi_0}{L} \cdot R \tag{4.93}$$

6. Identifying parameters: C_{a0}, h.

These two parameters are identified from the torque versus the angle of twist experimental results (Fig. 4.10) as well. Both are found by using the formula for $M_{II}(\theta)$ (Eq. 4.65), repeated here for convenience:

$$M_{II}(\theta) = A_1 + A_2 \cdot \theta + A_3 \cdot \frac{1}{\theta^3} \tag{4.94}$$

Similarly, the formula (Eq. 4.73) for $M_{III}(\theta)$ is repeated here as well:

$$M_{III}(\theta) = B_1\theta^{-3} + B_2\theta^{-2} + B_3\theta^{-1} + B_4 + B_5\theta + B_6\theta^2 + B_7\theta^{-3} ln\left[1 - A\left(\theta R - \gamma_\xi^p\right)\right] + B_8 ln\left[1 - A\left(\theta R - \gamma_\xi^p\right)\right] \tag{4.95}$$

The functions $A_1 \div A_3$ (Eqs 4.68÷4.70), and $B_1 \div B_8$ (Eqs 4.74÷4.81) depend on the parameters of the model. At this point, the parameters: A, γ_ξ^p, ξ_L and ν_a, E_a, γ_0 are already known. The remaining parameters C_{a0} and h can be identified from the best fit of theoretical curves (Eqs 4.94, 4.95) to experimental data (Fig. 4.10).

7. The Bauschinger parameter β is not needed for monotonic torsion. It can be identified from experimental results involving cyclic loads.

5. Circular rods subjected to monotonic torsion at 77K - experiments

In the previous chapters, multiaxial constitutive model of continuum undergoing plastic strain induced phase transformation was presented. Later on, in Chapter 4, the constitutive model was applied to the case of simple torsion. The expressions for stress as a function of strain, and torque as a function of the angle of twist have been derived. At the end of Chapter 4, calibration of parameters of the model was described. In order to obtain required material parameters, suitable experiments (tests) are necessary.

One can find in the literature many experimentally obtained parameters for 304 austenitic stainless steel. Yet, different constitutive models require different parameters. Often, the parameters found in the literature were obtained within different experimental conditions, or for different materials. Thus, application of these parameters introduces an error, by definition.

It is well known that the same material (e.g. ss 304) may be characterized by different mechanical or physical properties, as the samples come from different batches of production. The chemical composition of steels and the thermal treatment are not perfectly controlled, which leads to unavoidable variation of properties. For this reason, the best way to describe the behavior of a given material is to perform suitable tests and then, based on its results, identify material parameters. In such a manner, one is sure that correct material parameters are later used in the theoretical model.

The experiments provide a straightforward way to compare the behavior of various structures, as well. In the present work, the behavior of a classical austenitic homogeneous structures was compared with FGSM ones (Functionally Graded Structural Member) characterized by variable martensite content resulting from the phase transformation. The results of the comparison are presented at the end of the present chapter.

A comparison between the theoretical and the experimental results is carried out later on, in the course of Chapter 8.

5.1. Description of experimental set-up

The set-up for tests of torsion had to fulfill the following requirements:

- Allowing rotations in clockwise and anticlockwise directions,
- Allowing unlimited angles of twist (several turns),
- Allowing tests at room temperature as well as at 77K (liquid nitrogen temperature)
- Providing sufficient heat-insulation in the case of liquid nitrogen cooling (in order not to let liquid nitrogen evaporate too quickly, and gain enough time to perform monotonic or cyclic test at cryogenic temperature),
- Providing a way to fix the sample at the bottom,
- Providing a way to guide the sample at the top (no transverse loads allowed, only rotations around the axis of sample),

Keeping in mind all the above requirements, the set-up has been designed and its parts have been manufactured. One of the most important requirements was the one allowing to perform tests at cryogenic temperatures. For this reason the so called “cryostats” (vacuum insulated vessels containing cryogenic fluids) are used.

The cryostats are characterized by thermal insulation to facilitate maintaining constant temperature. Thermal insulation is usually achieved by building two walls of the cryostat with vacuum in between. The presence of vacuum cuts off heat conduction from the outside ambience. In the present case, a cylindrical cryostat has been used.
In order to fulfill all the requirements, the cryostat had to be additionally equipped for the torsion test. The additional parts have been designed and manufactured on purpose. In order to provide a support for the sample, a steel flange was mounted on the top of the cryostat. Thanks to thick walls the stiffness of the whole system was good enough. The top plate was supported with four columns mounted to the bottom plate of the system (Fig. 5.1). The columns additionally increased the overall stiffness. During the experiments no transverse deformations of the columns were observed.
3D model of the set-up is presented in Fig. 5.1. The set-up just after manufacturing is presented in Fig. 5.2a,b.

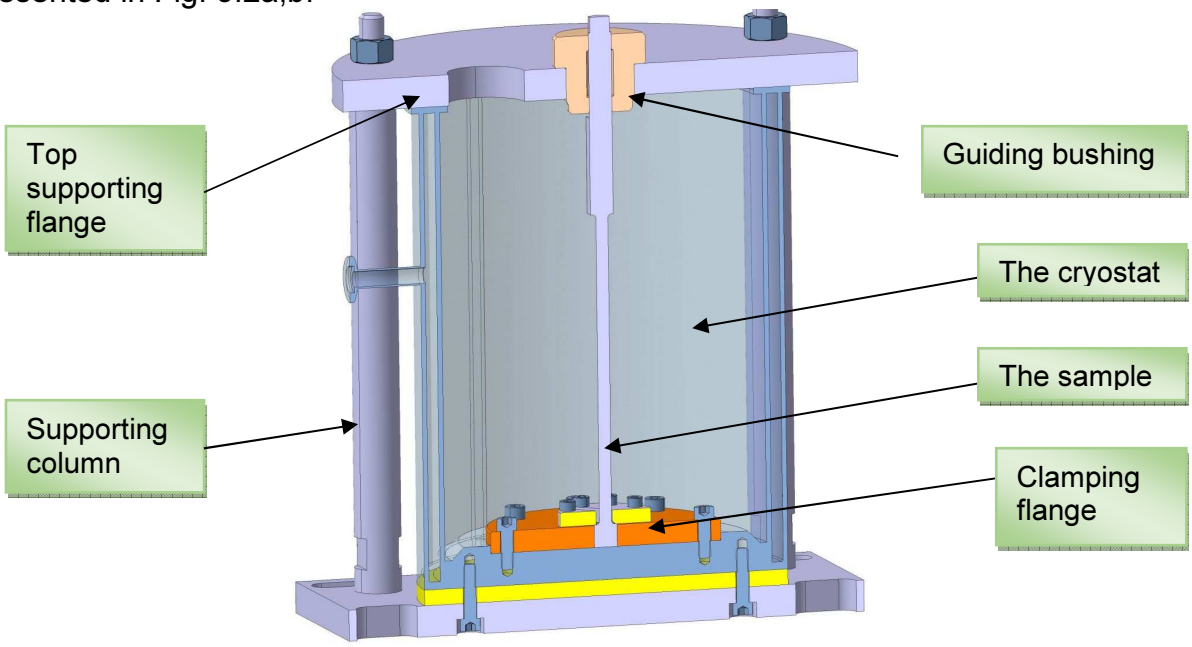

Fig. 5.1. Cross-section of the torsion set-up (model)

Figure 5.2. a) The interior of the cryostat with sample and bushing; b) The set-up with top flange

Two types of tests were performed: at room temperature (Fig. 5.3b), and at liquid nitrogen temperature (Fig. 5.3a). The set-up with the nitrogen container and the vacuum pump is presented in Fig. 5.4.

a b

Figure 5.3. a) Test at 77K (cold vapor and white frost visible), b) Test at 293K

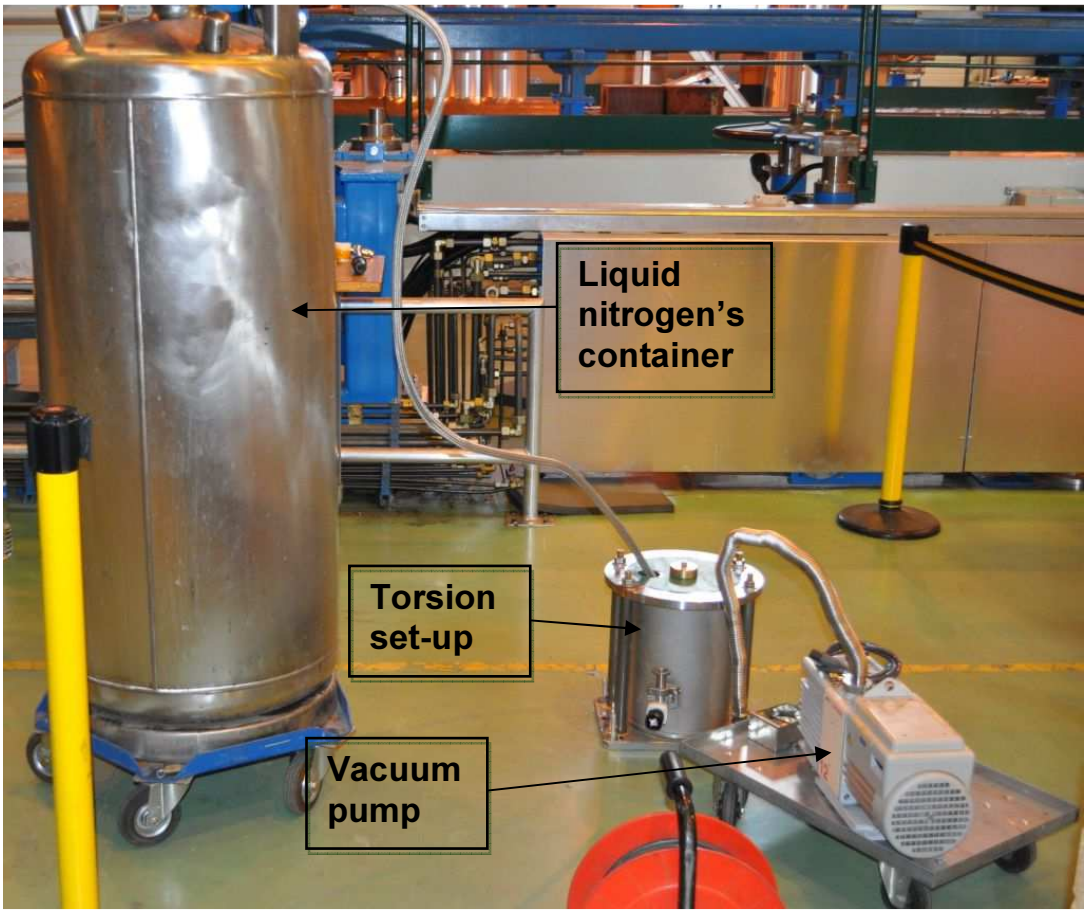

Figure 5.4. The set-up with liquid nitrogen container (on the left) and dynamic vacuum pump

Torque wrench was used to apply and to measure the torque. A wire was attached to the wrench, as indicated in Fig. 5.5. The angle was read directly on a printed scale with 0.5° resolution.

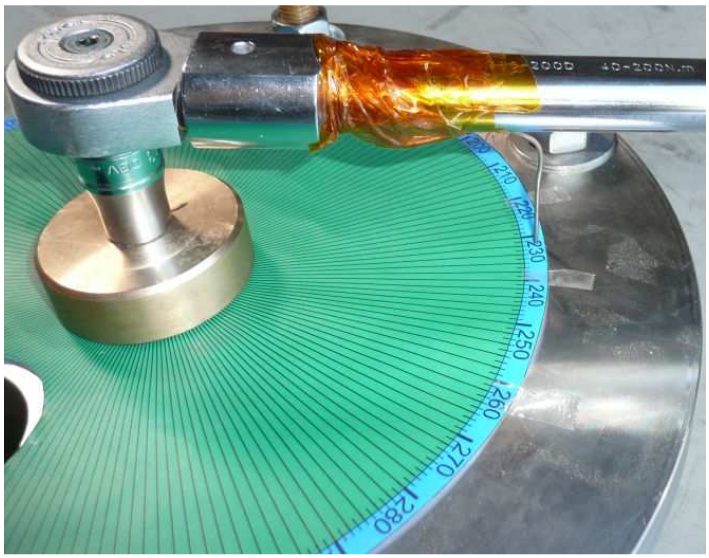

Figure 5.5. Set-up to measure the angle of twist

5.2. Geometry and material of the sample

In accordance with theoretical derivations (Chapter 4), bars of circular cross-section were used. Of course, perfect cylinders are in reality not possible to manufacture. Finite tolerances had to be used. The sample has been designed to fit into the set-up. The samples were machined from bars of square cross-sections 15x15. The final geometry was chosen to minimize its production cost (Fig. 5.6). The relevant technical drawing with all the tolerances is shown in Fig. 5.7.

Figure 5.6. Geometry of the sample

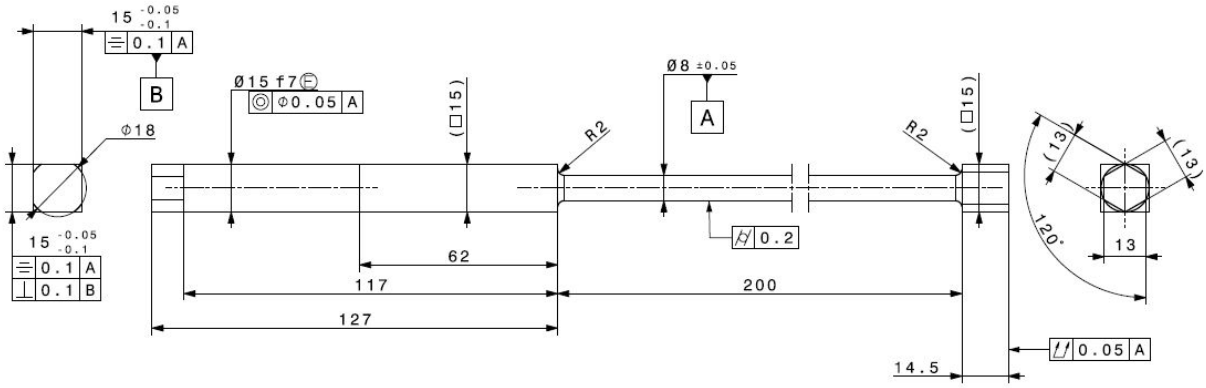

Figure 5.7. Detailed technical drawing of the sample.

The cylindrical part of the sample measured 200mm in length and 8mm in diameter. The square ending at the bottom was used to kinematically fix the sample against rotation. The hexagonal ending on the other side of the specimen was used as the interface for applying the loading via torque wrench.
The 304 austenitic stainless steel was chosen for the first set of samples. The steel is characterized by relatively high carbon content (0.07%), compared to other austenitic stainless steels (like 316L with 0.03%). The fraction of carbon is indicating a susceptibility to martensitic transformation. The greater the quantity of carbon, the easier the phase transformation occurs (with less cooling and smaller inelastic strain), and the higher fraction of martensite is possible to obtain (higher ξ_L). The chemical composition of 304 stainless steel is presented in Table 5.1.

	Fe	Cr	Mn max	Ni	P max	C max	S max	Si max
Quantity [%]	The rest	17-20	2	8.5-10	0.045	0.07	0.030	1.0

Table 5.1. Chemical composition of 304 austenitic stainless steel, according to EN 10088-1-3 – DIN 17440

5.3. Procedure of the test

The monotonic torsion tests at cryogenic temperatures have been performed following the sequence of steps:
1. Fixing the sample in the set-up.
2. Filling the cryostat with liquid nitrogen, and making sure that its level is well above the cylindrical part of the sample.
3. Setting the minimum value of the torque on the torque wrench (Fig. 5.8) (for the torque wrench used, the minimum torque was of 20 Nm). Yet, 3 different torque wrenches were used with different torque ranges.
4. Quasi-statically loading the sample until hearing “a clique sound”, indicating that the pre-set value was reached. Then, without moving the tool, recording the value of the angle of twist.
5. Checking the level of cryogenic fluid, by means of a hole in the top flange (Fig. 5.2b). If the cylindrical part of the specimen was not completely immersed in the coolant, refilling the cryostat and then continuing the test afterwards.
6. Unloading the sample, by releasing the wrench and reading the value of the residual angle of twist.
7. Setting next value of the torque (usually with the step of 1Nm or 2 Nm), and repeating the steps 4÷7 until the test was completed.

Figure 5.8. One of the torque wrenches used; the range of 20÷100 Nm

With respect to the above list of steps, it is important to notice that one does not perform “monotonic” torsion test in the classical meaning of this term. Using the torque wrench makes it necessary to load and unload the sample for each value of the torque. Thus, in fact one performs cyclic torsion with increasing amplitude of the torque for each subsequent cycle. It has been illustrated in Fig. 5.9.

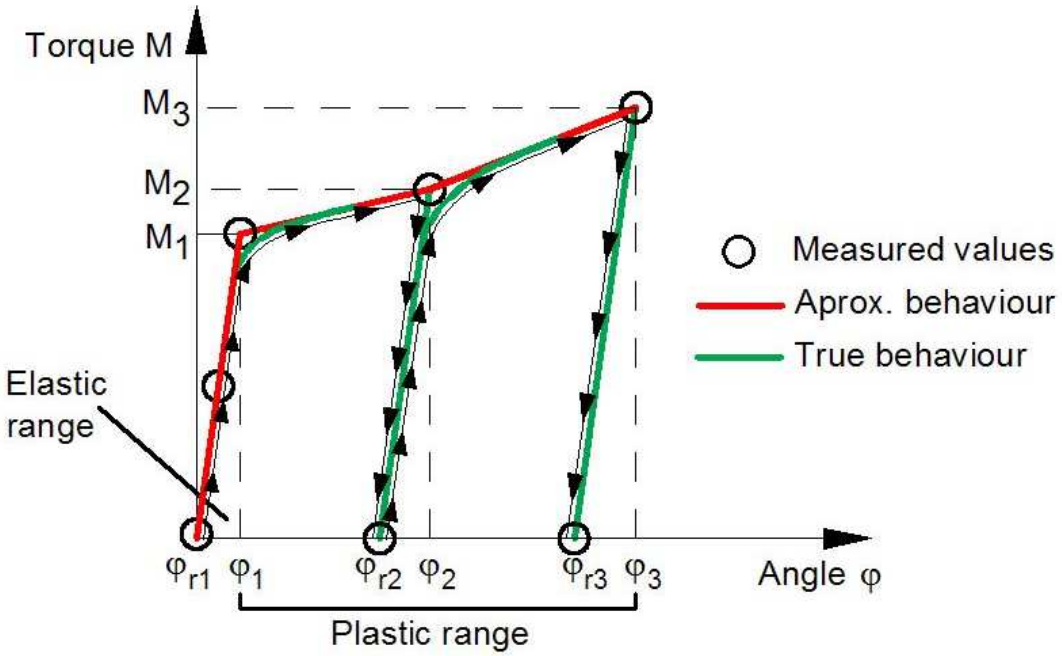

Figure 5.9. Torque versus angle of twist during loading by means of torque wrench

Red line in Fig. 5.9 connects the measured points The first three points remain within the elastic range. Thus, the loading and the unloading follow the straight line. After reaching the point denoted M_1, the sample has been unloaded and the value M_2 was set on the torque wrench. Now the material starts to flow plastically, thus, somewhere near the value M_1 the angle starts to increase (the green line in Fig. 5.9). Eventually, the value M_2 is reached, which corresponds to angle φ_2. Then, the sample was unloaded, and the residual angle φ_{r2} was reached. Between the points (M_2, φ_2) and (0, φ_{r2}) the straight line has been drawn, as one assumes that the unloading is elastic.

The next step in the process is setting M_3 as the next value of the torque. During the loading cycles the material plastically yields. At the moment of reaching the value M_3, the angle of twist was equal to φ_3.

The measurement has been made in a discrete way. A finite number of measurement points was registered, and they were interpolated by means of straight lines in order to obtain a continuous function. Yet, the real behavior resembles more the green line from Fig. 5.9. To obtain the green line, a continuous system of measurements of torque and angle of twist would be necessary. Such a system was too complex and expensive, only discrete measurements by using the torque wrench were possible. However, the difference between the red curves and the green one (Fig. 5.9) is rather small. Generally, the measurement that consists of cycles with increasing amplitude of the torque provides more interesting information compared to continuous loading. One obtains the residual angles of twist, from which it is possible to obtain the shear modulus (G), and the Young modulus as well (E). Having the evolution of the unloading modulus, one can easily calculate the evolution of damage parameter, which indicates the progression of the physical process of nucleation and growth of micro-cracks and micro-voids. This subject however is not treated in the present Thesis.

This type of loading (Fig. 5.9) is clearly not a monotonic loading. The presence of cycles causes additional hardening of the material. Yet, this hardening is not significant, as the torque was increased by small increments 1Nm or 2Nm.

Thus, still for the first comparison, this loading was treated as “monotonic” in the classical sense when compared to theoretically derived formulae. A more detailed theoretical derivation. that includes the cycles of increasing amplitude, cannot be obtained in analytical form. Only numerical simulations could provide a solution for this case. Such solution is not treated in the present Thesis, it is a subject of separate investigation.
For the tests performed at room temperature, almost the same procedure as described at the beginning of this chapter was used. The only difference consists in the fact that no cooling was needed. Such test was then much easier to realize.

5.4. Results of torsion test for 304 stainless steel samples

The goal of the very first torsion tests was to check the possibility of inducing martensitic transformation by twisting a bar beyond its yield limit. According to the concept of FGSM (Functionally Graded Structural Members), one needs to control the distribution of martensitic phase by controlled deformation (angle of twist). The first sample was loaded until rupture at room temperature. During this test no equipment to measure the martensite content was available. Thus, the simplest method was used, i.e. a qualitative magnetic method. It is commonly known that martensite is a ferromagnetic phase, whereas, the austenite is a paramagnetic one.
Before the test a magnet was moved along the surface of the sample and no magnetic force was detected. This indicated that the sample had fully austenitic structure. The same test was then repeated after loading. This time a magnetic force between the magnet and the sample was detected, clearly indicating that the martensite was present and confirming that the martensitic transformation could be induced via twisting. The result for sample 1 is presented in Fig. 5.10. In the plot, there is also a result for sample 4, which was loaded until rupture, but at 77K. Both curves provide an important information about the maximum values of the torque and the angle of twist, that the same material can carry at two different temperatures: 77K and 293K. In other words, such test provides the limit loads, which are very crucial for further tests. The experiment is the simplest way to obtain the torque and the angle of twist corresponding to rupture for this particular type of loading. Otherwise, relying exclusively on theoretical assumptions about the failure criterion, and having no material parameters relevant for the tested samples, one would commit significant error.

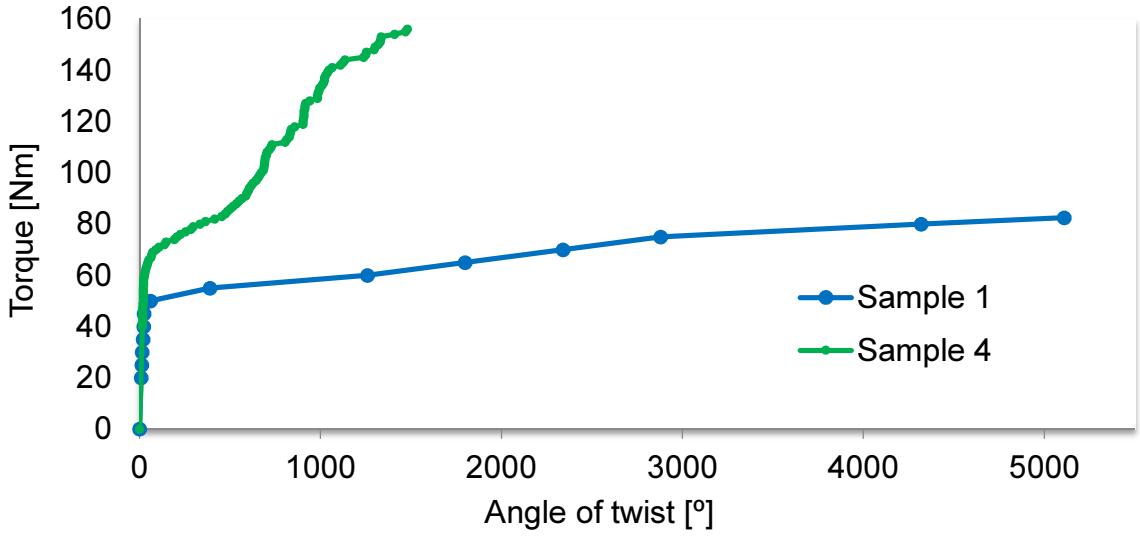

Figure 5.10. Torque versus angle of twist for Sample 1 and Sample 4

As one can see from Fig. 5.10, the sample loaded at 293K (room temperature) ruptured at about 82.5Nm and at about 5100°, so after more than 14 full (360°) rotations. This huge angle of twist proves very high ductility of 304 stainless steel at room temperature. At 77K the behavior is drastically different. The maximum angle of twist was 1480°, so 3 times smaller than at 293K. However, the maximum torque reached almost 160Nm, which was almost 2 times more than at 293K. So, as one would expect the ductility decreases with decreasing temperature and the strength increases. The hardening at 77K is caused by replacement of the austenitic microstructure by stronger martensite, thanks to the martensitic transformation.
It is clearly visible in Fig. 5.10, that the torque corresponding to the elastic limit is higher at 77K, and reaches about 60Nm, whereas at 293K it is only 45Nm. Thus, this 50% increase results only from the change of temperature. Even higher increase, by almost 100%, was noticed in terms of the maximum torque (160Nm at 77K compared to 82.5Nm at 293K). The steep parts at the beginning of both curves (in the elastic range) coincided very well. This confirmed equality of the Young modulus at both temperatures.
Two additional samples have been loaded at 77K and 293K, in order to compare the resultant microstructure, the micro-hardness and the martensite content profiles. According to the results presented in Fig. 5.10, for the samples 1 and 4, an intermediate value of the angle of twist has been selected: 870° in order to ensure significant yielding at both temperatures. This leads to larger martensite contents, easier to detect later on. The same angle of twist ensures practically the same plastic strains in the bars. According to the kinetics of the plastic strain induced phase transformation (Chapter 4), the rate of martensite formation is much higher at lower temperatures. One expects much higher martensite content at 77K, for the same angle of twist. The detailed results of the martensite distribution are presented in the Chapter 6.3.
Torque versus angle of twist for both samples (2 and 3) is presented in Fig. 5.11. The results obtained at 293K (sample 3) indicate very flat behavior for loading higher than 50Nm, and plastic yielding with weak hardening.
Very different behavior was identified at 77K, where the torque increases rapidly as a function of the angle of twist, reaching 100Nm at the angle of 870°. This is much more than at room temperature (about 55Nm).

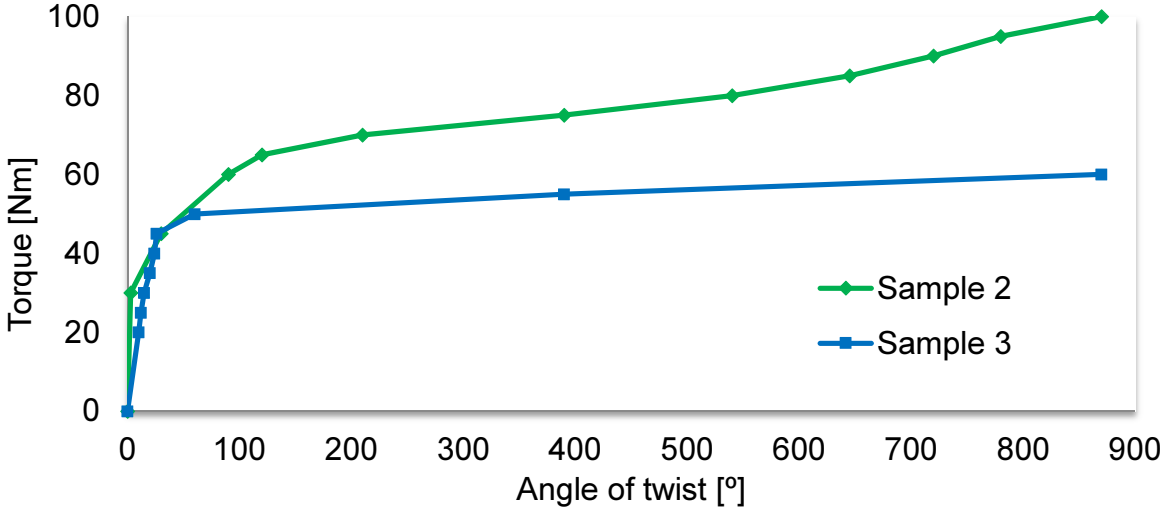

Figure 5.11. Torque versus angle of twist for Sample 2 and Sample 3

The sequence of loading (illustrated in Fig. 5.9) for sample 2 is presented in Fig. 5.12.

One can appreciate clearly the difference between the angle of twist in the elastic or plastic ranges. The slope of unloading lines (dashed ones) evolves in the course of micro-damage evolution.

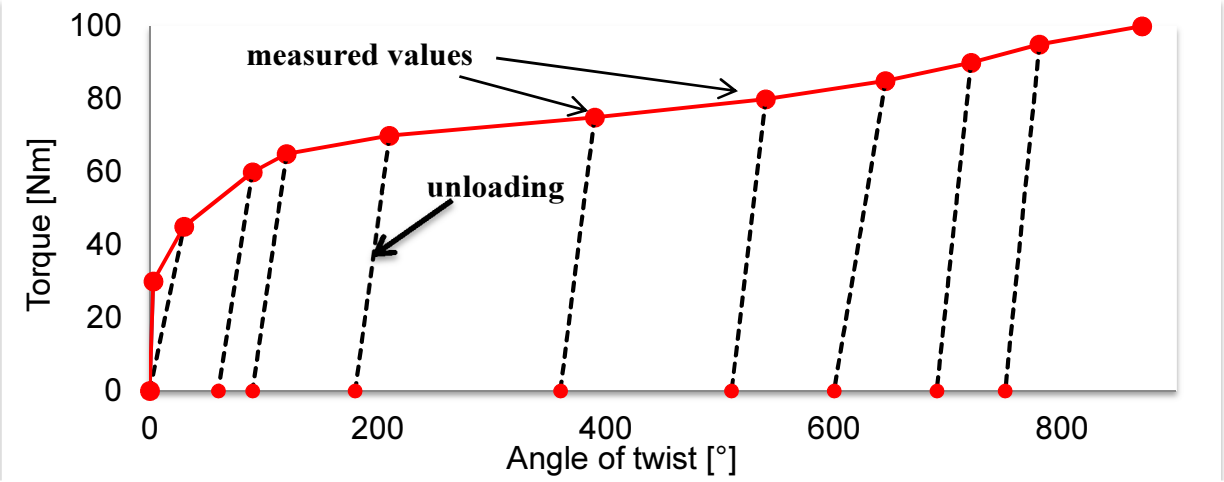

Figure 5.12. Detailed loading sequence for sample 2

5.5. Performance of the FGSM made of 304 stainless steel

In order to check the performance of FGSM in the form of a bar of circular cross-section, the sample has been subjected to a comparative test. First, the martensitic transformation was induced by means of torsion at 77K. High enough load was used to ensure inducing significant content of martensite. Later on, the same sample has been loaded again with torsional loading until rupture.

Two samples were prepared: one was first loaded at 77K and then at 293K, whereas, the second one was loaded at 77K and then again loaded at 77K, until rupture.

In other words, the samples were pre-strained in the first part of the test, and then tested again in order to check the influence of hardening caused by the first cycle.

In total 3 FGSM samples were created. All of them were loaded at 77K up to 120Nm. This value was selected, based on the results obtained in the course of test until rupture at 77K (Fig. 5.10). As the maximum measured torque was of 156Nm, the value of 120Nm was equal to 77% of the maximum value, ensuring significant hardening and significant increase of martensite content. The relationship between the torque and the angle of twist during the pre-strain loading at 77K is presented in Fig. 5.13, for all the samples.

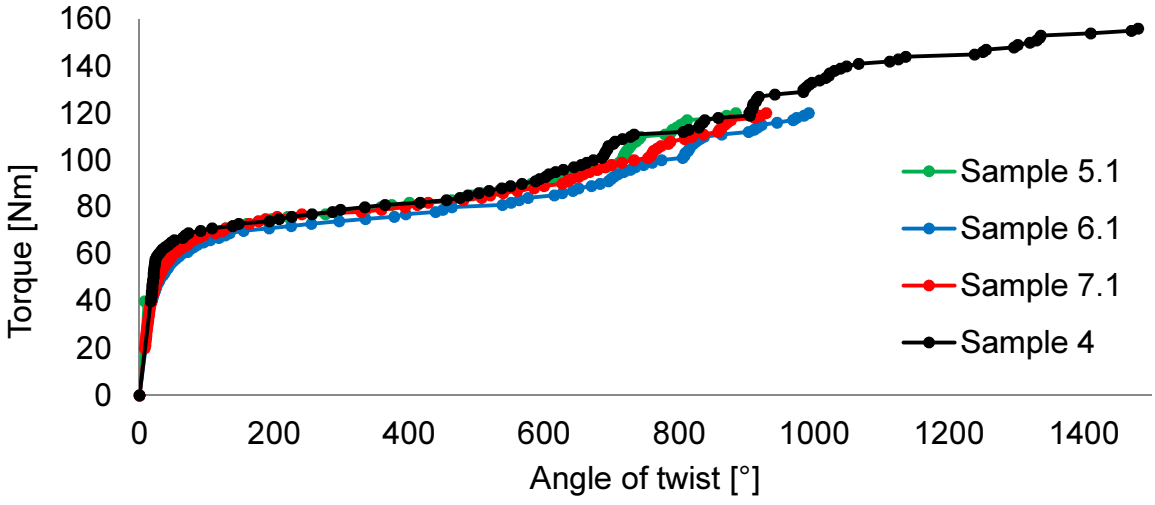

Figure 5.13. Torque versus angle of twist for samples 5.1, 6.1, 7.1, 4,twisted at 77K

Together with the samples denoted 5.1, 6.1 and 7.1, the result obtained from sample 4 is presented. All of them have been loaded using 1Nm of torque increase for each step.
It is interesting to notice in Fig. 5.13, that all of the obtained results differ from each other. One would expect almost the same results. Yet, this difference can be assigned to the character of loading (cycles with increasing amplitude). The progression of the phase transformation probably varied in all the samples, thus different mechanical behavior was obtained.
After the pre-straining (Fig. 5.13), two samples were loaded at room temperature: 5.2 and 6.2, and one sample at 77K (7.2). The results are presented in Fig. 5.14.

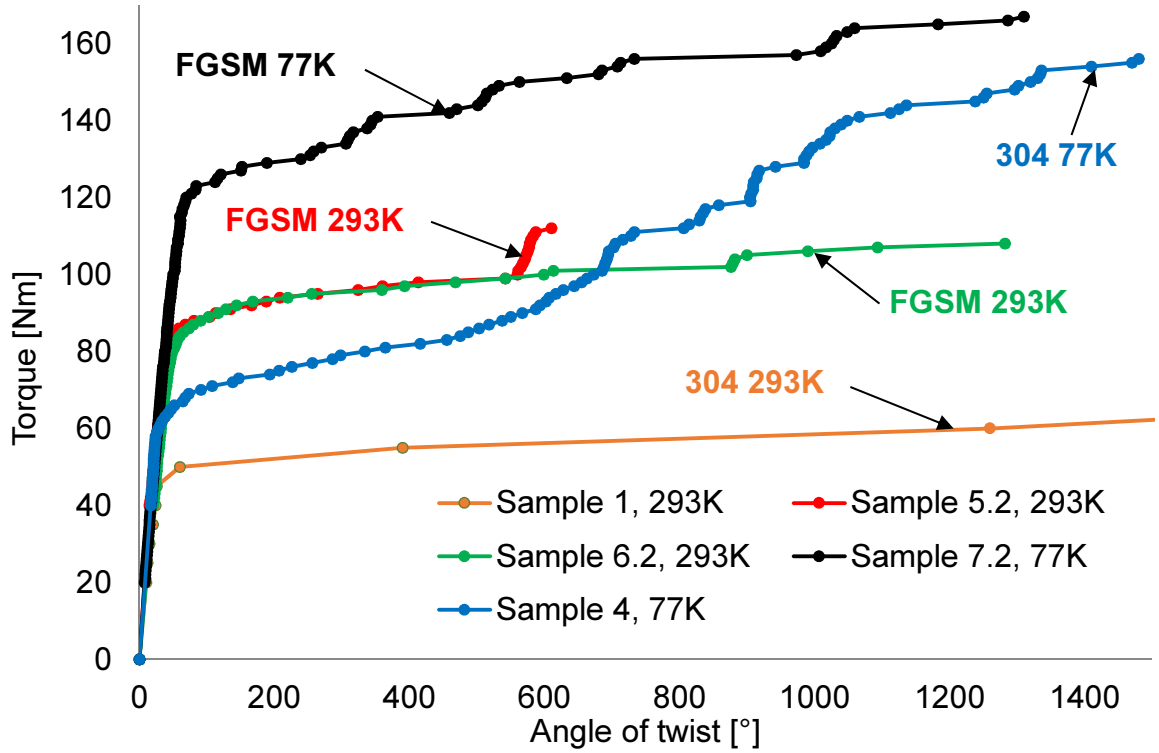

Figure 5.14. Torque versus angle of twist for the samples 5.2, 6.2, 7.2, 1, and 4, twisted at 77K or at 293K

The sample 5.2 has reached 85Nm, corresponding to the elastic range limit, and 112Nm as the maximum torque at rupture. The elastic torque increased from 45Nm (Sample 1), thus by 40 Nm, which is equivalent to 89%. The maximum torque increased from 82.5Nm for sample number 1, thus by 36%. Yet, the behavior of sample 5.2 was unexpected in the range of angle of twist preceding the rupture. In order to check if this is not a measurement error, the same test was repeated for sample 6.2. It turned out, that this “sudden increase” of torque registered for sample 5.2 was false No such behavior was observed for sample 6.2. The error was later on identified as coming from a blockage in the rack and pinion mechanism of the torque wrench. As it was blocked, the torque increased almost with no increase in the angle of twist. It is worth noticing, that the results for samples 5.2 and 6.2 are almost identical (Fig. 5.14). For sample 6.2 a maximum torque of 108Nm was reached, so actually 31% more than for sample 1. Thus, pre-straining at 77K has very beneficial effect. It caused the increase of elastic torque by 89%, and the maximum torque by 28%. Only the angle of twist decreases, from 5110° for sample 1 to 1282° for sample 6.2. The value of 1282° is equivalent to more than 3.5 full (360°) rotations, which is still substantial.

The samples 5.2 and 6.2 have higher elastic torque – 85Nm, than the sample loaded at 77K – 60Nm. Higher torque values are obtained in the whole angle range. It turned out that the FGSM sample was stronger at 293K, than the austenitic sample loaded at 77K. This is rather surprising. The yield stress of FGSM became higher at 293K, than previously at 77K. Again this proves that the mechanical properties became greatly improved, thanks to the phase transformation.
The sample 7.2 was loaded at 77K. Both at 77K until 120Nm, and later on at 77K until rupture, the sample was loaded in the clockwise direction. For sample 7.2 the torque at the end of elastic range reached about 120Nm. Thus, the end value of the torque in the pre-strain loading became the new elastic torque limit. Compared to 60Nm (for sample 4) the elastic torque increased by 100%.
The maximum torque registered for sample 7.2 was of 167Nm, which was 11Nm more (the maximum value for sample 4). So, the pre-straining process increased the maximum loading. Surprisingly, the angle of twist at rupture for sample 7.2 was equal to 1310°, which was only 170° less than for sample 4. Thus the FGSM performs better at 77K when compared to the untransformed austenitic structure.

5.6. Deformation of twisted samples

Several pictures of samples during and after torsion tests were taken. The purpose was to observe the deformation under torsion and the effects of the strain induced phase transformation. For some samples more than significant angles of twist were reached (for example, a bar of 200mm and 8mm in diameter can rotate 14 times around its axis).
The surface of the samples was photographed and it turned out that the surface texture evolved, compared to the initial sample. The reason for such a considerable surface change is related to motion of dislocations, which appear on the surface.

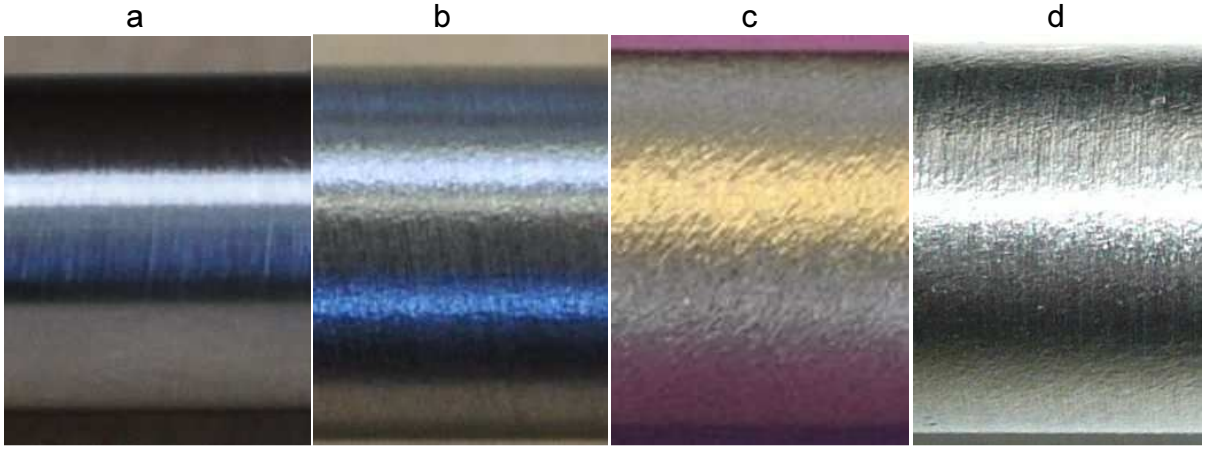

Figure 5.15 a) Texture of surface of the sample after machining, b) Texture of sample number 1 during the test, c) Texture of sample 1 after rupture, d) Texture of sample 2 after the test at 77K

Four different textures were shown in Fig. 5.15. The texture of the initial sample, just after machining, is presented in Fig. 5.15a. The residual traces of tooling, in the form of circumferential lines, are clearly visible. An intermediate photograph of sample 1 was taken in the course of loading and is presented in Fig. 5.15b. Still, traces of tooling are visible, yet, a different reflection was observed. Another photograph was taken after the rupture of sample 1 (Fig. 5.15c). In this case, the texture of the surface is drastically different, no traces of machining are visible. The surface became more rough and more glossy.

This effect is attributed to relatively high strain on the surface and the induced martensite. In Fig. 5.15d the texture was photographed for sample 2, after loading at 77K (to 870°). Compared to initial texture (Fig. 5.15a) the roughness has increased together with the glossiness, but still the traces of tooling are visible. The whole sample is presented in Fig. 5.16. In the second part, a trace of glued strain gauge is visible. Similarly to sample 2, sample 3 was twisted to 870° at room temperature. The sample after deformation is presented in Fig. 5.17. In this case, parallel lines were drawn before the test, so the angle 870° can be observed from the pattern of twisted lines.

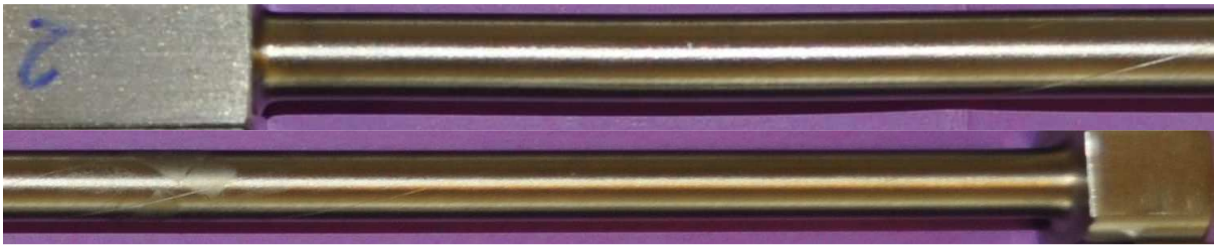

Figure 5.16. Sample number 2 after torsion test (divided into two portiones)

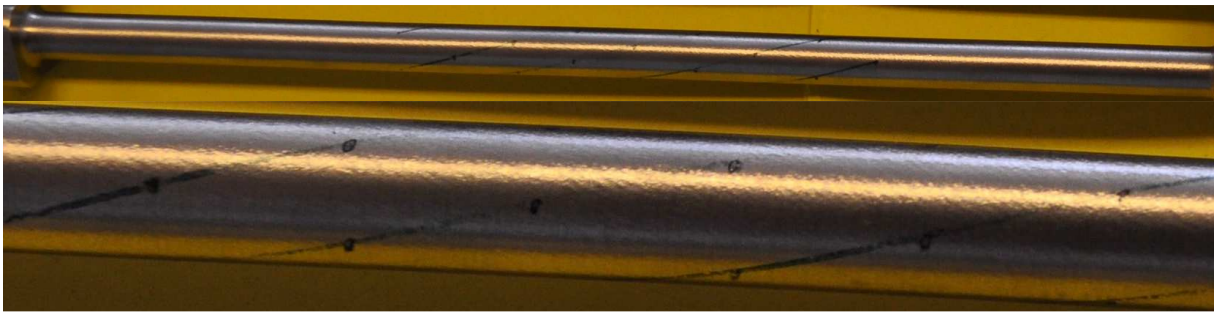

Figure 5.17. Deformation of sample 3 after 870°, together with a magnified view of the lines which were initially parallel

The samples 1, 2 and 3 were photographed together (Fig. 5.18). It is important to notice, that the length of the samples changes (specifically increases). Sample 1 has elongated almost by 10mm. Sample 2 by some 5mm, less than sample 1 but more than sample 3. Both samples 2 and 3 were twisted to 870°, yet sample 2 elongated more. This can be attributed to the difference in mechanical properties at cryogenic and at room temperatures. The cryogenic conditions lead to more elongation during torsion than in ambient conditions. Such a significant effect of elongation was unexpected, as it is not taken into account in the deformation pattern of classical torsion theory. Yet, this effect was studied in the literature, and it is known as the Swift effect (Swift 1947). This is a second order effect, according to Colak and Krempl (2005), value of the axial strain is of the order of 4% of the total shear strain.
In the present Thesis this effect was omitted in the theoretical formulation , as it would increase the complexity of already complicated model. Yet, the fact that the free-end torsion causes axial strain has very important consequence, as it can make a reason for the distribution of martensite measured in Chapter 6. The presence of axial strain caused non-zero martensite content in the middle of the cross-section. The subject of incorporating the observed elongation is not treated in the present Thesis. Incorporation of the Swift effect is a subject of separate study.

Figure 5.18. Samples 1, 2 and 3 after torsion test, axial elongation visible

The photograph of sample 4, that was loaded at 77K until rupture, is presented in Fig. 5.19. One can see that the sample became a little warped.
The fracture zone lies on the side of the hexagonal head, similarly to sample 1 (Fig. 5.18). The fracture surface is flat and perpendicular to the axis of the bar.

Figure 5.19. Sample 4 after torsion test until rupture at 77K

Sample 5.1 after the test at 77K until 120Nm is presented in Fig. 5.20. The sample was no longer straight, similarly to sample 4 (Fig. 5.19). The reason for such deformation could be the presence of a shear force when pressing the torque wrench, which produces bending. Bending was certainly possible because of unavoidable gap between the sample and the guiding bushing (Fig. 5.1).

Figure 5.20 Sample 5.1 after torsion at 77K (until 120Nm)

The same sample, after subsequent loading at 293K, has ruptured (Fig. 5.21). A magnified view of the surface is shown in Fig. 5.22.

Figure 5.21. Sample 5.2 after the test at 293K

Figure 5.22. Texture of sample 5.2 after torsion at 293K

From Fig. 5.22 it is clearly visible, how the surface is affected by relatively high plastic strains and by significant martensite content. The roughness and the glossiness have increased compared to the initial sample (Fig. 5.15a).

The sample 6.1, after torsion at 77K until 120Nm, is presented in Fig. 5.23. Again, the sample became considerably deformed. During subsequent loading at 293K and rupture (Fig. 5.24), the sample fractured near the center. It turned out that the sample straightened, compared to Fig. 5.23. This proves that the cycles of torsion and the progression of the phase transformation affect the evolution of shape. The sample can be subjected to a significant distortion.

Figure 5.23. Sample 6.1 after torsion at 77K (until 120Nm)

Figure 5.24. Sample 6.2 after rupture under torsion at 293K

For sample 7.1 more detailed photographic study of deformation was done. After several stages of loading, pictures of the shape were made. They are presented in Fig. 5.25. After 77Nm the sample was still straight. It became deformed after 79Nm, and as soon as the torque of 120Nm was reached, different deformation pattern was observed.

Figure 5.25. Deformation of sample 7.1 during loading at 77K

Figure 5.26. Several stages of deformation for sample 7.2 loaded at 77K

Similarly, for the second stage of loading (sample 7.2) at 77K, the process of twisting was photographed and is presented in Fig. 5.26. The deformation stays similar to the initial one, however, it becomes actually more straight, as can be seen in the photograph after rupture.

5.7. Summary of torsion experiments for 304 stainless steel

In total 10 samples were tested. The maximum values of torque and angle of twist are summarized in Table 5.2.

Sample number	Temperature of the test [K]	Max. angle of twist [°]	Max torque [Nm]
1	293	5110	82.5
2	77	870	100
3	293	870	60
4	77	1480	156
5.1	77	884	120
5.2	293	610	112
6.1	77	992	120
6.2	293	1282	108
7.1	77	929	120
7.2	77	1310	167

Table 5.2. The designations of samples by the temperature of test and the maximum values of angle of twist and torque

5.8. Conclusions

After the sequence of torsion tests on 304 stainless steel bars, the following conclusions have been drawn:
1. It is possible to induce the martensitic transformation by means of torsion at room and at the liquid nitrogen temperature. A magnetization test revealed the presence of magnetic force, indicating the existence of martensite in the samples.
2. The possibility of creation of FGSMs by means of torsion was demonstrated.
3. Analyzing the performance of FGSMs, created by twisting stainless steel bars at 77K until 120Nm, it turned out that at room temperature the elastic torque increased by 89%, and the maximum torque by 36%.
4. Analyzing the performance of FGSMs at 77K it turned out, that the elastic torque increased by around 100%, and the maximum one by 7%. The maximum angle of twist decreased only by 11%.
5. An increase of mechanical properties (yield strength, ultimate strength) has been observed for all the FGSMs.
6. Torque versus angle of twist response differs tremendously for the same material (304ss) at 293K and at 77K. The same sample can carry 100% more load at cryogenic temperature.

It has been demonstrated that it is possible to influence the microstructure of the sample by the phase transformation induced by torsion. In the next chapters detailed material science investigations are carried out, including microscopic observations, micro-hardness measurements and martensite content distribution measurements.

6. Microscopic analysis of FGSMs

The present chapter is devoted to investigation of the properties of newly created FGSMs, obtained by means of torsion at cryogenic temperatures. The results in terms of torque versus angle of twist were presented in the previous chapter.
In the present chapter, four samples have been studied, namely samples 1, 2, 3 (see Table 5.2), and not loaded reference sample, denoted “Raw”. First of all, round slices have been extracted from the bars, polished and etched to reveal martensite presence. The resulting micrographs are presented in the section 6.1. In the following section 6.2, the micro-hardness was measured across the cross-section. Micro-hardness informs indirectly about the martensite content, as this fraction is almost 3 times harder than austenite. In the section 6.3, the martensite content was measured on the surfaces of samples 1, 2, 3 as well as “Raw”. Quantitative measurements clearly indicate the resultant distribution of martensite, after reaching various angles of twist and at different temperatures. From these results, in section 6.3 the kinetics of phase transformation was identified.

6.1. Microscopic observations

6.1.1. Extracting material samples

Four from six samples (1,2,3, Raw) were subjected to microscopic investigation. Three transverse and one longitudinal cross sections were extracted from the samples (Fig. 6.1). One cross-section (cs2) was cut out from the central portion of the sample, and the remaining ones at a distance of 50mm from the centre. The longitudinal slice was cut out from the portion located closer to extremity of the sample. Generally, the longitudinal cuts were used to evaluate the content of ferrite in the structure. On the other hand, the perpendicular cuts were used to analyze the induced martensite content and its distribution.

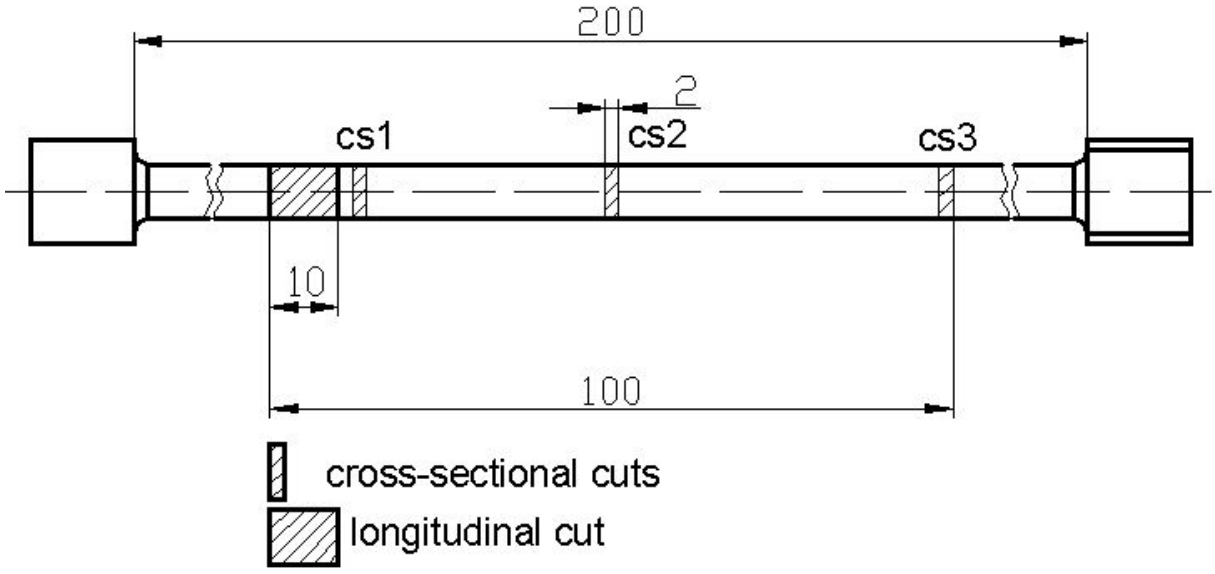

Fig. 6.1. Transverse and longitudinal cross-sections and their position

6.1.2. Ferrite content measurements

Longitudinal extractions were polished and etched with #98 of ASTM E407 to reveal ferrite. Ferrite content has been measured via the automatic image analysis associated with LEICA DMRME microscope (Fig. 6.2). The measurements were performed on dark field images, as shown in Fig. 6.3 a,b,c,d.

Figure 6.2. The LEICA DMRME optical microscope

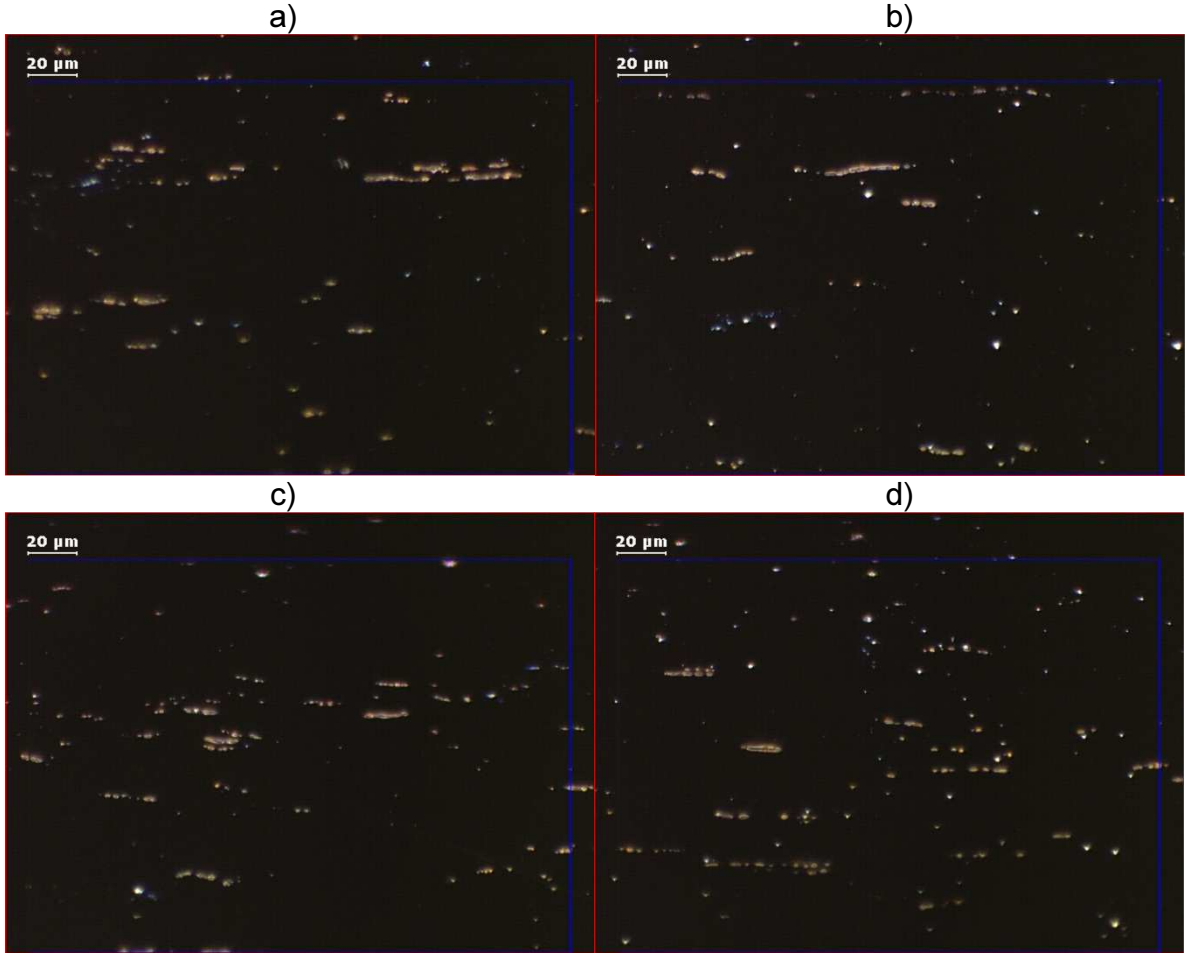

Fig. 6.3. Dark field images obtained from small portions of the longitudinal cross sections: a) Sample 1, b) Sample 2, c) Sample 3, d) Sample “Raw”

The resulting fraction of ferrite was calculated as the ratio between the area occupied by the ferrite (white dots) and the whole area. The results are presented in Table 6.1.

Cut	Area of ferrite [μm^2]	Ferrite content [%]
Sample 1	395.38	1.1
Sample 2	253.57	0.71
Sample 3	272.56	0.76
Sample Raw	428.82	1.19

Table 6.1. Integral area of ferrite and its content

The results confirmed the expectation of very low ferrite content in all the samples. The maximum value was equal to 1.2% for the "Raw" sample (Tab. 6.1). Yet, similar values were obtained for the other ones - around 1%.
The ferrite fraction was important for the martensite content measurements. The feritscope used to measure martensite content, identifies all the magnetic phases, thus ferrite as well. From the results shown in Tab. 6.1 it was confirmed that the ferrite content was very small. For this reason one was sure that the readout from the Feritscope was indicating only martensite. Small quantity of ferrite (1%) was ignored in the measurements by means of Feritscope.

6.1.3. Microstructure observations of martensite

The transverse cuts (Fig. 6.1) were polished and etched with the etchant #13a of ASTM E407. A digital microscope Keyence VHX-1000 was used (Fig. 6.4). The photographs were taken with 200x magnification. In order to obtain the pictures of the whole cross-section, a (8mm in diameter) stitching technique was used. Three cross sections were analyzed for each of 4 samples (1, 2, 3, Raw). Two types of lightings were used for better contrast.

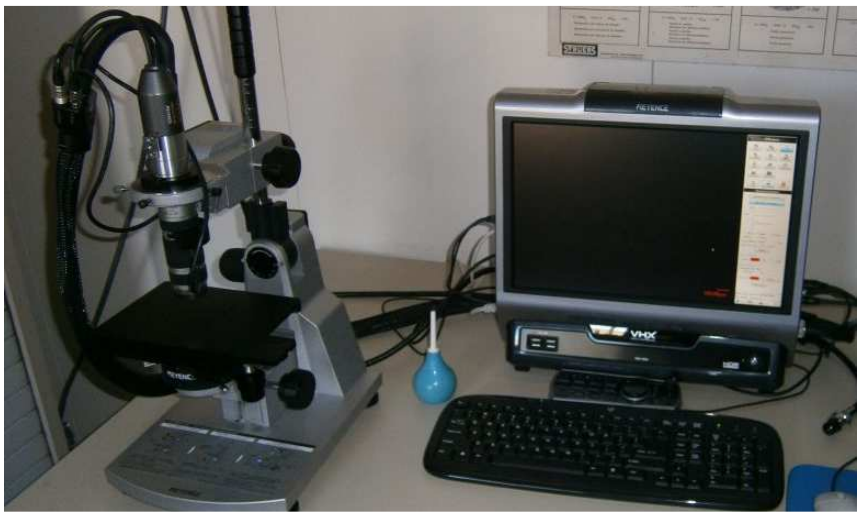

Figure 6.4. The Keyence VHX-1000 digital microscope

All the microscopic photos are presented in the following sections. The photographs are shown in the following sequence: sample 1, sample 2, sample 3, sample "Raw".

6.1.4. Sample 1 - loaded at 293K until rupture

The microscopic photographs were obtained from three perpendicular cross-sections and for one longitudinal cross-section per each of the samples. Two types of lighting were used. The stitched microscopic photographs from the first type of lighting are shown in Fig. 6.5.

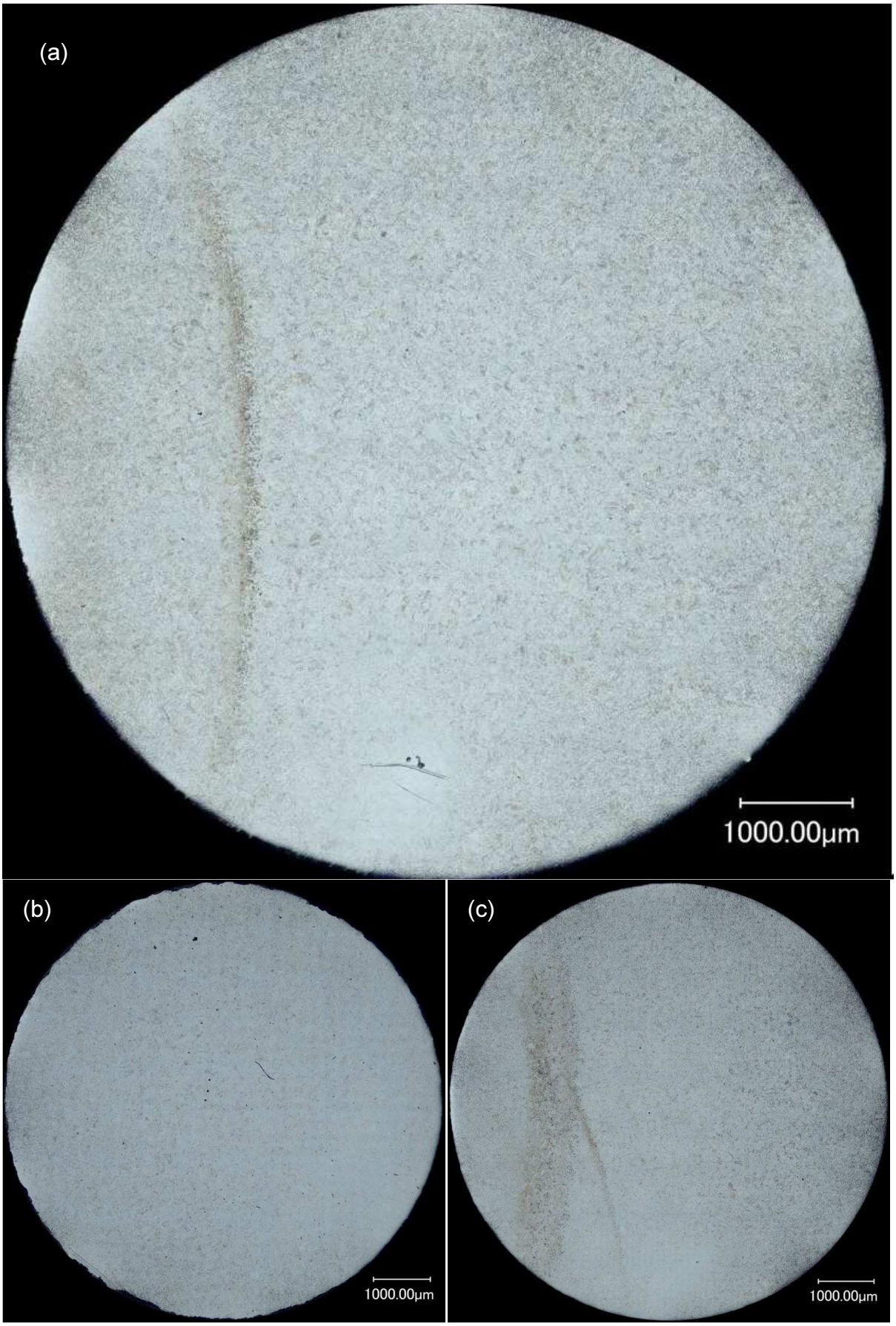

Figure 6.5. The microstructure of the sample 1 (loaded at 293K until rupture), lighting type 1, a) cross-section 2, b) cross-section 1; c) cross-section 3

The photograph of the cross-section 2 was the most representative one, thus, it has been enlarged (Fig. 6.5a). The microstructures of the cross sections 1 and 3 are presented in Fig. 6.5b, c. In Fig. 6.5a the scratch on the left-hand side was visible, yet the overall quality of the photo was good. One could see increasing concentration of darker spots towards the edge of the cross-section, which represents the martensitic phase.
The microscopic picture of the longitudinal sample is presented in Fig. 6.6. Again, stitching technique was used, as the area of the cross-section was relatively high – about 50 mm^2.

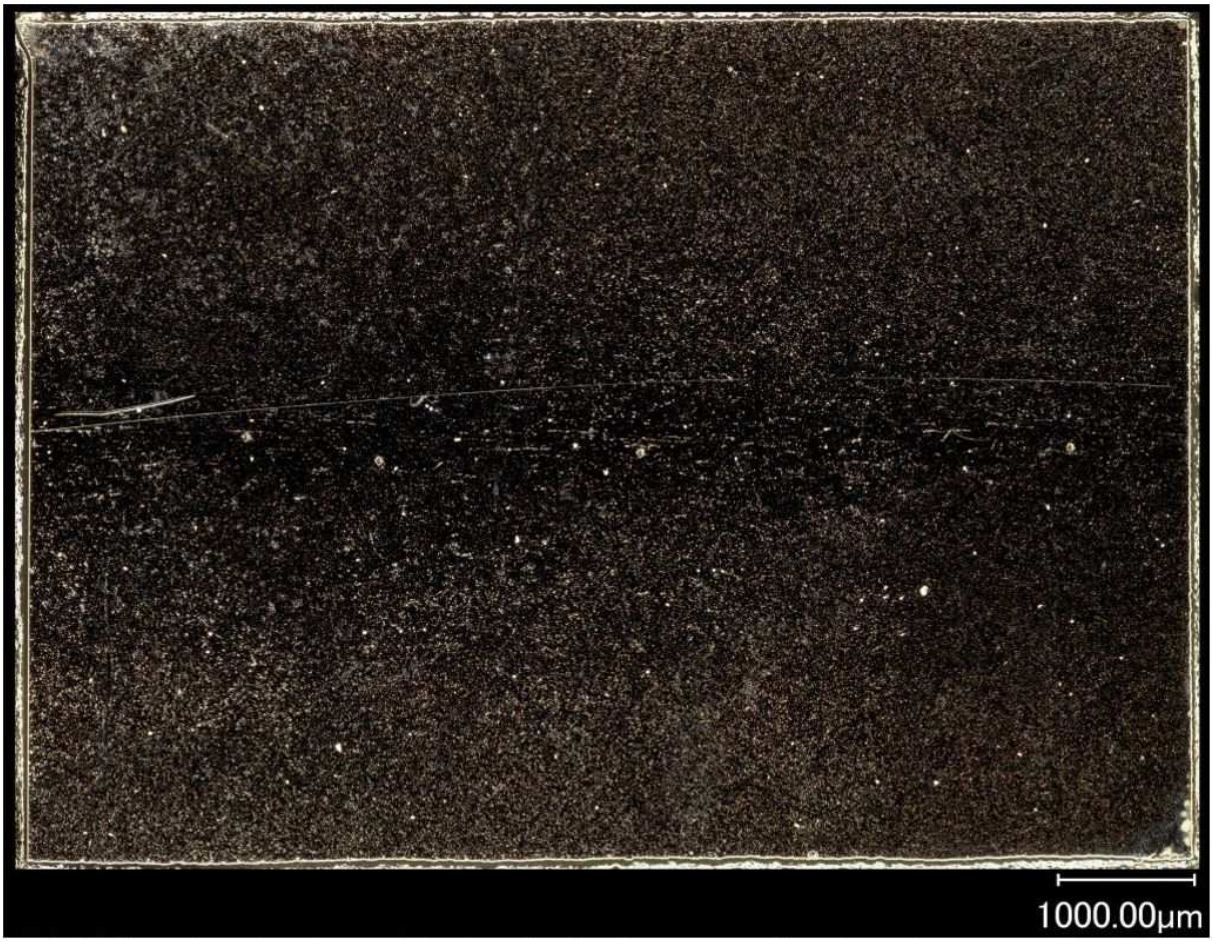

Figure 6.6. Microstructure of the longitudinal cross-section of sample 1 (loaded at 293K until rupture), dark field image

From Fig. 6.6 one can clearly identify the core of the bar, with rather smooth black color, and the outside layer with many bright dots. The dots represent the increasing content of martensite.
The photographs made with the second type of lighting are presented in Fig. 6.7. The picture of highest quality has been enlarged for more details (Fig 6.7a). The cross-sections 2 and 3 are shown in smaller pictures (Fig. 6.7b, c). The grain size in Fig. 6.7a is higher in the center of the sample and smaller towards its surface. The core is darker indicating more austenite, whereas the outside layer is brighter indicating more martensite. The photographs shown in Fig. 6.7b, c have lower quality because of the presence of scratches which occurred during the handling of the samples.

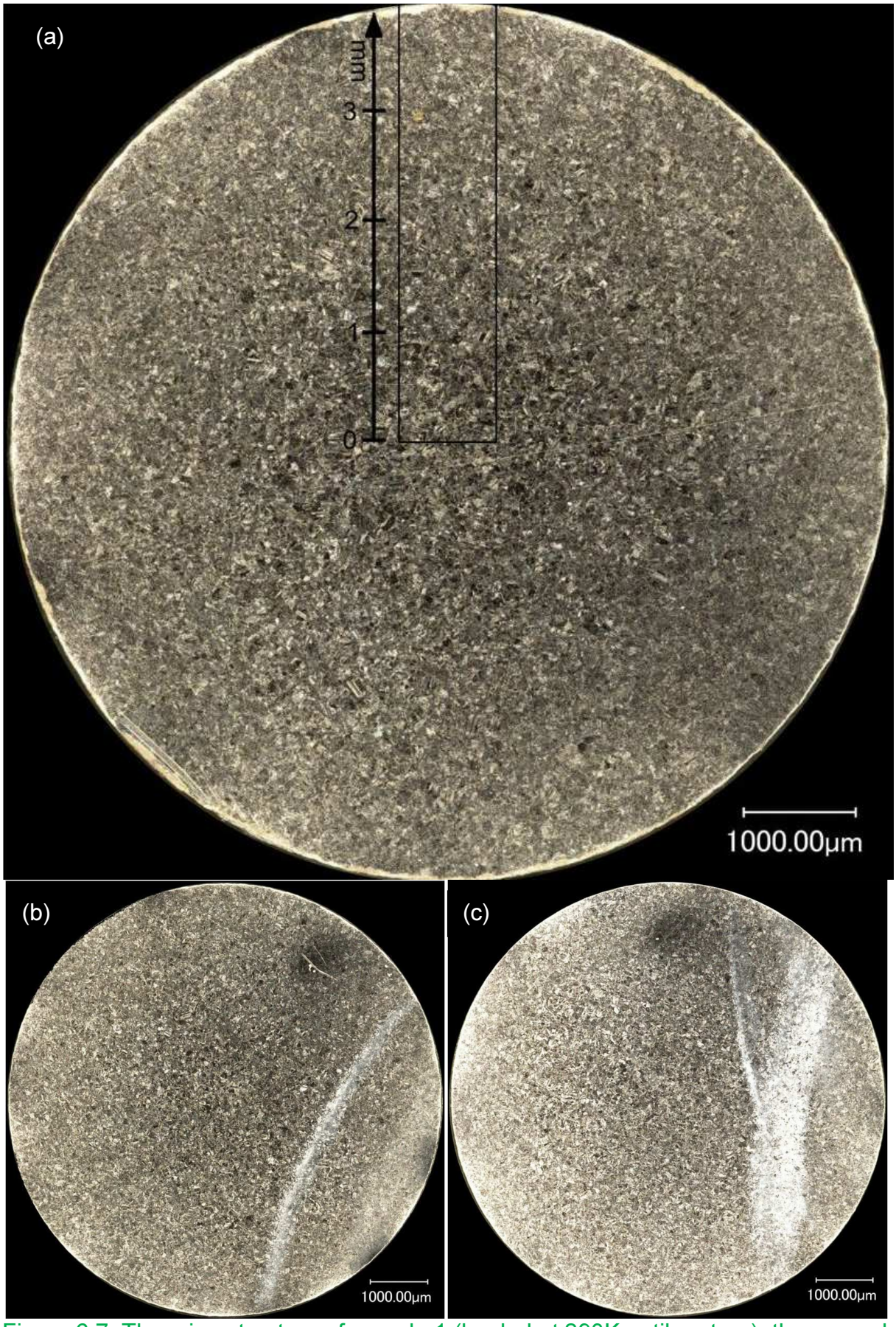

Figure 6.7. The microstructure of sample 1 (loaded at 293K until rupture), the second lighting type, a) cross-section 1, b) cross-section 2, c) cross-section 3

A strip from Fig. 6.7a has been magnified and is presented separately in two parts in Figs 6.8 and 6.9. It was magnified to highlight how the microstructure changes from the center towards the surface. First two milimeters of the microstructure, measured from right to left, are presented in Fig. 6.8. The dark colour represents the austenite, and the white colour the martensite. There are slightly more dark grains near the center than at 2 mm distance.

Figure 6.8. First two millimeters of the strip extracted from the cross-section number 1 of the sample 1 (Fig. 6.7a)

The second strip extracted from Fig. 6.7a is presented in Fig. 6.9. Compared to Fig. 6.8, there are much brighter grains indicating higher martensite content.

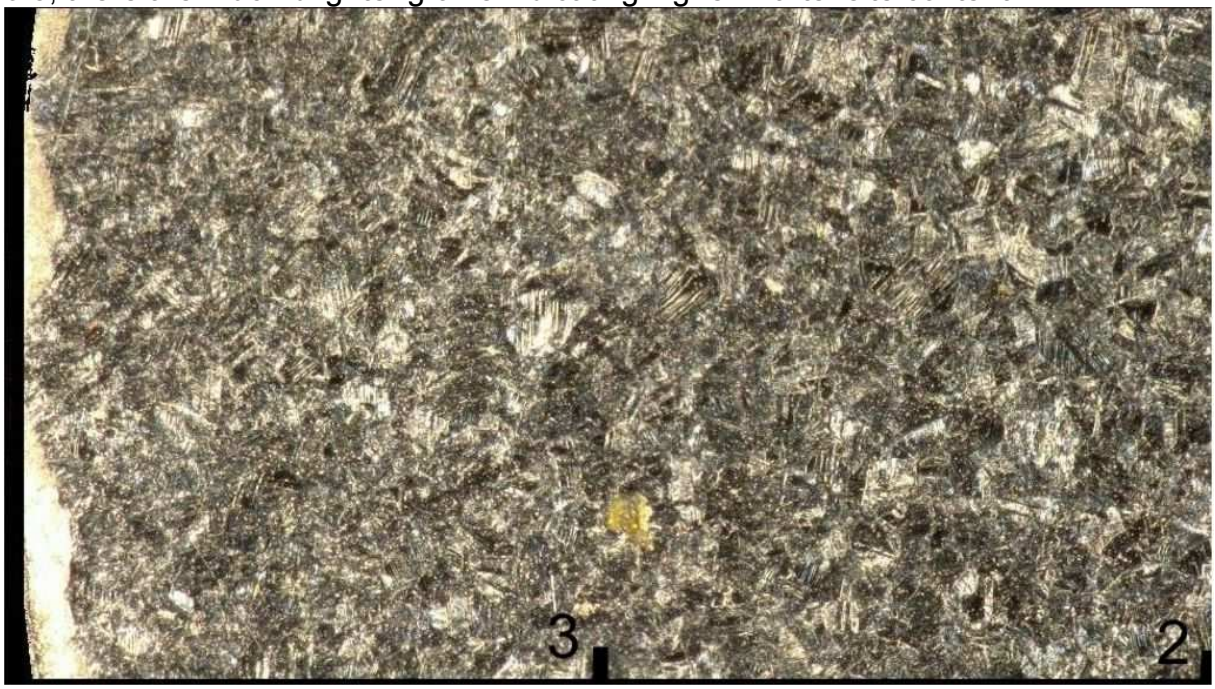

Figure 6.9. Second part of the strip extracted from the cross-section number 1 of the sample 1 (Fig. 6.7a)

The microscopic photographs (Figs 6.8, 6.9), however, did not provide quantitative measure of the martensite content and its variation along the radius. One can only say that the microstructure is changing and more martensite is observed towards the surface of the sample. Visual proof supported this statement.

6.1.5. Sample 2, loaded at 77K and twisted to 870°

Again, for sample 2 three cross-sections and one longitudinal section have been analyzed, according to Fig. 6.1. Only one photo with the first type of lighting was made, for the cross-section 1 (Fig. 6.10a). This type of lighting doesn't provide enough quality, so there is not much difference than one can see from Fig. 6.10a. Better pictures were made with the second type of lighting, presented in Fig. 6.11.
In Fig. 6.10b the longitudinal section is presented. Yet, there was not much that one could see, because of the presence of many scratches. No macro-cracks were seen in both figures 6.10a and 6.10b.

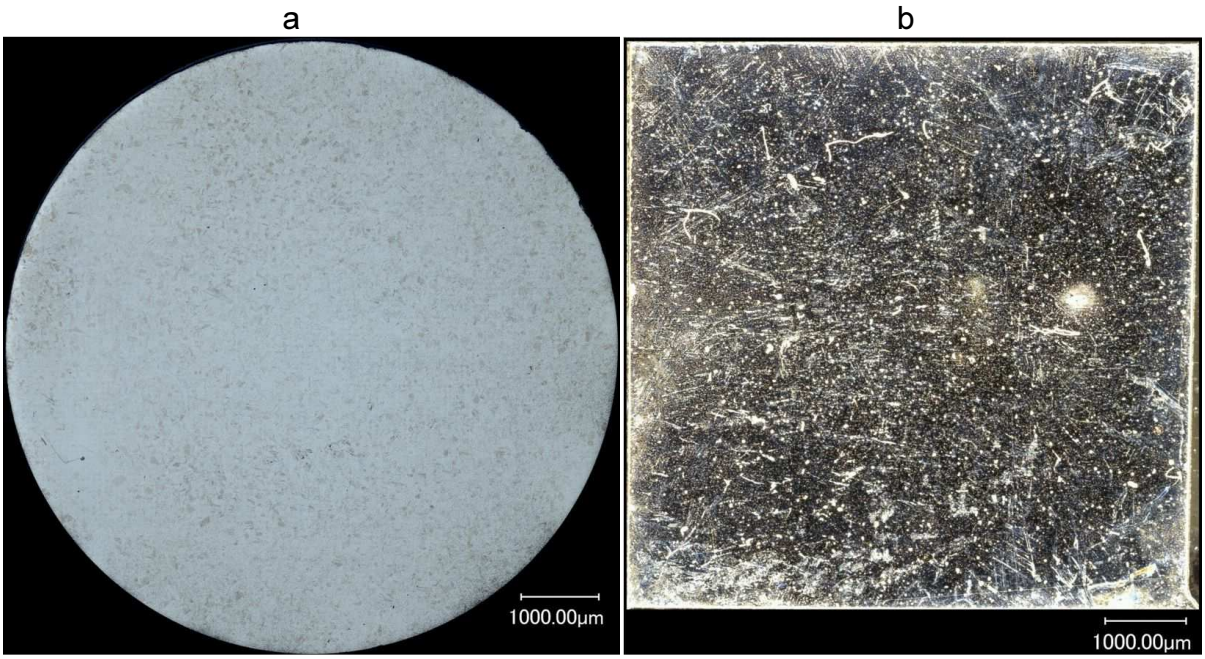

Figure 6.10 a) The microstructure of the cross-section 1 from the sample 2 (loaded at 77K up to 870°), lighting type 1, b) longitudinal cross-section, lighting type 2

The microscopic photographs of three cross-sections made with the second lighting type are presented in Fig. 6.11. The highest quality photo of the cross-section 1 is enlarged in Fig. 6.11a. Cross-sections 2 and 3 are presented in Figs 6.11b and 6.11c.
From Fig. 6.11a it is clearly visible that the darker area (austenite) is predominant in the center of the cross-section. Towards the surface, more brighter grains are present. The microstructure has symmetric character around the center, as expected from the theory (the strain field is axially symmetric). From Fig. 6.11b, c the symmetry is visible as well, yet their quality diminished because of the presence of a scratch.
A strip from the first cross-section (Fig. 6.11a), from the center towards the bottom of the cross-section, has been enlarged. It is divided into two pictures, presented in Figs 6.12 and 6.13, respectively.

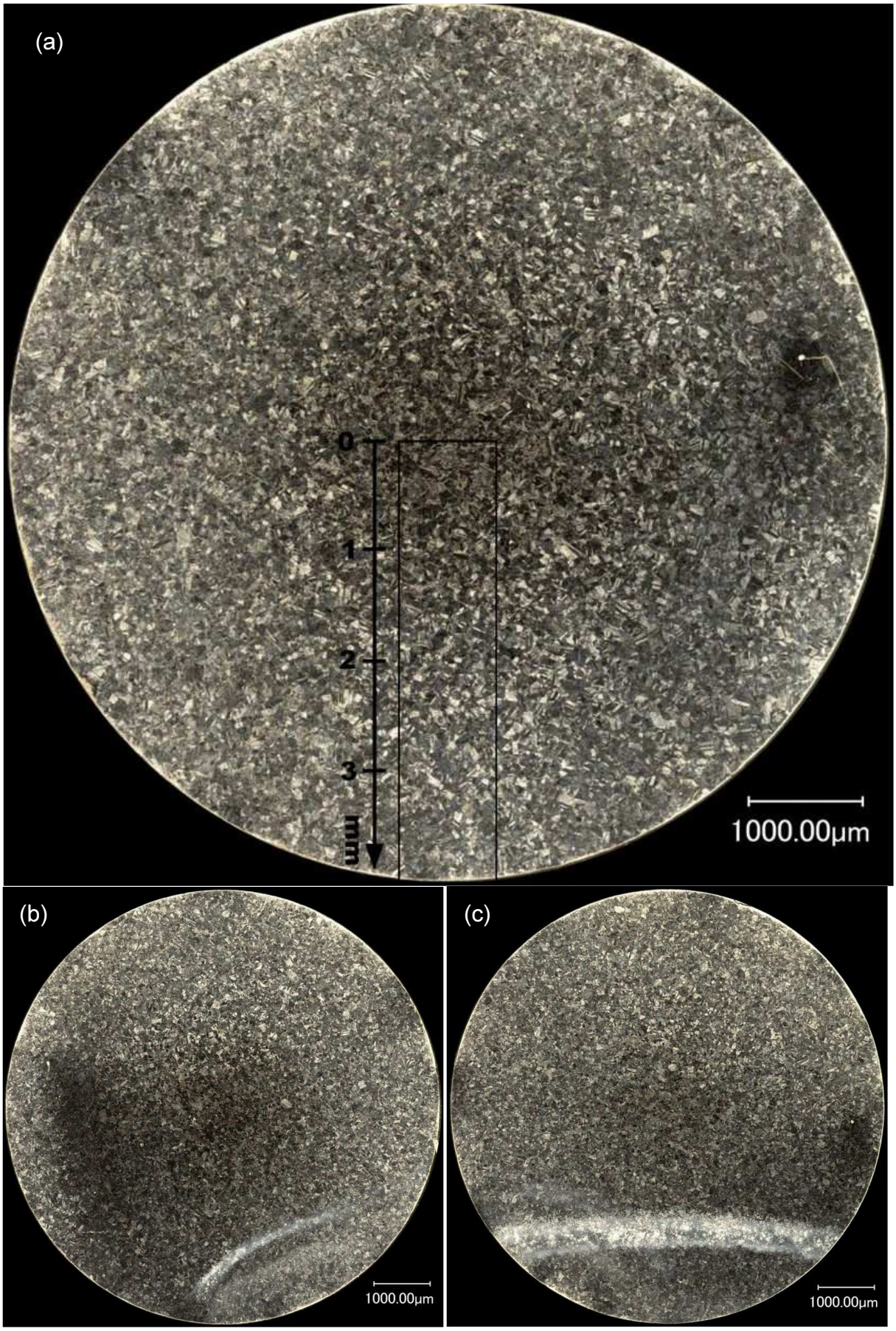

Figure 6.11. The microstructure of the sample 2 (loaded at 77K up to 870°), a) cross-section 1, b) cross-section 2, c) cross-section 3

A few martensite grains are present in the first millimeter of the cross-section from the center (Fig 6.12). The laths of martensite are clearly visible. One may notice the increasing amount of martensite grains towards the left edge (surface of the sample).

Figure 6.12. The first two millimeters of the strip extracted from the cross-section number 1 of the sample 2 (Fig. 6.11a)

In the second strip (Fig. 6.13) bright colors dominate, indicating high martensite content. As this sample was loaded at 77K up to 870° (about 2,5 turns), high martensite content was expected. So, actually, the photograph in Fig. 6.13 qualitatively confirms this expectation.

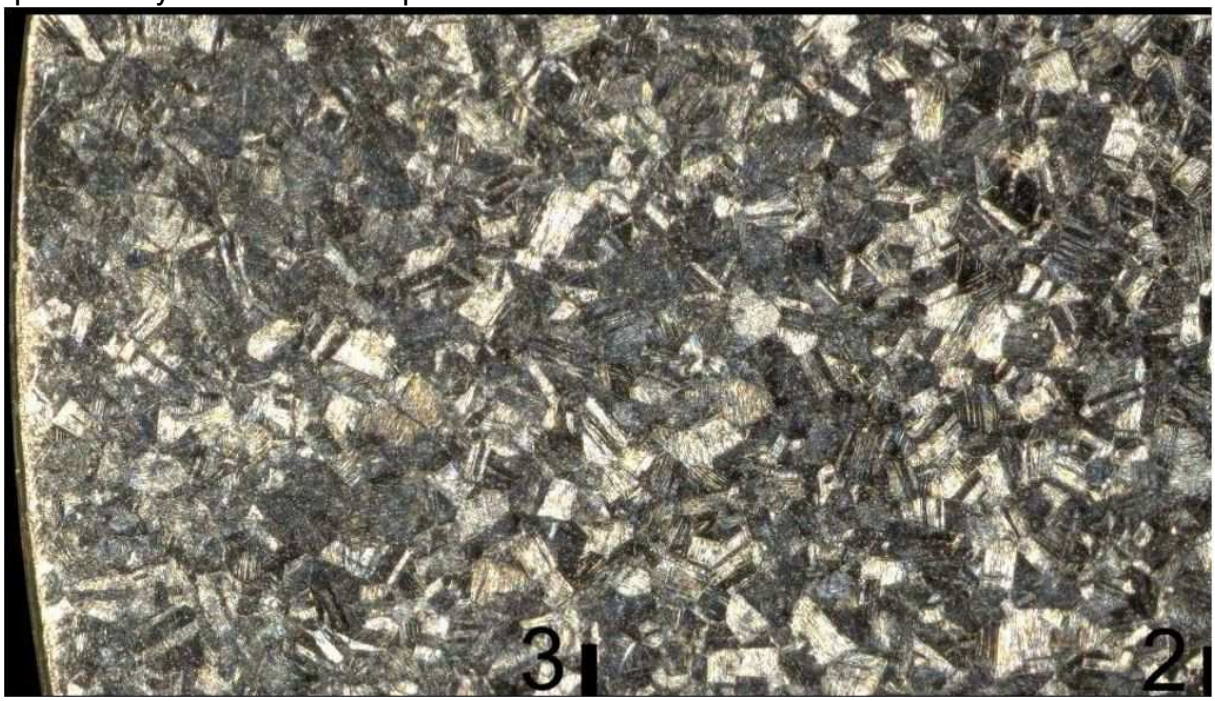

Figure 6.13. Second part of the strip, extracted from the cross-section number 1 of the sample 2 (Fig. 6.11a)

6.1.6. Sample 3, loaded at 293K and twisted to 870°

Sample 3 has been loaded at room temperature to the same angle of twist as the sample 2, specifically 870°. Because of the temperature conditions, small amount of martensite was expected.

The longitudinal microscopic photo is presented in Fig. 6.14. The second lighting type was used. The core in Fig. 6.14 is visible, characterized by almost continuous dark region with slightly elongated grains in the axial direction. Towards the top and the bottom brighter dots are visible, indicating the presence of martensite.

Figure 6.14. The microstructure of the longitudinal cross-section of sample 3 (loaded at 293K up to 870°), second lighting type

Three cross-sections photographed with the first lighting type are shown in Fig. 6.15. The second cross-section has been enlarged (Fig. 6.15a). The microstructure is symmetric around the center of the sample. Slightly more darker regions are visible near the surface, indicating more martensite there. Similar results can be seen in the third cross-section, presented in Fig. 6.15c. Not much can be said about the picture presented in Fig. 6.15b, as its quality is poor because of the presence of a scratch.

Microscopic photos made with the second lighting type are presented in Fig. 6.16 for all three cross-sections. The one of best quality, for the 3rd cross-section, has been enlarged (Fig. 6.16a). The remaining ones are presented in Fig. 6.16b (cs 1) and Fig. 6.16c (cs 2).

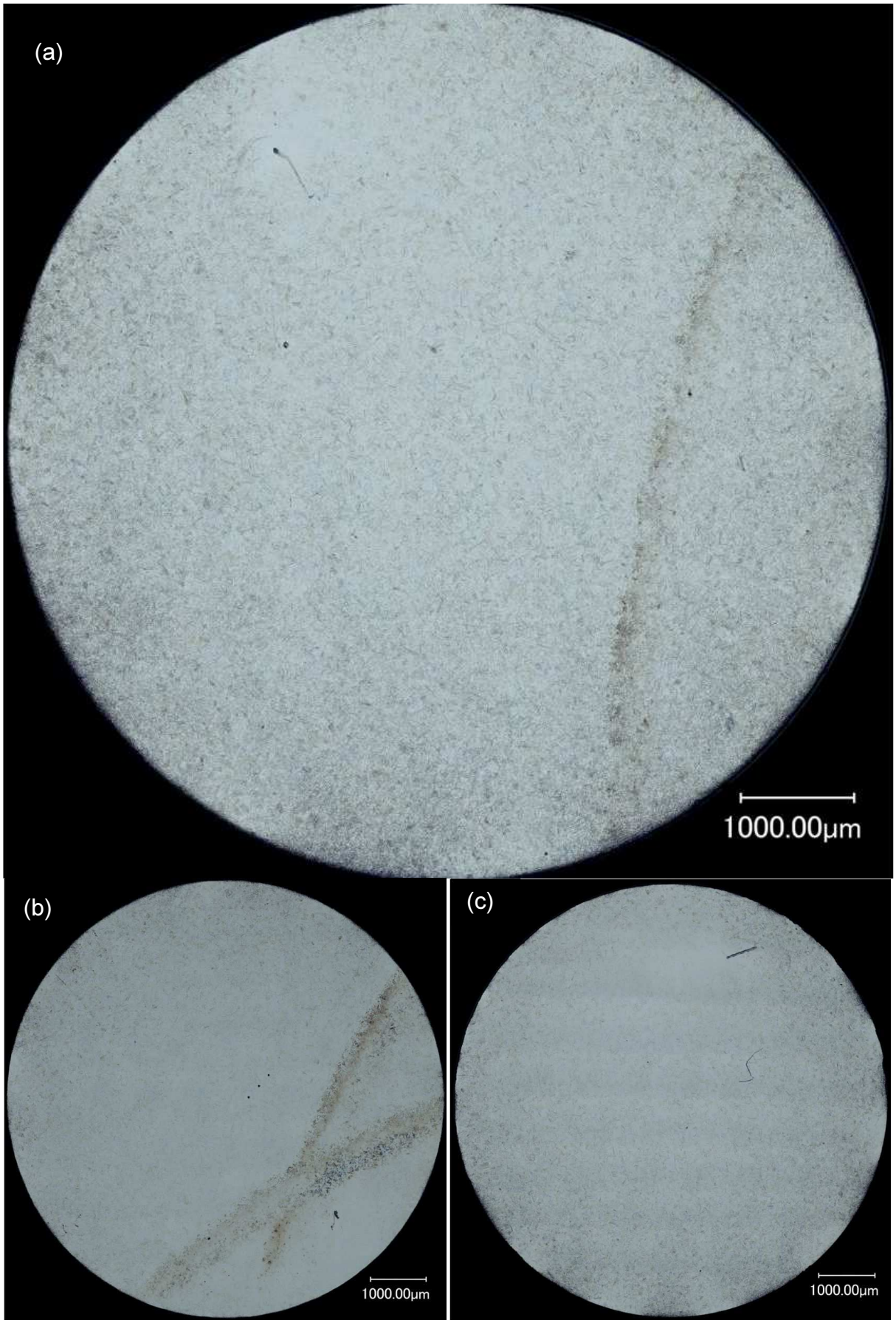

Figure 6.15. The microstructure of the sample 3 (loaded at 293K up to 870°), first lighting type, a) cross-section 2, b) cross-section 1, c) cross-section 3

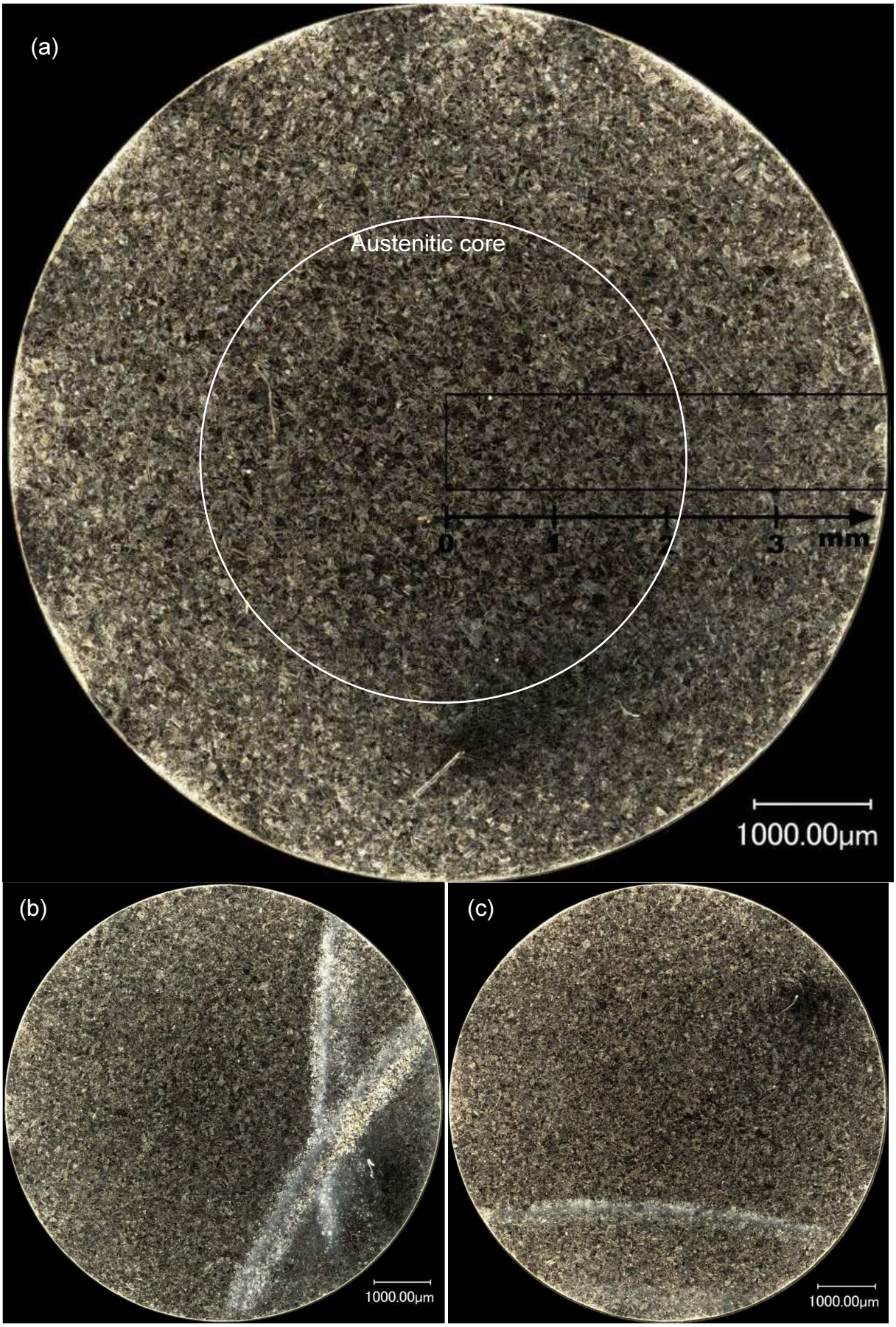

Figure 6.16 The microstructure of the sample 3 (loaded at 293K up to 870°), lighting type 2, a)cross-section 3, b) cross-section 1, c) cross-section 2

In Fig. 6.16a one may see predominantly dark color, indicating much more austenite than martensite. An austenitic core has been identified. Compared to Fig. 6.11a (sample 2), much wider dark zone is present in the sample 3. This confirmed theoretical expectation - more martensite was created at 77K with the same angle of twist. Also, for the remaining cross-sections (Fig. 6.16b, c) dark color predominated.
A strip has been extracted from third cross-section (Fig. 6.16a) and enlarged in two photos shown in Figs 6.17 and 6.18.

Figure 6.17. First two millimeters of the strip extracted from the cross-section number 3 of the sample 3 (Fig. 6.16a)

Figure 6.18. Second part of the strip extracted from the cross-section number 3 of the sample 3 (Fig. 6.16a)

The first two millimeters of the microstructure extracted from the center of sample 3 (Fig. 6.17) shows no radial variation. Bright grains are visible indicating the presence of martensite, however less laths are observed, compared to Fig. 6.12 (sample 2).
The second strip, presented in Fig 6.18, shows more martensite grains towards the surface. This clearly indicates increasing martensite content along the radius of the sample.

6.1.7. Sample in raw state

The “Raw” sample has been used for comparison. This sample was known to have almost purely austenitic structure. It was extracted from 304 stainless steel bar.
The longitudinal section is shown in Fig. 6.19. Yet, the quality is not very good. Thus, not much can be said about this microstructure.

Figure 6.19. The microstructure of the longitudinal cross-section from the “Raw” sample, second lighting type

Three cross-sections, observed with first lighting type, are shown in Fig. 6.20. Cross-section 3 has been enlarged (Fig. 6.20a). Actually, this photograph resembles the other pictures made with the first type of lighting (like Fig. 6.15). The quality of the photographs in Fig. 6.20b, c is very low. The general view did not inform about the presence of martensite, even though it might have looked similar to these observed previously.
Three cross-sections, photographed with the second type of lighting, are shown in Fig. 6.21. Cross-section 3 has been again enlarged (Fig. 6.21a). From this photo it appears that the bright areas are martensite. However, closer look into the magnified strip shown in Figs 6.22 and 6.23 reveals the difference in the morphology of the grains. The photos from Fig. 6.21b, c appear quite similar to the first one (Fig. 6.21a), yet they were overexposed.
The strip extracted from third cross-section, shown in Figs 6.22 and 6.23, clearly indicates that the microstructure is homogeneous. Different shape of grains is visible, compared to the other samples. Knowing that this sample could have only residual martensite content, a conclusion was drawn that these grains represented purely austenitic structure.

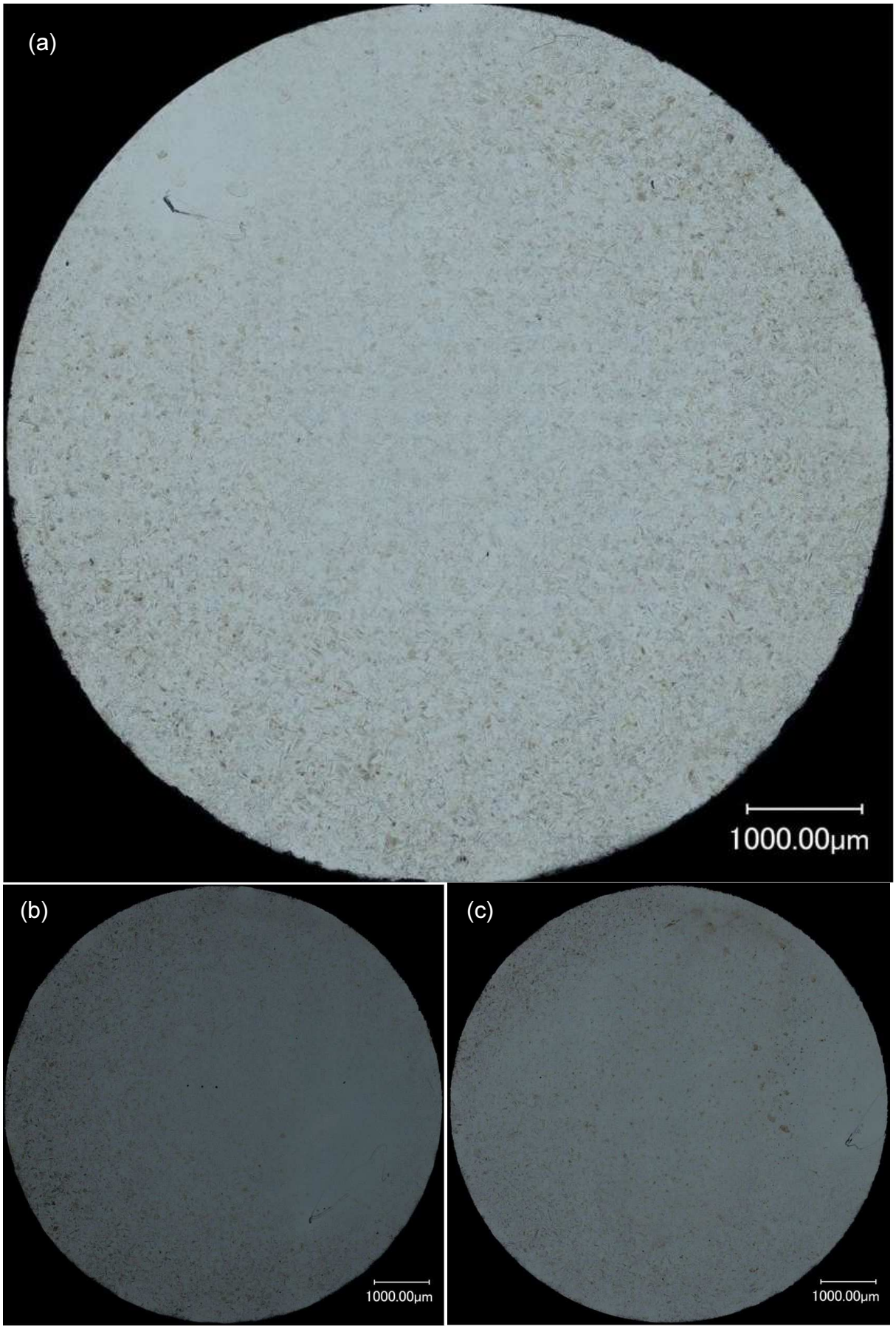

Figure 6.20. The microstructure of the ”Raw” sample, first lighting type, a) cross-section 3, b) cross-section 2, c) cross-section 1

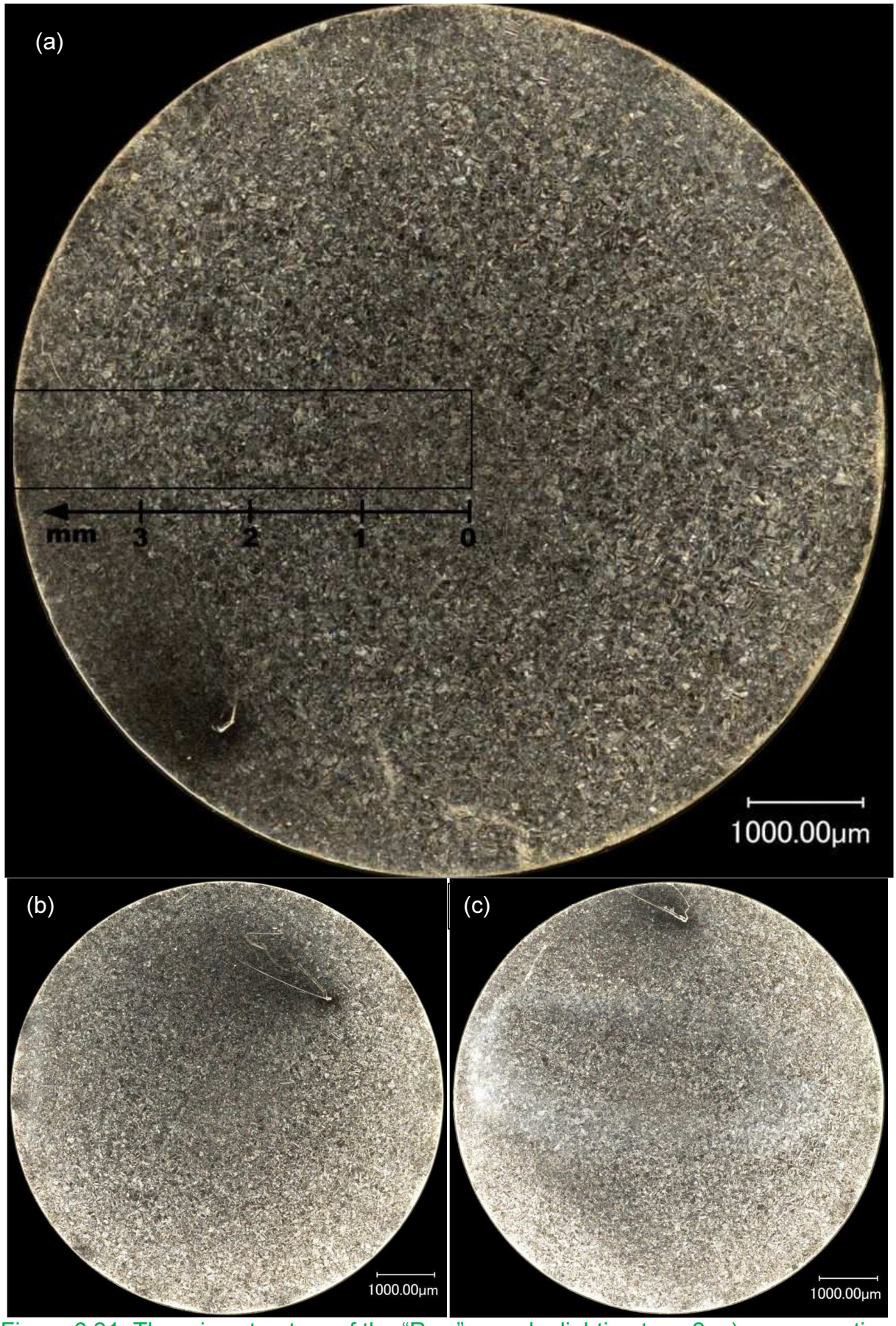

Figure 6.21. The microstructure of the “Raw” sample, lighting type 2, a) cross-section 3, b) cross-section 2, c) cross-section 1

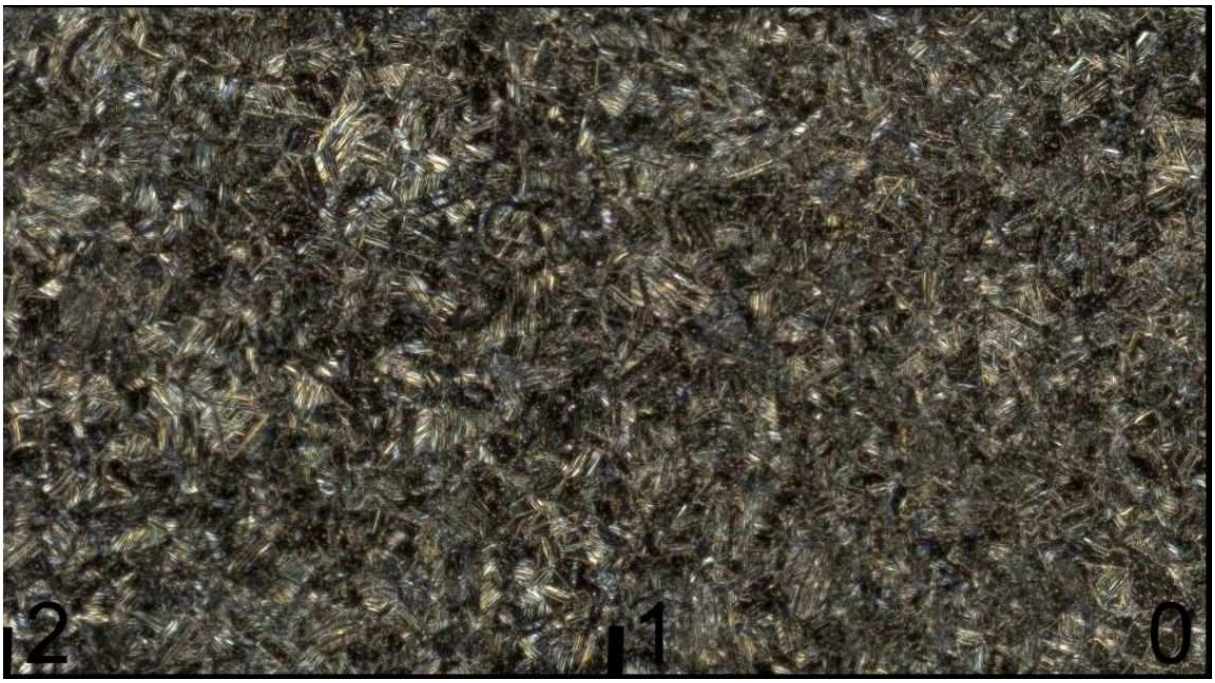

Figure 6.22. First two millimeters of the strip extracted from the cross-section number 3 of the “Raw” sample (Fig. 6.20a)

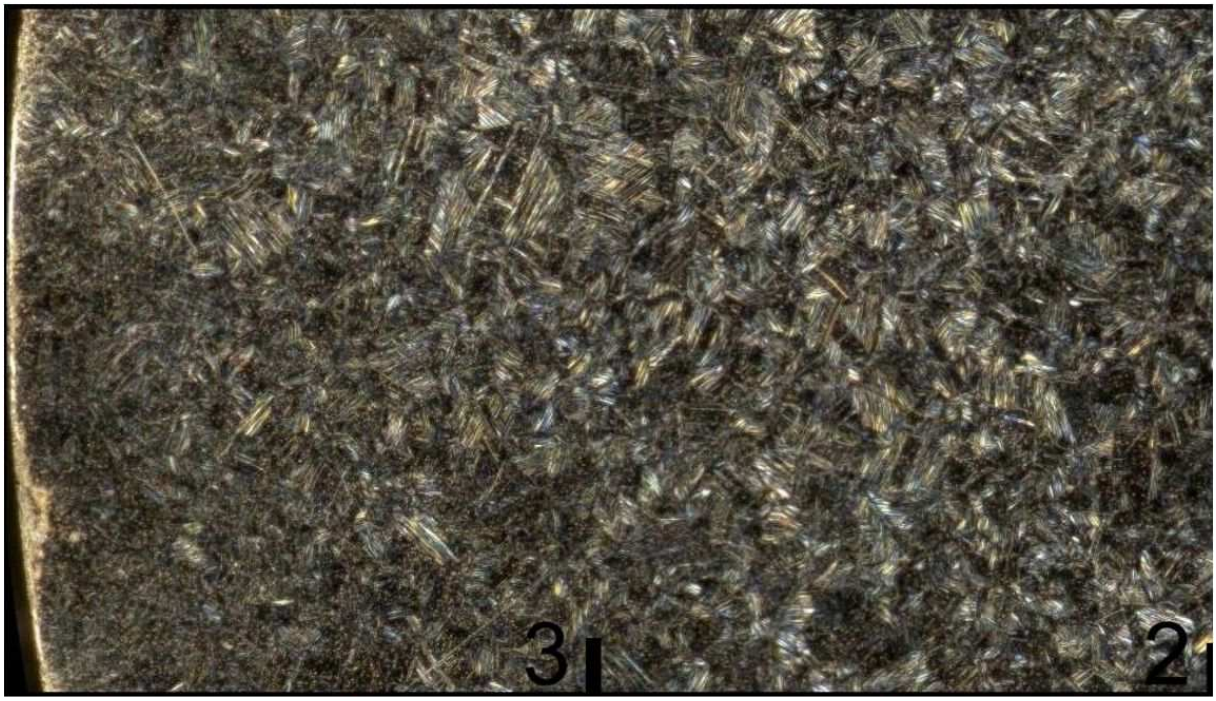

Figure 6.23 Second part of the strip extracted from the cross-section number 3 of the “Raw” sample (Fig. 6.20a)

6.1.8. Conclusions from the microscopic observations

The following conclusions have been drawn from the above observations:
1. Qualitatively, the martensite has been identified in the microstructures.
2. Radial increase of the martensite content has been demonstrated.
3. More martensite was obtained in the sample twisted at 77K, compared to the sample twisted at 293K, to the same angle of twist 870°.
Still, quantitative estimation of the martensite content appears necessary. More detailed results obtained by means of the Feritscope are presented in section 6.3.

6.2. Micro-hardness measurements

Martensitic and austenitic microstructures have very different mechanical properties. The martensite is hard and brittle, whereas, the austenite is soft and ductile. The hardness of martensite is almost 3 times higher than of the austenite. Therefore, it is expected that the mixture of austenite and martensite will have hardness in the range between the hardness of pure austenite and of pure martensite. Moreover, it is expected that the distribution of martensite along the radius of the sample is linear, because of linear function of the shear strain distribution. The micro-hardness can be measured locally by means of micro-indentations. It is a good, indirect way to check if the distribution of martensite has truly linear character. Such tests have been performed on six different samples (1, 2, 3, 4, Raw 304, Raw 304L, see Tab. 5.2).

6.2.1. Experimental method

Four cross sections have been analyzed for each sample: three transverse cross-sections and one longitudinal section, the same as in the microscopic observations (Fig. 6.1). The Wilson Micro-Vickers Hardness Tester 402 MVD (Fig. 6.24) has been used. The samples during the test are presented in Fig. 6.25 a, b. The load was set to 0,5 kg for each test. The results were indicated in the HV 0,5 scale, and the units were kilograms of force per square millimeter (kgf/mm^2).

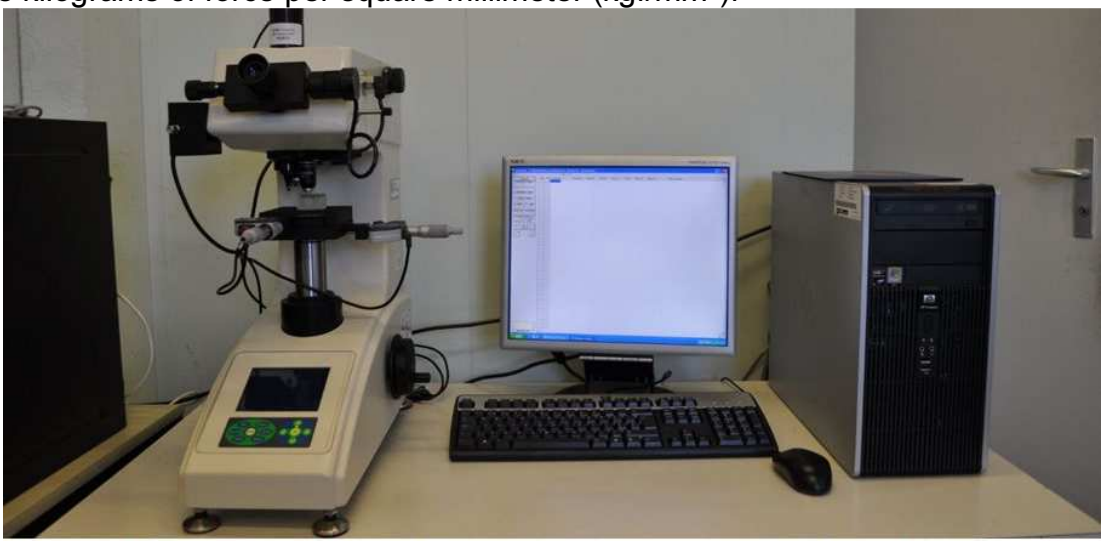

Figure 6.24. The Wilson Micro-Vickers Hardness Tester 402 MVD

The micro-hardness was measured along four radial lines within each cross-section, as illustrated in Fig. 6.25 a, b: from the center to the right, to the left, to the top, and to the bottom. Each cross-section was precisely centered before making the first indentation. For the first few tests, however, 250μm was used as the distance between indentations (making 15 points along the radial line). Later on, the distance was decreased to 200μm, according to the norm that specifies the minimum distance between indentations to be more than 2,5 times the maximum diameter of the indentation. For the average 60μm of its size, this condition was fulfilled for distances higher than 150 μm.
The last point from the center was the one at 3.8mm distance. For correct measurement, minimum distance of 3 diameters of an average indentation was necessary from the edge of the sample, which was satisfied.

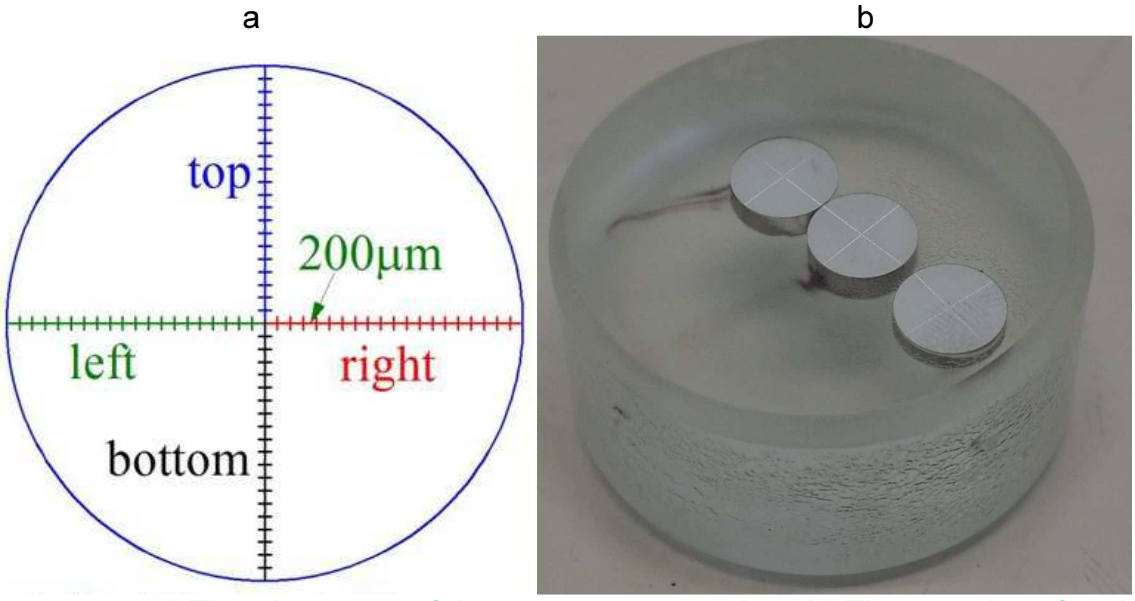

Figure 6.25. a) The placement of the measurement points, b) The samples after the indentation

The longitudinal sample has been cut parallel to the axis of the bar (Fig. 6.26a, b). The depth to which the sample has been extracted was around 2 mm. It is worth pointing out, that the direction of the hardness measurement was different between the transverse cross-sections and the longitudinal sections. The measurements within the longitudinal section were performed in the plane perpendicular w.r.t. the measurements in the cross-sectional cuts. The measurements in the longitudinal samples were cross-checked with the micro-hardness in the transverse direction. The measurements in two planes generate additional information about the hardness distribution inside the samples.

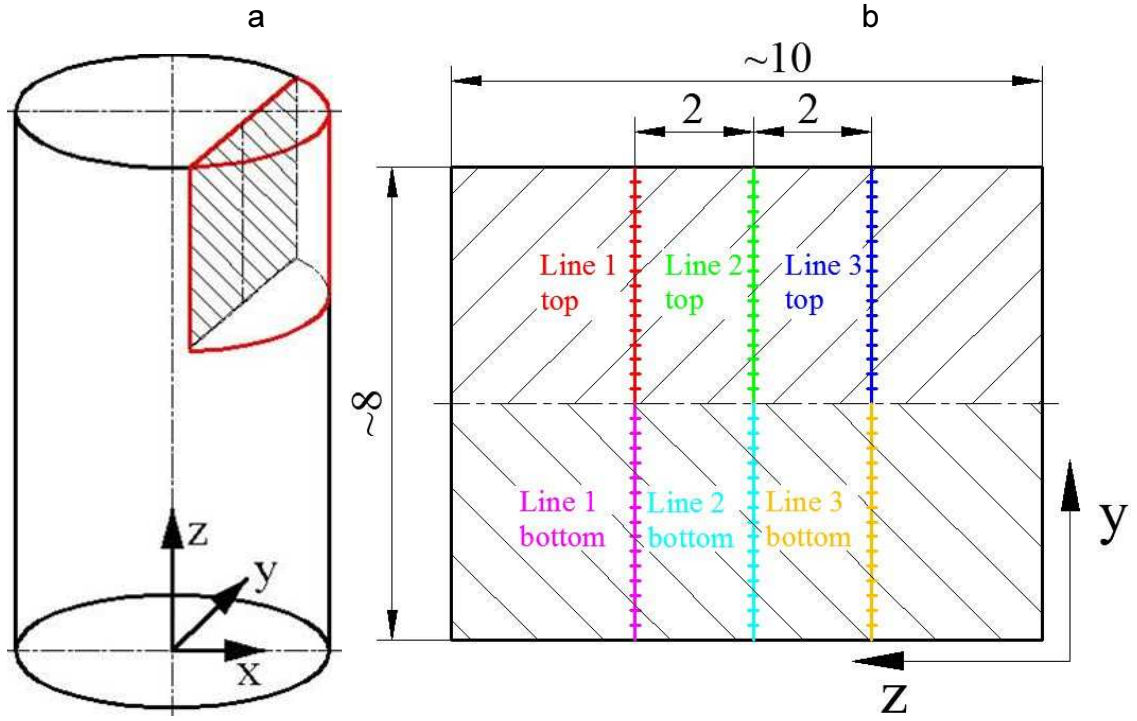

Figure 6.26. a) The sample extracted from cylindrical bar, b) lines and points on the plane of measurements

The measurements were performed on 6 lines, separated by 2 millimeters. The distance between the indentations on the longitudinal cuts was equal to 0,25 mm for all the samples. The longitudinal sample mounted in the Micro-Vickers tester is presented in Fig. 6.27a, whereas, the cross-sectional samples in Fig. 6.27b.

a b

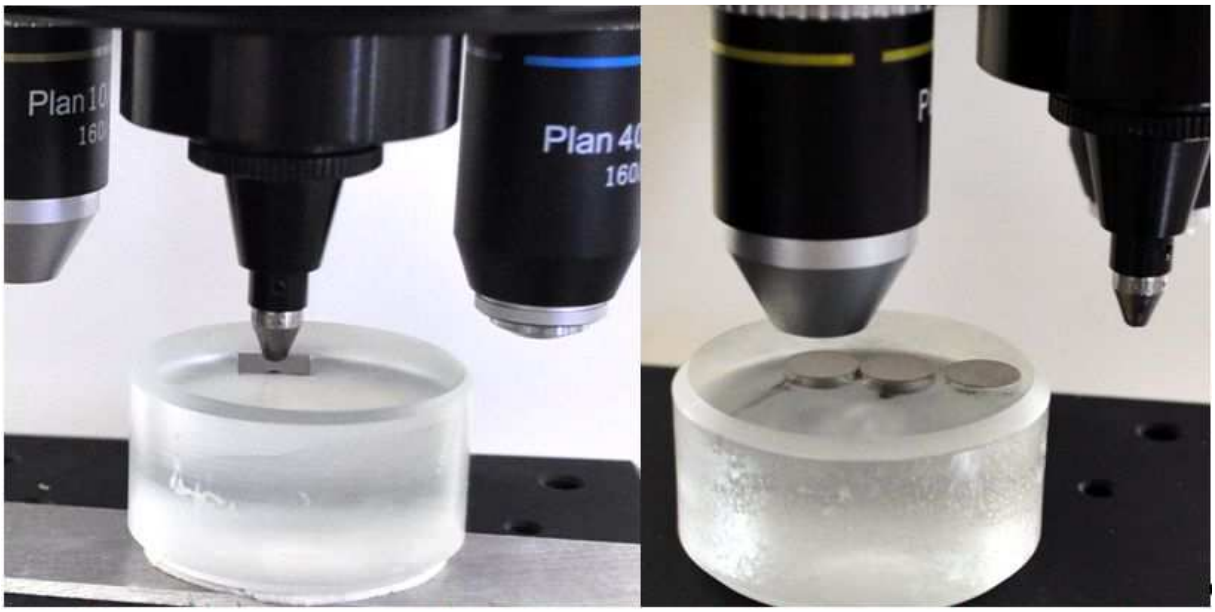

Figure 6.27. a) The longitudinal sample after indentation, b) The transverse cross-sections under lenses of the Micro-Hardness tester

Detailed results are presented in the following sections, for each of the samples. The results are presented in the following order: sample 1, 2, 3, 4, Raw 304, Raw 304L (Tab. 5.2). Later on, all the results are summed up, and conclusion are drawn at the end.

6.2.2. Results for Sample 1, loaded at 293K until rupture

The resulting micro-hardness distributions were colored according to Fig. 6.25a. Thus, the top line is always in blue, the left one in green, the right one in red and the bottom line is in black. All four measurements were formatted together into one plot, to check if the results were symmetric with respect to the center of the sample.
The results from the cross-section 1 are shown in Fig. 6.28, from the cross-section 2 in Fig. 6.29 and from the cross-section 3 in Fig. 6.30.

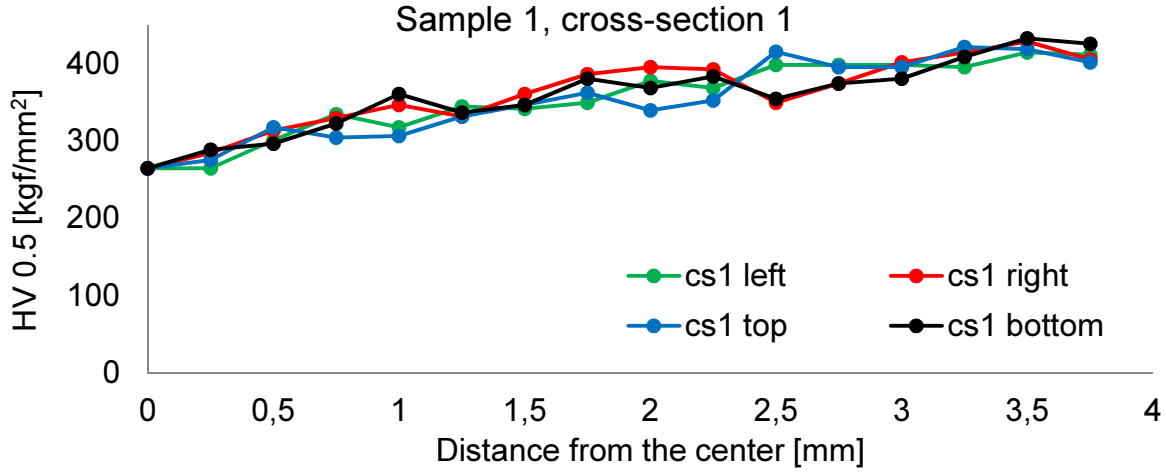

Figure 6.28. Micro-hardness results, sample 1, cross-section 1

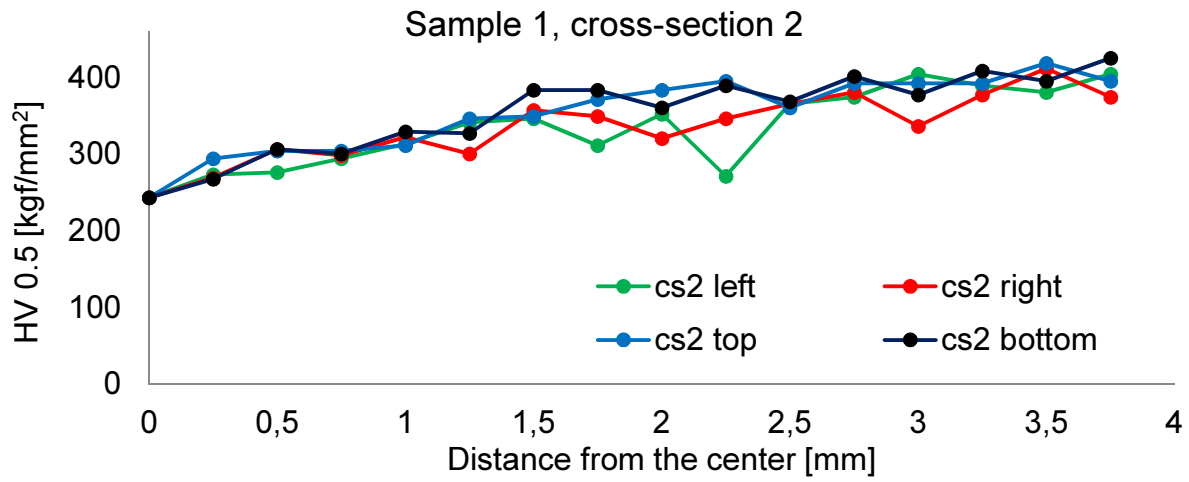

Figure 6.29. Micro-hardness results, sample 1, cross-section 2

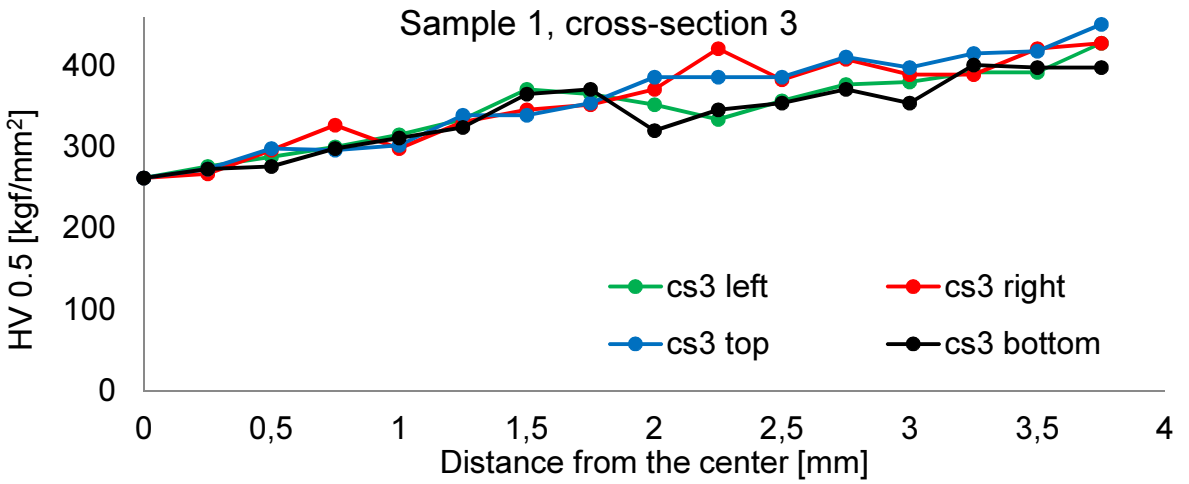

Figure 6.30. Micro-hardness results, sample 1, cross-section 3

From all the results for Sample 1 (Figs 6.28÷6.30) it is clear that the micro-hardness has its minimum in the center. Micro-hardness increases towards the surface of the sample, where it reaches its maximum. For all the results, the discrepancy between the top, the bottom, the left and the right lines is small. As expected for local measurements to have some necessary variations. In order to compare the results from three cross-sections, the average has been calculated from all four lines. The final results are shown in Fig. 6.31.

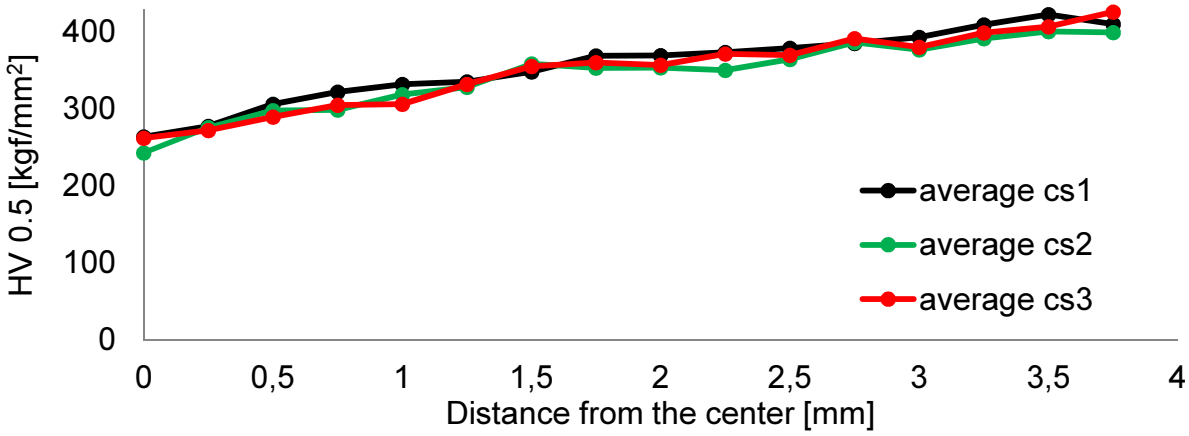

Figure 6.31. Average micro-hardness results for sample 1

From the results shown in Fig. 6.31, it turns out that a good agreement is obtained for all three cross-sections. As the cross-sections were extracted at a distance of 50mm from each other, it turns out that the micro-hardness variation in each cross-section of the sample is similar, which indirectly indicates similar martensite content along the sample. This follows the theoretical expectations, as the torque is constant along the sample and the strain distribution is expected to be independent of the axial coordinate.
The minimum micro-hardness is about 250 in the center (Fig. 6.31), and the maximum reaches some 420. The trend of the micro-hardness increase is close to linear.
Lastly, the micro-hardness measurements in the longitudinal section are shown in Fig. 6.32. There is 6 lines colored according to Fig. 6.26b. The minimum value was again found in the center – about 250, and the maximum one near the surface – about 440. For all six lines similar trend was observed, indicating increasing martensite content along the radius.

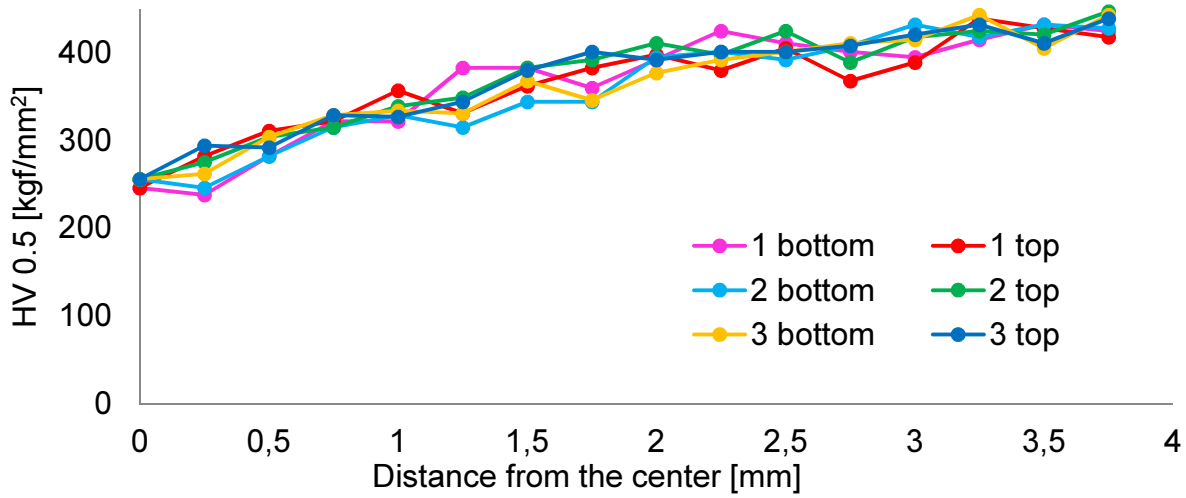

Figure 6.32. Micro-hardness results, sample 1, longitudinal section

From the longitudinal micro-hardness results (Fig. 6.32), and the cross-sectional measurements (Fig. 6.31), it can be concluded that the hardness distribution is similar in two perpendicular planes. Symmetry of these results suggests analogous martensite distribution.
In order to calculate the micro-hardness, the diameter of the indentations was measured. The Micro-Vickers tester was equipped with an ocular having 40x magnification.
Photographs of the indentations carried information about the microstructure as well. Two photographs are shown in Fig. 6.33, taken from the measurements made in the longitudinal section, for the first bottom line. In Fig. 6.33a, the indentation has been made in the center of the sample, whereas, in Fig. 6.33b the indentation has been made at 3.75mm distance from the center. A clear difference in size is visible. The indentation in the center is bigger, as the material is less hard (more soft) there, compared to the one near the surface (harder martensite).

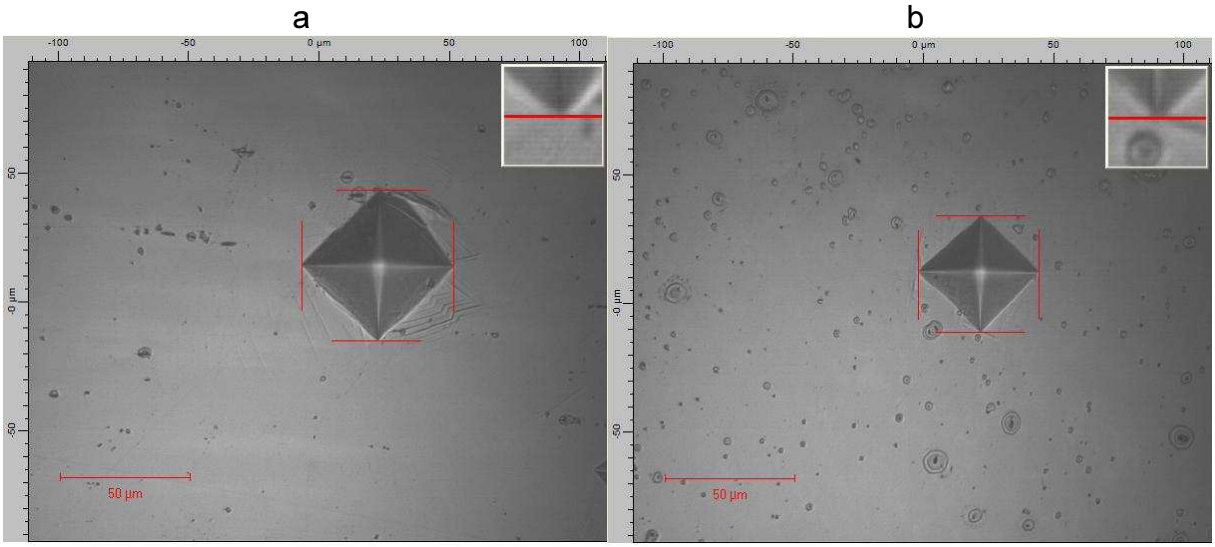

Figure 6.33. Pictures of the indentations made in the first bottom line, at a distance from the center of: a) 0.25 mm; b) 3,75 mm

6.2.3. Results for sample 2, twisted at 77K to 870°

The results of the micro-hardness measurements for three cross-sections, for Sample 2, are shown in Figs 6.34÷6.36: for cross-section 1 in Fig. 6.34, cross-section 2 in Fig. 6.35 and for cross-section 3 in Fig. 6.36.
Sample 2 has been loaded at 77K, twisted up to 870°. Thus, high martensite content was expected as well as higher micro-hardness record.

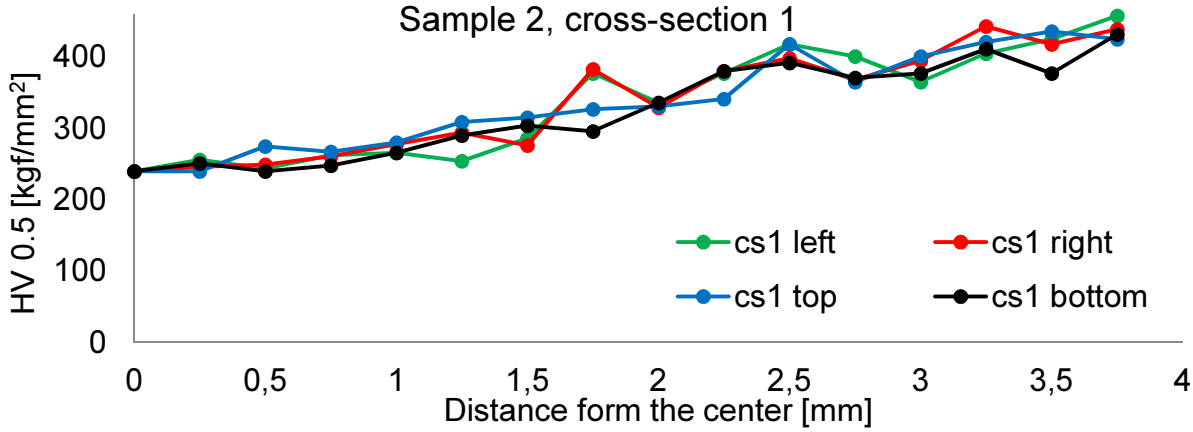

Figure 6.34. Micro-hardness results, sample 2, cross-section 1

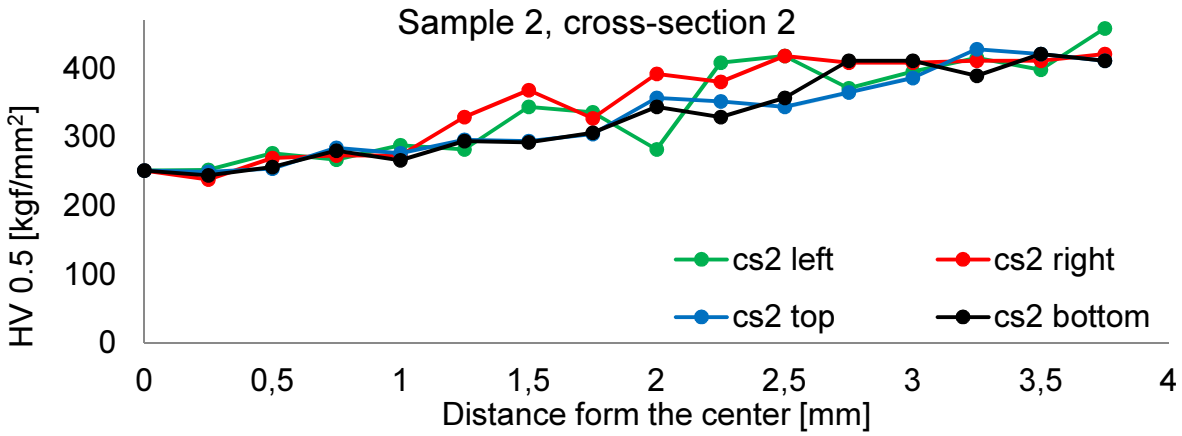

Figure 6.35. Micro-hardness results, sample 2, cross-section 2

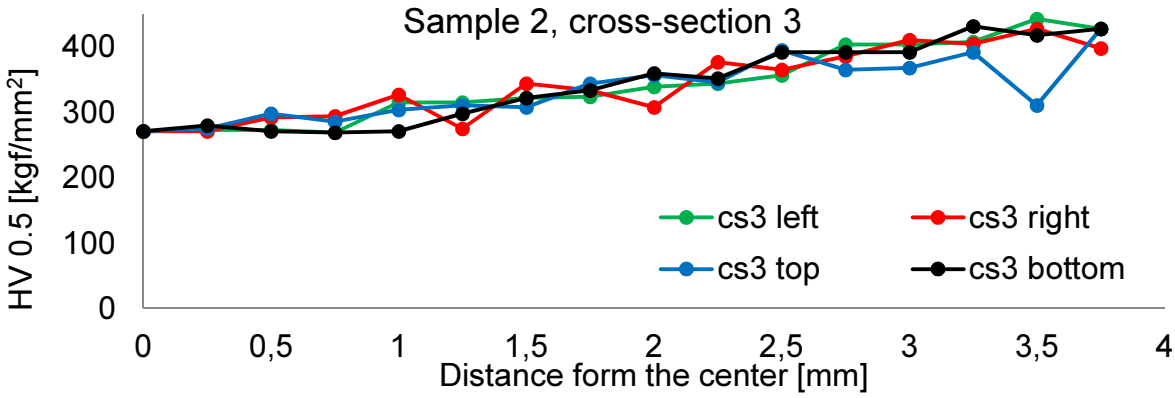

Figure 6.36. Micro-hardness results, sample 2, cross-section 3

In all the results (Figs 6.34÷6.36), the micro-hardness was similar in all directions (left, right, top, bottom). Again, similarly to sample 1, the micro-hardness distribution turns out to have axis-symmetric character. For all the samples, the micro-hardness was equal to about 250 in the center, and about 450 at a point located 0.25 mm from the surface.

The average results for all three cross-sections are shown in Fig. 6.37.

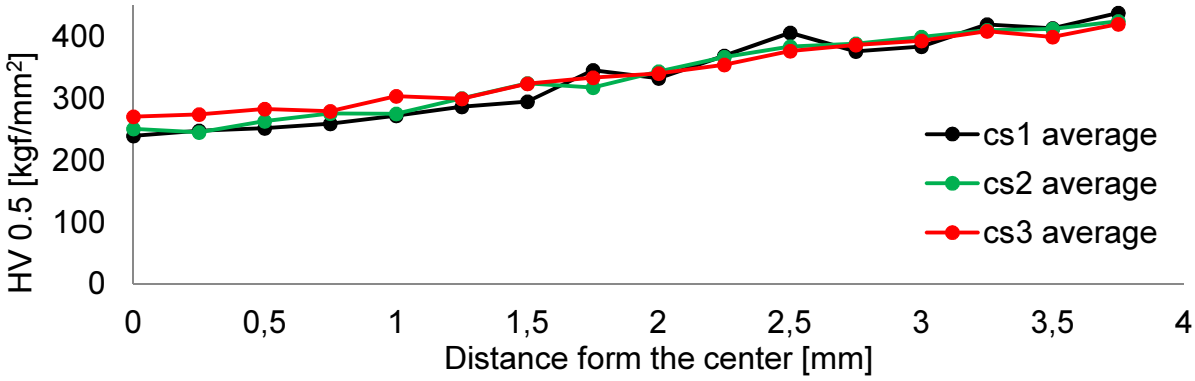

Figure 6.37. Average micro-hardness results for sample 2

Again, for all three cross-sections, the average results agree well with each other, confirming that the micro-hardness does not change along the length of sample 2. A trend very close to linear can be identified, indicating increasing martensite content along the radius of the sample.

Lastly, the results of the micro-hardness measured within the longitudinal section are presented in Fig. 6.38. For all six lines, nice correlation is observed. The micro-hardness increases from about 250 in the center, to about 440 at 3.75 mm distance. Thus, very similar results as in the cross-sectional cuts are obtained.

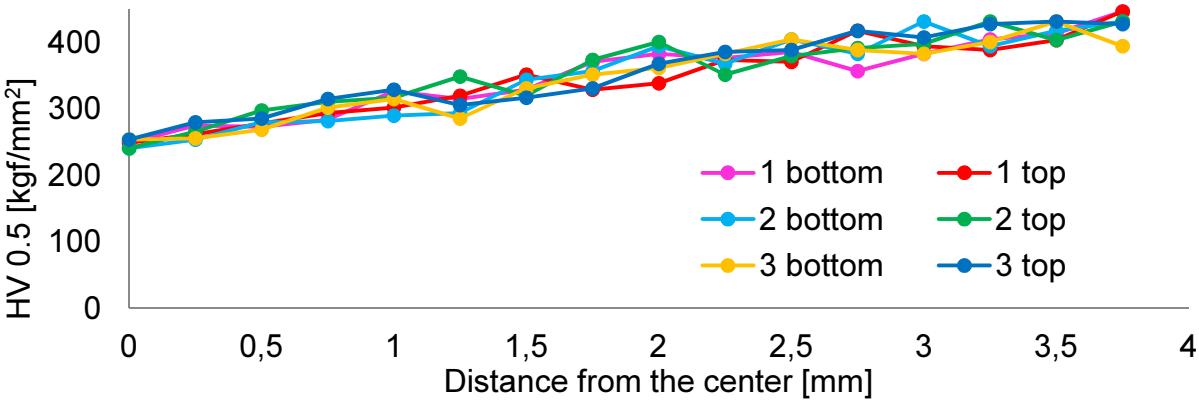

Figure 6.38. Micro-hardness results for the longitudinal section of sample 2

The micro-hardness depends strongly on microstructure at the point of measurement. An example is shown for cross-section 3, for the top line (Fig. 6.39). At 1.5 mm distance from the center (Fig. 6.39a), the microstructure clearly shows grains with martensite laths. The red cross symbolizes the targeted center of indentation. Yet, the indenter slipped a little, thus, the real indentation border has been sketched as well. The value of the micro-hardness measured at this point is 322.

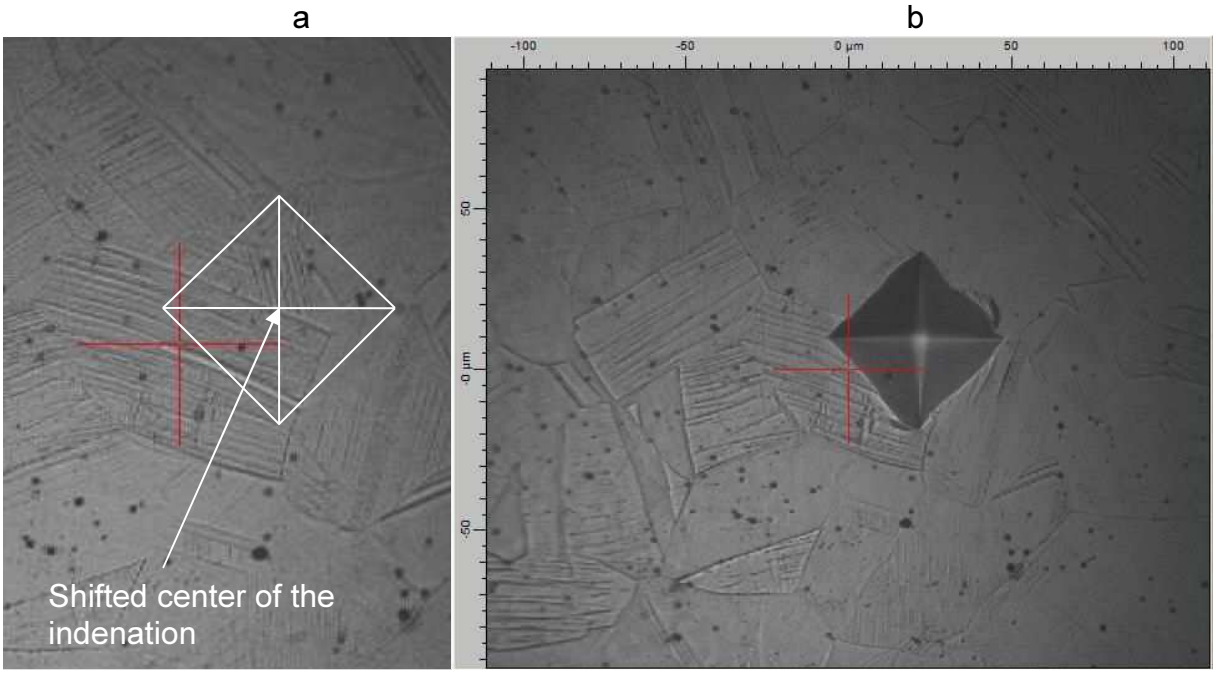

Figure 6.39. Microstructure of the cross-section 3, top line, at 1.5mm distance from the center, a) before indentation, b) after indentation

The microstructures with the indentation imprints, for the measurements made within the longitudinal section for the first bottom line, are shown in Fig. 6.40. Note the size of the indentation imprints, larger in the center of the sample (Fig. 6.40a) compared to the point located at a distance of 0.25mm from the surface (Fig. 6.40b). Again, harder micro-structure was present near the surface, as expected from higher strains and higher martensite content.

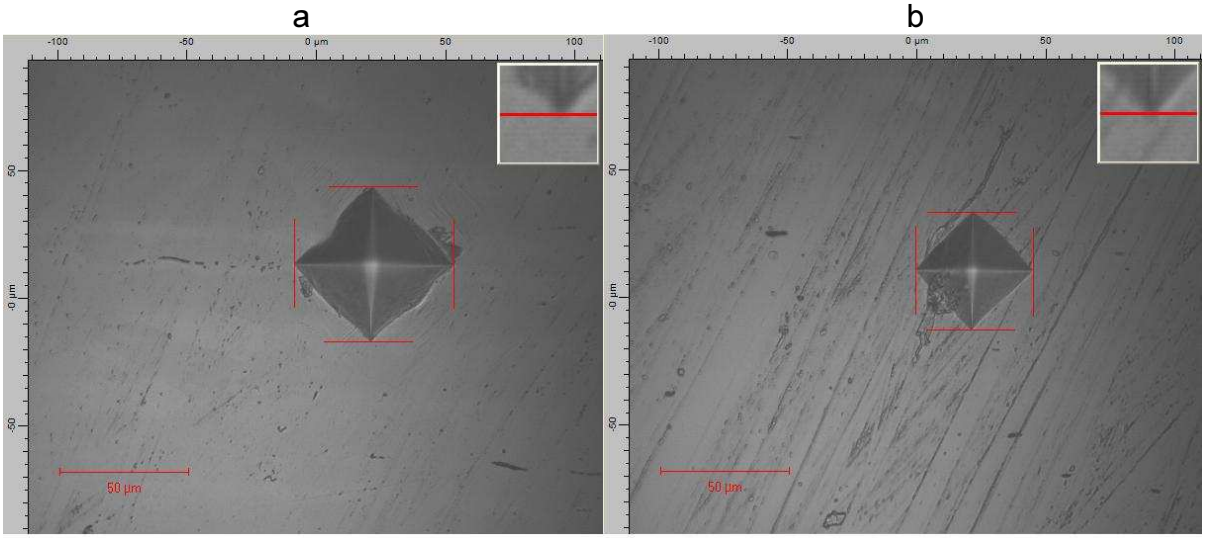

Figure 6.40. Pictures of the indentation imprints made in the first bottom line, at a distance from the center of: a) 0 mm; b) 3,75 mm

6.2.4. Sample 3, twisted at 293K to 870°

Sample 3 has been twisted at 293K, to 870° of angle of twist. Compared to Sample 2, much less martensite content was expected, because of small rate of martensitic transformation at room temperature. Thus, smaller values of micro-hardness were expected as well as smaller increase in its distribution from the center towards the surface.

The results from cross-section 1 are shown in Fig. 6.41. Variation in the results along four radial lines is shown. Yet, all the results agree well, keeping in mind local character of the measurement. One point drastically differs from the other ones. This can be attributed to some kind of defect or void in the microstructure of the material, that could naturally happen.

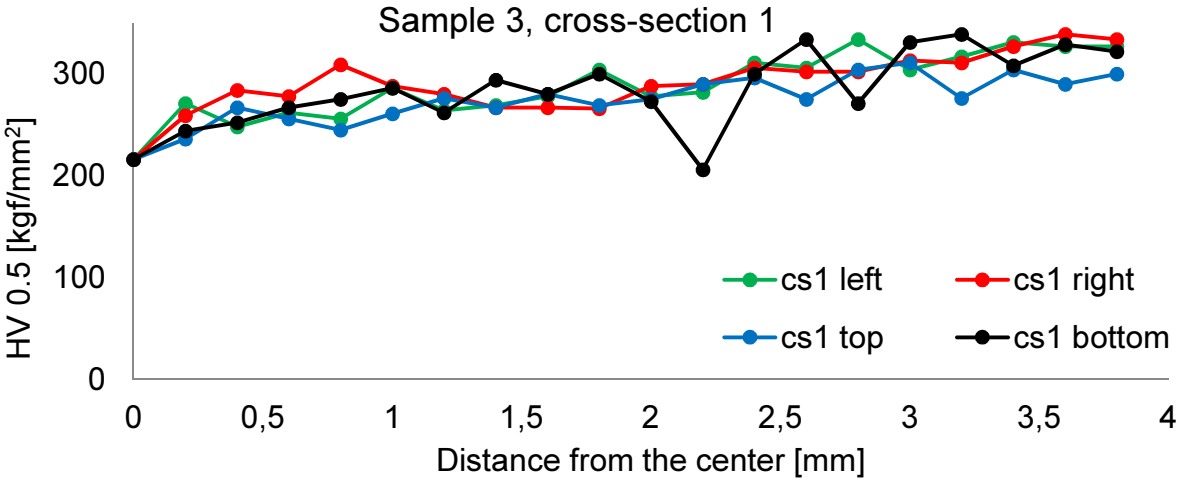

Figure 6.41. Micro-hardness results, sample 3, cross-section 1

The results from cross-section 2 are shown in Fig. 6.42. Good correlation is observed for all the lines. Lastly, for the cross-section 3 the results are shown in Fig. 6.43. Again, similar function for all four measurements is observed.

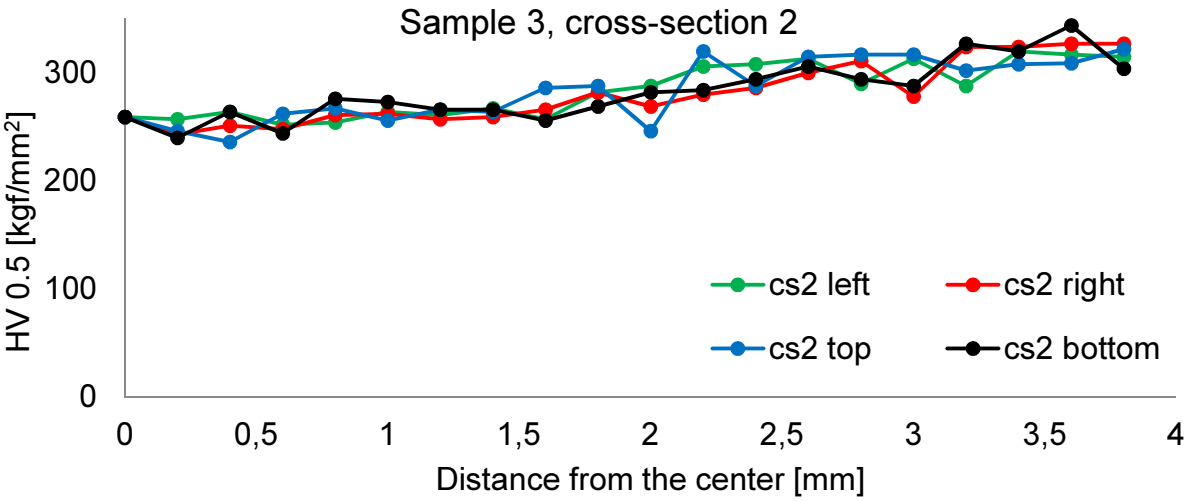

Figure 6.42. Micro-hardness results, sample 3, cross-section 2

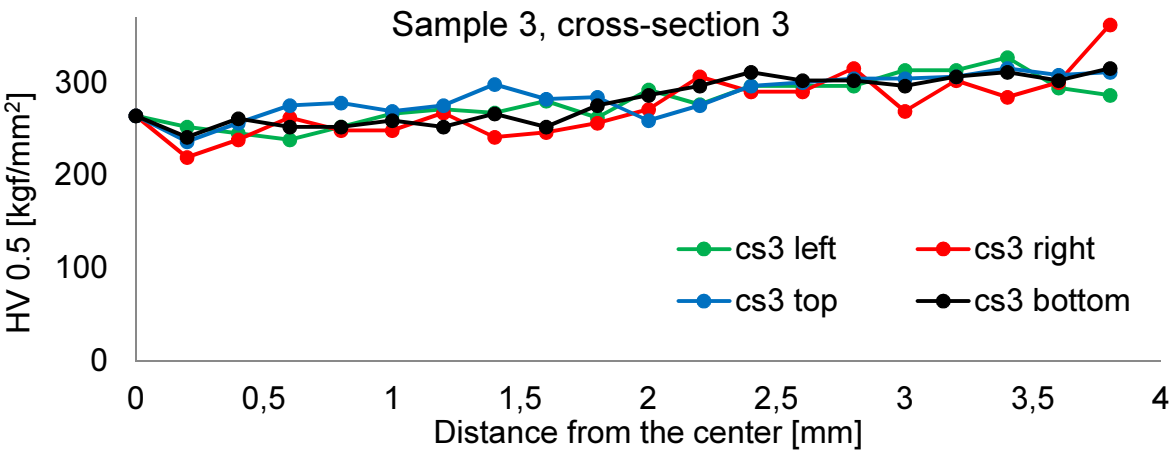

Figure 6.43. Micro-hardness results, sample 3, cross-section 3

The average results are shown in Fig. 6.44. It turns out, that very good agreement is obtained. Micro-hardness increased from about 250 in the center of the sample, to some 320 at a distance of 0.2 mm from the surface. A linear trend of the increase is clearly observed.

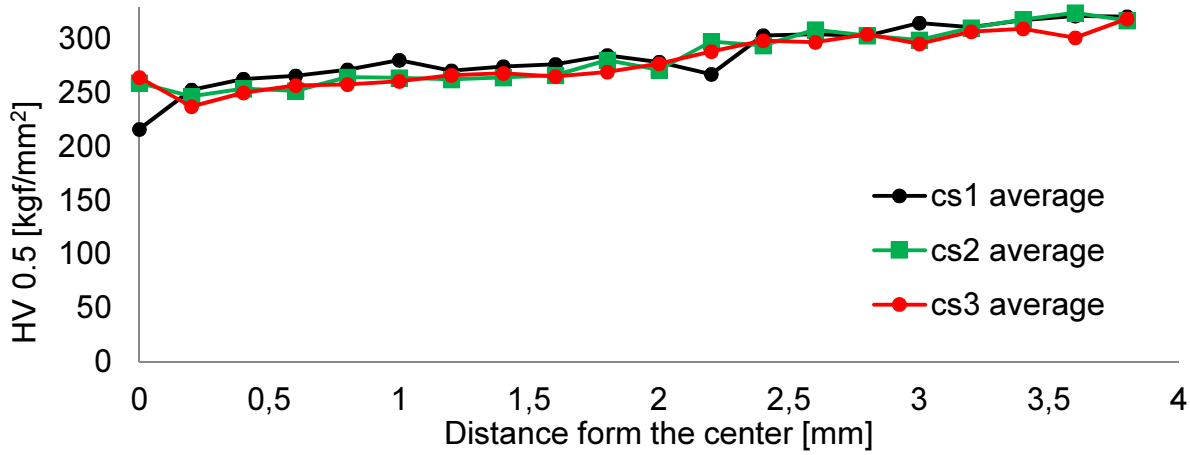

Figure 6.44. Average micro-hardness results for sample 3

Finally, the results for the longitudinal cut are shown in Fig. 6.45. For all 6 lines similar results were obtained.
Micro-hardness increased from 250 in the center to about 340 at a distance of 0.25 mm from the surface. Again, linear trend of increase is observed.

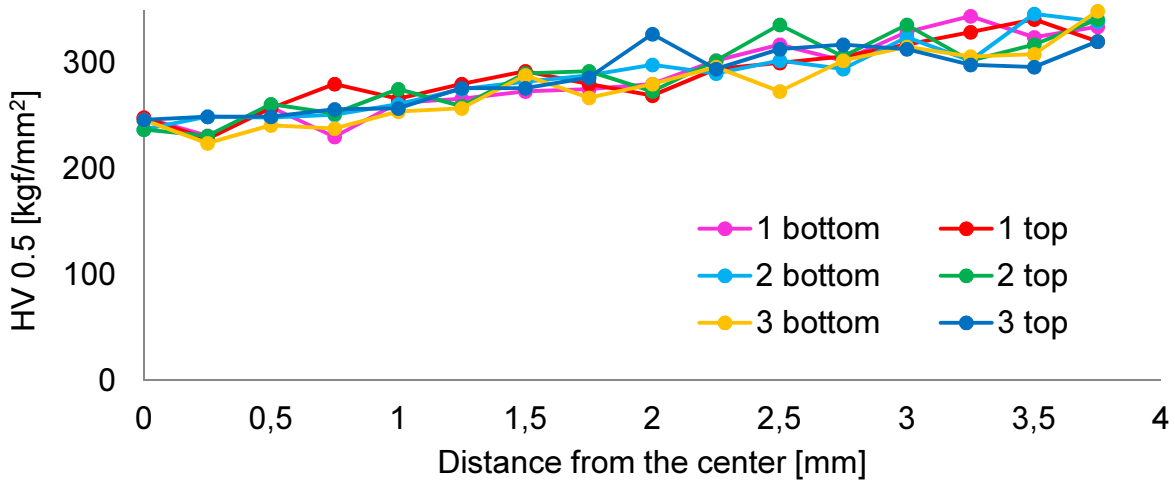

Figure 6.45. Micro-hardness results for the longitudinal section of sample 3

At this point, it is worth comparing the results obtained from the samples 2 and 3, as both of them were twisted to 870 degrees, yet at two different temperatures 77K and 293K. At 77K much more martensite was expected, because of higher rate of the phase transformation. For sample 3, maximum micro-hardness obtained near the surface was about 320, whereas, for sample 2 about 420. Thus, 31% higher maximum micro-hardness was measured for sample 2. This result strongly indicates, that much more martensite has been induced in the sample twisted at the liquid nitrogen temperature.
Two indentation imprints are shown in Fig. 6.46. They were obtained at the third bottom line in the longitudinal cut. First indentation is located in the center of the sample (Fig. 6.46a), and the second one at a distance of 0.25 mm from the surface. Again, the second indentation is smaller, indicating harder material near the surface compared to the portion in the center. Higher hardness is attributed to the presence of martensite.

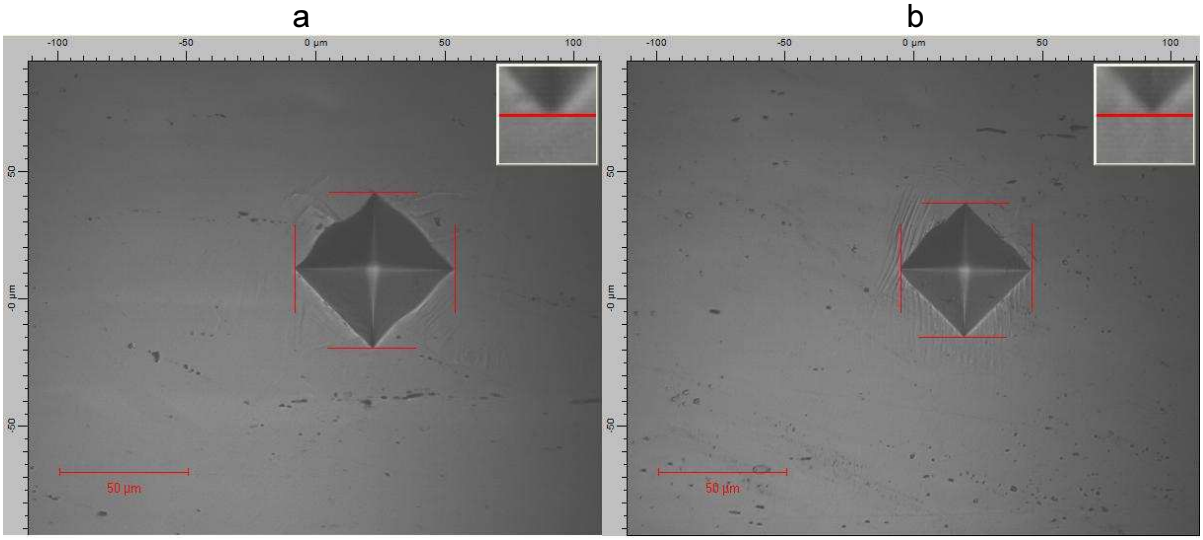

Figure 6.46. Pictures of the indentation imprints made in the third bottom line, at a distance of: a) 0 mm; b) 3,75 mm

6.2.5. Sample 4, twisted at 77K until rupture

Sample 4 was twisted at 77K until rupture. For this type of loading conditions and material maximum possible martensite content was obtained. As strain increased to the limit, which was the fracture, no more strain could be applied by means of torsion to the material. As maximum martensite content was expected to occur, consequently, high micro-hardness was also expected.
For Sample 4 three cross-sections were analyzed only. The resulting micro-hardness distribution along the radius is shown in Fig. 6.47 for cross-section 1, in Fig. 6.48 for cross-section 2, and in Fig. 6.49 for cross-section 3.
For all the cross-sections, the results are similar along all the lines (left, right, top, bottom). This indicates that the properties are symmetric with respect to the center of the sample.

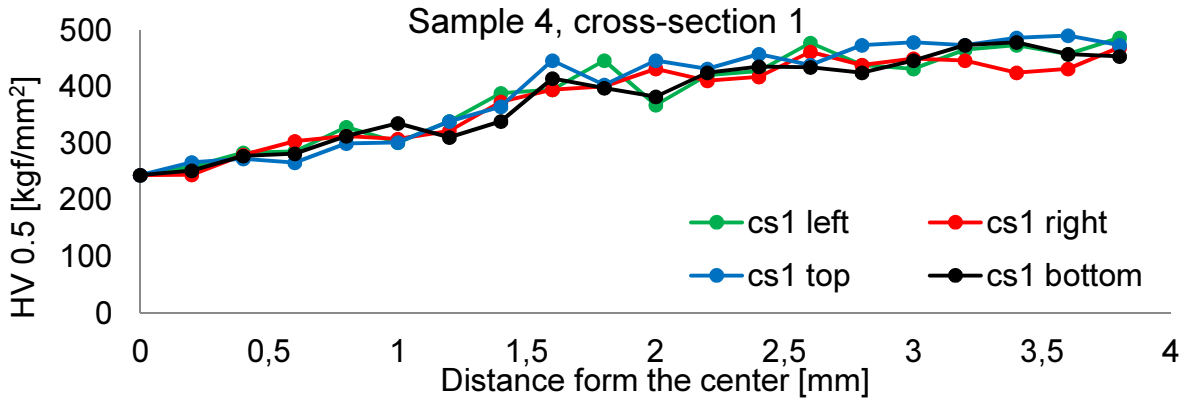

Figure 6.47. Micro-hardness results, sample 4, cross-section 1

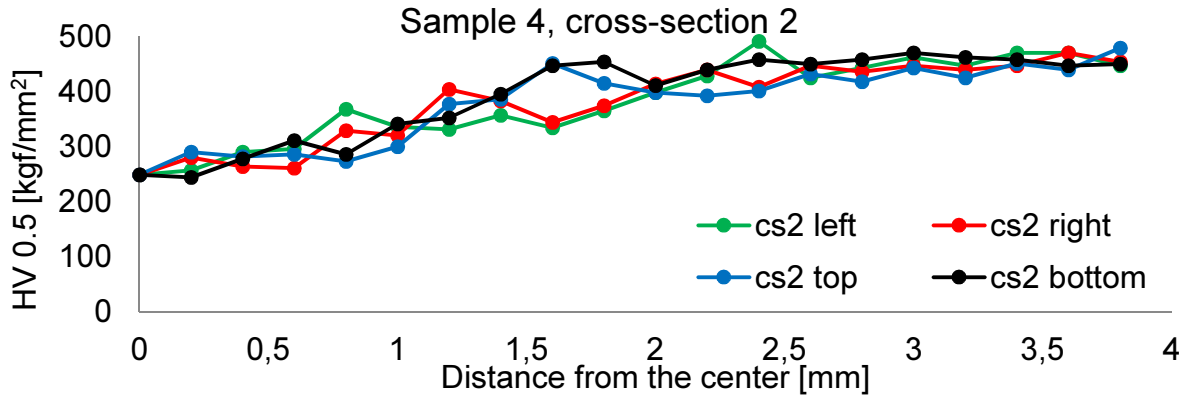

Figure 6.48. Micro-hardness results, sample 4, cross-section 2

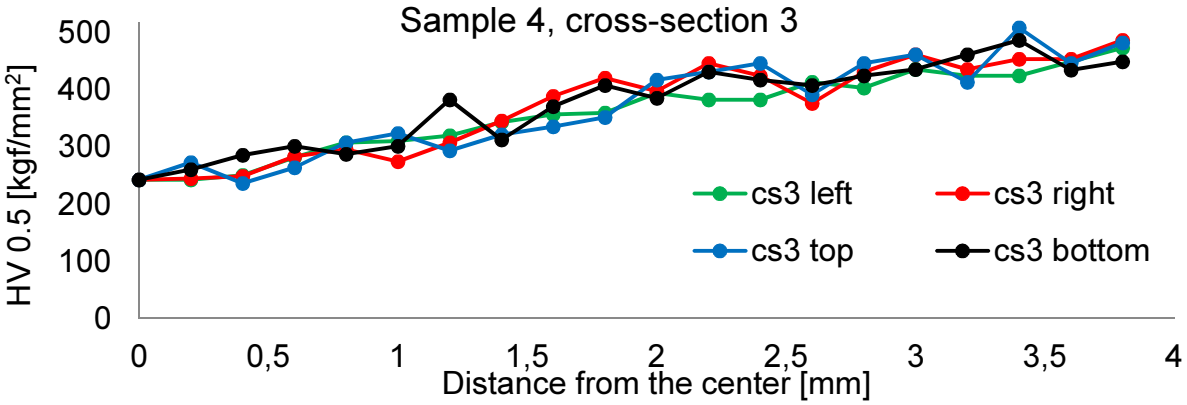

Figure 6.49. Micro-hardness results, sample 4, cross-section 3

The average results of all the cross-sections were shown in the Fig. 6.50.

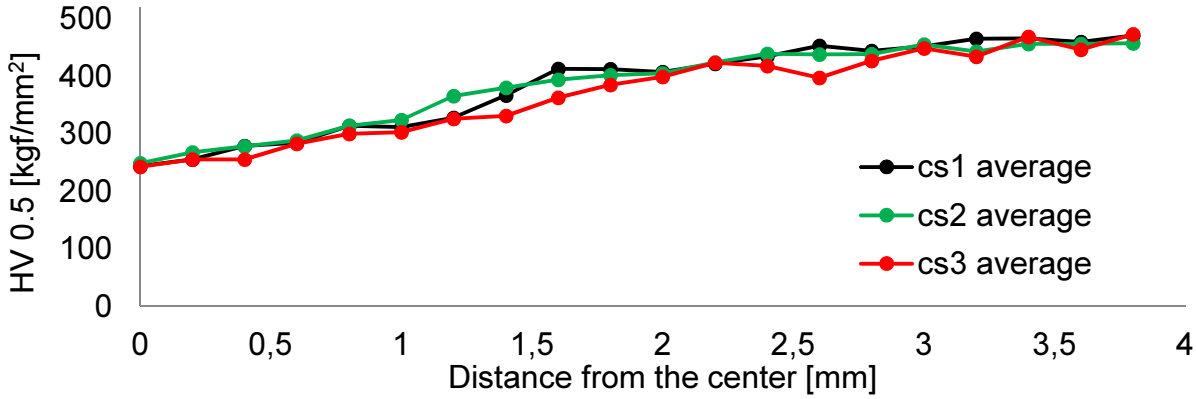

Figure 6.50. Average micro-hardness results for sample 4

From the average results (Fig. 6.50) it is clear, that all three results are very similar, again confirming that the properties are similar along the length of the sample. The value of 250 micro-hardness is measured in the center, and about 470 near the surface. Thus, the micro-hardness possible to obtain during torsion at 77K, for 304 stainless steel, is as high as 470. Compared to sample 2 with the micro-hardness of 440, it is 7% higher.
However, locally for sample 4 even higher values than 470 were obtained. For example, for cross-section 2 (Fig. 6.48) at a distance of 2.4 mm from the center for the left line, the micro-hardness was equal to 491. This means that locally even higher values than 470 could be obtained.

6.2.6. Raw sample from 304 stainless steel

Raw sample from 304 stainless steel was tested for comparison with the samples presented before and characterized by mixed structure (austenite and martensite). Three cross-sections were analyzed. The micro-hardness results are presented in Fig. 6.51 for cross-section 1, in Fig. 6.52 for cross-section 2, and in Fig. 6.53 for cross-section 3.

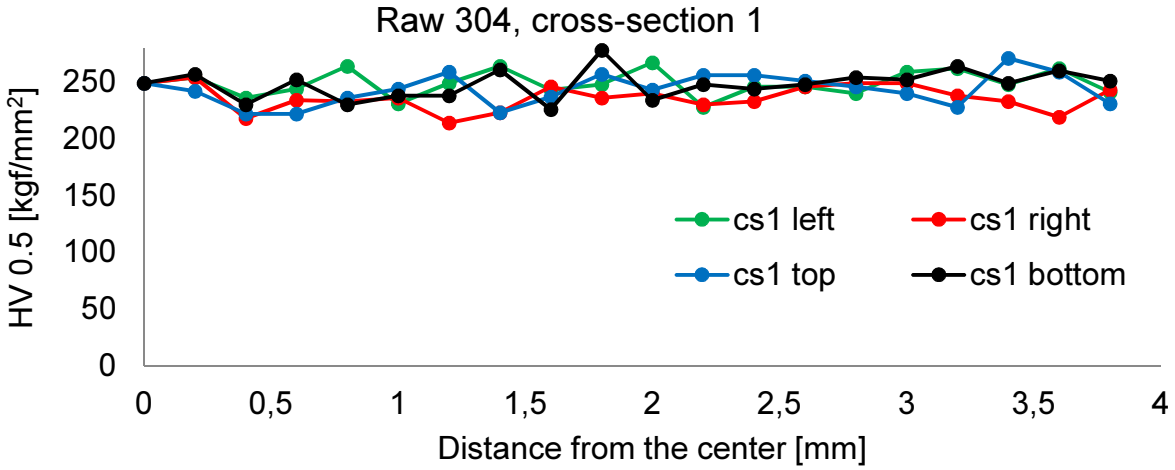

Figure 6.51. Micro-hardness results, raw 304 stainless steel sample, cross-section 1

For cross-sections 1 and 2 (Figs 6.51, 6.52) the results for all four lines are similar, indicating rather isotropic properties of the material. In addition, the micro-hardness varied around a constant value, as expected.

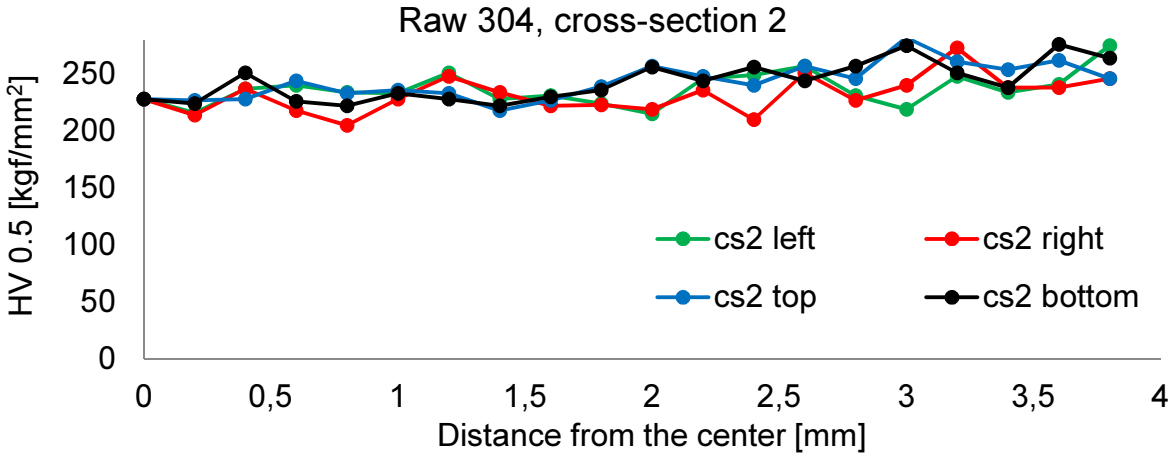

Figure 6.52. Micro-hardness results, raw 304 stainless steel sample, cross-section 2

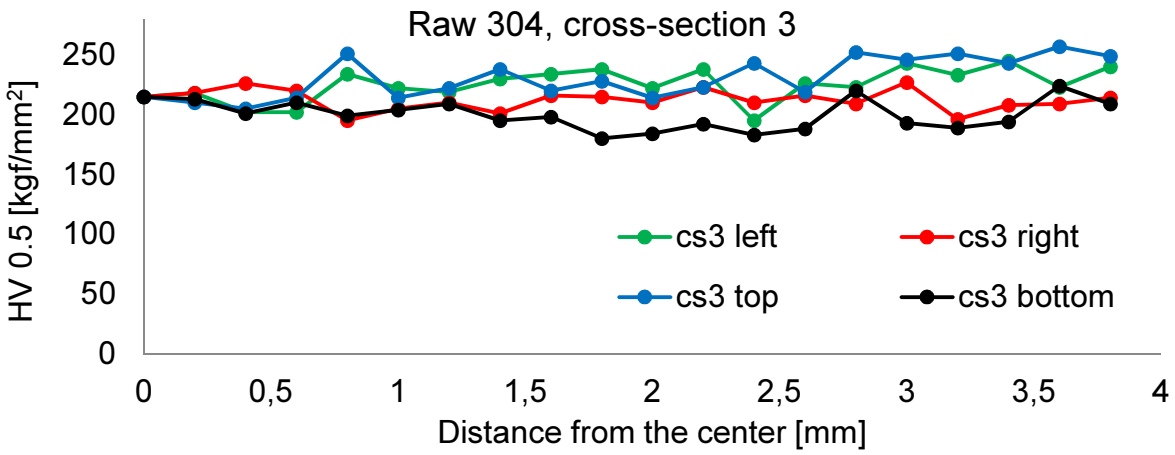

Figure 6.53. Micro-hardness results, raw 304 stainless steel sample, cross-section 3

For cross-section 3 (Fig. 6.53), the results for the bottom and the right lines deviated from the top and the left lines. This indicated rather non-homogeneous distribution of the micro-hardness. Yet, as for the remaining two cross-sections the results were quite similar, it was assumed that they indicated true properties of 304 austenitic stainless steel. Naturally, the microstructure of the raw material can exhibit variations that might lead locally to rather anisotropic properties. The average results are presented in Fig. 6.54.

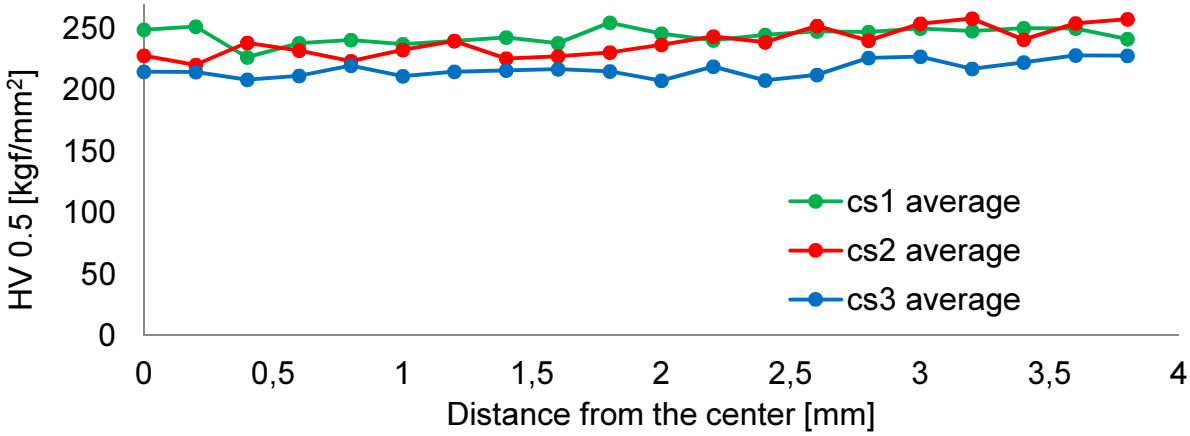

Figure 6.54. Average micro-hardness results for raw 304 stainless steel sample

In Fig. 6.54 a clear constant trend in the micro-hardness values is observed for all the samples.

Yet, for samples 1 and 2 similar values are obtained, whereas, for sample 3 slightly smaller micro-hardness is recorded, which is certainly caused by the differences shown in Fig. 6.53. The micro-hardness shows constant value, equal to about 240, along the radius of the sample. This conclusion agrees with the expectations for an austenitic structure.

Two indentations are shown for cross-section 1, for the right line. The first made in the center of the sample (Fig. 6.55a), and the second made at a distance of 0.2 mm from the surface (Fig. 6.55b). The size of both indentations (imprints) was similar, indicating similar hardness of the material, as reflected in the results presented in Fig. 6.51. The microstructure indicated similar pattern as for martensite laths (see Fig. 6.39), yet, these were rather twins as both micro-hardness and precise martensite content measurements revealed only residual contents of martensite.

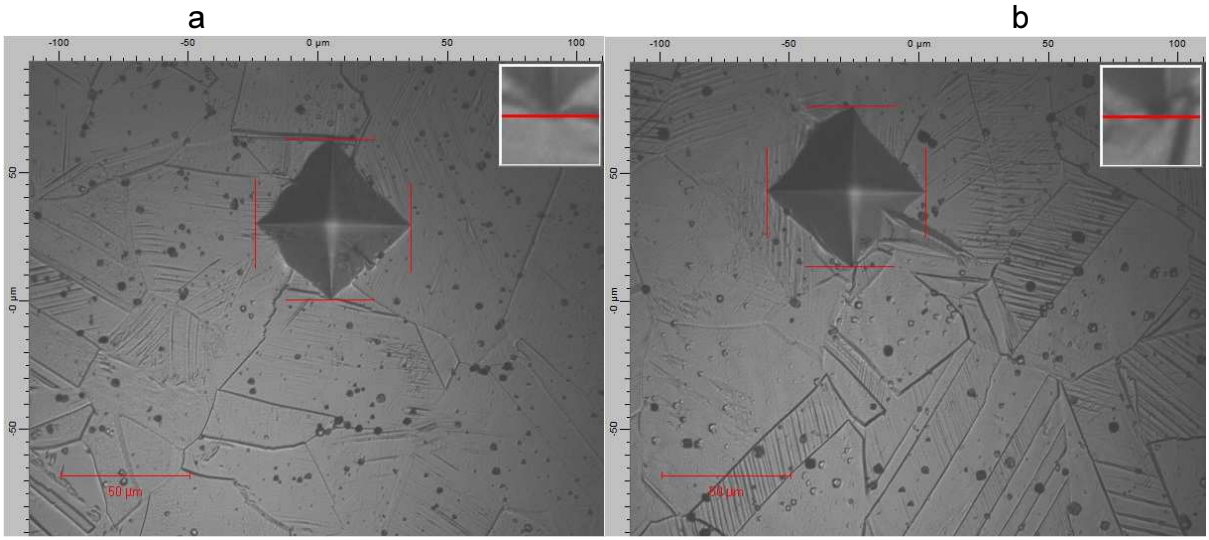

Figure 6.55. Microstructure and indentations for cross-section 1 for the right line, a) in the center of the sample, b) at a distance of 0.2 mm from the surface

6.2.7. Raw sample of 304L austenitic stainless steel

Apart from the raw sample made of 304 stainless steel, from which most of the samples for torsion were made, another material was tested as well – 304L stainless steel. The samples were cut out from a bar in the raw state. Similarly to previous samples, three transverse cross-sections and one longitudinal section were prepared and analyzed. The results for cross-section 1 are shown in Fig. 6.56, for cross-section 2 in Fig. 6.57, and for cross-section 3 in Fig. 6.58.

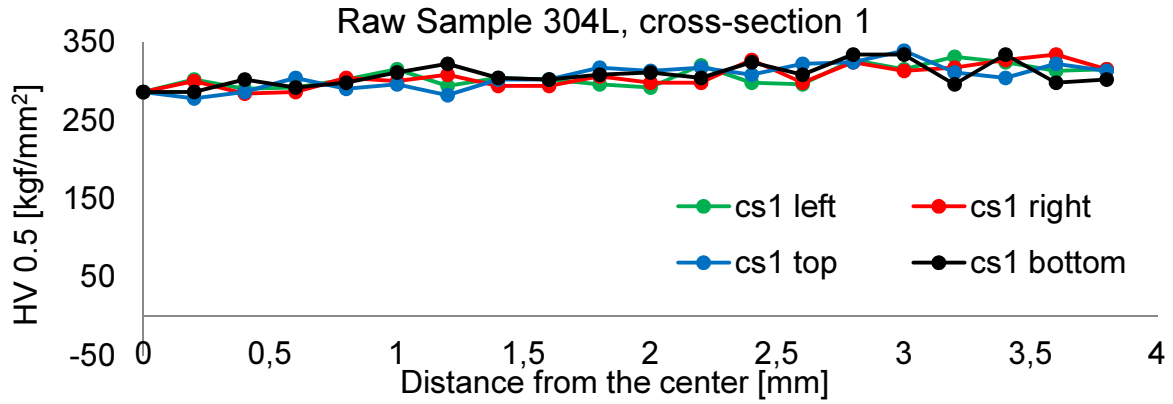

Figure 6.56. Micro-hardness results for cross-section 1 of the raw 304L stainless steel sample

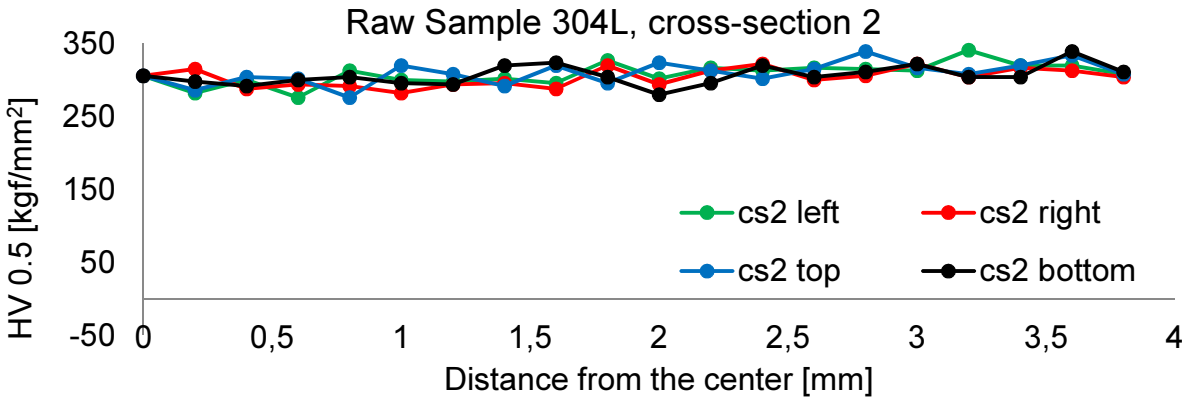

Figure 6.57. Micro-hardness results for cross-section 2 of the raw 304L sample

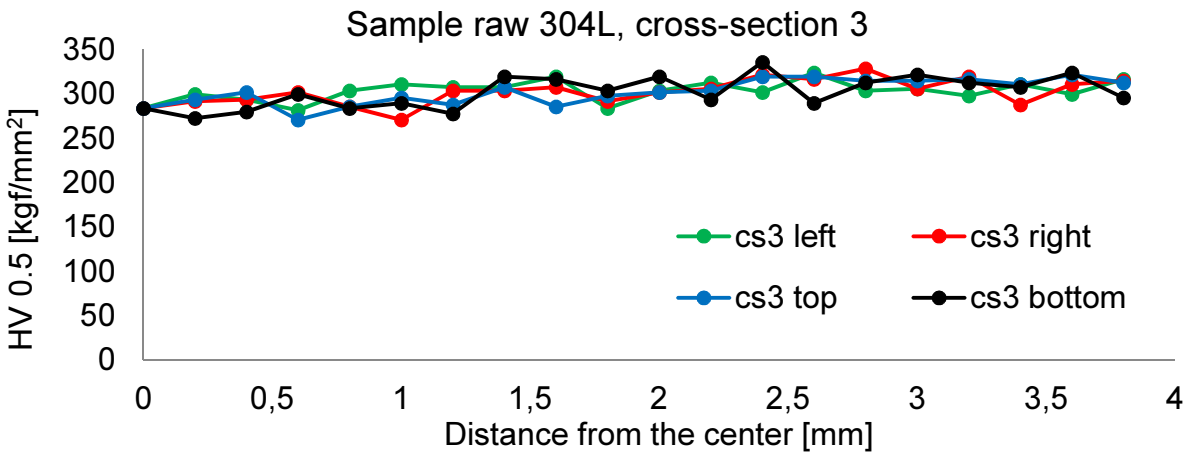

Figure 6.58. Micro-hardness results for cross-section 3 of the raw 304L sample

From all three cross-sections, similar results were obtained for all four lines (left, right, top, bottom), indicating rather isotropic properties. The constant trend is clearly visible in all the results. The average results are shown in Fig. 6.59.

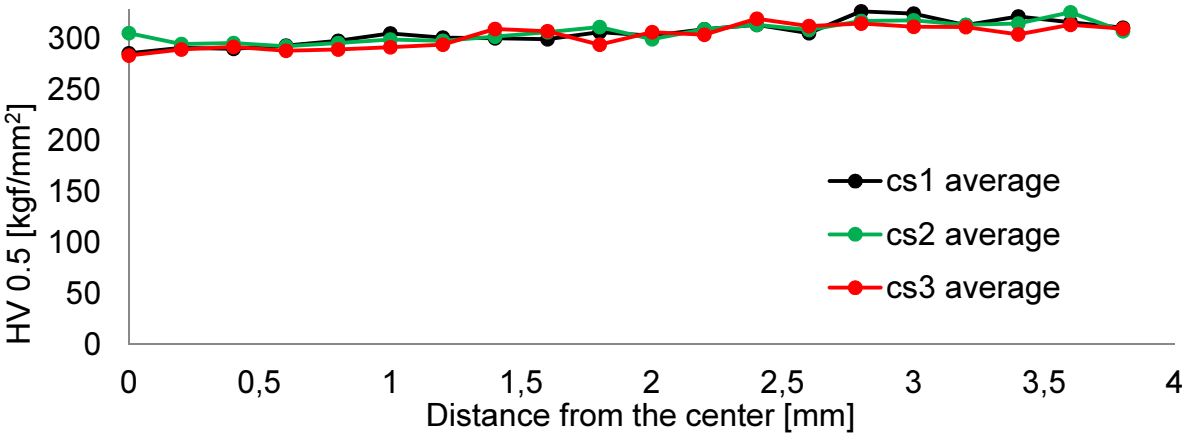

Figure 6.59. Average micro-hardness results for 304L raw sample.

In Fig. 6.59 very good agreement is obtained for all three cross-sections. Very small variations of micro-hardness around the value of 300 occur. Compared to raw sample made of 304 stainless steel, the 304L stainless steel is characterized by higher micro-hardness of around 300, whereas, 240 was a typical value of 304 ss.
The results for the longitudinal section are shown in Fig. 6.60.

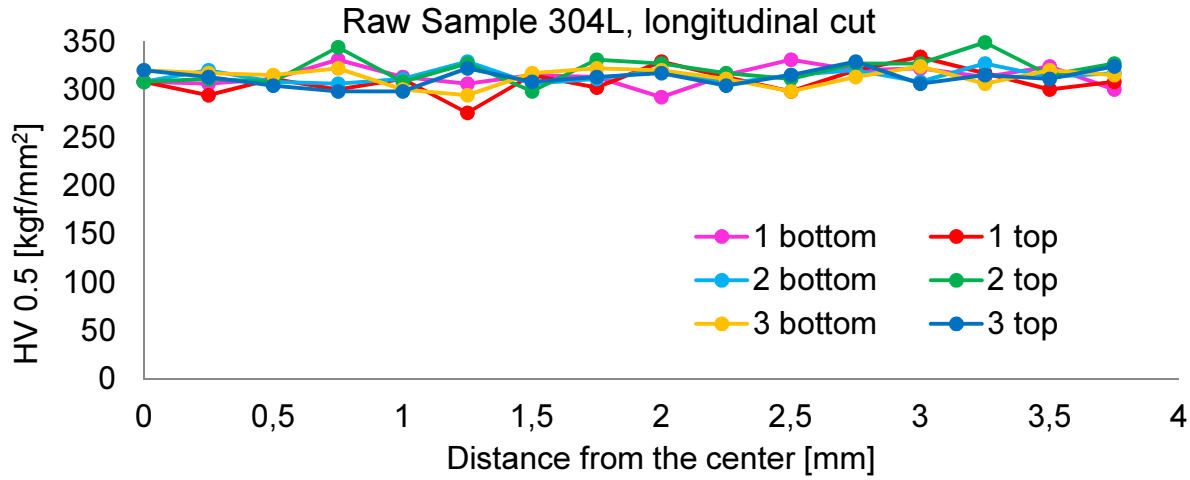

Figure 6.60. Micro-hardness results for the longitudinal section, raw 304L sample

Again, in Fig. 6.60 similar results were obtained, and the micro-hardness varied around the value of 300. This result shows that the same austenitic structure can have different properties, as the chemical composition of 304 and 304L steels is different. The austenite in 304 stainless steel was more soft, than the austenite in the grade 304Lstainless steel.
Two sample indentations are shown in Fig. 6.61, made within the longitudinal section, in the third bottom line. Indentation in the center is shown in Fig. 6.61a, and the imprint made at a distance of 0.25 mm from the surface is illustrated in Fig. 6.61b. Both indentations were of similar size, indicating constant hardness of the material in the center and near the surface.

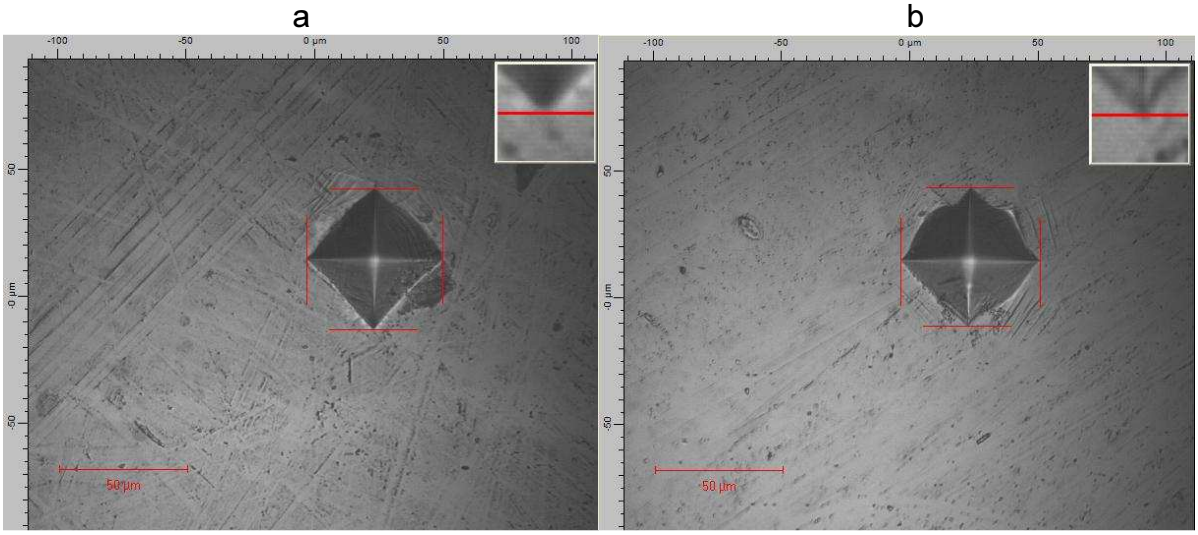

Figure 6.61. Indentation made within the longitudinal section, in the third bottom line, a) at the center, b) at a distance of 0.25mm from the surface

6.2.8. Summary and conclusions of the micro-hardness measurements

In order to compare all the obtained results, an average has been calculated from all the above presented results. In case of the micro-hardness measurements made within the longitudinal sections, the results from 6 lines were averaged. In case of transverse cross-sections, average from 12 results was calculated (3 cross-sections per sample and 4 lines per cross-sections).

The average results from transverse cross-sections are shown in Fig. 6.62. The lowest micro-hardness was found for the raw sample of 304 stainless steel. Its value is nearly constant and equal to around 240. Slightly higher values were obtained for sample 3, which was twisted at 293K to 870°. Even higher values were obtained for sample 2, which was twisted at 77K to 870°. Similar results were measured for sample 1, which was twisted at room temperature until rupture. Higher micro-hardness was obtained for sample 4, which was twisted until rupture at the liquid nitrogen temperature (77K). However, for small distances from the center of sample 1, the micro-hardness was even higher than for sample 4, which was rather unexpected. The results for the raw sample, made of 304L stainless steel, were constant and equal to around 300.
The highest micro-hardness obtained in sample 4, twisted at 77K until rupture, is equal to around 470. It increased almost by 100% compared to the raw sample where the hardness of around 240 was measured. Thus, considerable increase is possible by means of the process of twisting stainless steel bars at cryogenic temperatures.

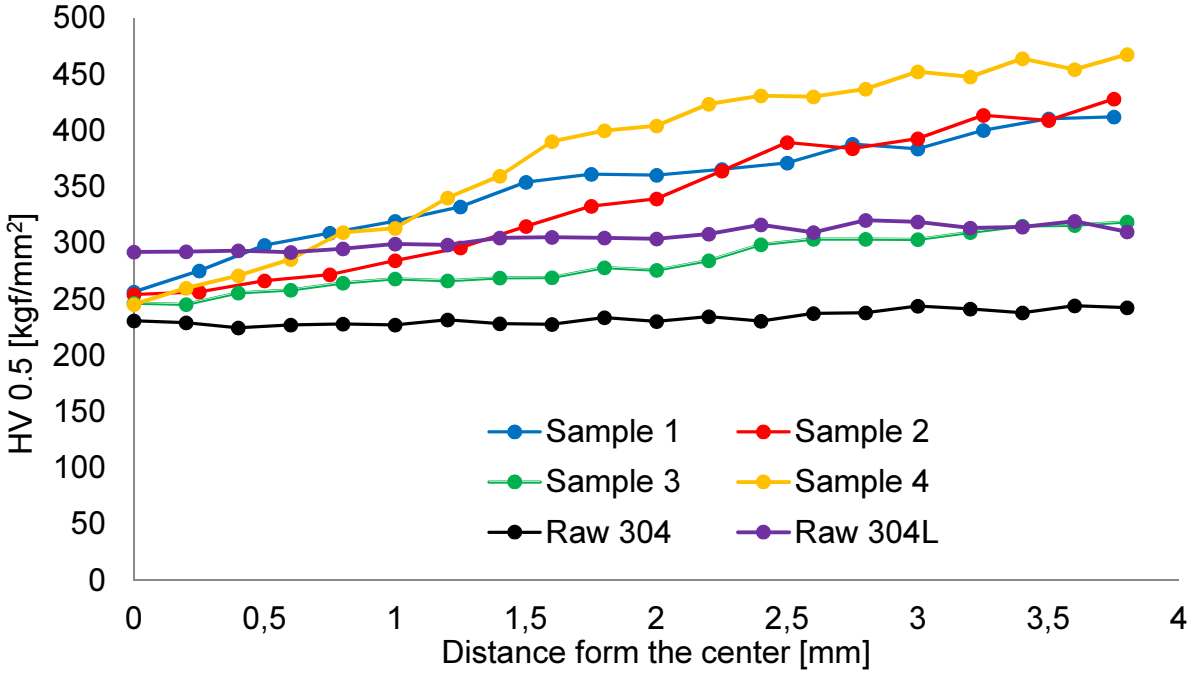

Figure 6.62. Average micro-hardness results for all the cross-sectional samples made of 304 stainless steel

Similar comparison was made for the longitudinal samples (Fig. 6.63). Similar trends were obtained like for transverse samples. The smallest values of the micro-hardness were obtained for sample 3. Higher values were measured for samples 2 and 1. The micro-hardness of sample 1 was higher than for sample 2 within the whole range of radial coordinate. This was not the case for transverse samples (Fig. 6.62), where the micro-hardness of sample 1 was higher than of sample 2 only to some 2.25 mm distance. After that the micro-hardness for sample 2 was slightly higher.

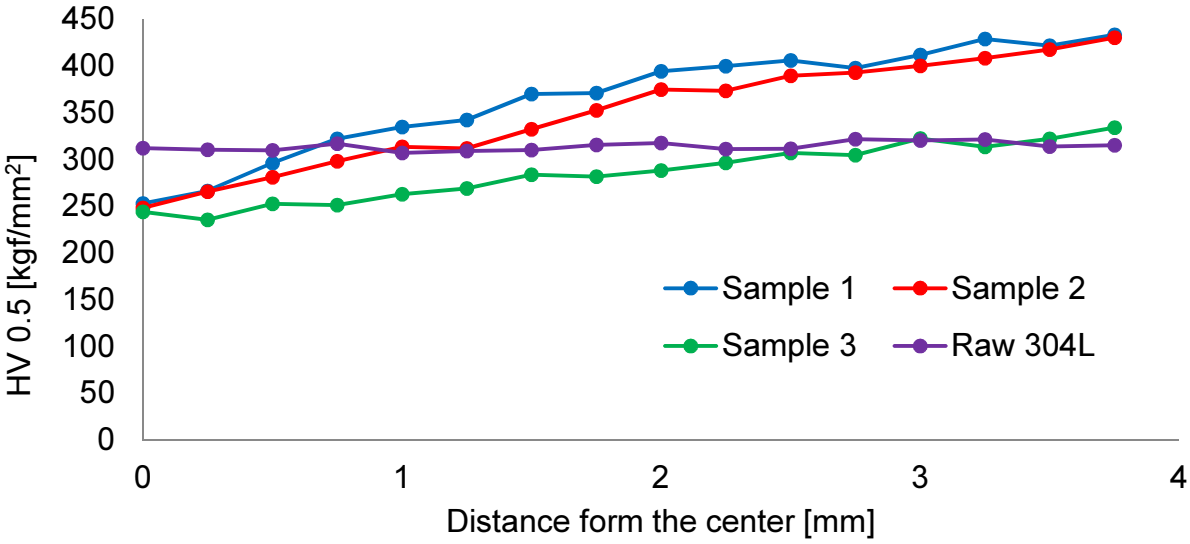

Figure 6.63. Average micro-hardness results for the longitudinal sections

To summarize all the micro-hardness measurements, all the results from transverse and longitudinal sections are illustrated in Fig. 6.64 (combined from Fig. 6.62 and 6.63). The cross-sectional and the longitudinal results are shown with the same colors. Although both were measured in different planes, and the axial coordinate is not the same, the results do not substantially differ from each other.

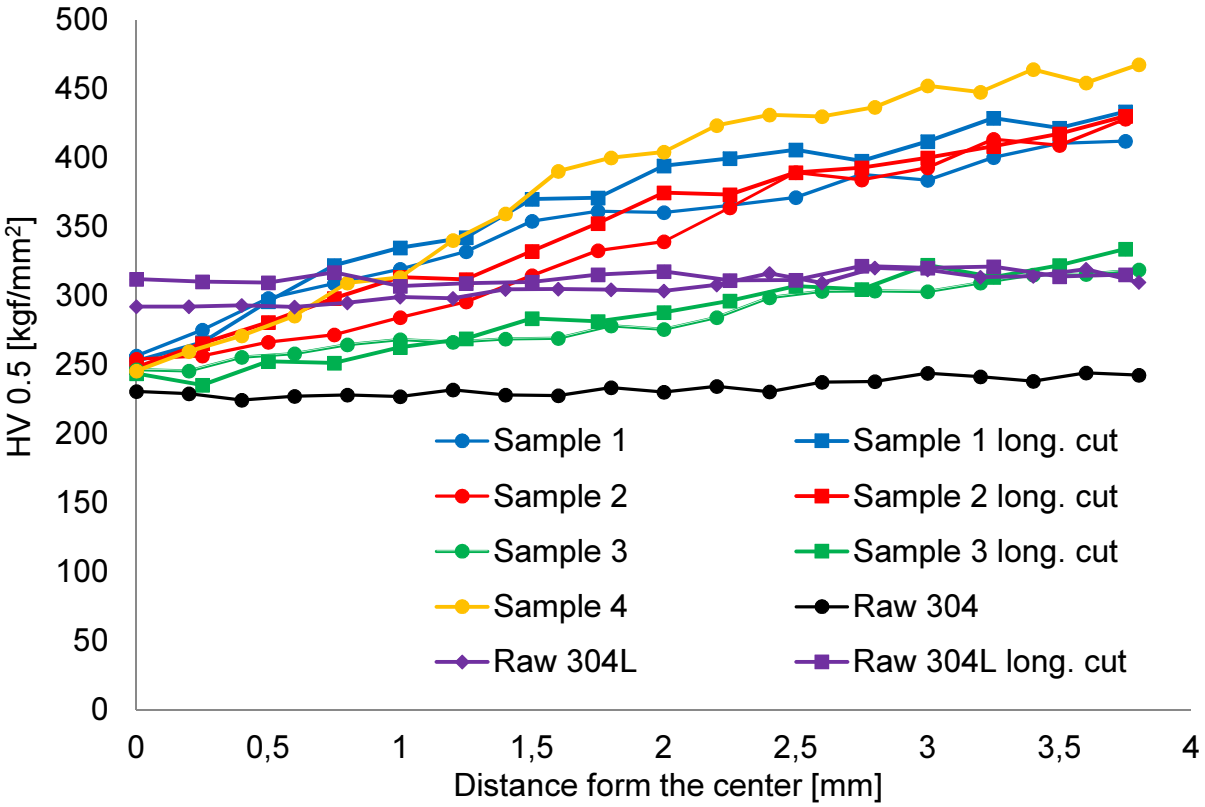

Figure 6.64. Average micro-hardness results for all the samples made of 304 stainless steel

6.2.9. Conclusions

Based on the micro-hardness measurements the following conclusions are drawn:

1. Practically constant micro-hardness was obtained for the raw samples of 304 and 304L stainless steels.
2. The micro-hardness values increasing along the radius of the sample were obtained for all the samples loaded by means of torque.
3. The trend of radially increasing micro-hardness was approximately linear.
4. The highest distribution of micro-hardness was obtained for the sample twisted at liquid nitrogen temperature (77K) until rupture.
5. Generally, the micro-hardness values were higher for samples twisted to higher angles.

6.3. Martensite content measurements

One of the main goals of this work was the experimental confirmation of the possibility of obtaining functionally graded structural members by means of torsion. Thus, the aim is to obtain a structure with functionally varying content of austenite and martensite. Torsion tests were performed on cylindrical samples. In order to introduce plastic strains, rather high values of the angle of twist were applied. The plastic strain induced phase transformation led to the evolution of microstructure from the parent austenitic phase to the secondary martensitic one. In order to recognize the presence of secondary phase, the martensite content measurements were necessary. Two methods have already been presented (microscopic observations and microhardness measurements). During microscopic observations the martensite grains were clearly visible, and their distribution on the surface of the samples. Yet, only qualitative results were obtained. The micro-hardness measurements confirmed the findings from the microscopic observation, indicating an increasing content of martensite along the radius of the sample.

Quantitative measurements are of high importance for the present work. Especially, the distribution of the martensitic phase in the cross sections of the twisted bars is sought. Several attempts have been made to achieve this goal. The first test is based on the magnetic properties of the austenite and the martensite. It is known that austenite is paramagnetic, whereas the martensite is ferromagnetic. The content of martensite is proportional to the magnetic permeability of the material (Garion et al. 2006). Thus, an experimental set-up was created in order to measure the magnetic permeability. All details of this set-up are described in the subsequent sections. Yet, this measurement could only provide average permeability of cylindrical slice of the sample, but not the function of magnetic permeability along the radius. Even though this measurement doesn't lead to most precise results, the experimental method is worth mentioning. The set-up works properly, however, the method is not precise enough, as shown in the results. Yet, the attempt is valid, and the results offer an important feedback.

Another approach is a technique called Electron Backscatter Diffraction (ESBD). This technique is used with scanning electron microscopes. The samples need very fine polish, and a long time of preparation. According to the direction of the crystallographic planes of slip, it is possible to distinguish between the body center cubic (martensite) and the face center cubic unit cell (austenite). One sample has been carefully prepared. The program allowed automatic scanning and identification of selected region. A thin radial square was selected. It turned out that the percentage of the recognized microstructure was rather low (less than 20%) around the surface, and about 50% near the center. This was probably caused by distortion of the original lattice, caused by very high angles of twist, and existence of residual stressed in the sample.

Another technique was the measurement by using X-rays. The measurements with X-rays allow differentiation between BCC and FCC microstructures. Yet, the samples with known martensite content were needed to calibrate the machine. Lack of such samples made it impossible to evaluate quantitatively the martensite fraction in the material.

Finally, the Feritscope MP3C was used. The device was designed to measure local volume fraction of ferrite, especially in the welds. It turns out, that it can be used to measure the quantity of martensite as well. Point-like measurements were possible, and this method provided the results which were precise enough.

6.3.1. Martensite content measurement based on magnetic permeability. Set-up 1

Four samples were prepared for the test (Fig. 6.65): sample 1, sample 2, sample 3 and the raw sample (see the parameter of loading in Tab. 5.2). The samples were cut to 40 mm length. A coil has been prepared in order to induce magnetic field. The induced voltage in the coil was measured in two cases: without core, and with core in the form of 40mm long samples of various martensite content.
The coils were powered by a current source (Fig. 6.66). There were two main variables in the measurement: amplitude of current and frequency of signal. Ultimately, a constant amplitude of current was used in the measurement. A wide range of frequencies was tested to calculate the inductance of the coil from the induced voltage. The inductance is constant for a given coil with a given core.
The measurement consisted of measuring the induced voltage by means of a multimeter for different frequencies of the current. Constant amplitude of current was used.
The photograph of the set-up is shown in Fig. 6.66. The current source was connected to the coil. Two multimeters and one oscilosope were used. The oscilloscope was applied to observe the signal from the generator. First multimeter was used to measure the amplitude of the current (for verification only). The second one was used to measure the induced voltage in the coil.

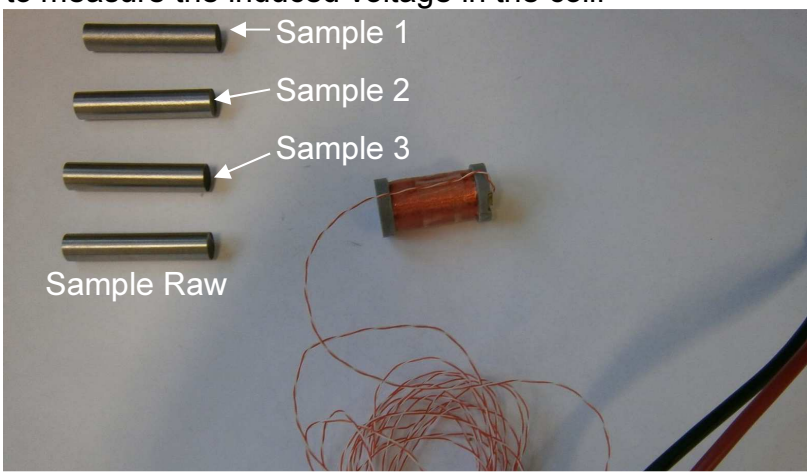

Figure 6.65. The coil and the samples with various martensite content

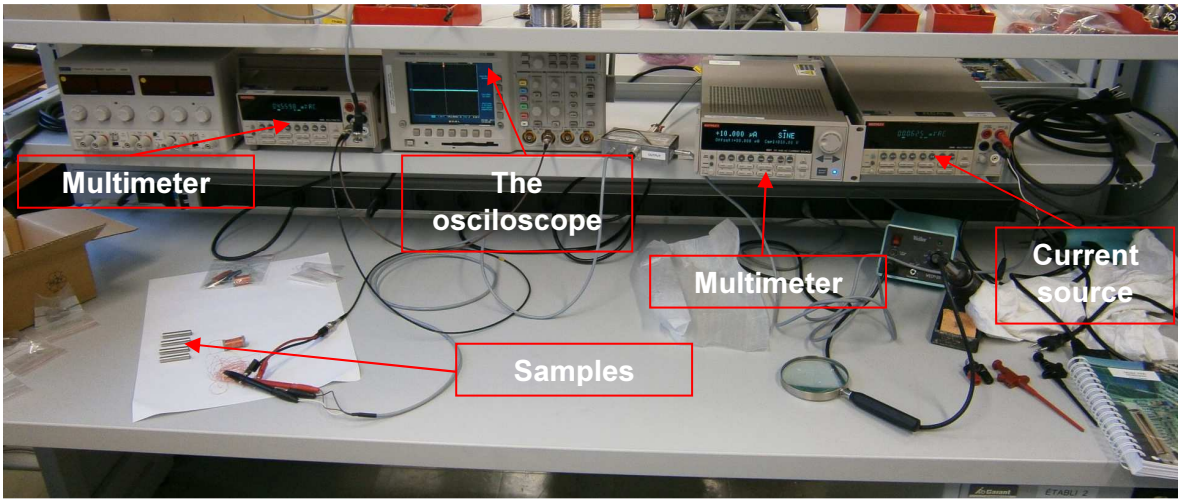

Figure 6.66. Experimental set-up for average permeability measurements

In the following paragraphs the mathematical model used to calculate the magnetic permeability is described.
The inductance of a coil can be calculated from well-known formula:

$$L = \frac{N_t^2 \cdot A_c \cdot \mu}{l_c} \tag{6.1}$$

$$\mu = \mu_0 \cdot \mu_r \tag{6.2}$$

where:
L - denotes inductance of the coil
N_t - is the number of circumvolutions in the coil
l_c - is the length of the coil
μ - denotes total magnetic permeability
μ_0 - is a constant, magnetic permeability of the vacuum
μ_r - denotes relative magnetic permeability
A_c - is the area of cross-section of the coil, which can be calculated from the formula:

$$A_c = \pi \frac{D_c^2}{4} \tag{6.3}$$

Here, D_c is the diameter of the core in the coil. Thus, it is the diameter of the sample (8 mm). The values of these constants are listed in Table 6.3.

μ_0	l_c	D_c	A_c	N_t
[H/m]	[m]	[m]	[m^2]	[-]
$4\pi\ 10^{-7}$	0.023	0.008	$5.027\ 10^{-5}$	10000

Table 6.3.Parameters for the mathematical model

From Eqs 6.1 and 6.2 one can express the relative permeability as:

$$\mu_r = \frac{L \cdot l_c}{N_t^2 \cdot A_c \cdot \mu_0} \tag{6.3}$$

All the quantities in equation 6.3, apart from the inductance of the coil (L), were known. The inductance can be calculated from well known formula describing the voltage induced in the coil, through which alternating current is passing. Namely:

$$u = -L \frac{di}{dt} \tag{6.4}$$

where di/dt is derivative of the current with respect to time. Assuming that the current is represented by a harmonic function $i = i_0 \cdot \sin(\omega t)$, as provided by the generator in the set-up, one obtains from Eq. 6.4:

$$u = -L \cdot i_0 \cdot \omega \cdot \cos(\omega t) \tag{6.5}$$

Thus, again a harmonic function is obtained, as L, i_0, ω are constants. Using definition of the root mean square value of the voltage one has:

$$u_{RMS} = \sqrt{\frac{1}{T}\int_0^T u^2\, dt} = \sqrt{\int_0^T \frac{1}{T}(-Li_0\omega)^2 \cdot [\cos(\omega t)]^2\, dt} \tag{6.6}$$

which is equal to:

$$u_{RMS} = Li_0\omega \sqrt{\frac{1}{T}\int_0^T [\cos(\omega t)]^2\, dt} = Li_0\omega \sqrt{\frac{1}{T}\int_0^T \frac{1+\cos(\omega t)}{2}\, dt} \tag{6.7}$$

where the integral is:

$$\sqrt{\frac{1}{T}\int_0^T \frac{1+\cos(\omega t)}{2}dt} = \sqrt{\frac{1}{T}\cdot\frac{T}{2}} = \frac{1}{\sqrt{2}} \tag{6.8}$$

Thus, from Eq. 6.7 one gets:

$$u_{RMS} = \frac{Li_0\omega}{\sqrt{2}} \tag{6.9}$$

where ω denotes angular frequency that can be expressed as a function of frequency (f):

$$\omega = 2\pi f \tag{6.10}$$

Thus, Eq. 6.9 takes the form:

$$u_{RMS} = \frac{Li_0 2\pi f}{\sqrt{2}} \tag{6.11}$$

Finally, the inductance is calculated from 6.11 as:

$$L = \frac{u_{RMS}\sqrt{2}}{2\pi f i_0} \tag{6.12}$$

Using definition from Eq. 6.3 and the formula 6.12, the unknown relative permeability can be expressed as:

$$\mu_r = \frac{u_{RMS}}{f}\frac{\sqrt{2}\cdot l_c}{2\pi i_0 \cdot N_t^2 \cdot A_c \cdot \mu_0} \tag{6.13}$$

The u_{RMS} voltage and the frequency f were measured during the experiment only. The other parameters were constants.

The results of experiment are shown and described below. The first test was performed in a wide range of frequencies in order to check the response. The induced voltage u_{RMS} has been measured. The results are shown in Fig. 6.57. The amplitude of the current was set to $i_0 = 10\mu A$.

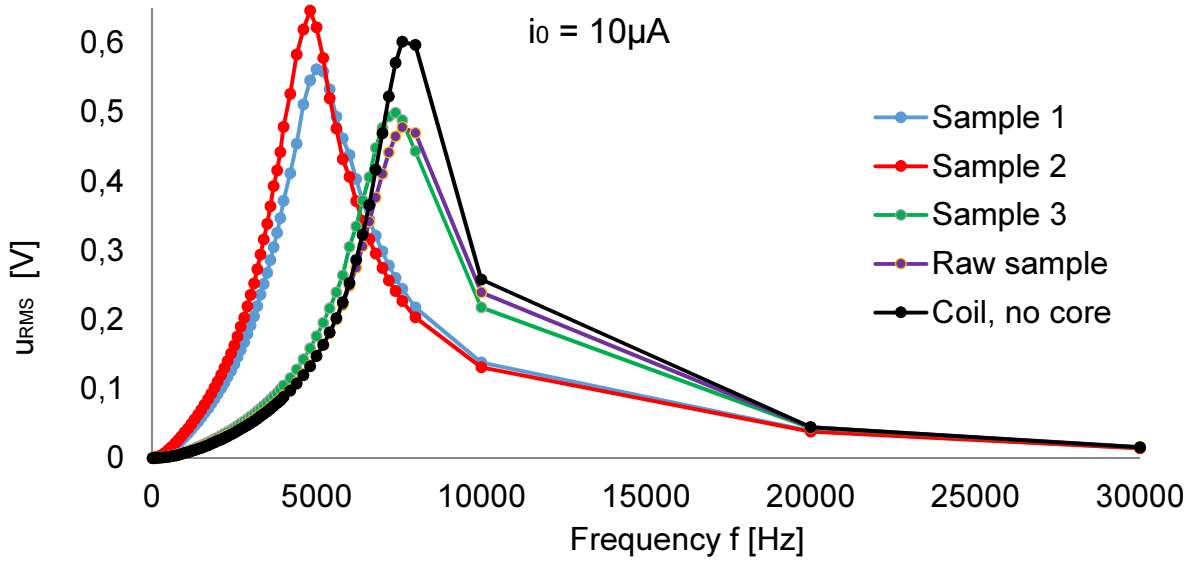

Figure 6.67. Induced voltage u_{RMS} as a function of frequency

Based on the measured RMS voltage (Fig. 6.67), the inductance was calculated by using Eq. 6.12. The results are shown in Fig. 6.68.

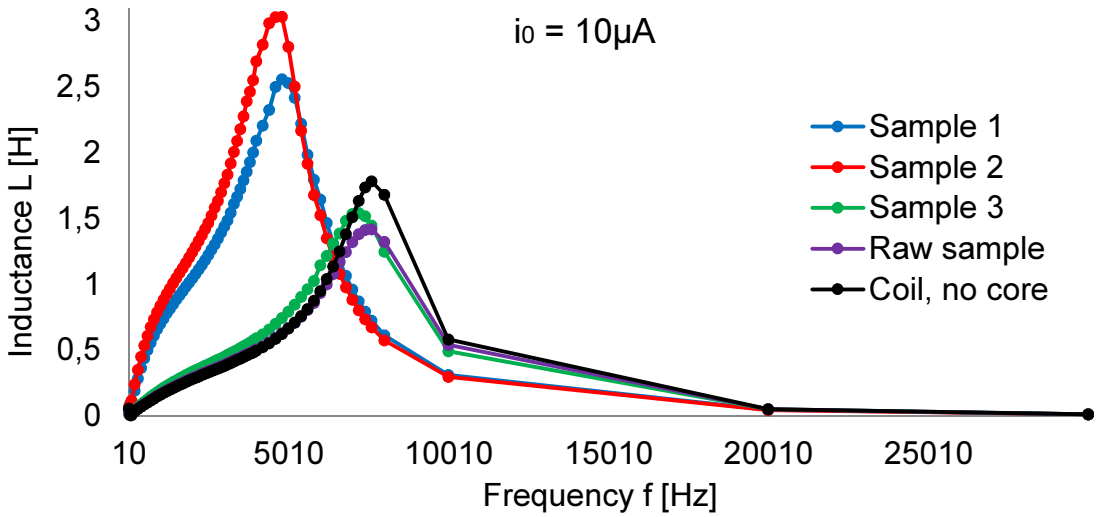

Figure 6.68. Inductance of the coil as a function of frequency

The plots of inductance in Fig. 6.68 indicate its dependence on the frequency. This result is false, because inductance is a constant parameter, related to the number of convolutions and geometry of the coil. Variable function, shown in Fig. 6.68, was rejected as contradictory w.r.t. inductance definition. Even for small values of frequency (Fig. 6.69), the inductance was not constant.

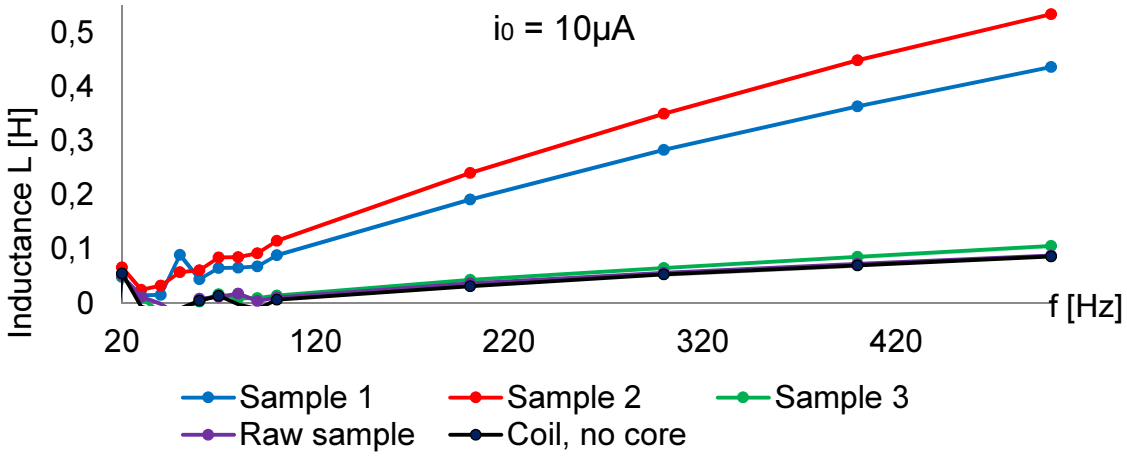

Figure 6.69. Inductance of the coil as a function of frequency for f < 500 Hz

The expected value of inductance of the coil without core is calculated based on the formula 6.1, and inserting μ_0 instead of μ. After inserting the data from Table 6.3, one obtains:

$$L = \frac{N_t^2 \cdot A_c \cdot \mu_0}{l_c} = \frac{10000^2 \cdot 5.027 \cdot 10^{-5} \cdot 4\pi \cdot 10^{-7}}{0.023} \cong 0.27\ [\mathrm{H}] \qquad (6.14)$$

The calculated inductance (Eq. 6.14) differs drastically from the results obtained (Fig. 6.58). Thus, another set of tests was performed. This time with different amplitude of current, much higher than before $i_0 = 1mA$. The results in terms of induced voltage as a function of frequency, for all samples, are shown in Fig. 6.70. The calculated inductance from the formula 6.12 is shown in Fig. 6.71.

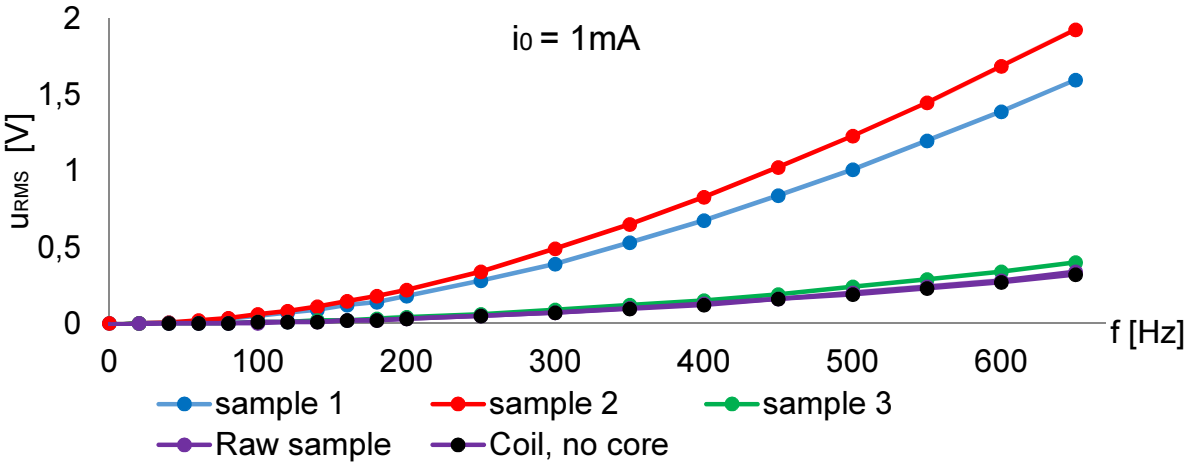

Figure 6.70. Induced voltage as a function of frequency, for i_0=1mA

This time different results were obtained (Fig. 6.70), compared to the previous ones (Fig. 6.67). Yet, the calculated inductance is still not constant (Fig. 6.71). Thus, one has to reject these results as well.

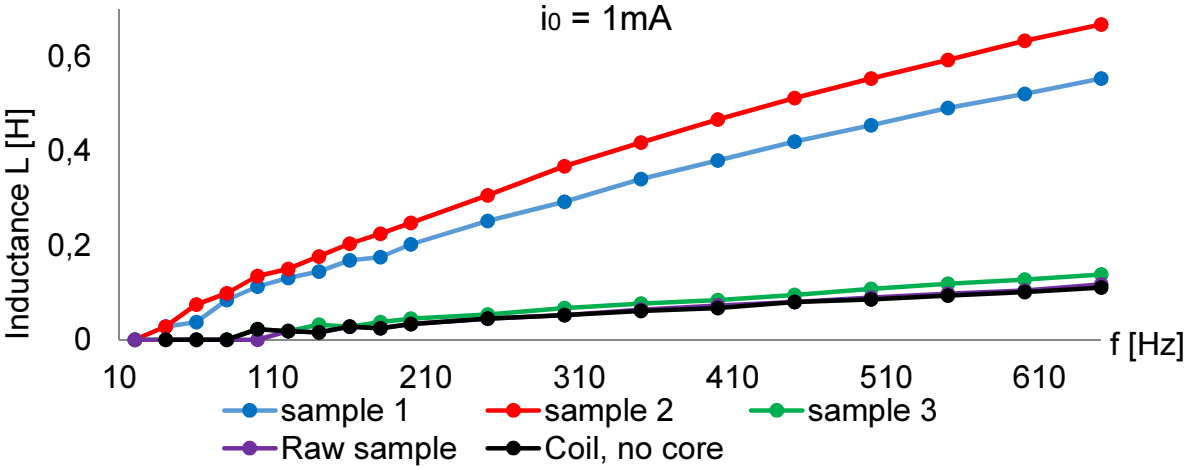

Figure 6.71. Calculated inductance as a function of frequency, i_0=1mA

A solution of the problem consists in introducing another source of magnetic field outside the coil, and measuring the induced voltage in the small coil. Thus, another set-up was built. A detailed description is presented in the following section.

6.3.2. Martensite content measurement based on magnetic permeability. Set-up 2

The set-up used for measurements has been modified in comparison with the previous one. A magnet has been added. The photograph of the set-up is shown in Fig. 6.72. A cylindrical holder made of “Plexiglas” has been used. The coil with the samples was placed inside this holder, as shown in Fig. 6.73 a, b.
Like in the previous test, the voltage induced in the coil was measured as a function of frequency. The results for five samples have been recorded.

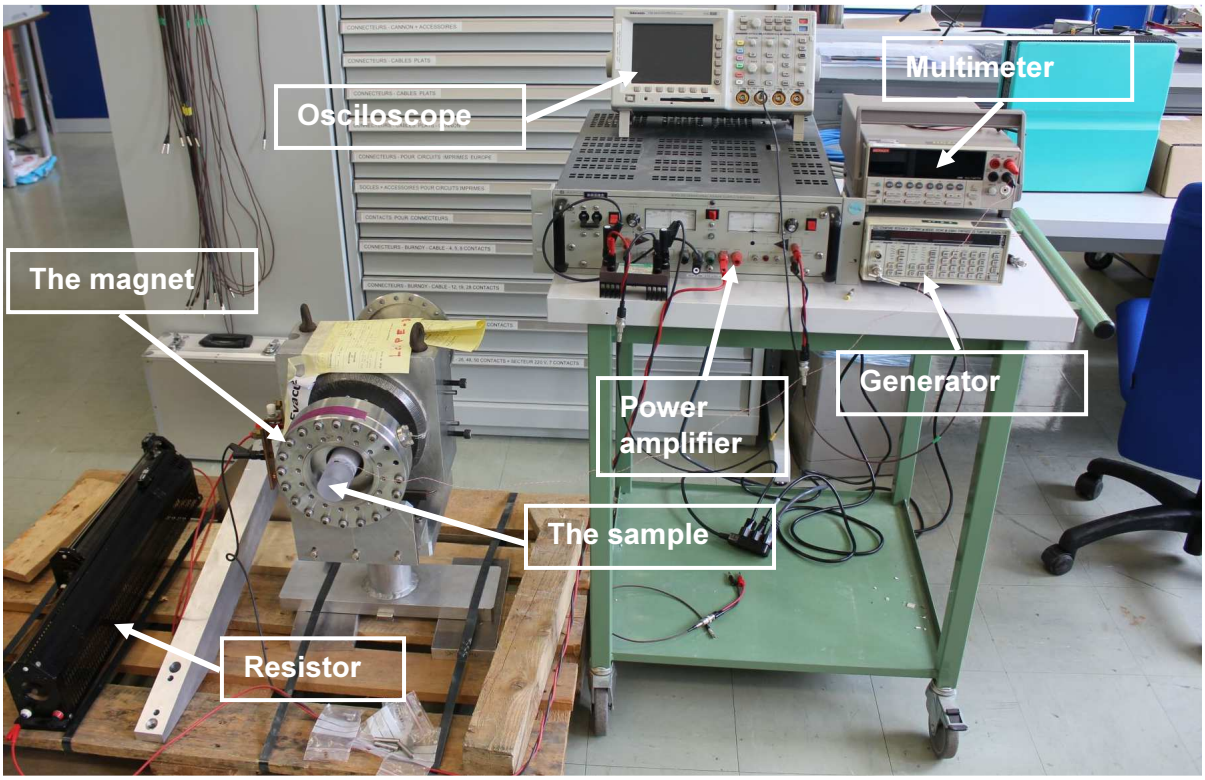

Figure 6.72. Set-up for magnetic permeability measurements with a magnet

a b

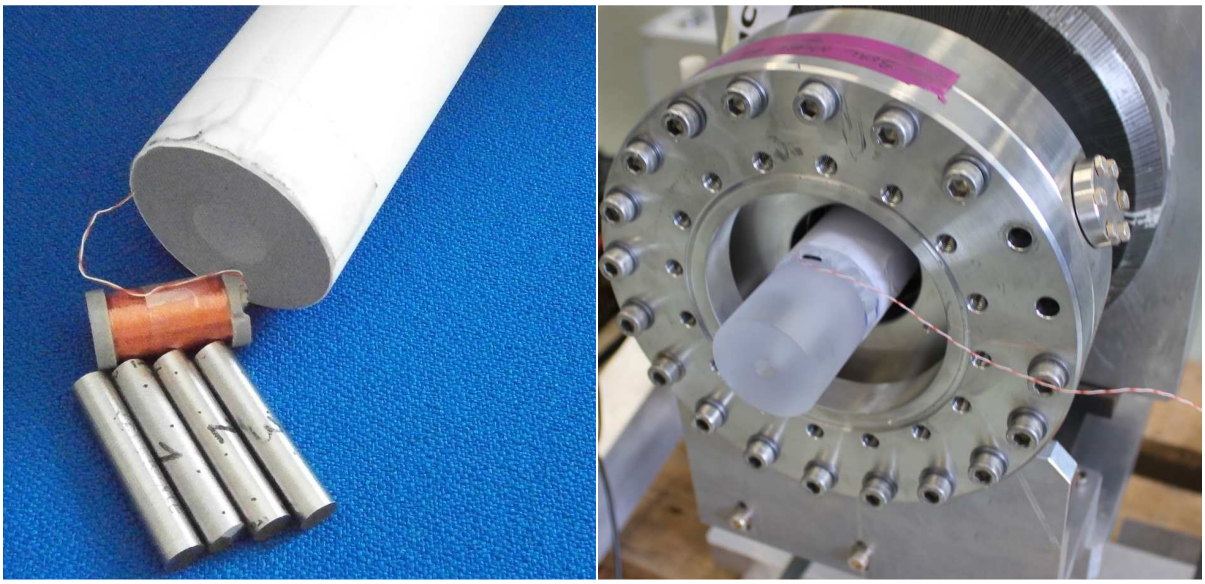

Figure 6.73. a) holder for the coil with the samples, b) magnet with the holder inside

The procedure of calculating relative permeability is shown in the following paragraphs. Taking into account formula 6.1 for the inductance of the coil, and 6.11 for the RMS value of the induced voltage, one obtains:

$$u_{RMS} = \frac{N_t^2 \cdot A_c \cdot \mu}{l_c} \frac{i_0 2\pi f}{\sqrt{2}} \tag{6.15}$$

For the coil without core one has to insert into Eq. 6.15 the permeability of the air ($\mu = \mu_0$):

$$u_{RMS0} = \frac{N_t^2 \cdot A_c \cdot \mu_0}{l_c} \frac{i_0 2\pi f}{\sqrt{2}} \tag{6.16}$$

For the sample with core, after introducing Eq. 6.2 into 6.15, one obtains:

$$u_{RMS\_Sample} = \frac{N_t^2 \cdot A_c \cdot \mu_r \cdot \mu_0}{l_c} \frac{i_0 2\pi f}{\sqrt{2}} \tag{6.17}$$

Combining equations 6.16 and 6.17, one derives:

$$u_{RMS\_Sample} = \mu_r \cdot u_{RMS0} \tag{6.18}$$

where:

$$\mu_r = \frac{u_{RMS\_Sample}}{u_{RMS0}} \tag{6.19}$$

Thus, very simple formula is obtained for relative permeability of the core. It is calculated as the ratio between the RMS values of the voltage induced in the coil without core and with core. This value does not depend on frequency. Yet, this has been examined experimentally. The induced voltage was measured for several values of frequency. The results for the frequency range 0÷400 Hz and the current amplitude $i_o = 6A$, for the induced voltage u_{RMS}, are shown in Fig. 6.74. As the amplitude of current is another parameter, second measurement was performed for comparison, for $i_o = 3A$ (Fig. 6.75).

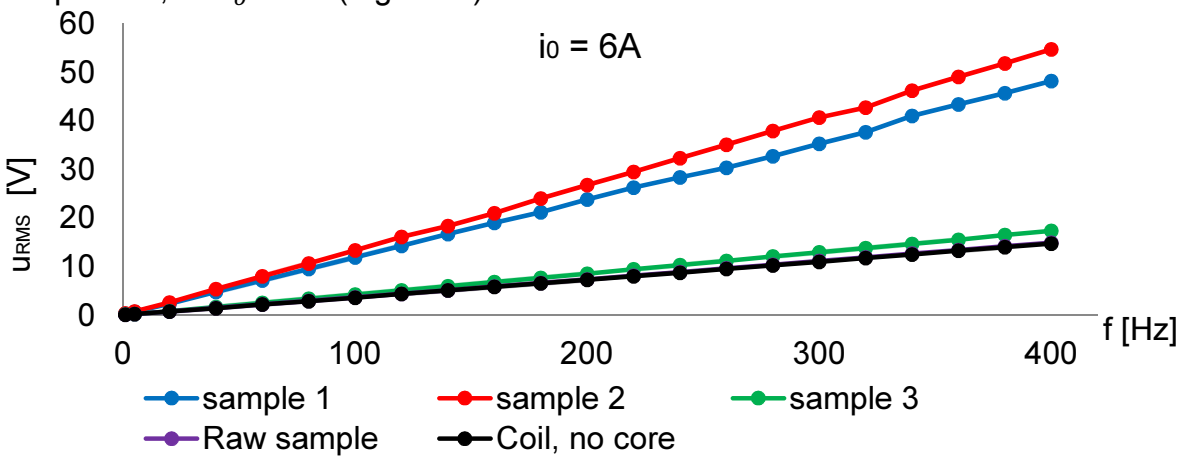

Figure 6.74. Induced voltage versus frequency, i_0=6A

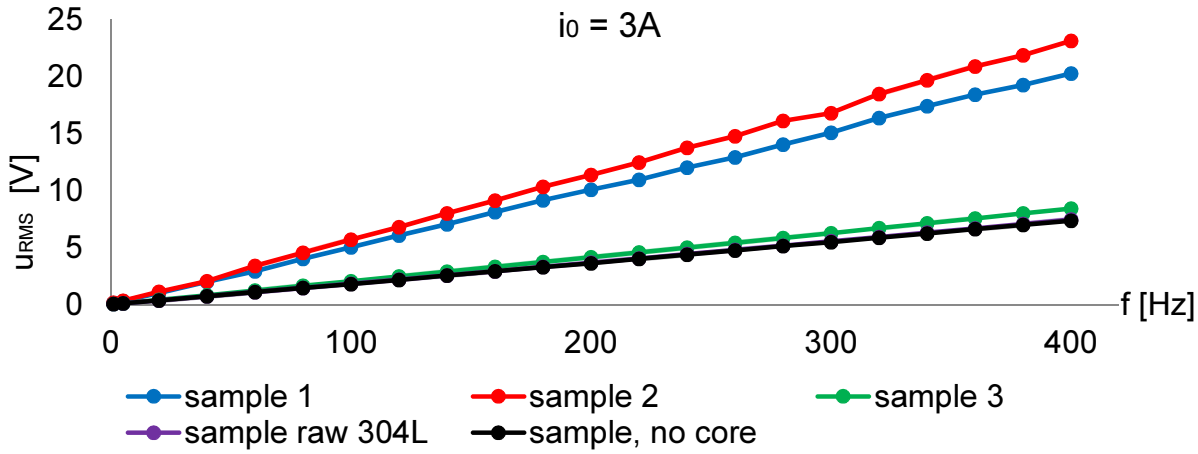

Figure 6.75. Induced voltage versus frequency, i_0=3A

From both results (Figs 6.74, 6.75) a linear dependence of voltage on the frequency is obtained. Based on formula 6.19, the relative magnetic permeability of the samples was calculated and is shown in Figs 6.76 and 6.77.

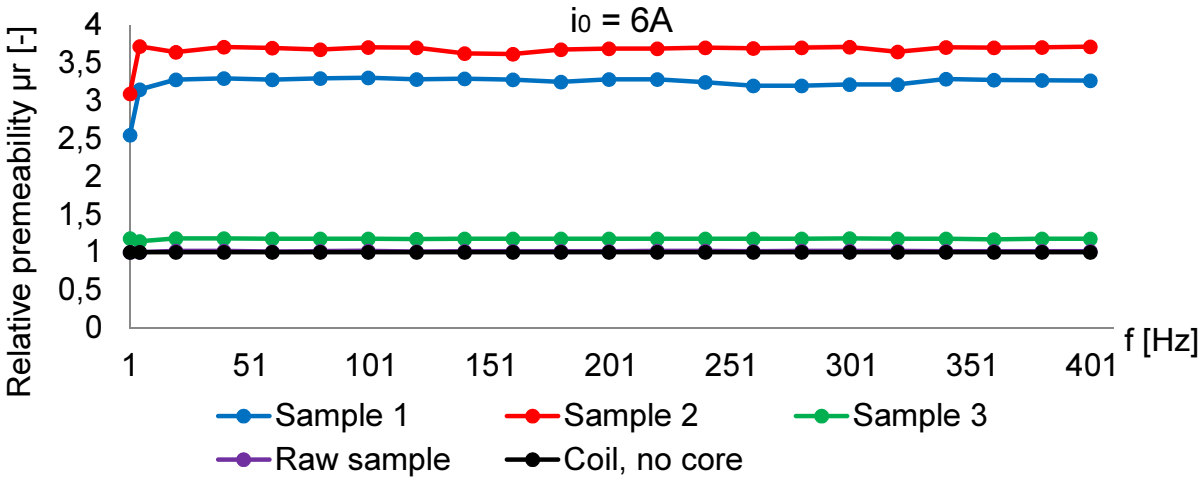

Figure 6.76. Calculated relative permeability versus frequency, i_0=6A

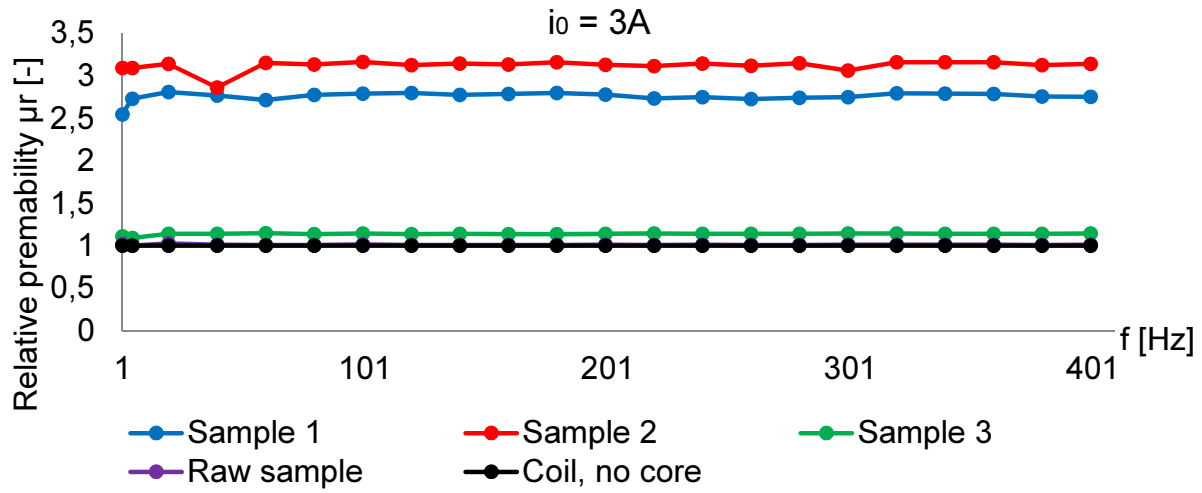

Figure 6.77. Calculated relative permeability versus frequency, i_0=3A

The resultant relative magnetic permeability (Figs 6.76, 6.77) is approximately constant for all the samples. Because of paramagnetic properties of the raw sample, its results were almost exactly the same as for the coil without core. For this reason, one cannot distinguish between these two results in Figs 6.76 and 6.77.
The results obtained agree with the theory as the relative magnetic permeability does not depend on the frequency. In order to draw further conclusions, the results from Figs 6.76 and 6.77 were averaged, and are reported in Tab. 6.4. The average has been calculated from the formula:

$$\mu_r = \frac{1}{n}\sum_{i=1}^{n} \mu_{ri}(f_i) \tag{6.20}$$

where:
n – is the number of measured voltage values,
$\mu_{ri}(f_i)$ - are the values of the relative magnetic permeability measured for finite frequencies (f_i).
The difference between these values, shown in Tab. 6.4, was calculated as:

$$Difference = \frac{\mu_r(6A) - \mu_r(3A)}{\mu_r(6A)} \cdot 100\% \tag{6.21}$$

	$i_0 = 6A$	$i_0 = 3A$	Difference
	μ_r [−]	μ_r [−]	[%]
Sample 1	3,22	2,75	14,5
Sample 2	3,66	3,12	14,7
Sample 3	1,17	1,14	3,2
Raw sample	1,01	1,01	0

Table 6.4. Average values of the relative magnetic permeability

From Tab. 6.4 different values were obtained for different amplitudes of current. For example, for sample 1 and i_0=6A the result is μ_r=3,22, whereas, for i_0=3A the result is μ_r=2,27, thus, 14,5% smaller. Such dependence on the amplitude of current was not expected. For this reason, the results have to be treated as preliminary only.

In order to relate the relative permeability of the sample to martensite content, the results of the work by Larbalestier and King (1973) are used. Larbalestier and King obtained experimental relations between the content of martensite and the relative magnetic permeability. They performed the measurements under 1000Oe and 100Oe (Oe=oersted) of strength of magnetic field. The content of α' martensite is identified by using the Sucksmith's balance. The results for 1000Oe were taken into account and are shown in Fig. 6.78 as points. A linear trendline has been added to reach good agreement. Although this measurement was taken at 4.2 K, it is assumed that the same holds for room temperature conditions. The martensite is stable up to the temperature of 400 °C, which offers large safety factor w.r.t. 25 °C. The measurements were performed for three types of stainless steel, namely 304L, 321 and 347. It was assumed that the same properties hold for 304 stainless steel, which is used in the present work.

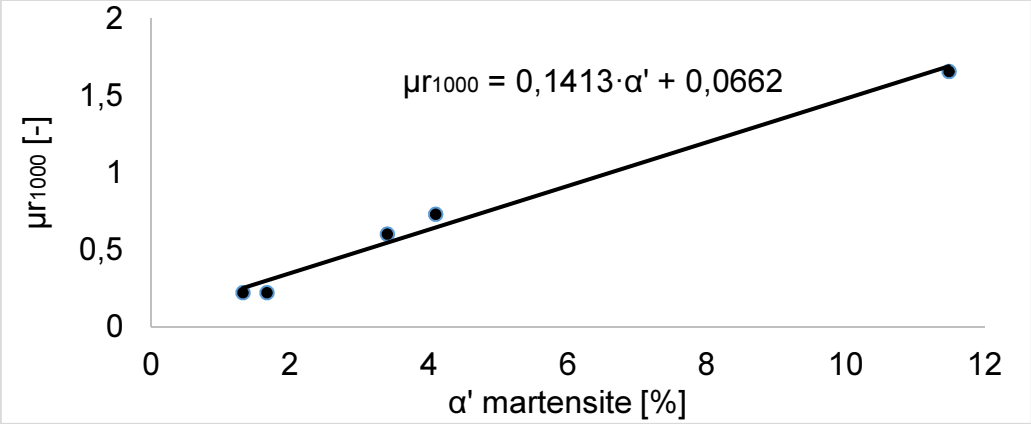

Figure 6.78. Relative magnetic permeability μ_r versus α' martensite content at 4.2K, for steels 304L, 321, and 347 at the field of 1000 Oe, from Larbalestier and King (1973)

Taking into account the phenomenological formula obtained from the approximation (Fig. 6.78), the martensite content is calculated as:

$$\alpha' = 6{,}982 \cdot \mu_r - 0{,}4026 \qquad (6.22)$$

The martensite content is calculated based on the results from Tab. 6.4 and formula 6.22. The resulting martensite content is shown in Tab. 6.5.

	$i_0 = 6A$	$i_0 = 3A$
	Martensite content α' [%]	
Sample 1	22,9	19,6
Sample 2	25,9	22,2
Sample 3	8,6	8,3
Raw sample	7,5	7,5

Table 5.6. The calculated values of martensite content

The results indicate that the raw sample has 7.5 % of martensite, which is highly improbable, as it should stay rather close to zero. A simple test with a magnet revealed no magnetic force compared to the other samples. Another issue was the difference with respect to amplitude of current. On the other hand, the values for the samples 1, 2 and 3 are reasonable, yet, more precise measurements are necessary in order to confirm this.

6.3.2.1. Conclusions from magnetic measurements

Based on the results presented in the preceding sections, it is concluded that the results have only a preliminary character. The first test didn't succeed at all, because of the inductance which turned out to vary with the frequency of the signal. The second approach solved this issue, and the voltage was a linear function versus frequency. Still, the relative magnetic permeability which was constant versus frequency, depended on the amplitude of current. Another questionable assumption reflects the relation between the relative magnetic permeability and the martensite content. Based on the work by Larbalestier and King (1973), many assumptions have been adopted. The first consisted in using the curve of μ versus α' for 1000 Oe field strength, whereas, a different result was obtained for 100 Oe (Larbalestier and King (1973). The results showed in Fig. 6.78 were obtained at 4.2 K, whereas in the present experiments the temperature was 293K. Thus discrepancy was big.
As a general conclusion, the magnetic method is not recommended as it requires many assumptions, and it is rather indirectly related to the martensite content. Too many variables influence the results, which decreases the confidence in them. Therefore, a different method should be applied.

6.3.3. Measurements via the EBSD technique (Electron Backscatter Diffraction)

The EBSD technique has many useful applications, among them it allows to identify the phases of microstructure. This technique makes it possible to recognize the seven crystallographic systems on a sub-micro level, for grains larger than 20nm. Because of difference in crystallographic structure between the α' martensite (BCC – body center cubic) and the austenite (FCC - face center cubic), this technique can efficiently be used.
The EBSD measurements of the phase content in austenitic stainless steels were reported in many works (cf. Nakajima et al. 2011, Müller-Bollenhagen et al. 2010, Kisko et al. 2013, Weidner et al. 2010).
Shen et al., 2012, concluded that the EBSD technique underestimates the content of martensite when compared to results obtained via the X-ray technique. X-ray measurement gave around 1.3 times higher result than EBSD. Similar conclusion was drawn by Gussev et al., 2013. The reason was limited resolution of EBSD, which couldn't identify martensite particles smaller than 0.2 μm.
In the present study, three cross sections have been carefully prepared for EBSD measurements (Fig. 6.85a). They have been immersed in a conductive resin, and then electro polished to achieve very fine surface finish.

The aim of the measurement was to estimate the martensite content within a narrow strip, starting from the center of the cross section and ending up at the surface.
It turned out from the EBSD technique, that the phase recognition was good exclusively near the center of each sample. At distances larger than half of the radius, the phase recognition was smaller than 20%. With such low indexing, the quantitative measurements were not possible. The reason of this poor recognition were high strains applied during the torsion. These strains caused deformation of the lattice. The distance between the atoms changed. The software could not recognize the pattern, as the database was provided for unstrained crystal orientations.
Again, the EBSD technique didn't solve the problem of the martensite content identification and quantitative evaluation within the cross-section.

6.3.4. Martensite content measurements by means of X-ray technique

X-ray diffraction is a commonly used technique to identify phases, including austenite or martensie. Many researchers have successfully used this technique. For example, De et al., 2004, carried out quantitative measurement for 304 stainless steel, identifying volume fractions of austenite, α' and ε martensite. Solomon & Solomon, 2010, measured the strain induced α' martensite in 316 stainless steel.
In the present study, the variation of martensite content along the radius of the sample was sought. It turned out, that the available equipment was not satisfactory. Quantitative martensite content measurement was not possible because of the lack of calibration samples. Only the qualitative results were obtained.
The results for the raw, unstrained sample are shown in Fig. 6.79, the important region is magnified in Fig. 6.80.

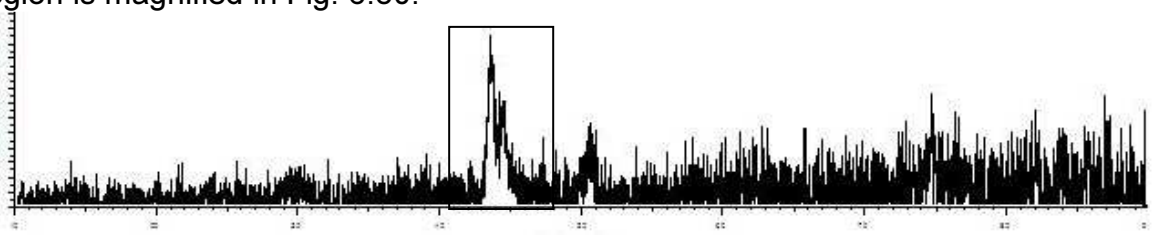

Figure 6.79. Results from XRD measurements for the reference sample (304ss)

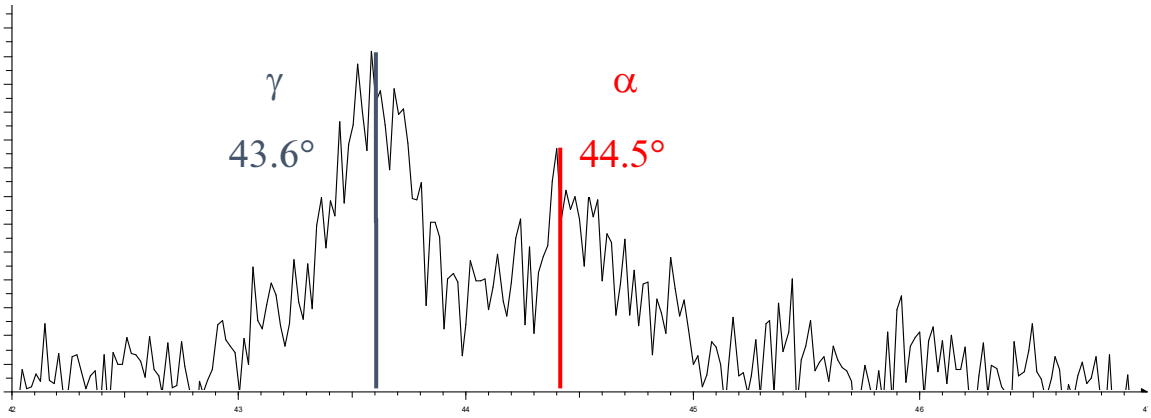

Figure 6.80. The highest peaks detected for the reference sample, γ is the austenitic phase and α' is the martensitic one

The results for twisted sample are shown in Fig. 6.81, and in Fig. 6.82 where the peak is magnified.

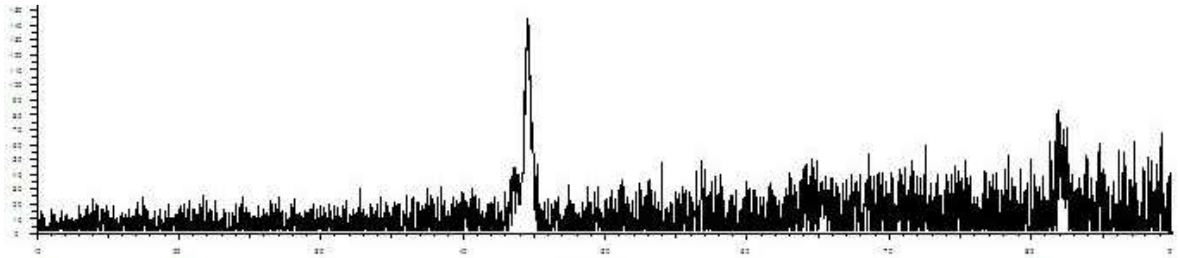

Figure 6.81. XRD results from the sample after torsion

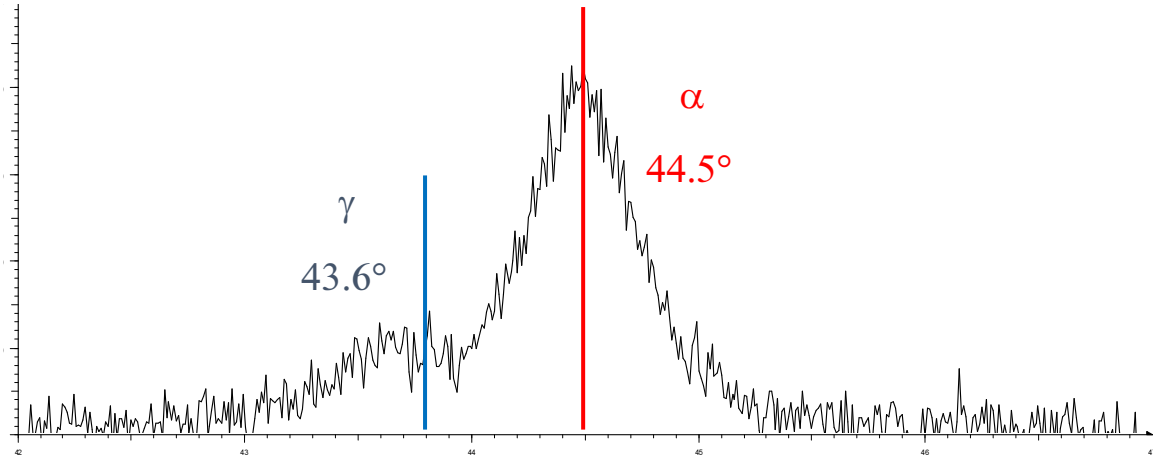

Figure 6.82. The highest peaks for the deformed sample (α' martensite content is much higher than in the undeformed sample)

One can clearly see the difference between the results presented in Figs 6.82 (after deformation) and 6.80 (undeformed sample). The *γ*-phase peak found at the angle of 43.6° has considerably decreased. At the same time the α' martensite peak at 44.5° has increased. This result confirms the presence of martensite that was induced by the phase transformation triggered by torsion.
In the following section, more precise method is described, which allows quantitative measurement of martensite content within the cross-section of the sample.
A successful method was found: the measurement by means of the so-called Feritscope.

6.3.5. Measurements by using Feritscope

The Feritscope measures locally the quantity of ferromagnetic microstructure in the material. Both ferrite and martensite exhibit ferromagnetic properties. The Feritscope is devoted to ferrite content measurements, yet, it can be used as well for martensite content measurements. The detailed procedure is described later in this section.
There are essentially two types of martensite structure, the so called α' martensite and the ε martensite. The α' has body centered cubic (BCC) crystallographic structure, and the ε martensite occurs in the hexagonal closed packed (HCP) crystallographic form. The α' is ferromagnetic, whereas, the ε martensite is paramagnetic. Because of the paramagnetic properties of the ε martensite, it cannot be measured using the Feritscope. Yet, this intermediate phase is much less important. Many studies have shown, that the quantity of ε martensite decreses with increasing plastic strain. Also, ε martensite is an intermediate phase that transforms into the α' martensite. For higher plastic strains, only α' martensite is present.
The Feritscope principle is based on the measurement of voltage, which is proportional to the magnetic properties of ferrite structure. Yet, magnetic properties (like magnetic permeability) of martensite are somewhat different.

For this reason, the readout of martensite content cannot be interpreted directly. A conversion procedure of the readout values to the correct martensite content is needed.
The Feritscope has been extensively used by other researchers. This method is quite convenient, as non-destructive and very fast. While reading through the publications, an interesting fact has been found. Different authors have obtained different correlation factors between the readout of the Feritscope and the correct martensite content. In the works by Glage et al. (2009), Talonen (2007), Somani et al. (2009), Naraghi (2009), Man et al. (2011), Talonen et al. (2004), a linear dependence has been found with 1.7 as the proportionality coefficient. This result means that the content of martensite is 1.7 times higher than the readout of the Feristcope. However, in other works different proportionality coefficients have been found. In the work by Müller-Bollenhagen et al. (2009), the Authors found the coefficient of 1.58. On the other hand, in the publications by Backer et al. (2001), Shin et al. (2001), Glage et al. (2011), Meyer et al. (2011), the Authors applied Feritscope, yet, they did not mention using any proportionality factor. This leads to a simple conclusion, that no correction was applied to the readout, leading to a significant error.
Actually, the correlation coefficient of 1.7 has been found by Talonen et al. (2004). All the other authors referred to this work. These results seem very reliable, and as they are often referred to, in the present work the same correlation has been applied.
In the publication by Talonen et al. (2004), the Authors compared several methods of measuring the martensite content. They concluded that the martensite content has almost linear dependence on the Feritscope reading, up to some 55% of ferrite (Fig. 6.83a). For higher readings this relation turned out nonlinear. As the content values up to 100% of martensite were expected, the whole possible range was approximated with two linear functions.

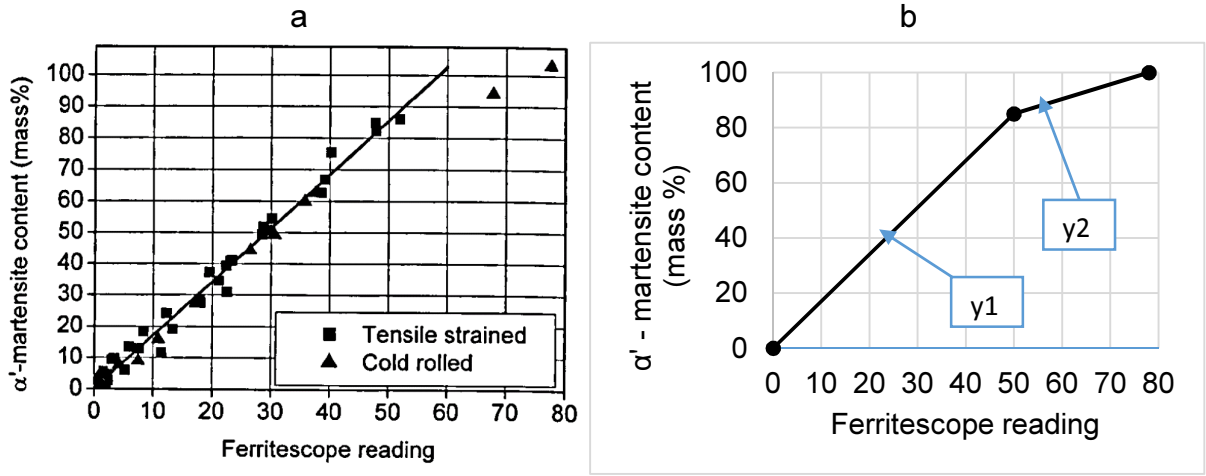

Figure 6.83 a) α' martensite content measured and calculated from the density of the specimen (Talonen et al. (2004)), b) Bilinear approximation of experimental data obtained by Talonen et al. (2004)

Based on the experimental points obtained by Talonen et al. (2004) (Fig. 6.83a), a simplified approximation was proposed (Fig. 6.83b). The first and the last points of the second line from Fig. 6.83b have the following coordinates: (50,85) and (78,100). From these two coordinates, the formula for the linear function was easily found. Finally, the martensite content can be calculated from the Feritscope reading according to the following formula:

$$M(\%) = \begin{cases} 1.7 \cdot Fr, & Fr \leq 50 \\ 0.5357 \cdot Fr + 58.2143, & Fr \epsilon \langle 50, 78 \rangle \end{cases} \quad (6.23)$$

where:

- Fr is the readout from Feritscope expressed in percents (%),
- $M(\%)$ is the mass content of martensite in percents (%).

The mass content of martensite M(%) has been assumed equal to the volume fraction of martensite. Thus, constant density was assumed. In the theoretical description, volume fraction of martensite was used as the variable describing the phase transformation kinetics.

Formula 6.23 is correct under the assumption that no ferrite is present in the material. Otherwise, the Feritscope will show the contribution of both phases: martensite and ferrite. For austenitic stainless steels, the ferrite is not expected. Yet, in order to confirm this expectation, the ferrite content was measured by using the microscopic method for several samples. The method has been described in the section 6.1.2, and the results are shown in Table 6.1. For all tested samples about 1% of ferrite was found. As this value is small compared to 100% of martensite, that was achieved for some samples, the content of ferrite was ignored. Thus, all the readout from Feritscope was converted to martensite content, according to the formula 6.23.

In order to better understand the physical basis of the measurement, next section is devoted to this subject.

6.3.5.1. The principle of measurement by means of Feritscope

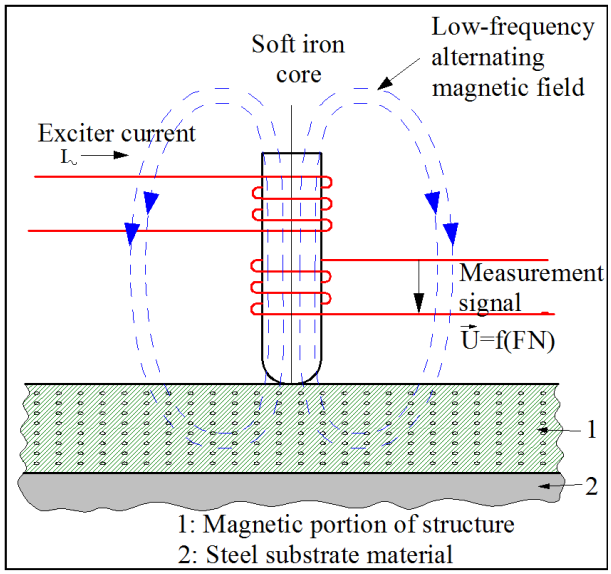

Figure 6.84. The physical principle of martensite content measurement [130]

The principle of martensite content measurement by means of Feritscope is presented in Fig. 6.84. The Feritscope operates according to the magnetic induction method. Magnetic field generated by the coil interacts with magnetic fractions in the microstructure of the specimen. Changes in magnetic field induce voltage in the secondary coil, which is proportional to the content of ferromagnetic phases (martensite, ferrite, other ferritic components). Finally, this voltage is measured and scaled in percents of ferrite. As can be seen from Fig. 6.84, the magnetic field induced by the probe interacts with certain volume of the material. Thus, the final result is rather an average of a small volume around the point of contact of the probe with the specimen.

6.3.5.2. The method of measurement

The Feritscope with the probe and the sample with three cross-sections are shown in Fig. 6.85a.

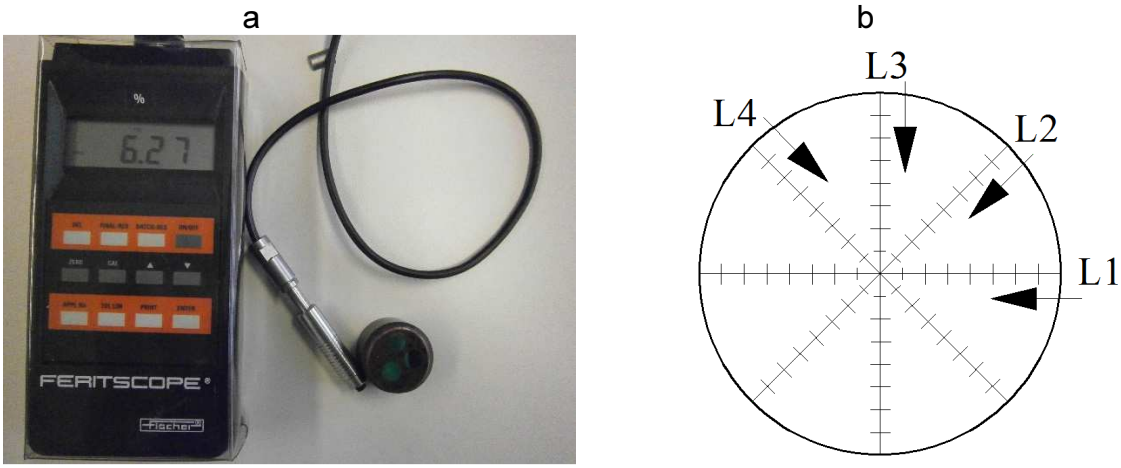

Fig. 6.85. a) The Feritscope Mp3C with the probe and the sample with 3 cross-sections; b) Positions of the measurement points in the cross-sections

The goal of the measurement was to obtain radial distribution of the martensite content. Three transverse and one longitudinal cross-sections, extracted from cylindrical samples (Fig. 6.1), have been used to measure the martensite distribution. The measurement was performed along several radial lines in order to capture the distribution over the whole cross-section. According to theoretical predictions, the results were supposed to be symmetric w.r.t. the center of the sample. Four diagonal lines (Fig. 6.85b) were denoted by: L1, L2, L3, L4. The direction of the measurement was defined from outside (the surface) towards the center. The distance between the measurement points was 0,5 mm. Three measurements were made per each of these points. Later on, the average was calculated and used as the final result.
According to Feritscope manual [131], there are several factors that influence the results, like the thickness of sample, the surface curvatures, the distance from the edge, etc. They are described in details in the following section.

6.3.5.3. Correction factors for measurements with Feritscope

According to Feritscope Mp3C manual [114], it is necessary to apply the correction factors that take into account:

- surface roughness,
- cladding thickness,
- specimen curvature,
- specimen thickness,
- edge distance to the measurement location.

The influence of the surface roughness cannot be estimated quantitatively according to the manual [114]. However, its influence can be reduced by combining sufficient number of single readings to one meaningful value [114]. For this reason, 3 measurements have been done at each point.
The influence of cladding thickness was used exclusively for measurements on welding seams. Thus, it was ignored in the present study.
The remaining three factors: the specimen curvature, thickness and the distance from the edge are discussed in the following sections.

True ferrite content can be calculated as:

$$Fr = Fm \cdot CF_T \cdot CF_D \cdot CF_C \tag{6.24}$$

where:
Fr - stands for the true ferrite content,
Fm - denotes the measured ferrite content,
CF_T - is the correction factor to cover the thickness of the sample,
CF_D - is the correction factor to cover the distance from the edge,
CF_C - denotes the correction factor involving curvature of the sample.

These correction factors (CF_T, CF_D, CF_C) can be found in the Feritscope manual [113, pp 116-123]. They are functions of the ferrite number (FN), which is another unit used in the device. In all the performed measurements, the ferrite content was measured in percents. Thus it was necessary to convert the ferrite content in % to ferrite number FN. The relationship between these two was provided by the certificate of the device, as shown in Fig. 6.86.

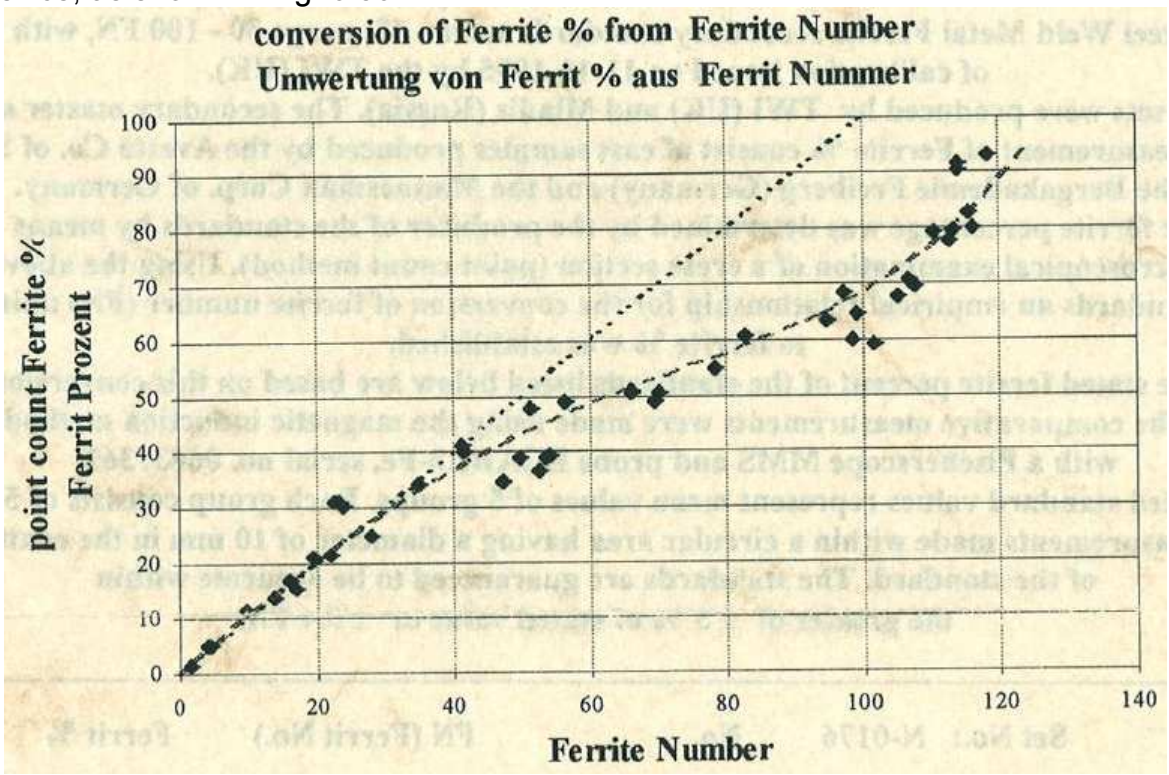

Fig. 6.86. The relationship between the ferrite content in % and the ferrite number FN (cf. the certificate of the device)

The relationship between the ferrite content in % and the ferrite number FN was measured in a finite number of points (Fig. 6.28). The certificate provided an approximation, indicated by dotted line. In order to facilitate calculations, the approximate function from Fig. 6.82 was interpolated with 4th order polynomial, which took the form indicated in (Fig. 6.87):

$$FN(Fr) = -4.99 \cdot 10^{-6} \cdot Fr^4 + 6.727 \cdot 10^{-4} \cdot Fr^3 - 0.0169 \cdot Fr^2 + 1.057 \cdot Fr - 0.0612 \tag{6.25}$$

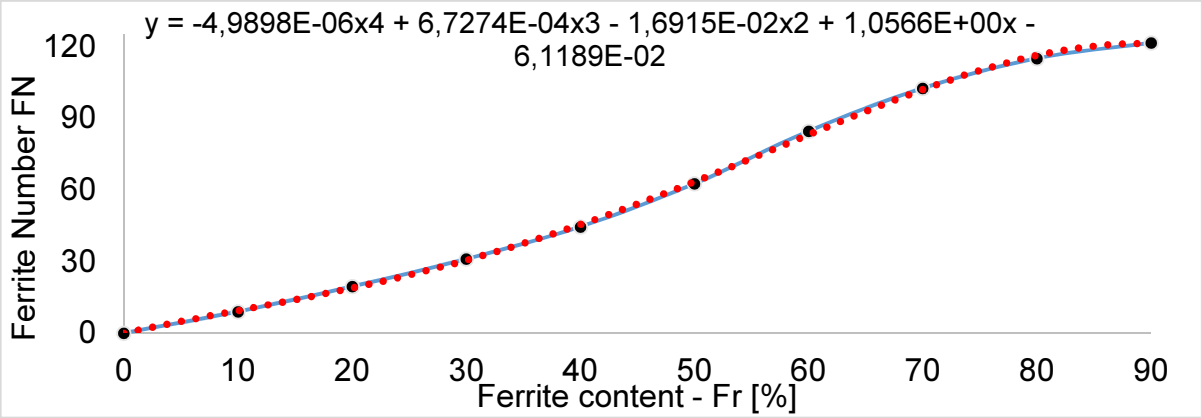

Figure 6.87. Ferrite number FN as a function of the ferrite content in % - red curve (Eq. 6.24), blue curve from the certificate (Fig. 6.82)

The 4th order approximation described by Eq. 6.25 and shown in Fig. 6.87 agrees very well with the curve extracted from Feritscope certificate (Fig. 6.86).
Having defined the relationship between Fr and FN, one can obtain the correction factors listed in Eq. 6.24.

6.3.5.4. Correction factor to cover the influence of thickness CF_T

The influence of thickness, taken from the Feritscope manual [114], is shown in Fig. 6.88. For thickness higher than 2mm, the correction coefficient is very close to unity. Its maximum is equal to 1.03 for small values of FN. As the thickness of the slices extracted from the samples was always greater than 2 mm, the results were not affected. Thus, the correction factor CF_T was ignored.

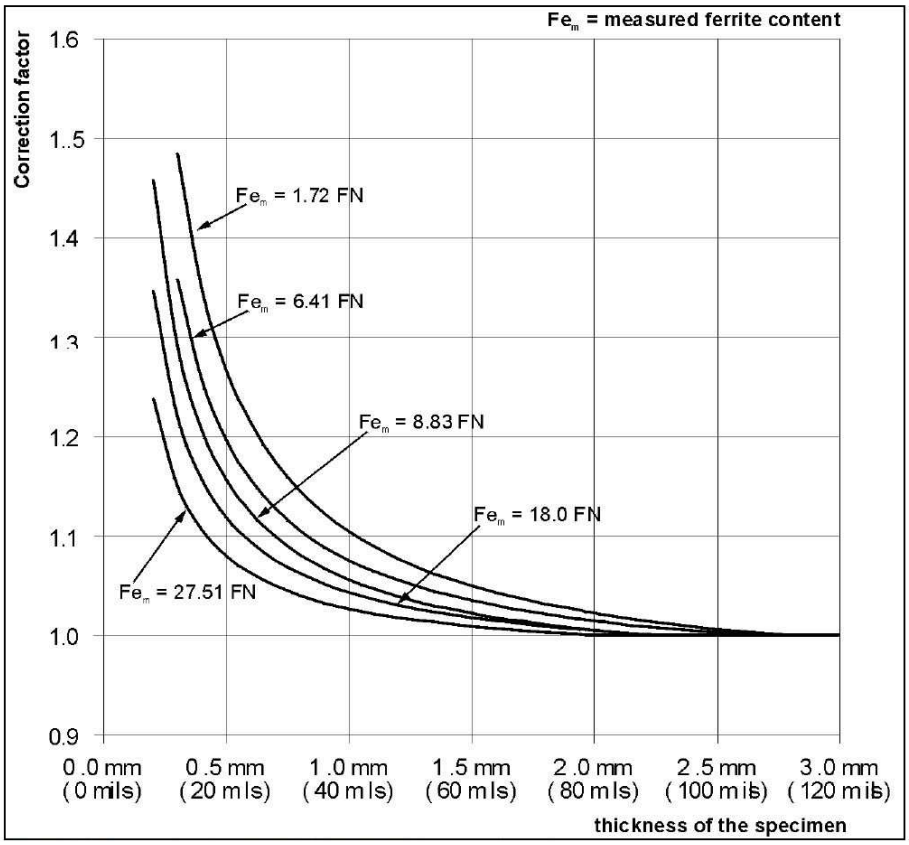

Fig. 6.88. Correction factor to cover the influence of thickness [114]

6.3.5.5. Correction factor to cover the influence of curvature CF_C

The measurements were performed either on flat surfaces (samples extracted from the cross-sections), or on the surface of the bar of 8mm diameter. For the convex surfaces, the correction factor is a function of two variables: the ferrite number FN and the diameter of curvature (Fig. 6.89, from [114]). As there is no specific curve for diameter Φ_c=8mm, it has been interpolated. The line has been drawn roughly in the mid distance between the lines Φ_c=5mm and Φ_c=10mm, Fig. 6.89. Again, this function was approximated by using 4th order polynomial to facilitate the calculations. The polynomial takes the following form:

$$CF_C(FN) = 2.767 \cdot 10^{-9} \cdot FN^4 - 6.167 \cdot 10^{-7} \cdot FN^3 + 5.462 \cdot 10^{-5} \cdot FN^2 - 3.125 \cdot 10^{-4} \cdot FN + 1.0758 \quad (6.26)$$

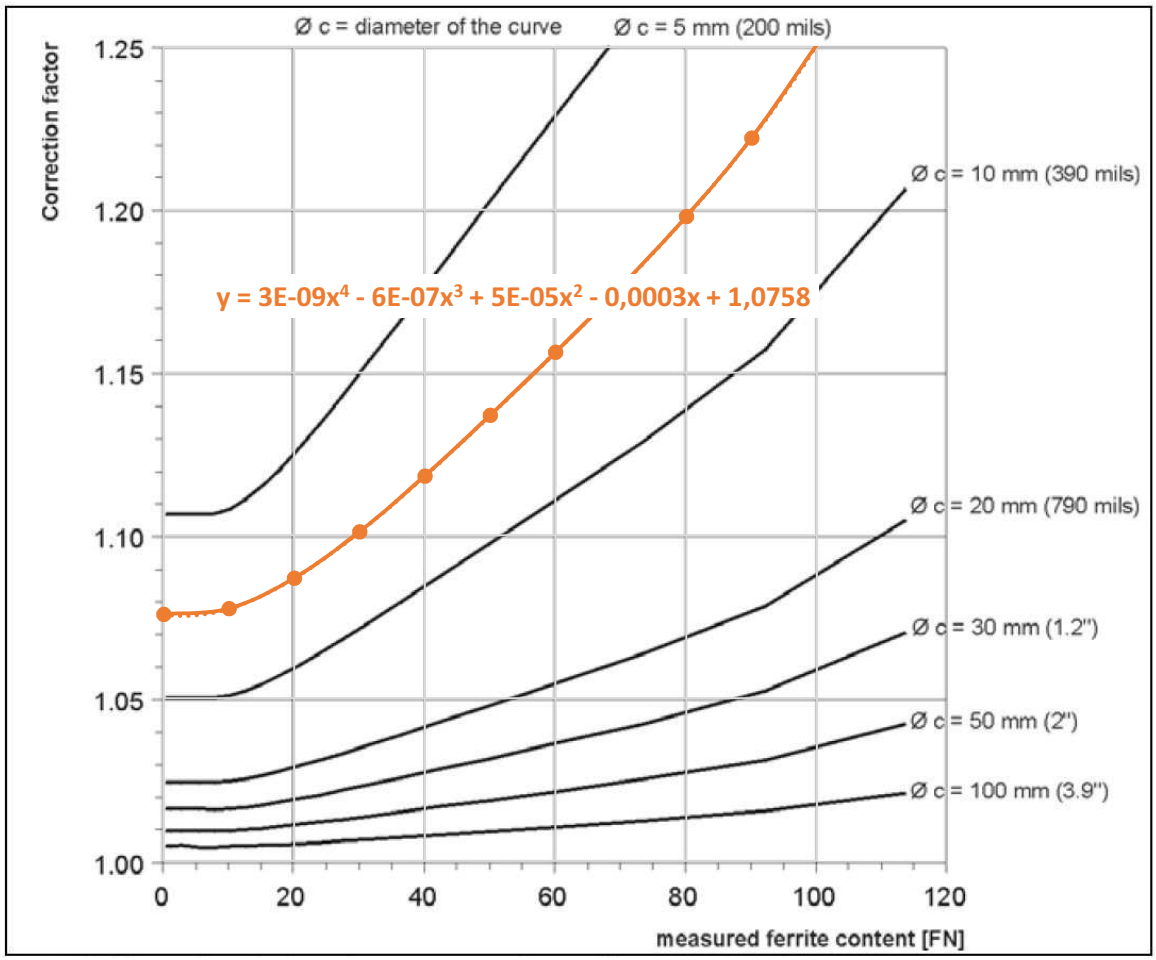

Figure 6.89. Correction factor as a function of the measured ferrite number FN and the diameter (cf. Feritscope manual, [114])

6.3.5.6. Correction factor to cover the distance from the edge CF_D

The plot from the Feritscope manual [114] is presented in Fig. 6.90. The correction factor CF_D depends on two variables: the distance from the edge, and the value of measured ferrite content in FN. In this case, for each of the measurement points along the radius of the sample, one would have to define the correction factor separately from Fig. 6.90. For large amount of data, this process would be very laborious. Only one intermediate function for all the ferrite numbers FN has been assumed (Fig. 6.90). Thus, the correction factor depends only on the distance from the edge now (denoted as Δ). The smallest distance from the edge in all the measurements was equal to 0.5 mm.

Actually, all the lines for different FN lie close to each other, so only small error was introduced. For the distances greater than 1.5 mm, all the lines for different FNs almost overlap.

The relationship between the correction factor CF_D and the distance from the edge (Δ) has been approximated with 4th order polynomial, in the following form:

$$CF_D(FN) = 6.515 \cdot 10^{-3} \cdot \Delta^4 - 6.813 \cdot 10^{-2} \cdot \Delta^3 + 0.265 \cdot \Delta^2 - 0.478 \cdot \Delta + 1.379 \quad (6.27)$$

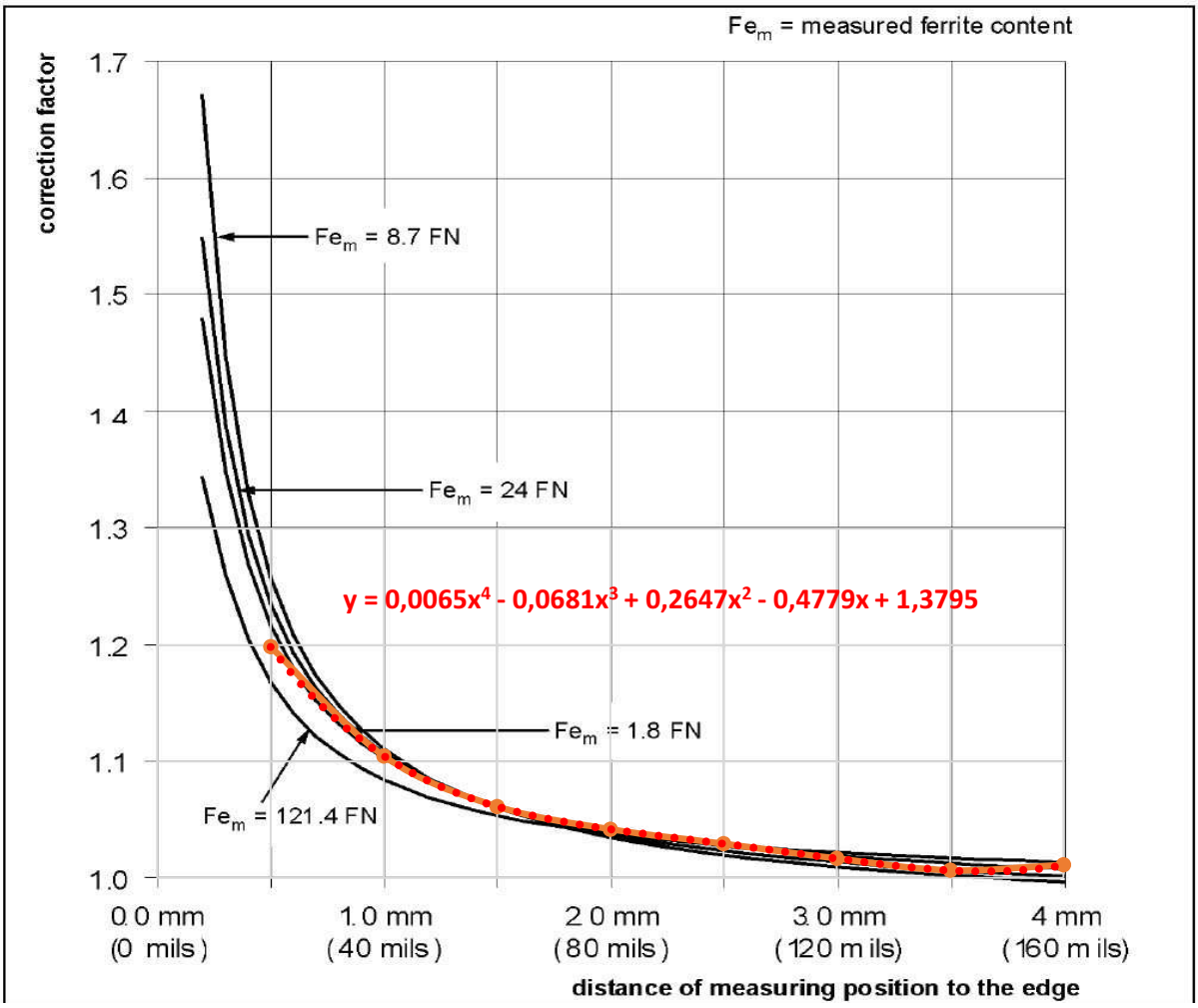

Figure 6.90. Correction factor to cover the distance from the edge [114], red line – approximation for all FN values

6.3.5.7. The summary

The procedure to obtain the correct martensite content consists of the following steps, performed for every single measurement:

1. Calculating the ferrite number FN from the measured ferrite content Fm (in %), using Eq. (6.25):

$$FN(Fm) = -4.99 \cdot 10^{-6} \cdot Fm^4 + 6.727 \cdot 10^{-4} \cdot Fm^3 - 0.0169 \cdot Fm^2 + 1.057 \cdot Fm - 0.0612$$

2. Calculating the correction factor for the curvature CF_C, according to Eq. (6.26):

$$CF_C(FN) = 2.767 \cdot 10^{-9} \cdot FN^4 - 6.167 \cdot 10^{-7} \cdot FN^3 + 5.462 \cdot 10^{-5} \cdot FN^2 - 3.125 \cdot 10^{-4} \cdot FN + 1.0758$$

3. Calculating the correction factor that takes into account the distance from the edge CF_D, according to Eq. (6.27):

$$CF_D(FN) = 6.515 \cdot 10^{-3} \cdot \Delta^4 - 6.813 \cdot 10^{-2} \cdot \Delta^3 + 0.265 \cdot \Delta^2 - 0.478 \cdot \Delta + 1.379$$

4. Calculating the real ferrite content from Eq. (6.24), assuming $CF_T = 1$:

$$Fr = Fm \cdot CF_D \cdot CF_C \tag{6.28}$$

5. Application of the biaxial formula, according to Eq. (6.23):

$$M(\%) = \begin{cases} 1.7 \cdot Fr, & Fr \leq 50 \\ 0.5357 \cdot Fr + 58.2143, & Fr \epsilon \langle 50, 78 \rangle \end{cases}$$

6.3.6. Results of ferrite content measurements by means of Feritscope

The results of the martensite content measurement are presented in the form of 3D plots. The measurement points are separated by the distance of 0,5mm (Fig. 6.26 for the longitudinal samples, and Fig. 6.85b for the transverse ones). The results are presented in the following sequence:

1. Sample twisted at 77K to 870°, cross-sections 1, 2, 3
2. Sample twisted at 293K to 870°, cross-sections 1, 2, 3
3. Sample twisted at 293K to rupture, cross-sections 1, 2, 3
4. Raw sample of 304 stainless steel, cross-sections 1, 2, 3

6.3.6.1. Sample twisted at 77K to 870°

The results measured within the longitudinal sample are shown in Fig. 6.91, whereas, these measured by using transverse cross-sections (the slices were cut out according to Fig. 6.1) are illustrated in Figs 6.92 through 6.94.
The maximum martensite content for the longitudinal sample (Fig. 6.91) was equal to almost 50%, and was reached close to the edge. Very similar results were obtained along all three lines. The minimum martensite content was obtained in the center, and was equal to about 10%.

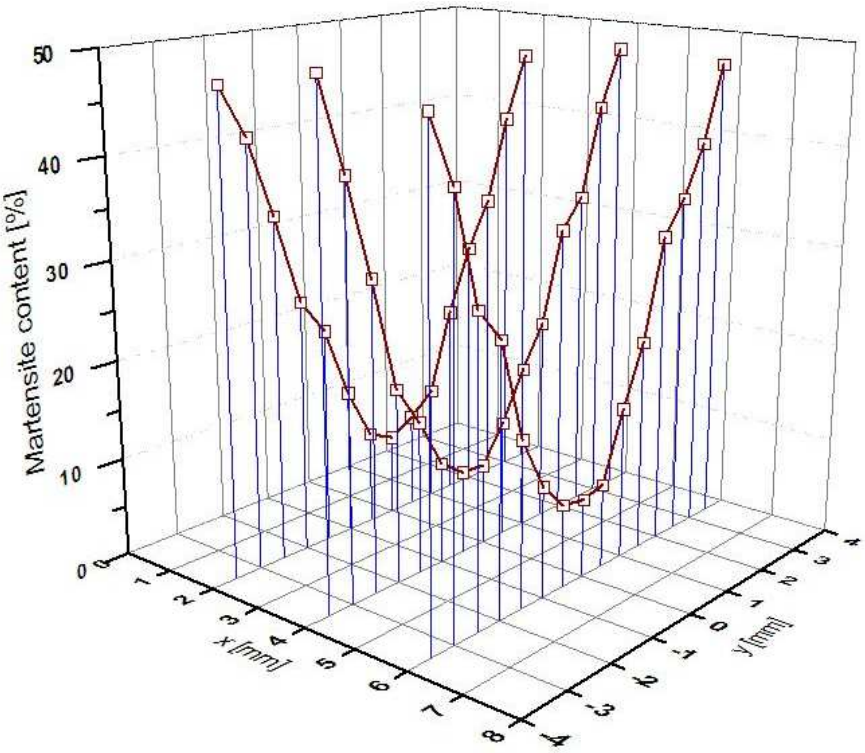

Figure 6.91. Martensite content measured within the longitudinal section, for the sample loaded at 77K and twisted to 870°

For the transverse cuts (Figs 6.92 through 6.94), similar maximum values (about 50%), and the same minimum values (about 10% in the center) were obtained.

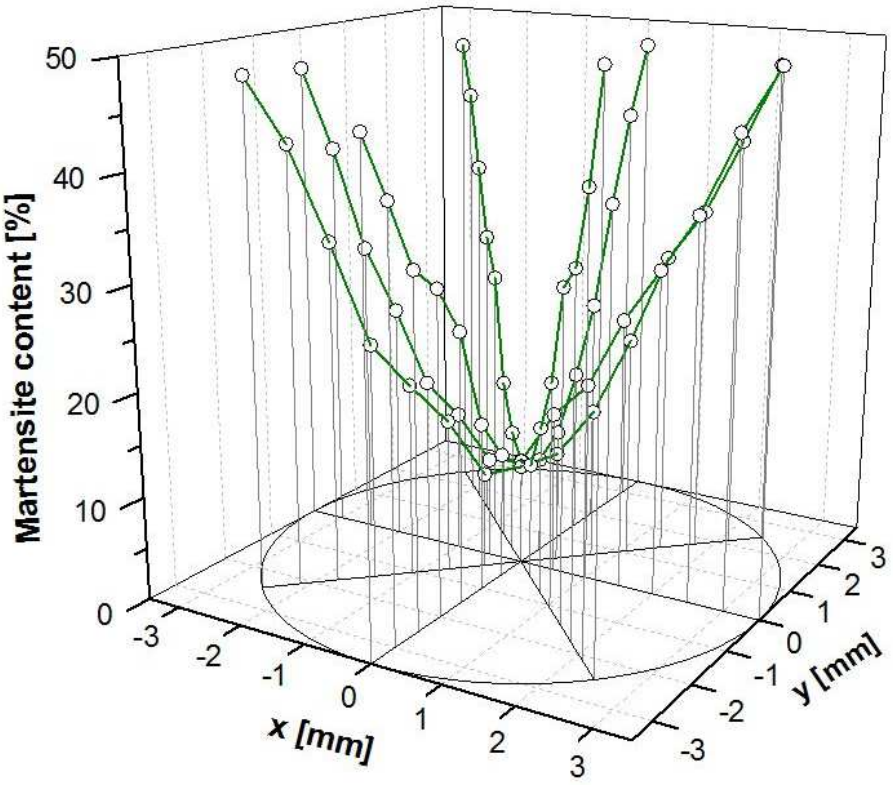

Figure 6.92. Martensite content results within cross-section 1, for sample loaded at 77K and twisted to 870°

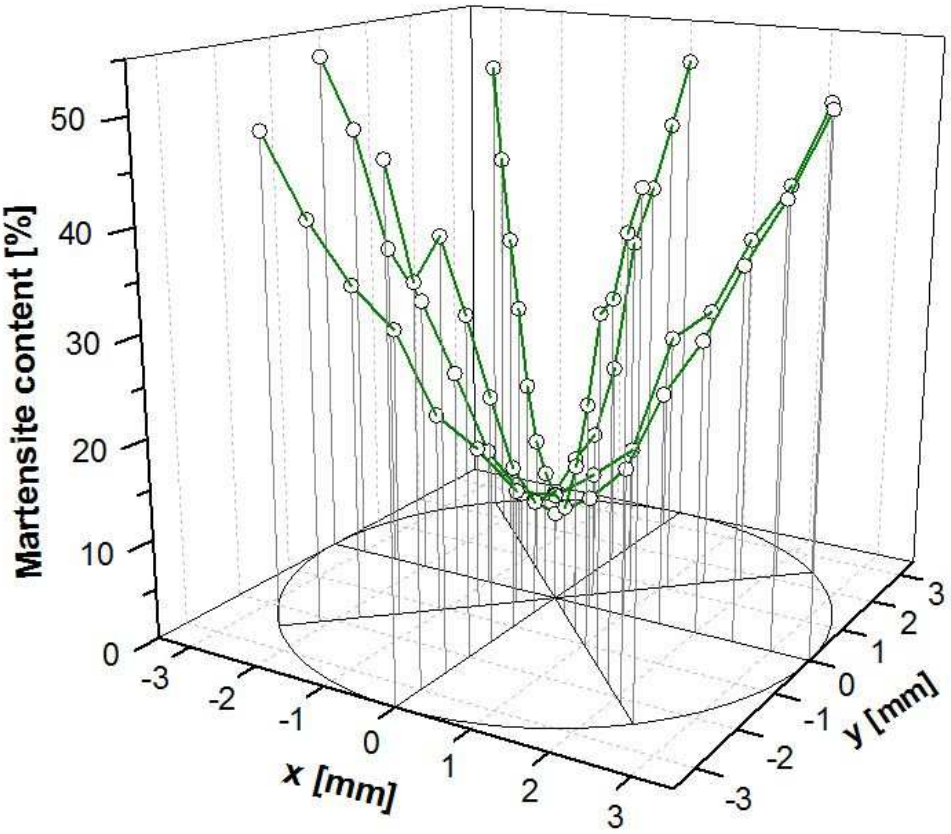

Figure 6.93. Martensite content results within cross-section 2, for sample loaded at 77K and twisted to 870°

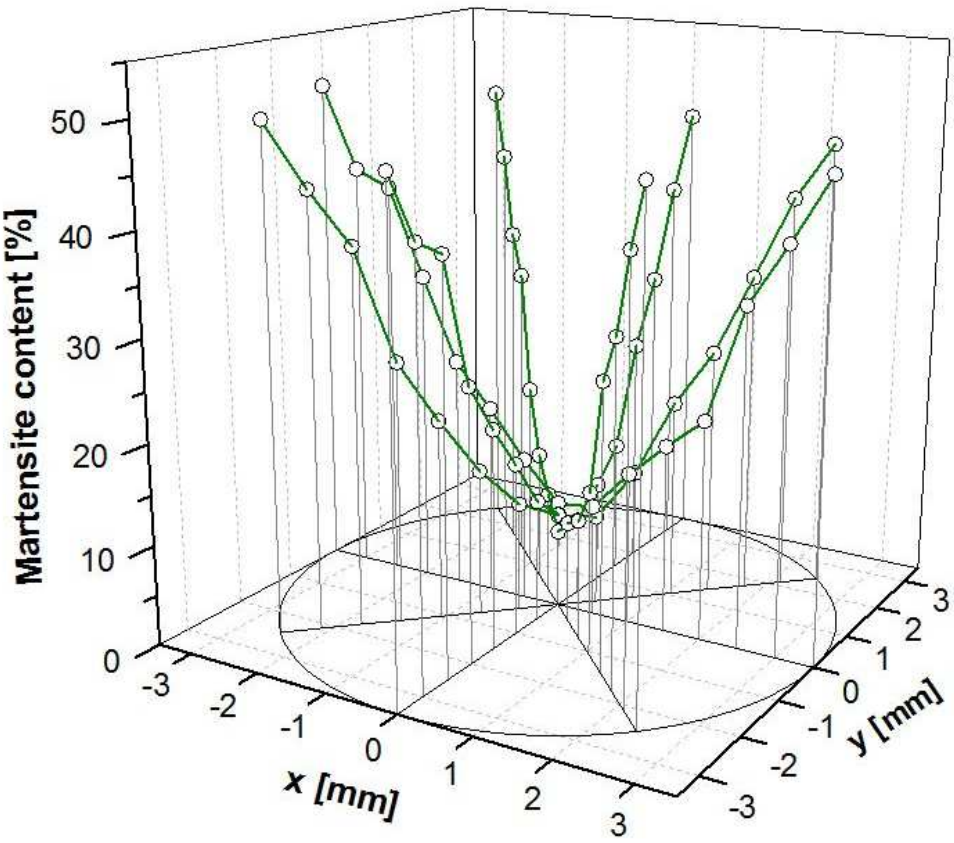

Figure 6.94. Martensite content results within cross-section 3, for sample loaded at 77K and twisted to 870°

6.3.6.2 Sample twisted at 293K to 870°

This sample was twisted at 293 K to the same angle of twist like the previous one. Thus, much smaller martensite content was expected.
The results measured within the longitudinal sample are shown in Fig. 6.95. In this case, about 5% of martensite was found near the edge only. The minimum value reached about 1% in the center of the sample.
The results for transverse cuts are shown in Figs 6.96 through 6.98. In this case, for all three results a maximum of 4÷5 % was found near the surface. Simultaneously, in the center of all samples about 1% of martensite was present.

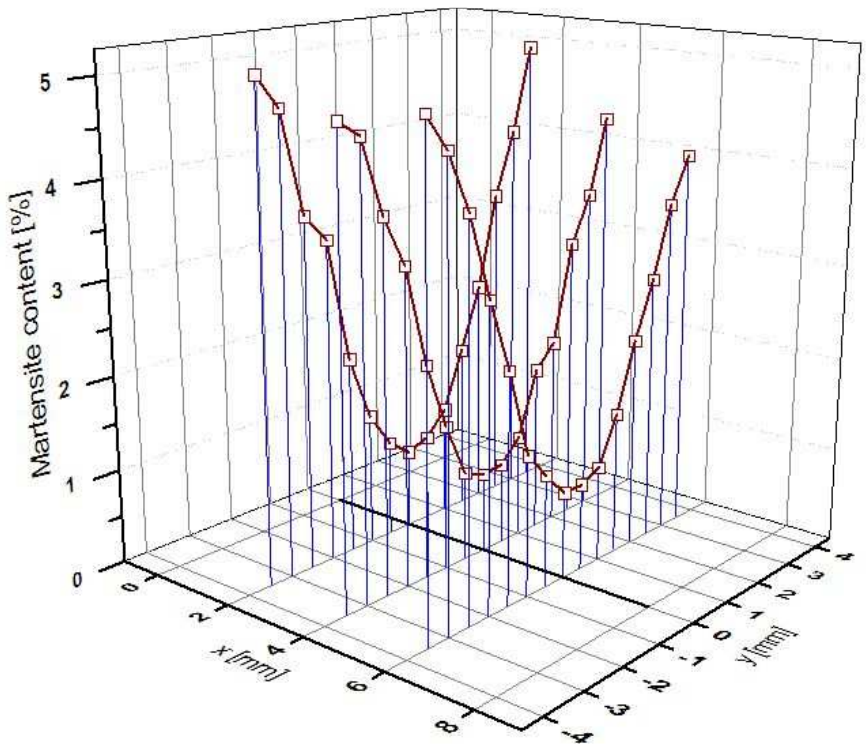

Figure 6.95. Martensite content results within the longitudinal section, sample twisted until rupture at 293K

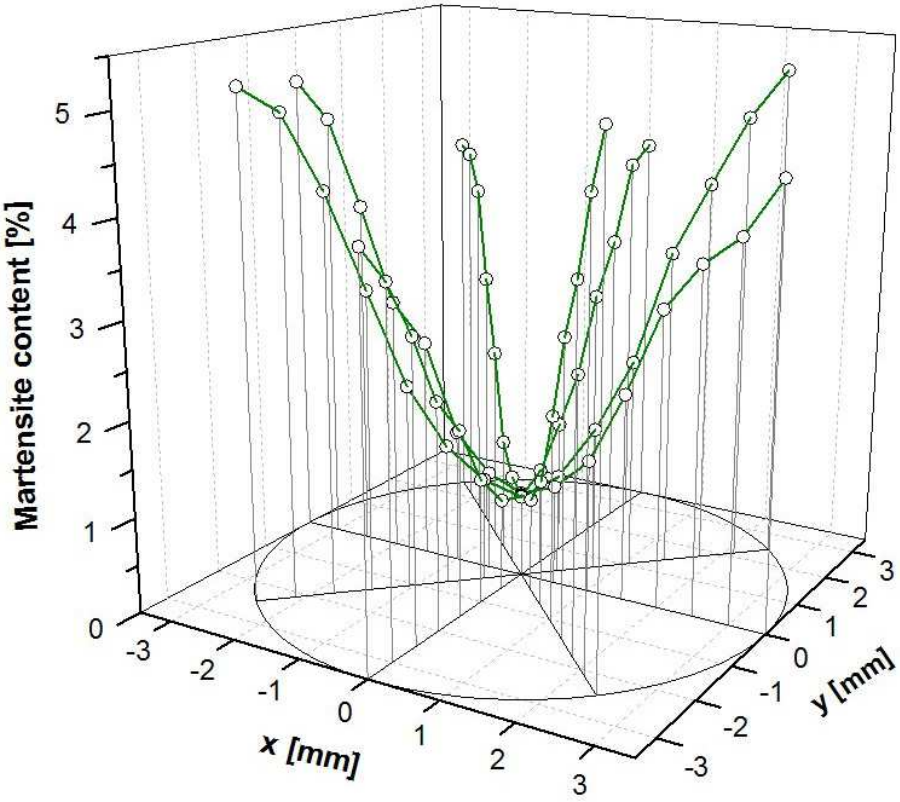

Figure 6.96. Martensite content results within cross-section 1 for sample loaded at 293K and twisted to 870°

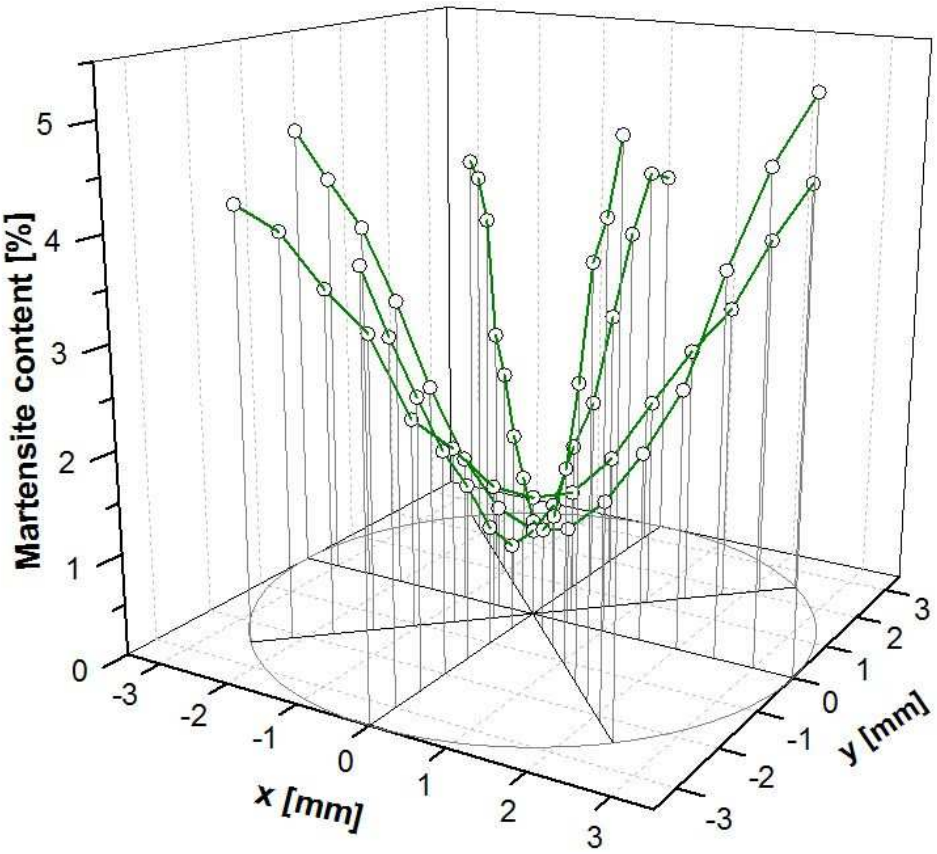

Figure 6.97. Martensite content results within cross-section 2, for sample loaded at 293K and twisted to 870°

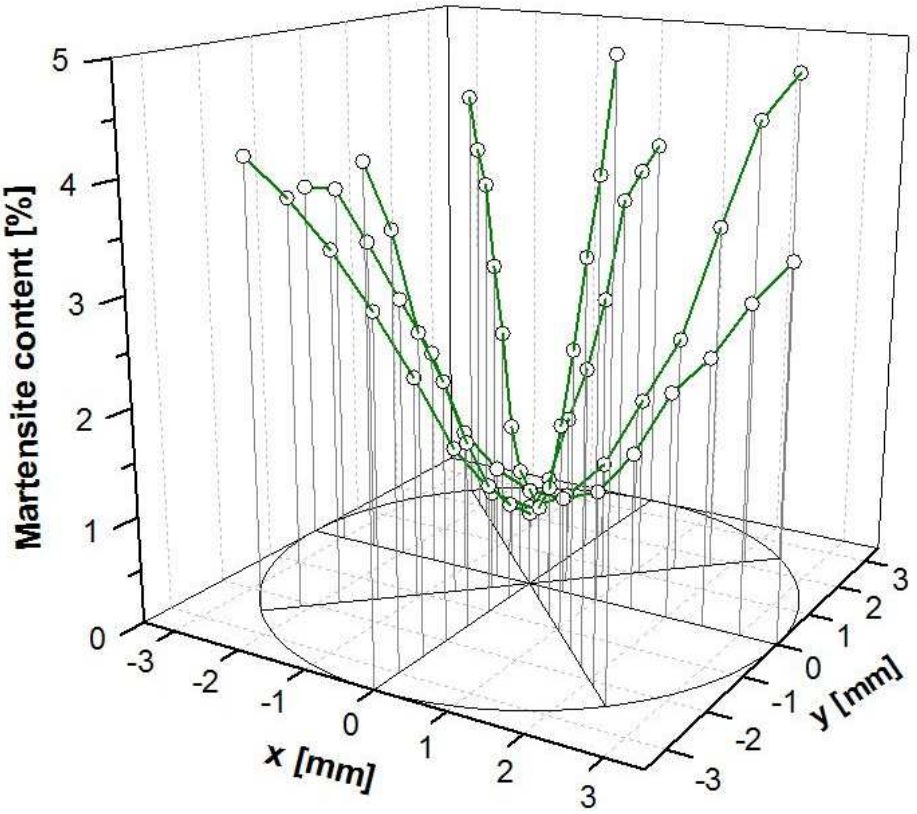

Figure 6.98. Martensite content results within cross-section 3, for sample loaded at 293K and twisted to 870°

Thus, for the sample twisted at room temperature to 870°, about 10 times less martensite was obtained, compared to the sample twisted at 77K to 870°. This experimental result confirms the theoretical prediction, drawn from the kinetics of the phase transformation.

6.3.6.3 Sample twisted at 293K until rupture

In the sample twisted at room temperature until rupture high martensite content was expected, because of extremely large value of the angle of twist (5110°). For this angle of twist and such geometry of sample, a maximum of 1.78 of shear strain was reached.
The results for longitudinal section are shown in Fig. 6.99. More than 40% of martensite was found near the edge of the sample, and about 10% in the center.
The results for transverse cross-sections are shown in Figs 6.100 through 6.102. Again, about 40% of martensite was measured at 0.5 mm distance from the surface of the samples, whereas, in the center - similarly to the longitudinal sample - about 10% was reached.

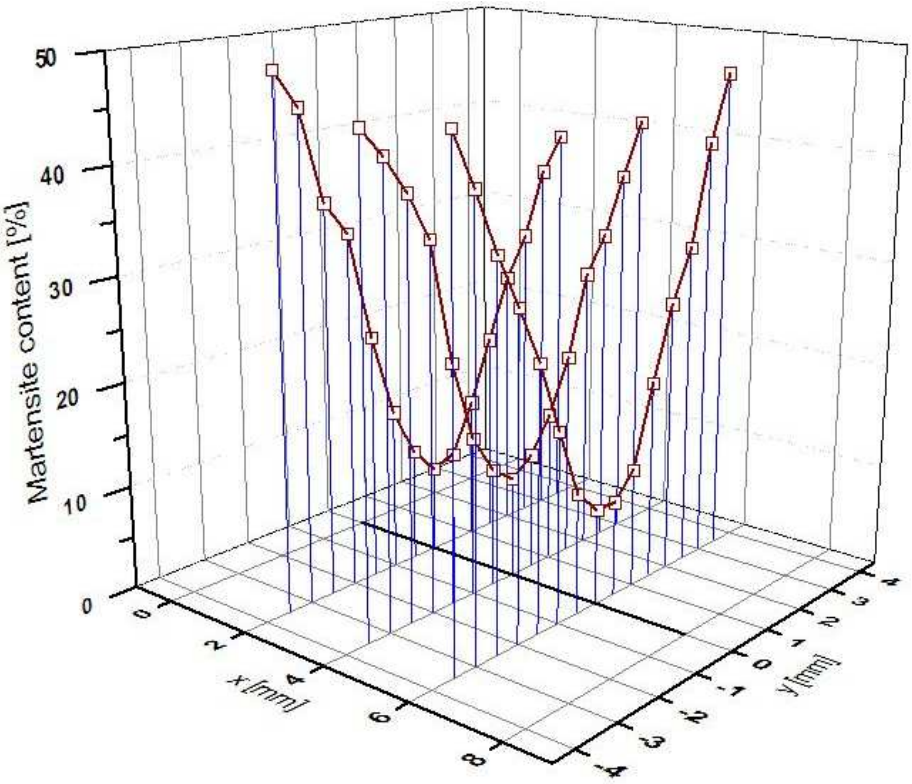

Figure 6.99. Martensite content results within the longitudinal section, for sample twisted until rupture at 293K

It turned out, that similar martensite distributions were obtained for samples twisted at 77K to 870°, and twisted at 293K until rupture. Large angles of twist introduced at room temperature, which were almost 6 times higher (5110/870=5.86) at 293K compared to 77 K, compensated for the rate of transformation which is much higher at 77K than at 293K.

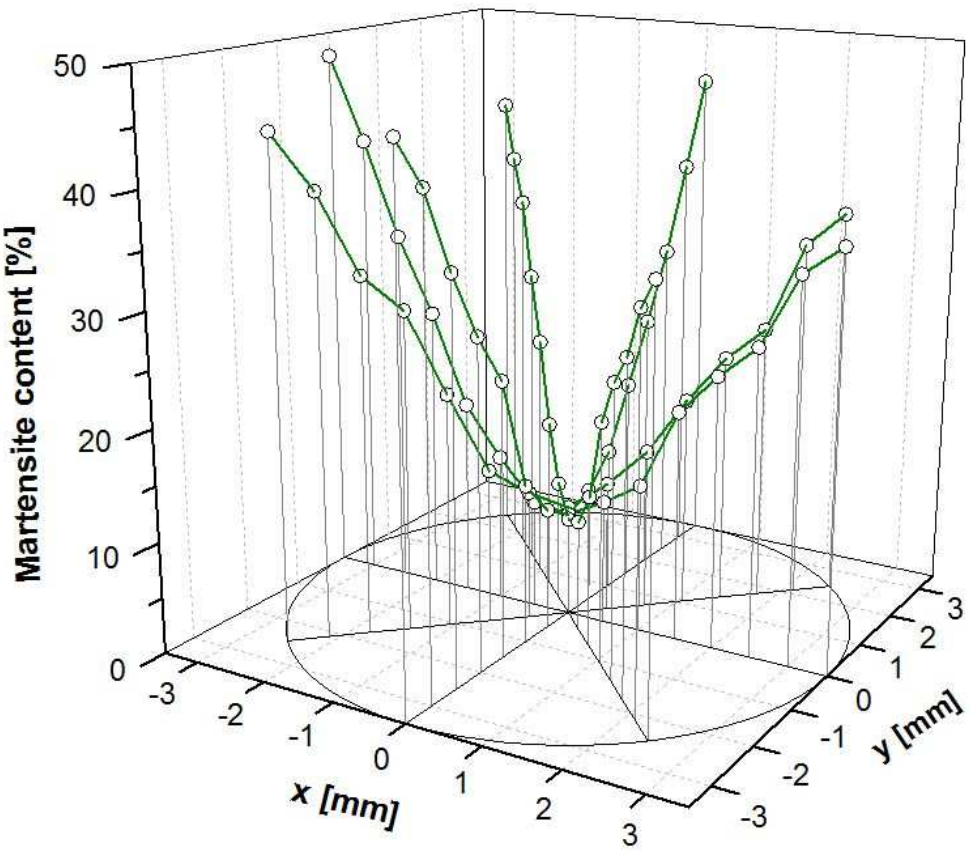

Figure 6.100. Martensite content results within cross-section 1, for sample twisted at 293K until rupture

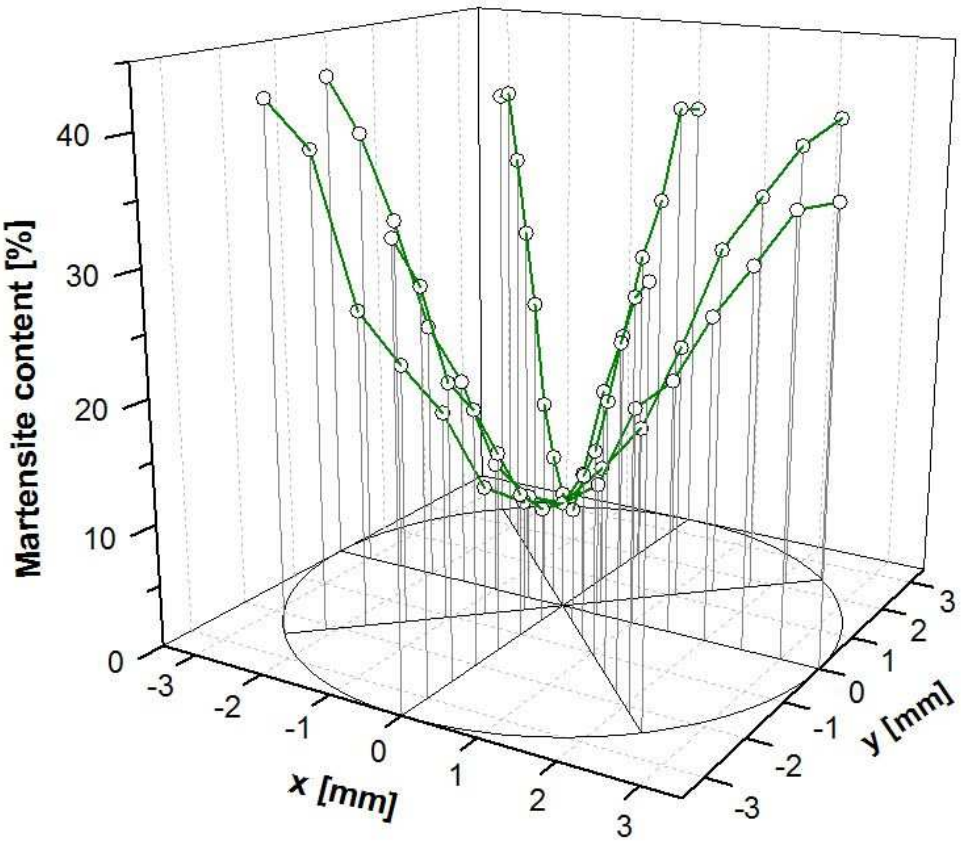

Figure 6.101. Martensite content results within cross-section 2, for sample twisted at 293K until rupture

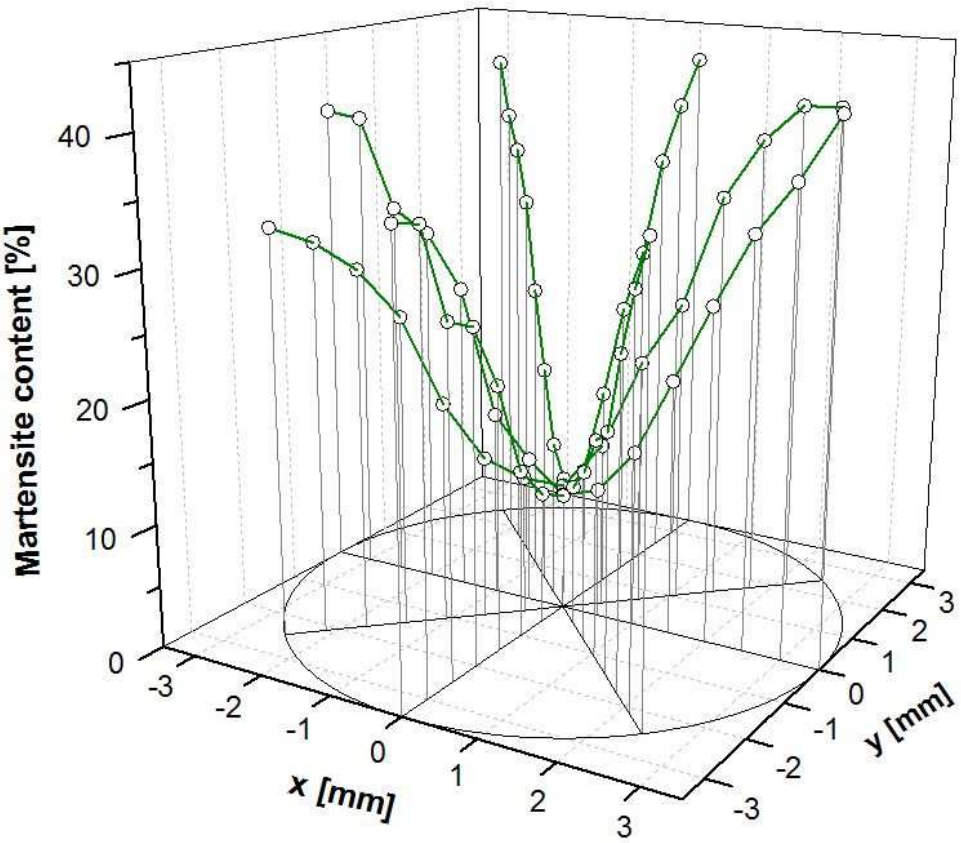

Figure 6.102. Martensite content results within cross-section 3, for sample twisted at 293K until rupture

6.3.6.4. Raw sample of the 304 steel

In order to obtain a reference, the samples from raw material were tested as well. The results obtained within the longitudinal section are shown in Fig. 6.103. In this case, the martensite content is smaller than 0.6%, so it is close to zero, as expected. The results for transverse cuts are shown in Figs 6.104 through 6.106. Similarly, the maximum martensite content of 0.6% was found in all samples.
This measurement confirmed that practically all martensite was generated by the plastic strain induced phase transformation. It is now clear, that the distribution of martensite can be entirely controlled by the angle of twist and the temperature.

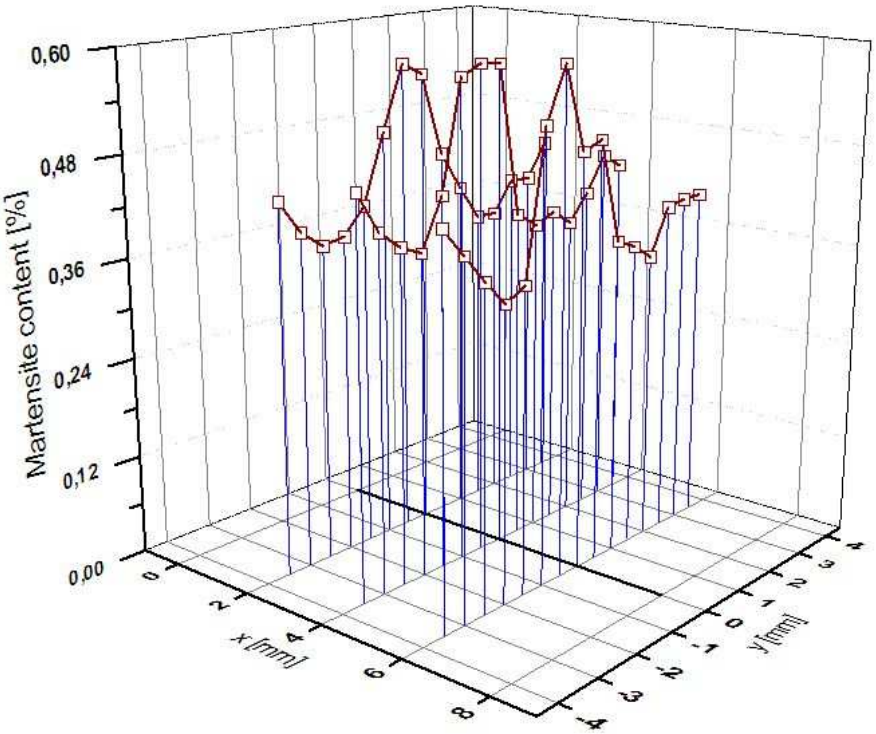

Figure 6.103. Martensite content results within the longitudinal section, for raw 304L stainless steel sample

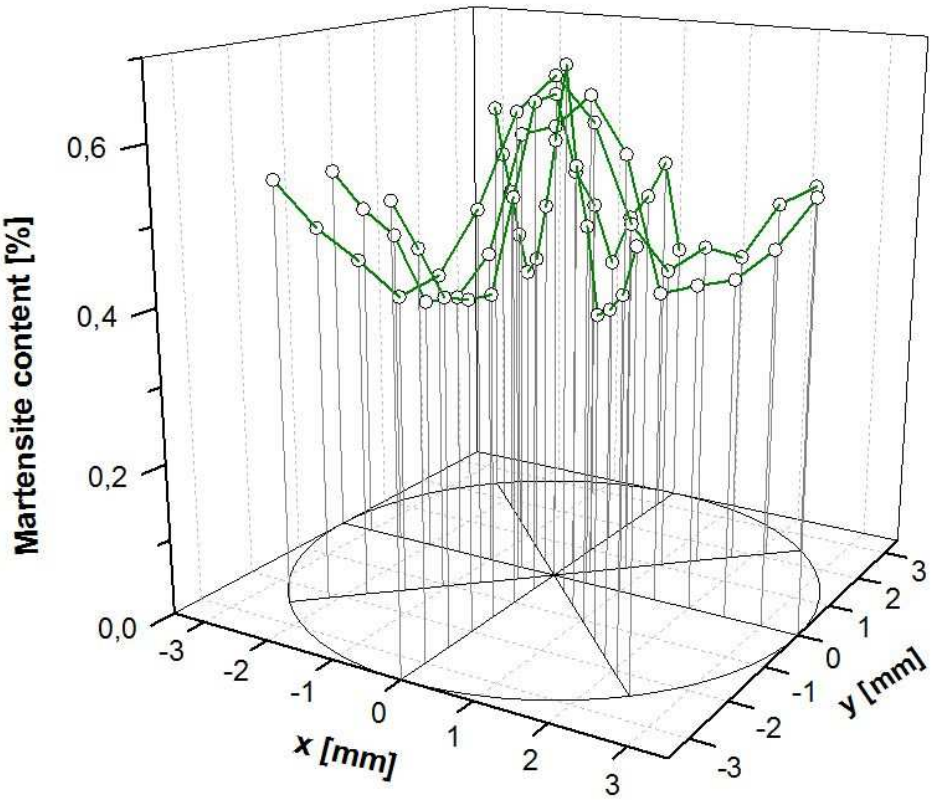

Figure 6.104. Martensite content results within cross-section 1, for raw 304L ss sample

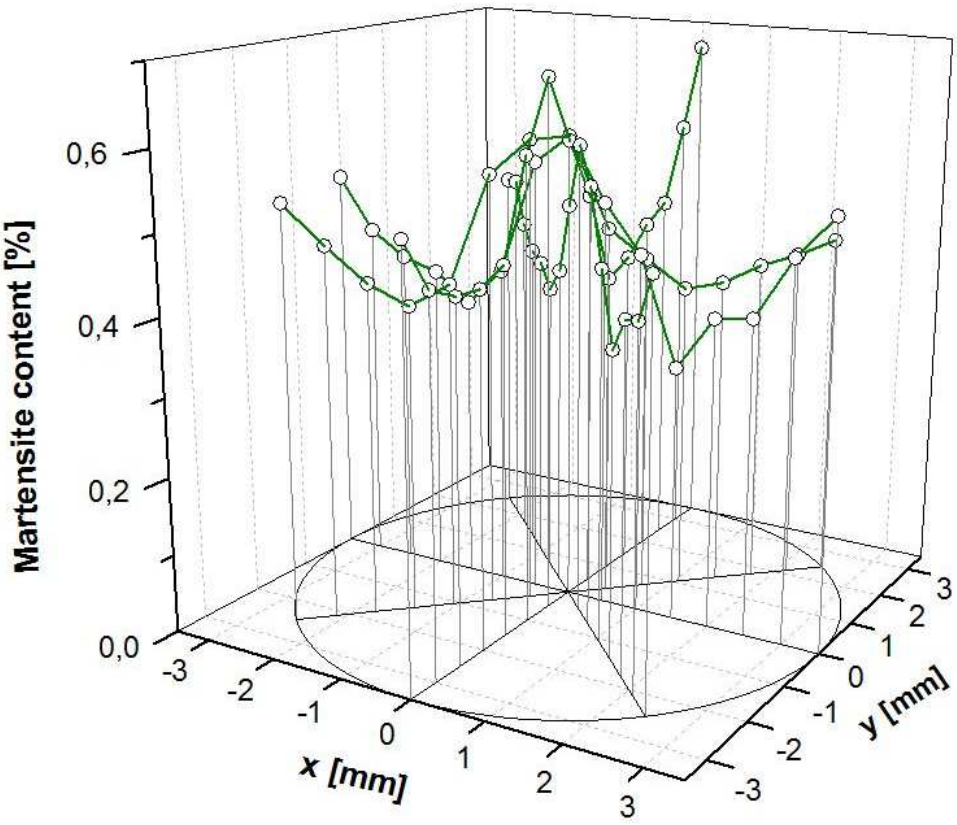

Figure 6.105. Martensite content results within cross-section 2, for raw 304L ss sample

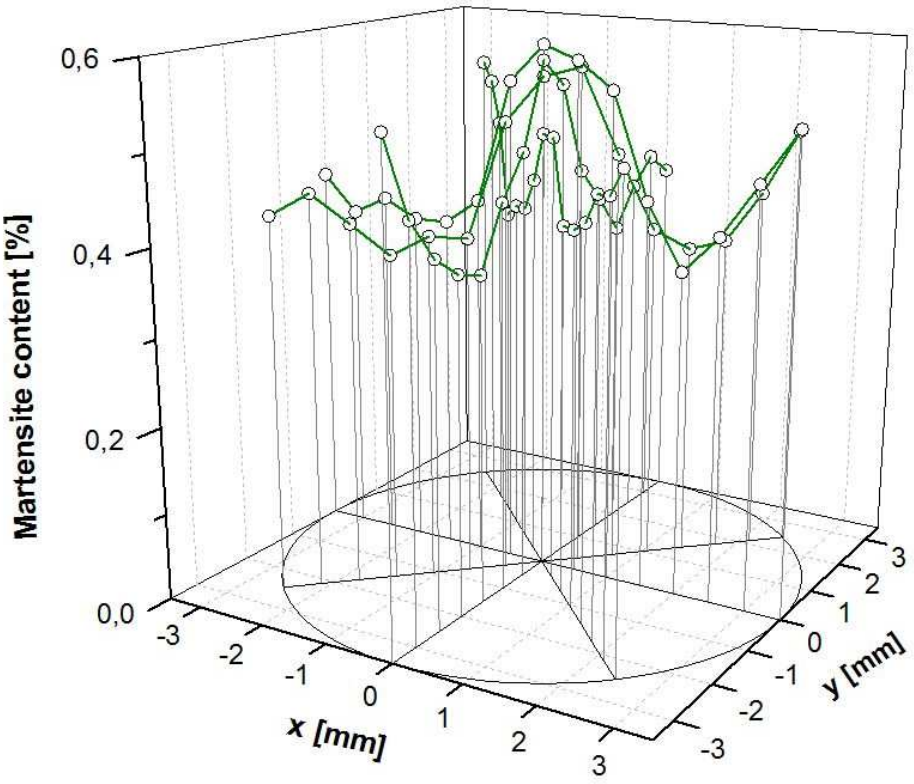

Figure 6.106. Martensite content results within cross-section 3, for raw 304L ss sample

6.3.7. Summary of the martensite content measurements by means of Feritscope

In order to compare all the obtained results, the data presented in the form of 3D plots were averaged. It means, that the results from all 4 diagonal lines were averaged and shown together in one plot, for all three cross-sections. In such way, the results from different axial coordinates along the bar were easily compared.
The results are shown in the following order: the sample twisted at 77K to 870°, at 293K to 870°, at 293K until rupture, raw 304 ss sample.

6.3.7.1 Sample loaded at 77K, twisted to 870°

The results shown in Fig. 6.107 indicate, that martensite distributions are very similar for all the three cross-sections. Actually, this result confirms the theoretical predictions, as the twisting moment was constant along the bar Thus, the same shear strain distribution was expected.

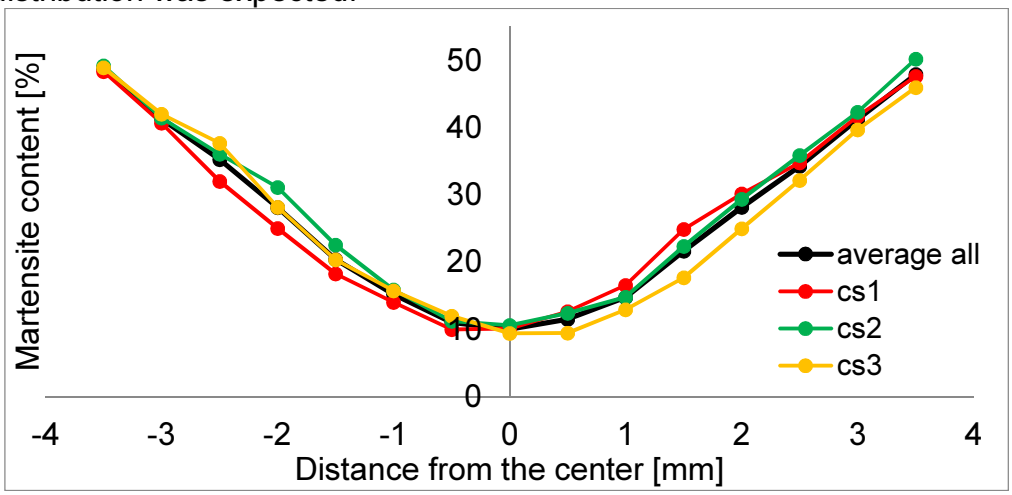

Figure 6.107. Average martensite content results for sample twisted at 77K to 870°

6.3.7.2. Sample loaded at 293K, twisted to 870°

For the sample twisted at room temperature to 870°, the results from all three cross-sections again agreed with each other (Fig. 6.108).

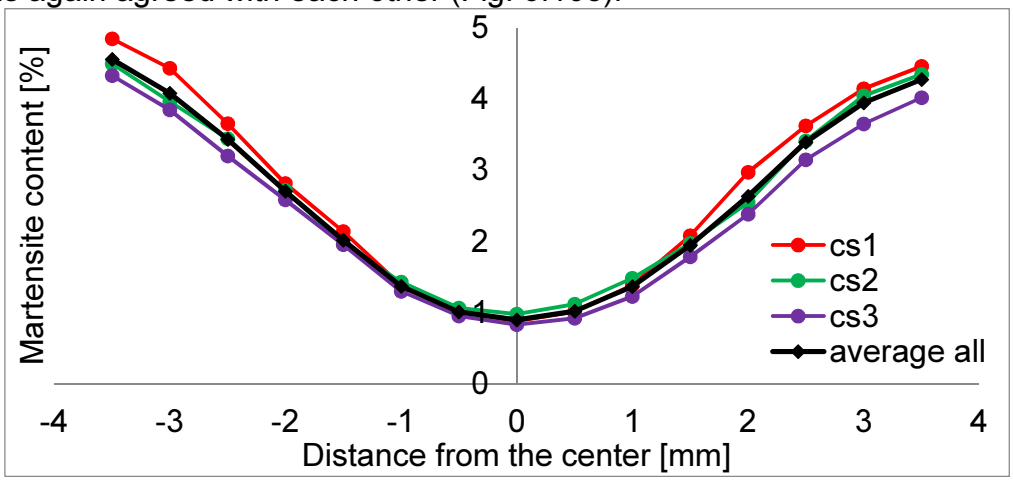

Figure 6.108. Average martensite content results for sample twisted at 293K to 870°

6.3.7.3. Sample loaded at 293K until rupture

For the sample twisted until rutpure at room temperature (Fig. 6.109), martensite content distributions along the radius were again similar for all three cross-sections.

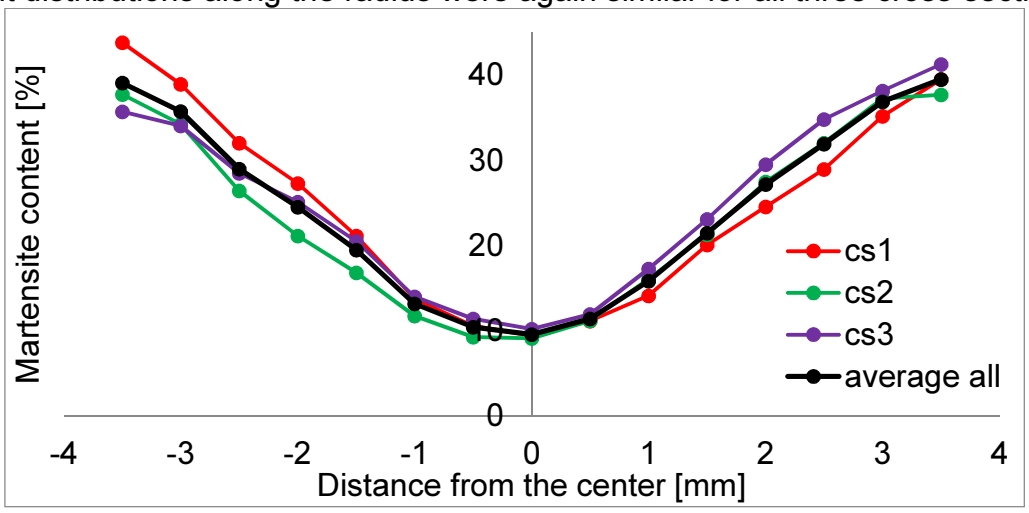

Figure 6.109. Average martensite content results for sample twisted to rupture at 293K

6.3.7.4. Raw sample from 304 stainless steel

The results for raw sample shown in Fig. 6.110 indicate similar results as well. The recorded martensite content remained between about 0.4% and 0.65%.

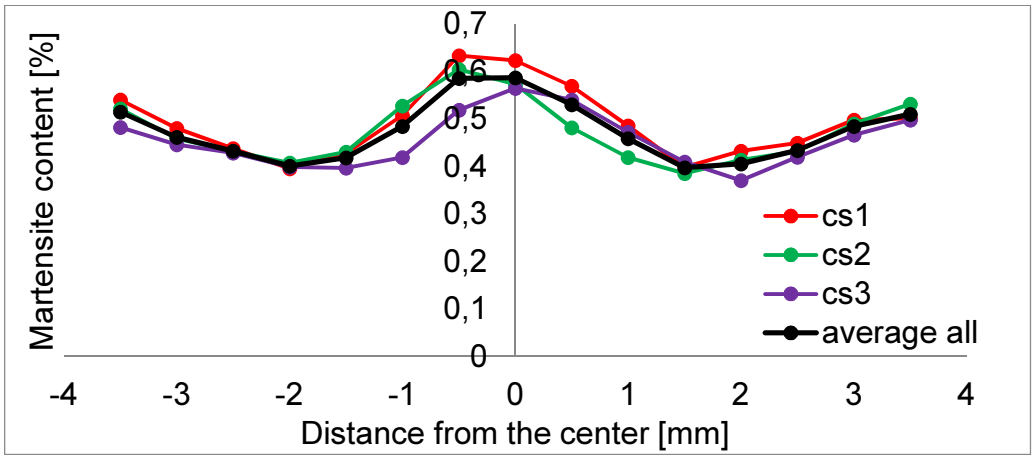

Figure 6.110. Average martensite content results for raw 304 ss sample

6.3.7.5. Average results from transverse cross-sections

The results measured in all three cross-sections, for all four samples, were averaged and are shown in Fig. 6.111. It is clearly visible, that for raw sample the martensite content is close to zero. In the sample twisted at room temperature to the angle of 870°, the martensite content is about 1% in the center and some 5 % near the surface. Much higher martensite content was found in the sample twisted at 77K to 870°, and in the sample twisted until rupture at room temperature. One can conclude, that at room temperature it is possible to obtain martensite distributions that are limited by the blue and the red curves in Fig. 6.111. The red line for the sample twisted until rupture indicates a limit, since no more martensite can be induced at room temperature.

At the liquid nitrogen temperature (blue curve in Fig. 6.111), more martensite can be obtained than at 293 K. Yet, only the torsion test until rupture provides the limit values, for this specific case of pure torsion.

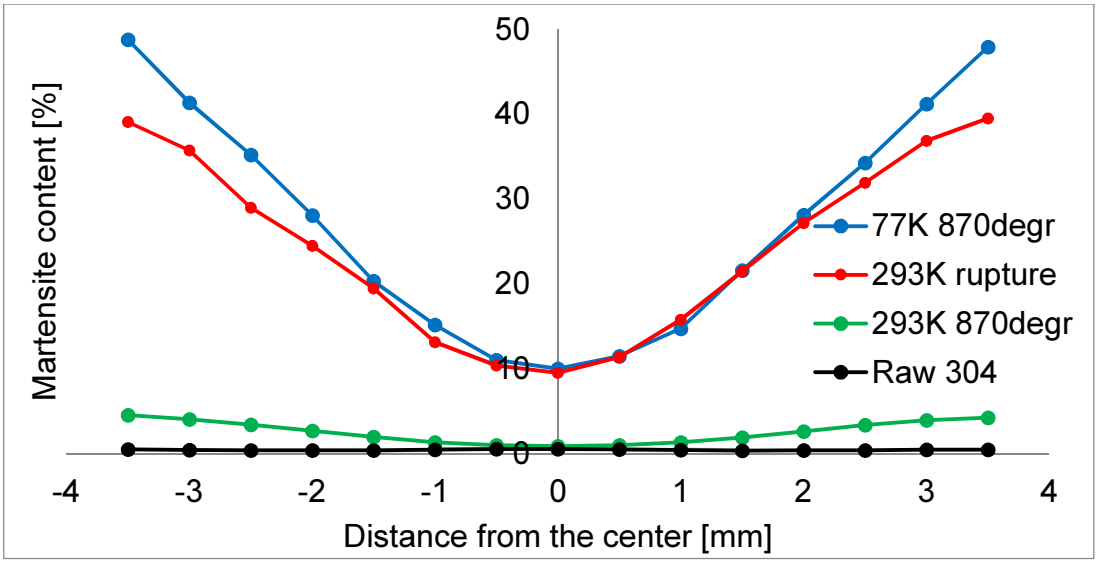

Figure 6.111. Average martensite content results for all samples (transverse cross-sections)

6.3.7.6. Average results from the longitudinal samples

One longitudinal section was extracted per each of four samples. The martensite content was measured along three lines. These values have been averaged, and are presented in Fig. 6.112.

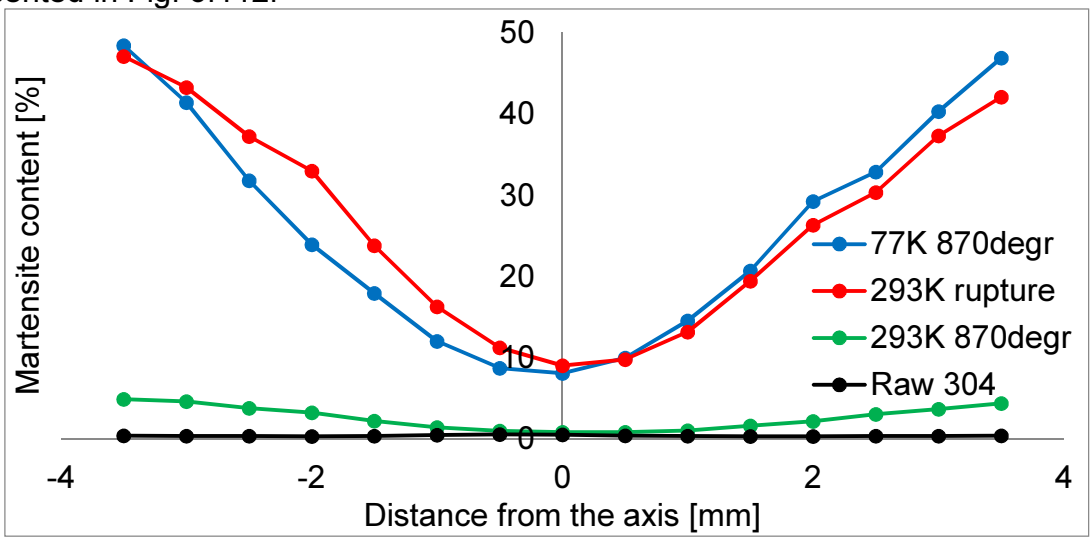

Figure 6.112. Average martensite content results for all samples (longitudinal sections)

The results are similar like for the round samples (Fig. 6.111). Yet, some asymmetry was obtained in the sample twisted at 77K, and in the other one loaded at 293 K until rupture.Higher martensite contents were obtained on the left hand side in the sample twisted at room temperature.In the raw sample near zero values were found, and in the sample twisted to 870° at 293K, a maximum of about 6% martensite content was found.

6.3.7.7. Comparison between the results from longitudinal and transverse samples

The results of average martensite content, measured in the longitudinal and in the transverse samples (Figs 6.111 and 6.112), are presented within one plot in Fig. 6.113. It is clearly visible, that the results for the raw sample and the sample twisted at 293K to 870° are almost identical for transverse and longitudinal samples. Similar results were found for the sample twisted in liquid nitrogen to 870°. Only for the sample loaded until rupture at room temperature the results are visibly different, especially on the left hand side.

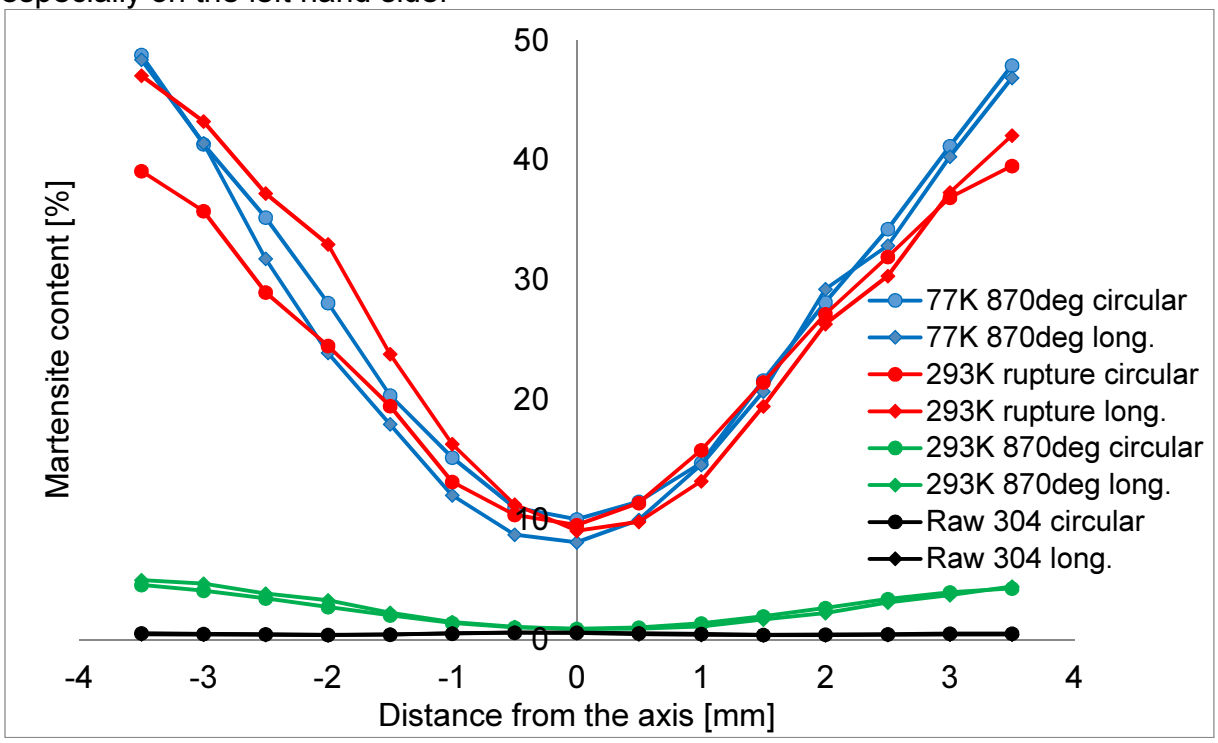

Figure 6.113. Average martensite content results for all samples (transverse and longitudinal cross sections)

6.3.8. Conclusions from the martensite content measurements

Based on the above presented methods, the best results were obtained by means of Feritscope, which allowed point like measurements within the cross-section of the sample. From the summarized results presented in Figs 6.111 through 6.113, it has been confirmed that the martensite content distribution varies along the radius. It reaches a minimum in the center and a maximum near the surface. According to theoretical predictions, based on the linearised kinetics of phase transformation, the martensite content was supposed to follow a linear function of the radius. The experimental results show that it is not the case. For all samples a nonlinear variation is observed, which corresponds to the exact, sigmoidal profile of transformation kinetics (Fig. 3.1a).

The most important conclusion, however, is a possibility to control distribution of martensite content along the radius by means of the angle of twist and the temperature. At room temperature, maximum content of martensite possible to obtain by means of torsion is represented by red curve in Fig. 6.113.

In the liquid nitrogen conditions, the rate of phase transformation is much higher than at room temperature. Thus, more martensite can be obtained. The difference can be clearly observed for samples twisted at these two temperatures to the same angle of twist 870° (Fig. 6.113). Almost 10 times more martensite near the surface of the sample was obtained at 77K. Thus, much smaller angles of twist were necessary.

The limit curve of martensite distribution, obtained during torsion at 77K, was not measured.

7. Torsion tests: round bars made of 304L, 316L and 316LN stainless steel

In Chapter 4 the experimental results of torque versus angle of twist were presented, for twisted bars made of 304 stainless steel. In the section 6.3, the martensite content measurements in the cross-sections of samples extracted from the bar were shown.
In the present chapter another set of experimental results is presented for samples made of other austenitic stainless steels: 304L, 316L and 316LN. It is expected, that all of these steels have very different mechanical properties, as well as different parameters of the kinetics of plastic strain induced phase transformation, that depend on temperature.
Torsion tests until rupture were performed at 77K for one sample of each of three steels: 304L, 316L, 316LN. On the top of the mechanical response, the content of martensite was measured on the surface of the samples during the test. The increasing amount of the secondary α' phase was captured.

7.1. The measurement method

The same equipment like in the monotonic torsion tests was used. The same cryostat, the vacuum pump and the torque wrenches were applied. During the test at 77K, because of the liquid nitrogen evaporation, the cryostat has been refilled several times in order to maintain constant temperature conditions. The set-up is shown in Fig. 7.1a, whereas, the sample in the bath of boiling nitrogen is presented in Fig. 7.1b.

a b

Figure 7.1. a) Set-up with the vacuum pump and the liquid nitrogen dewar , b) sample immersed in the boiling nitrogen

An important difference compared to the monotonic torsion experiments, was the measurement of martensite content evolution during the loading. The volume fraction of martensite has been measured by means of Feritscope, after several stages of loading. Martensite content was measured on the surface of cylindrical sample along four straight lines. It gave more detailed results concerning the symmetry of the martensite content around the center of the sample. Three measurements were made in each of the points.
Afterwards, an average was calculated from these three measurements and accepted as the real result in this particular point. Distribution of the measurement points is shown in Fig. 7.2.

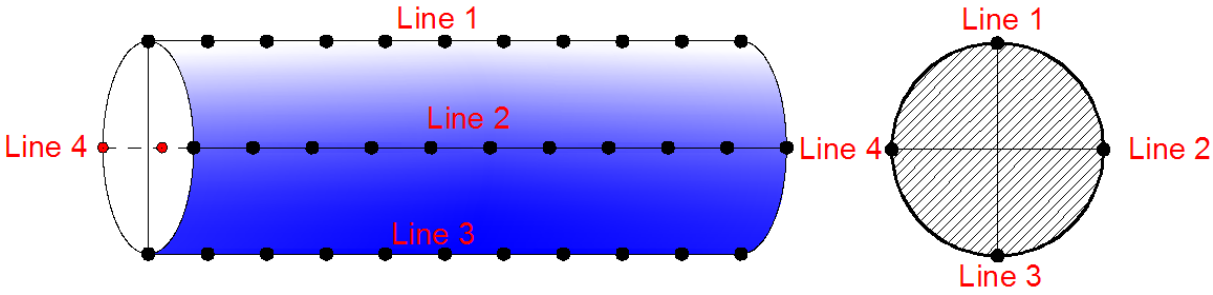

Figure 7.2. Distribution of the measurement points on the surface of sample

At the beginning, the cryostat is filled with liquid nitrogen 3-4 times. This allows cooling down all the parts of the cryostat and achieve stable temperature conditions. The process takes about 30 minutes. Afterwards, the rate of evaporation of liquid nitrogen becomes small enough to start the test.

The test is stopped several times to measure the content of martensite on the surface of the sample. In order to remove the sample, the guiding element made of copper is removed and then the sample is lifted from the square hole at the bottom of the cryostat. The measurement of the martensite content on the surface takes up to 15 minutes. During this time interval a considerable quantity of liquid nitrogen is evaporating. Thus, before restart of loading, the cryostat is refilled with liquid nitrogen. This is repeated after each sequence of measurements. For this reason, high volumes of liquid nitrogen are consumed.

The photograph of the sample before test, with the measurement for martensite content, is shown in Fig. 7.3. The sample after twisting is shown in Fig. 7.4. It is important to notice, that the position of the measurement points changed because of twisting. Thus, after torsion the martensite content is measured along straight lines, as shown in Figs 7.3 and 7.4. It is done not in the points marked in Fig. 7.3 along the twisted lines, but along the straight lines, to maintain distance between the points.

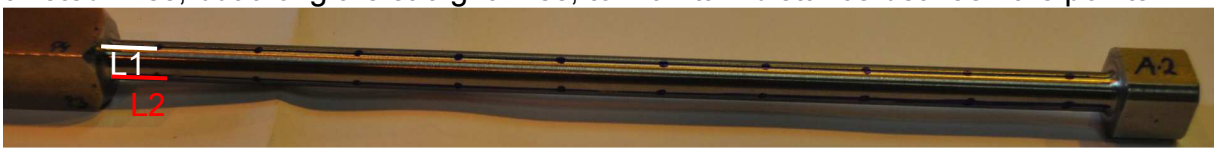

Figure 7.3. Sample before test, with the measurement points

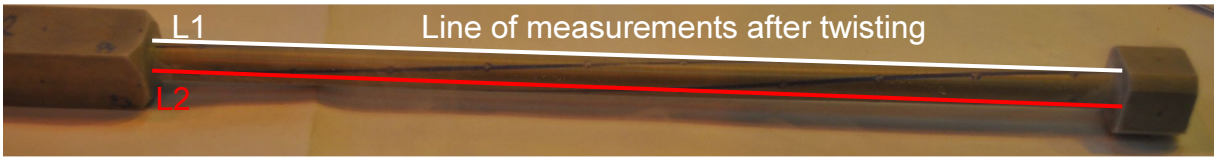

Figure 7.4. Sample removed from the liquid nitrogen bath for martensite content measurements (angle of twist visible)

The geometry of samples has been modified, compared to the samples made of 304 stainless steel. The sample was machined from a bar with square cross section 15x15 (Fig. 7.5), whereas, the sample made of 304L ss was machined from a bar ϕ22mm (Fig. 7.6), and the sample made of 316LN stainless steel from a bar ϕ25mm (Fig. 7.7).

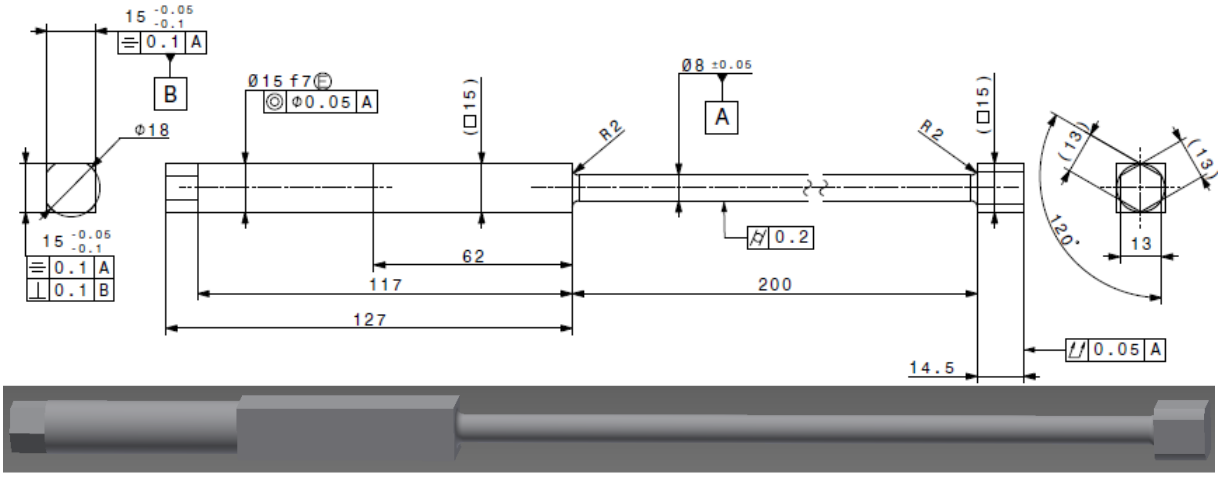

Figure 7.5. Geometry of the sample made of 316L stainless steel

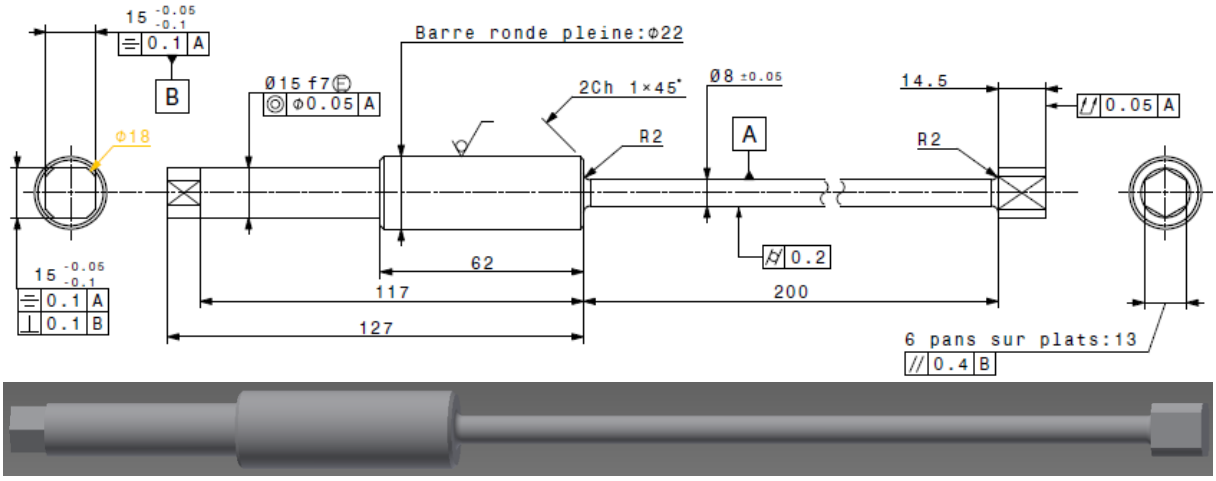

Figure 7.6. Geometry of the sample made of 304L stainless steel

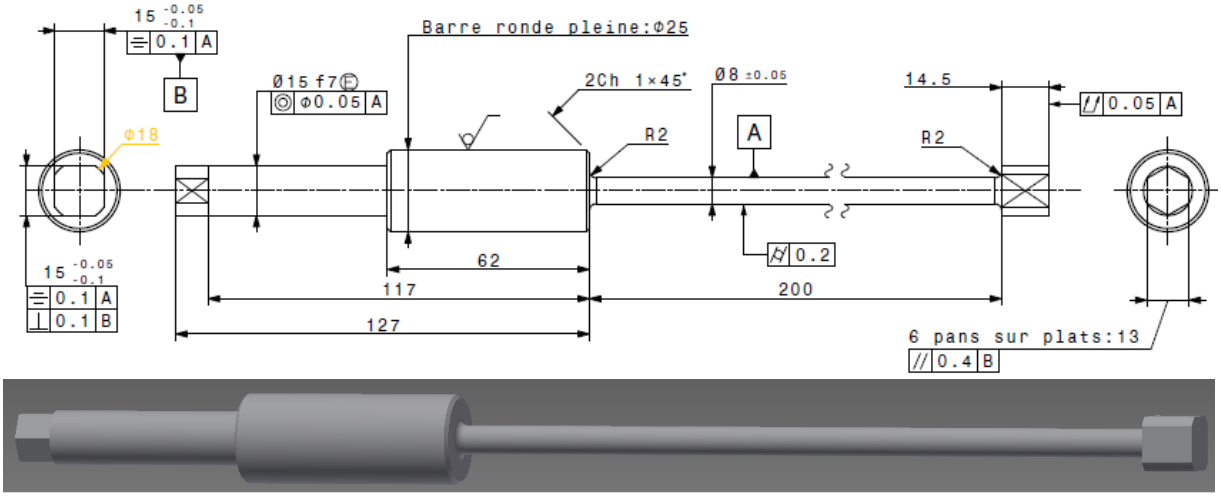

Figure 7.7. Geometry of the sample made of 316LN stainless steel

The chemical composition of steels 304L and 316LN is presented in Tabs 7.1 and 7.2, respectively.

304L	Fe	Cr	Mn max	Ni	P max	C max	S max	Si max
Quantity [%]	The rest	18-20	2	10-12	0.045	0.03	0.030	1.0

Table 7.1. Chemical composition of 304L (X2CrNi 19.11) austenitic stainless steel, according to EN 10088

316LN	Fe	Cr	Mn max	Ni	Mo	N	P max	C max	S max	Si max
Quantity [%]	The rest	16-18.5	2	12-14	2-3	0.14-0.2	0.045	0.03	0.030	1.0

Table 7.2. Chemical composition of 316LN (Cr Ni 18.12. Mo N) austenitic stainless steel, according to EN 10088

The temperature conditions and the loading are shown in details in Tab. 7.3. Apart from three tests until rupture for steels 304L, 316L and 316LN, two samples from 304 stainless steel were tested as well. These are the samples denoted by 6.1, 6.2 and 7.1, 7.2 (see Tab. 5.2). The torque versus the angle of twist for these four tests were already shown in Chapter 5. However, for these tests evolution of martensite content was measured as well, and is presented in this chapter. In addition, the torque versus the angle of twist results are repeated for clarity.

Lp	Symbol	Material	Temperature	Max torque	Max angle	ξ_{max}
			[K]	[Nm]	[°]	[%]
1	6.1	304	77	120	992	71.1
	6.2	304	293	108	1282	94.3
2	7.1	304	77	120	992	67.2
	7.2	304	293	167	1310	95.0
3	C1	316L	77	167	3820	93.7
4	D1	304L	77	171	2120	95.5
5	E1	316LN	77	156	4130	52.5

Table 7.3. Parameters of the samples dedicated to the monotonic torsion tests

The results are described in the following sequence:
1. Torsion test of sample C1 (316L)
2. Torsion test of sample D1 (304L)
3. Torsion test of sample E1 (316LN)
4. Sample 6.1 (304)
5. Sample 6.2 (304)
6. Sample 7.1 (304)
7. Sample 7.2 (304)

7.2. Torsion test at 77K of sample made of 316L stainless steel

The results in terms of torque versus angle of twist for sample C1 (316LN) loaded at 77K are shown in Fig. 7.8. The intermediate torque values, after which the test was stopped for martensite content measurements, are indicated by arrows. Twelve measurements were made in total. Apart from the measurements during the test, the martensite fraction was measured before the loading and after the rupture, as well.
It is very important to recall that the torque was increased step by step (by 1Nm), and the results exposed in Fig. 7.8 represent cycles with increasing amplitude of the torque (Fig. 5.9), and not continuous monotonic torsion.

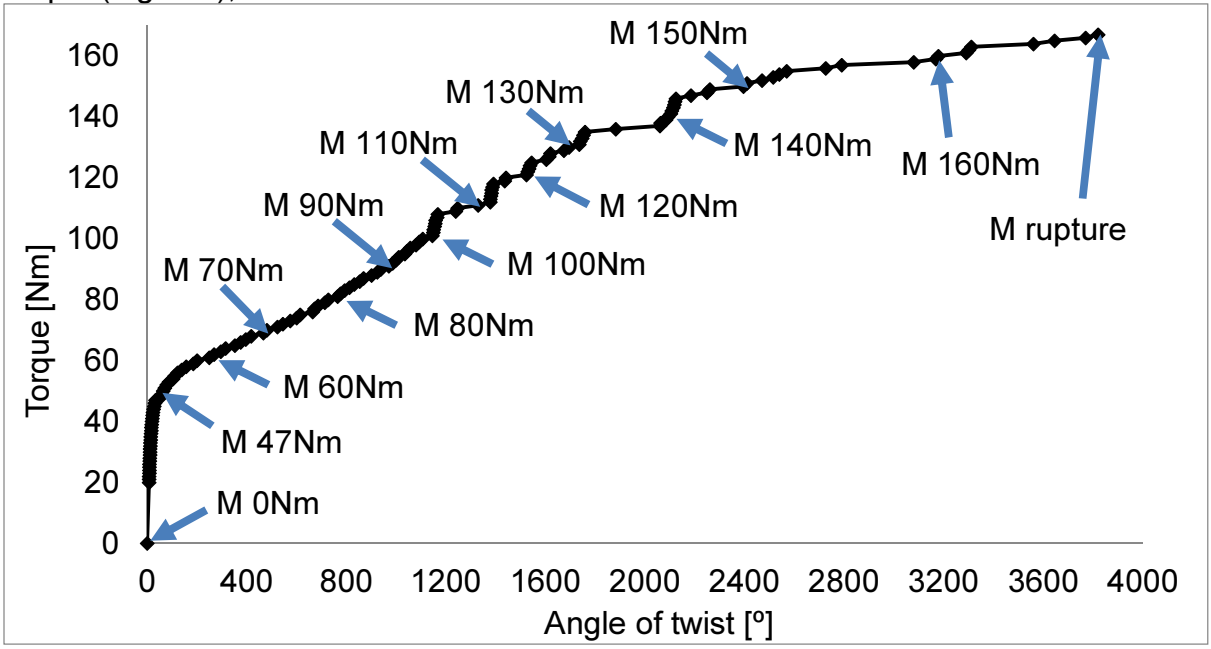

Figure 7.8. Torque versus the angle of twist for sample C1 (316L), loaded at 77 K

The value of the torque at rupture was equal to 167Nm, which was higher than for the sample made of 304 stainless steel, for which the torque of 156Nm was obtained. The angle of twist at rupture for sample C1 was equal to 3820° (10.6 turns), so actually above 2 times more than for the sample made of 304 ss with 1480° (see Tab. 5.2). The elastic range was exceeded at about 45Nm, yet, the sample supported above 3 times more until rupture. In the first half of the test, the torque increased almost linearly with the angle of twist. In the second part a decreasing positive slope was observed.

7.2.1. Martensite content evolution on the surface, for sample C1

In sample C1 the martensite content was measured along the surface of the sample at 5 points, and along four lines as shown in Fig. 7.2. The average of 4 lines was accepted as the final result at each loading step. All the measurements are summarized in Fig. 7.9.

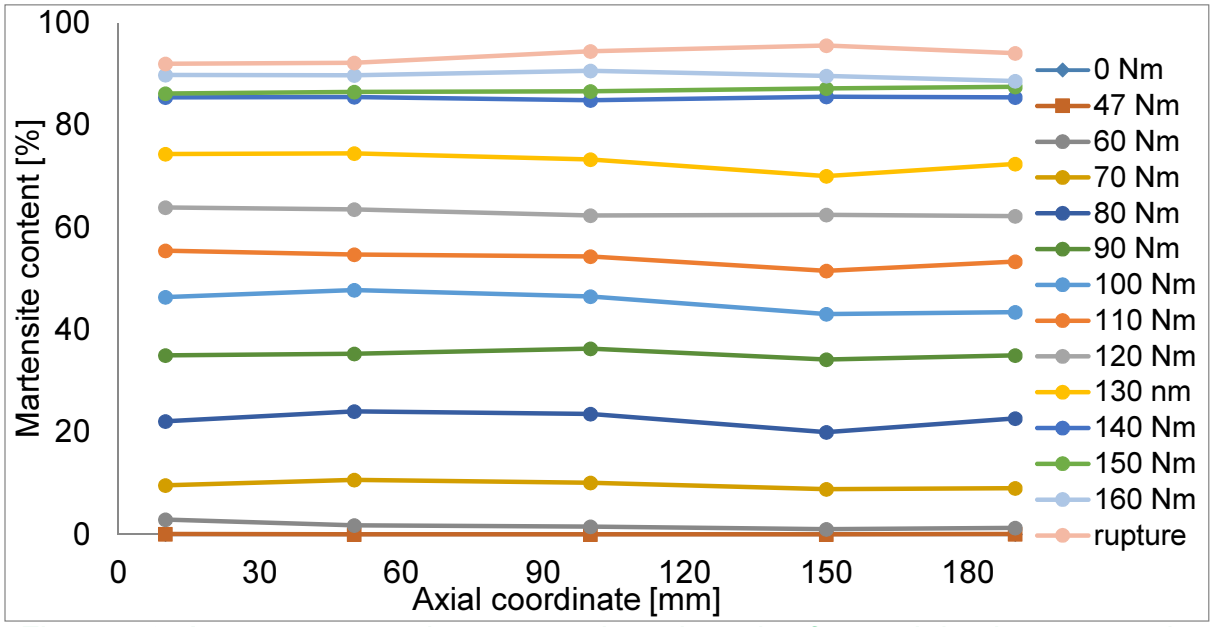

Figure 7.9. Average martensite content along the axis after each load step, sample C1, 77 K

As demonstrated in Fig. 7.9, the martensite content was almost the same in all 5 measurement points along the surface of the sample. This results confirmed theoretical expectations, as the torque was constant along the axis of the sample. Thus, every cross-section had the same state of stress and strain. According to the kinetics of the phase transformation, for the same strain intensity the same martensite content was expected.

Before, very small fraction of martensite was found (0.04%). After having reached 47Nm, very small increase (to 0.1%) was found. In the next measurement, at the level of 60Nm the martensite content reached some 1.7%, still very small. Higher increase was noticed after the next loading step (70Nm), to some 10%. Then, for the next 7 measurements, the increase remained between 8% and 13%. In the last four measurements (at 140Nm, 150Nm, 160Nm and at rupture) the increase was smaller. After the rupture, about 90% of martensite was recorded.

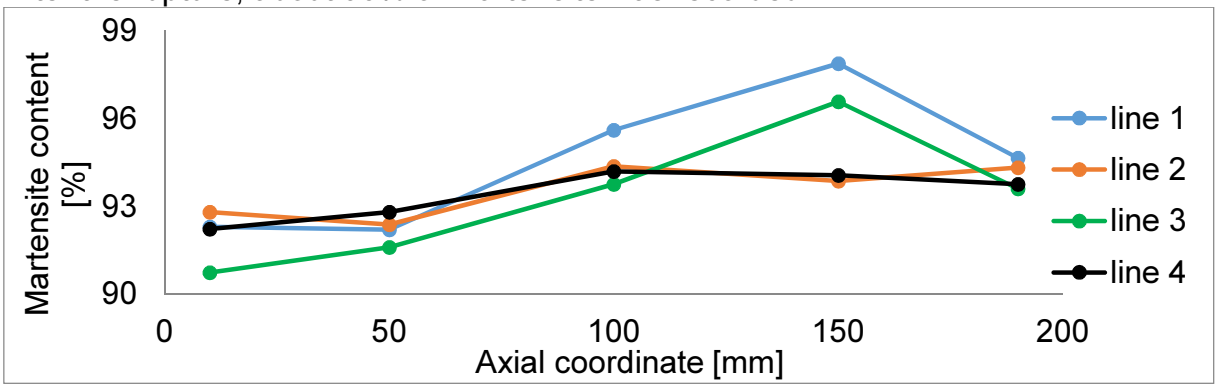

Figure 7.10. Martensite content measurement along 4 lines after the rupture of sample C1

Martensite fraction along four lines (see Fig. 7.2) after the rupture is shown in Fig. 7.10. Maximum difference between the measurements was of 4%. These results indicated clearly, that there was some asymmetry in the martensite distribution. Yet, the difference was rather small, so that the average results presented in Fig. 7.9 can be treated as constant on the whole surface of the sample.

For the sake of compactness, detailed results of martensite content measurements along 4 lines are not shown for the other stages of loading. Yet, the results were analogous to the ones shown in Fig. 7.10. The difference between all the measurements was quite small for all the stages of the loading.

7.2.2. Deformation of sample C1

The sample was photographed before the measurement of martensite content. It was important to observe the deformation, as it distorted from the straight initial geometry. The photographs are summarized in Fig. 7.11.

Figure 7.11. The deformation of sample C1 after each stage of loading

What was interesting, the distortion first increased, as shown in the stages corresponding to the torque of 100Nm, 110Nm, 120Nm. Yet, just before (150Nm, 160Nm) and at the rupture, the sample has become more straight again.
This distortion and the straightening was probably caused by the process of phase transformation, which causes local changes in the mechanical properties. Some kind of adaptation took place, and the straight geometry was promoted for very high torques in order to withstand the load.

7.3. Torsion test at 77K of sample made of 304L stainless steel

The results of torque versus the angle of twist for sample made of 304L stainless steel twisted at 77K are shown in Fig. 7.12. Again, torque values at which the martensite was measured on the surface of the sample are denoted by arrows. The martensite content was measured 10 times during the test. In addition, the martensite fraction was measured before the test and then after the rupture.

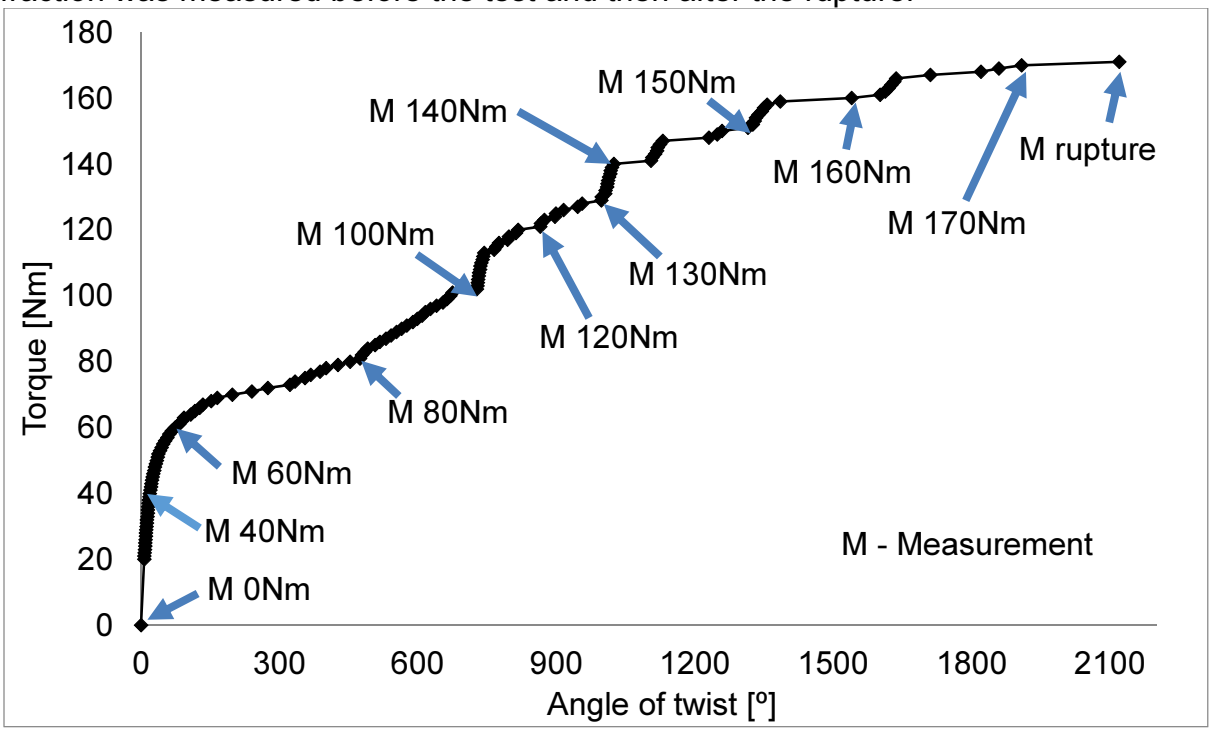

Figure 7.12. Torque versus the angle of twist for sample D1 (304L), loaded at 77 K

During the test, the torque was increased by 1Nm steps. Again, one has to remember that the results from Fig. 7.12 represent cycles with increasing amplitude of the torque (as shown in Fig. 5.9), and not continuous monotonic type of loading.
The elastic torque limit was around 40Nm. Afterwards, nonlinear torque versus the angle of twist response was observed. The maximum value of the torque was equal to 171Nm, which was more than 4 times greater than the elastic torque limit (40Nm). In the first part of the test (up to 100Nm), smooth response was observed, whereas, in the second one jumps in the response were recorded. The sample failed at 2120° (almost 6 full rotations), which was substantially more than for the sample made of 304 stainless steel, for which the angle of 1480° was obtained.

7.3.1. Martensite content evolution on the surface, for sample D1

For sample D1, the martensite content was measured along the surface of the sample at 5 points, and along four lines as shown in Fig. 7.2.
The average of four results, from these 4 lines, was accepted as the final result at each step. All the measurements are summarized in Fig. 7.13.

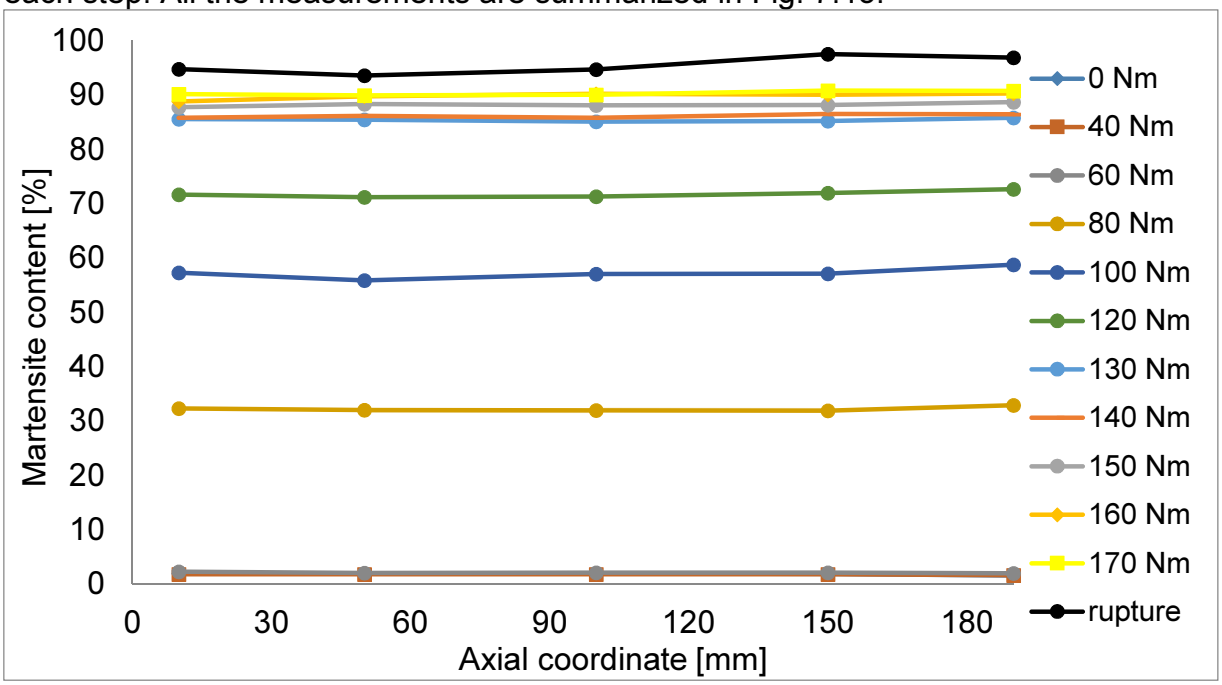

Figure 7.13. Average martensite content on the surface after each load step for sample D1 (304L), 77 K

Before the test, about 2% of martensite was detected on the surface of the sample. This non-zero martensite fraction was attributed to the previous plastic work and the tooling. For the measurements made at the level of 40Nm and 60Nm, no increase in the martensite content was noticed. However, at 80Nm substantial increase of martensite fraction was observed, to about 32%. At 100Nm it was equal to some 56%, then at 120Nm some 72% occurred, and at 130Nm some 86% was reached. Then, the increments were smaller. After the rupture about 95% of martensite was found, thus, almost pure martensite was obtained at the surface of the sample.
All the measured results showed that the content of martensite did not depend on the axial coordinate of the sample, or very little. Almost the same values were found in all 5 measurement points.

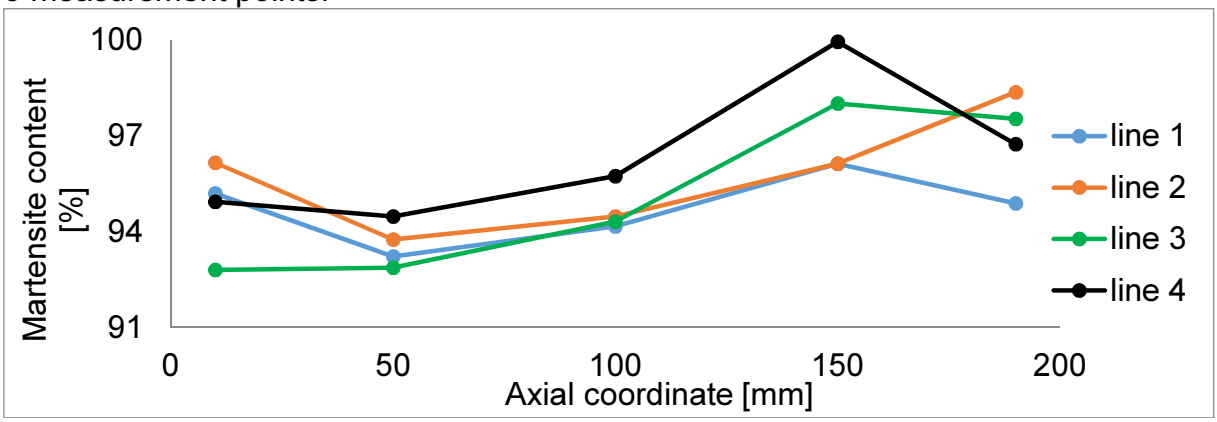

Figure 7.14. Martensite content measurement along 4 lines after the rupture of sample D1 (304L)

Detailed results of the volume fraction of martensite after the rupture and along four lines on the surface (as explained in the Fig. 7.2) are shown in Fig. 7.14.
Similarly, as for sample C1 (Fig. 7.10), the maximum difference between the results was less than 5% (at 10mm distance and 150mm distance). These results demonstrate again, that the martensite fraction was almost constant around the axis of the sample, confirming nearly axisymmetric martensite distribution.

7.3.2. Deformation of sample D1 (304L)

Deformation of sample D1 after each loading stage, before the measurement of the martensite content on the surface took place, is shown in Fig. 7.15.

Figure 7.15. Deformation of sample D1 (304L) after each stage of loading

For this sample distortion was observed as well, even higher than for sample C1 (7.11). The distortion was increasing with the loading.
At 60Nm the sample was still almost straight. However, soon above 80Nm spatial distortion was clearly visible. This distortion was increasing to the level of torque of about 150Nm. Then, it started to decrease, which was visible already at some 160Nm and 170Nm. Finally, after the rupture the straightness was greatly recovered.

7.4. Torsion test at 77K of sample made of 316LN stainless steel

The results in terms of torque versus the angle of twist for sample E1 (316LN), twisted at 77K, are shown in Fig. 7.16. The points at which the test was stopped for martensite content measurements are denoted by arrows. In total, 9 measurements of the martensite fraction were made, 7 during the test, one before start and one after the rupture.
One has to remember that the torque was applied in a cyclic manner (as shown in Fig. 5.9), with the amplitude increasing by 1Nm within each cycle. This was not a monotonic type of torsional loading.
The torque at the end of elastic range reached some 70Nm (more than for sample C1 – 45Nm and sample D1 – 40Nm). Maximum torque at rupture was equal to 155Nm, about the same as for sample made of 304 stainless steel (156Nm, see Tab. 5.2). The angle of twist at rupture was of 4103°, thus, 11.4 full rotations. This was the highest value among all the materials (304 -1480° , 304L - 2120° , 316L - 3820°). The torque in the plastic range smoothly increased with the angle of twist.

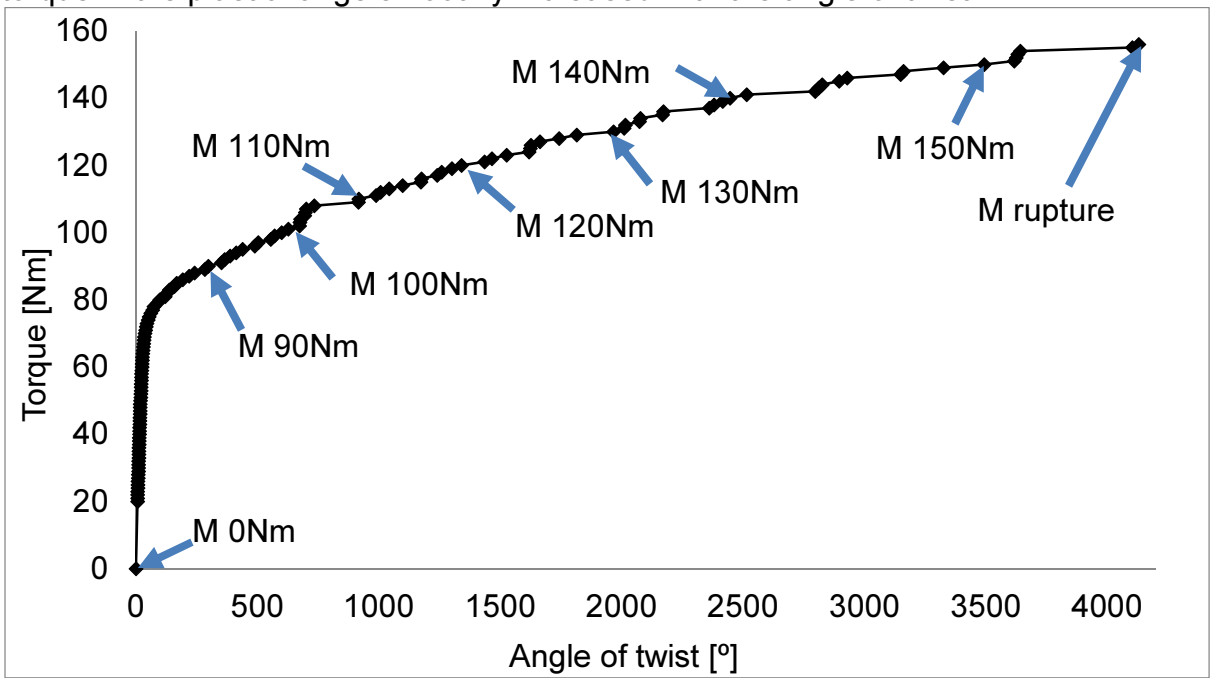

Figure 7.16. Torque versus the angle of twist for sample E1, loaded at 77 K

7.4.1. Martensite content evolution on the surface, for sample E1

Martensite content measurements on the surface of sample E1 during the test are shown in Fig. 7.17. Again, almost constant results were found along the axis of the sample during all the measurements.

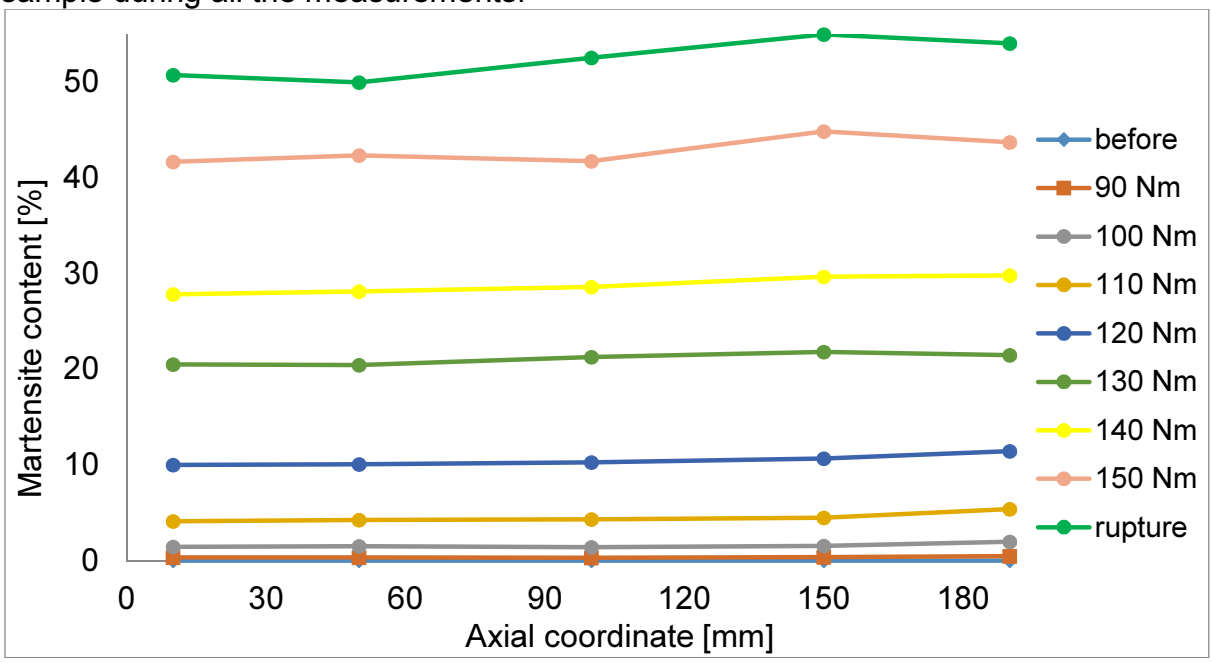

Figure 7.17. Average martensite content along the axis after each load step, for sample E1 at 77 K

Before the test 0% of martensite was found on the surface. At 90Nm only about 0.4% martensite was induced, then, at 100Nm some 1.4% was reached. The subsequent increments were higher. At the rupture, some 55% martensite was found. So, actually much less compared to the samples made of 304L (95%) and 316L (90%) stainless steels.

Detailed martensite content measurements along 4 lines are presented in Fig. 7.18 for the last loading stage (at the rupture). Again, like for the previous samples, the maximum difference was rather small, less than 7% (for the measurement at 150mm distance). This confirms again, that the martensite content was close to symmetric around the axis of the sample.

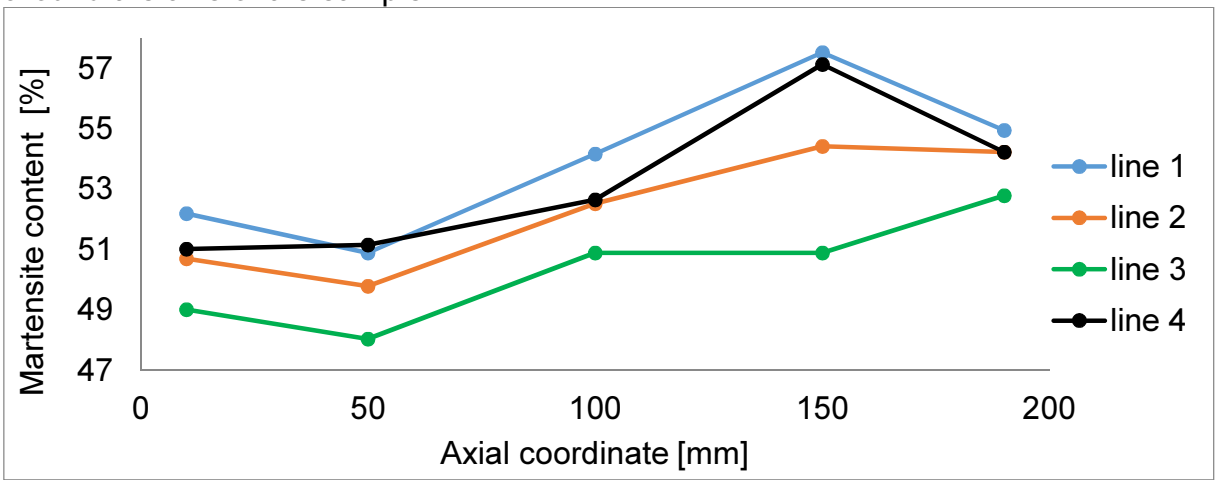

Figure 7.18. Martensite content measurement along 4 lines after the rupture of sample E1

7.4.2. Deformation of sample E1 (316LN)

The photographs of the deformed sample were taken before the test and after each loading stage. They were summarized in Fig. 7.19. Again, similarly to samples C1 and D1, the distortion first increases with the torque and - at some point - starts to decrease. A visible distortion occurred at 100Nm, near the center of the sample. Later on, the distortion moved to the left side of the sample, which is shown in the photo after the rupture. The fracture occurred very near the left side of bar (Fig. 7.19).

Figure 7.19. Deformation of sample E1 (316LN) after each stage of loading

In the last photo (Fig. 7.19), the surface of the sample has been magnified. One can clearly see the difference compared to the state before the test. The texture has changed, indicating the influence of modified martensitic microstructure.

7.5. Torsion test at 77K of sample made of 304 stainless steel

7.5.1. Sample 6.1 (304 ss)

Torque versus angle of twist for the sample denoted as 6.1 (see Tab. 5.2), made of 304 stainless steel and twisted at 77K, is shown in Fig. 7.20. Again, 7 measurements of martensite content were made during the test. Additionally, the martensite fraction was measured before the test and after reaching 120Nm (preset value).
This test was performed in order to repeat the test for sample 5.2, where rather strange behavior was observed (Fig. 5.14). In order to reproduce this result the sample was first twisted at 77K to 120Nm, to be afterwards twisted at 293K until rupture.
Again, one has to remember that the torque was increased in 1Nm steps, in the form of cycles with increasing amplitude (see Fig. 5.9). This cannot be interpreted as pure monotonic torsional loading test.

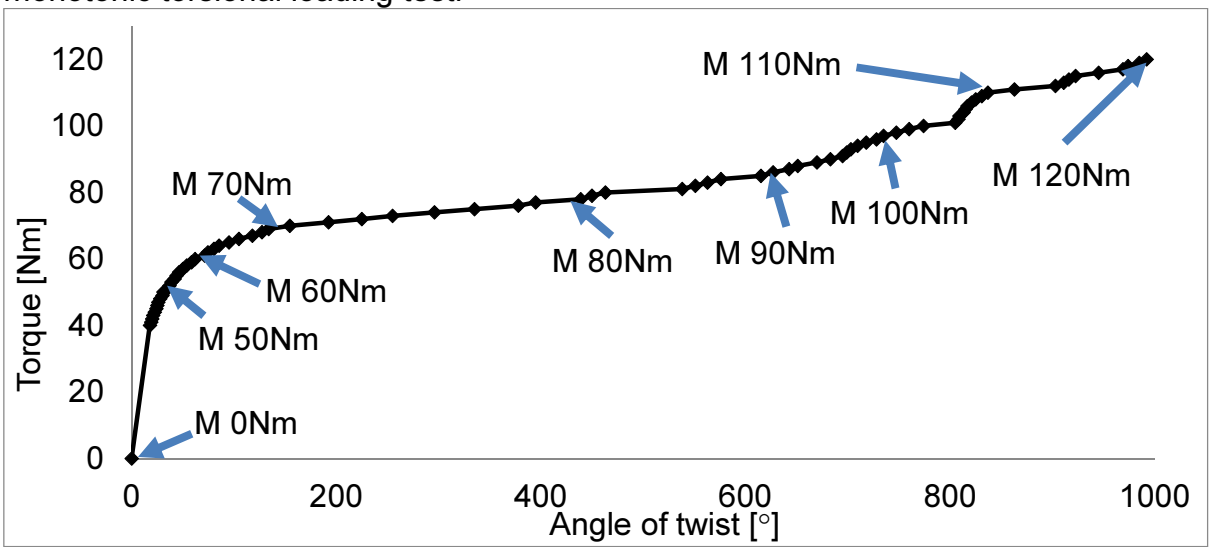

Figure 7.20. Torque versus the angle of twist for sample 6.1 twisted at 77K

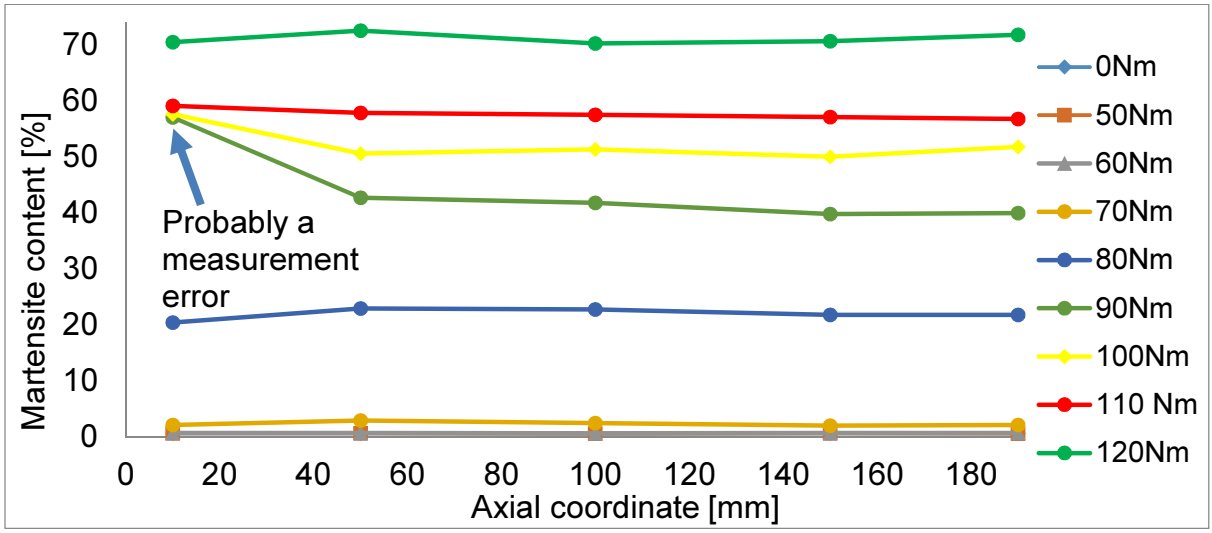

Figure 7.21. Average martensite content along the axis after each load step, sample 6.1 twisted at 77K

The evolution of martensite content is shown in Fig. 7.21. Again, the results are almost the same in all 5 measurement points and at every stage of the test. However, one result substantially differed from the rest, precisely during the measurement at 90Nm made at 10mm distance. This measurement was probably mistaken, as it did not fit with all the other results where a linear trend was observed.
Before the test, some 0.6% of martensite was found on the surface. At 60Nm about 0.1% increase was measured. At 70Nm around 2.5% was recorded, and at 80Nm much higher increase was observed, to some 23%. After reaching the pre-set value of the torque – 120Nm, about 70% of martensite was induced on the surface.

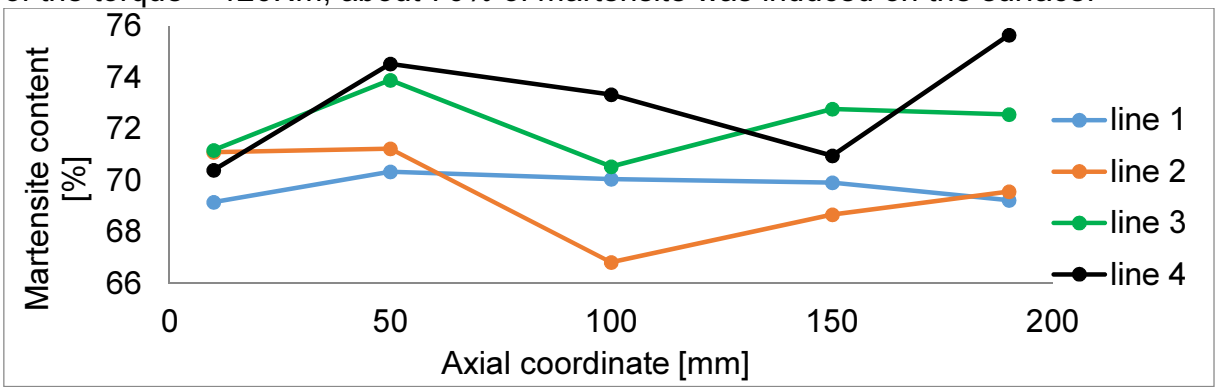

Figure 7.22. Martensite content measurement along 4 lines after the rupture of sample 6.1

The martensite content measured after the rupture along 4 lines is shown in Fig. 7.22. The results differ from each other. The biggest difference was of some 6.5% for the measurement at 100mm. Thus, the relative difference around the sample was less than 10%. Therefore, one can conclude that the martensite content was rather symmetric around the axis of the sample.
Photograph of the deformed sample after loading to 120Nm is shown in Fig. 7.23. One can clearly see relatively high resulting distortion.

Figure 7.23. Deformation of sample 6.1 after loading to 120Nm

7.5.2. Sample 6.2 (304 ss)

After torsion to 120Nm at 77K, the same sample has been loaded at room temperature until rupture.
Again, multiple loading/unloading procedure with increasing amplitude of torque was applied. The loading increment was set to 1Nm.
The results are shown in Fig. 7.24. In this case, the elastic torque limit reached almost 80Nm, so much higher than previously at 77K (40Nm, Fig. 7.20). High martensite fraction, induced during the test at 77K (70% on the surface), caused strong increase of yield strength. At the same time, big part of the material (plastic austenite) transformed into elastic martensite.
The sample fractured at 108Nm, similarly to the sample 5.2 (112Nm, see Tab. 5.2), which has been loaded in exactly the same conditions. Yet, the angle of twist at rupture for sample 6.2 was equal to 1282°, so much larger than for the sample 5.2 (610°). For sample 6.2, smooth torque versus the angle of twist response was obtained, confirming that for sample 5.2 some problem with the torque wrench occurred.

The martensite content was measured 7 times during the test. The results are summarized in Fig. 7.25.

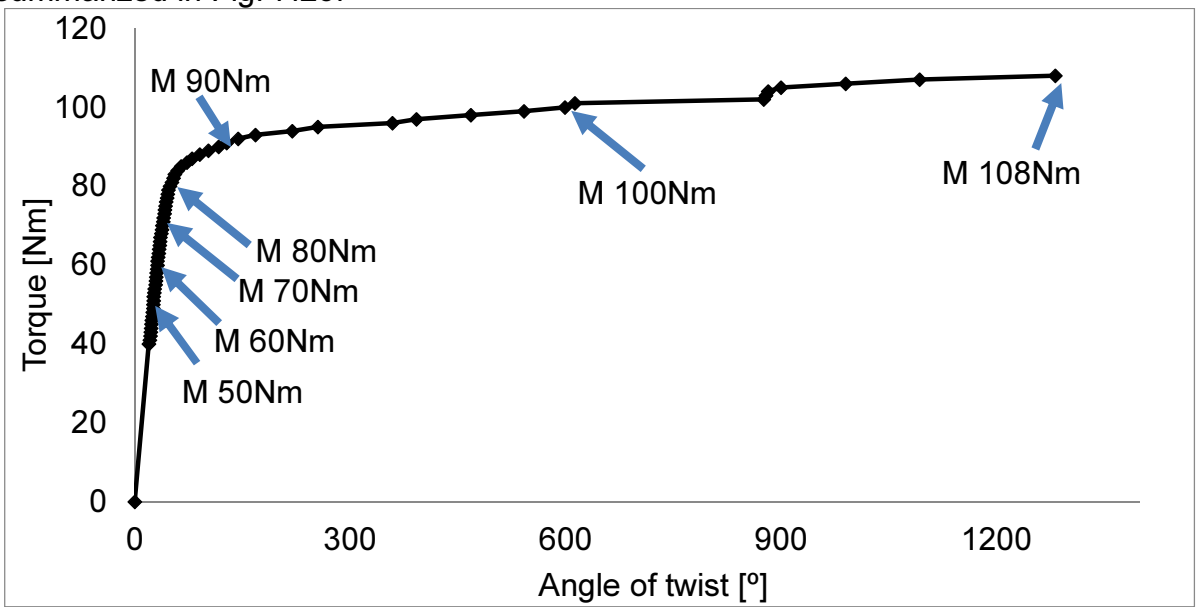

Figure 7.24. Torque versus the angle of twist for sample 6.2 loaded at 293 K

From the previous test at 77K, about 70% of martensite was induced on the surface of the sample. After the first loading stage at 50Nm, the martensite content increased to about 75%. Then, after subsequent loading stages to: 60Nm, 70Nm, 80Nm, almost no increase was measured. At 90Nm the martensite fraction increased to 80%. Finally, after the rupture, 94% of martensite was recorded.

Again, all results from Fig. 7.25 present almost straight lines, confirming that the martensite content was constant along the axis of the bar.

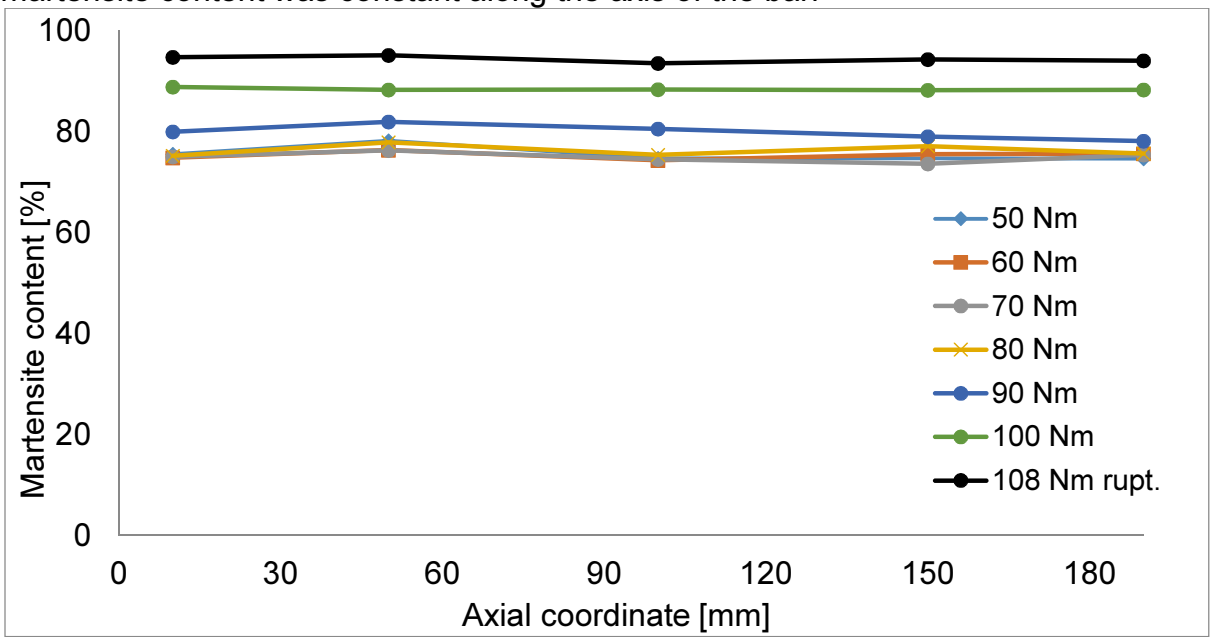

Figure 7.25. Average martensite content on the surface of sample 6.2, twisted to rupture at 293K

Detailed results of the martensite fraction at rupture, tracked along four lines, are shown in Fig. 7.26. The biggest difference of 6%, occurred for the measurement at 10mm distance. Thus, compared to the average value which was about 94%, the results were very similar around the axis of the sample.

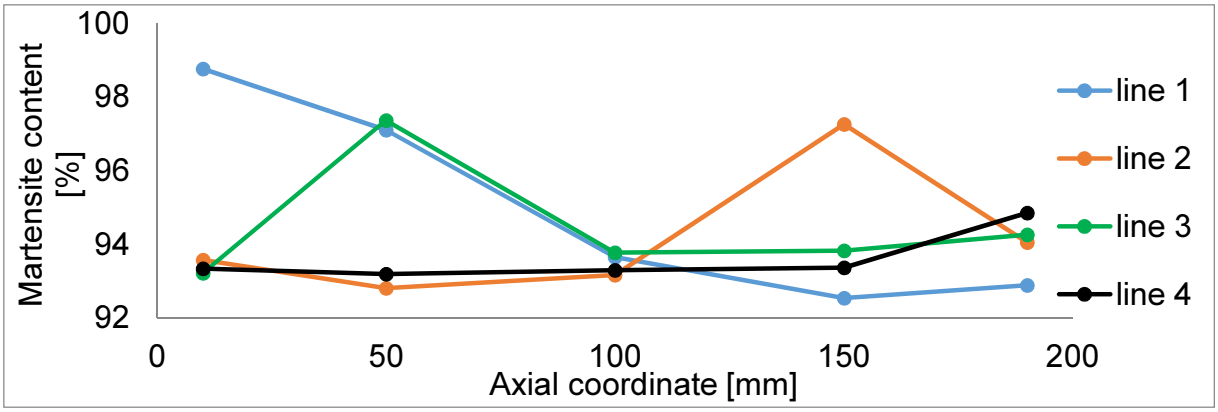

Figure 7.26. Martensite content measurement along 4 lines, after the rupture of sample 6.2 (see Tab. 5.2)

The photograph of the sample after rupture is shown in Fig. 7.27. Here, the fracture occurred further from the left side than for the other samples (C1 – Fig. 7.11, D1 – Fig. 7.15, E1 – Fig. 7.19), and closer to the center. Compared to Fig. 7.23, at the torque of 120Nm, the distortion decreased a lot. This effect of straightening before rupture was observed for the previous samples as well (C1, D1, E1).

Figure 7.27 Deformation of sample 6.2 after the rupture by torsion at 293K

7.5.3. Sample 7.1 (304 ss)

The sample denoted as 7.1 (see Tab. 5.2) has been loaded similarly to the samples 6.1 and 5.1. Here, the initial goal was to induce the martensitic transformation by twisting the sample to 120Nm at 77K. The next goal consisted in checking the performance under torsion in the liquid nitrogen temperature.

The results in terms of the torque versus the angle of twist, for sample 7.1 twisted at 77K, are shown in Fig. 7.28.

Slight difference w.r.t. previous tests consists in the fact, that the present test started from 20Nm torque, whereas, for samples 5.1 and 6.1 the test started from 40Nm. Again, the torque was increased by 1Nm steps. The loading/unloading process, with increasing amplitude of the torque at each loading stage was applied.

This test differed as well in the values of the torque, at which the martensite content was measured. For sample 6.1 it was every 10Nm, however, in the present case the measurements were carried out approximately every 120 deg. Constant increase of the angle of twist, resulted in the constant increase of strain between the measurements. Thus, roughly the same increase in martensite content was expected between the measurements, according to the kinetics of the phase transformation.

In total, 10 martensite content measurements were done: 8 during the test, one before and one after the test. The results of martensite fraction on the surface are shown in Fig. 7.29.

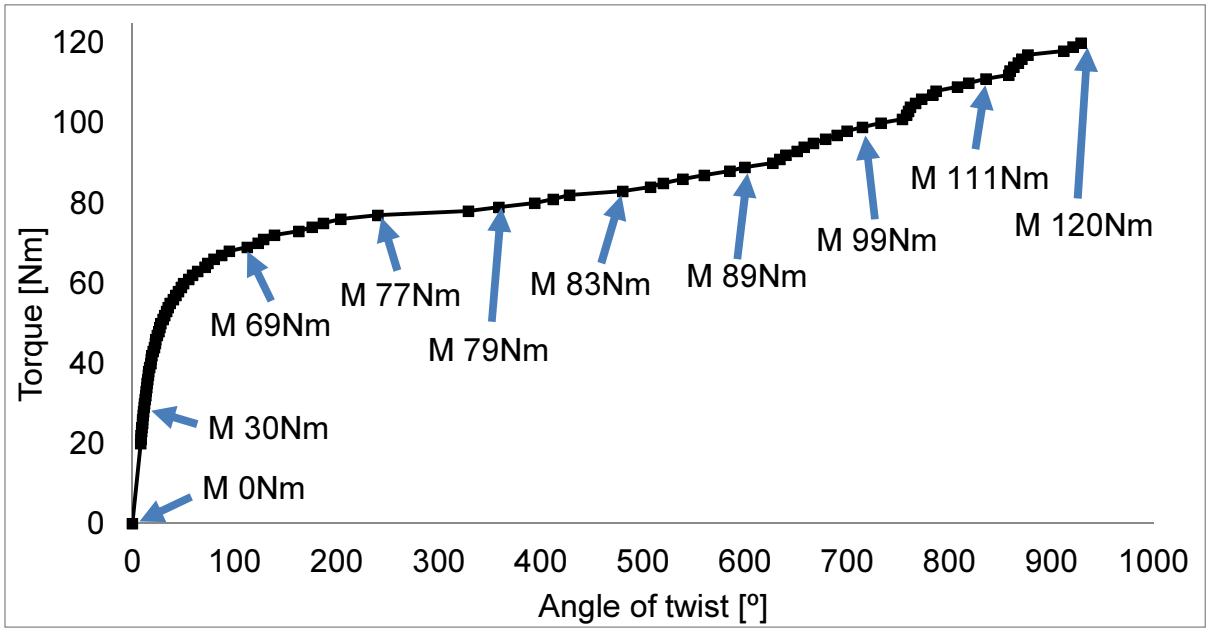

Figure 7.28. Torque versus the angle of twist for sample 7.1 loaded at 77 K

About 0.7% of martensite was found on the surface before the test. At 30Nm no increase was noticed. At 69Nm the martensite content increased to 1.7%. The following increments were much higher, of about 6÷8 %. Finally, after having reached 120Nm, about 70% of martensite was found. So, actually the same value when compared to sample 6.1 (Fig. 7.21) was obtained.

Yet, for this sample the results were not entirely constant along the axis of the sample. In the first 3 measurement points (at 10, 50 and 100 mm distance) they were almost constant, however, for the last points (at 150 and 190 mm) smaller values were found. The same tendency continued throughout all stages of loading.

The increase of martensite content between the stages was nearly constant, confirming the theoretical expectations.

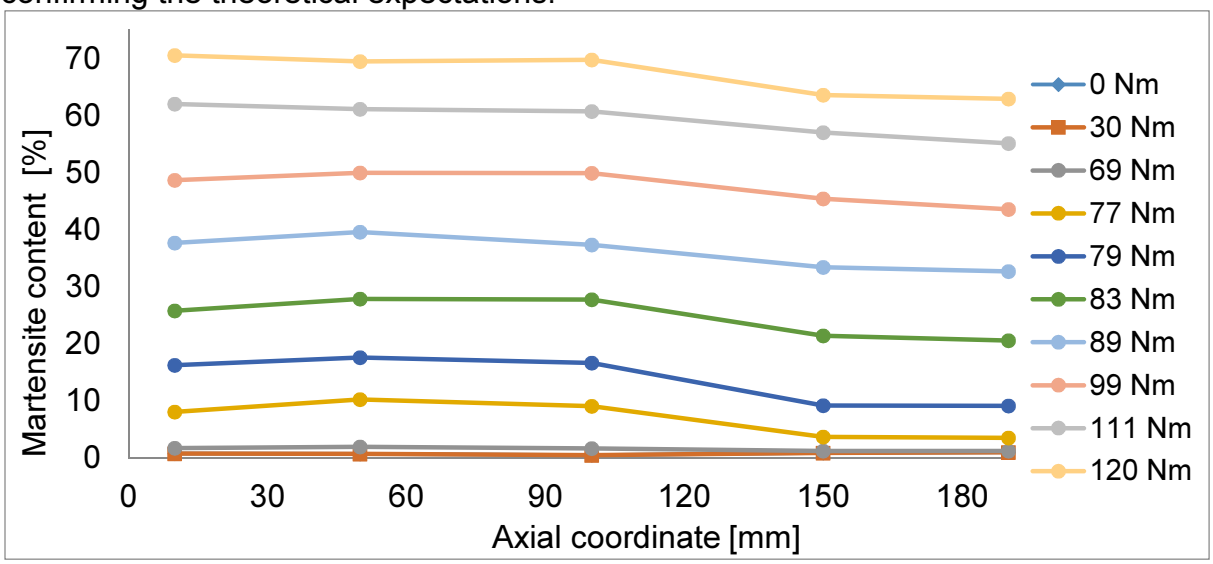

Figure 7.29. Average martensite content on the surface of sample 7.1, twisted at 77K

Martensite content measurements at rupture, along 4 lines (according to Fig. 7.2), are shown in Fig. 7.30. The biggest difference between the results was equal to 7% (at 10mm distance).

Still, the difference is relatively small compared to the average value of about 70%. Thus, the symmetry of martensite content was maintained, as for the previous samples.

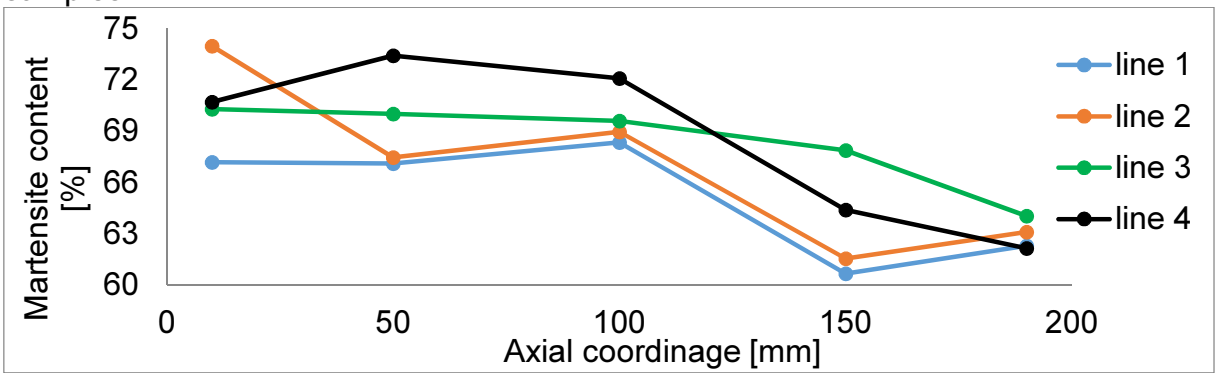

Figure 7.30. Martensite content measurements at rupture, along 4 lines for sample 7.1

The deformation of sample 7.1 was photographed after each loading stage. The pictures are summarized in Fig. 7.31. The distortion is clearly visible, especially at the torque of 83Nm. At the level of 111Nm (the photograph after 120Nm was not taken) the distortion changed.

Figure 7.31. Deformation of sample 7.1 twisted at 77K

7.5.4. Sample 7.2 (304 ss)

After twisting the sample 7.1 (304 ss) to 120Nm at 77K, the sample was loaded again at 77K. The direction of rotation vector was the same in both tests. This test at 77K was supposed to show the performance in torsion of the sample strengthened by means of the plastic strain induced phase transformation.
The torque versus the angle of twist response is shown in Fig. 7.32. The martensite content measurement points are denoted by arrows.
The elastic torque limit was equal to almost 120Nm, the same as the final value of torque obtained in the previous test (Fig. 7.28). Compared to the elastic torque limit obtained in the first test (40Nm – Fig. 7.28), it has increased 3 times. It is worth pointing out, that the value of the torque at rupture was of 167Nm, thus, even higher than for the test until rupture (156Nm, see Tab. 5.2). The preloading by torsion to 120Nm did not change the maximum carrying capacity. It has actually increased, together with tremendous yield stress increase. The angle of twist at rupture was equal to 1310°, so it remained very high, only slightly smaller than for the sample loaded until rupture in one go (1480°, sample 4, Tab. 5.2).

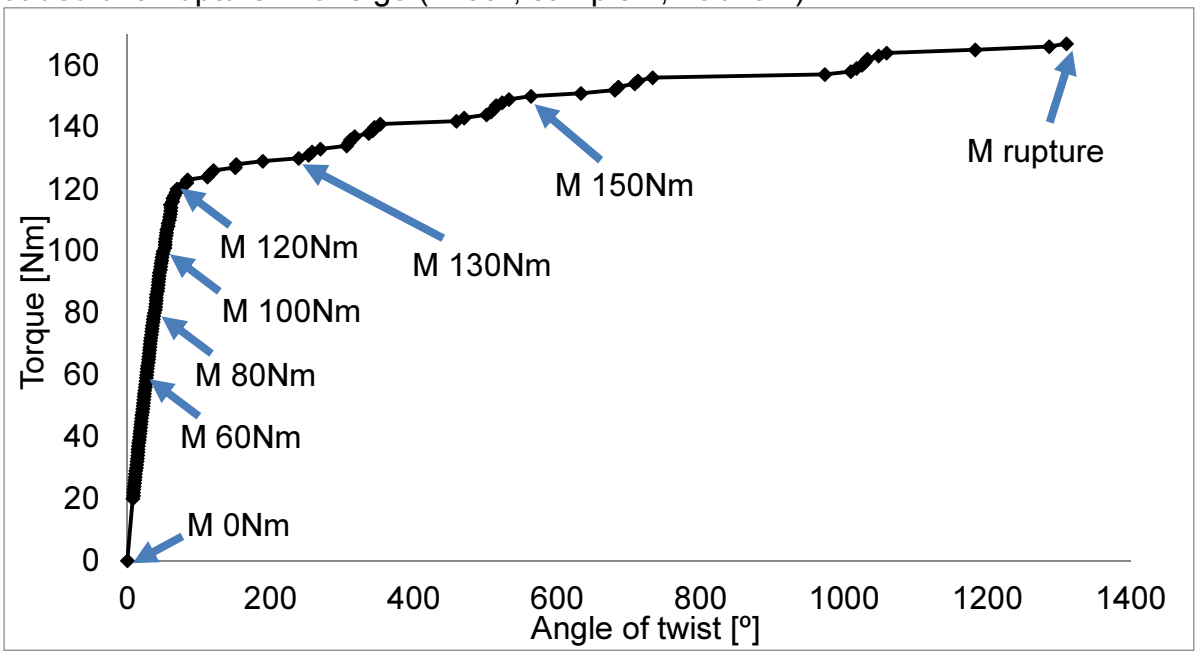

Figure 7.32. Torque versus the angle of twist for sample 7.2 loaded at 77 K

The martensite content results for sample 7.2 are shown in Fig. 7.33. In the first 4 loading stages (at 60, 80, 100 and 120Nm), the martensite content was not constant along the axis - similarly to the results obtained for sample 7.1 (see Fig. 7.29). Yet, in the last stages (130Nm, 150Nm and at rupture), the content of martensite at the extremity of the sample has increased, making the results almost constant along the sample. This effect was probably related to the distortion of the bar during the test. The martensite content was higher in the regions of higher distortion, and smaller in the regions of straight sections. For large torque values the sample straightened, which caused the martensite content to become nearly equal along the whole bar.
Almost no increase in martensite content was noticed at 60, 80, 100 and 120Nm. At 130Nm it increased to about 79%, then, at the level of 150Nm the martensite content reached 87%, and at the rupture some 95% was recorded.

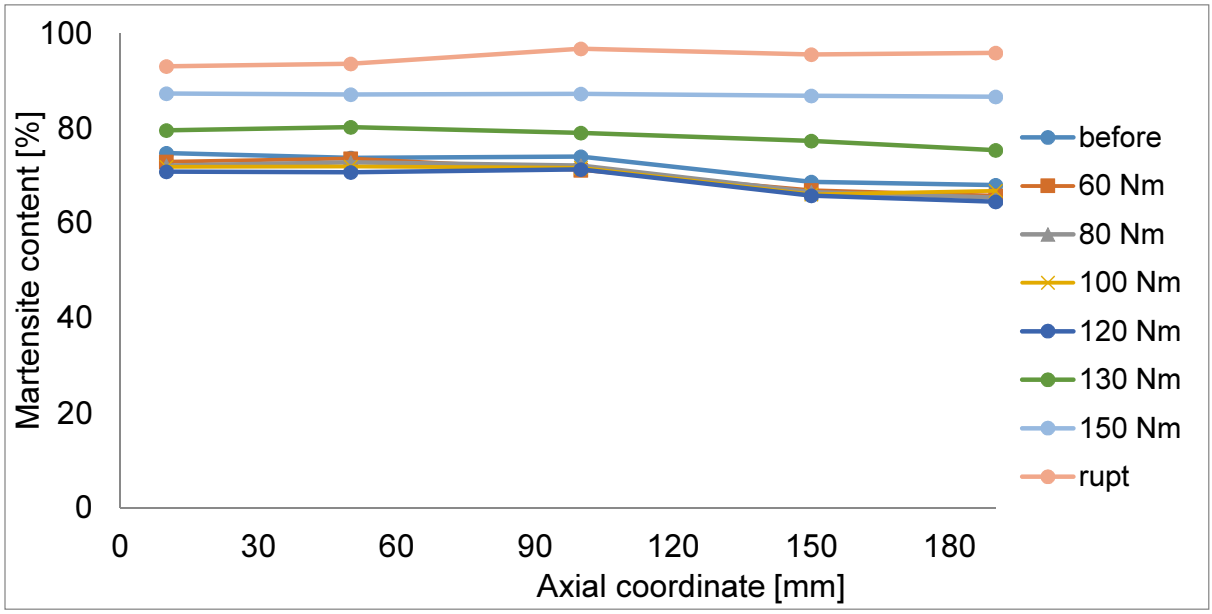

Figure 7.33. Average martensite content on the surface of sample 7.2, twisted at 77K

The martensite content at the rupture, along 4 predefined lines, is presented in Fig. 7.34. As can be seen, there is some discrepancy between all four measurements, with the biggest difference equal to about 4% (at 10mm distance). So, very good convergence was obtained, confirming that the martensite content was symmetric around the axis of the sample.

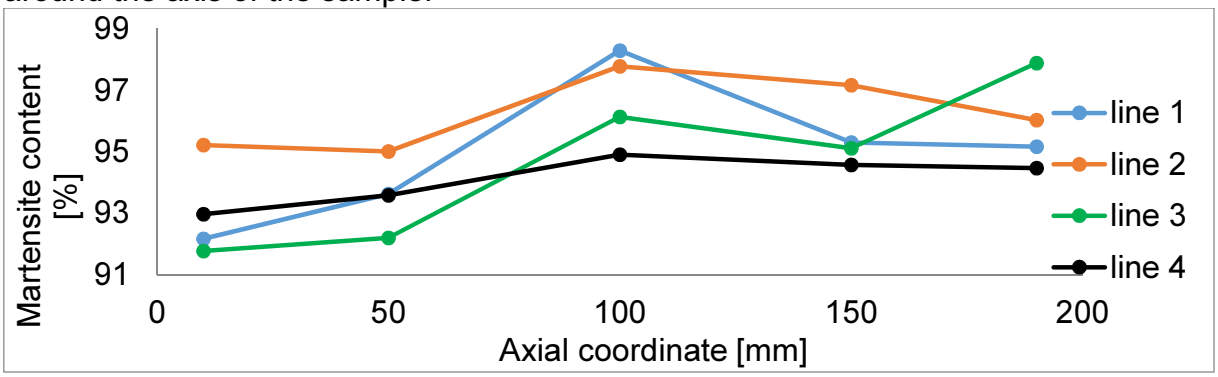

Figure 7.34. The martensite content measurements along 4 lines, at the rupture of sample 7.2

The deformation of sample 7.2 is shown in Fig. 7.35. One can see how the distortion was evolving during the test.

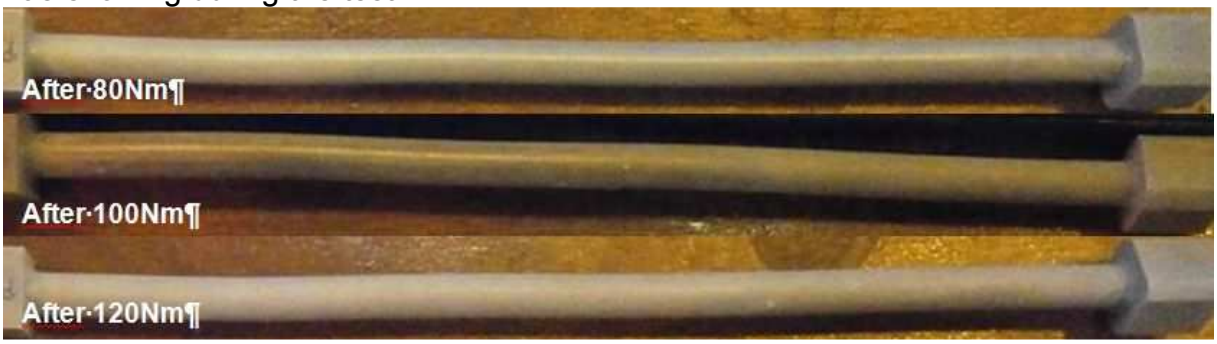

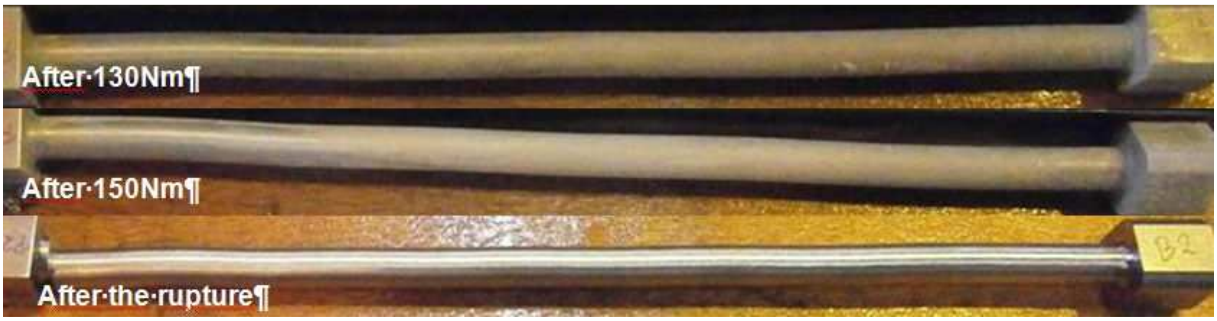

Figure 7.35. Deformation of sample 7.2 twisted at 77K

7.6. The summary of results for stainless steels: 304, 304L, 316L, 316LN

The results in terms of torque versus angle of twist for 77K are shown in Fig. 7.36 for all samples. For what concerns the maximum torque, the samples made of 304L, 316L, 304, 316LN reached the torque of 171Nm, 167Nm, 156Nm and 156Nm, respectively. Thus, the strongest material turned out to be the stainless steel 304L, then the grade 316L.

On the other hand, with respect to the maximum angle of twist, the following sequence was obtained: 316LN - 4130°, 316L - 3820°, 304L - 2120° and 304 - 1480°. Similar behavior was found for the samples made of the grades 304 and 304L. The results almost coincided with each other.

The character of the resulting curves for samples C1, D1, Sample 4 is similar. One can observe very steep part in the elastic region, then softening in the beginning of plastic yielding, subsequent hardening causing increasing slope and lastly decreasing slope the rupture point.

Completely different behavior was found for sample E1, made of 316LN stainless steel, for which, steep part in the elastic region was similar as for the other samples, but then only decreasing slope in the torque – angle of twist curve was recorded.

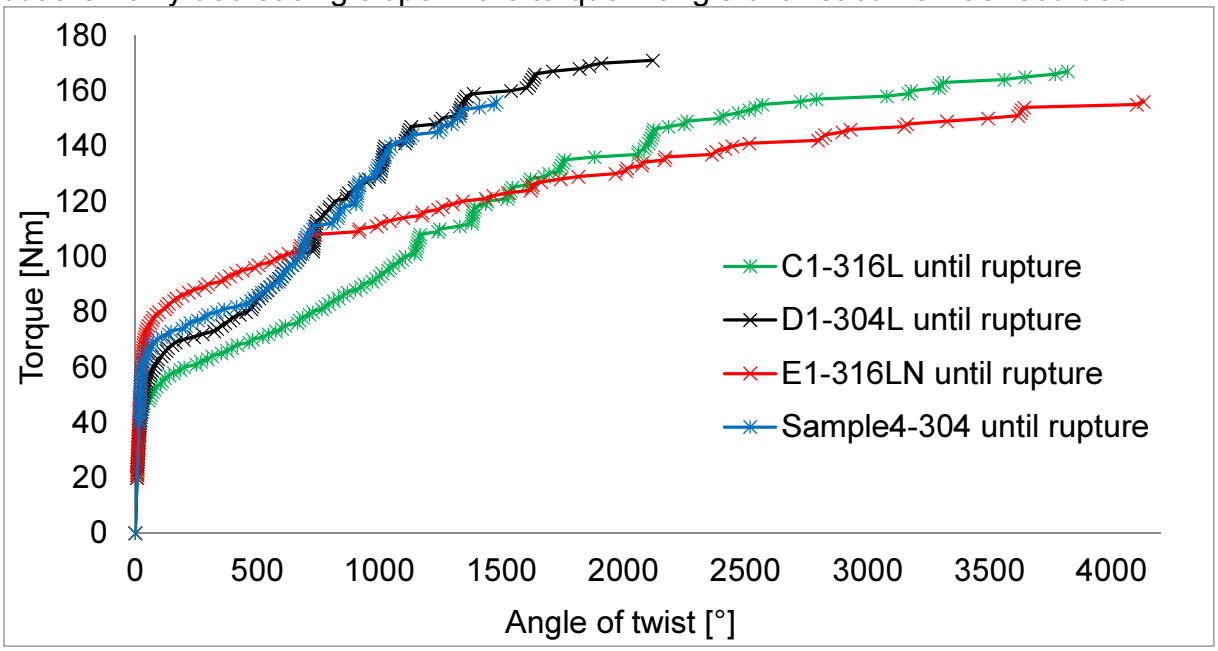

Figure 7.36. Torque versus the angle of twist for samples twisted at 77K until rupture (C1, D1, E1, Sample4)

The martensite content distribution on the surface of the samples was always nearly constant (Fig. 7.9, 7.13, 7.17, 7.21, 7.25, 7.29, 7.33) along the axis of the sample.

The measurements were made at 5 points, at the distances of 10, 50, 100, 150 and 190mm. An average has been calculated from these 5 values. These average values have been plotted as functions of the angles at which the tests were stopped for martensite content measurements. These results were shown in Fig. 7.37 for samples: C1, D1, E1 and 6.1, 7.1.
The highest transformation rate was found for 304L stainless steel, then for the grades 304, 316L and 316LN. For 304 stainless steel, the martensite content was measured only up to 120Nm at 77K. Most probably more martensite would be induced in the sample, if the test was continued until rupture.
For samples 6.1 and 7.1, which were loaded in the same conditions, the same martensite contents were obtained (violet and orange lines in Fig. 7.37). This confirms reliability of the results.

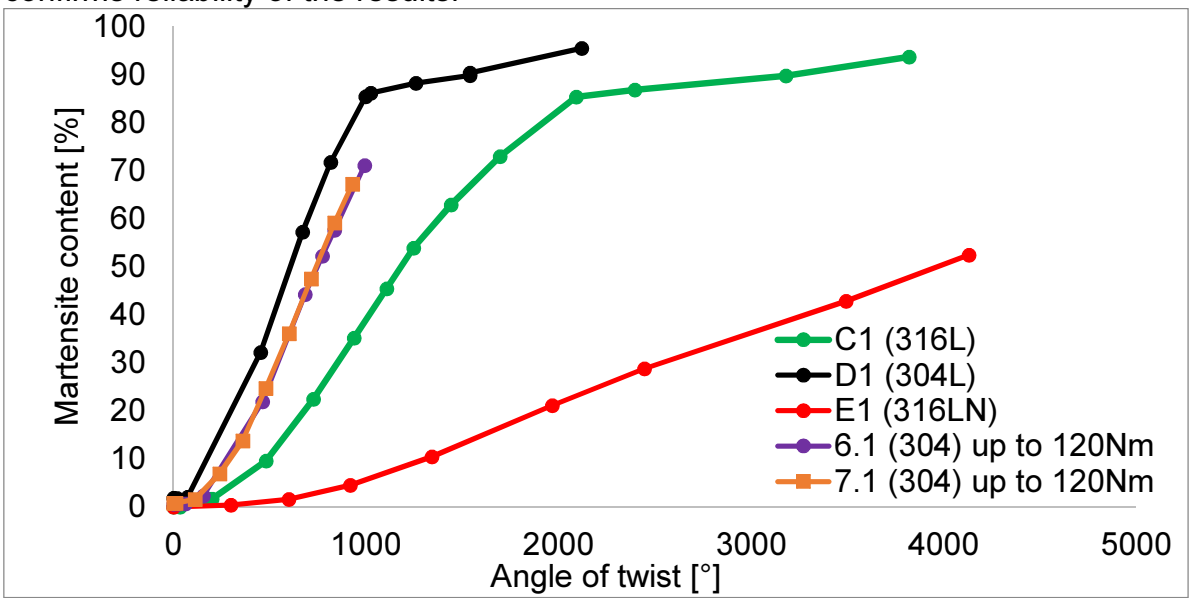

Figure 7.37. Martensite content measured on the surface as a function of angle of twist at 77K

The martensite content is presented as a function of torque in Fig. 7.38. Here, it is more clearly seen that a torque threshold exists, after which the phase transformation starts to develop. From this result it turns out, that for samples C1, D1, 6.1 and 7.1 the results are similar. Only the results for sample E1 are far different.

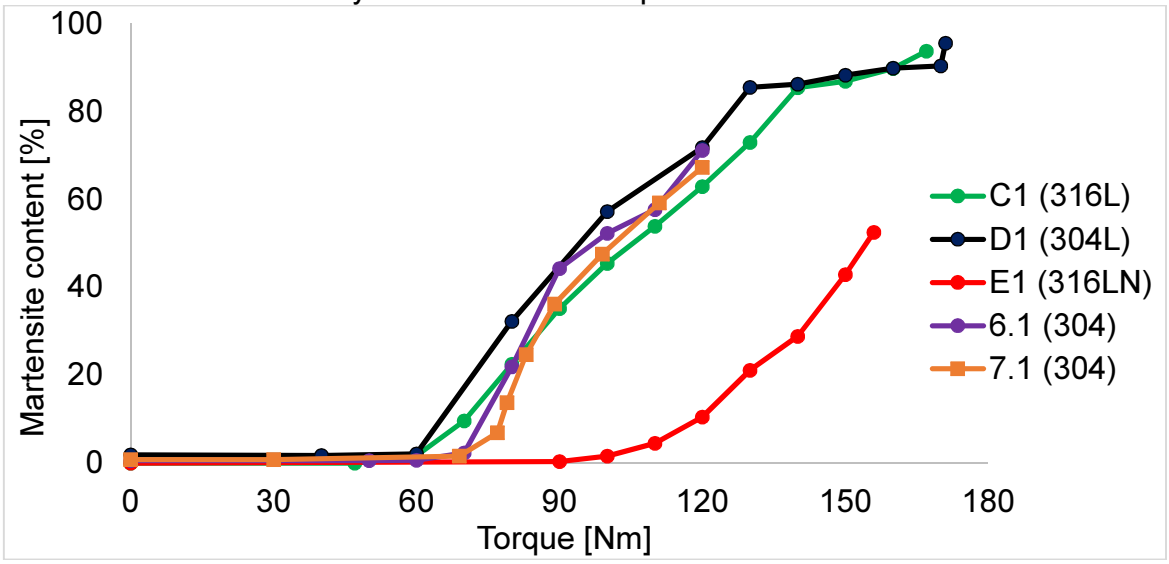

Figure 7.38. Martensite content on the surface as a function of torque at 77K

Lastly, the shear strain on the surface of the sample was calculated based on the angle of twist. Combining Eqs 4.53 and 4.56, one gets:

$$\gamma = \frac{\varphi}{L} R \tag{7.1}$$

where the length of the sample (L) was equal to 200mm, and the radius (R) was equal to 4mm. Translating the results presented in Fig. 7.37 into functions of the shear strain, one obtains the curves shown in Fig. 7.39. Actually, these results represent the kinetics of the phase transformation, as the martensite content is related directly to the strain.

One may notice, that the shear strain reaches rather high values, up to almost 1.5 for the sample made of grade 316LN, and up to 1.3 for the sample made of grade 316L. Thus, large plastic strains are needed to fracture these materials.

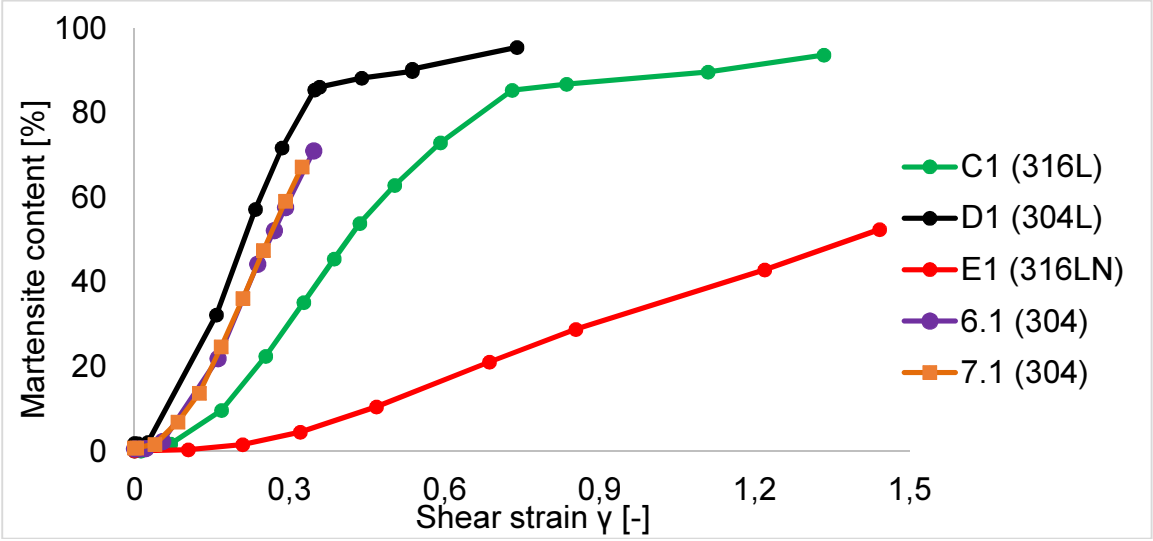

Figure 7.39. Martensite content as a function of shear strain at 77K

Later on, in the next chapter, these results are used in order to identify the parameters of the constitutive model.

The samples made from grade 304 were compared separately in terms of torque versus angle of twist (cf. Fig. 7.40). Actually, the results for samples 6.1, 7.1 and for sample 4 differed from each other. Theoretically, they were supposed to be similar. Yet, the difference was still acceptable.

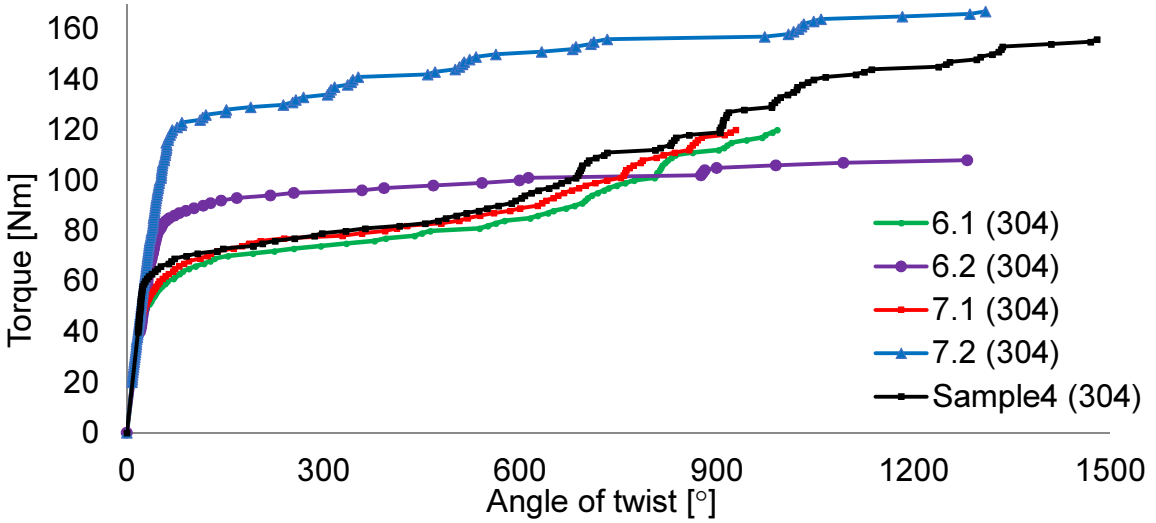

Figure 7.40. Torque versus angle of twist for samples 6.1, 6.2, 7.1, 7.2, and sample 4, twisted at 77K

The martensite content was measured for samples 6.2 and 7.2 during the test until rupture. The results are shown in Fig. 7.41 as a function of the angle of twist. A surprising effect was found, namely, the martensite content was increasing more during the test at room temperature (the red curve). In the last two measurement points, the martensite content was the same. However, at the beginning almost no increase was observed in sample 7.2, whereas, in the sample loaded at room temperature steady increase was found.
This result was rather unexpected, because the rate of phase transformation is usually smaller at 293K, and smaller saturation values are expected. Yet, the experimental results showed that this was not the case, and that at room temperature the martensite content on the surface of the sample during torsion can reach even 95%.

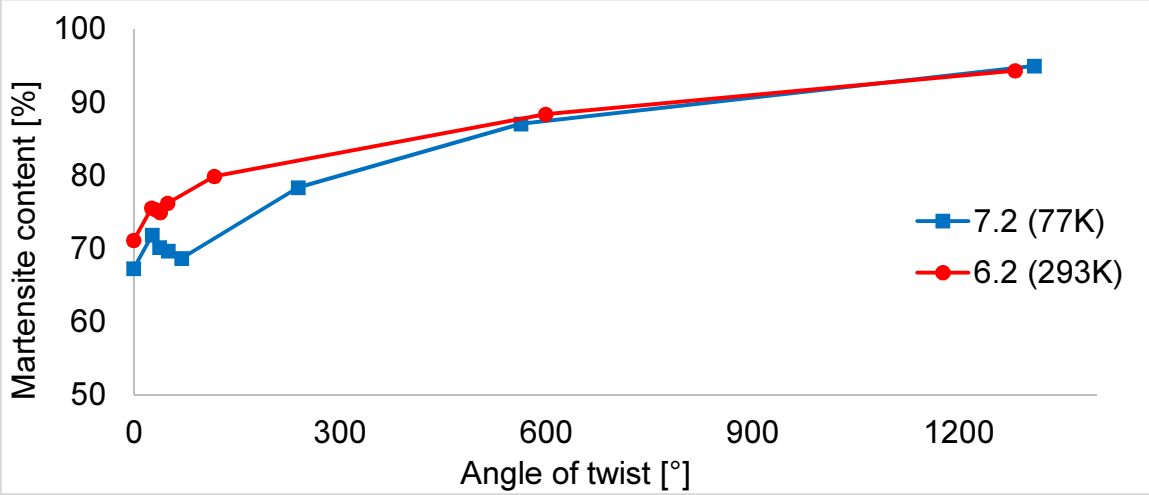

Figure 7.41. Martensite content as a function of the angle of twist for samples 6.2 and 7.2

7.7. Conclusions

The following conclusions are drawn from the above presented results:

- the behavior of twisted bars differs a lot for different grades of the austenitic stainless steel (304, 304L, 316L, 316LN),
- the kinetics of the phase transformation (the relationship between the rate of the volume fraction of martensite and the plastic strain rate) was obtained for several samples made of different grades,
- the evolution of martensite content was captured during the torsion test along the axis of the sample,
- distortion of the samples due to torsion was observed, possibly caused by the presence of bending moment, resulting from imperfect geometry of the samples and the way the loading was applied.

8. Comparison between the theory and the experiment

8.1. Introduction

Equations for torque versus the unit angle of twist ($M(\theta)$), and the shear stress versus shear strain have been derived in Chapter 4. The "monotonic" torsion experiments have been performed at 77K and 293K for the sample made of 304 stainless steel, and at 77K for the grades: 304L, 316L and 316LN. Torque versus angle of twist was experimentally measured. Based on the experiments, the following parameters were calibrated: h (coefficient for the hardening caused by the Orowan mechanism), C_{a0} (the tangent stiffness modulus of austenite) and E_a (Young's modulus of austenite). The Poisson ratio of austenite $\nu_a = 0.5$ has been assumed like for incompressible materials, and for martensite $\nu_m = 0.3$ (like for elastic materials).

8.2. Calibration of the model based on the kinetics of phase transformation

8.2.1. Calibration for 304 stainless steel

For 304 stainless steel, the martensite content measurements were performed within the cross-sections of several samples (see sections 6.3.6 and 6.3.7). Based on these results, the parameters of the kinetics of phase transformation (A, γ_ξ, ξ_L) have been identified. Based on the average martensite content along the radius of the sample, presented in section 6.3.7 (Fig. 6.111), the sought parameters were found for two temperature levels: at 77K from the results obtained for sample 2 which was twisted up to 870 degrees, and at 293K from the results obtained for sample 3 twisted to 870 degrees as well. The final values of the parameters are shown in Table 8.1.

Temperature [K]	A [−]	γ_ξ [−]	ξ_L [%]
77	1.95	0.01	Saturation not observed
293	0.2	0.02	Saturation not observed

Table 8.1. Parameters of the kinetics of phase transformation, identified from data presented in Fig. 6.111

Third parameter of the kinetics (ξ_L) was not identified, as the saturation effect was not observed neither for sample 2 nor for sample 3.

Taking into account the equation for the kinetics (Eq. 4.4), the expression for shear strain ($\gamma = \theta r$), and the expression for the unit angle of twist (Eq. 4.56), the martensite content is expressed as a function of the radius of the cross-section by:

$$\xi = \begin{cases} 0, & \gamma^p \le \gamma_\xi \\ A(T) \cdot \left(\dfrac{\varphi^{\mathrm{M}}}{\mathrm{L}} \cdot \mathrm{r} - \gamma_\xi \right) & \gamma_\xi < \gamma^p \le \gamma_L^p \\ \xi_L & \gamma^p > \gamma_L^p \end{cases} \tag{8.1}$$

where:

- R is the radius of the bar (Tab. 8.2),
- L denotes the length of the bar (Tab. 8.2),
- φ^{M} is the angle up to which the sample was twisted (Tab. 8.2).

Sample	$R\ [m]$	$L\ [m]$	$\varphi^{\mathrm{M}}[°]$	$\varphi^{\mathrm{M}}[rad]$
2 (77K)	0.004	0.2	870	15.18
3 (293K)			870	15.18

Table 8.2. The radius (R) and the length (L) of twisted bar

After inserting the parameters of the kinetics of phase transformation from Tab. 8.1, and the parameters of the geometry (R, L) and the loading (φ^{M}), the functions $\xi(r)$ were obtained. For 77K the following equation holds:

$$\xi = \begin{cases} 0, & \gamma^p \le 0.01 \\ 1.95 \cdot \left(\frac{15.18}{0.2} \cdot \mathrm{r} - 0.01\right) & \gamma^p > 0.01 \end{cases} \tag{8.2}$$

whereas, for room temperature:

$$\xi = \begin{cases} 0, & \gamma^p \le 0.02 \\ 0.2 \cdot \left(\frac{15.18}{0.2} \cdot \mathrm{r} - 0.02\right) & \gamma^p > 0.02 \end{cases} \tag{8.3}$$

A comparison between the experimental results obtained for sample 2 (77K) and the approximated kinetics described by Eq. 8.1 is shown in Fig. 8.1, and for sample 3 (293K) in Fig. 8.2, respectively.

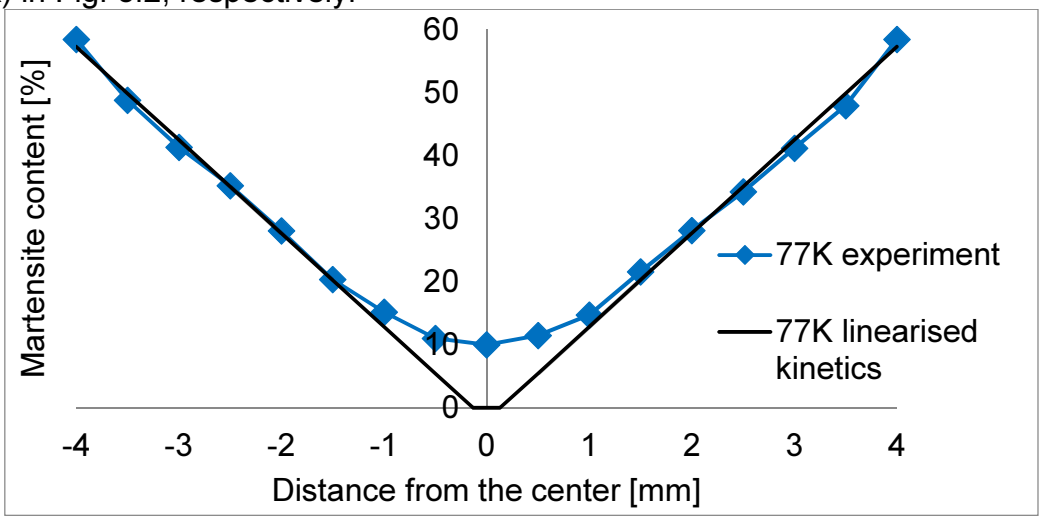

Figure 8.1. Experimental and theoretical distribution of martensite along the radius of sample 2, twisted at 77K up to 870°

Of course, the theoretical kinetics expressed by formula 8.1 does not depend on the angular coordinate, just on the radius. In reality, perfect symmetry was never possible to obtain (see Figs 6.92÷6.94). Yet, the average martensite content turned out to be very close to symmetric. Thus, good agreement was obtained between the experimental and the theoretical results at 77K. Only in the center of the sample some discrepancy appeared. The model did not predict any martensite content in the center of the sample. This experimental fact is directly related to the axial strain which turns out non-zero in torsion, and which drives the phase transformation in the axial direction as well. This results in non-zero martensite content there.

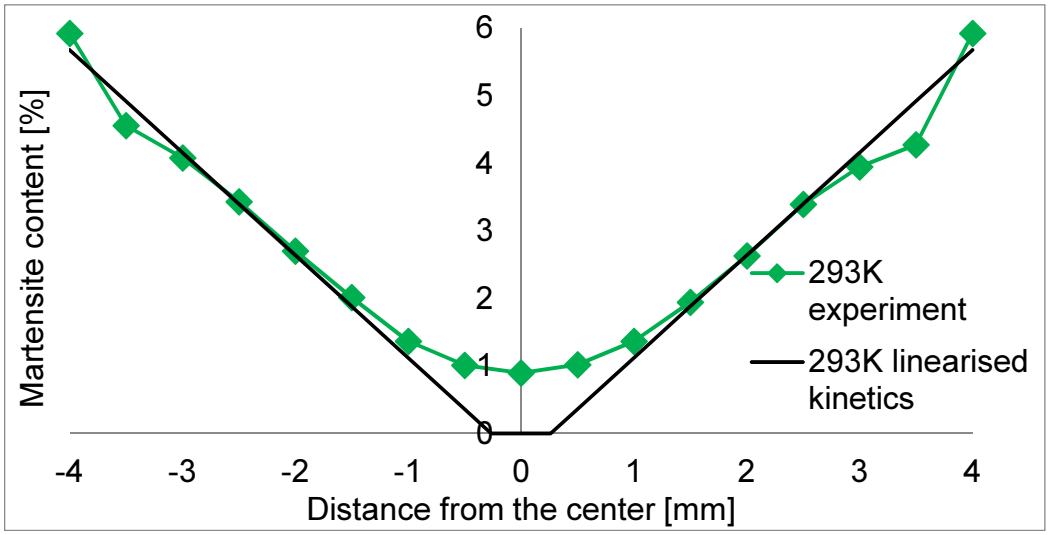

Figure 8.2. Experimental and theoretical distributions of martensite along the radius of sample 3, twisted at 293K up to 870°

At room temperature (Fig. 8.2), reasonably good agreement was obtained between the theory and the experiment as well. Again, the biggest difference was observed in the center, where the model predicted zero martensite content. Slight deviation was observed at a distance of 3.5 mm from the center.

The experimental results were measured within the cross-sections (see section 6.3.6), giving more data regarding the symmetry of martensite distribution. In order to better compare the theoretical results with the experimental data, both types of results were collected together. For sample 2, the martensite measurements were extracted from 1st cross section (Fig. 6.92). Theoretical and experimental results are shown in Fig. 8.3.

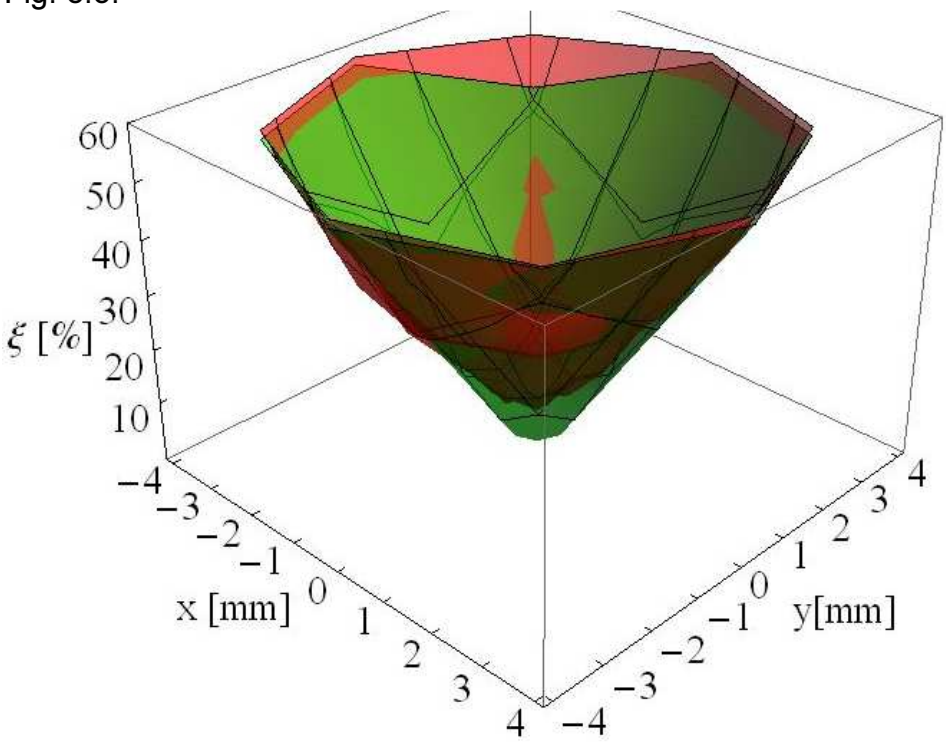

Figure 8.3. Theoretical (red) and experimental (green) martensite content within the cross-section of sample 2 (cross-section 1)

As can be seen in Fig. 8.3, very good agreement was obtained between the theory and the experiment. Thus, the linear kinetics has been confirmed to be applicable in predicting the experimental results.
For sample 3, the martensite measurements were extracted from 1st cross section (Fig. 6.100). The theoretical results, calculated from Eq. 8.3, with the experimental results are shown in Fig. 8.4. Again, good correlation was obtained proving, that the linearized kinetics predicts well the experimental results.

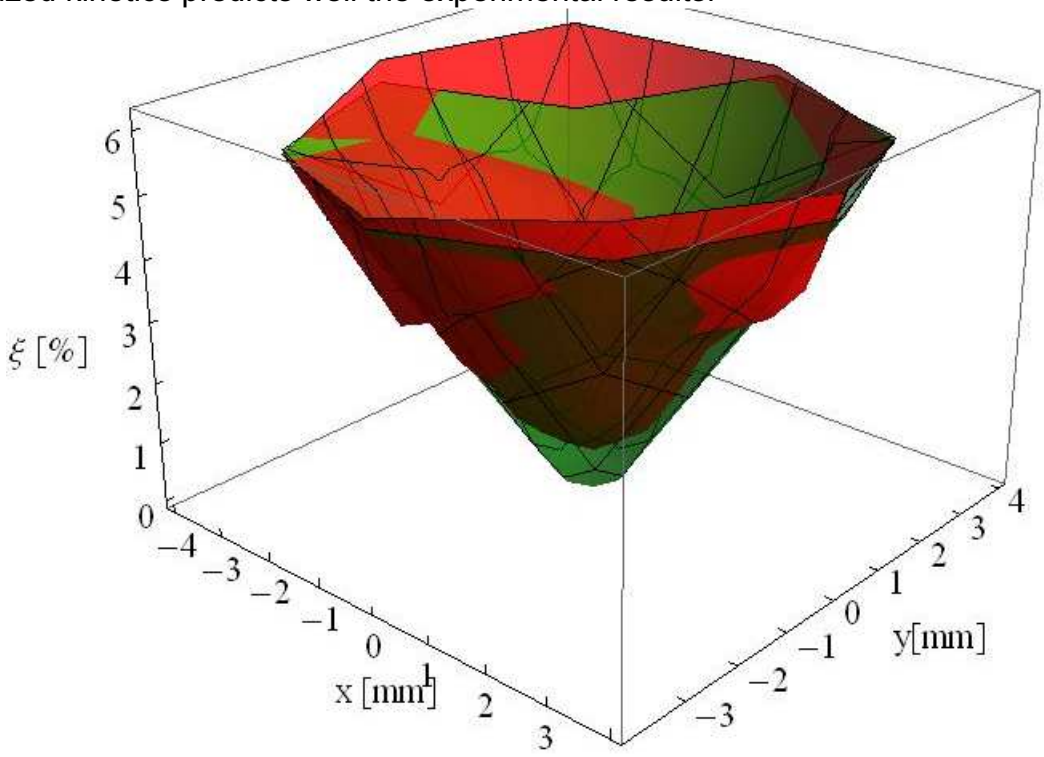

Figure 8.4. Theoretical (red) and experimental (green) martensite content within the cross-section of sample 3 (cross-section 1)

8.2.2. Samples made of grades: 304L, 316L, and 316LN

Based on the martensite content measurements versus the angle of twist, presented in Fig. 7.37, the parameters of the kinetics of phase transformation were identified. In this case, the formula 8.1 was slightly changed. The radius is now constant ($r = R$), and the angle of twist is represented by the variable (φ). The formula takes the form:

$$\xi = \begin{cases} 0, & \varphi \le \varphi_\xi \\ A \cdot \left(\frac{\varphi}{\mathrm{L}} \cdot \mathrm{R} - \gamma_\xi\right) & \varphi_\xi < \varphi \le \varphi_L^p \\ \xi_L & \varphi > \varphi_L^p \end{cases} \qquad (8.4)$$

The parameters identified for grades: 304L, 316L and 316LN are summarized in Tab. 8.3:

Steel	A [-]	γ_ξ [-]	ξ_L [%]
304L	2.6	0.02	91.9
316L	1.42	0.08	89.8
316LN	0.42	0.19	No saturation observed

Table 8.3. Parameters of the kinetics of phase transformation for grades 304L, 316L and 316LN

The length and the radius of the sample are given in Tab. 8.2. Summary of the experimental data and the theoretical kinetic law of phase transformation is illustrated in Fig. 8.5. The theoretical kinetics is plotted using the parameters from Tables 8.2 and 8.3, and Eq. 8.4.

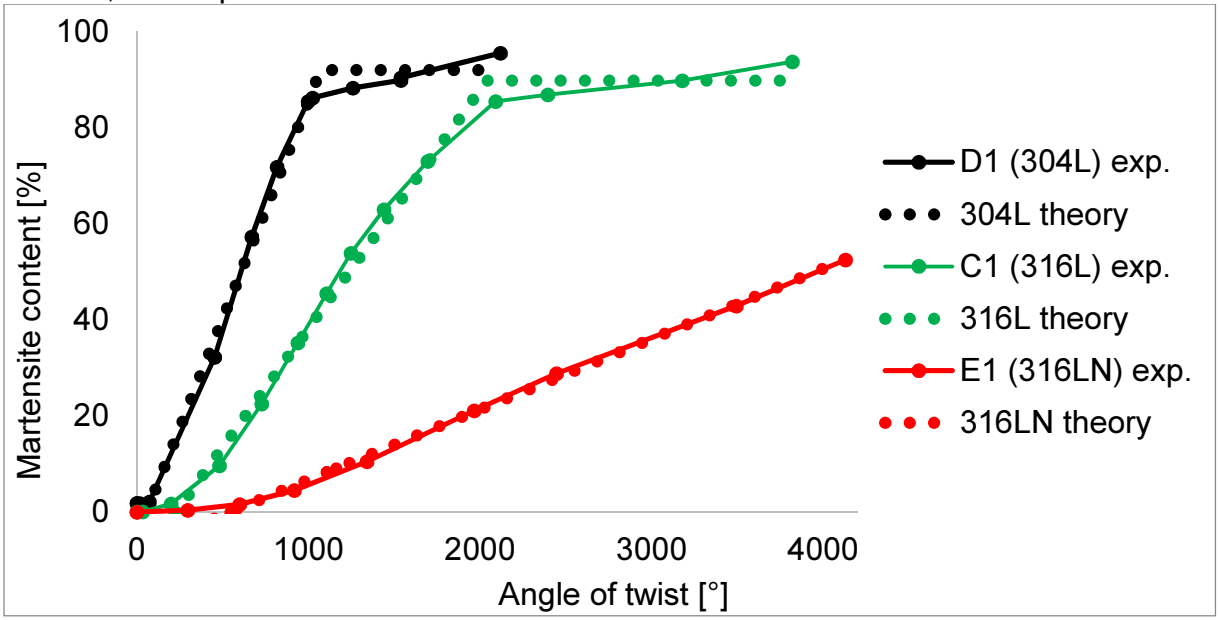

Figure 8.5. Experimental data versus theoretical kinetics of phase transformation, measured and plotted for grades 304L, 316L and 316LN

Good correlation between the linear kinetics and the experimental results was obtained, especially for 316LN stainless steel. For grades 304L and 316L, the saturation level slightly differed from the experimental results, for which rather bilinear behavior was obtained.

8.3. Torque versus the angle of twist, theory and experiment

8.3.1. Identification for grade 304 stainless steel

Two parameters of the constitutive model (A,γ_ξ) were identified, based on the measurements of the volume fraction of martensite within the cross section. The remaining parameters were identified based on the torque versus the angle of twist measurements $(E_a,h,C_{a0},\ \tau_0)$. The Poisson ratio was assumed $\nu_a = 0.5$, like for incompressible plastic materials. All the parameters are presented in Table 8.4, for temperatures 77K and 293K.

Temperature [K]	E_a [MPa]	ν_a [-]	τ_0 [MPa]	C_{a0} [MPa]	h [-]	A [-]	γ_ξ [-]
77	1.95e11	0.5	490	1100	0.5	1.95	0.01
293	1.95e11	0.5	370	350	0.1	0.2	0.02

Table 8.4. Parameters of the constitutive model at 77K and 293K, for grade 304 ss

Based on the parameters listed in Table 8.4, other secondary parameters have been calculated, like the shear modulus G_a, the shear stress at the beginning of the phase transformation τ_ξ, the unit angles of twist: at the end of the elastic range (θ_0), at the beginning of the phase transformation range (θ_ξ) and the maximum one (θ_{max}), corresponding to the shear strain limit of the model (γ_{max}).

Also, the values of the angle of twist (φ_0, φ_ξ, φ_{max}), corresponding to the until angles of twist (θ_0, θ_ξ, θ_{max}), were obtained. All of these parameters are presented in Tables 8.5 and 8.6.

Temperature [K]	G_a [GPa]	τ_ξ [MPa]	γ_0 [-]	γ_{max} [-]	R [m]	L [m]
77	650	492.7	7.54E-03	0.3464	0.004	0.2
293	650	375.0	5.69E-03	0.3464	0.004	0.2

Table 8.5. Secondary parameters of the constitutive model for 304 ss

Temperature [K]	θ_0 [1/m]	θ_ξ [1/m]	θ_{max} [1/m]	φ_0 [°]	φ_ξ [°]	φ_{max} [°]
77	1.885	2.5	86.60	21.6	28.7	992.4
293	1.423	5.0	86.60	16.3	57.3	

Table 8.6. Secondary parameters of the model including the angle of twist and the unit angle of twist

Parameters $B_1 \div B_8$, defined in Eqs. (4.74 ÷ 4.81), were listed for both temperatures in Table 8.7.

Temperature [K]	77	293
B_1	-4075963.8	-1.70E+09
B_2	1614700.3	338669064
B_3	6176.88	134927.9
B_4	97.91842	121.863
B_5	-0.111303	0.011719
B_6	0.000115	7.5063E-07
B_7	211049611	4.2503E+11
B_8	-94.51629	-215.02456

Table 8.7. Parameters $B_1 \div B_8$ defined by Eqs (4.74 ÷ 4.81) for 304 ss

Based on the equations of the torque versus the unit angle of twist (Eq. 4.64 for M_I, Eq. 4.67 for M_{II} and Eq. 4.73 for M_{III}), and the parameters listed in Tables 8.4 and 8.7, the theoretical prediction for temperature 293K is plotted in Fig. 8.6.
In the equations, the unit angle of twist was assumed constant according to Eq. (4.56) ($\theta = \varphi/L$), such that the torque was expressed as a function of the angle of twist.

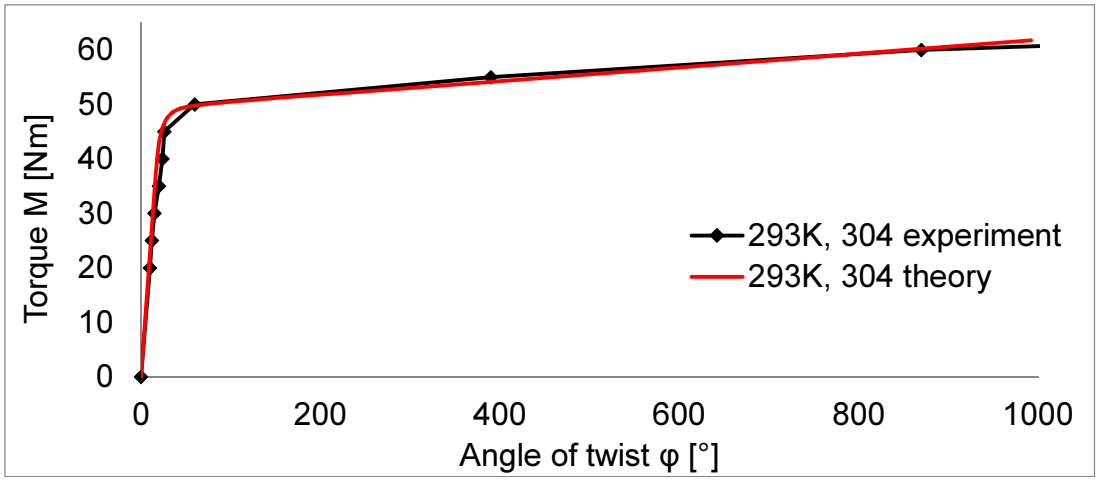

Figure 8.6. Theoretical and experimental functions of the torque versus the angle of twist for 304 ss at 293K

It is important to keep in mind, that the constitutive model has a limitation related to the small strains framework. For this reason, the maximum angle of twist was limited to 992° (see Tab. 8.6). In order to describe the complete curve of the torque versus the angle of twist until rupture, large strain framework is required. Yet, this has not been considered in the present work. It is a subject of a separate study.
There is very good agreement between the experimental and the theoretical results presented in Fig. 8.6, in the range up to about 1000° (almost 3 full rotations).
In the same manner, the torque was plotted for the liquid nitrogen temperature (77K) in Fig. 8.7. The black line represents the theoretical function, whereas, 4 color lines represent different experimental results. Namely, for sample 4 loaded until rupture (Tab.5.2), and samples 5.1, 6.1 and 7.1 loaded until 120Nm. The experimental results differ from each other. This may be attributed to:

- variation of the chemical composition between the samples,
- slight difference in the loading programs, which started from 40Nm for samples 5.1, 6.1 and 4, and from 20Nm for sample 7.1.

The parameters of the theoretical model have been identified such, that the resulting function was located between the experimental results. Yet, the approximation was still good, with the discrepancy not higher than 10%.

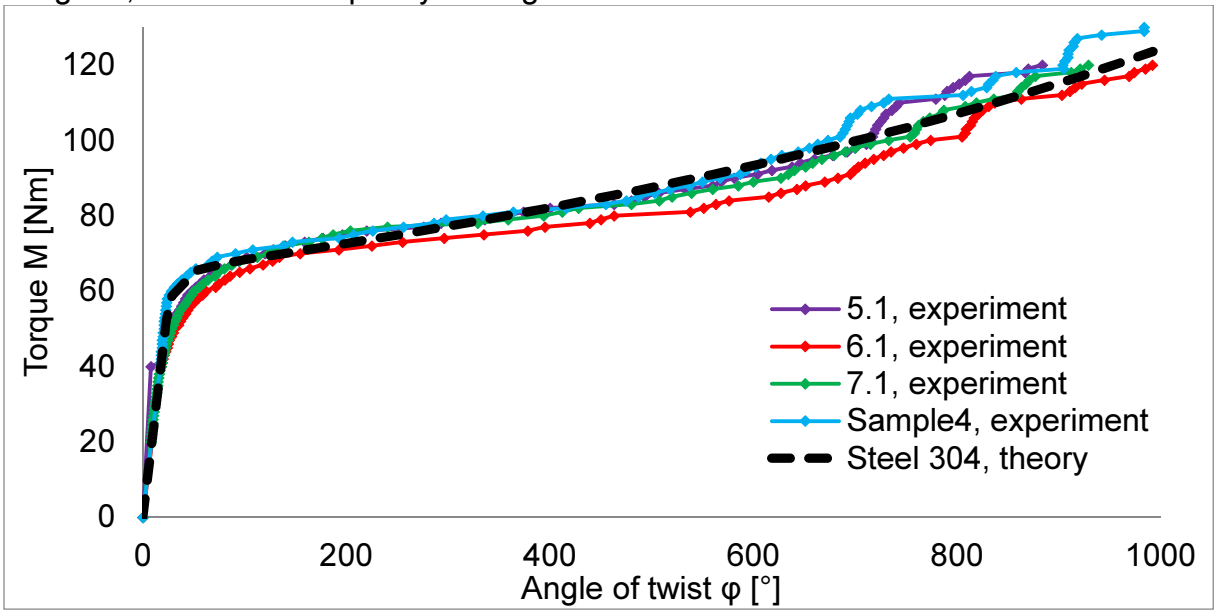

Figure 8.7. Theoretical and experimental functions of the torque versus the angle of twist at 77K

8.3.2. Identification for grades 304L, 316L, and 316LN ss

In the same manner like for 304 stainless steel, the parameters of the constitutive model (E_a,h, C_{a0}, τ_0) were identified to best fit the experimental results of the torque versus the angle of twist. All the parameters, including the parameters of the kinetics of phase transformation, were summarized in Tab. 8.8 for grades 304L, 316L, and 316LN. Additional secondary parameters, based on the parameters from Tab. 8.8, are shown in Tabs 8.9 and 8.10.
The parameters $B_1 \div B_8$, defined in Eqs (4.74 ÷ 4.81), are listed in Tab. 8.11.

Temperature 77K								
Steel	E_a	ν_a	τ_0	C_{a0}	h	A	γ_ξ	ξ_L
	[MPa]	[-]	[MPa]	[MPa]	[-]	[-]	[-]	[%]
304L	1.95e11	0.5	420	1400	0.2	2.6	0.02	91.9
316L	1.95e11	0.5	400	990	0.5	1.42	0.08	89.8
316LN	1.95e11	0.5	610	890	0.1	0.42	0.19	-

Table 8.8. Parameters of the constitutive model at 77K, for 304L, 316L, and 316LN ss

Temperature 77K						
Steel	G_a	τ_ξ	γ_0	γ_{max}	R	L
	[GPa]	[MPa]	[-]	[-]	[m]	[m]
304L	650	439.0	64.6E-03	0.3464	0.004	0.2
316L		473.1	61.5E-03			
316LN		770.7	93.8E-03			

Table 8.9. Secondary parameters of the constitutive model for 304L, 316L, and 316LN ss

Temperature 77K						
Steel	θ_0	θ_ξ	θ_{max}	φ_0	φ_ξ	φ_{max}
	[1/m]	[1/m]	[1/m]	[°]	[°]	[°]
304L	1.615	5	86.60	18.5	57.3	992.4
316L	1.538	20		17.6	229.2	
316LN	2.346	47.5		26.9	544.3	

Table 8.10. Secondary parameters of the model related to the angle of twist and the unit angle of twist, for 304L, 316L, and 316LN ss

Parameter	304L	316L	316LN
B_1	-3787008.231	-94720814.03	-5307844363
B_2	738512.884	4490112.516	107561989.3
B_3	3650.443913	11451.07718	83674.82037
B_4	82.89988347	105.0582804	188.2281803
B_5	-0.000975821	-0.10329436	0.029348192
B_6	7.80656E-05	7.53741E-05	4.00837E-06
B_7	74703418.65	880315017.2	69134188144
B_8	-72.17607737	-116.8141494	-260.36988

Table 8.11. Parameters $B_1 \div B_8$, defined by Eqs (4.74 ÷ 4.81), for 304L, 316L, and 316LN ss

Based on Eqs 4.64, 4.67, 4.73 for the torque versus the unit angle of twist, including Eq. 4.56, the theoretical results are compared to the experimental ones for grade 304L in Fig. 8.8. Good agreement has been obtained, with a few Nm maximum difference between the points.

The results for grades 316L and 316LN are compared in Fig. 8.9. For both materials good agreement has been found between the experiment and the theory. Only at the end of elastic range, the theoretical results were substantially greater than the experimental ones. In the plastic range, very good agreement was obtained, especially for 316L stainless steel.

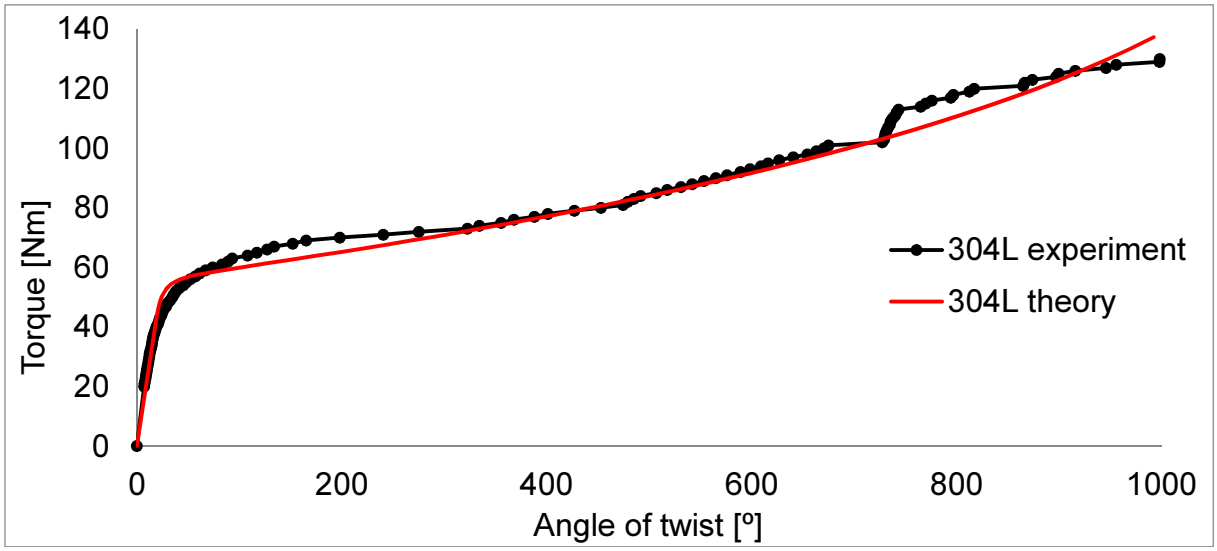

Figure 8.8. Torque versus the angle of twist, experimental and theoretical results for 304L stainless steel

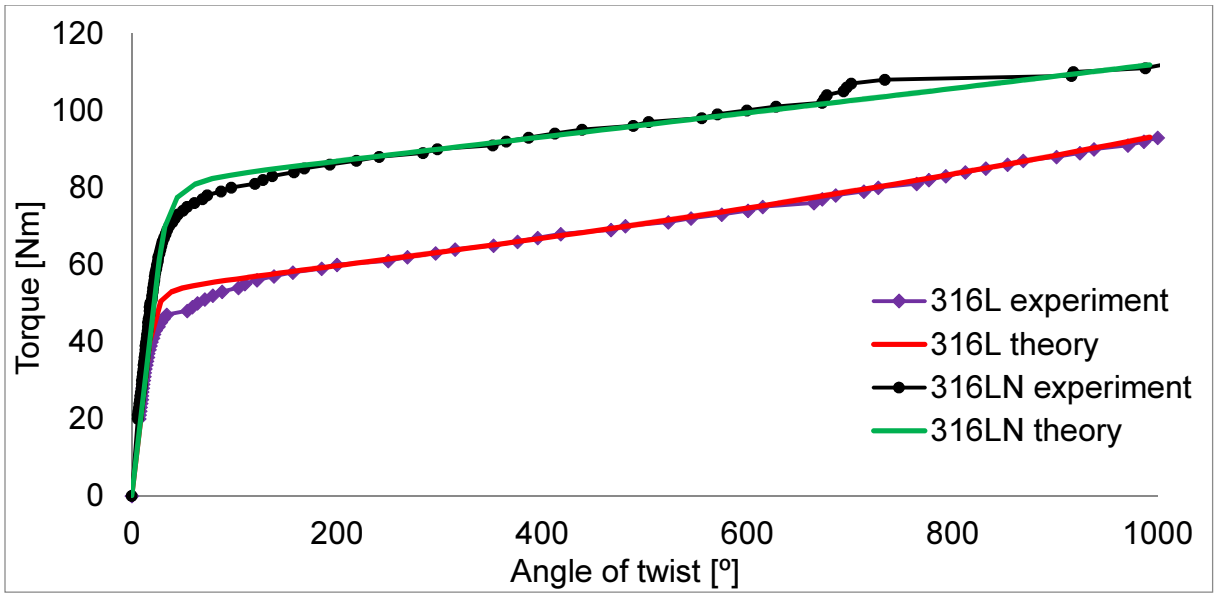

Figure 8.9. Torque versus the angle of twist, theoretical and experimental results for grades 316L and 316LN

8.4. Prediction of stress versus strain based on the constitutive model

8.4.1. Prediction for grade 304 ss

In the course of experimental work, the torque versus the angle of twist was measured. Thanks to the constitutive model, one can calculate the stress versus strain relationship, as well.

One has to recall, that the model has its limitation with respect to maximum strain, which is $\varepsilon_{max} = 0.2$, thus, $\gamma_{max} = 0.34$. Taking into account the geometry of the sample, the limit angle of twist was equal to $\varphi_{max} = 992°$. In conclusion, this part of the experimental results was simulated only. The same was true for the stress versus strain calculations, limited to $\gamma_{max} = 0.34$. Still, these calculations provide useful information about the state of stress during twisting.

The equations derived for the shear stress versus shear strain, were derived in Chapter 4, where closed form analytical solutions were found (see Eqs 4.46 ÷ 4.48).

However, these equations were derived using simplified expression for the homogenized modulus C_{a+m}. Having defined the parameters of the model, one can numerically evaluate the exact formula with no simplifications (Eq. 4.87), as well. In order to do so, two more parameters of the model are needed: the Young modulus of pure martensite and the Poisson ratio of pure martensite. These parameters are listed in Tab. 8.12. The Young modulus was assumed the same like for the austenitic phase, and the Poisson ratio was assumed like for standard low ductility steels. Both moduli do not substantially evolve at cryogenic temperatures.

Steel 304	
$E_m\ [MPa]$	$\nu_m\ [-]$
$E_m = E_a = 1.95 \cdot 10^5$	0.3

Table 8.12. Parameters of the martensitic phase, for grade 304 ss

Both curves of shear stress versus shear strain, calculated including the simplified formula and using the exact approach, are presented in Fig. 8.10. The exact results have been calculated using Mathematica software, based on numerical integration of Eq. 4.87.

The results illustrated in Fig. 8.10 indicate that the simplified and the exact formulae lead to almost the same values for both temperatures. This fact validates the correctness of simplification of the modulus C_{a+m} (see Chapter 4), and closed form analytical formulae for the shear stress versus shear strain.

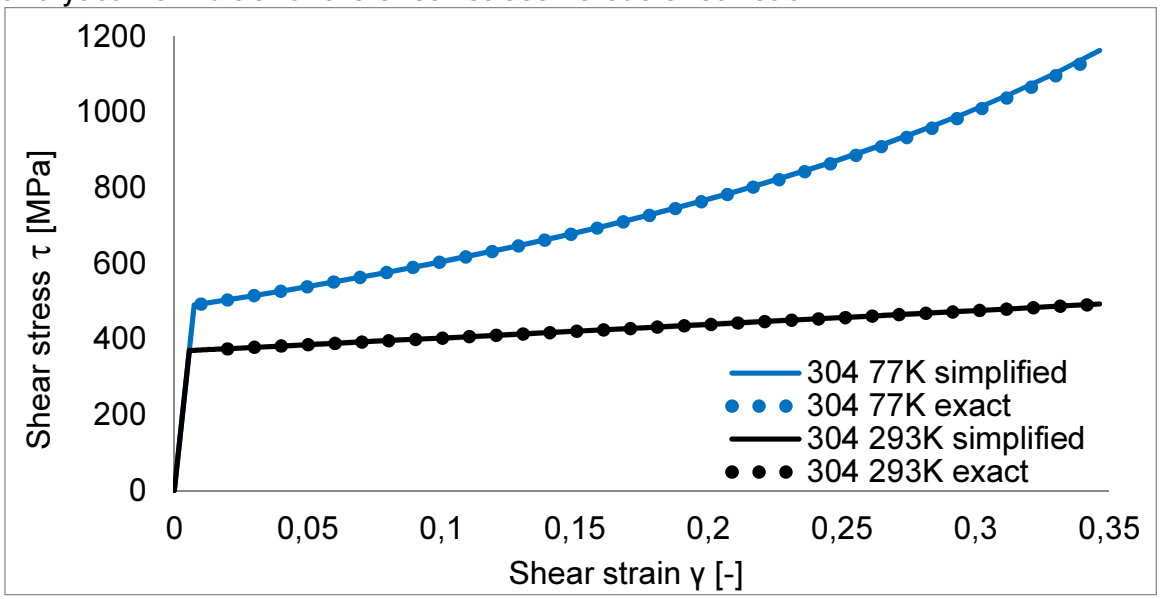

Figure 8.10. Shear stress versus shear strain at 77K and 293K for 304 ss, calculated from simplified (Eqs 4.46÷4.48) and exact formulae (Eq. 4.87)

It turns out from Fig. 8.10, that at 293K the function of stress versus strain has bilinear character. Its maximum reaches 490 MPa. On the other hand, much higher stress of 1140 MPa is reached at 77K, with nonlinear increase of stress versus the shear strain.

8.4.2. Prediction for grades 304L, 316L, and 316LN

Similarly to the procedure described in the previous section (8.4.1), based on the parameters identified for grades 304L, 316L, 316LN, the stress versus strain is plotted in Fig. 8.11.

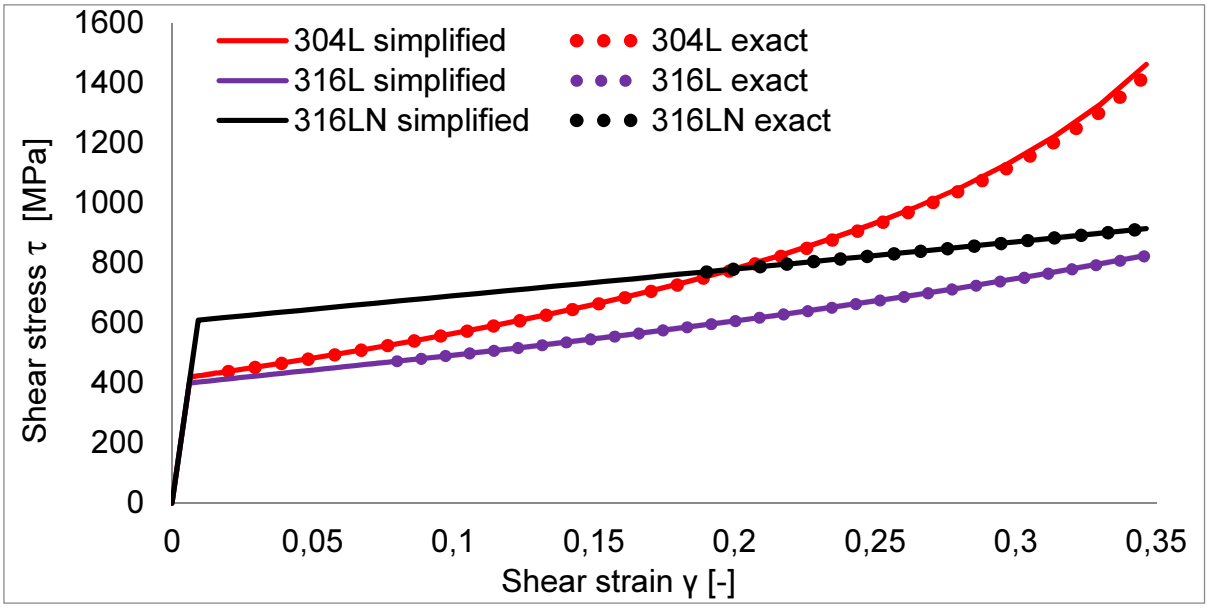

Figure 8.11. Shear stress versus shear strain at 77K for steels 304L, 316L, and 316LN

For grade 316L nearly bilinear character of the curve shown in Fig. 8.11 was found, with a maximum of 826 MPa at $\gamma = 0.34$. Slightly higher maximum stress (914 MPa) was obtained for 316LN stainless steel. The highest stress of 1460 MPa was obtained for grade 304L, where strong nonlinear increase is clearly visible.
For all the results shown in Fig. 8.11, the exact and simplified curves are almost the same. Thus, the same conclusion is drawn as for 304 stainless steel (Fig. 8.10), that the simplified formulae for the stress versus strain introduce negligible error. Their validity is therefore confirmed.

8.5. Error estimation for the exact and simplified formulae C_{a+m}

In the previous section shear stress was calculated based on parameters of the model. Both simplified and exact formulae were used. In the present section explicit comparison is made between the simplified and exact functions of modulus $C_{a+m}(\gamma)$. Difference between them is sought to validate assumed simplifications (see section 4.3.3).
In the course of Chapter 4 the simplified expression for the homogenized tangent stiffness modulus C_{a+m} was derived (Eq. 4.41). Simplified formula was compared to the exact one ($C_{(a+m)Ex}$, Eq. 4.84 with Eq. 4.85) within the shear strains range from γ_ξ and γ_{max} (0.34).
The functions $C_{a+m}(\gamma)$ and $C_{(a+m)Ex}(\gamma)$ were plotted after inserting numerical values of the parameters of the constitutive model listed in Tab. 8.4 for 304 ss at 77K and 293K and in Tab. 8.8 for grades: 304L, 316L and 316LN at 77K.
The results for 304L stainless steel were showed in Fig. 8.12, for steels 316L (77K) and 304 (77K) in Fig. 8.13 and for steels 316LN (77K) and 304 (293K) in Fig. 8.14.

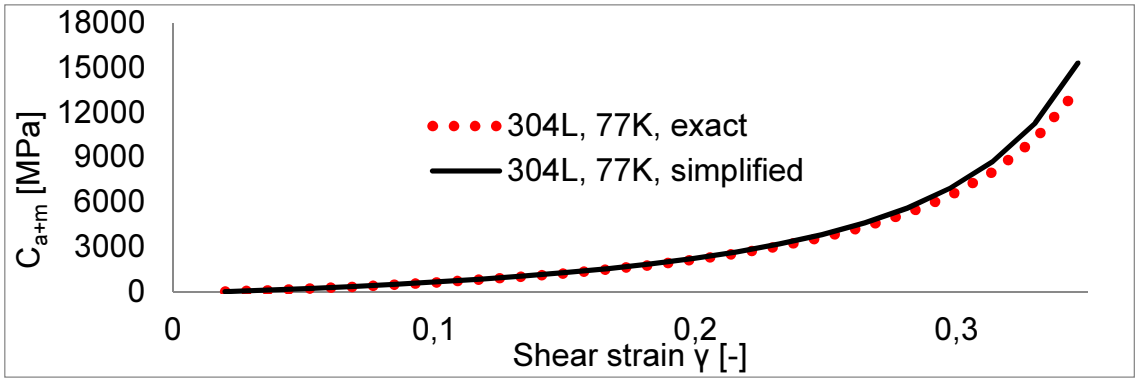

Figure 8.12. Homogenized module C_{a+m}; simplified (Eq. 4.41) and exact (Eq. 4.21), grade 304L, 77K

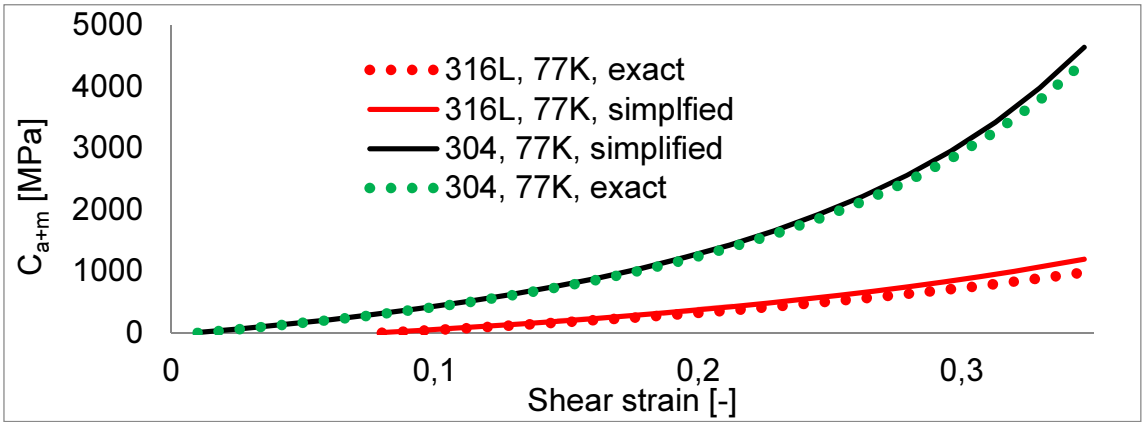

Figure 8.13. Homogenized module C_{a+m}; simplified (Eq. 4.41) and exact (Eq. 4.21), grade 316L and 304, 77K

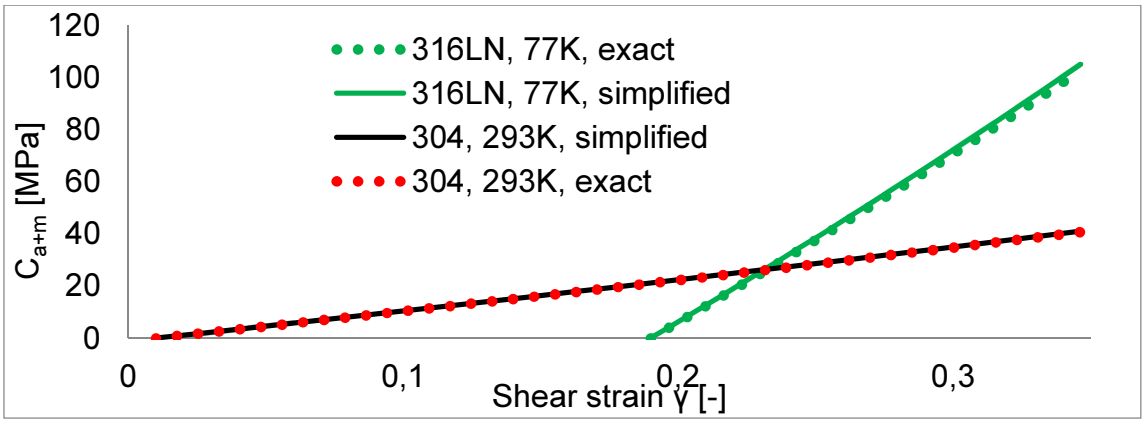

Figure 8.14. Homogenized module C_{a+m}; simplified (Eq. 4.41) and exact (Eq. 4.21), grade 316LN - 77K, 304 – 293K

The highest values of the module $C_{a+m}(\gamma)$ is obtained for grade 304L – some 15000 MPa, then for grade 304 – abut 4600 MPa, about 1200 MPa for 316L. Much smaller values are obtained for 316LN ss – about 100 MPa and for 304 ss at 293K – only about 40MPa.

Good convergence is obtained for all the presented result (Figs 8.12 ÷ 8.14). Thus for the identified values of parameters of the model (Tab. 8.4, 8.8), simplified and exacts formulae for modulus $C_{a+m}(\gamma)$ are reasonably similar. This proves validity of the simplified formula.

8.6. Error estimation for the exact formulae of the torque versus the angle of twist

8.6.1. Error estimation for grade 304 stainless steel

In order to evaluate the correctness of the calculated function of the torque versus the angle of twist (Eq. 4.73), a comparison with the exact formula (Eq. 4.89) has been performed. The calculation was performed using Maple software. The function was integrated within 30 points. Both plots are presented in Fig. 8.15, for grade 304 stainless steel.

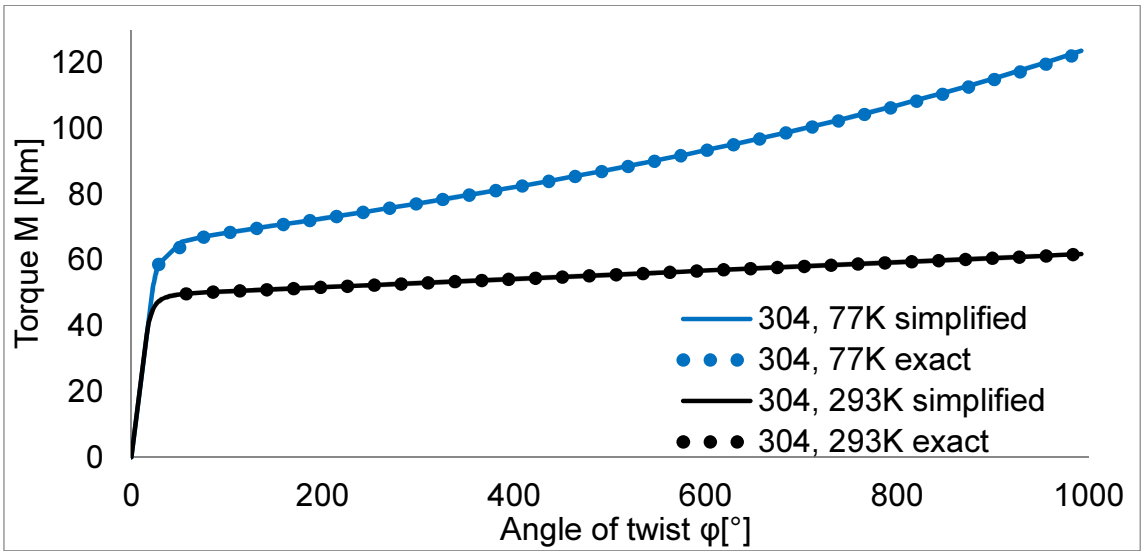

Figure 8.15. Torque versus the angle of twist for 77K and 293K, calculated using the simplified (Eq. 4.73) and the exact formulae (Eq. 4.89)

Similarly to the stresses, the differences between the simplified and the exact formulae were very small. Thus, the simplified analytical formulae were confirmed to be reasonably precise.

8.6.2. Error estimation for grades 304L, 316L, and 316LN

Similarly to the previous section, the results of the torque versus the angle of twist are compared for simplified (Eq. 4.73) and exact (Eq. 4.89) formulae. The results for three steels: 304L, 316L, and 316LN, are summarized in Fig. 8.16.

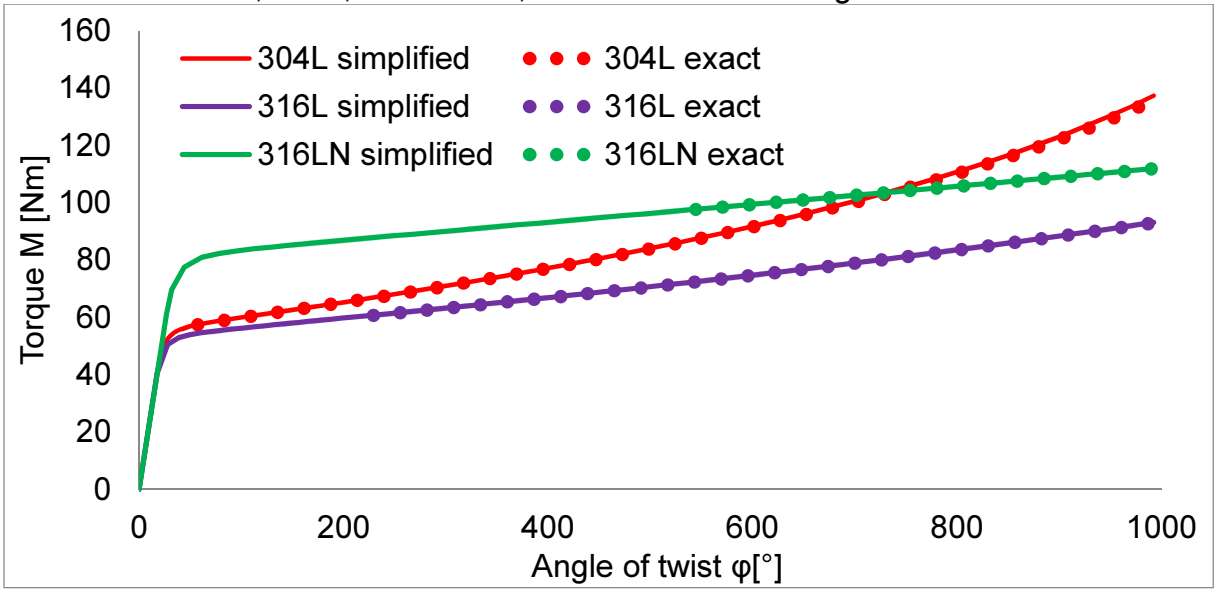

Figure 8.16. Torque versus the angle of twist, simplified (Eq. 4.73) and exact (Eq. 4.89) formulae for steels 304L, 316L, and 316LN

Again, it turns out from Fig. 8.16, that the results are very similar for the exact and the simplified formulae. This proves validity of the simplified closed form analytical solution for the torque versus the angle of twist (Eq. 4.73).

8.6. Conclusions

In the light of the above analysis, the following conclusions are drawn:

- good agreement between the experimentally measured kinetics of the plastic strain induced phase transformation, and the theoretical model for steels: 304, 304L, 316L, and 316LN, was obtained,
- good correlation for the torque versus the angle of twist between the experimental results and the theoretical ones (in the range up to 992 angular degrees) was obtained,
- simplified analytical equations for the torque versus the angle of twist, as well as the stress versus strain, proved to be almost equal to the exact formulae (which were treated by means of numerical methods because of their complexity).

9. Cyclic torsion of round bars at 77K and 293K

9.1. Introduction

A series of cyclic torsion tests has been carried out. The aim was to evaluate material behavior and the phase transformation under cyclic torsional loading. Cyclic torsion was performed at room temperature (293K), and at the liquid nitrogen temperature (77K). Several grades of austenitic stainless steels were tested, namely 304, 304L, 316L, and 316LN.

One of the most important purposes of these experiments was to verify the possibility of controlling the martensite content and its distribution within cross-section, via cyclic torsion. There is two possible ways of introducing plastic strains into the sample, by monotonic and by cyclic torsion. In the case of monotonic torsion, predefined angle of twist has to be reached, whereas, for cyclic torsion the same predefined angle of twist can be obtained by application of several cycles of known amplitude. Thus, it is important to verify the latter possibility via series of cyclic torsion tests.

In order to capture the micro-structural changes from the austenitic phase to the martensitic one, the measurements of martensite content were performed by using the Feritscope. After each half cycle (denoted “hf” in the plots) of the test, the sample was removed from the clamping system and the martensite content was measured on the surface. The measurements were carried out along four axial lines and at several points (Fig. 7.2), thus, axial distribution of martensite content on the surface of the sample was obtained. Combining all the half cycles (usually 20), the evolution of the content of martensite was captured during all cycles.

The methods of measuring the torque and the angle of twist, as well as the martensite content, were the same like in the monotonic torsion tests, described in Chapters 5 and 7.

9.2. Plan of the measurements

Set of samples, made of four grades of austenitic stainless steel, were tested: 304, 304L, 316L, and 316LN. The parameters of loading are presented in Tabs 9.1 and 9.2. Some 10 samples made of 304 stainless steel were tested: 5 of them were loaded by applying torque control (±60Nm at 293K, ±60Nm at 77K, ±70Nm at 77K, ±80Nm at 77K, ±100Nm at 77K), and 3 samples were loaded by using kinematic control (±60° at 77K, ±180° at 77K and ±180° at 293K). One sample was loaded with the first cycle to 90°, and then by cycles ±90°. Finally, one sample was loaded at 77K with asymmetric cycles (sample A10).

Regarding the samples made of 304L, 316L and 316LN steels, 3 samples of each material were tested. All of them were tested by applying torque control at the liquid nitrogen temperature, with the amplitudes of ±70Nm, ±80Nm and ±100Nm.

The following goals of these tests were defined:

- measuring the evolution of martensite on the surface during cyclic loading,
- checking the possibility of creating Functionally Graded Structural Members by means of cyclic torsion, via much smaller amplitudes of the angle of twist,
- monitoring the distortion of the samples during cyclic loading,
- checking in the course of torque control the possibility of the material to plastically adapt (shakedown),
- measuring in the course of cyclic loading the hardening on cycle.

Lp	Symbol	Material	Temperature	Number of cycles	Loading control	
					M [Nm]	φ [°]
1	A1	304	77 K	10	± 70 Nm	-
2	A2	304	77 K	10	± 80 Nm	-
3	A3	304	77 K	10	± 60 Nm	-
4	A4	304	77 K	10	± 100 Nm	-
5	A5	304	77 K	3	-	± 180°
6	A6	304	77 K	10	-	± 60°
7	A7	304	293 K	10	-	± 180°
8	A8	304	293 K	10	± 60 Nm	-
9	A9	304	293 K	10	-	90° ± 90
10	A10	304	77 K	3	-	Non-symmetric
10	C2	316L	77 K	10	± 100 Nm	-
11	C3	316L	77 K	10	± 80 Nm	-
12	C4	316L	77 K	10	± 70 Nm	-
13	D2	304L	77 K	10	± 100 Nm	-
14	D3	304L	77 K	10	± 80 Nm	-
15	D4	304L	77 K	10	± 70 Nm	-
16	E2	316LN	77 K	10	± 100 Nm	-
17	E3	316LN	77 K	10	± 80 Nm	-
18	E4	316LN	77 K	10	± 70 Nm	-

Table 9.1. Parameters of samples for the cyclic torsion tests

In the subsequent section, all the experimental results are shown. The results are presented in the following order:

- samples made of 304 stainless steel
- samples made of 316L stainless steel
- samples made of 304L stainless steel
- samples made of 316LN stainless steel

The results in terms of the torque versus the angle of twist, as well as the evolution of the martensite content on the surface, are presented as well. Later on, in section 9.4, the results are compared with each other to draw further conclusions. Short description is provided for each of the obtained results.

9.3 Experimental results

9.3.1. Data for 304 stainless steel

10 samples made of 304 stainless steel were twisted. The conditions of the tests are specified in Tab. 9.1. The results are presented in the following sections.

9.3.1.1. Sample A1

The results of the torque versus the angle of twist for sample A1 loaded at 77K are shown in Fig. 9.1. The first half cycle is missing because of a problem that occurred during the measurements of the torque. The subsequent cycles were correctly measured. Under the loading of ±70Nm, the maximum angle of twist was equal to 80°.

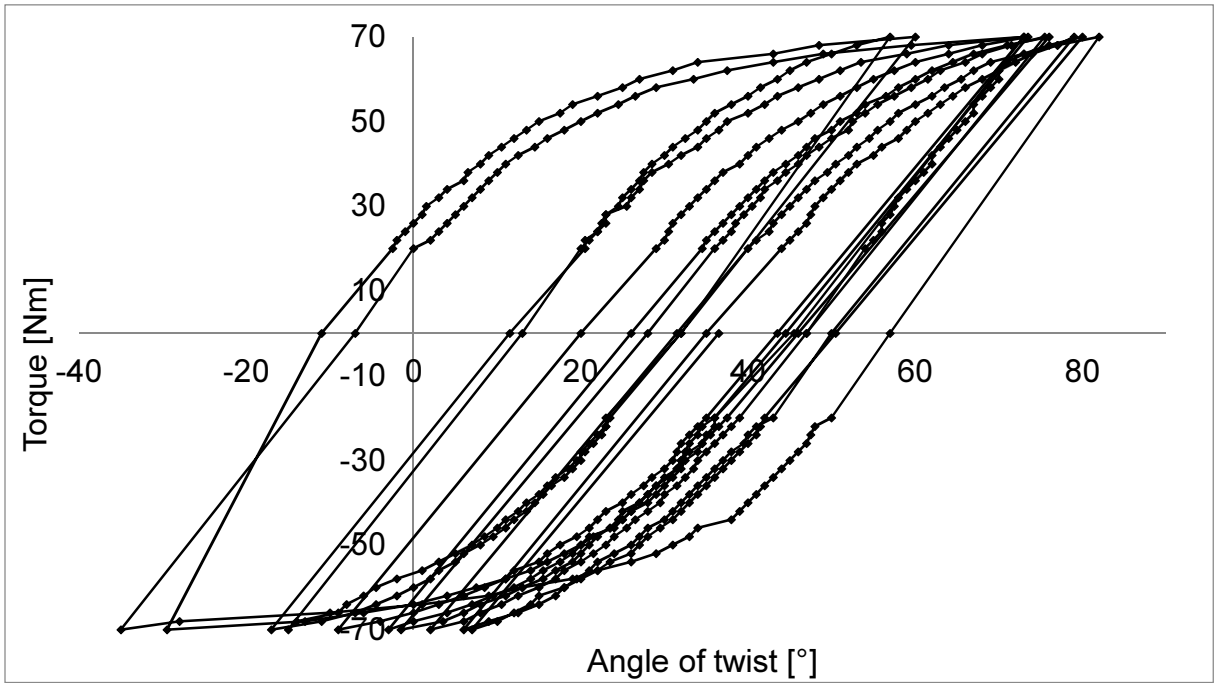

Figure 9.1. Torque versus the angle of twist for sample A1, ±70Nm, 10 cycles at 77K

Evolution of martensite content on the surface is shown in Fig. 9.2. The maximum of around 20% was reached in the course of the last cycle. The martensite content decreases from the left side of the sample towards the right end (see Figs 7.3, 7.4, where the measurement points are denoted).

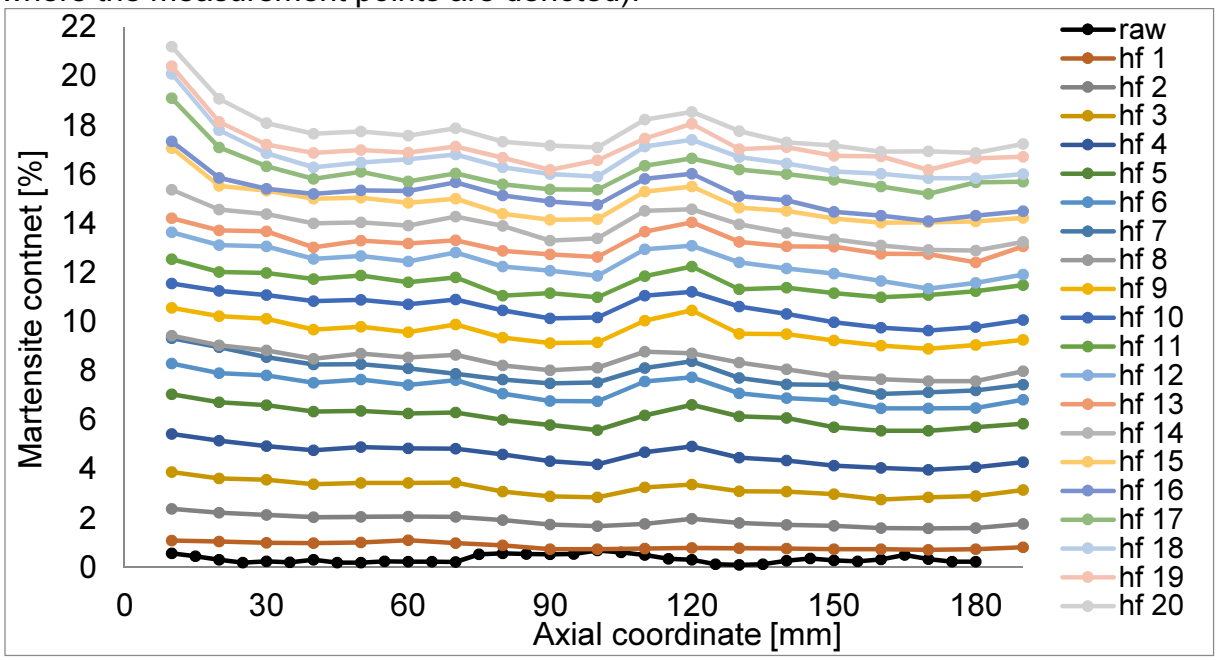

Figure 9.2. Martensite content on the surface of the sample after each half cycle, sample A1, ±70Nm, 10 cycles at 77K

9.3.1.2. Sample A2

For sample A2 loaded to ±80Nm at 77K (Fig. 9.3), the maximum angle of twist was of 242°. Constriction of the loops was clearly observed. The last few loops almost coincided with each other.

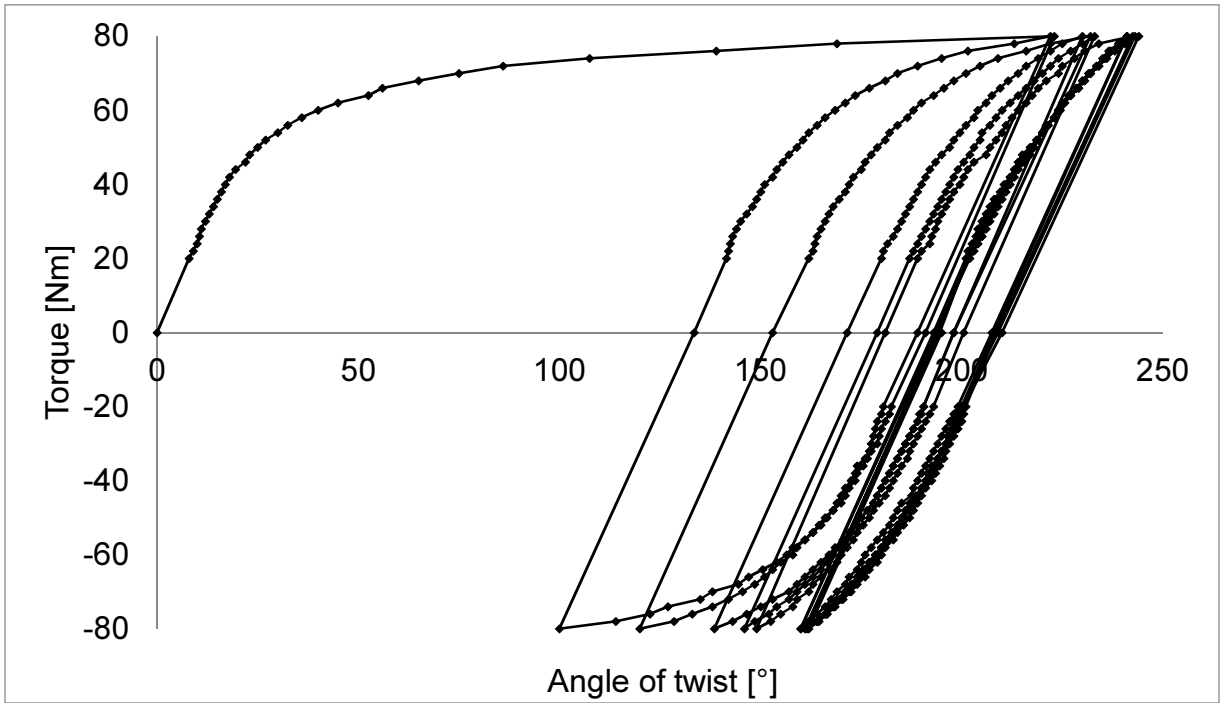

Figure 9.3. Torque versus the angle of twist for sample A2, ±80Nm, 10 cycles at 77K

Evolution of martensite content is shown in Fig. 9.4. During all measurements, some variations were observed along the axis of the sample. About 27% of martensite content was obtained after all 10 cycles. It is slightly more compared to sample A1, loaded to ±70Nm (martensite content of about 20%).

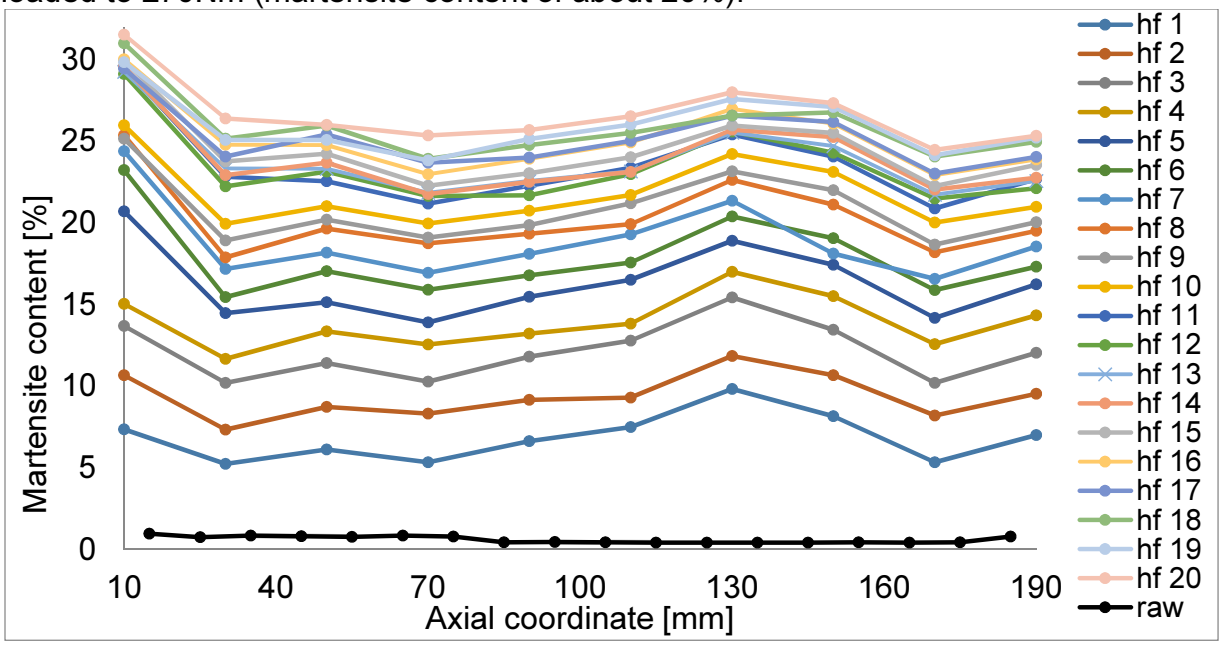

Figure 9.4. Martensite content on the surface of the sample after each half cycle, sample A2, ±80Nm, 10 cycles at 77K

9.3.1.3. Sample A3

Sample A3 was loaded at 77K to ±60Nm (Fig. 9.5). In this case, very small angles of twist were measured (39° at maximum). Yet, the elastic limit was exceeded, and the subsequent loops got narrower.

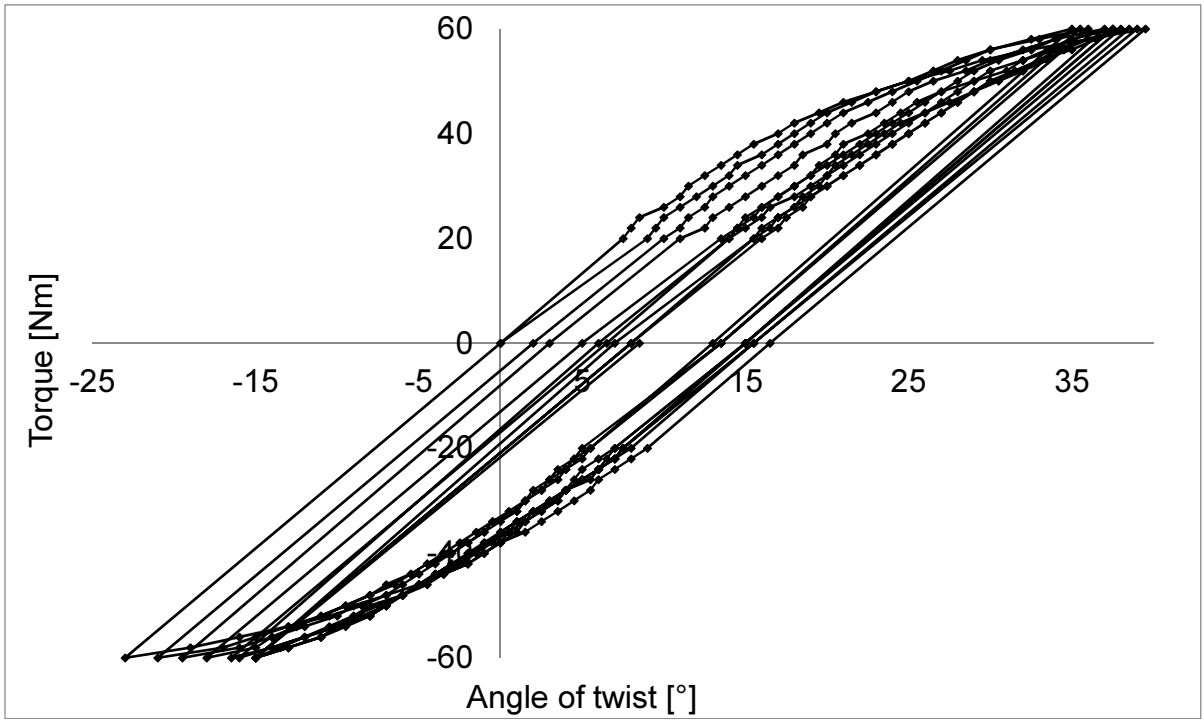

Figure 9.5. Torque versus the angle of twist for sample A3, ±60Nm, 10 cycles at 77K

The evolution of martensite content on the surface is shown in Fig. 9.6. For this sample, rather small values were obtained, i.e. 4% at maximum after all cycles. Still, progressive transformation was captured after each half-cycle, with about 0.2% increase between them. Again, higher martensite content was found near the left end of the bar compared to the right end, especially for the last few half-cycles.

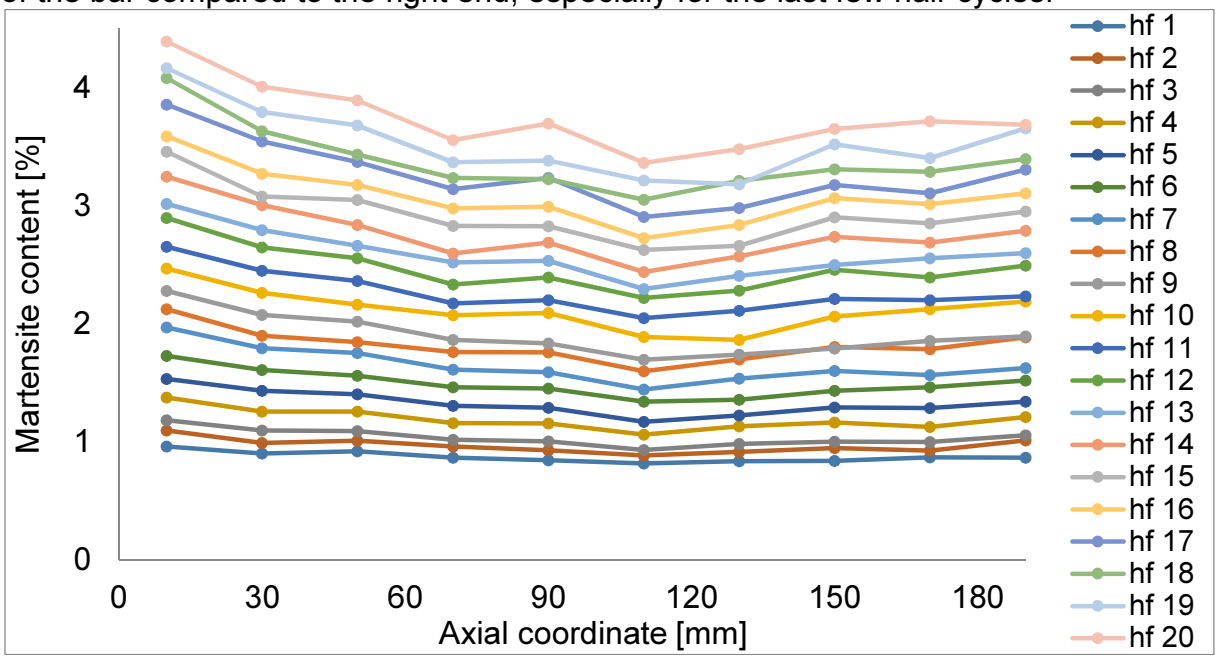

Figure 9.6. Martensite content on the surface of the sample after each half cycle, sample A3, ±60Nm, 10 cycles at 77K

9.3.1.4. Sample A4

For sample A4, loaded at 77K to ±100Nm (Fig. 9.7), the maximum angle of twist was of 719°, much higher when compared to sample A2 (±80Nm and 242°, respectively). After the first half-cycle, very narrow loops were obtained.

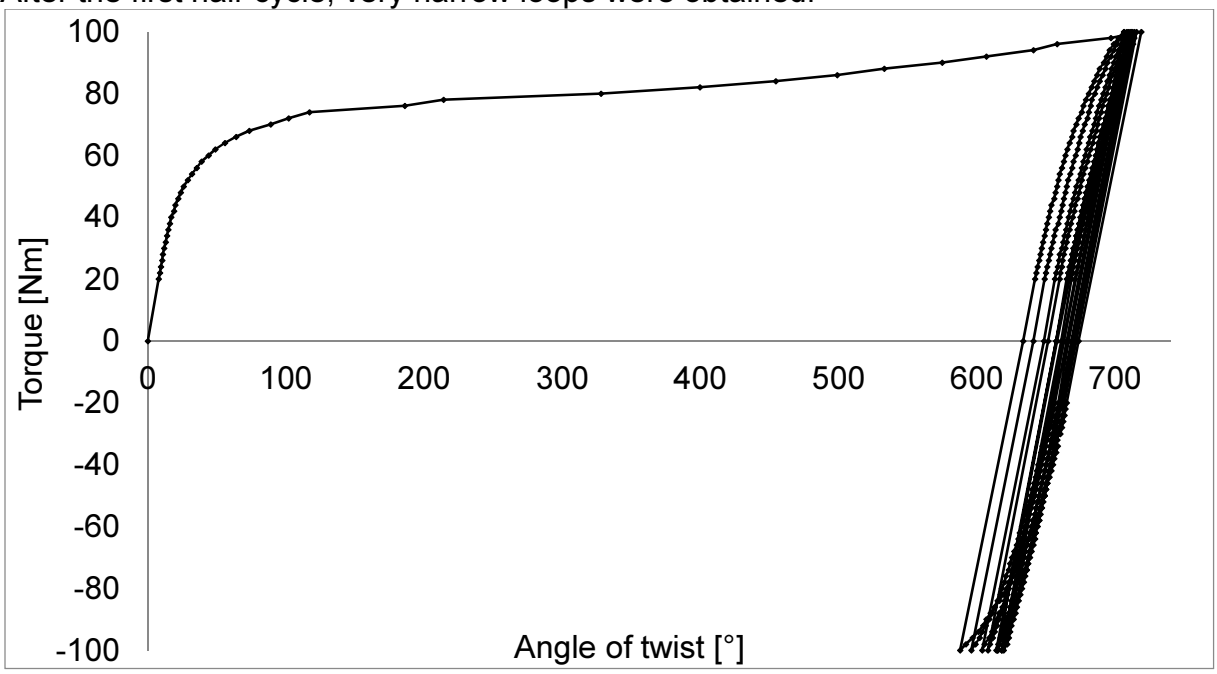

Figure 9.7. Torque versus the angle of twist for sample A4, ±100Nm, 10 cycles at 77K

The evolution of martensite content on the surface is shown in Fig. 9.8. Already after the first half-cycle, about 50% of martensite was induced. The process continued up to about 70% after all cycles. During the last few half-cycles, very small increase in martensite content was measured (overlapping curves).

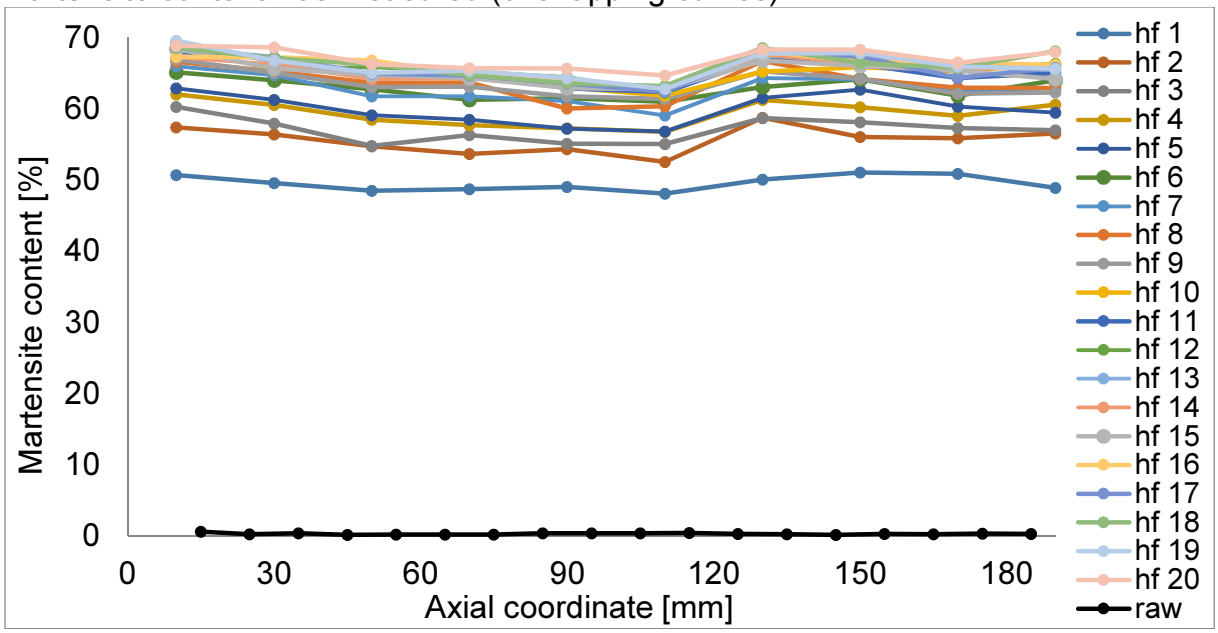

Figure 9.8. Martensite content on the surface of the sample after each half cycle, sample A4, ±100Nm, 10 cycles at 77K

9.3.1.5. Sample A5

Sample A5 was twisted at 77K under controlled angle of twist (±180°). Only 3 full cycles were performed to prevent fracture, which occurred at 157Nm (see sample 4, Tab. 5.2). Very strong hardening was observed after each half-cycle, resulting in increasing amplitude of the torque by about 25Nm.

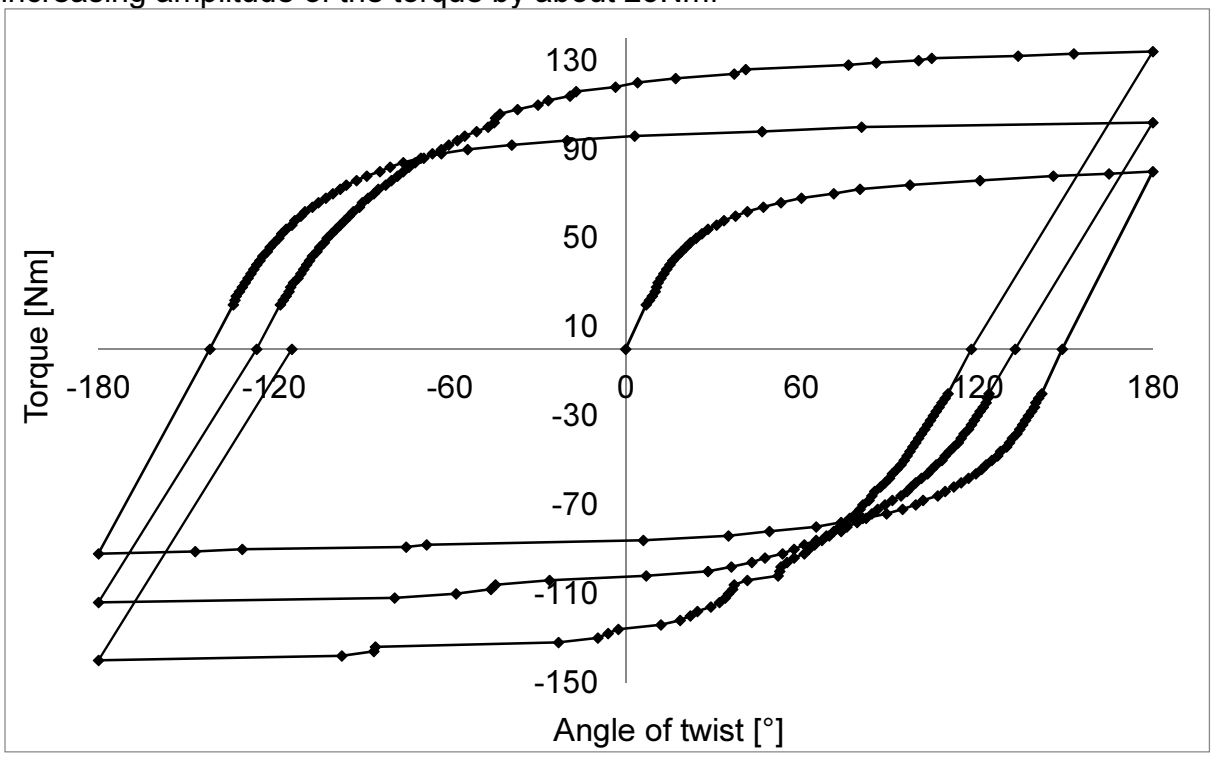

Figure 9.9. Torque versus the angle of twist for sample A5, ±180°, 3 cycles at 77K

The evolution of martensite content is shown in Fig. 9.10. After the first half-cycle, the martensite content was equal to about 4%, and was constant along the surface of the sample. After the 2nd half-cycle, it reached about 20%, then about 40% after the 3rd one, and about 58% after the 4th half-cycle. Finally, after the last one, about 85% martensite fraction was found. Thus almost full transformation occurred.

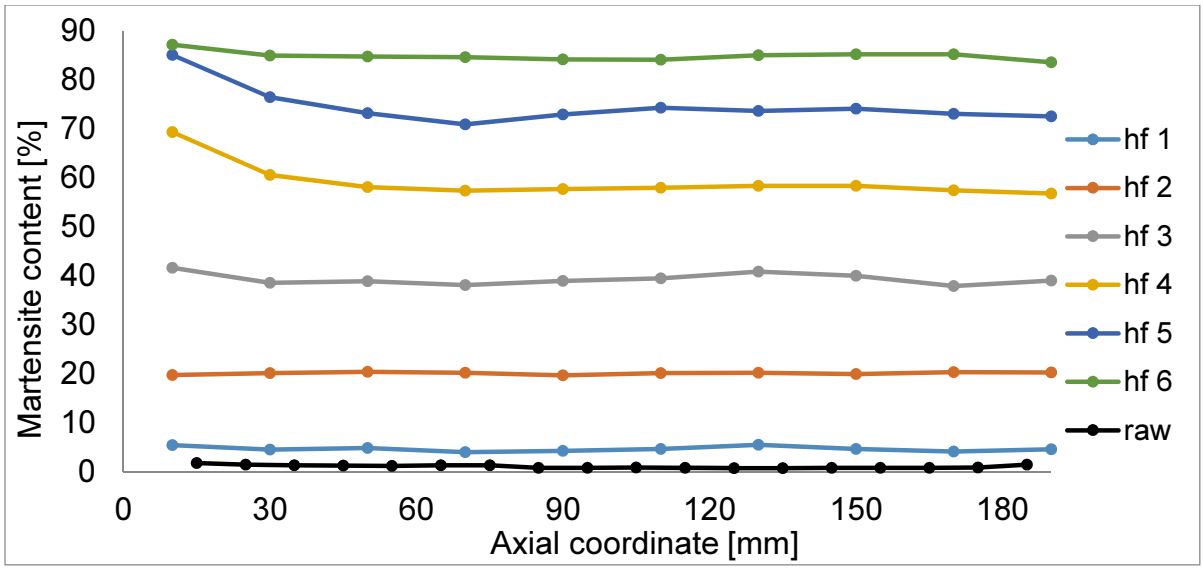

Figure 9.10. Martensite content on the surface of the sample after each half cycle, sample A5, ±180°, 3 cycles at 77K

9.3.1.6. Sample A6

Sample A6 was twisted at 77K to ±60°. Similarly to sample A5, after each half-cycle the torque amplitude was increasing from 64Nm after the first half-cycle, to 99Nm after the 20th half-cycle.

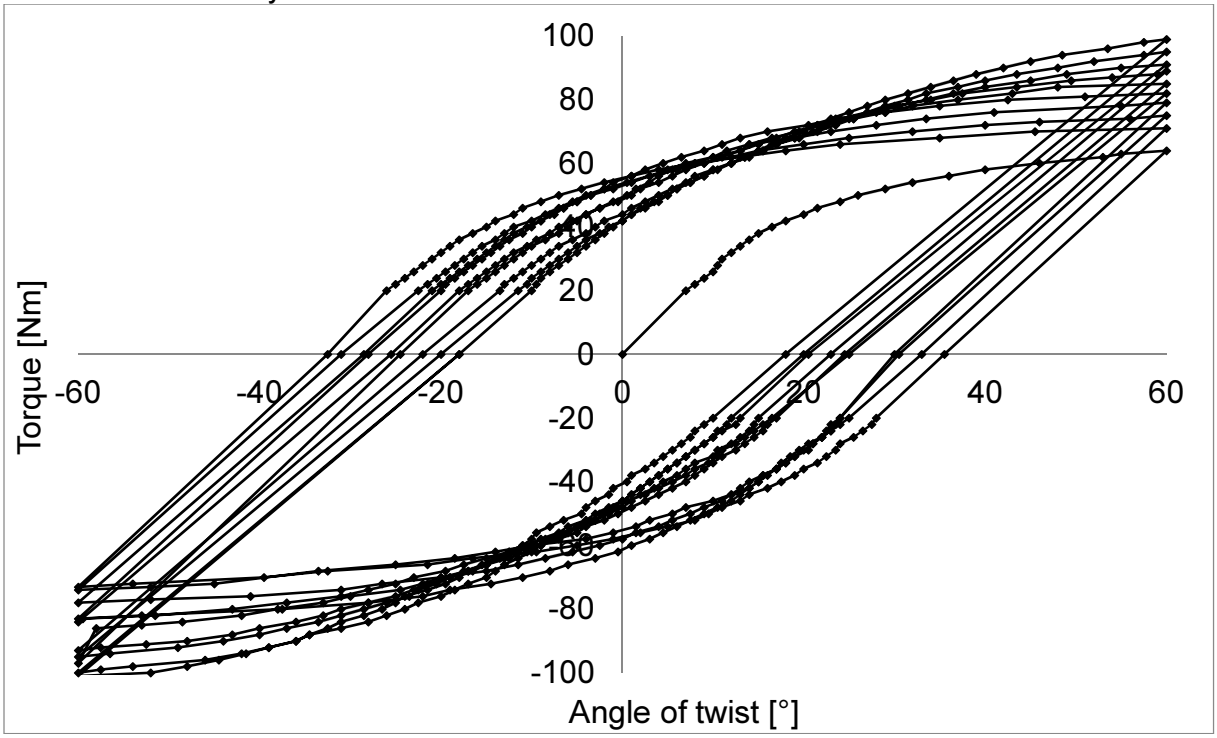

Figure 9.11. Torque versus the angle of twist for sample A6, ±60°, 10 cycles at 77K

The evolution of martensite content for sample A6 is shown in Fig. 9.12. Nearly constant values were obtained along the axis for almost all the measurements. After each half-cycle, the martensite fraction increased by some 1.5 ÷ 4 %. About 50% martensite content was obtained in the course of the test.

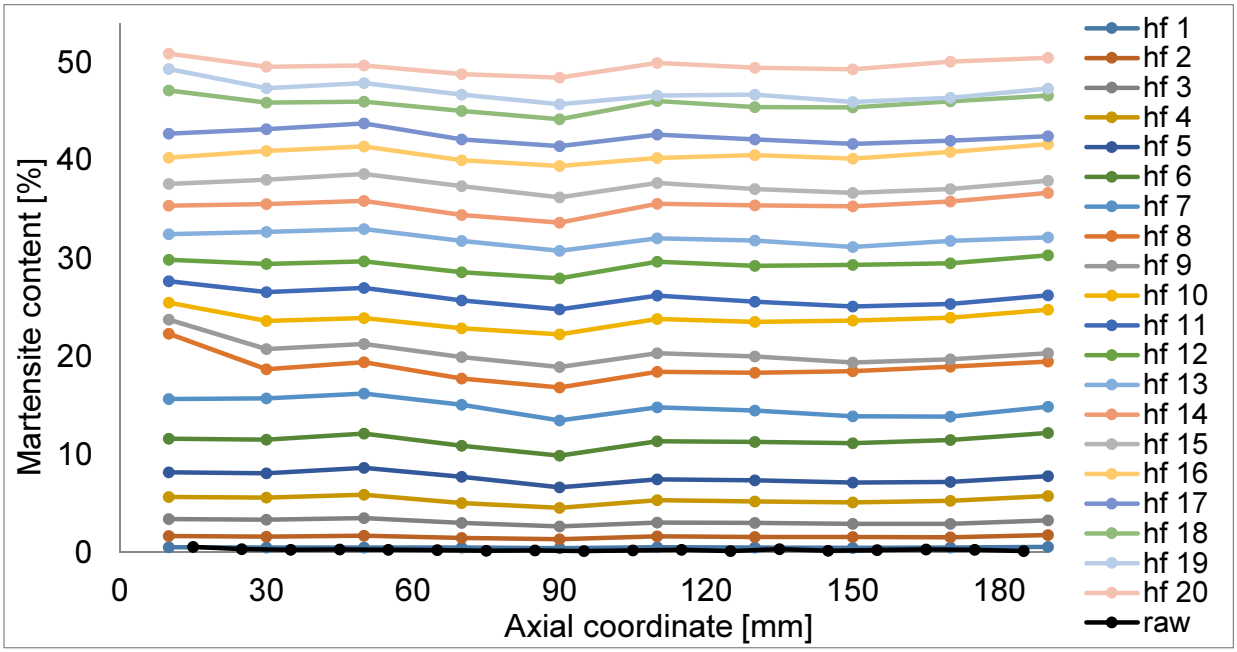

Figure 9.12. Martensite content on the surface of the sample after each half cycle, sample A6, ±60°, 10 cycles at 77K

9.3.1.7. Sample A7

Experimental results for sample A7, twisted at room temperature to ±180° are shown in Fig. 9.13. An increasing amplitude of torque was observed, but much smaller values were reached compared to the same test performed at 77K (sample A5, Fig. 9.9). For sample A7, the torque increased from 52Nm after 1st half-cycle to some 60Nm after the last one.

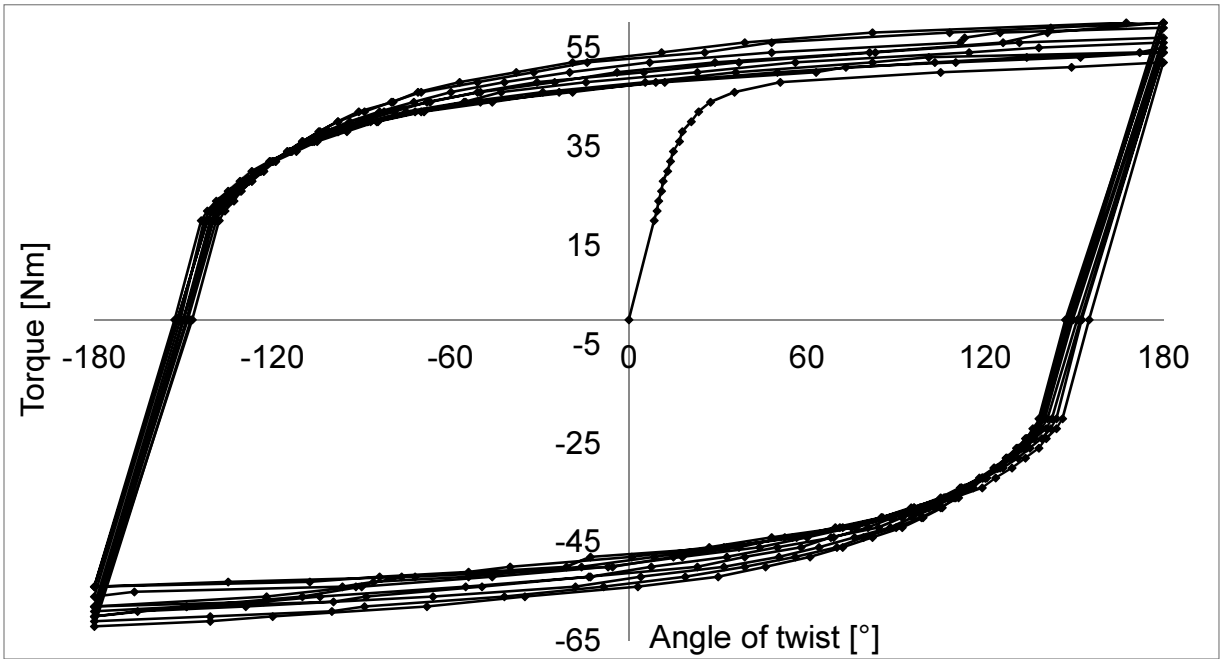

Figure 9.13. Torque versus the angle of twist for sample A7, ±180°, 10 cycles, 293K

The evolution of martensite fraction on the surface is shown in Fig. 9.14. After the first 8 half-cycles, more or less uniform martensite increment per cycle was observed. During the subsequent cycles a "valley" with smaller values was visible at lengths between 90 mm and 150 mm. After the test, about 32% of martensite was induced in the sample. Much less in comparison with sample A5, for which some 85% was reached.

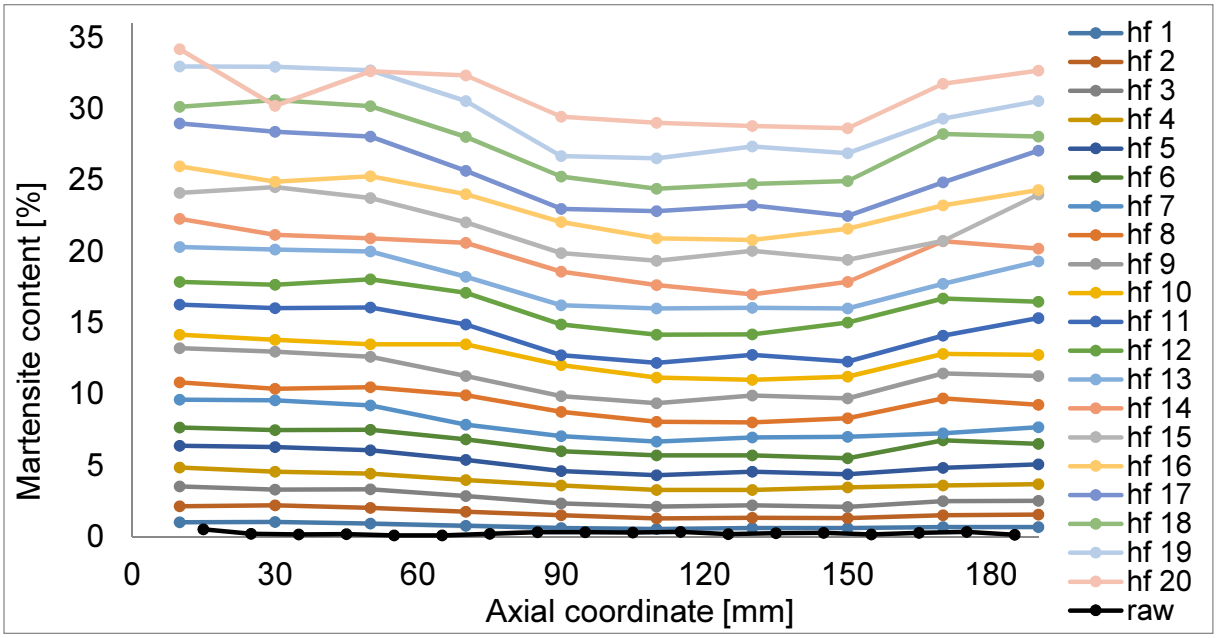

Figure 9.14. Martensite content on the surface of the sample after each half cycle, sample A7, ±180°, 10 cycles at 293K

9.3.1.8. Sample A8

The results for sample A8, twisted at 293 K to ±60 Nm, are shown in Fig. 9.15. After the first half-cycle, the value of angle of twist was 1110°. The loops got narrower during the test, but were still quite wide. Compared to sample A3, loaded in the same way at 77K, a completely different behavior was observed. For sample A3, the angle of twist was equal to 39° only.

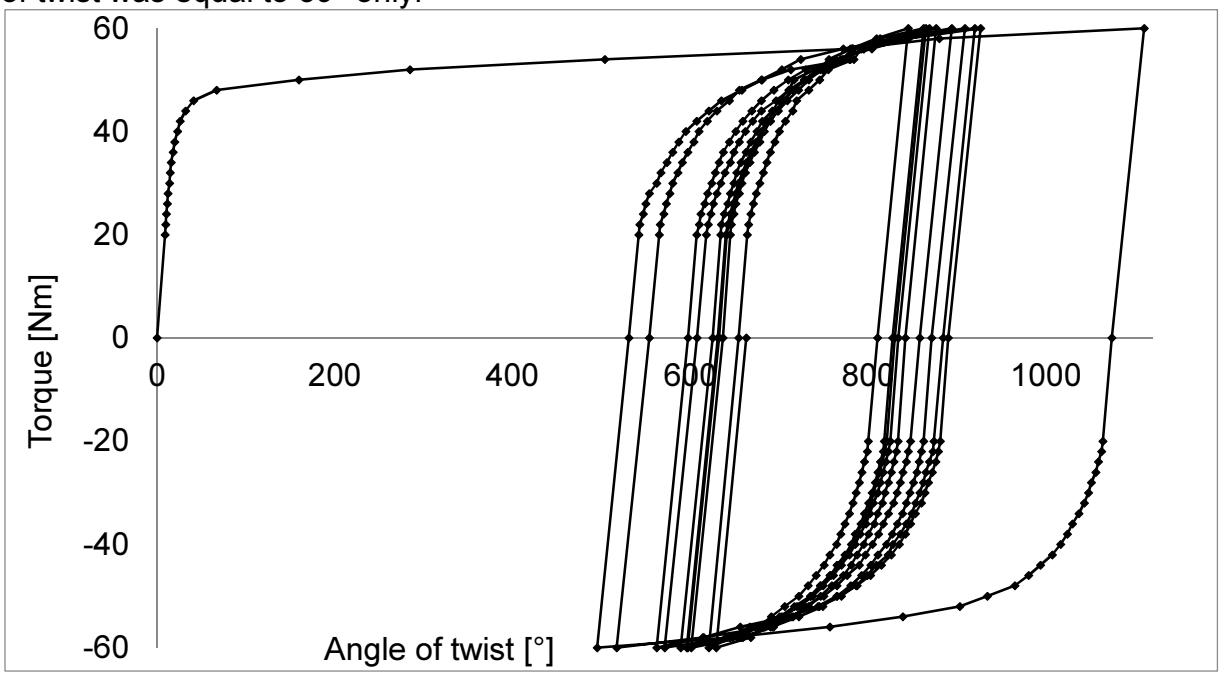

Figure 9.15. Torque versus the angle of twist for sample A8, ±60Nm, 10 cycles at 293K

The evolution of martensite is shown in Fig. 9.16. After the test, about 44% of martensite fraction was obtained. A gap between the 11th and 12th half-cycles was observed. It was caused by stopping the test for about 18 hours, during which some spontaneous transformation probably occurred. No other rational explanation of this experimental fact has been found.

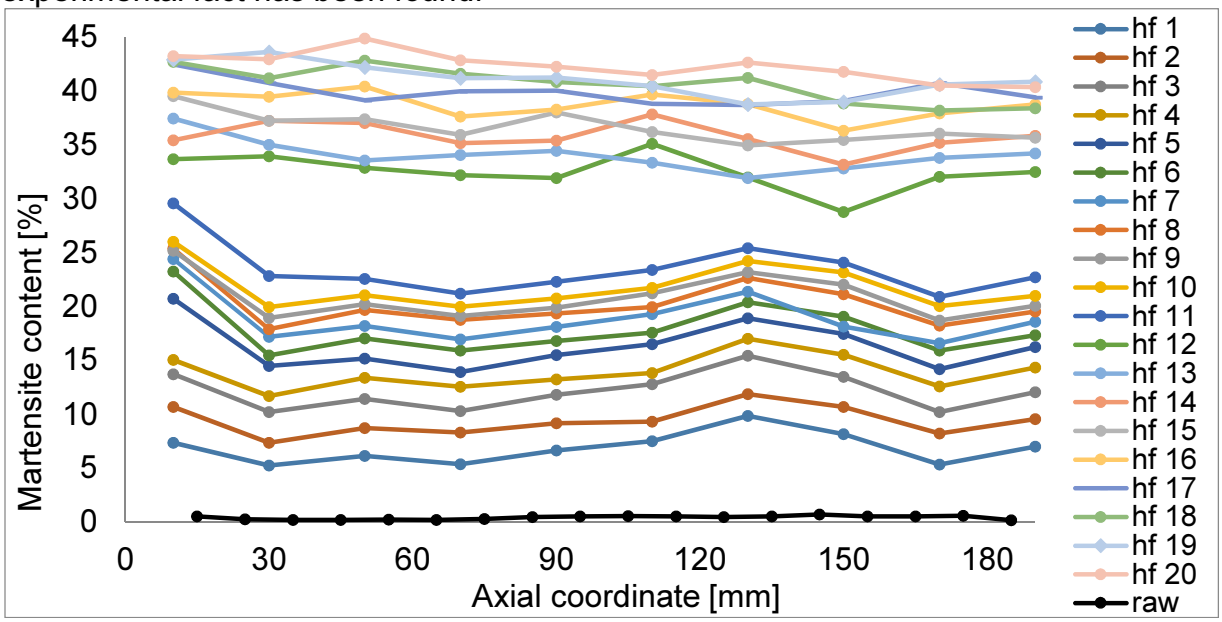

Figure 9.16. Martensite content on the surface of the sample after each half cycle, Sample A8, ±60Nm, 10 cycles at 293K

9.3.1.9. Sample A9

Sample A9 was loaded at 293K. It was supposed to be loaded by using kinematic control to ±180°. Yet, because of an omission, the angle of twist varied from 0 to 180° (in other words 90°±90°). The results in terms of the torque versus the angle of twist are shown in Fig. 9.17. Half cycles 3 and 19 are missing because of problems with the torque wrench. An interesting conclusion was drawn from these results, that some softening was observed, since the first half-cycle had higher torque values when compared to the next ones.
In this test, the martensite evolution was not measured. It is important to point out, that these results are meaningful to validate the constitutive models. Such asymmetric cyclic torsion results are very rare in the literature.

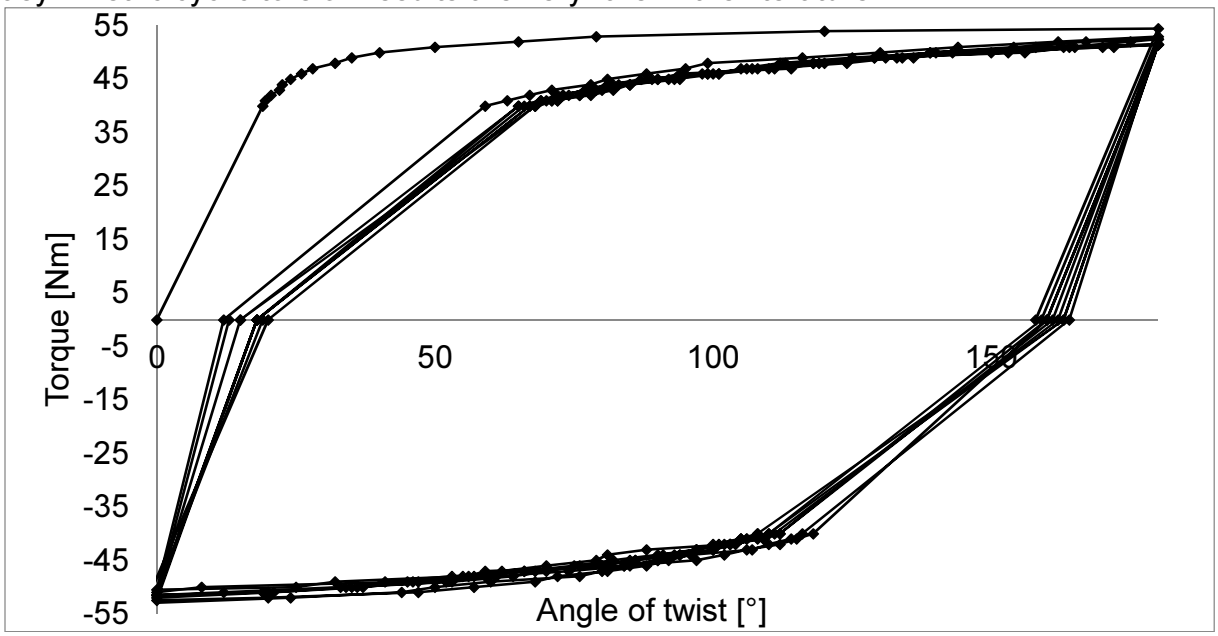

Figure 9.17. Torque versus the angle of twist for sample A9, 90° ± 90, 10 cycles at 293 K

9.3.1.10. Sample A10

Sample A10 was supposed to be loaded by applying kinematic control to ±180°, at 77K. Yet, similarly to sample A9, because of an omission, the cycles became asymmetric (Fig. 9.18). In the 1st half-cycle the sample was loaded to 180°, yet, the results were not captured because of a problem with the torque wrench. The second half-cycle was performed from +180° to -180° properly, then the 3rd one to 180° ,the 4th one to -180°, the 5th one was finished at 55°, and the 6th was completed at -305°.
These experimental results provide great benchmarks for complex constitutive models. Often, the constitutive models are only able to capture monotonic or cyclic behavior under symmetric loading. Decent models should simulate correctly asymmetric loading as well, like for sample A10.
These results provide a direct proof of damage evolution inside the volume of the sample, which can be deduced from decreasing slope of unloading stages.

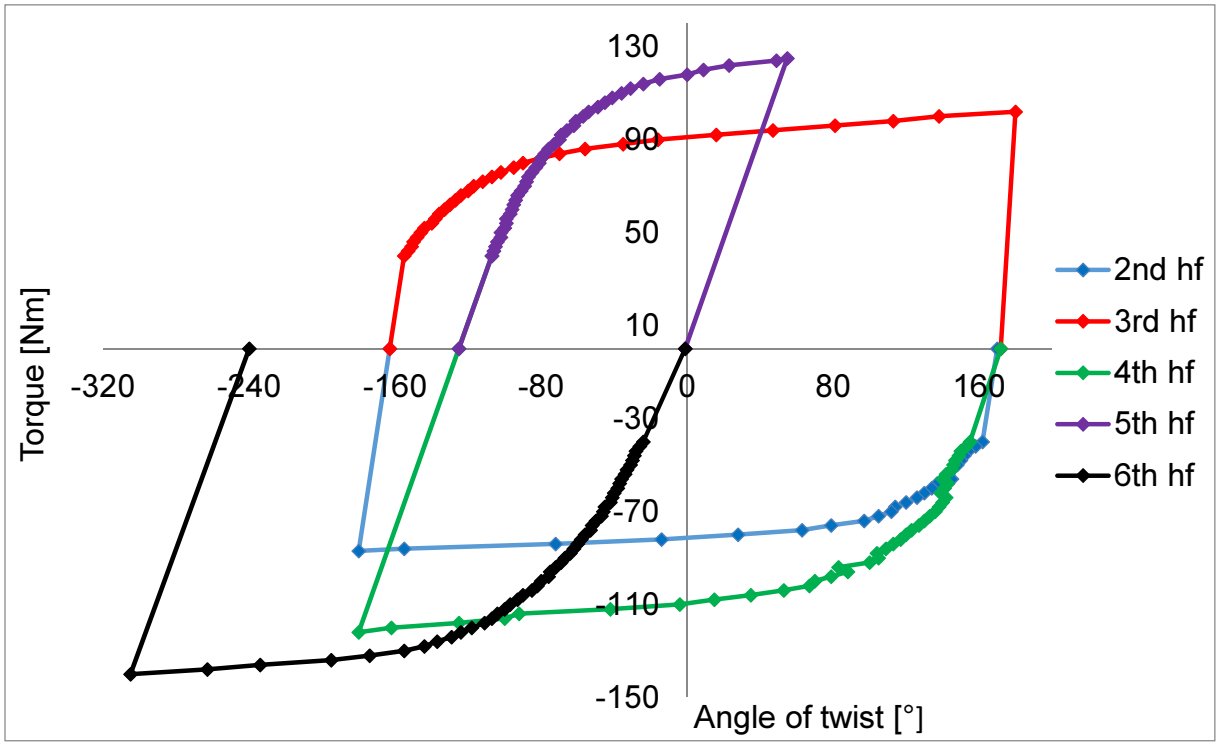

Figure 9.18. Torque versus the angle of twist for sample A10, asymmetric cycles

9.3.2 Data for 316L stainless steel

In the subsequent sections, the results in terms of torque versus the angle of twist are presented, for samples made of grade 316L stainless-steel. All the tests were performed at the liquid nitrogen temperature. For all of them, the martensite content evolution was measured on the surface of the sample.

9.3.2.1 Sample C2 at 77 K

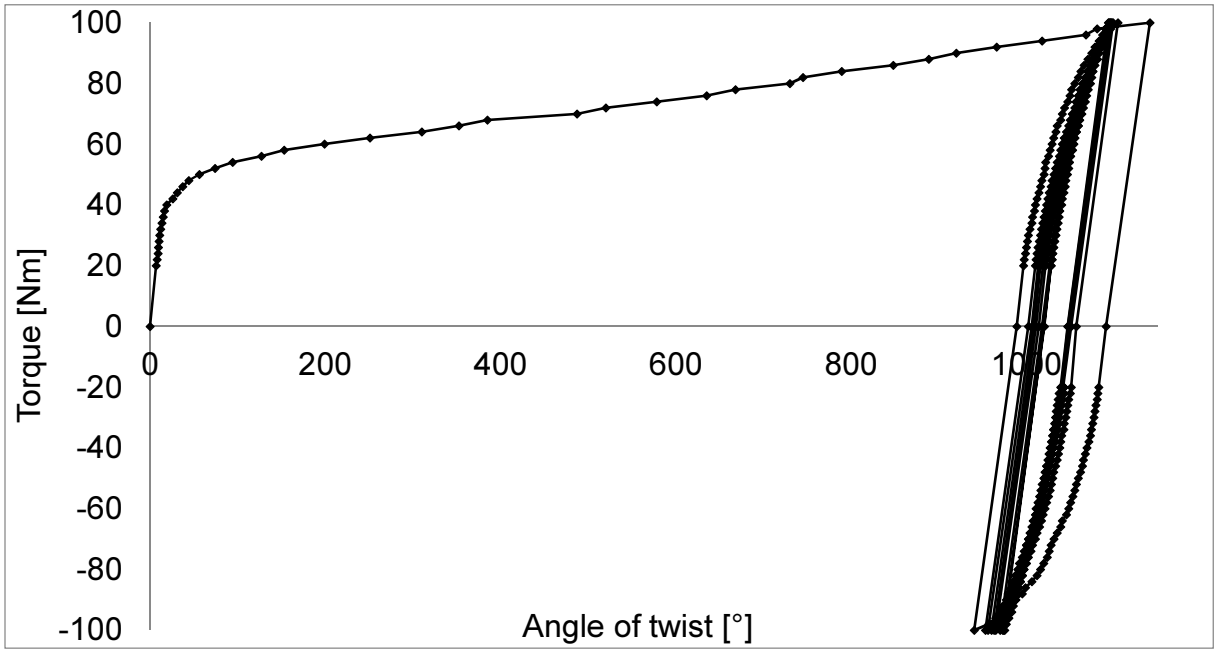

Figure 9.19. Torque versus the angle of twist for sample C2, ±100Nm, 10 cycles at 77 K

The results in terms of torque versus the angle of twist for sample C2 are shown in Fig. 9.19. In total, 10 cycles controlled by torque (±100Nm) were performed.

After the first half-cycle, the angle of twist was rather high and reached 1141°. During the subsequent cycles, gradually reduced (narrower) hysteresis loops were observed.
The evolution of martensite fraction on the surface is shown in Fig. 9.20. After the first half-cycle, about 49% of martensite was induced. In the subsequent cycles only small increase were observed. Interestingly enough, the martensite content was oscillating between cycles. For example, after the 7th half-cycle 62.1% was measured, whereas, after the 8th half-cycle 58% occurred. Similarly, after the 13th half-cycle 63.9% was detected, and after 14th half-cycle only 61.6% was observed. This phenomenon can probably be attributed to measurement errors, since there is no reason for which the reverse transformation would cause a decreasing martensite content.

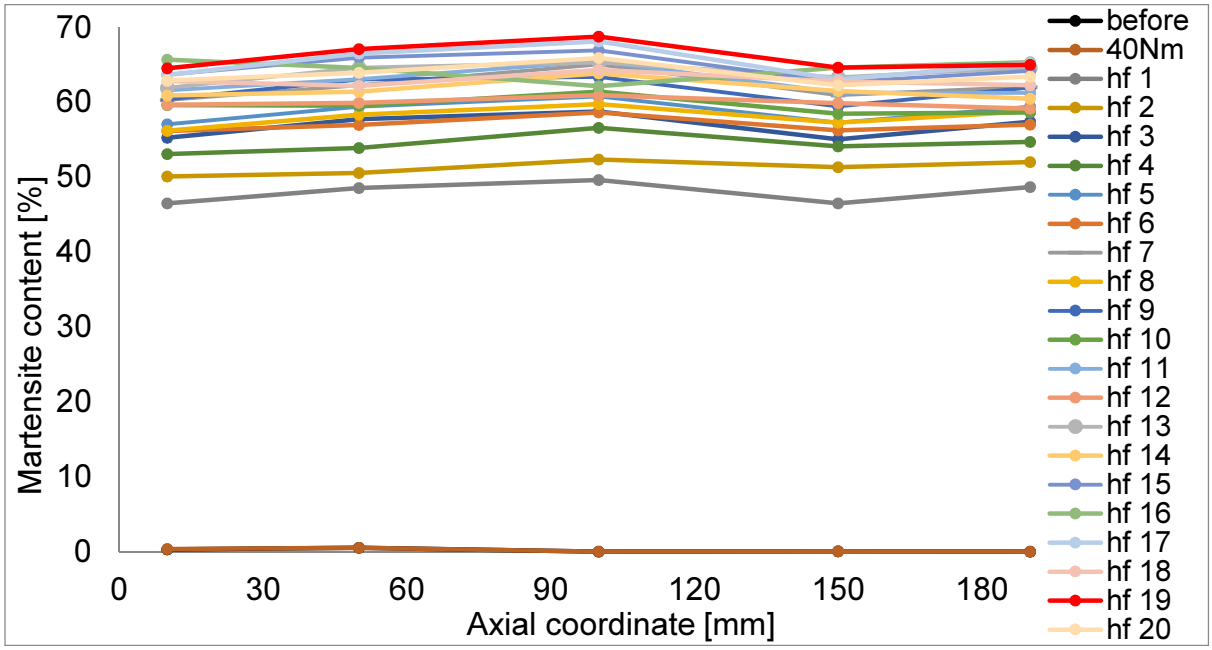

Figure 9.20. Martensite content on the surface of the sample after each half cycle, sample C2, ±100Nm, 10 cycles at 77 K

9.3.2.2. Sample C3 at 77 K

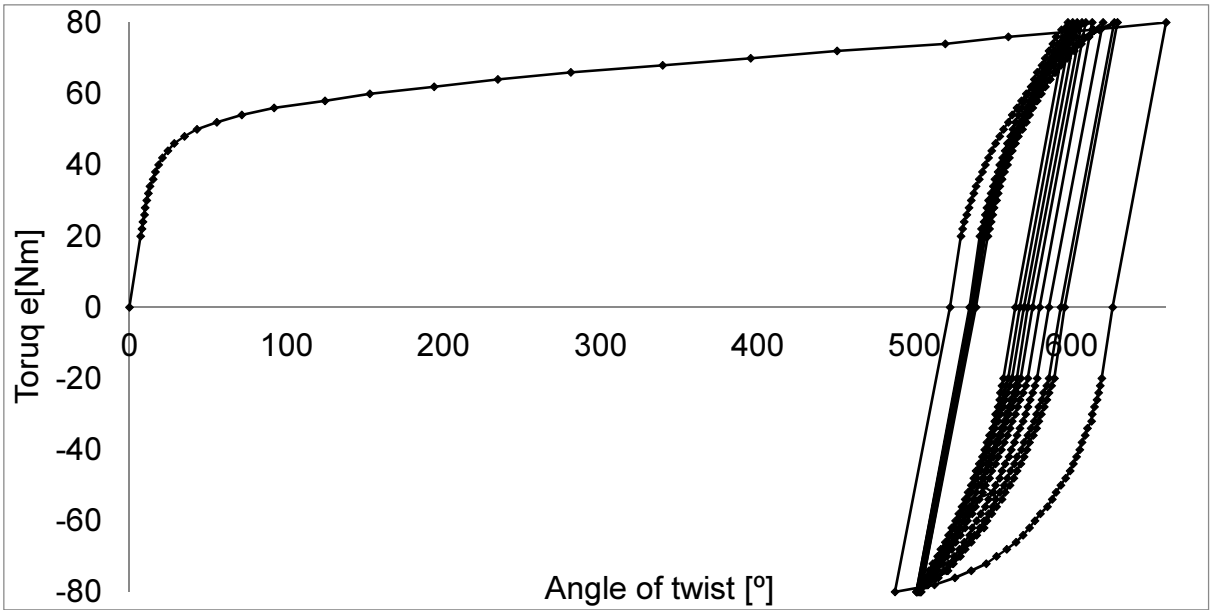

Figure 9.21. Torque versus the angle of twist, Sample C3, ±80Nm, 10 cycles, 77 K

The results for sample C3 are shown in Fig. 9.21. The sample was loaded to ±80Nm at 77K. After the 1st half-cycle, the angle of twist of 660° was reached. Gradual reduction of the hysteresis loops is clearly visible.
The evolution of martensite content on the surface of the sample is shown in Fig. 9.22. For this sample, the measurements were made after every 2nd half-cycle, thus at the end of each full cycle. This was motivated by extremely long time of full torsion test, with such many martensite content measurements, and high consumption of liquid nitrogen (almost 200 liters per one full test) as well as its cost.
After the 1st half-cycle, about 20% of martensite was induced. Then the content of martensite was monotonically increasing, after each subsequent cycle. At the end of the test, about 34% of martensite on the surface was reached.

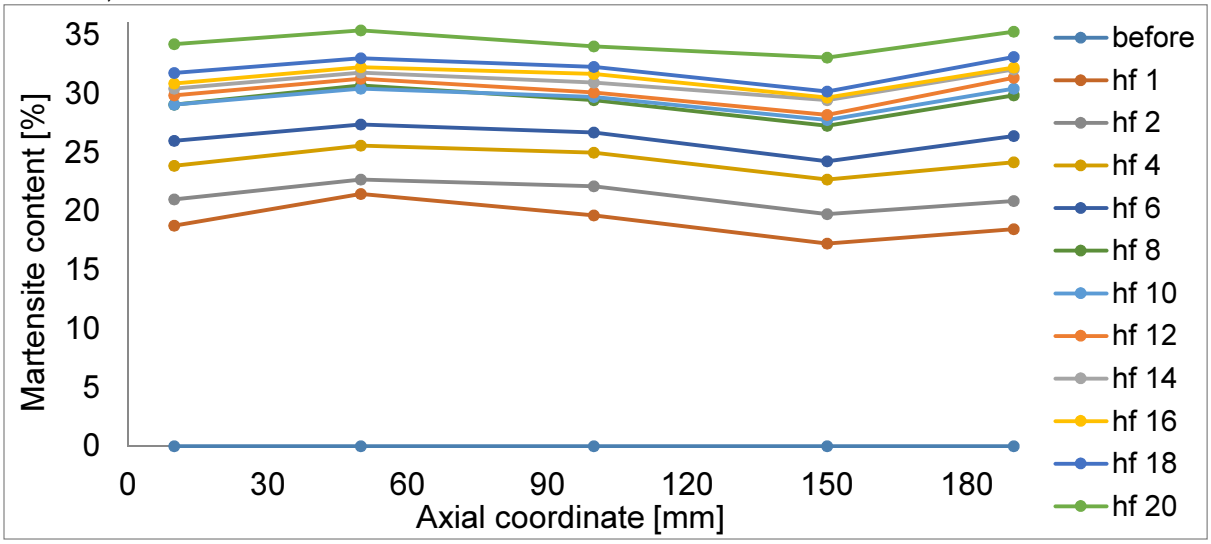

Figure 9.22. Martensite content on the surface of the sample after each half cycle, sample C3, ±80Nm, 10 cycles at 77 K

9.3.2.3. Sample C4 at 77 K

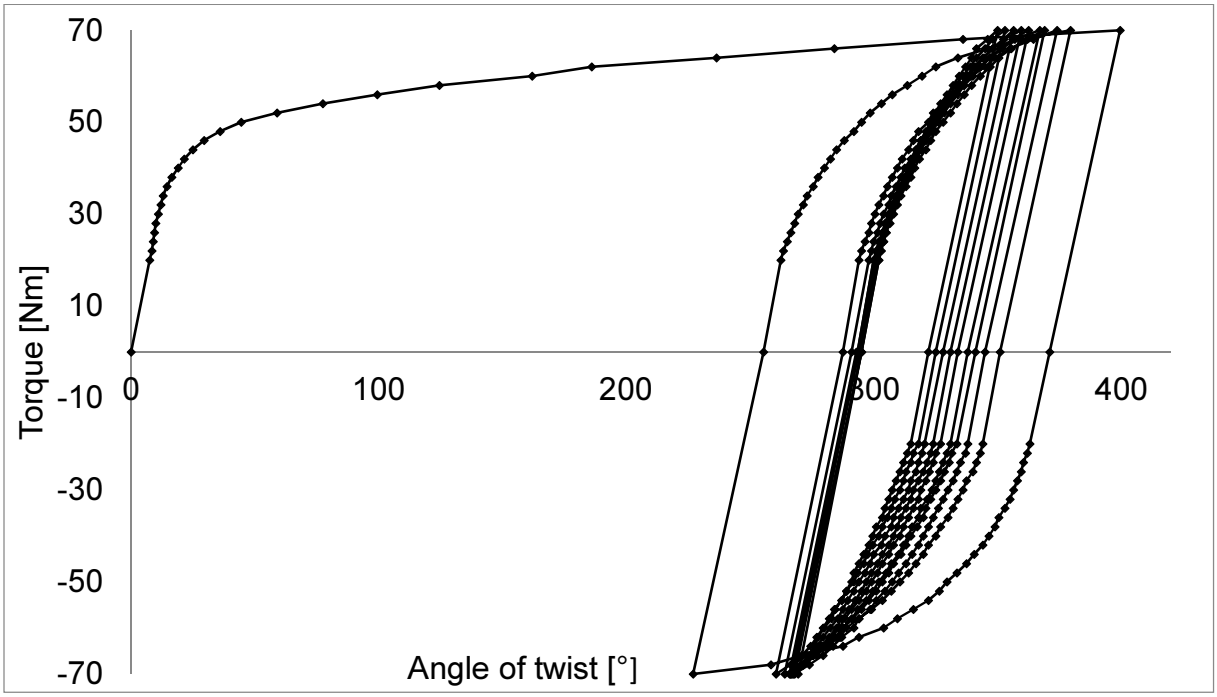

Figure 9.23. Torque versus the angle of twist for sample C4, ±70Nm, 10 cycles, 77 K

The results for sample C4 loaded to ±70Nm at 77K are shown in Fig. 9.23. The maximum angle of twist was equal to 399.5°. Similarly to the samples C2 and C3, progressively reduced hysteresis loops were observed.
Evolution of martensite content on the surface is shown in Fig. 9.24. The measurements were performed every 2nd half-cycle. Apart from additional measurement after the 1st half-cycle, where about 8% of martensite was found, after the test completion about 20% of martensite was obtained. What is noticeable, the martensite content is slightly smaller at the end of the sample (measurements at 150 and 190mm), and this tendency appears during all the test.

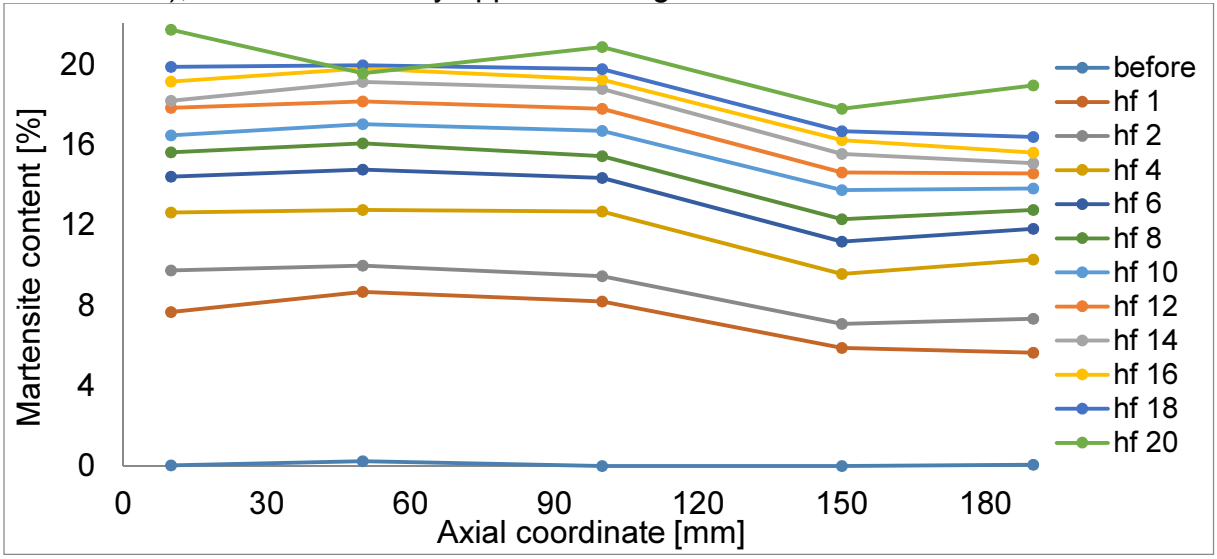

Figure 9.24. Martensite content on the surface of the sample after each half cycle, sample C4, ±70Nm, 10 cycles at 77 K

9.3.3 Data for 304L stainless steel

In this section the results for three samples (D2, D3, D4), made of the 304L stainless steel, are presented. The temperature and the loading are exactly the same like for the samples C2, C3, C4. All samples were loaded by using torque control: ±100Nm, ±80Nm, ±70Nm. Together with the measurements of the torque versus the angle of twist, the martensite content was measured during the test on the surface of the samples.

9.3.3.1. Sample D2 at 77K

The results for sample D2 loaded to ±100Nm at 77K are shown in Fig. 9.25. After the 1st half-cycle, the angle of twist reached 702°, which is much less than for the sample C2 (1141°). The width of the hysteresis loops strongly decreased after all cycles.

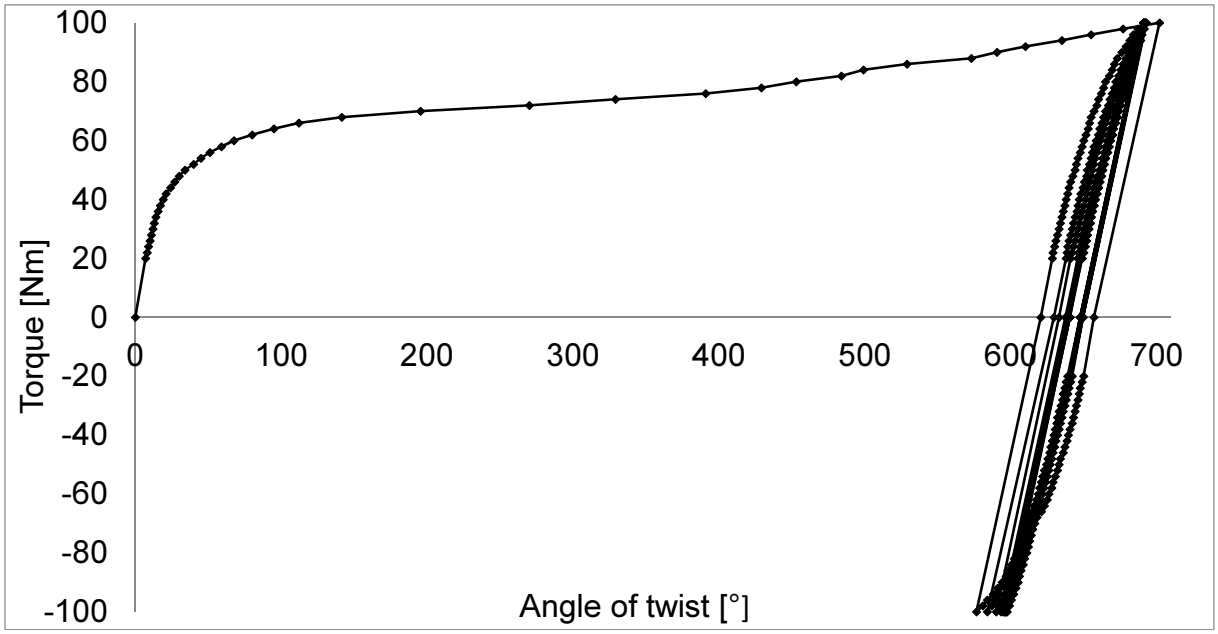

Figure 9.25. Torque versus the angle of twist, sample D2, ±100Nm, 10 cycles, 77 K

The evolution of martensite fraction on the surface of the sample is shown in Fig. 9.26. After the first half-cycle, the biggest increase was found, to about 60% of martensite. Afterwards, small increments were observed only. After the whole test, about 73% of martensite was obtained. After the 7th half-cycle, the test was stopped for about 24 hours. For this reason, the measurement was repeated at room temperature before immersing the sample in the coolant. After the 1st measurement, about 70% of martensite fraction was found, whereas, after the 2nd one about 72.5% was found in average. Such a difference could be explained by the difference in measurement conditions. After removing the sample from the bath of liquid nitrogen, it was always covered with white frost (frozen humidity). This created an additional layer between the material of the sample and the head of the Feritscope. At 293K, when the sample was warmed up, no such layer occurred, thus slightly higher martensite content was possibly registered.

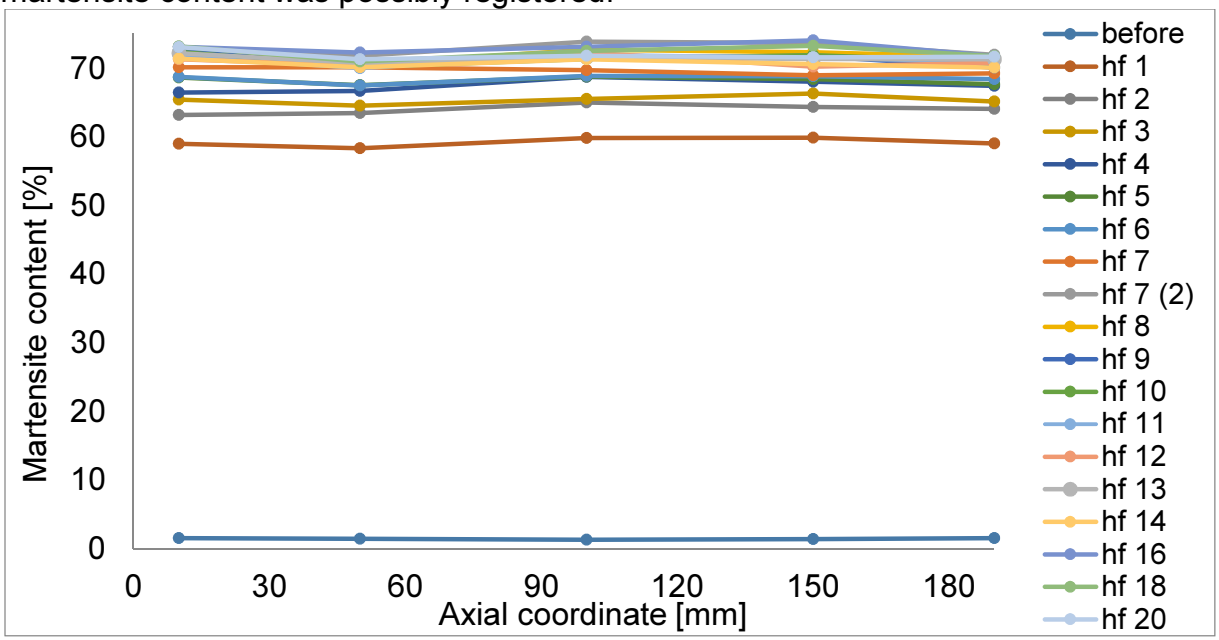

Figure 9.26. Martensite content on the surface of the sample after each half cycle, sample D2, ±100Nm, 10 cycles at 77 K

9.3.3.2. Sample D3 at 77K

The results for sample D3 twisted at 77K to ±80Nm are shown in Fig. 9.27. The maximum angle of twist was equal to 436°. Progressive reduction of the hysteresis loops was also observed.

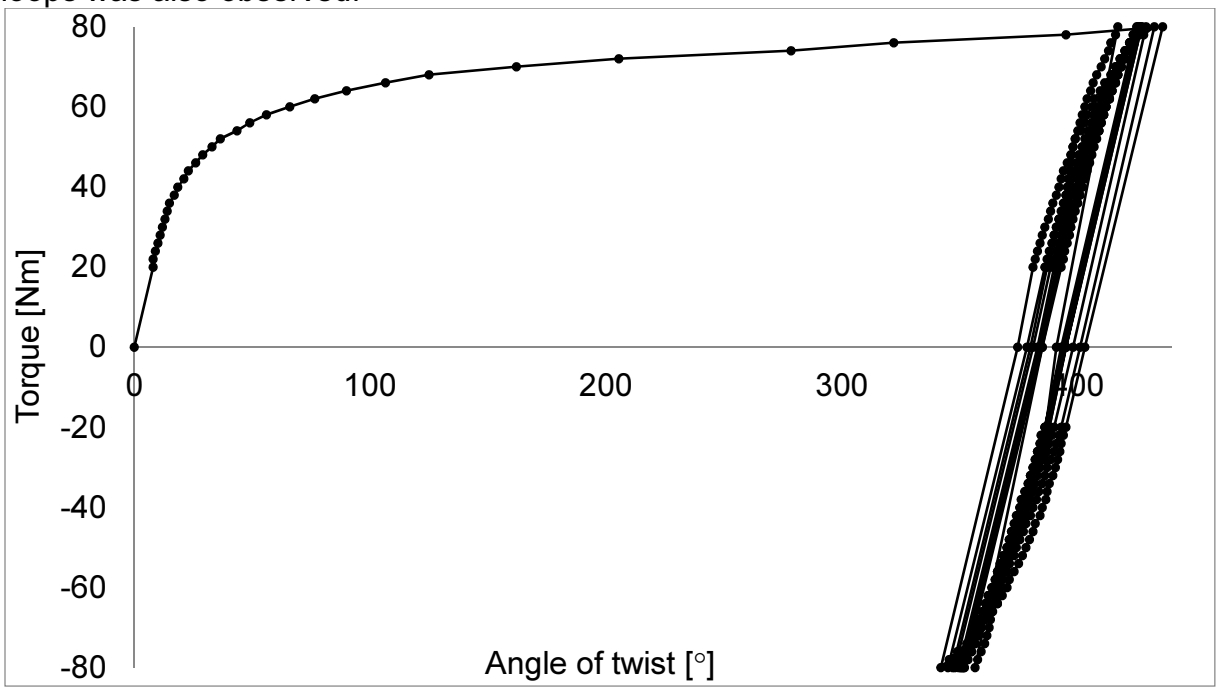

Figure 9.27. Torque versus the angle of twist, sample D3, ±80Nm, 10 cycles at 77 K

Evolution of martensite content on the surface is shown in Fig. 9.28. No measurement were carried out before the test, however, based on the previous samples near zero values were expected. After the 1st half cycle about 30% of martensite was induced. Afterwards, the subsequent increments of martensite content were decreasing. After the test, in total, about 45% of martensite was obtained. In all the measurements, the martensite fraction values were almost constant along the sample.

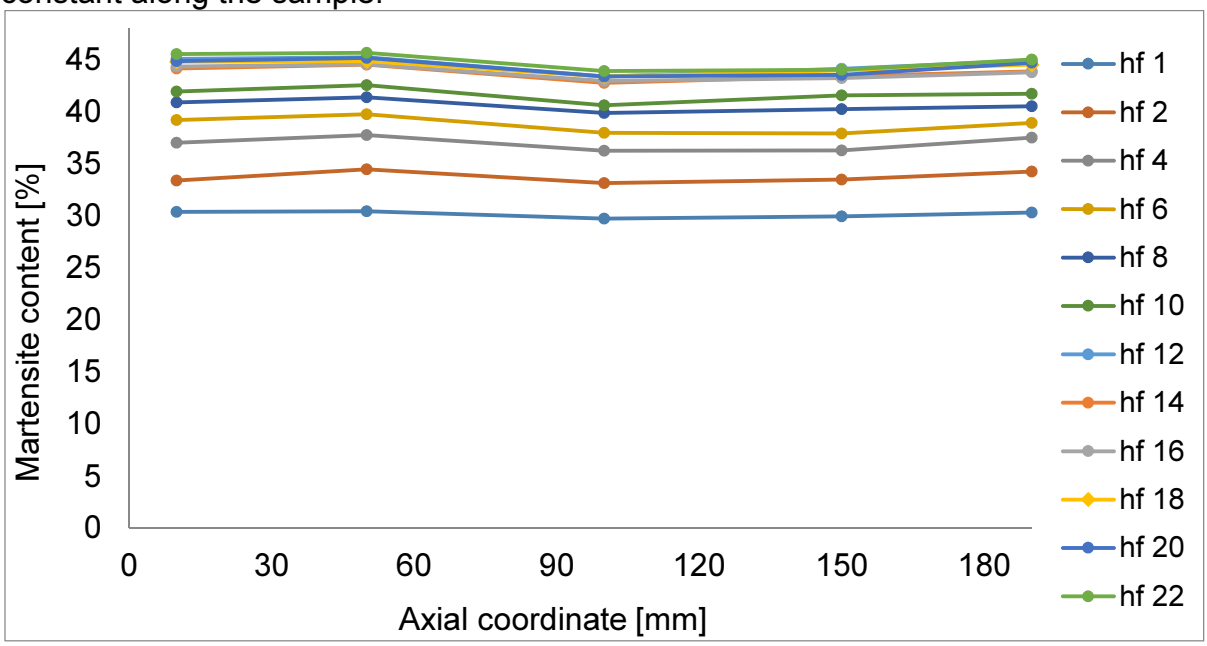

Figure 9.28. Martensite content on the surface of the sample after each half cycle, sample D3, ±80Nm, 10 cycles at 77 K

9.3.3.3. Sample D4 at 77K

The results of the torque versus the angle of twist for sample D4, twisted at 77K to ±70Nm, are shown in Fig. 9.29. After the 1st half-cycle, the angle of twist reached 174°. The hysteresis loops were progressively reduced in size, but much less when compared to the samples D2 and D3.

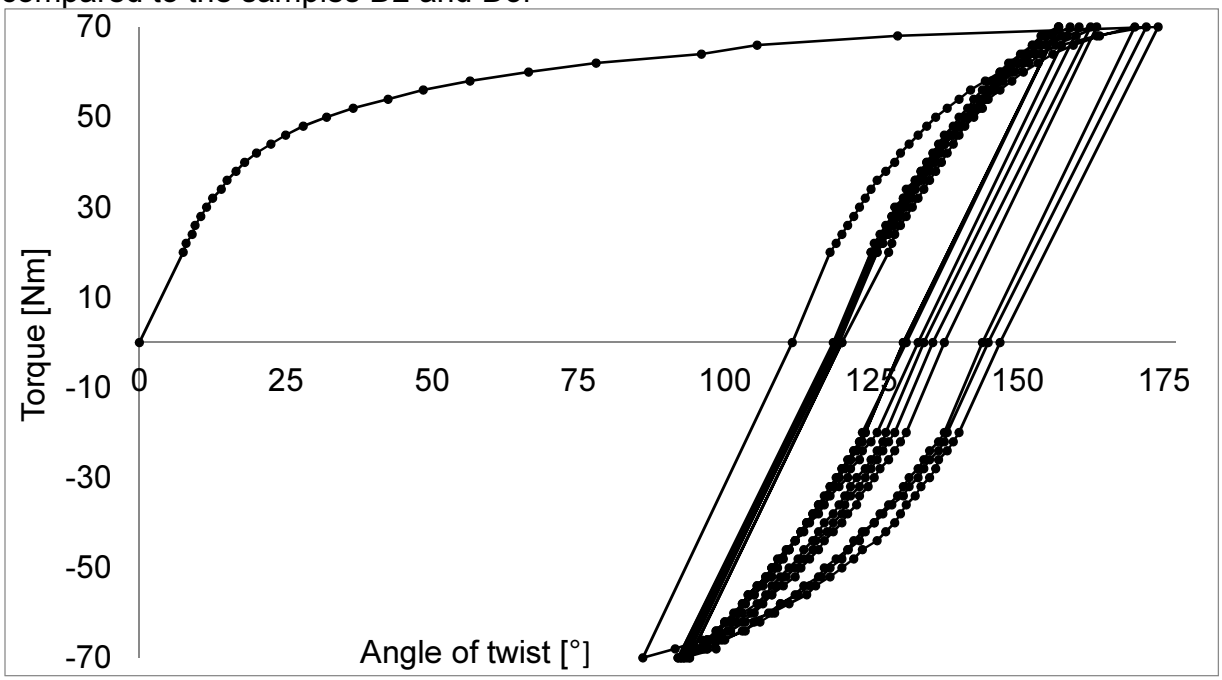

Figure 9.29. Torque versus the angle of twist, sample D4, ±70Nm, 10 cycles at 77 K

The evolution of martensite content on the surface of the sample is presented in Fig. 9.30. Actually, before the test about 1.3% of martensite was found. After the 1st half-cycle about 5.5% was measured. Within each subsequent measurement, the martensite fraction increased, reaching finally about 22% after the whole test.

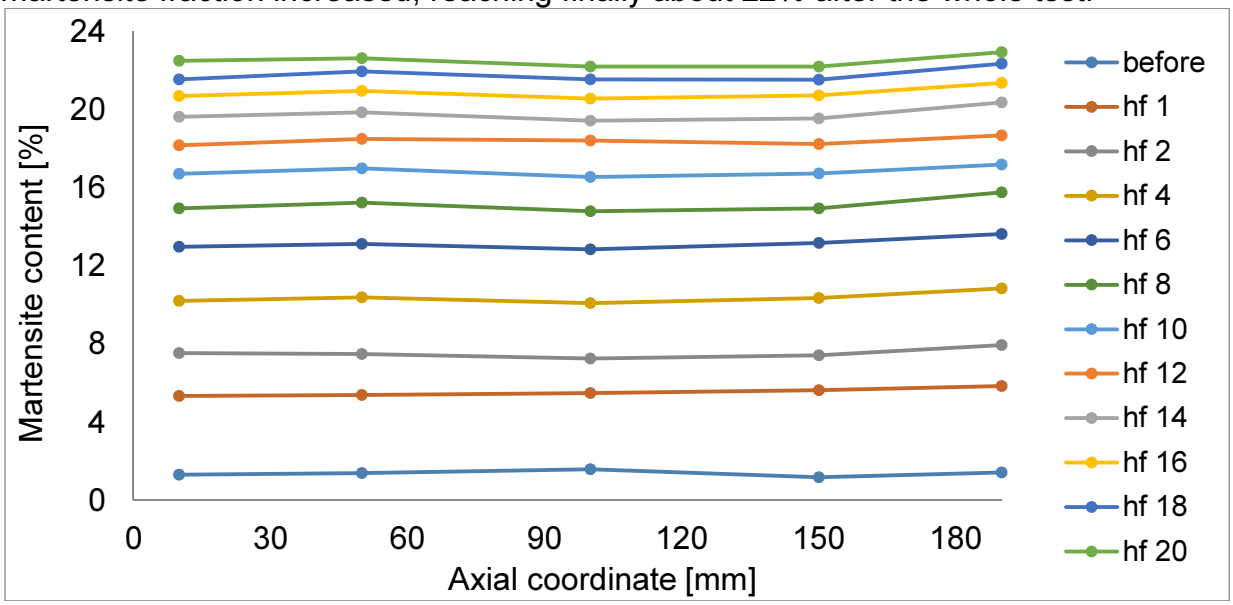

Figure 9.30. Martensite content on the surface of the sample after each half cycle, sample D4, ±70Nm, 10 cycles at 77 K

9.3.4. Data for 316LN stainless steel

Three samples made of grade 316LN stainless steel were tested. The same temperature and loading conditions were applied like for the samples made of 304L and 316L steels. Namely, the torque control was imposed to the predefined levels: ±100Nm, ±80Nm and ±70Nm, all of them were tested at 77K.

9.3.4.1. Sample E2 at 77K

The results for sample E2 twisted at 77K to ±100Nm are presented in Fig. 9.31. The angle of twist after the first half-cycle was equal to 574°. The width of the hysteresis loops was much larger compared to the samples made of grades 304, 304L and 316L ss. Each consecutive loop decreased slightly in size, making the width of the last 10th cycle almost 300° in terms of angle of twist.

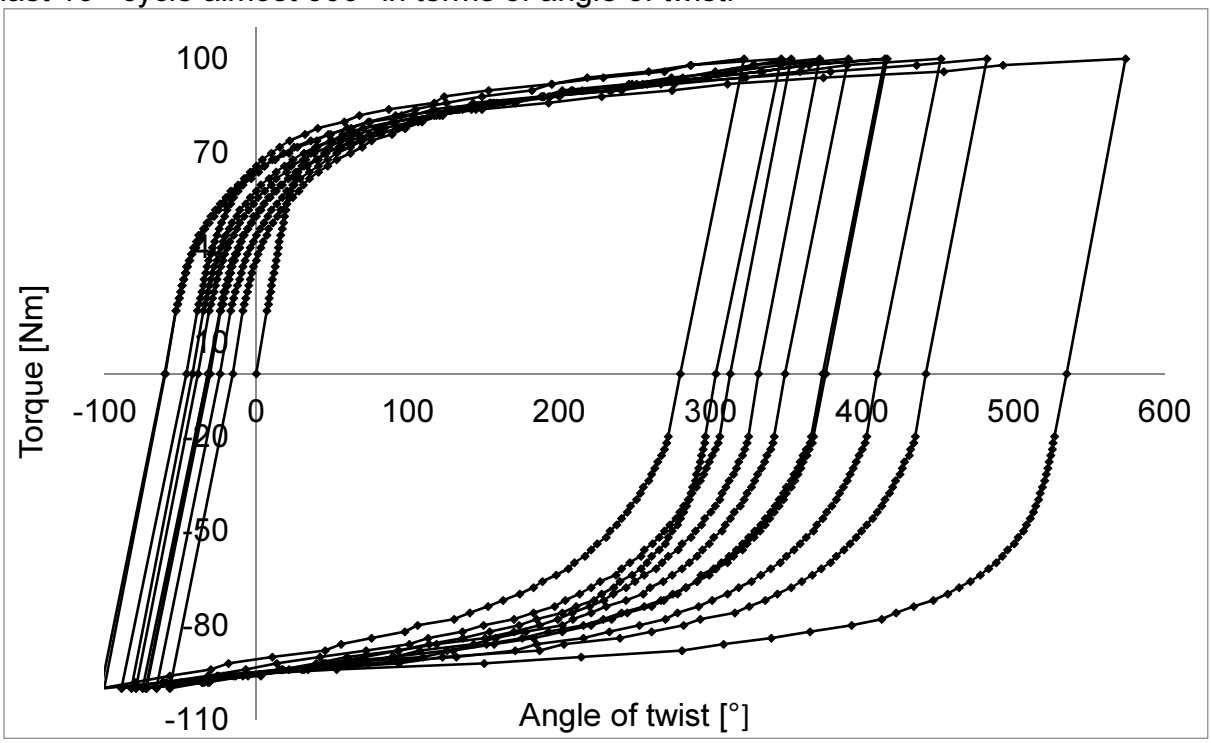

Figure 9.31. Torque versus the angle of twist, sample E2, ±100Nm, 10 cycles at 77 K

The evolution of martensite content on the surface of the sample is presented in Fig. 9.32. After the 1st half-cycle, about 1.3% of martensite was induced only. After the whole test, about 9% of martensite was induced. This was much less compared to all the other samples: sample A4 with 70% martenstie (304), sample C2 with 67% martensite (316L), sample D2 with 72.5% martensite (304L).

Thus, grade 316LN stainless steel is much more stable against the plastic strain induced phase transformation.

Almost constant values of the volume fraction of martensite along the axis of the sample were observed in all the measurements. This confirmed the theoretical expectations, because of constant torque along the sample, leading to the same state of stress and strain in every cross-section.

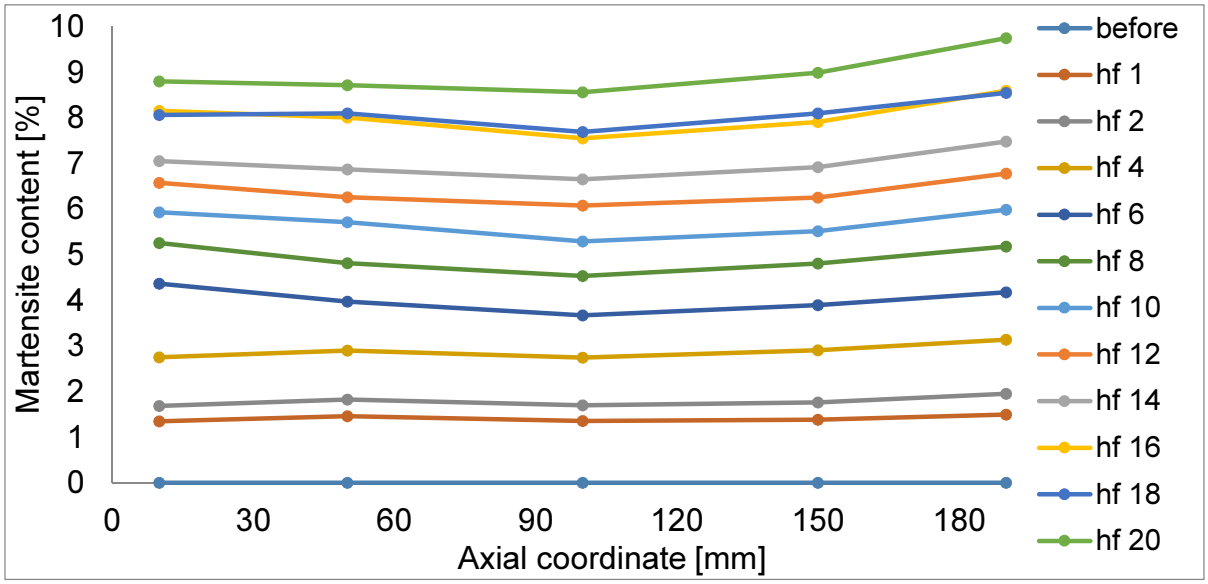

Figure 9.32. Martensite content on the surface of the sample after each half cycle, sample E2, ±100Nm, 10 cycles at 77 K

9.3.4.2. Sample E3 at 77K

The results for sample E3 twisted at 77K to ±80Nm are shown in Fig. 9.33. The maximum angle of twist was equal to 105°. Thus, much less when compared to the other samples loaded in the same conditions (D3 made of 304L reached 436°, C3 made of 316L reached 660°, A2 made of 304 reached 242°). The hysteresis loops slightly decreased in size during the test.

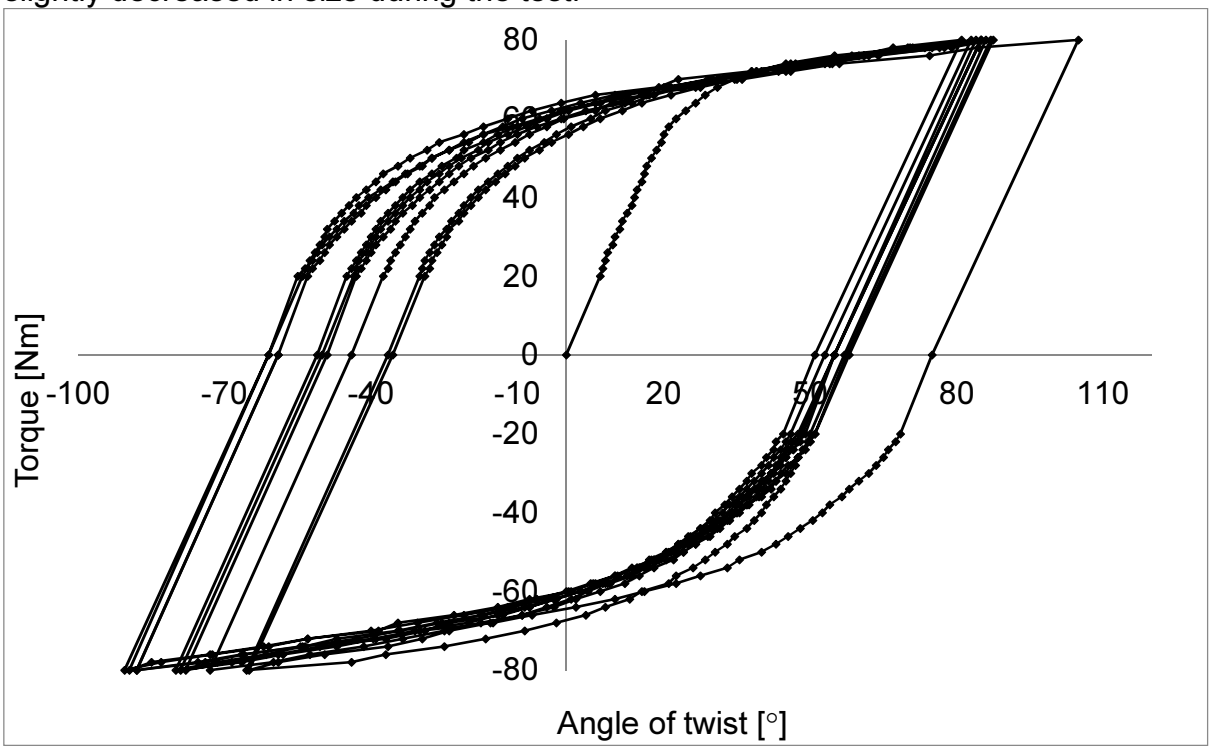

Figure 9.33. Torque versus the angle of twist, sample E3, ±80Nm, 10 cycles at 77 K

The evolution of martensite content on the surface of sample E3 is shown in Fig. 9.34. Actually, only negligible martensite content of 0.09% was induced at 150mm.

This measurement confirmed stability of grade 316LN against the strain induced phase transformation. For the samples loaded at 77K to ±80Nm, the martensite fractions reached after 10 cycles were as follows: D3 – 45%, C3 – 34%, A2 – 27%.

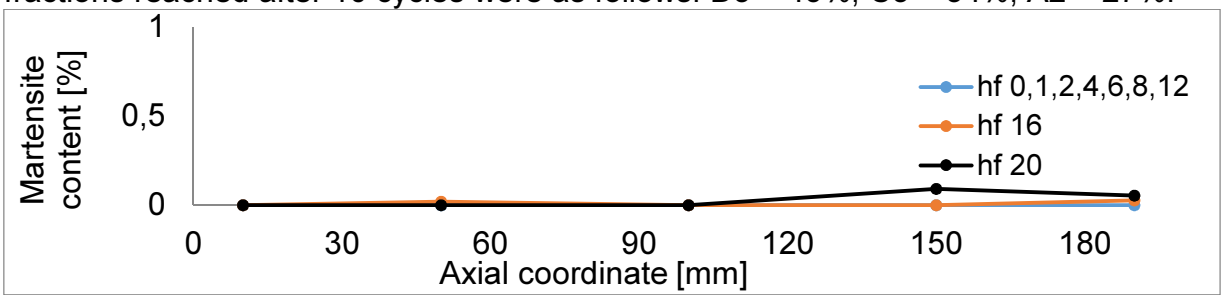

Figure 9.34. Martensite content on the surface of the sample after each half cycle, sample E3, ±80Nm, 10 cycles at 77 K

9.3.4.3. Sample E4 at 77K

The results for sample E4 twisted at 77K to ±70Nm are shown in Fig. 9.35. The maximum angle of twist reached in the course of test was equal to 35.5°. Only small reduction of size of the hysteresis loops was observed.

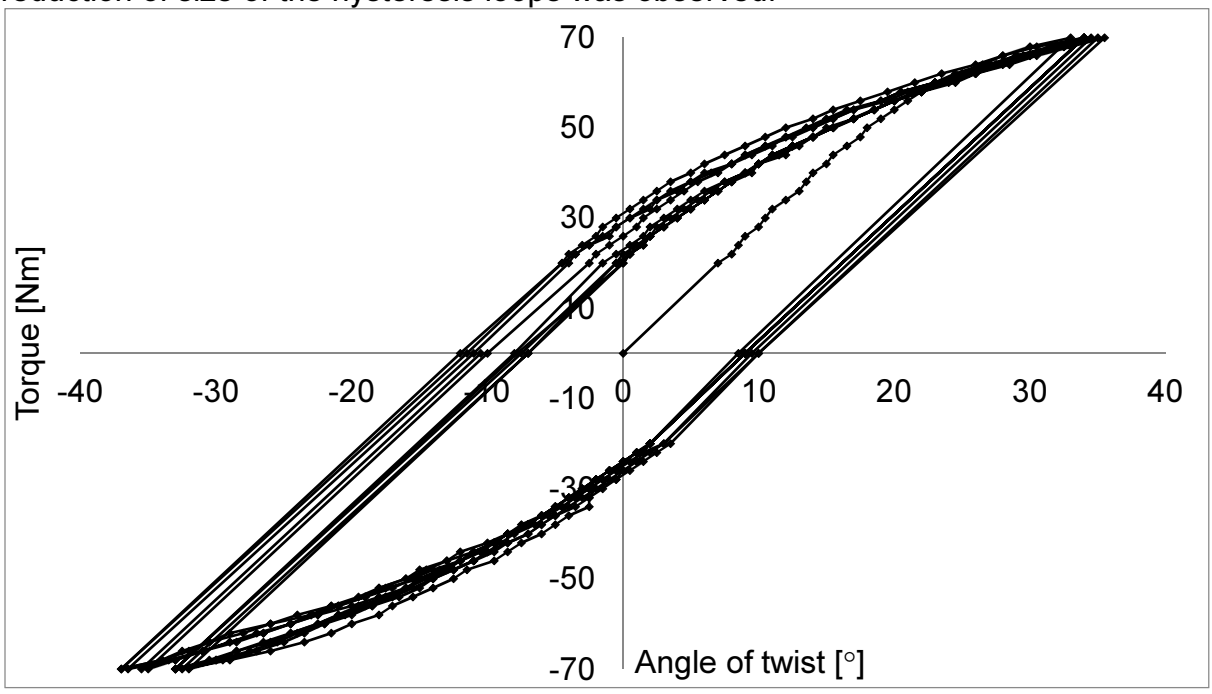

Figure 9.35. Torque versus the angle of twist, sample E4, ±70Nm, 10 cycles at 77 K

The evolution or martensite content on the surface is shown in Fig. 9.36. For this sample, practically no martensite was induced in all the measurements. The value of the plastic strain was not large enough to induce any phase transformation.

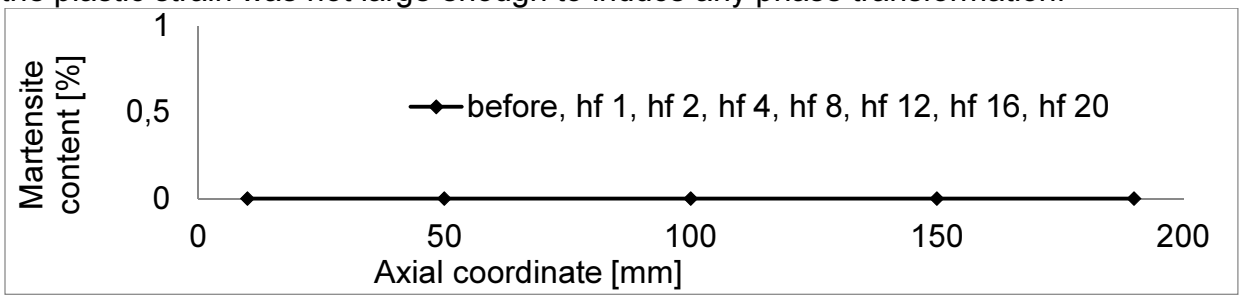

Figure 9.36. Martensite content on the surface of the sample after each half cycle, sample E4, ±70Nm, 10 cycles at 77 K

9.4. Discussion of results of the cyclic torsion

9.4.1. Results for torque ±70 Nm (A1, C4, D4, E4)

All the samples A1, C4, D4, E4 (Table 9.1) were twisted at 77K. 10 cycles of ±70Nm were carried out. Different values of the maximum angle of twist were obtained. For sample E4 (316LN) φ_{max} was equal to 35.5º, for sample A1 (304) φ_{max} was equal to 82º, for D4 (304L) φ_{max} of 174º was reached, and for C4 (316L) the highest φ_{max} of 399.5º was obtained. For samples C4 and D4 considerable hardening was observed, resulting in non-negative values of the angle of twist after the second half-cycle. For samples A1 and E4, minimum angle of twist was equal to -35º for sample A1 and -36.5º for sample E4.

The martensite content (measured as the average along the axis of the sample for the last half-cycle) was the smallest for sample E4 (0 %). For sample A1 it was equal to 17.8%, for sample C4 the value of 19.8% was obtained, and the highest value of 22.5% was reached for D4.

The average martensite content on the surface of the sample is plotted against the accumulated angle of twist for samples A1, C4, D4, E4 (Fig. 9.38). The accumulated angle of twist has been calculated according to the following formula:

$$\varphi_{acum} = \sum_{i=1}^{n} |\Delta\varphi_i| \tag{9.1}$$

where $\Delta\varphi_i$ is the change of the angle of twist between the measurements of the martensite content (Fig. 9.37).

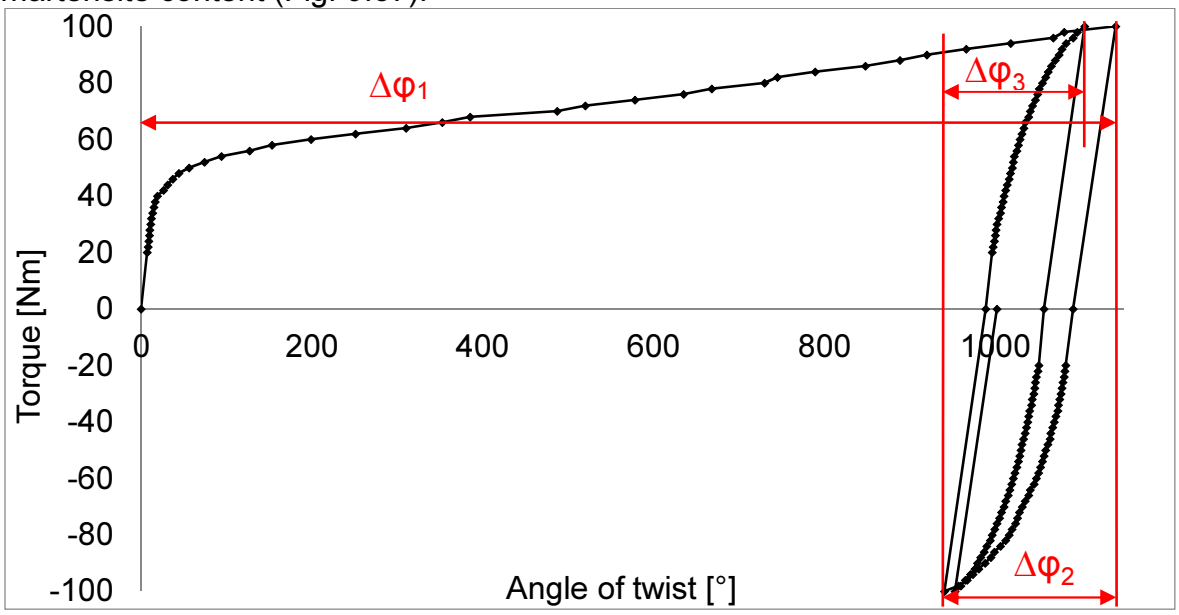

Figure 9.37. The angle of twist increments between the half-cycles, sample C2

No martensite was induced in sample E4. For sample A1, made of grade 304 stainless steel, nearly linear relationship was obtained. For samples C4 and D4, the relevant function has exponential character. The highest amount of martensite was found for the sample made of grade 304L stainless steel.

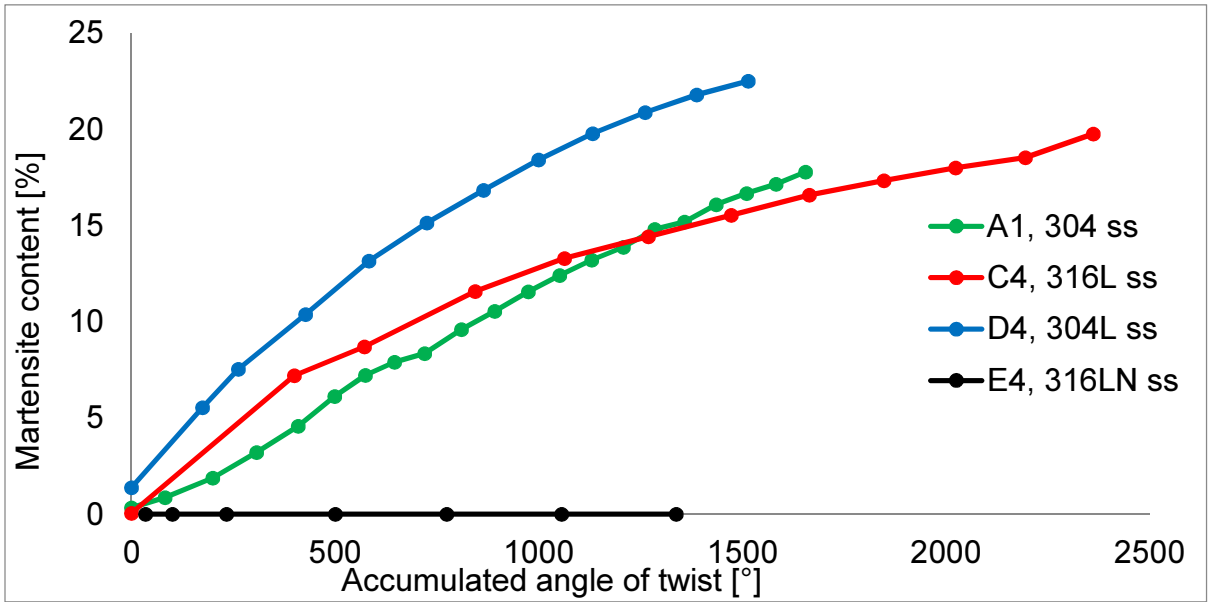

Figure 9.38. Martensite content versus the accumulated angle of twist, samples loaded to ±70Nm at 77K

9.4.2. Results for torque ±80 Nm (A2, C3, D3, E3)

The samples A2, C3, D3, E3 (Table 9.1) were twisted at 77K to the torque level of ±80Nm. The maximum angle of twist measured for sample E3 was of 105º, while 244º was obtained for sample A2, 436º was reached for D3 and 660º was registered for C3. For samples A2, C3 and D3 the angle of twist was always positive. For sample E3 it became negative, with the minimum of -89.5º. The hysteresis loops were the widest for sample E4, then for the samples A2 and C3. The narrower hysteresis loops were registered for sample D3. The martensite content on the surface of the sample was equal to 0% for sample E3, 26.7% for sample A2, 34.4% for sample C3 and 44.8% for sample D3.

Evolution of the average martensite content on the surface of all samples as a function of the accumulated angle of twist is presented in Fig. 9.39.

No martensite was induced in the sample E3 made of grade 316LN stainless steel. Maximum martensite content was obtained for sample D3 made of grade 304L stainless steel, then for sample C3 (316L). Slightly less martensite was obtained in sample A2, made of grade 304 ss. For the samples A2, C3 and D3 exponential relationship was observed in the evolution of martensite content on the surface as a function of the accumulated angle of twist.

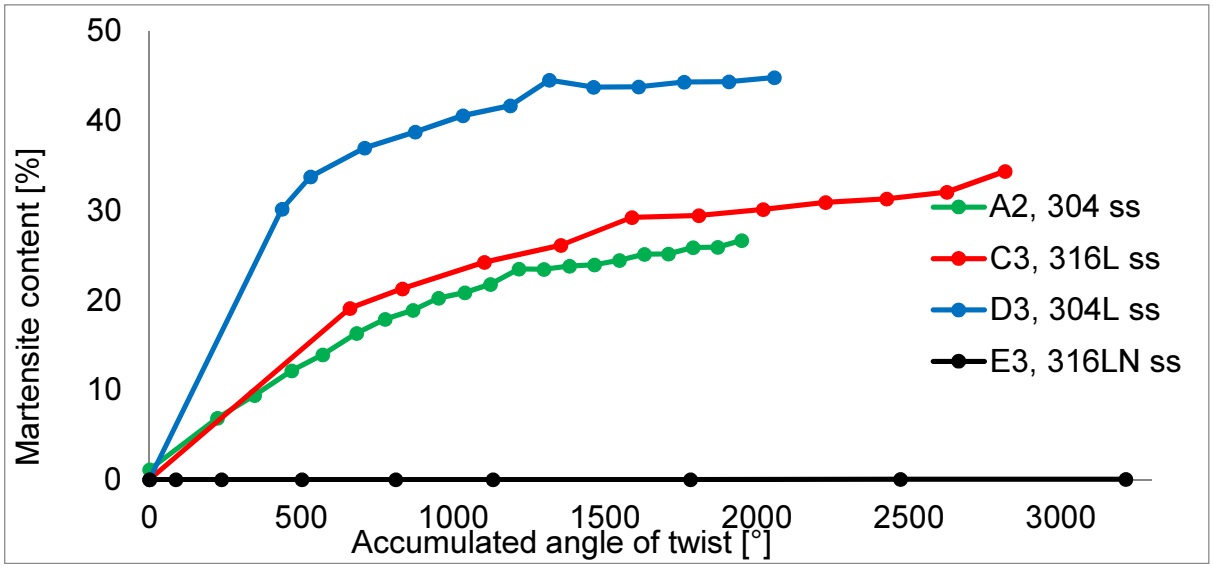

Figure 9.39. Martensite content versus the accumulated angle of twist, samples loaded to ±80Nm at 77K

9.4.3. Results for torque ±100 Nm (A4, C2, D2, E2)

The samples A4, C2, D2, E2 (Table 9.1) were twisted at 77K to the torque level of ±100 Nm. The maximum angle of twist obtained was equal to 574º for sample E2, 702º for sample D2, 719º for sample A4 and 1141º for sample C2. For samples A4, C2 and D2 the minimum angle of twist was non-negative, whereas, for sample E2 it was negative and equal to -100.5º. The widest hysteresis loop was observed for sample E2, and much narrower loops occurred for samples C2, A4 and D2. The martensite content measured on the surface after all 10 cycles was of 9% for sample E2, 63.7% for sample C2, 67.1% for A4 and 71.9% for sample D2.

The average martensite content on the surface of the samples is plotted against the accumulated angle of twist in Fig. 9.40.

The smallest increase of martensite content was measured in sample E2 made of grade 316LN stainless steel. About 9% was induced on the surface only, after almost 10^4 degrees of accumulated angle of twist. Much higher values were obtained for samples C2 (up to 65%), D2 (up to 67%) and A4 (up to 72%).

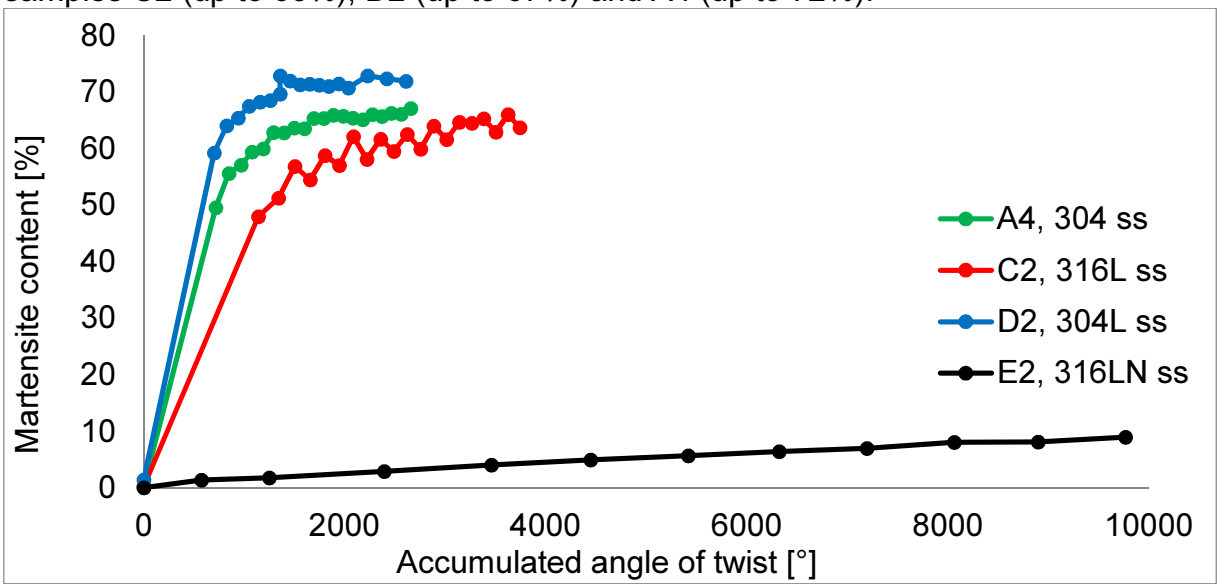

Figure 9.40. Martensite content versus the accumulated angle of twist, samples loaded to ±100Nm at 77K

9.4.4. Results for all the load controlled tests (±70 Nm, ±80 Nm, ±100 Nm)

Samples made of 316LN stainless steel have shown the smallest values of the maximum angle of twist during the cyclic tests. They have shown as well the smallest martensite content and the widest hysteresis loops in comparison with the samples made of 304, 304L and 316L ss.

Lp	Symbol	φ_{max}	φ_{min}	γ_{max}	γ_{min}	M_{max}	M_{min}	ξ_{max}
		[°]	[°]	[-]	[-]	[Nm]	[Nm]	[%]
1	A1	82	-35	0.029	-0.012	70	-70	17.8
2	A2	244	0	0.085	0	80	-80	26.7
3	A3	39.5	-23	0.014	-0.008	60	-60	3.7
4	A4	719	0	0.251	0	100	-100	67.1
5	A5	180	-180	0.063	-0.063	134	-140	84.9
6	A6	60	-60	0.021	-0.021	95	-100	49.7
7	A7	180	-180	0.063	-0.063	60	-61	31.0
8	A8	1110.5	0	0.388	0	60	-60	42.3
9	A9	180	0	0.063	0	54.5	-52.5	-.
10	A10	180	-305	0.063	-0.106	125	-140	-.
10	C2	1141	0	0.398	0	100	-100	63.7
11	C3	660	0	0.230	0	80	-80	34.4
12	C4	399.5	0	0.139	0	70	-70	19.8
13	D2	702	0	0.245	0	100	-100	71.9
14	D3	436	0	0.152	0	80	-80	44.8
15	D4	174	0	0.061	0	70	-70	22.5
16	E2	574	-100.5	0.200	-0.035	100	-100	9.0
17	E3	105	-89.5	0.037	-0.031	80	-80	0.0
18	E4	35.5	-36.5	0.012	-0.013	70	-70	0.0

Table 9.2. Maximum and minimum: angle of twist, shear strain and torque

For samples A1, C4, D4, E4, which were loaded to ±70Nm at 77K, the highest angle of twist of 399.5° was achieved in sample C4 (Tab. 9.2), while 174° was obtained in sample D4, 82° in sample A1 and 35.5° in sample E4.

For samples A2, C3, D3, E3, loaded to ±80Nm, the highest angle of twist of 660° was obtained in sample C3 (similarly to the case of ±70Nm). Smaller values were obtained in the remaining samples: in sample D3 the angle of 436° was reached, in A2 - 244°, and in E3 - 105°. Thus, exactly the same order as in the case of ±70Nm.

For cycles with the torque of ±100Nm, again, the highest angle of twist was obtained in the sample made of grade 316L stainless steel (C2), namely 1141°. Then, the angle of 719° was obtained for sample A4 made of grade 304 ss, slightly smaller angle of 702° was reached in sample D2. Finally, the angle of 574° was obtained in sample E2, made of grade 316LN stainless steel.

It is worth pointing out, that the highest shear strain, calculated from Eqs 4.53 and 4.56 by setting the radius equal to R, was equal to 0.398 (corresponding to the angle of 1141° for sample C2, Tab. 9.2). Similar value was obtained for sample A8 with the angle of twist of 1110.5° ($\gamma = 0.388$). Only these two values were slightly above the limit shear strain of the model, which was equal to $\gamma_{max} = 0.346$ (Eq. 4.10). Thus, apart from the results for samples C2 and A8, all the other results could be described using similar approach, presented in the Chapter 4, based on the small strains theory.

The amount of martensite measured on the surface was the smallest for samples made of grade 316LN stainless steel: 0% in the test with torque of ±70Nm, 0% in the test with torque of ±80Nm, and 9% in the test with torque of ±100Nm. The samples made of grade 304 stainless steel have shown higher martensite contents: 17.8% for the loading ±70Nm, 26.7% for the loading ±80Nm, and 67.1% for the loading ±100Nm. The samples made of grade 316L stainless steel have shown similar values to the previous ones: 19.8% in the test to ±70Nm, 34.4% in the test to ±80Nm, and 63.7% in the test to ±100Nm. The samples made of grade 304L stainless steel have shown the highest values: 22.5% for the loading to ±70Nm, 44.8% for the loading to ±80Nm, and 71.9% for the loading to ±100Nm.
Based on the previous comparison one concludes, that during cyclic torsional loading with the torque control, the amount of martensite induced on the surface is the smallest for the samples made of grade 316LN stainless steel, while it is increased for the samples made of grade 304 ss, as well as for the samples made of 316L and of 304L ss. The only exception from this sequence was observed for the torque of ±100Nm, when slightly more martensite was obtained for sample A4 made of grade 304 stainless steel (67.1%), whereas, for sample C2 made of grade 316L ss some 63.7% was reached. Yet, this difference was relatively small, only 3.4%. For this reason, it is concluded that the ability to form martensite during cyclic torsion at 77K increases according to the following sequence: from grade 316LN ss, through 304 and 316L, to 304L (Fig. 9.41).

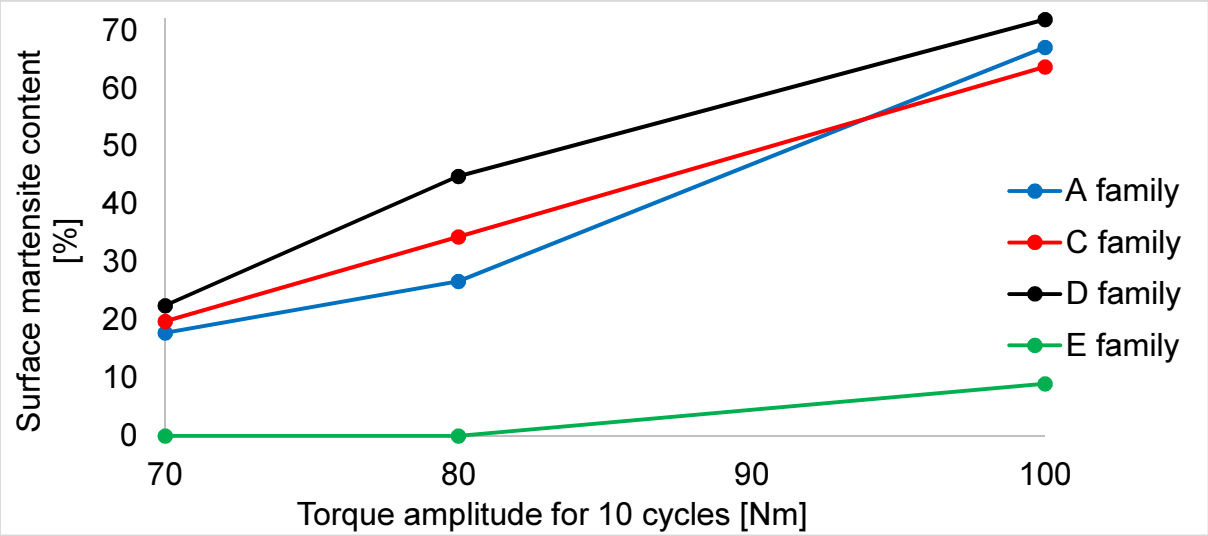

Figure 5.41. Martensite content on the surface of the sample for different stainless steel grades (A – 304, C - 316L, D – 304L, E – 316LN)

9.5. Deformation of the samples

All samples loaded via cyclic torsion, were photographed during the test. The photographs were taken after removing the samples from the bath of liquid nitrogen, and before the measurements of martensite content on the surface. The photographs were taken in order to evaluate the shape of the samples during loading and after the test. The reason for this was a need to check if the samples remain straight or if they become distorted.
Several pictures were obtained for each of the samples. Usually about 20 photographs per sample were made, one photograph after each half-cycle. For the sake of conciseness, only two photographs are presented per sample: one before and one after the end of the test.

Evaluation of deformation of all samples has been done, and the results are presented in Table 9.3. Some samples were only slightly distorted. Thus, their final shape is denoted as “almost straight”. For many samples the distortion was more clearly visible. For them the distortion was marked “large”.

Sample	Deformation (large or small)	Final shape (straight or deformed)
A1	Small	Almost straight
A2	Small	Almost straight
A3	Small	Almost straight
A4	Large	Deformed
A5	Large	Deformed
A6	Small	Almost straight
A7	Large	Deformed
A8	Large	Deformed
C2	Small	Almost straight
C3	Large	Deformed
C4	Large	Deformed
D2	Large	Deformed
D3	Large	Deformed
D4	Small	Almost straight
E2	Small	Almost straight
E3	Small	Almost straight
E4	Small	Almost straight

Table 9.3. Evaluation of deformation of samples after the cyclic torsion tests

In total, 8 samples remained almost straight after the test (A1, A2, A3, A6, C2, E2, E3, E4), whereas, 14 samples became deformed (Tab. 9.3). This statistics revealed the problem of distortion of the samples during twisting. It should be solved if the samples were to be applied in the real structures. Such a technological process, that consists of twisting cylindrical bars should produce samples of straight geometry. One could think of such structural elements like shafts, for which straight shape is obligatory.

The initial and the final shapes are presented below for all tested samples. The sequence is the same as in Table 9.3. The samples made of grade 304 stainless steel (A1÷A8) are shown in Figs 5.42 ÷ 5.49. The samples made of grade 316L stainless steel (C2 ÷ C4) are shown in Figs 5.50 ÷ 5.52. The samples made of grade 304L stainless steel (D2 ÷ D4) in Figs 5.53 ÷ 5.55. Finally, the samples made of grade 316LN stainless steel (E2 ÷ E4) are illustrated in Figs 5.56 ÷ 5.58.

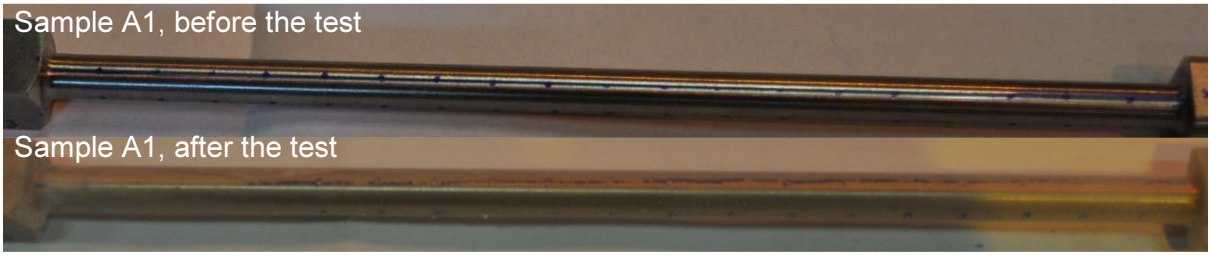

Figure 5.42. Photographs of sample A1 before and after cyclic torsion test

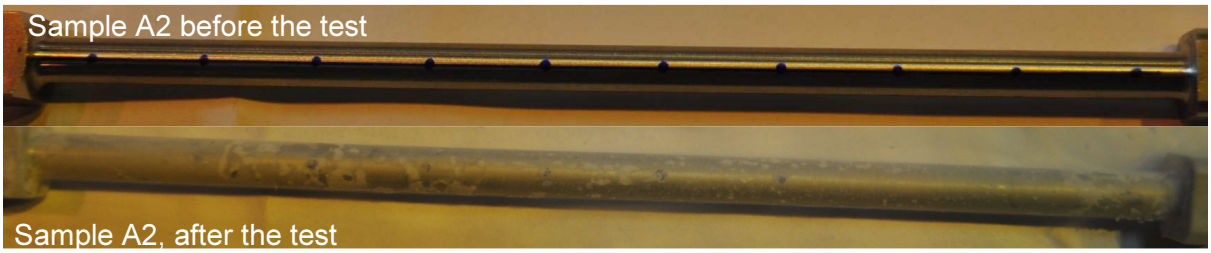

Figure 5.43. Photographs of sample A2 before and after cyclic torsion test

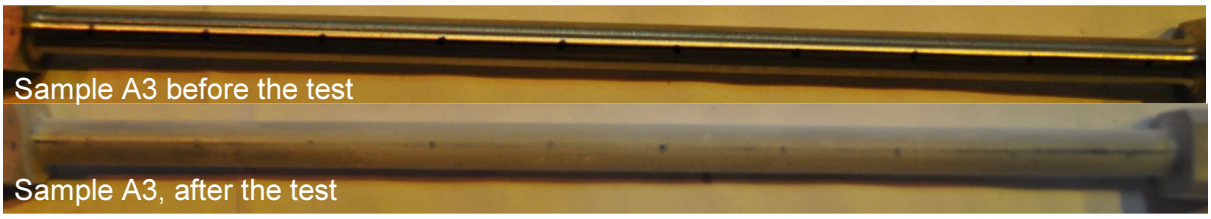

Figure 5.44. Photographs of sample A3 before and after cyclic torsion test

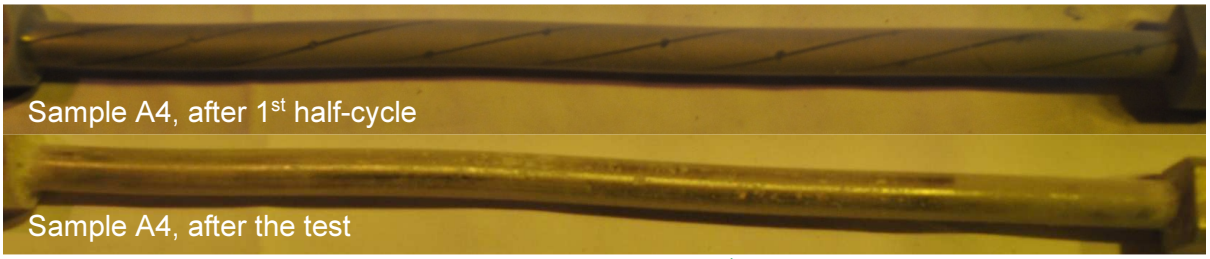

Figure 5.45. Photograph of sample A4 after the 1st half-cycle and after the test (no picture was made before the test)

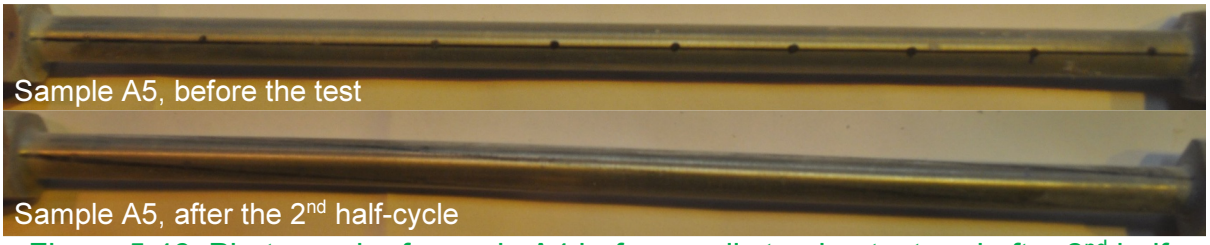

Figure 5.46. Photograph of sample A4 before cyclic torsion test and after 2nd half-cycle (no picture was made after the test)

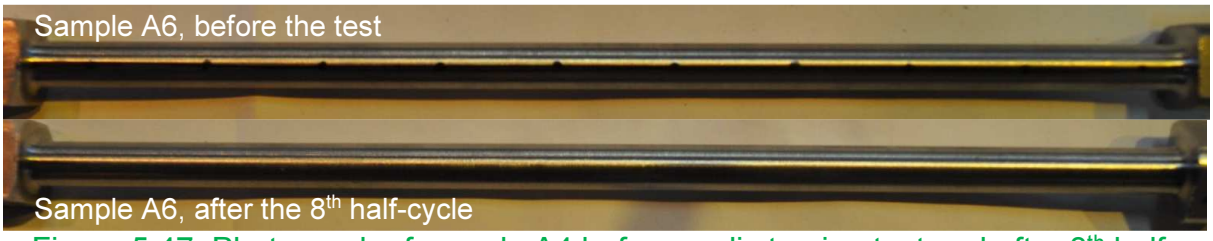

Figure 5.47. Photograph of sample A4 before cyclic torsion test and after 8th half-cycle (no pictures were made after the test)

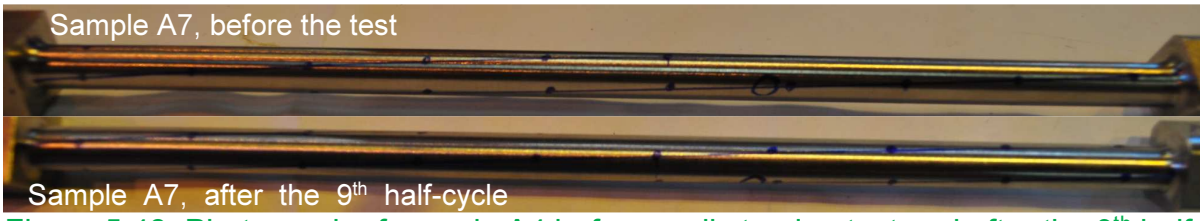

Figure 5.48. Photograph of sample A4 before cyclic torsion test and after the 9th half-cycle (no pictures were made after the test)

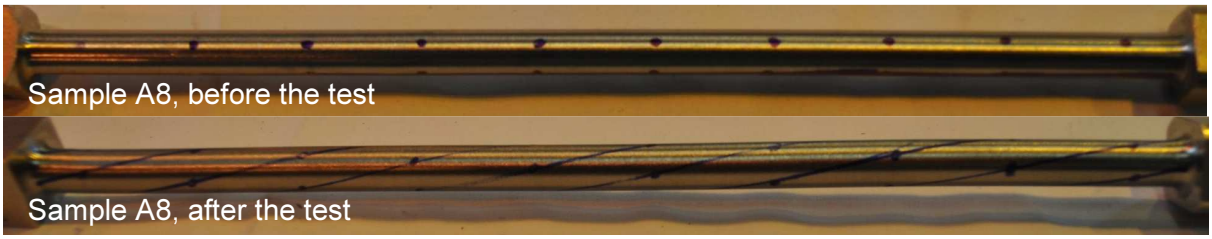

Figure 5.49. Photographs of sample A8 before and after cyclic torsion test

Figure 5.50. Photographs of sample C2 after the 1st half-cycle and after the test (no picture was made before the test)

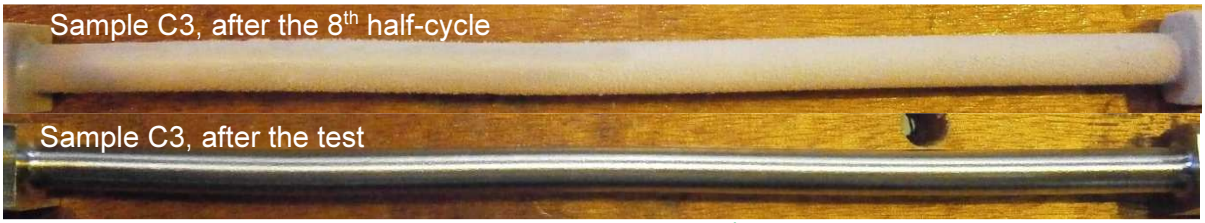

Figure 5.51. Photographs of sample C3 after the 8th half-cycle and after the test (no picture was made before the test)

Figure 5.52. Photographs of sample C4 before and after cyclic torsion test

Figure 5.53. Photographs of sample D2 before and after cyclic torsion test

Figure 5.54. Photographs of sample D3 before and after cyclic torsion test

Figure 5.55. Photographs of sample D4 before and after cyclic torsion test

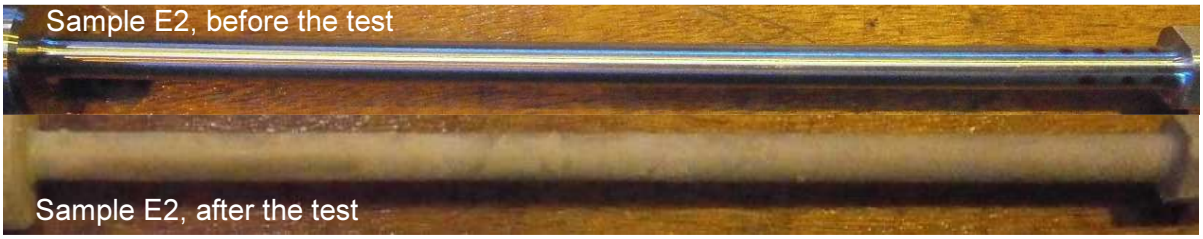

Figure 5.56. Photographs of sample E2 before and after cyclic torsion test

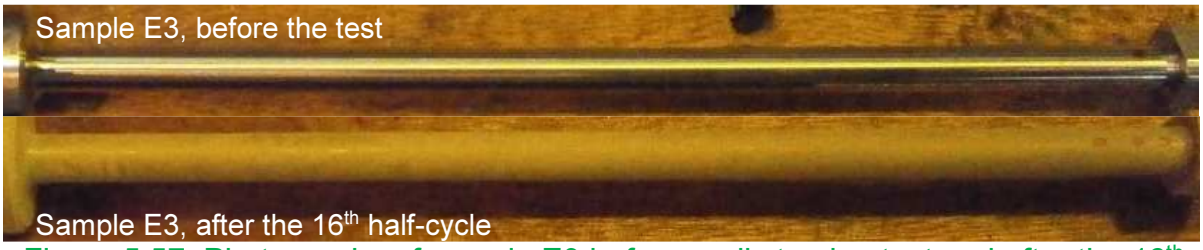

Figure 5.57. Photographs of sample E3 before cyclic torsion test and after the 16th half-cycle (no picture was made after the test)

Figure 5.58. Photographs of sample E4 before and after cyclic torsion test

9.6. Summary and conclusions

The following results were discussed in the present chapter:
1. The torque was measured as a function of the angle of twist during cyclic torsion for 4 different austenitic stainless steels (grade 304 ss – 10 samples, grade 304L ss – 3 samples, grade 316L ss – 3 samples, grade 316LN ss – 3 samples).
2. The evolution of martensite content on the surface, along the axis of the sample, was measured for almost all samples (A1÷A8, C2÷C4, D2÷D4, E2÷E4).
3. The distortion of the samples was captured, by making photographs after almost each half-cycle of loading.
4. The evolution of martensite on the surface was related to the accumulated angle of twist, resulting in generalized kinetics of the phase transformation during torsion.

The following conclusions are drawn:

- The martensite content has almost constant distribution on the surface of the sample along its length, which corresponds to the theoretical prediction,
- Different martensite contents were obtained for all four grades of the austenitic stainless steel. The highest martensite content was found in grade 304L stainless steel, then in 316L, 304 and, finally, in 316LN (Fig. 5.41).
- Cyclic torsion allows generation of phase transformation by means of smaller angles of twist, when compared to monotonic torsion.
- Cyclic torsion allows obtaining straight geometry of the samples, in the course of cyclic deformation process.

10. Plastic shakedown

10.1. Introduction

In the previous Chapter, the results of cyclic torsion tests were presented. Most of the samples were twisted at liquid nitrogen temperature. A few were tested at room temperature. Five samples were loaded by using kinematic control, i.e. by controlling the angle of twist. The other samples were loaded by using torque control (14 samples, Tab. 9.1).
Cyclic torsion tests controlled by means of torque (constant amplitude of torque on cycle), were performed in order to test the possibility of reaching shakedown of newly created Functionally Graded Structures. The phenomenon of elastic shakedown consists in such a deformation mode, that the sample behaves in elastic way after several dissipative cycles. In many cases it is accompanied by increasing yield stress, caused by hardening of the material in the course of loading. Such a phenomenon is beneficial because of lack of energy dissipation due to plastic strains.
Apart from elastic shakedown, in the literature the term “plastic shakedown” is used. Plastic shakedown leads to stabilization of hysteresis loops during cyclic loading, and decreasing energy dissipation to a minimum corresponding to given loading configuration. Similarly to the elastic shakedown, the plastic shakedown is beneficial as well, because of strong limitation of energy dissipation on cycle, resulting in the increase of fatigue life of structure.
The phenomenon of shakedown is often related to hardening, and to increase of the yield stress. In the present Thesis, additional elements are added, namely the effect of micro-structure evolution in the course of loading. Because of the phase transformation, the volume of the material gradually evolves from the austenitic phase to the martensitic one. As the martensite has much higher yield strength than the austenite, and it behaves in nearly brittle way, it is defined by many sources (e.g. Sitko et al. (2010), Sitko and Skoczeń (2012)) as purely elastic phase.
Thus, the phase transformation leads to a new phenomenon called structural “shakedown”, which consists of replacing the parent ductile and dissipative phase by the secondary elastic phase. Assuming an extreme case, that all the volume of the material is replaced by the elastic phase, the shakedown occurs by definition as the secondary phase behaves in purely elastic way with no dissipation of energy. In practical applications, only some part of the volume will change into the secondary phase, resulting in the elastic properties of this part of the volume. The phenomenon of structural shakedown is explained in detail in the subsequent section.

10.2. Mechanism of structural shakedown

The mechanism of structural shakedown is represented in Fig. 10.1. A three dimensional body of an arbitrary shape is loaded by means of general loadings (forces, continuously distributed forces, body forces, torques etc.). The body is supported in order to remain in static equilibrium.
Let us assume that the loadings acting on the body increase. In the first stage the loadings are still small, such that the yield stress is not exceeded and the continuum behaves in an elastic way. In the second stage, the loading causes at least one point of the material to reach the yield point, and the plastic strains occur.
Yet, in this stage the plastic strains are small, such that the limiting strain threshold for the phase transformation to occur is not reached.

In the next stage, the loading increases even more, such that the amplitude of the plastic strains increases. Now, the initial threshold strain has been surpassed and the secondary phase starts to develop. The inclusions of martensitic phase are denoted as yellow ellipsoids with laths representing the texture.
In the last – fourth loading stage, the plastic strains reach their maximum possible values (not causing fracture). The parent phase transforms into the secondary phase within the maximum allowable quantity. In theory, this could be 100% of the volume of the material. In practice, some smaller values are expected, especially in the cases where more complex loadings are applied.

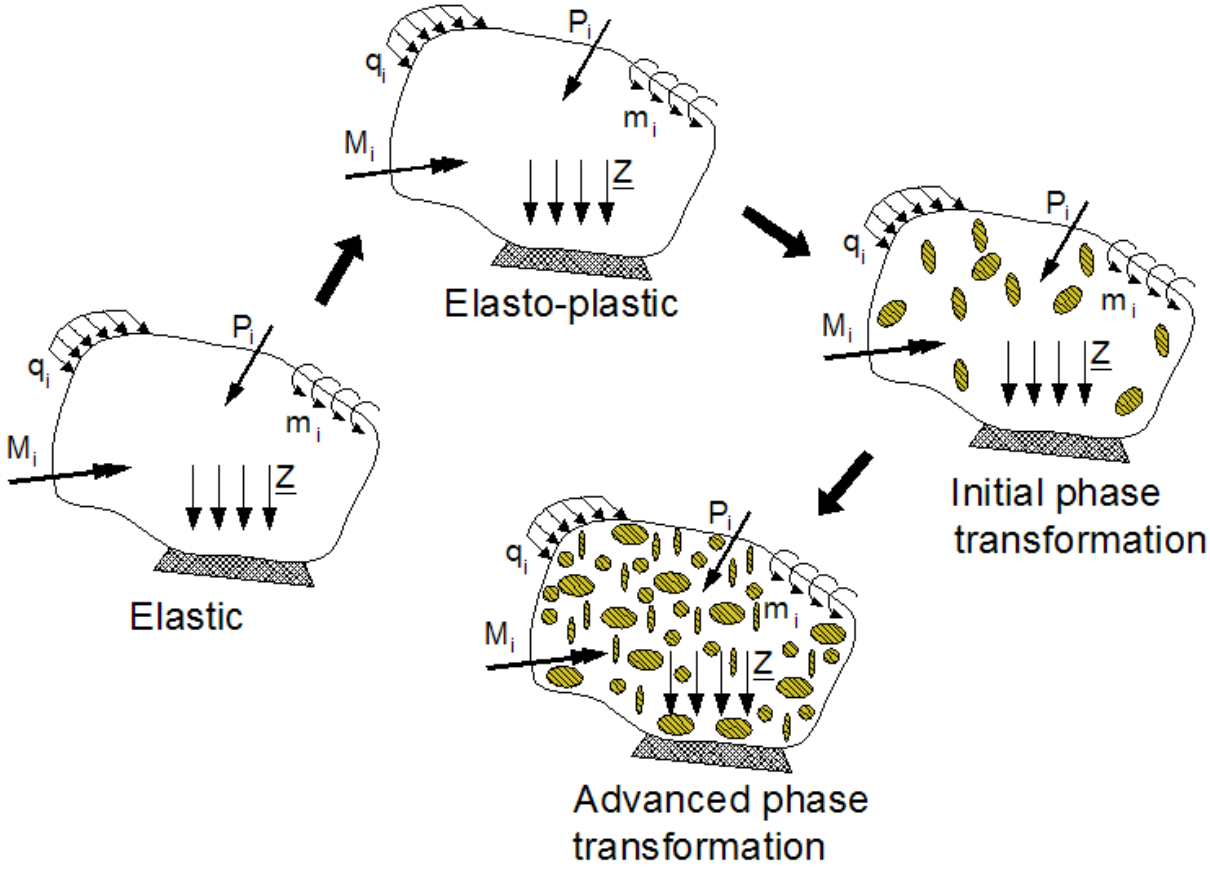

Figure 10.1 Loading stages associated with the micro-structural changes in two-phase continuum

Taking into account the general principle of structural shakedown presented in Fig. 10.1, the specific case of structural shakedown due to pure torsion is shown in Fig. 10.2. A bar with circular cross-section has been loaded by means of twisting moment, which is constant along its length. A slice has been enlarged to reveal progression of the phase transformation during the increase of loading. For small values of torque, the elastic strains occur in the area of the cross-section (stage 1). Then, in the subsequent cycle, upon the increase of the torque, the sample begins to flow plastically from the surface towards the center of the sample. When the amplitude of inelastic strain exceeds the threshold value for the phase transformation, the secondary (martensitic) phase starts to emerge. In the final stage, the plastic zone covers almost all the cross-section, only a small area around the center remains elastic. Large quantity of secondary phase is generated from the parent austenitic one.

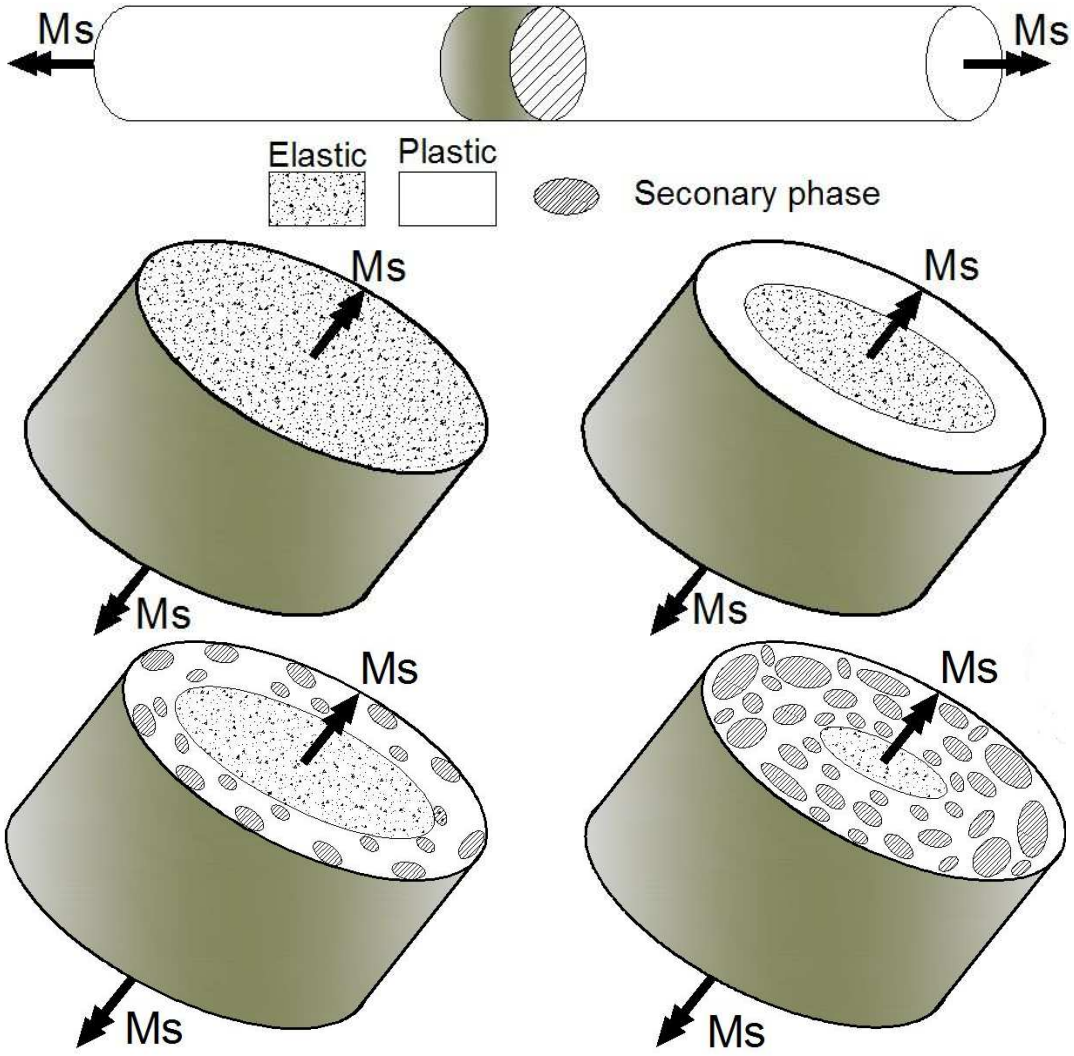

Figure 10.2. The scheme of structural shakedown due to torsion of circular bar

According to the classical shakedown theory, it can occur if the dissipation of energy is limited (less than infinity). It can be proven that for a body undergoing phase transformation the dissipation of energy is limited as well. In addition, the process of structural evolution from plastic ductile austenite into elastic martensite further decreases energy dissipation. It is explained in details in the subsequent section.

10.3. Boundedness of energy dissipation during structural shakedown

During the shakedown process the volume of the structure can be subdivided into dissipative volume (undergoing plastic strains) and elastic volume. According to the formula:

$$V = V^{diss} + V^{el} \tag{10.1}$$

the volume of the structure remains constant (assuming no dilatation effect), whereas the dissipative volume decreases with time (Fig. 10.3).

The dissipated energy can be calculated by integrating its rate (power)over the time of loading. The power defined at the level of a material point can be calculated as:

$$P_i^{diss} = \underline{\underline{\sigma}} : \underline{\underline{\dot{\varepsilon}}}^p \tag{10.2}$$

Thus, the power over the whole body can be achieved by integrating Eq. 10.2 over the volume:

$$P^{diss} = \int_V \underline{\underline{\sigma}} : \underline{\underline{\dot{\varepsilon}}}^p dV \tag{10.3}$$

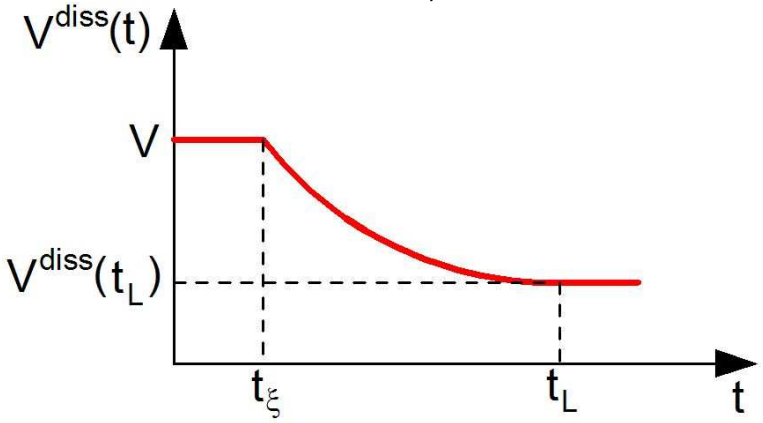

Figure 10.3. Decreasing dissipative volume $V^{diss}(t)$ with time

Recalling the relationship between the power and the energy:

$$P^{diss} = \frac{dW^{diss}}{dt} \tag{10.4}$$

The total dissipated energy equals:

$$W^{diss} = \int_0^t P^{diss}(t)dt \tag{10.5}$$

Thus, inserting Eq. 10.3 into Eq. 10.5, one obtains total energy dissipation in the form:

$$W^{diss} = \int_o^t \left(\int_V \underline{\underline{\sigma}} : \underline{\underline{\dot{\varepsilon}}}^p dV \right) dt \tag{10.6}$$

Eq. 10.6 represents the dissipation of energy for a body without phase transformation, for which the dissipative volume remains constant during the whole process and equal to the initial volume *V*.

For a body with the phase transformation, the total dissipation of energy can be calculated by decomposing Eq. 10.6 with respect to time, in order to take into account three time intervals (according to Fig. 10.3):

- $t \in < 0, t_\xi >$ before the phase transformation,
- $t \in < t_\xi, t_L >$ during the phase transformation,
- $t \in < t_L, t >$ after the phase transformation.

In the first time interval, the dissipative volume is equal to the initial volume *V*. Thus, the dissipation of energy equals:

$$W_{pt1}^{diss} = \int_0^{t_\xi} \left[\int_V \underline{\underline{\sigma}} : \underline{\underline{\dot{\varepsilon}}}^p dV \right] dt \tag{10.7}$$

In the second time interval, one integrates over the volume which remains a decreasing function of time (see Fig. 10.3). The dissipated energy equals:

$$W_{pt2}^{diss} = \int_{t_\xi}^{t_L} \left[\int_{V^{diss}(t)} \underline{\underline{\sigma}} : \underline{\underline{\dot{\varepsilon}}}^p dV \right] dt \tag{10.8}$$

In the 3rd time interval, the phase transformation reaches saturation, and the dissipative volume decreased to its minimum $V^{diss}(t_L) = const.$ The dissipated energy equals:

$$W_{pt3}^{diss} = \int_{t_L}^{t} \left[\int_{V^{diss}(t_L)} \underline{\underline{\sigma}} : \underline{\underline{\dot{\varepsilon}}}^p dV \right] dt \tag{10.9}$$

Finally, total dissipated energy for a body which undergoes phase transformation equals:

$$W_{pt}^{diss} = W_{pt1}^{diss} + W_{pt2}^{diss} + W_{pt3}^{diss} \tag{10.10}$$

and:

$$W_{pt}^{diss} = \int_{0}^{t_\xi} \left[\int_{V} \underline{\underline{\sigma}} : \underline{\underline{\dot{\varepsilon}}}^p dV \right] dt + \int_{t_\xi}^{t_L} \left[\int_{V^{diss}(t)} \underline{\underline{\sigma}} : \underline{\underline{\dot{\varepsilon}}}^p dV \right] dt + \int_{t_L}^{t} \left[\int_{V^{diss}(t_L)} \underline{\underline{\sigma}} : \underline{\underline{\dot{\varepsilon}}}^p dV \right] dt \tag{10.11}$$

Comparing the total dissipated energy for a classical body (Eq. 10.6), and a body undergoing phase transformation (Eq. 10.11) it is straightforward to conclude that:

$$W_{pt}^{diss} \leq W^{diss} \tag{10.12}$$

So:

$$\int_{0}^{t_\xi} \left[\int_{V} \underline{\underline{\sigma}} : \underline{\underline{\dot{\varepsilon}}}^p dV \right] dt + \int_{t_\xi}^{t_L} \left[\int_{V^{diss}(t)} \underline{\underline{\sigma}} : \underline{\underline{\dot{\varepsilon}}}^p dV \right] dt + \int_{t_L}^{t} \left[\int_{V^{diss}(t_L)} \underline{\underline{\sigma}} : \underline{\underline{\dot{\varepsilon}}}^p dV \right] dt \leq \int_{0}^{t} \left[\int_{0}^{V} \underline{\underline{\sigma}} : \underline{\underline{\dot{\varepsilon}}}^p dV \right] dt \tag{10.13}$$

If no phase transformation occurs, one has $V^{diss}(t) = V$, and both sides of inequality 10.13 are equal. For all other cases, because the dissipative volume is decreasing with time, integration over smaller volume will of course lead to smaller value of dissipated energy.

If the phase transformation consumes all the volume of the material, then the shakedown will occur by definition (Fig. 10.4). In such a case, all the volume of the material is replaced by the secondary phase which is elastic.

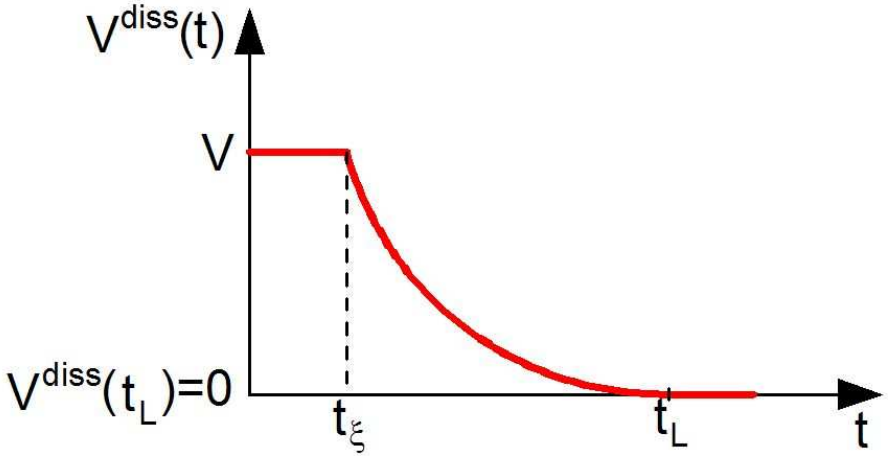

Figure 10.4. Dissipative volume in the case of complete phase transformation

The following conclusions can be drawn from the previous considerations:

1. Boundedness of dissipated energy in the continuum without phase transformation, implies boundedness of dissipated energy in the continuum with phase transformation.

2. If the structure composed of elastic-plastic matrix shakes down, the structure made of the same matrix undergoing phase transformation to secondary elastic phase, will also shake down.
3. If the transformation to secondary elastic phase occurs in the total volume of the structure, the shakedown occurs by definition.
In the following sections, the experimental results from cyclic torsion tests are presented. The dissipation of energy is calculated for several different materials (grades: 304, 304L, 316L, 316LN).

10.4. Experimental results: energy dissipation during elastic-plastic torsion

The results of cyclic torsion tests were presented in the Chapter 9. The torque was related to total angle of twist. It is worth recalling, that the loading was carried out with a torque wrench, which imposed a necessity of unloading the sample before setting slightly higher value of the torque. For this reason, at each measurement point the angle of twist after unloading (residual value) was measured as well.
In the present section, the results in terms of torque versus residual angle of twist in the elastic-plastic range are shown.
The dissipated energy, corresponding to plastic work, is calculated based on the following formula:

$$W = \int_0^{\varphi*} |M(\varphi^p)| d\,\varphi^p \qquad (10.14)$$

where φ^p is the residual angle of twist, $\varphi*$ is the upper limit of integration
Eq. 10.14 represents the area under the torque – residual angle of twist curve, expressed in the units of energy [J]. The dissipated energy has been calculated for full range of cycles. An example is shown for sample C2 (Tab. 9.1). The areas representing the dissipated energy after the 1st and the 2nd cycles are illustrated in Fig. 10.5 a, b.

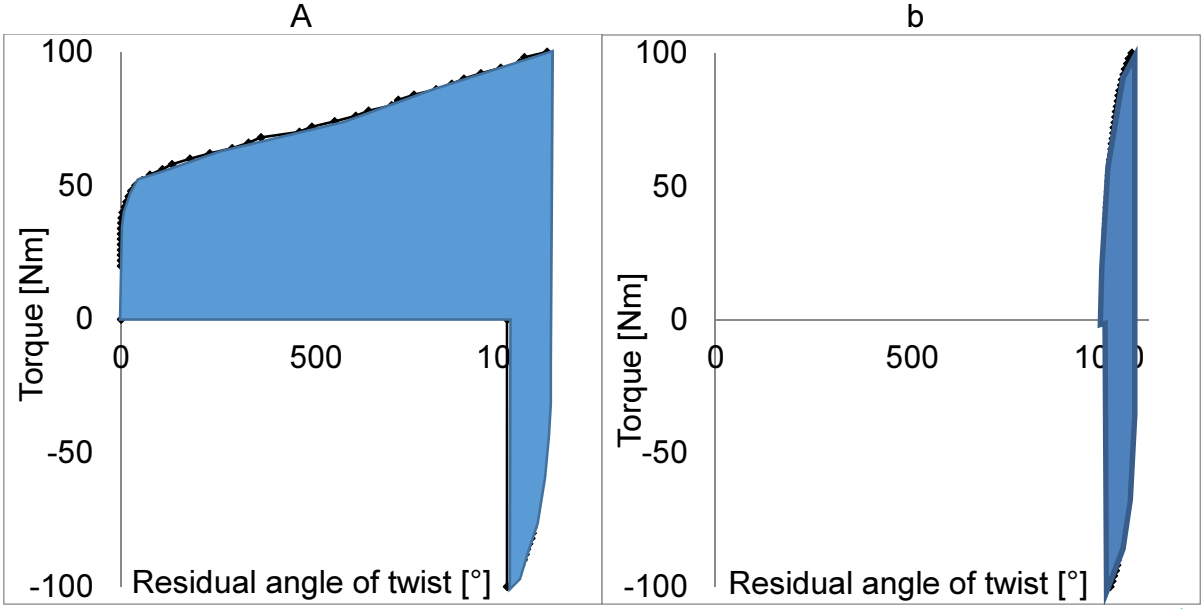

Figure 10.5. Area representing the dissipation of energy for sample C2 a) after 1st cycle, b) after 2nd cycle

The results in terms of torque versus residual angle of twist are shown for all samples in Figs 10.6 through 10.19, in the following order C2, C3, C4, D2, D3, D4, E2, E3, E4, A1, A2, A3, A4, A5, A6, A7, A8 (see Tab. 9.1).

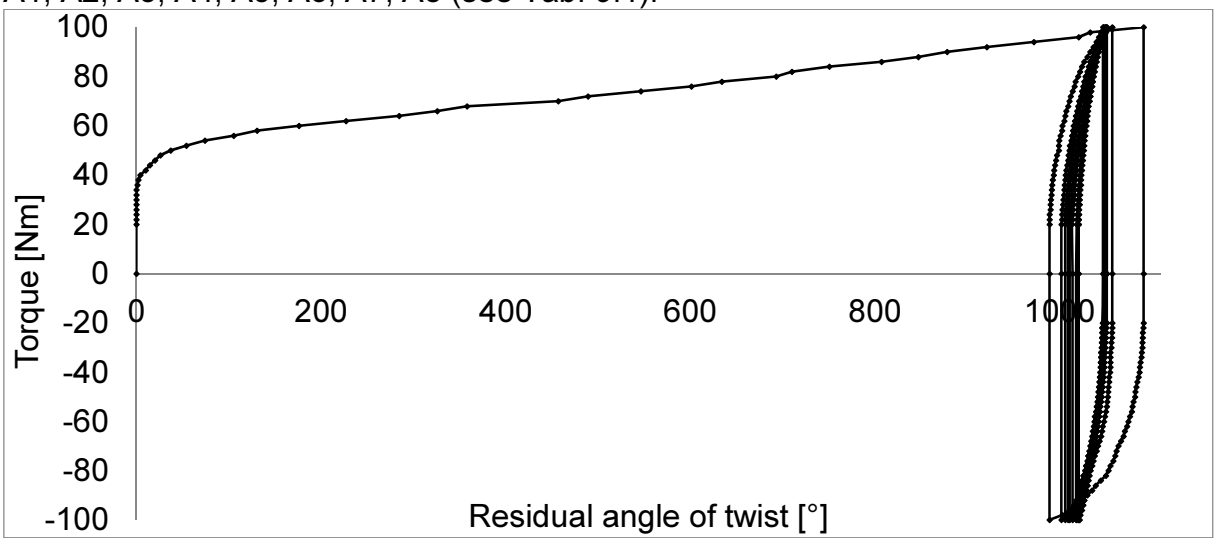

Figure 10.6. Torque versus residual angle of twist for sample C2, 77K, ±100Nm

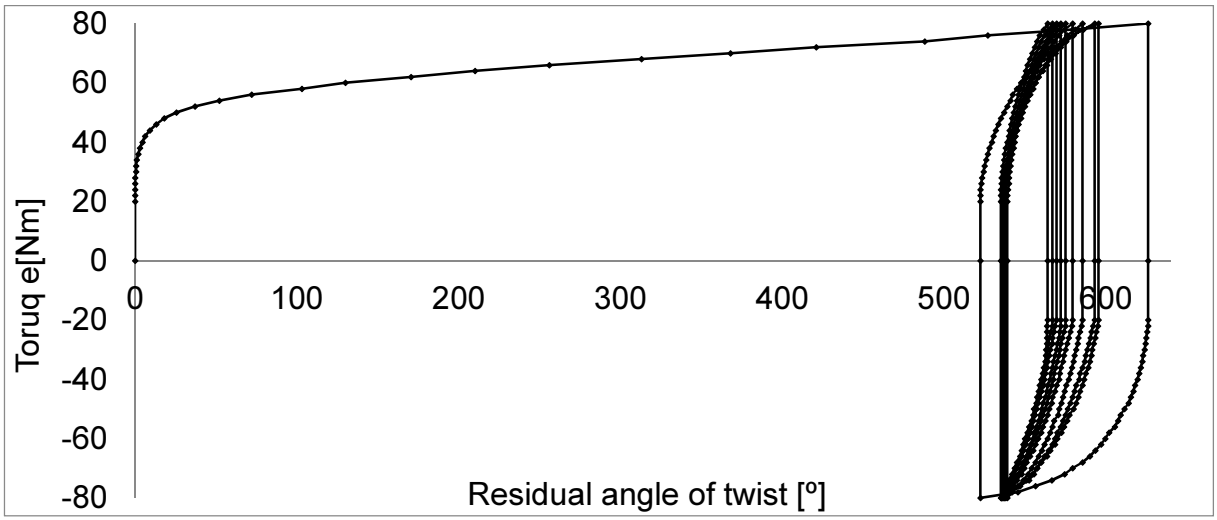

Figure 10.7. Torque versus residual angle of twist for sample C3, 77K, ±80Nm

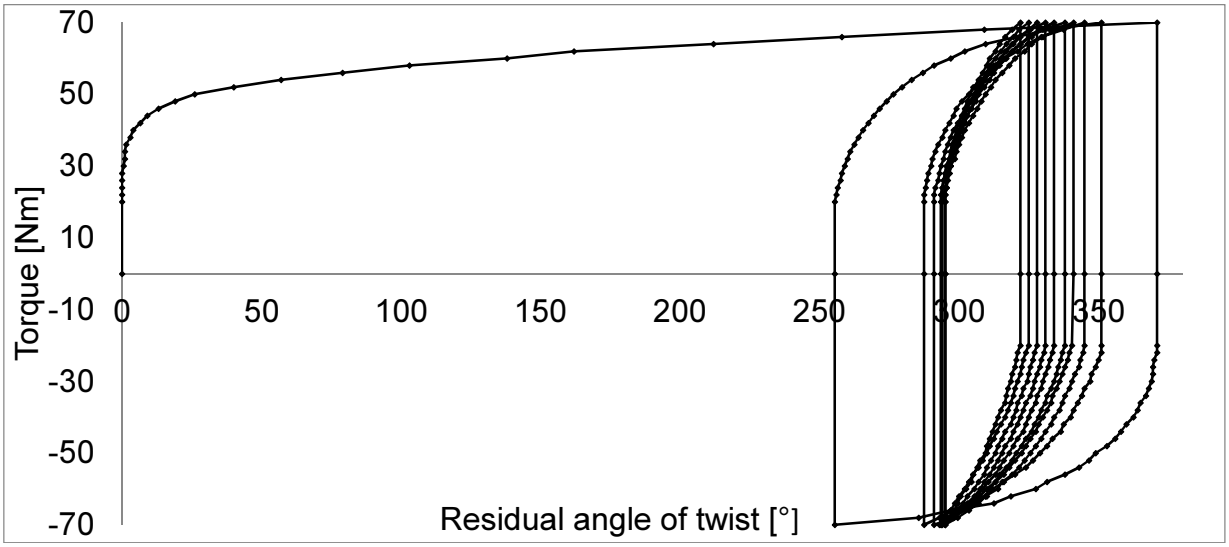

Figure 10.8. Torque versus residual angle of twist for sample C3, 77K, ±70Nm

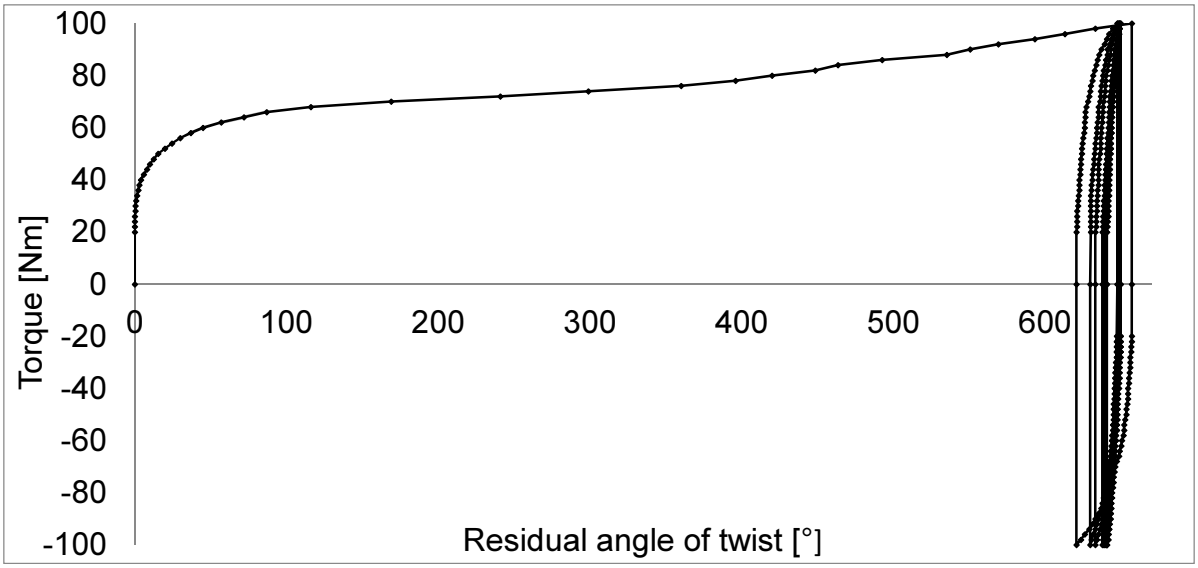

Figure 10.9. Torque versus residual angle of twist for sample D2, 77K, ±100Nm

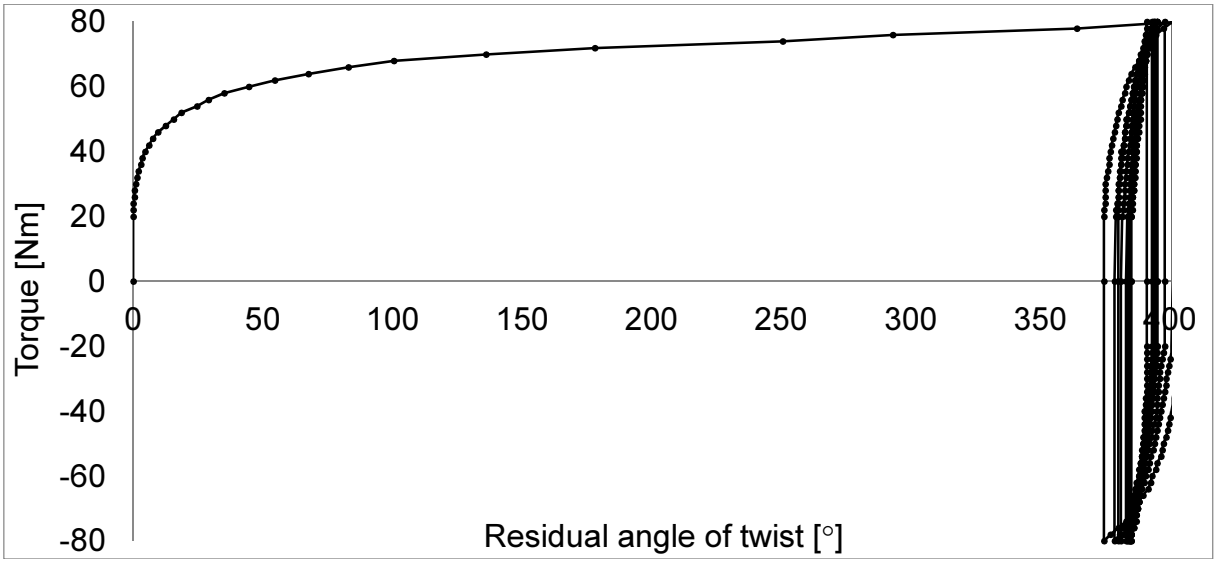

Figure 10.10. Torque versus residual angle of twist for sample D3, 77K, ±80Nm

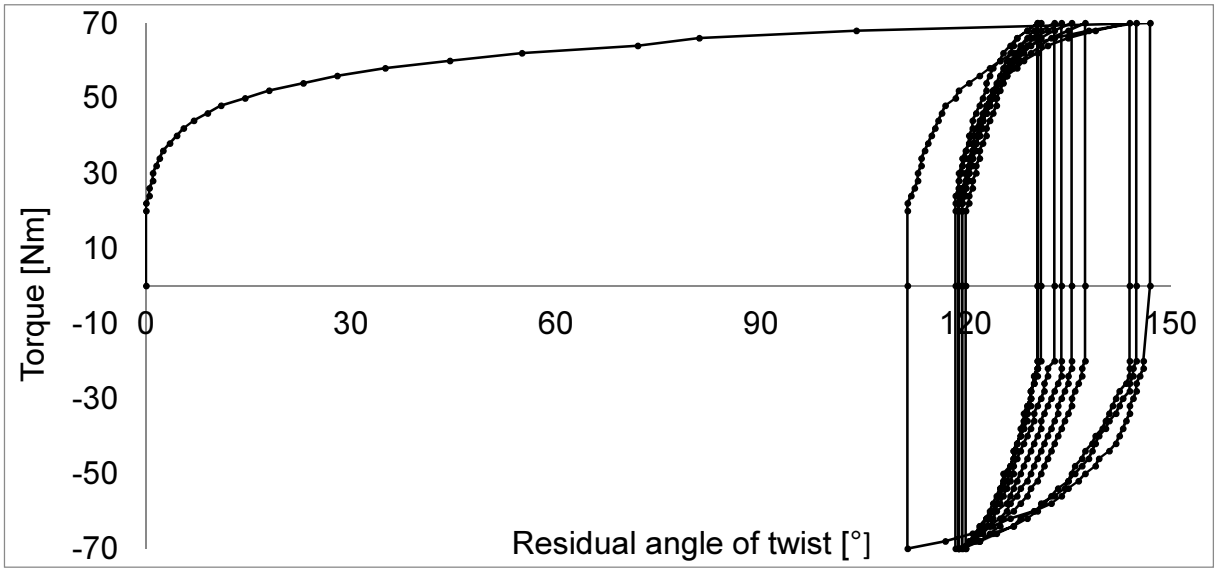

Figure 10.11. Torque versus residual angle of twist for sample D4, 77K, ±70Nm

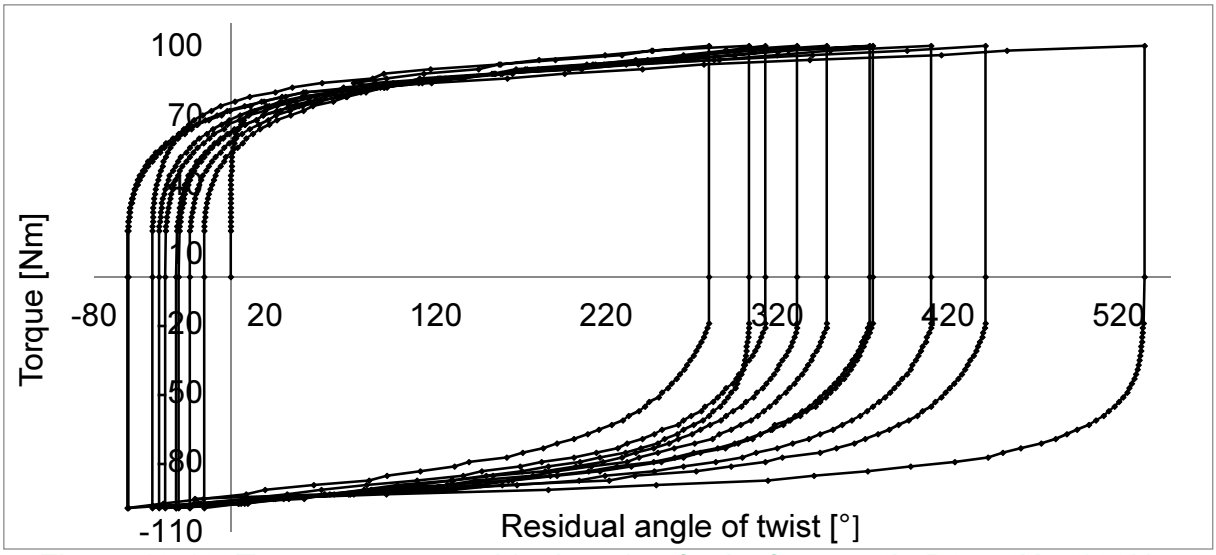

Figure 10.12. Torque versus residual angle of twist for sample D2, 77K, ±100Nm

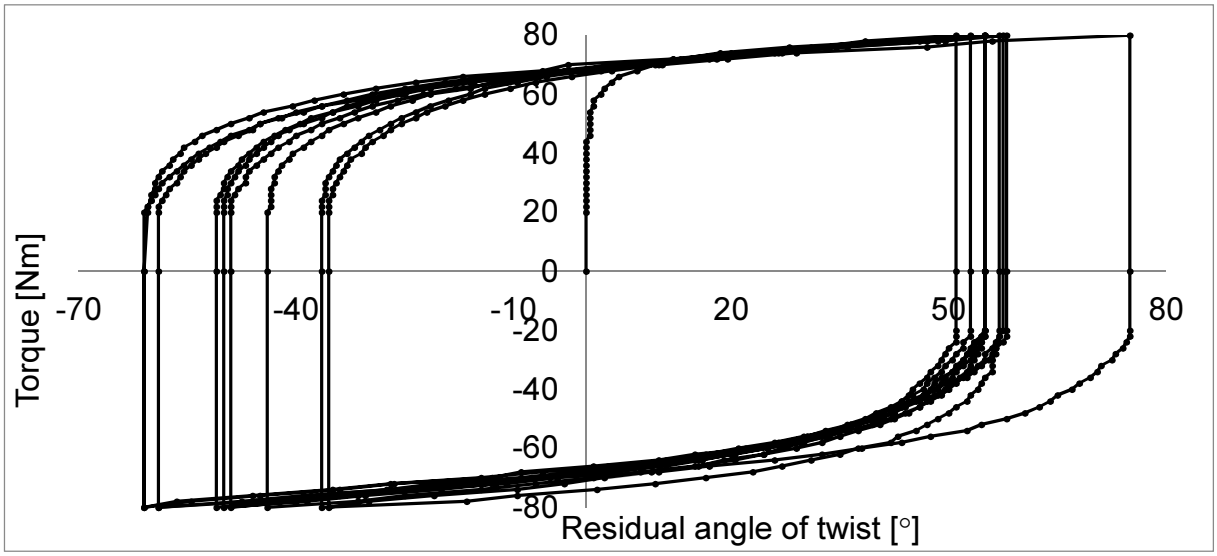

Figure 10.13. Torque versus residual angle of twist for sample E3, 77K, ±80Nm

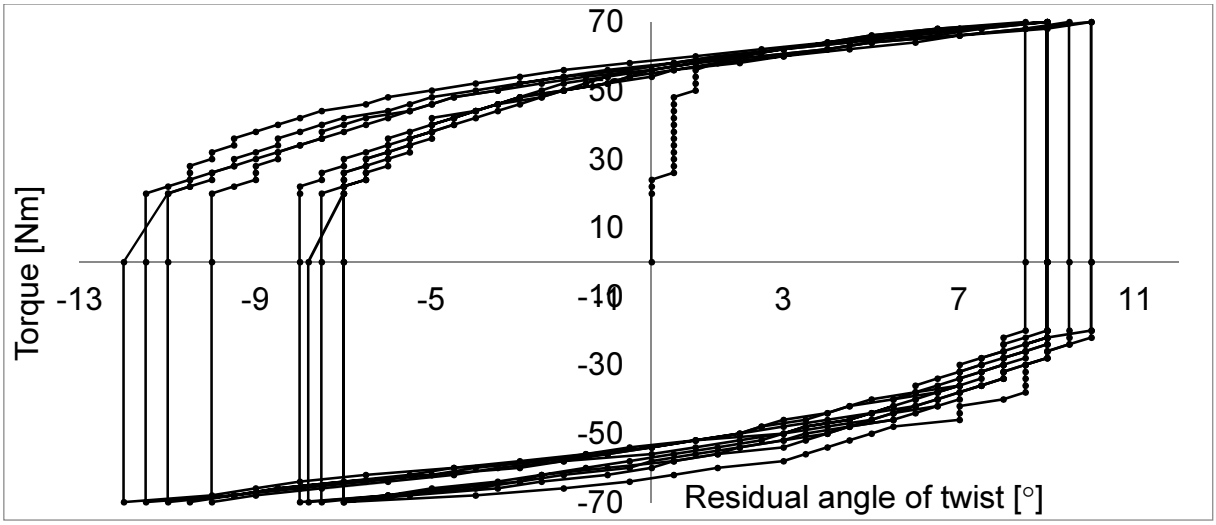

Figure 10.14. Torque versus residual angle of twist for sample E4, 77K, ±70Nm

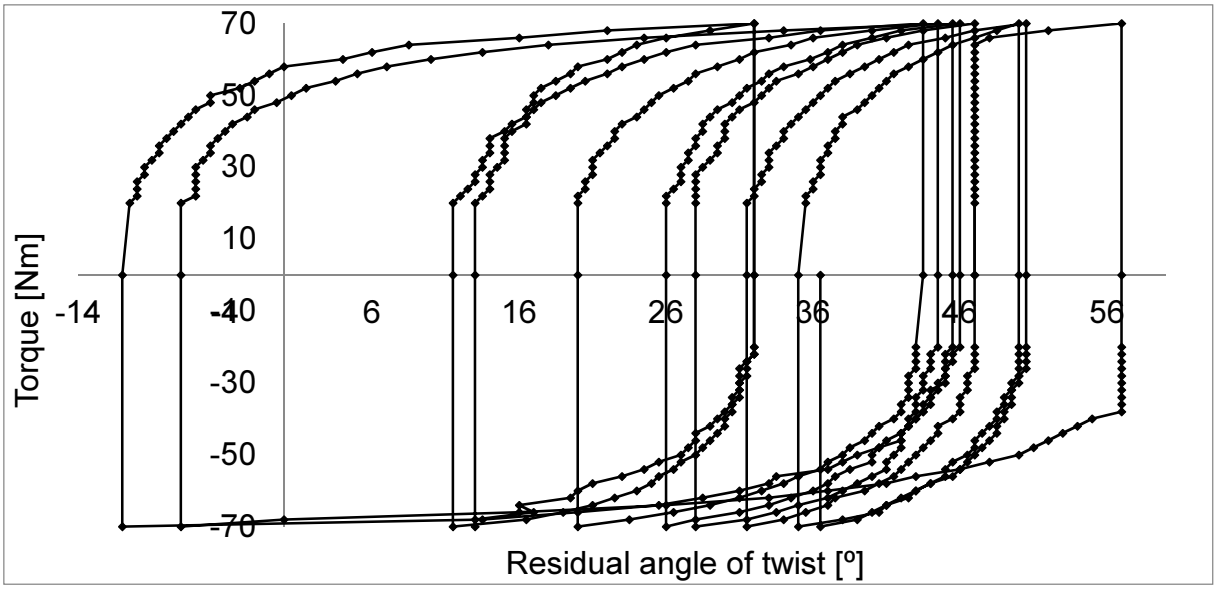

Figure 10.15. Torque versus residual angle of twist for sample A1, 77K, ±70Nm

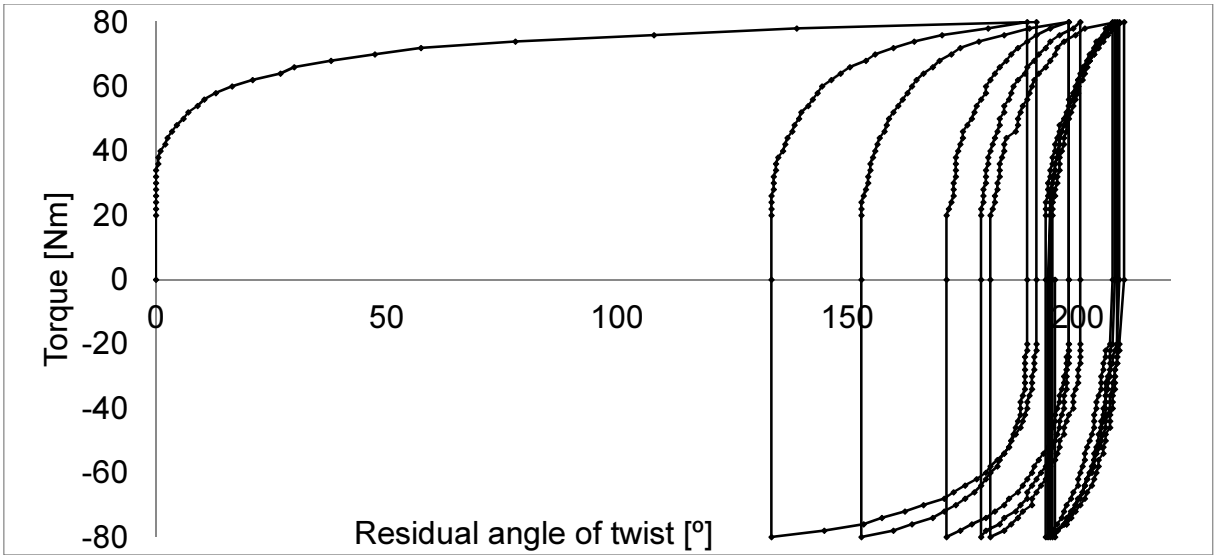

Figure 10.16. Torque versus residual angle of twist for sample A2, 77K, ±80Nm

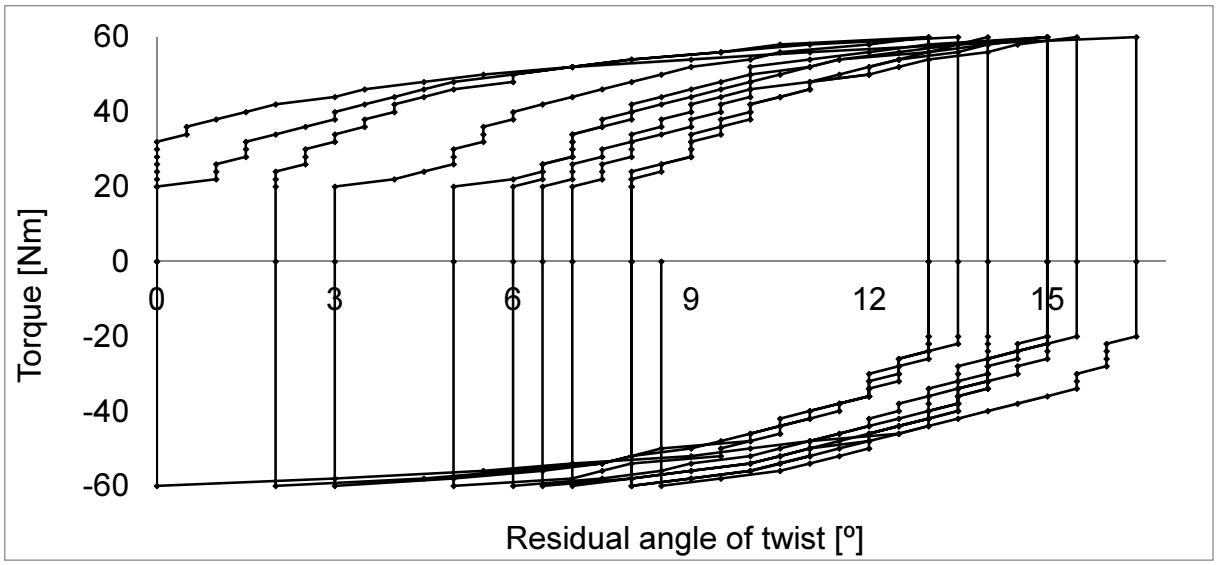

Figure 10.17. Torque versus residual angle of twist for sample A3, 77K, ±60Nm

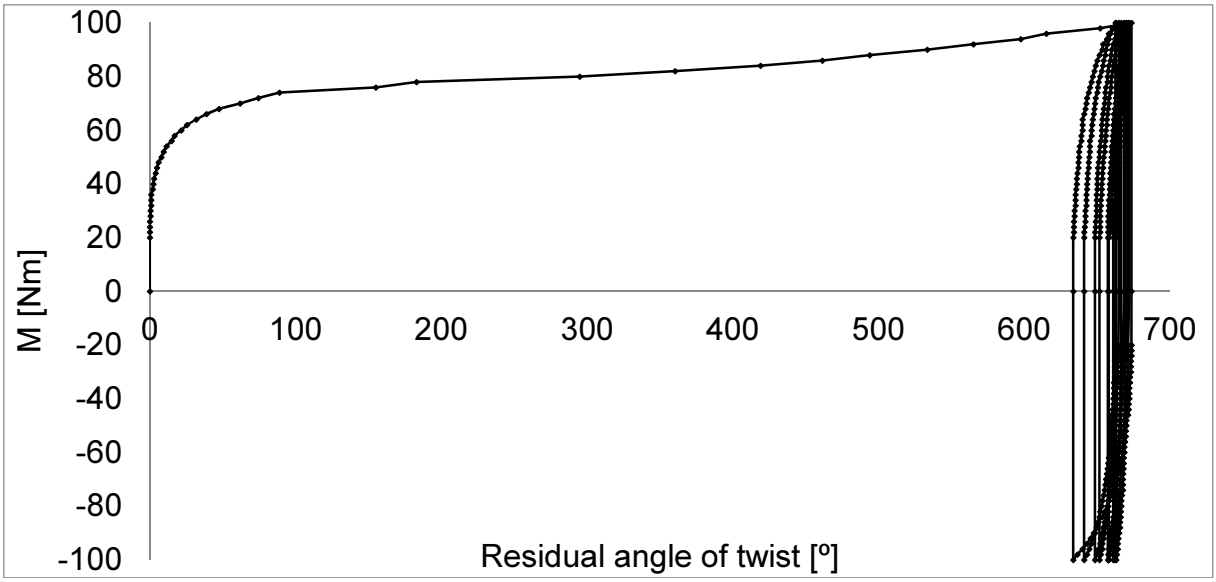

Figure 10.18. Torque versus residual angle of twist for sample A4, 77K, ±100Nm

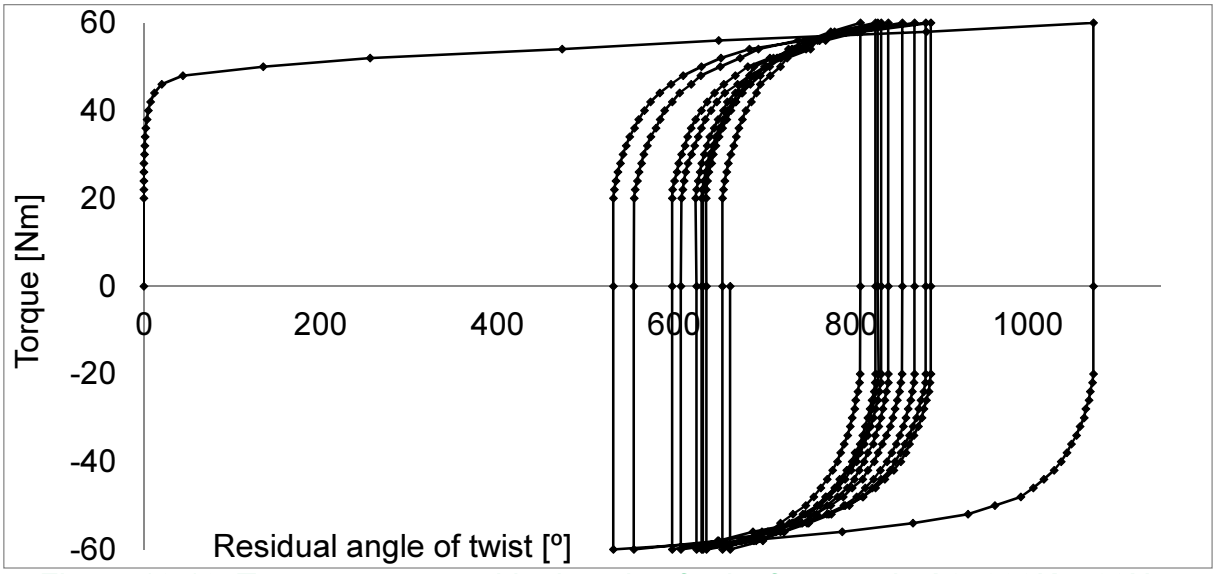

Figure 10.19. Torque versus residual angle of twist for sample A8, 293K, ±60Nm

10.5 Energy dissipated in subsequent cycles

The dissipated energy has been calculated according to Eq. 10.14, for all the results obtained in the course of torque controlled cyclic torsion tests illustrated in Figs 10.6 through 10.19. The results for samples made of grade 316L stainless steel are shown in Fig. 10.20. Similarly, for the samples made of grade 304L stainless steel the results are illustrated in Fig. 10.21, for 304 ss in Fig. 10.22, and for 316LN ss in Fig. 10.23.

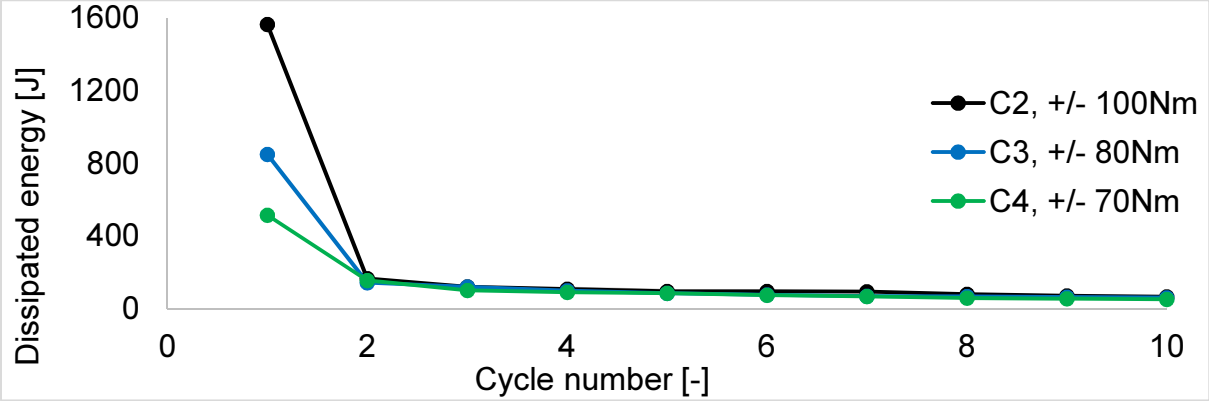

Figure 10.20. Energy dissipated during cyclic torsion at 77K for samples made of grade 316L stainless steel

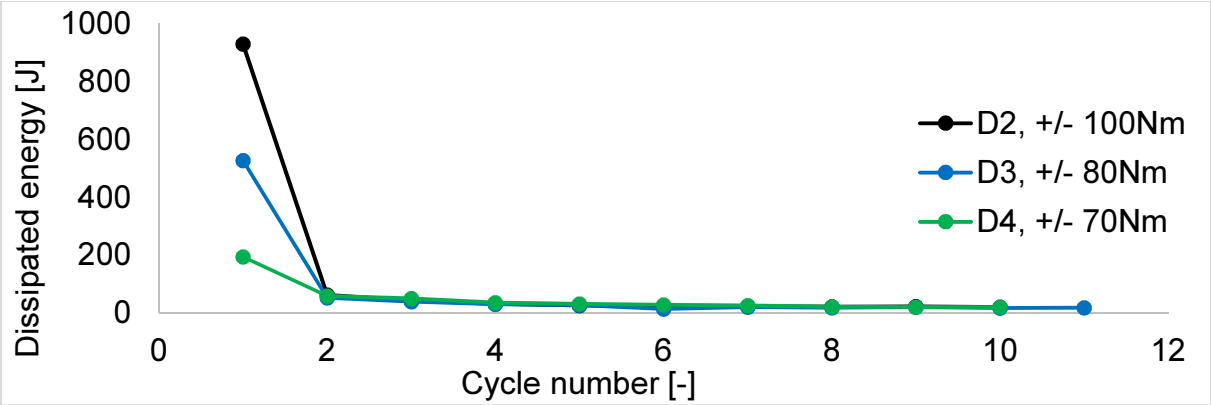

Figure 10.21. Dissipated energy during cyclic torsion at 77K for samples made of grade 304L stainless steel

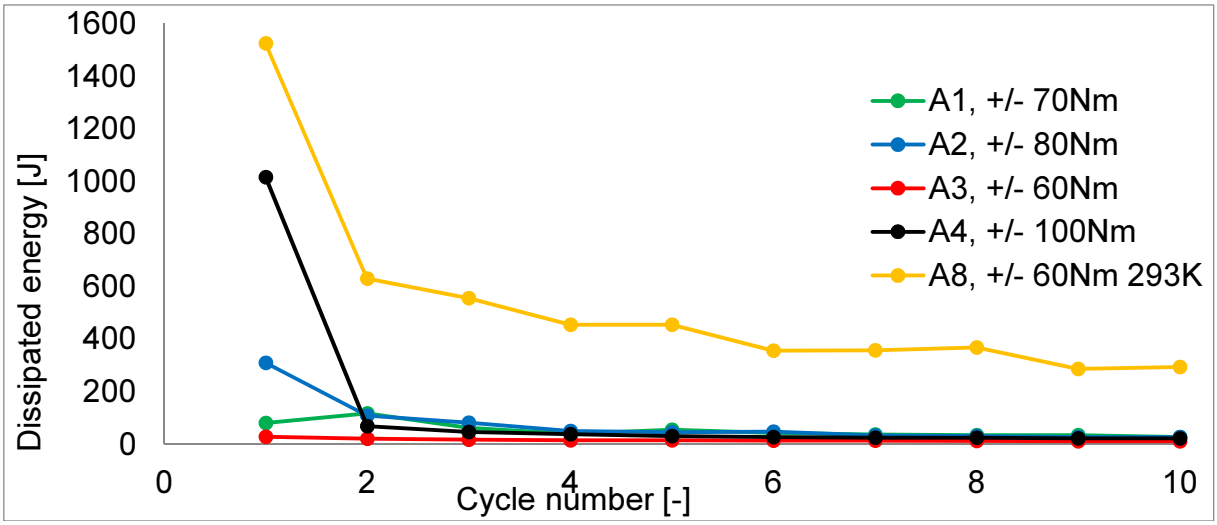

Figure 10.22. Energy dissipated during cyclic torsion at 77K and 293K (A8) for samples made of grade 304 stainless steel

For all the samples made of grade 316L (Fig. 10.20), 304L (Fig. 10.21) and 304 (Fig. 10.22), the dissipated energy decreases in the course of subsequent cycles. However, for the sample made of grade 316LN stainless steel loaded to ±80Nm and to ±70Nm (Fig. 10.23), the dissipated energy increases with subsequent cycles, showing increasing dissipation of energy. For clarity, these two results are shown separately in Figs 10.24 and 10.25.

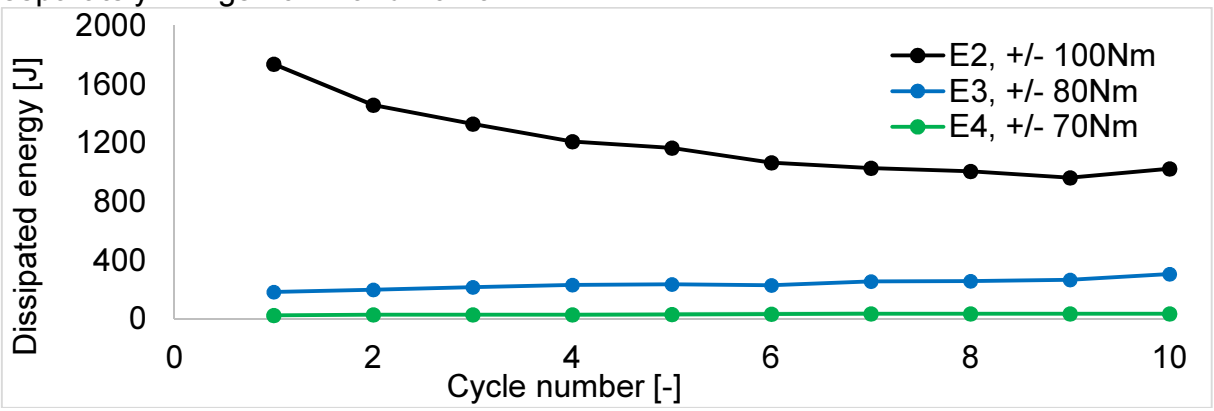

Figure 10.23. Dissipated energy during cyclic torsion at 77K for samples made of grade 316LN stainless steel

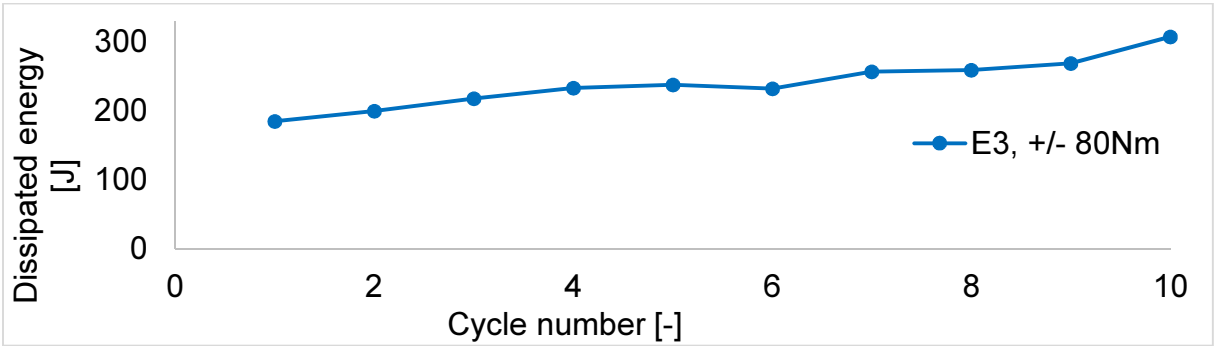

Figure 10.24. Dissipated energy during cyclic torsion at 77K, obtained for sample E3

The dissipated energy within sample E3 has increased from 185J after the 1st cycle, to 308J after the last 10th cycle. Thus, it increased by some 65%.

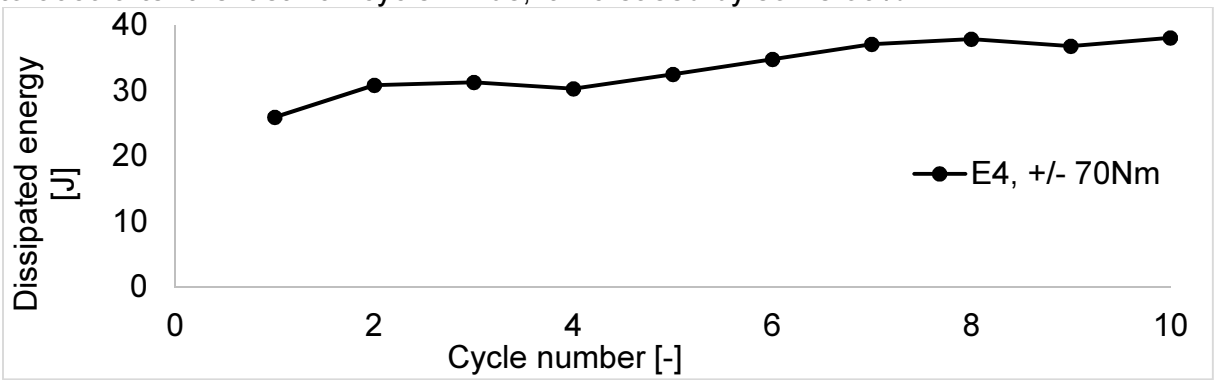

Figure 10.25. Dissipated energy during cyclic torsion at 77K, obtained for sample E4

For sample E4 the dissipated energy increased from 26J to 38J, thus by around 46%. The increase of dissipated energy was quite unexpected. This effect may possibly have to do with the occurrence of phase transformation. Indeed, in samples E3 and E4 no martensite was induced, whereas, in sample E2 the phase transformation occurred and the energy dissipation decreased.

A summary of all results, expressed in terms of dissipated energy, is made in Tab. 10.1, and is further illustrated in Fig. 10.26.

cycle	C2	C3	C4	D2	D3	D4	E2	E3	E4	A1	A2	A3	A4	A8
1	1566	851	516	929	526	193	1739	185	26	81	310	29	1016	1524
2	167	144	156	62	52	59	1459	200	31	117	109	21	69	630
3	120	121	102	42	39	50	1331	218	31	63	82	18	47	556
4	108	99	90	31	30	35	1212	233	30	40	51	15	38	455
5	96	86	85	25	26	31	1168	238	32	56	45	15	31	455
6	96	77	75	23	14	28	1067	232	35	43	48	14	27	355
7	94	70	68	22	20	25	1029	257	37	38	34	14	25	357
8	81	67	60	22	18	21	1007	259	38	34	31	13	25	368
9	72	63	55	22	20	20	964	269	37	34	28	12	22	287
10	66	60	51	20	17	19	1026	308	38	27	28	11	22	294

Table 10.1. Dissipated energy as a function of the number of cycles, corresponding to Tab. 9.1

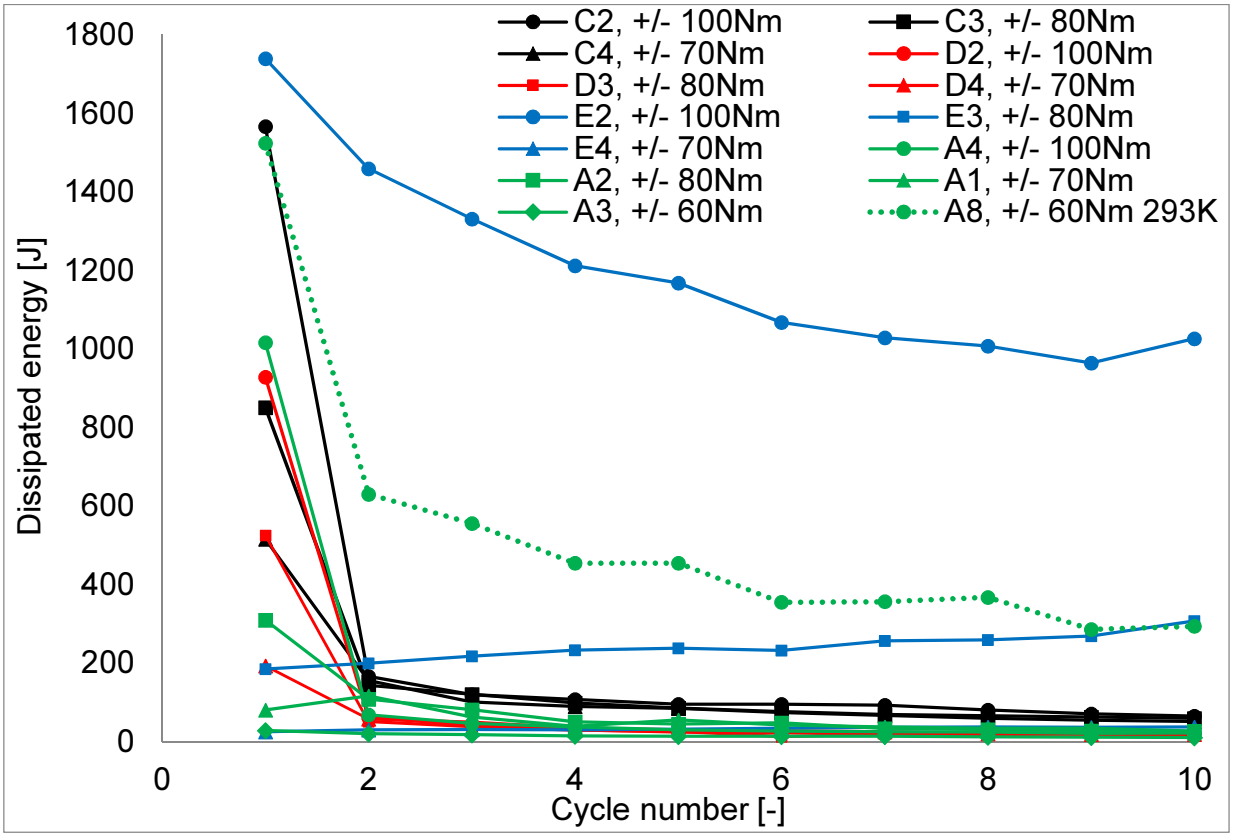

Figure 10.26. Dissipation of energy illustrated in all samples

From Fig. 10.29 it is clearly visible that dissipated energy is the smallest for the sample made of grade 304L stainless steel, then for the samples made of grades 304 and 316L. For 316LN ss, the dissipated energy is the highest for samples E2 and E3, however, for sample E4 it is even smaller than for the other materials. Here, the largest spread of response is encountered.

10.4. Conclusions

Based on the results contained in the present chapter, the following conclusions are drawn:

- dissipated energy decreases during cyclic torsion in the samples twisted at 77K, which has been proven experimentally for samples made of grades 304, 304L and 316L,
- for samples made of grade 316LN, the dissipated energy decreased for one loading (±100Nm) only, whereas, for the samples loaded to ±80Nm and to ±70Nm it somewhat increased,
- full elastic shakedown was not observed, yet, the dissipated energy decreased by several orders of magnitude after only 10 cycles,
- plastic shakedown was found for a number of samples.

11. Tensile tests at room temperature

Tensile test is used to obtain important mechanical properties like the Young modulus, the yield strength, the ultimate strength, the maximum strain, distortion of the cross-section, type of fracture (ductile, brittle), etc.
Tensile test has been carried out at room temperature for several samples pre-strained by means of torsion at 77K and at 293K. Thus, the samples had different martensite distributions. The test allows to evaluate the performance of newly created Functionally Graded Structural Members (FGSMs). One of the concerns was related to possible brittle behavior, resulting from very high martensite content. Several samples, from small to very high martensite contents, were tested and the above question was further elaborated.
The experimental procedure is covered in the next section, and the results are discussed in the subsequent sections.

11.1. Samples for the tensile test

In total, 11 tensile tests were performed on 8 different samples. All the samples, together with their preloading conditions, are summarized in Tab. 11.1. Some 4 of them were loaded by applying “monotonic” torsion (samples 1 through 4, see Tab. 5.2). These samples had only several centimeters of length. Sample 1 was pre-loaded until rupture. In addition, one raw sample from 304 stainless steel was tested, as well as the samples: 6.2 (Tab. 5.2), A9 and A10 (Tab. 9.1).
In the case of samples named 4, A9, A10, 62, two identical pieces were cut out in order to perform two separate tensile tests and to evaluate repeatability of the results. The samples cut out from sample 4 were named 41 and 42. Similarly, the ones cut out from sample A9 were denoted by A9.1 and A9.2, and from sample A10 in the same manner A10.1, A10.2 were obtained. Finally, from sample 6.2 (Tab. 5.2), two samples 62.1 and 62.2 were created.

Sample number	Material	Temperature [K]	Pre-loading conditions	Max. martensite content on the surface [%]
1	304	293	Torsion until rupture	49.5
2	304	77	Twisting to 870°	58.4
3	304	293	Twisting to 870°	5.9
41, 42	304	77	Torsion until rupture	88.5
A9.1, A9.2	304	293	10 cycles, 90°+/- 90 °	6.7
A10.1, A10.2	304	77	Unsymmetrical cycles	82.9
62	304	77K, 293K	Torsion at 77K until 120Nm then torsion at 293K until rupture	99.9 (after tensile test)
Raw	304	-	No loading	0,2

Table 11.1. Loading conditions for samples used in the tensile test

For most of the samples, extensometer could not be used because the samples were shorter w.r.t. the minimum necessary gauge length of 70 mm, defined for the available extensometer.

For these samples the gauge strain was not measured, only the displacement of the head of the tensile machine was registered. The nominal stress was calculated from the measured force for all samples.
Sample number 1 was twisted at room temperature until rupture, which occurred at about 5100º angle (more than 14 full rotations around its axis). Samples number 2 and 3 were loaded to 870 degrees (almost 2,5 turns). Sample 2 was loaded at cryogenic conditions (77K), whereas, sample 3 at room temperature. Sample number 4 was twisted at 77K until rupture. Sample A9 was loaded by applying cyclic torsion: 10 cycles to 90±90º at room temperature. Sample A10 was loaded at 77K with asymmetric cycles (see Fig. 9.18 for detailed results). Sample 6.2 was twisted at 77K to 120Nm, then twisted again at room temperature until rupture. The raw sample provided a reference for tensile properties of fully austenitic 304 stainless steel.
After torsion, all the samples (apart from the raw one) had various martensite distributions. The martensite content was measured by using Feritscope before the tensile tests. The results are shown in the subsequent sections.

11.2. Martensite content measurements before tensile test

Martensite content was measured on the surface of cylindrical samples before the tensile test at room temperature. The measurement was performed by using Feritscope on the surface of the samples, similarly to the procedure described in section 7.1. Three measurements were carried out in each of the points, and along four predefined lines. The read-outs were multiplied by the correction factors, according to the procedure described in section 6.3.5.

11.2.1. Sample 1 (grade 304 ss)

Sample number 1 was twisted at 293K until rupture (Fig. 11.1). Smaller samples were extracted for microscopic observations and micro-hardness measurements. Several pieces were generated. The pieces were assembled (Fig. 11.2) in order to measure the axial distribution of martensite content on the surface. The measurement points spaced by 10mm were marked on the surface.

Figure 11.1. Sample number 1 after rupture by torsion

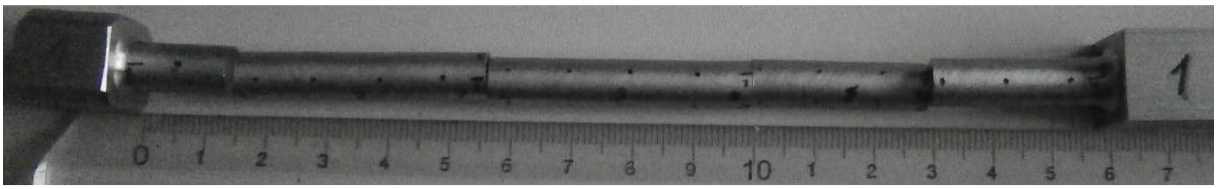

Figure 11.2. Fractions of sample number 1 with the measurement points of martensite content

The results of the measurement are shown in Fig. 11.3. Variations in martensite content were found between and along the measurement lines. Higher martensite content was detected near the ends of the sample, which suggested that the phase transformation in these regions was influenced by other parameters like the stress state (apart from temperature and strain). Stress concentrations caused by change in cross-section from square 15x15 to Φ8.
However, 5% difference could have been only a measurement error, and this issue was not studied in more details, as it was not the main topic of this work.

Average value of martensite content in the central part of the bar was about 50%. It is worth noticing, that the content of martensite was measured within the cross-section for the same sample (Fig. 6.109), where about 44% of martensite was found at 0.5mm distance from the surface. Slightly higher values were expected on the surface, so both measurements corresponded very well. The average of four measurements (violet line in Fig. 11.3) was indicated as the final result.

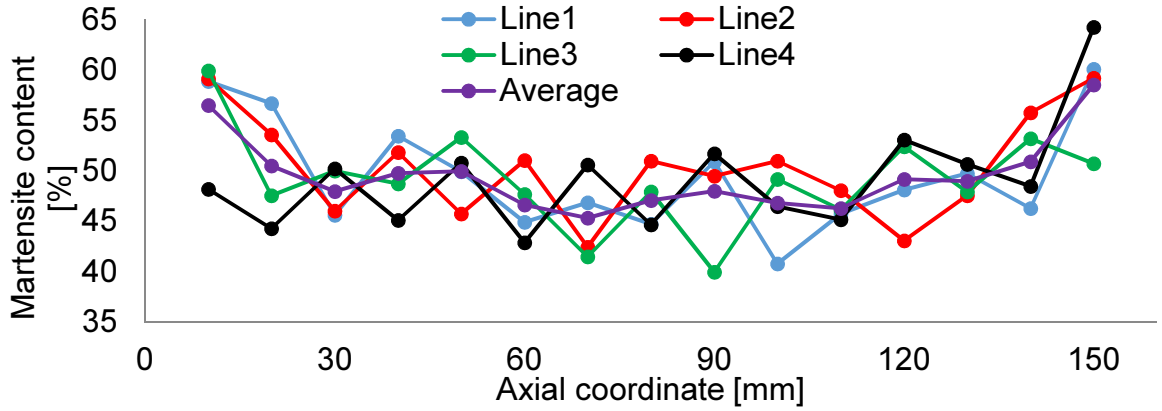

Figure 11.3. Martensite content measured for sample 1, loaded at 293K until rupture

11.2.2. Sample 2 (grade 304 ss)

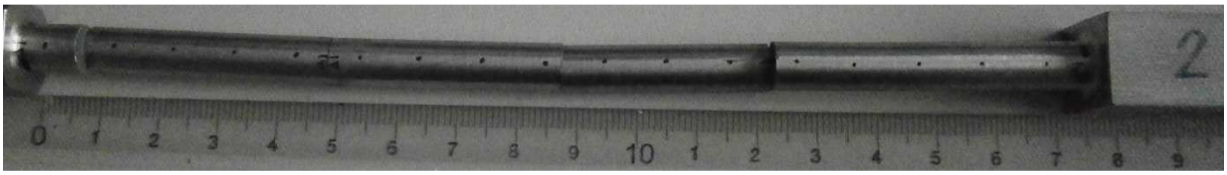

Figure 11.4. Fractions of sample 2 with the measurement points of martensite content

Sample number 2 was cut into fractions for the microscopic and micro-hardness measurements in the same manner as sample number 1 (Fig. 11.4). The results of martensite measurements on the surface are presented in Fig. 11.5. All four martensite content distributions fit well to each other, proving the axisymmetric distribution of martensitic phase on the surface. Between the axial coordinates from 120mm to 165mm, the martensite content increases from about 60% to almost 75%, indicating again the possibility of influence of other parameters like stress state, etc. However, this fact was not studied more deeply in the present work.

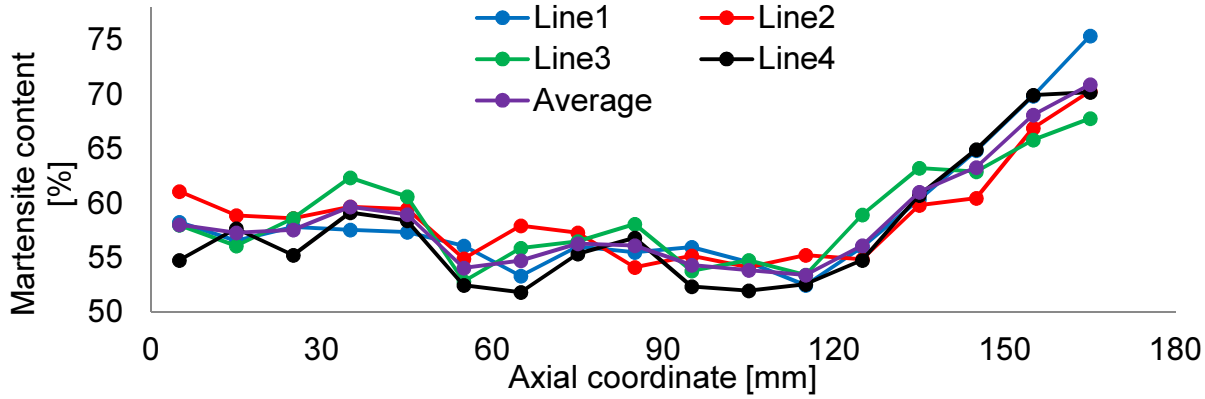

Figure 11.5. Martensite content measured for sample 2, loaded at 77K to 870°

The average content of martensite was about 55%, and correlated well with the results of measurements made within the cross-section (see Fig. 6.107), where the martensite content measured at 0.5mm distance from the surface was about 50%.

11.2.3. Sample 3 (grade 304 ss)

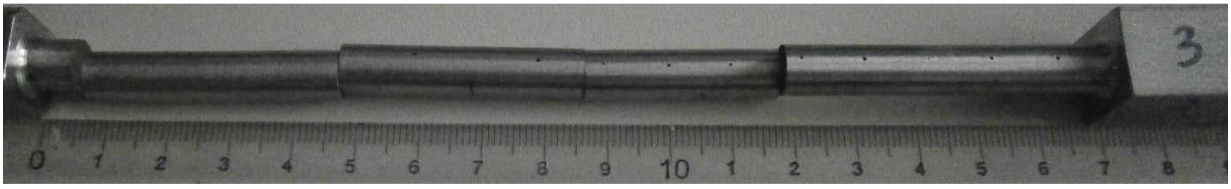

Figure 11.6. Fractions of sample 3 with the measurement points of martensite content

The fractions of sample number 3 are presented in Fig. 11.6. The results of martensite content measurements on the surface are presented in Fig. 11.7. The martensite content is relatively small (6%), compared to the previous results (50% or more). Here, the axial distribution varied from about 5% to 7%. Again, comparing the above with the results obtained from the cross-section of this sample (Fig. 6.108), a good correlation is found. At 0.5mm distance from the surface, about 4.5% of martensite was found, thus slightly less than 5% obtained on the surface.

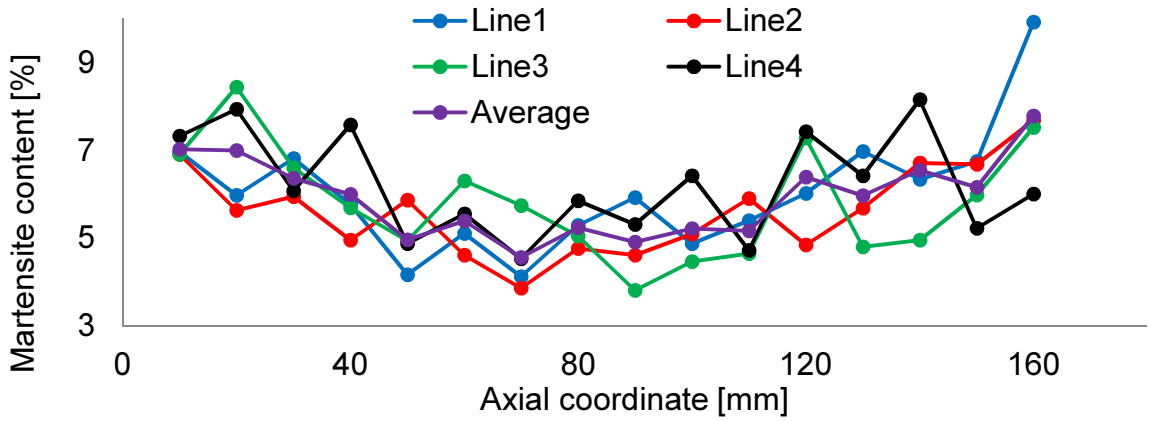

Figure 11.7. Martensite content measured for sample 3, twisted at 293K to 870º

11.2.4. Sample 4 (grade 304 ss)

Figure 11.8. Sample 4 after rupture by torsion, before tensile test

A photograph of sample number 4, which was twisted until rupture at 77K, after the test is shown in Fig. 11.8. The martensite content results from the surface are shown in Fig. 11.9. In average, about 88% was obtained, with a slight increase towards the right end to 92%.

As the phase transformation rate is much higher at 77K than at 293K, one expects high martensite content at the temperature of liquid nitrogen. As the sample 4 was twisted until rupture, the highest possible martensite content was obtained under given conditions. Thus, for grade 304 stainless steel, during torsion at 77K, about 88% was the maximum martensite content induced on the surface.

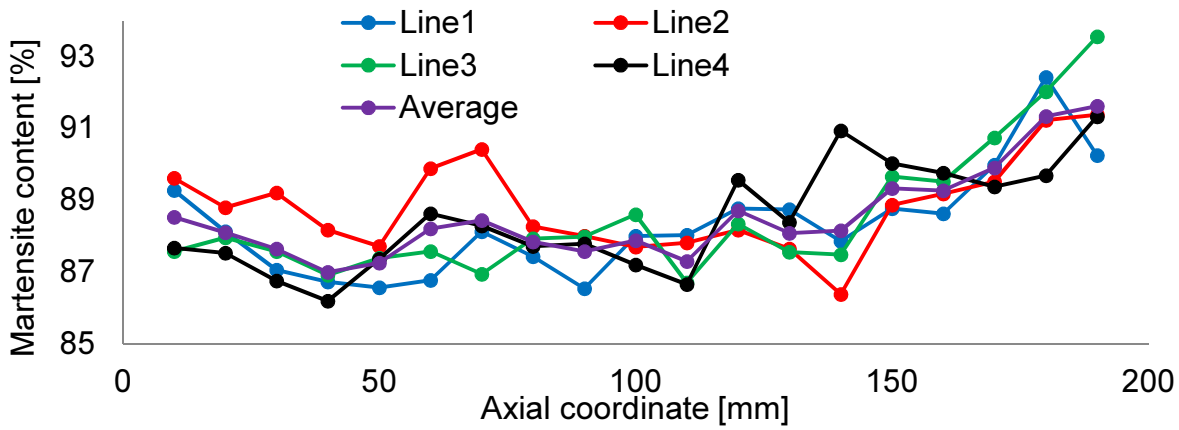

Figure 11.9. Martensite content measured on the surface of sample 4, loaded at 77K until rupture

11.2.5. Sample A9 (grade 304 ss)

Figure 11.10. Sample A9 after cyclic torsion at 293K, 10 cycles to 90±90º

Sample A9 after cyclic torsion test is shown in Fig. 11.10. The results of the martensite content measurements on the surface are shown in Fig. 11.11. Small angles of twist lead to small plastic strains in the bar, and to small content of induced martensite. It turned out, that the average content of α' phase was about 7%. Again, martensite content increased towards the left and the right ends of the bar, suggesting the influence of stress concentration. The average of four measurements along the predefined lines, was computed as the final result.

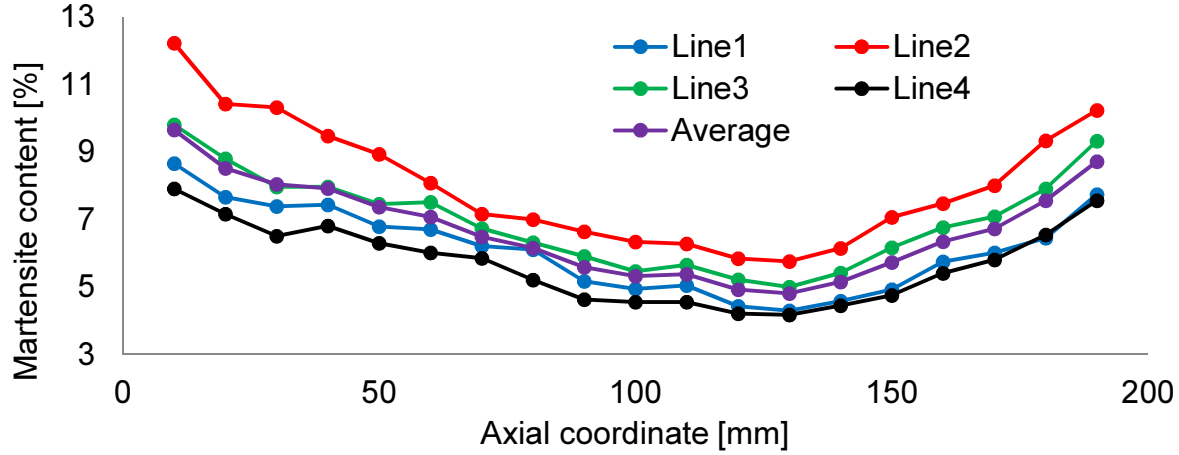

Figure 11.11. Martensite content measured for sample A9, loaded at 293K by cyclic torsion, 10 cycles to 90±90º

11.2.6. Sample A10 (grade 304 ss)

Figure 11.12. Sample A10 after cyclic torsion at 77K, before tensile test

The photograph after torsion test is shown in Fig. 11.12. The resulting martensite fraction on the surface is illustrated in Fig. 11.13. The results in terms of the torque versus the angle of twist are shown in Fig. 9.18. The torque reached some 140Nm, very close to the maximum one of 156Nm (sample 4, Tab. 5.2). Similar results were obtained for all four measurements. The average value reached about 83%. Higher values were measured at both ends, similar to previous samples.

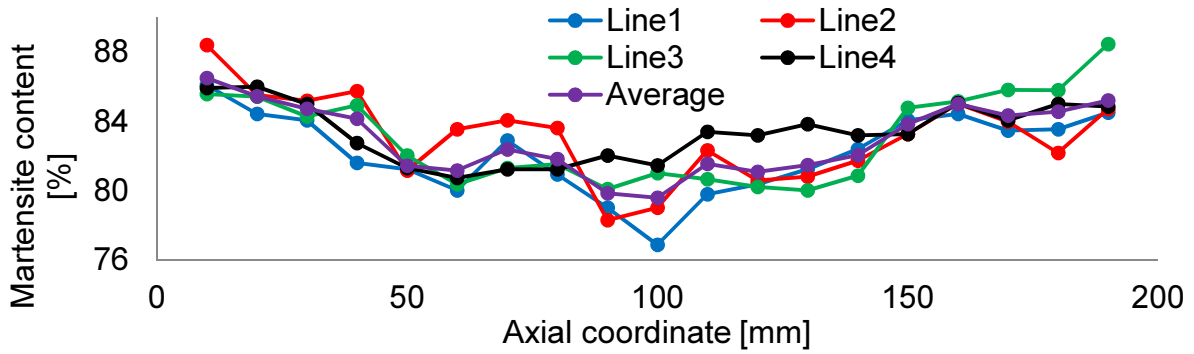

Figure 11.13. Martensite content measured for sample A10, loaded at 77K by cyclic torsion

11.2.7. Summary of the martensite content measurements

The averages of the results measured in four planes for each sample are presented for comparison in Fig. 11.14. The results for six samples are shown. Tensile test was performed for two more samples, the raw sample and the sample 62 (Tab. 11.1). For sample 62, the martensite content was not measured before tensile test, only after the test (see section 11.3). For the raw sample, almost zero martensite content was expected, similarly to the results obtained within the cross-sections (see Fig. 6.110). Samples 4 and A10 showed very high volume fraction of the α' martensite (more than 80%). Samples 1 and 2 showed high martensite contents on the surface (around 50÷60%). On the other hand, less than 10% of martensite was measured for samples number 3 and A9.

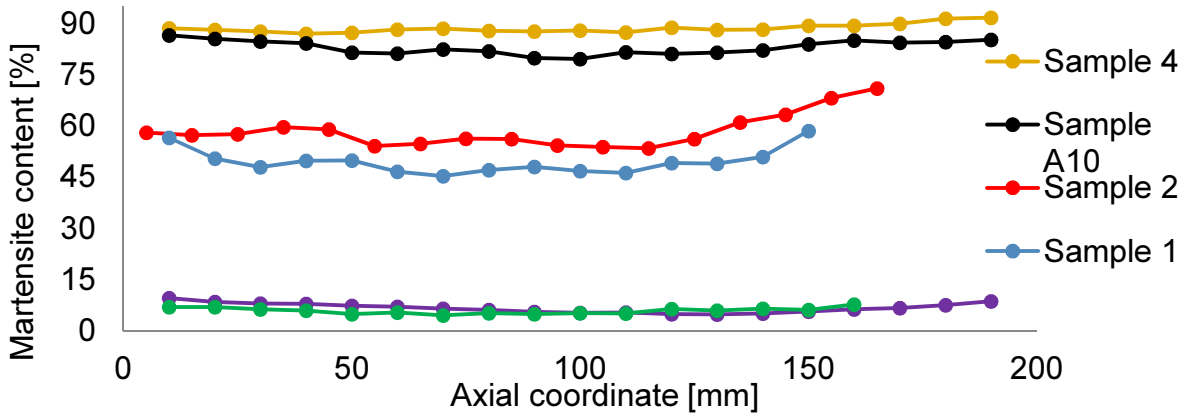

Figure 11.14. Average martensite content measured on the surface of the samples in the axial direction

11.3. Martensite content measurements after tensile test

Figure 11.15. Sample 62 after rupture by torsion and tensile test until rupture

The photograph of sample 62 after the tensile test is shown in Fig. 11.15. The fractions were assembled together, so that martensite content was measured on the surface. It turned out, that after applying the procedure with relevant correction factors and calibration, described in section 6.3.5, the martensite content was higher than 100% (but less than 110%). This overestimation has its roots in the approximation of the calibration curve, based on the paper by Talonen et al. 2004. In the experimental results only two points were available for very high Feritscope readings, thus some discrepancy was expected. As the values higher than 100% are not physically admissible, they have been reduced to 100% (Fig. 11.16).
It is worth noticing, that in this sample the phase transformation was first driven by shear strain during torsion, and afterwards by axial strains during the tensile test. For this reason, full transformation was reached on the surface of this sample.

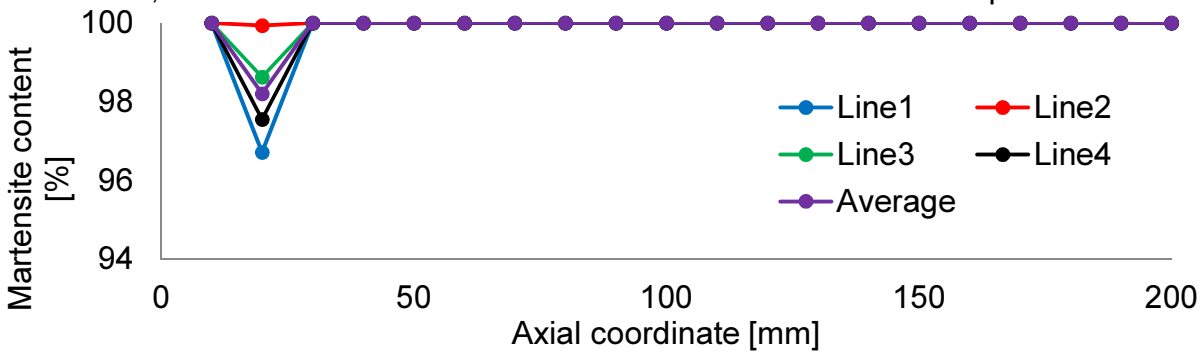

Figure 11.16. Martensite content measured in the sample 62, after tensile test

11.4. The experimental method

All tensile test were performed at room temperature using the standard tensile test machine. For two samples an extensometer has been used, allowing the measurements of elongation and, thus, the strain. For the other samples, as their gauge lengths were too small to use the available extensometer, only force versus displacement of the machine head were measured. All samples had circular cross-sections. Grip with the grooves was used for all the samples (the marks of grooves are clearly visible in sample 62, shown in Fig. 11.15). All samples before the test are presented in Figs 11.17 and 11.18. The raw sample is denoted by “10” in Fig. 11.18. The tensile test machine is presented in Fig. 11.19.

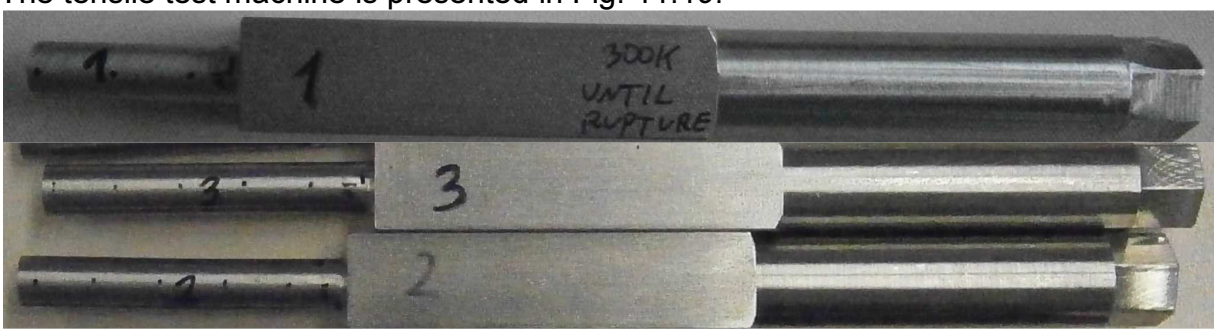

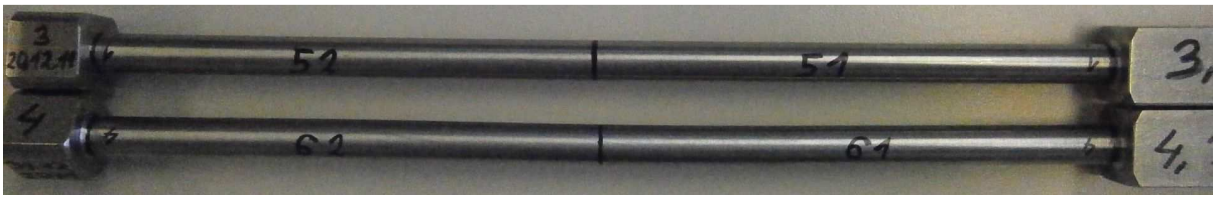

Figure 11.17. Samples number 1, 2, 3, A9.1, A9.2, A10.1, A10.2 before tensile test

Figure 11.18. Samples number 10 (raw), 41, 42, before tensile test

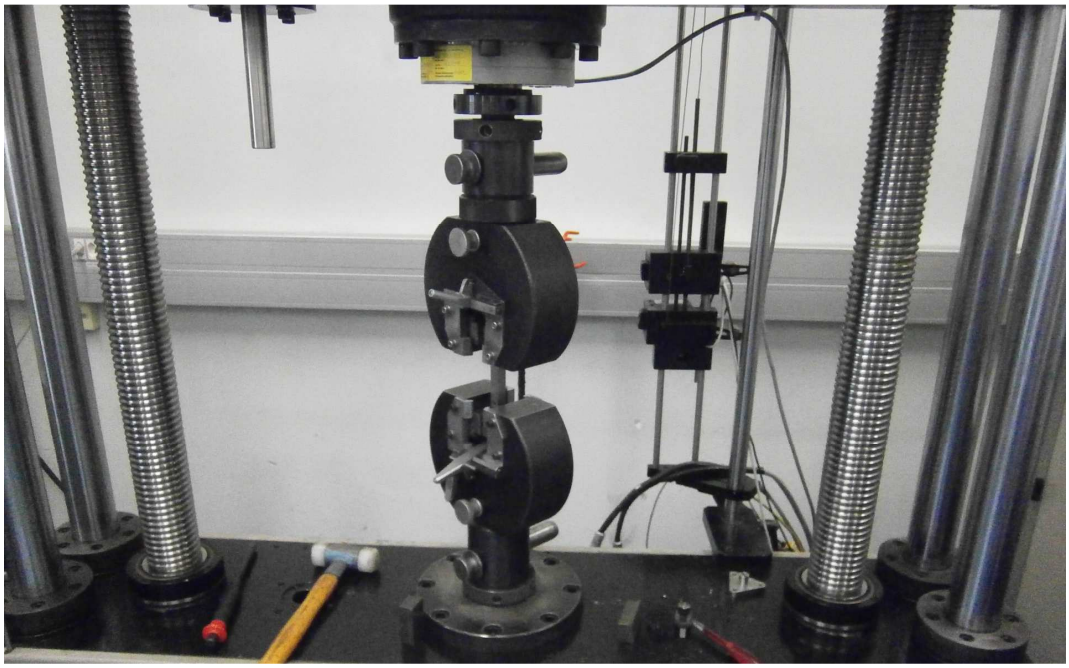
Figure 11.19. Tensile test machine with sample 1 in the clamps

11.5. Results of tensile test

In the following sections, the results of tensile test are presented for each sample. The measurements and the photographs of samples during the test and after the fracture are presented. For all samples, the clamps with grooves have been utilized. During the test, the grips squeeze the sample and make the imprints in the material. The marks are visible in many samples shown in the following section.
The clamps were not perfect because the grooves created stress concentrations. As the samples had axisymmetric distribution of the martensitic phase, no machining was possible since this would remove the layer with the highest martensite fraction. Thus, the clamps were the only solution to successfully perform tensile tests.

11.5.1. Tensile test results for sample 1

The photographs of sample 1 mounted in the clamps of tensile machine are shown in Fig. 11.20a. The maximum martensite content measured on the surface was about 55% for this sample (Fig. 11.14). Because of such high martensite content, a brittle behavior was expected. This was confirmed by the character of the fracture (Fig. 11.20b), since very small necking was observed. The sample ruptured after relatively small values of plastic strain. In Fig. 11.21 the fracture zone is magnified, the plane of the fracture being angled by about 45º to the axis of the sample.

a b

Figure 11.20. a) Sample 1 mounted in the clamps, b) photographs of the fracture zone

Figure 11.21. Magnified view of the fracture zone for sample 1

The results of the tensile test, where the force was measured against the stroke (displacement of the head of the tensile machine), are presented in Fig. 11.22. The maximum force reached about 58kN (corresponding to 5.8 tons). At the rupture, the stroke was equal to 11mm.

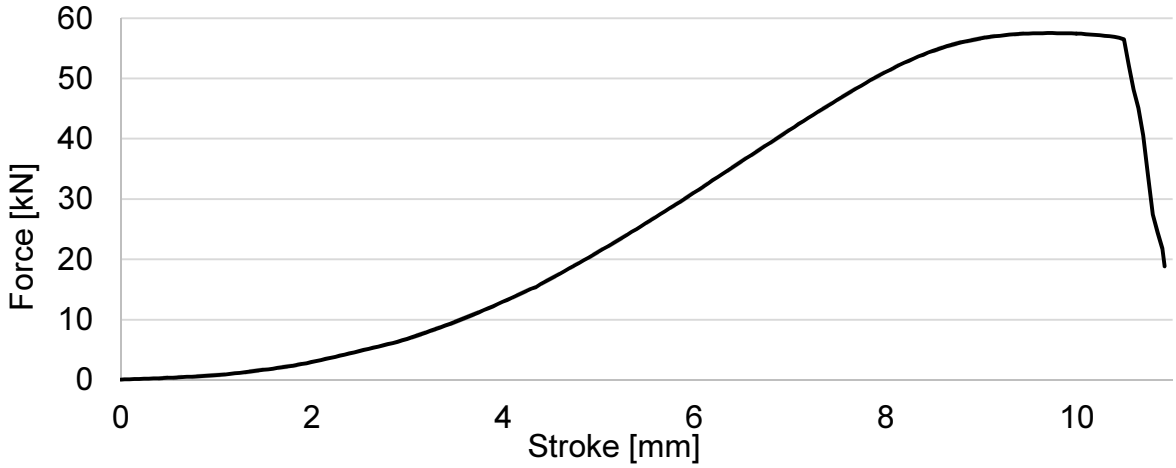

Figure 11.22. Force versus stroke during tensile test for sample number 1

11.5.2. Tensile test results for sample 2

The photograph of sample 2 mounted in the clamps is shown in Fig. 11.23a. The fracture zone was magnified in Fig. 11.23b. The sample after the rupture is shown in Fig. 11.24. The necking is clearly visible. Thus, the plastic strains occurred before rupture, and the character of the fracture is rather ductile. Force versus stroke results are presented in Fig. 11.25. Average martensite content on the surface reached about 60% for this sample, a few percent more than for sample 1. Actually, brittle behavior was expected, but the results were different than for sample 1 (Fig. 11.20). The explanation of this fact remains in the conditions of pre-straining by torsion. For sample 1 it was made at 293K until rupture, whereas, for sample 2 at 77K. In addition the strain (proportional to the angle of twist) in the sample 1 was several orders of magnitude higher than for the sample 2 (5110° and 870°). Clearly, after twisting at 77K and inducing 60% of martensite on the surface, the behavior in tension was still ductile, whereas, after twisting at 293K until rupture (advanced damage in sample) and inducing similar martensite content it was brittle.
The maximum force was equal to 60kN (6 tons), some 2kN more than for sample 1 (as expected from the higher martensite content, and higher strength). The stroke at rupture was about 16.5mm, 4.5mm more than for the previous sample. As the strain is proportional to the elongation (stroke), one can conclude that sample 2 failed at higher strain than sample 1. Thus, sample 2 showed higher maximum strain and stress when compared to sample 1, with similar martensite content.

a b

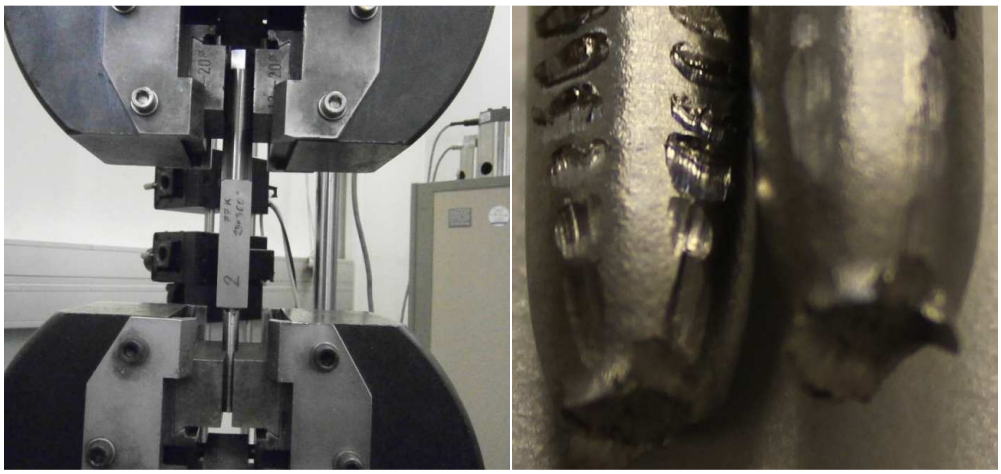

Figure 11.23. a) Sample 2 mounted in the clamps, b) magnified fracture zone

Figure 11.24. Sample 2 after fracture in tension

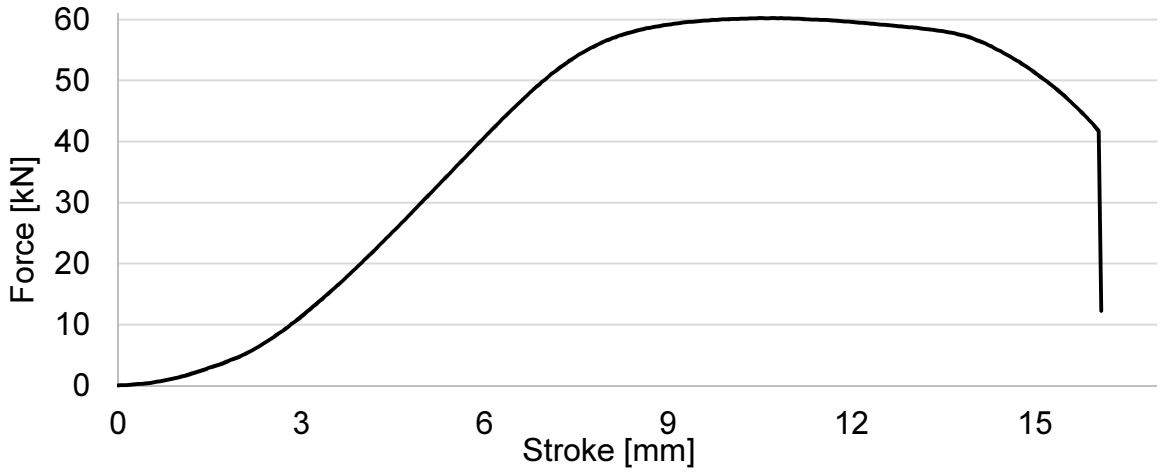

Figure 11.25. Force versus stroke in the tensile test for sample 2

11.5.3. Tensile test results for sample 3

The photograph of sample 3 after the rupture is presented in Fig. 11.26. In Fig. 11.27a the fracture zone has been magnified, whereas, in Fig. 11.27b the fracture is shown side view. In this sample necking is clearly visible. Reduction of the area at rupture was higher compared to the samples 1 and 2. Again, the rupture was followed by plastic yielding and necking, and the fracture was ductile like for sample 2. Average martensite content on the surface was about 5% for this sample. Thus, the material was almost purely austenitic. Much smaller force was expected as the austenite has smaller yield strength than the martensite.

In Fig. 11.28 force versus stroke results are shown. The maximum force was equal to 44kN, i.e. 16kN less than for sample 2. The maximum stroke was of 21mm, i.e. 4.5mm more than for sample 2. In the range of strokes between 7÷17mm, the force was almost constant. This was the range of plastic flow with constant yield stress.

Figure 11.26. Sample 3 after the tensile test

a b

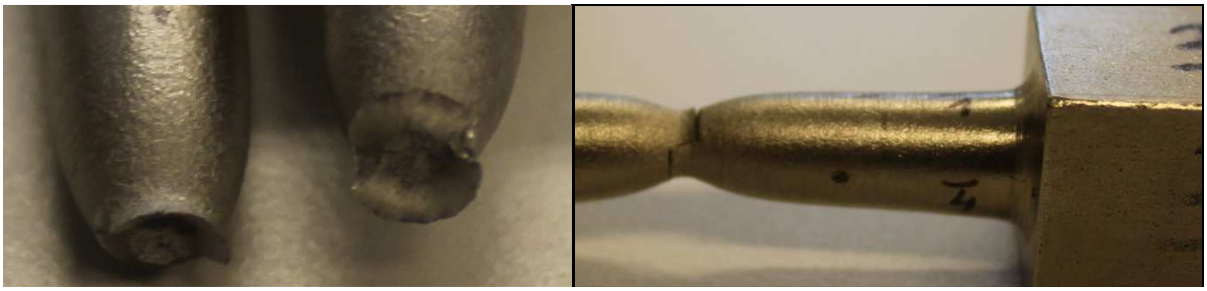

Figure 11.27. The fracture zone in sample 3, a) front view b) side view

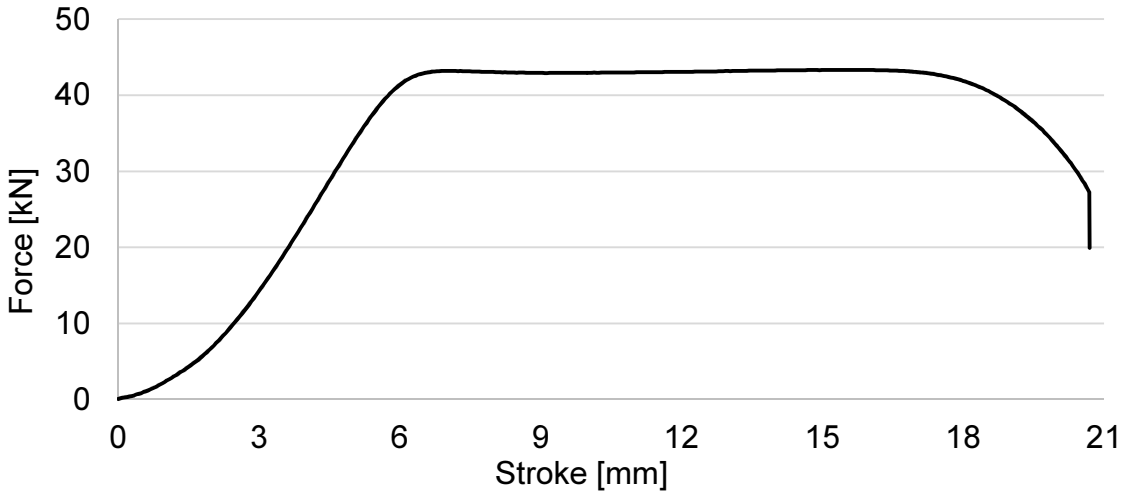

Figure 11.28. Force versus stroke in the tensile test for sample 3

11.5.4. Tensile test results for sample 4

Sample 4 was cut into two samples: 41 and 42 (Fig. 11.18). The sample number 41 after tensile test is presented in Fig. 11.29. Magnified fracture zone is presented in Fig. 11.30a together with the side view of fracture shown in Fig. 11.30b. The necking is clearly visible. As the average martensite content on the surface reached approximately 88%, one expected high force and small elongation. This has been confirmed in the results of the force versus stroke (Fig. 11.33). The maximum force was equal to 62kN, 2kN more than for sample 2 with 55% martensite content on the surface, and 4kN more than for sample 1. The maximum stroke for sample 41 was of 18mm, so 1.5mm more than for sample 2 with smaller martensite content. Yet, the stroke did not correspond to the strain, as the grips penetrated and slid on the sample.

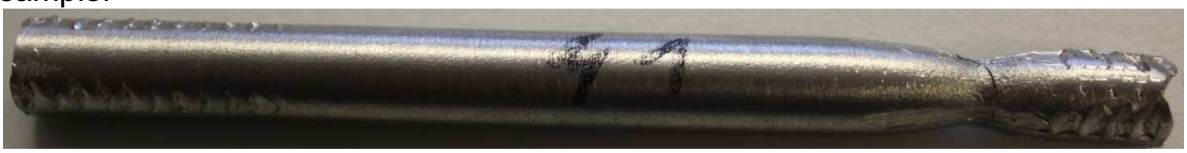

Figure 11.29. Sample number 41 after the tensile test

a b

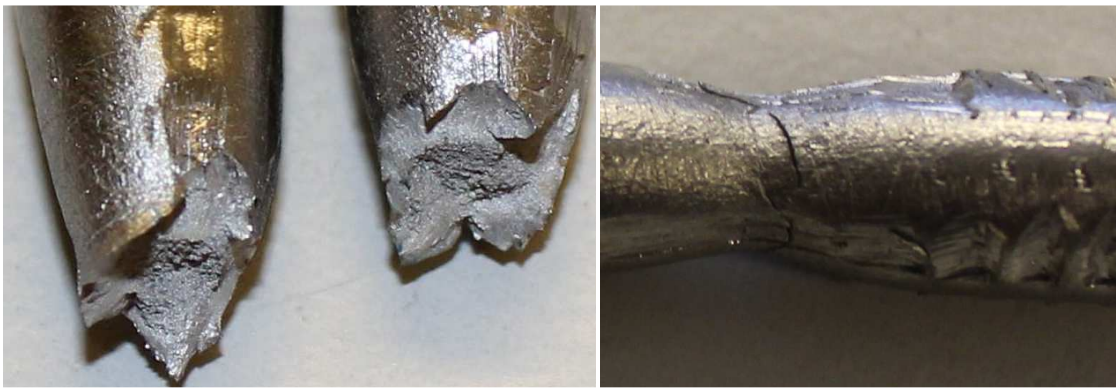

Figure 11.30. Magnified view of the fracture zone for sample 41

Sample number 42 after rupture is presented in Fig. 11.31. Magnified fracture zone and side view of the fracture region are shown in Fig. 11.32a, b. The necking is visible but of small size, and placed near the left grip. It was expected that both samples 41 and 42 would have almost the same properties.

This was confirmed, as very similar results were obtained in terms of force versus stroke for both samples.
The maximum force for sample 42 was of 62kN (Fig. 11.33), the maximum stroke was equal to 17mm. Sample 42 fractured at a smaller stroke of 17mm, when compared to sample 41 with the stroke of 18.5mm.

Figure 11.31. Sample 42 after the tensile test

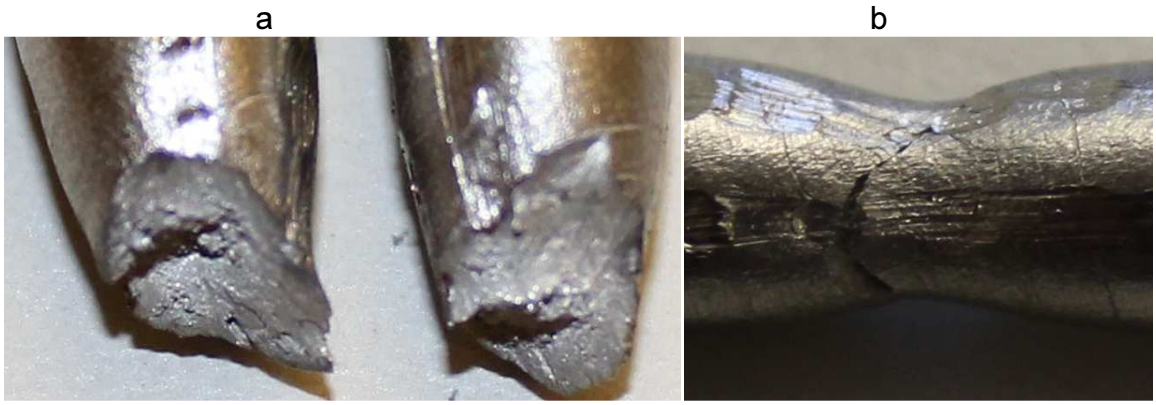

Figure 11.32. Magnified view of the fracture zone for sample 42

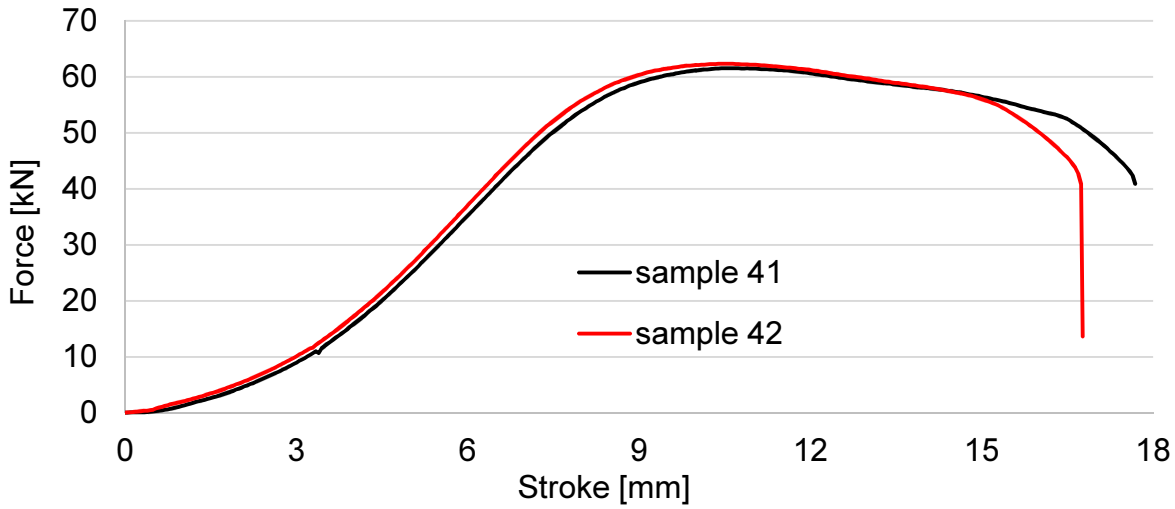

Figure 11.33. Force versus stroke in the tensile test for samples 41 and 42

11.5.5. Tensile test results for sample A9

Sample A9 was divided into two separate samples: A9.1 and A9.2. Sample A9.1 was equipped with an extensometer shown in Fig. 11.34a. The photograph after rupture is presented in Fig. 11.35, and the magnified view of the fracture zone is shown in Fig. 11.34b. The results in terms of force versus stroke are shown in Fig. 11.36. The average martensite content on the surface was of 7%, similar to sample 3 with 5% of martensite. As expected from minor martensite content, the maximum force was of only 39kN, i.e. 6kN less than for sample 3. However, the maximum stroke for sample A9.1 was equal to 38mm, almost twice as large as for sample 3 (21 mm). This shows very big difference in the maximum axial strains among these two samples with very similar martensite content.

This difference could possibly be caused by the character of pre-straining. Sample A9 was twisted by using symmetric cycles of 90±90º at 293K, whereas, sample 3 was loaded in a “monotonic” way at 293K.
The angle of twist for sample 3 was much higher and equal to 870°. This situation is similar to the case of samples 1 and 2 (with similar martensite content on the surface), where much higher stroke was obtained for sample 2, which was twisted to 870°, whereas, sample 1 was twisted to 5110°. This means that applying smaller angles of twist leads to higher strain at rupture during tensile test.

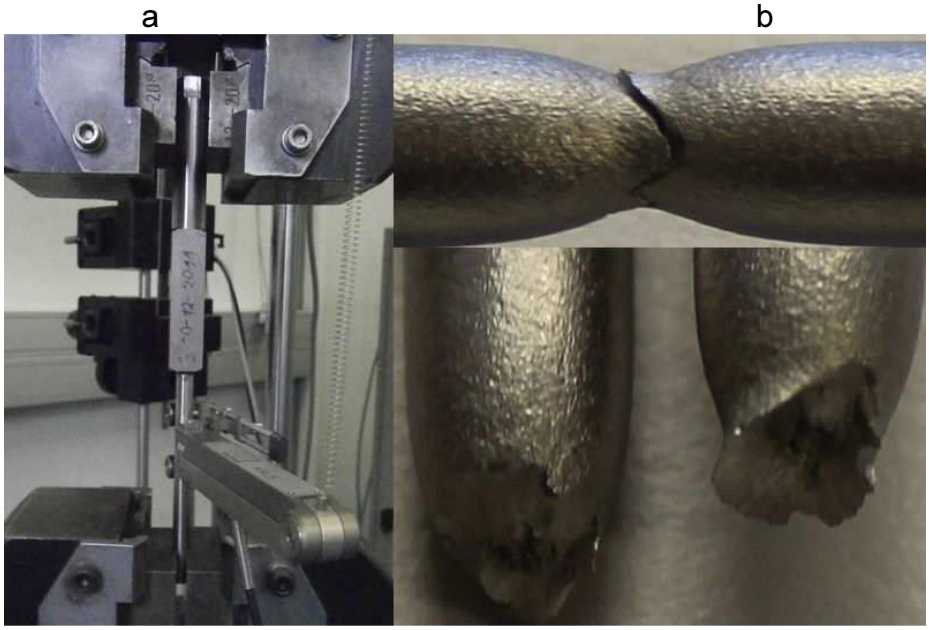

Figure 11.34. a) Sample A9.1 mounted in the clamps, b) magnified fracture zone

Figure 11.35. Sample A9.1 after the tensile test

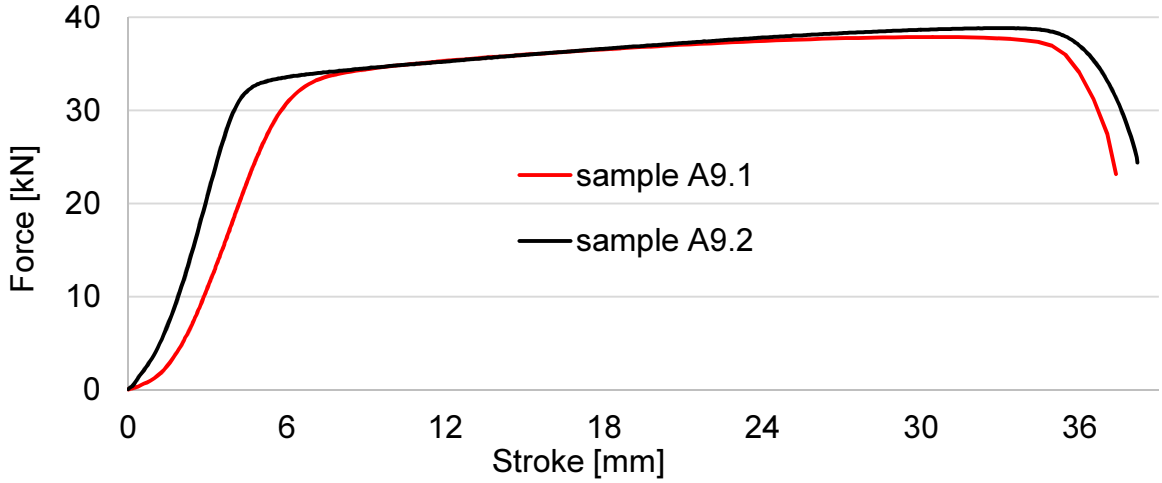

Figure 11.36. Force versus stroke in the tensile test for samples A9.1 and A9.2

Sample A9.2 was tested without extensometer (Fig. 11.37a). The moment preceding the fracture (1 second before) was captured and is shown in Fig. 11.37b. The whole sample after rupture is presented in Fig. 11.38, and the magnified fracture zone is shown in Fig. 11.39a,b.

The force versus stroke is similar for both samples: A9.1 and A9.2 (Fig. 11.36). The maximum force for sample A9.2 was of 38kN, and the maximum stroke was equal to 37mm. In the range of stroke from 8 to 35mm, a linear increase of force was observed indicating linear hardening.

a b

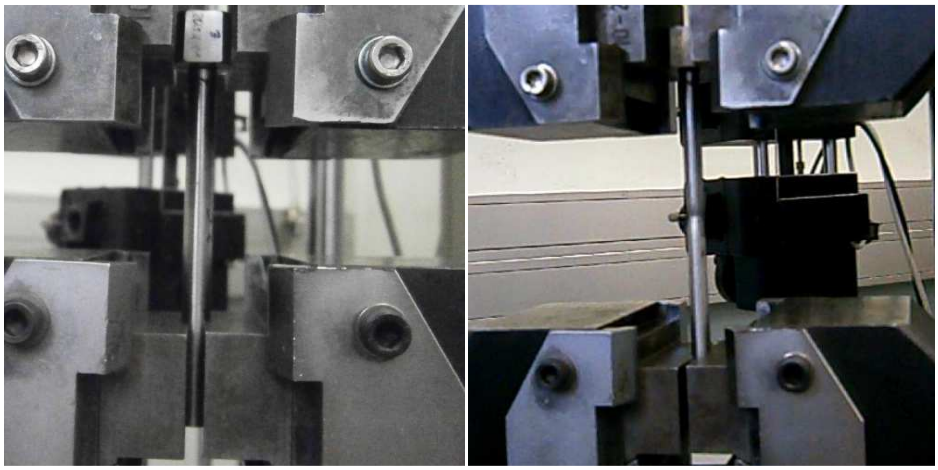

Figure 11.37. Sample A9.2 mounted in the clamps just before test (left), sample A9.2 one second before fracture (right)

Figure 11.38. Sample A9.2 after the tensile test

a b

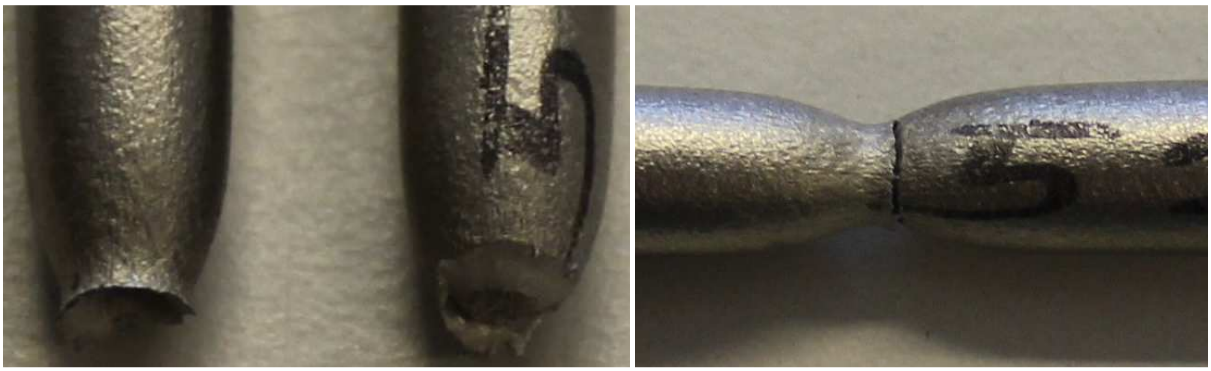

Figure 11.39. Magnified view of the fracture zone for sample A9.2, a) front view, b) side view

11.5.6. Tensile test results for sample A10

Sample A10.1 has been tested with the use of extensometer (Fig. 11.41a). The sample after fracture is presented in Fig. 11.40, and the magnified fracture zone is shown in Fig. 11.41b. The average martensite content on the surface reached about 83%, almost as much as for sample 4 with 88% of martensite. Maximum force registered during tensile test (Fig. 11.42) was equal to 63kN, almost the same as for sample 4 (with 62kN). The maximum stroke reached some 16mm for sample A10.1, which was 1mm less than for sample 42. Thus, the results were comparable. Moreover, necking was clearly visible.

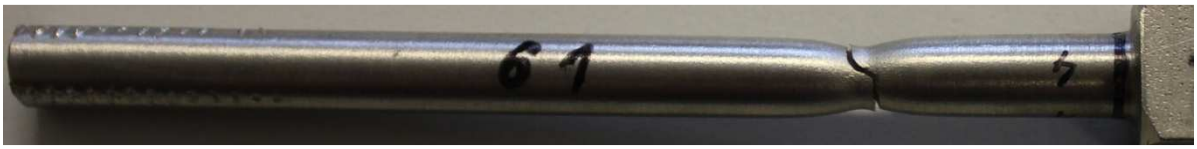

Figure 11.40. Sample A10.1 after the tensile test

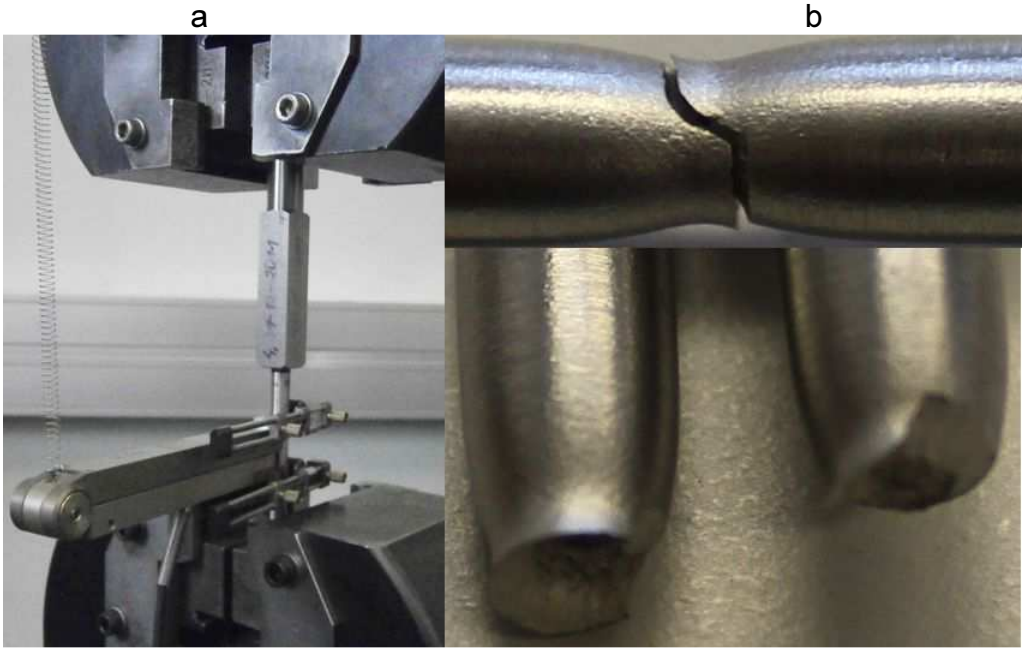

Figure 11.41. a) Sample A10.1 mounted in the clamps, b) magnified fracture zone

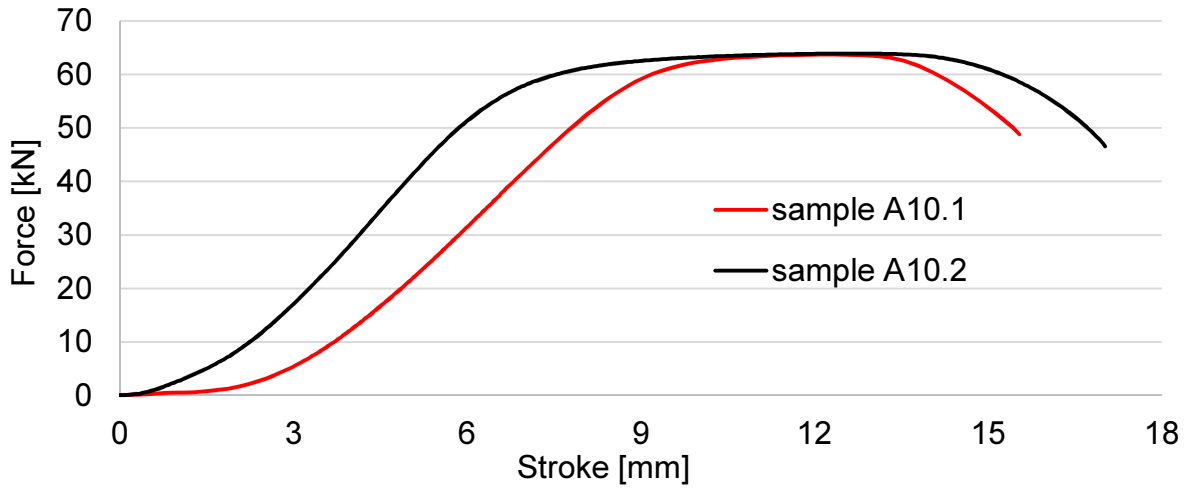

Figure 11.42. Force versus stroke in the tensile test for samples A10.1 and A10.2

Sample A10.2 was tested without extensometer (Fig. 11.44a). The sample after fracture is presented in Fig. 11.43, and the magnified fracture zone is shown in Fig. 11.44b.

Maximum force for sample 62 was the same as for sample 61, i.e. 63kN, and the maximum stroke at rupture reached 17mm. The results for both samples were different at the beginning of the test for strokes from 0 to 9mm, and in the range greater than 13mm. This difference was not expected, as both pieces were cut from the same sample. The reason of such a difference can be attributed to sliding of the grips, especially in the early range of the stroke.

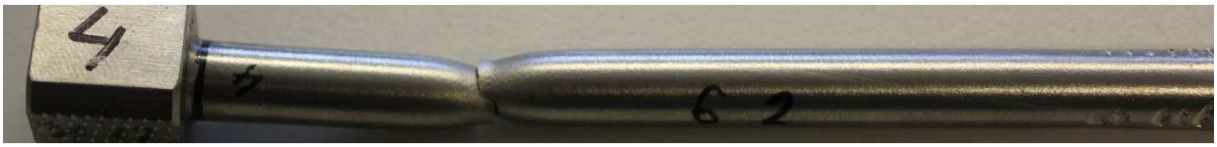

Figure 11.43. Sample A10.2 after the tensile test

a b

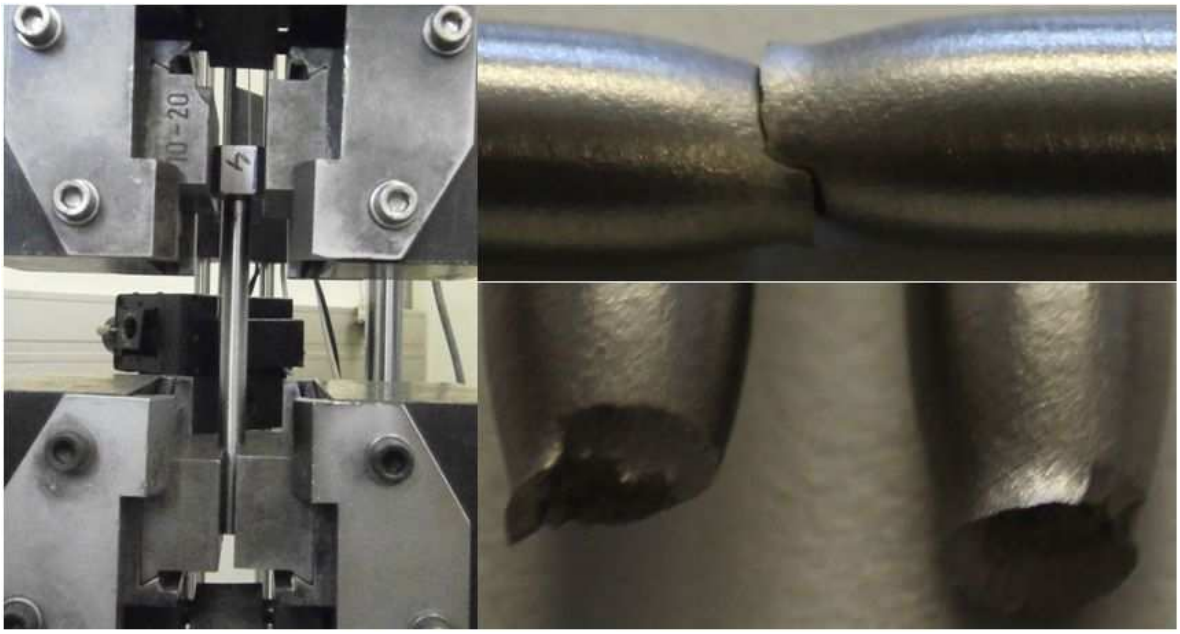

Figure 11.44. a) Sample A10.2 mounted in the clamps, b) magnified fracture zone

11.5.7. Tensile test results for sample 62

Sample 62 after the tensile test is presented in Fig. 11.45. Necking is clearly visible. The fracture zone has been enlarged in Fig. 11.46a, b. The martensite content has been measured after the test only, and it reached on the surface 100%. One would expect the highest strength of this sample (because of the highest martensite content), and it was confirmed by the force versus stroke results (Fig. 11.47). The maximum force was equal to 68kN, which is 5kN more than for sample number 6, where the martensite content on the surface reached 83%.

Figure 11.45. Sample number 7 after the tensile test

a b

Figure 11.46. Magnified fracture zone for sample 62, a) side view, b) front view

The stroke at rupture was about 17mm, still comparable to the previous samples, like sample number 6 (16÷17mm) and sample number 4 (16.5÷17mm). Thus, the plastic strain was always higher than zero, even for very high martensite content at the surface (>80%). Moreover, brittle behavior was never observed, some ductility always remained.

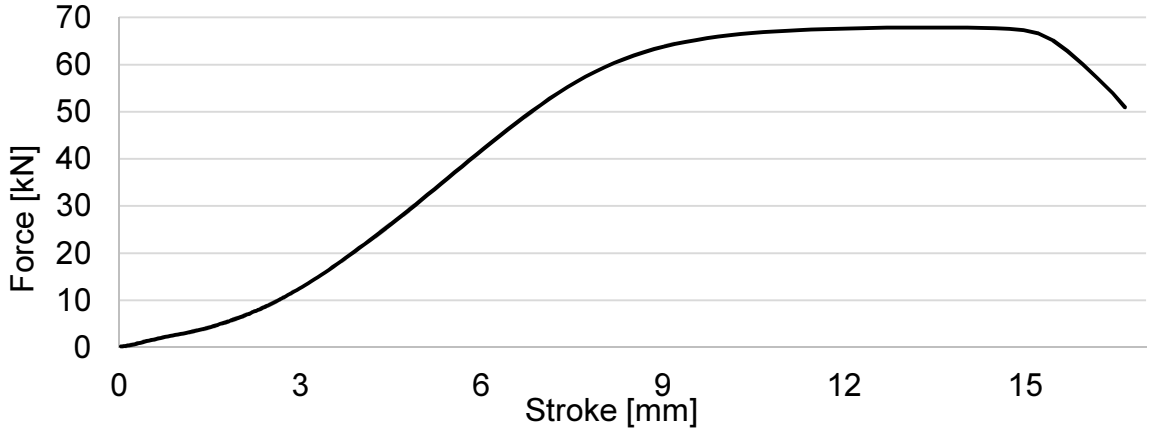

Figure 11.47. Force versus stroke during the tensile test for sample 62

11.5.8. Tensile test results for the raw sample (grade 304 ss)

The raw sample after the rupture during tensile test is shown in Fig. 11.48. Substantial necking is visible. The fracture has ductile character, and it is magnified in Fig. 11.49a, b. One would expect the smallest strength and the highest ductility for the raw sample of fully austenitic structure. The first expectation was confirmed, as the maximum load from the force versus stroke curve (Fig. 11.50) reached 37kN. This was the smallest value from all the tested samples. However, it was only 1kN smaller than for sample number A9.1 with 7% average martensite content on the surface.

Figure 11.48. Sample 10 (raw) after the tensile test

a b

Figure 11.49. Magnified fracture zone for the raw sample (10) a) side view, b) front view

The maximum stroke was equal to 31mm, which was not the highest value. Higher values were obtained for samples: A9.1 (38mm) and A9.2 (37mm).
This means that the process of cyclic torsion at room temperature increased both ductility and strength. This result needs to be verified, as there is always a chance of an experimental error due to sliding of grips.

Yet, the well-known TRIP effect, caused increased plasticity thanks to the phase transformation. The hardening doesn't allow the necking to occur until much higher stress values. Such effect is very favorable for the performance of the structure.

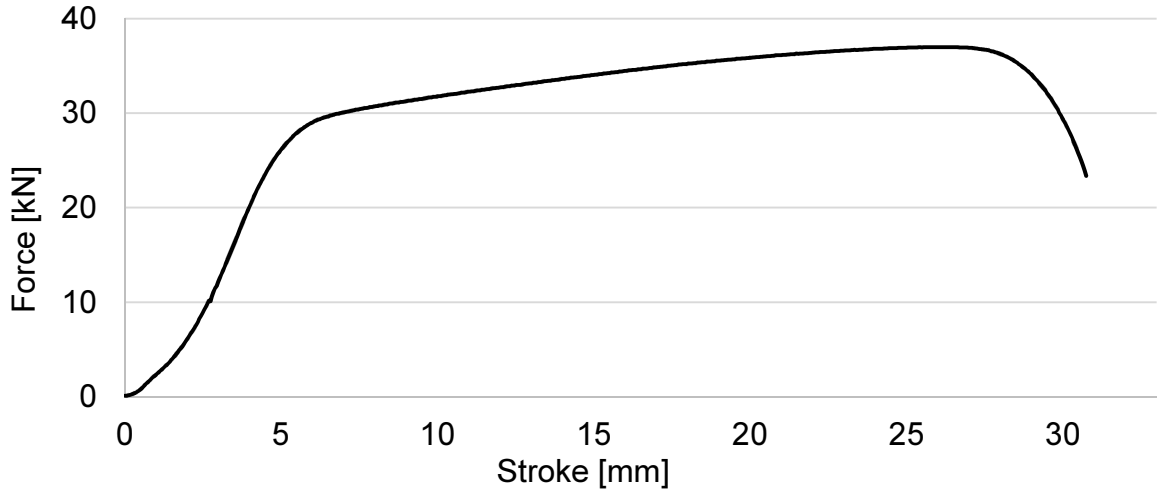

Figure 11.50. Force versus stroke during tensile test for sample 10 (raw)

11.5.9. Summary of tensile tests

All the results from tensile tests are summarized in Fig. 11.51. In terms of the maximum force, the raw sample reached 37kN. The sample 62 reached almost 68kN, thus, 84% more in comparison. This result shows the possibility of carrying much higher loads by the samples with high martensite contents, that were induced thanks to the plastic strain induced phase transformation during torsion.

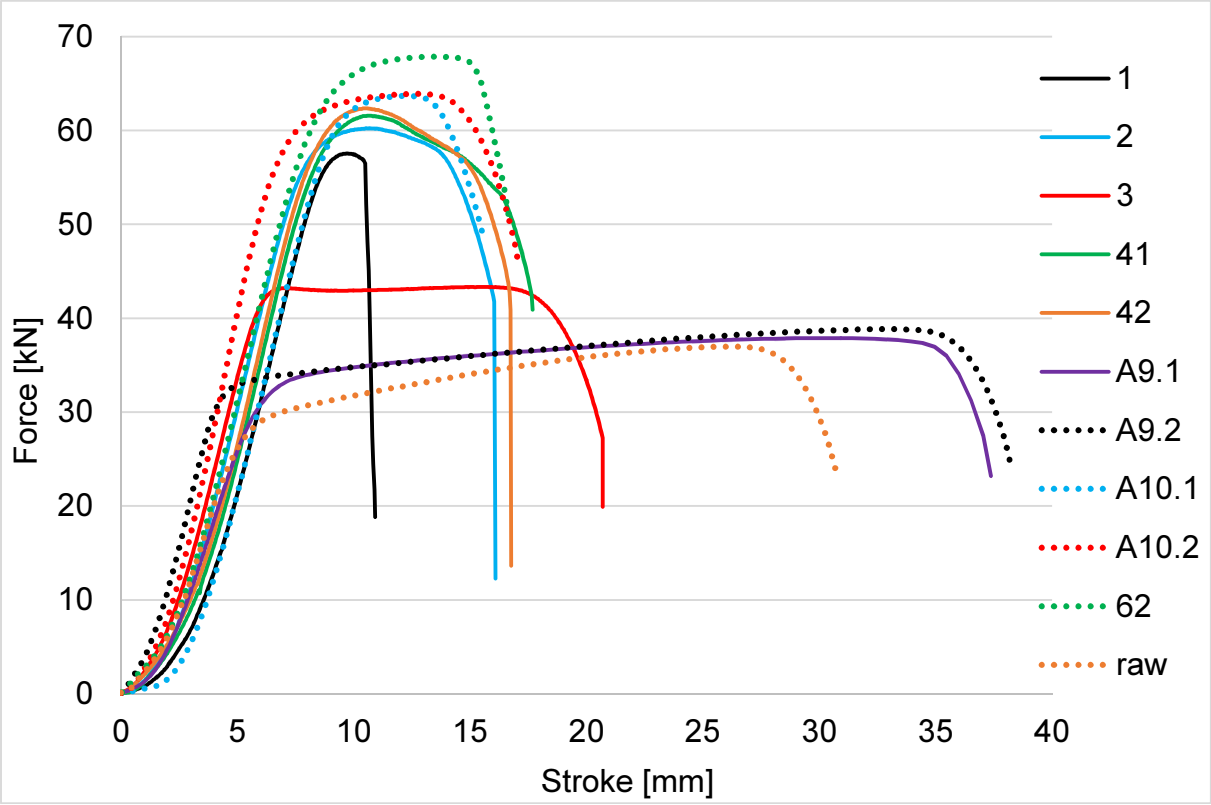

Figure 11.51. Force versus stroke for all tested samples

11.6. Stress - strain curves

Based on the measurements of the force versus stroke stress was calculated. For each sample the diameter was measured before tensile test, and the cross-section area was calculated (Tab. 11.2).

Sample number	Reference length L_0	Diameter D_0	Area A_0
[-]	[mm]	[mm]	[mm^2]
1	-	7.83	48.15
2	-	7.95	49.64
3	-	8.02	50.52
41	-	7.97	49.89
42	-	7.92	49.27
A9.1	25	8.02	50.52
A9.2	-	8.02	50.52
A10.1	25	7.93	49.39
A10.2	-	8.03	50.64
62	25	7.98	50.01
Raw	-	8.02	50.52

Table 11.2. The diameter and the area of samples before the tensile test

The stress was then calculated according to the known formula:

$$\sigma = \frac{F}{A_0} \tag{11.1}$$

where:

- σ is the nominal stress,
- F is the measured force,
- A_0 is the reference area (Tab. 11.2).

The nominal stress as a function of the stroke is plotted for all the samples in Fig. 11.52.

The smallest stress was obtained for the raw sample. Slightly higher values were obtained for samples A9.1 and A9.2, with 6.7% of martensite on the surface. For sample 3, which showed 5.9% of martensite on the surface, the yield stress was of the order of 850MPa. The remaining samples reached the maximum stresses higher than 1200MPa (samples: 1, 2, 41, 42, A10.1, A10.2, 62). In particular, the samples: 1, 2, 41 had the maximum stress of about 1200MPa, whereas, the samples 42, A10.1, A10.2 reached about 1250MPa at maximum. The highest stress was obtained for sample 62, i.e. about 1350MPa.

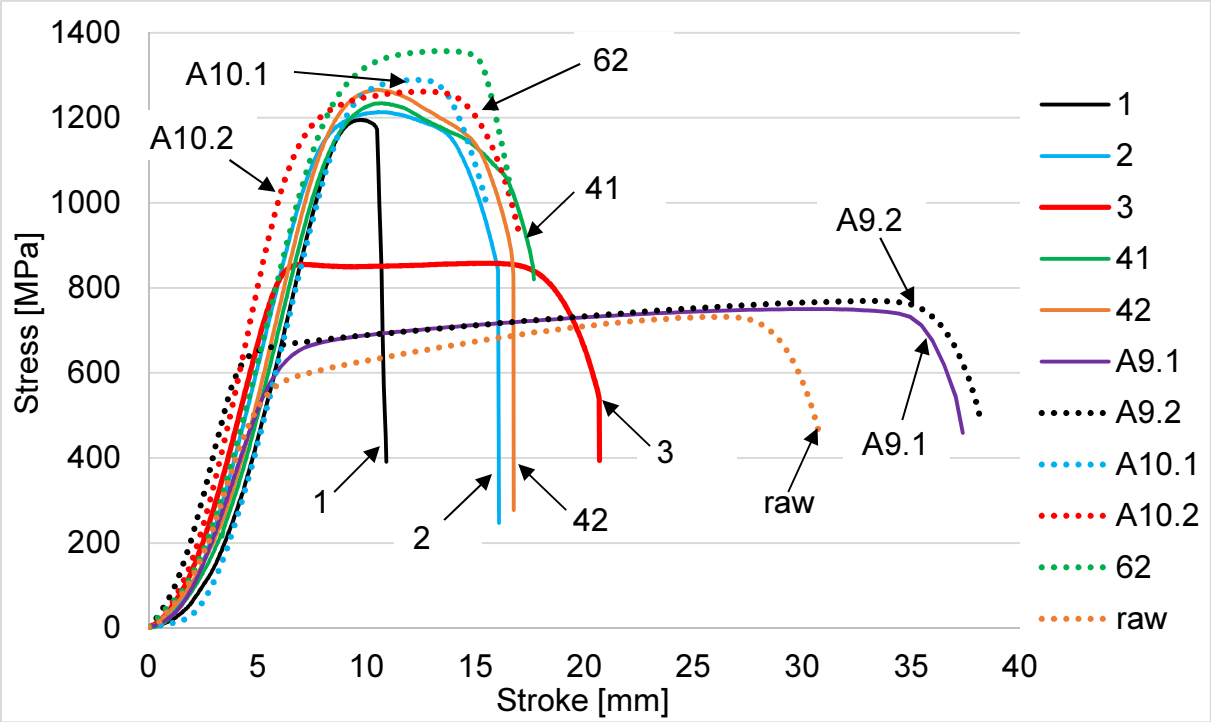

Figure 11.52. The calculated stress versus stroke for all tested samples

For samples A9.1, A10.1 and 62, the extensometer was used and the strain was calculated precisely. The results for these three samples are shown in Fig. 11.53.

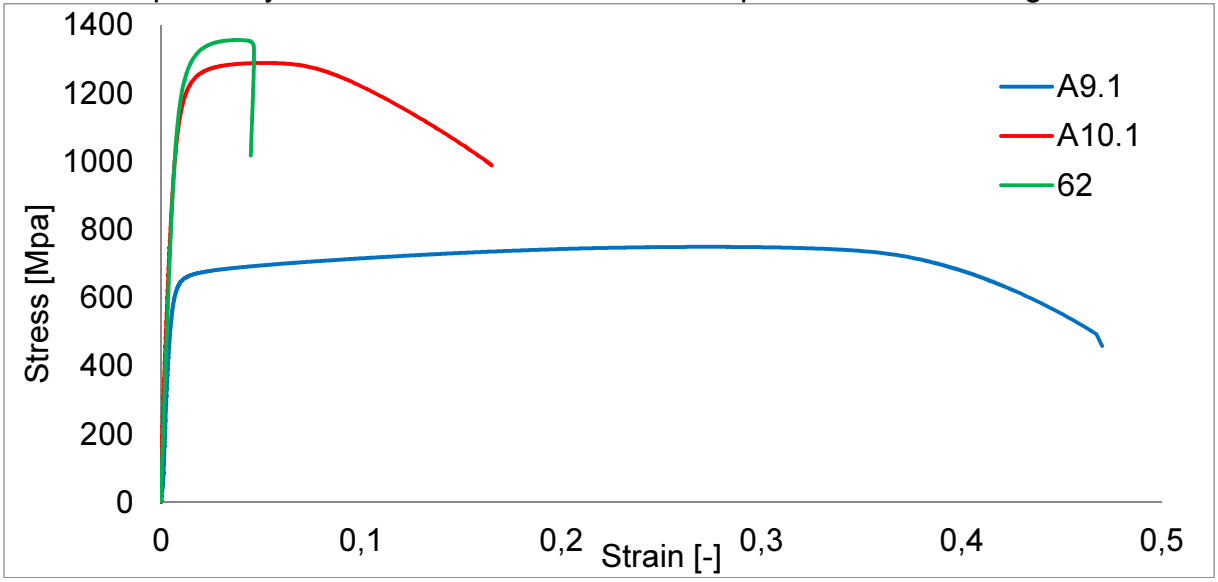

Figure 11.53. Stress versus strain for the samples: A9.1, A10.1, and 62

The highest strain was obtained for sample A9.1, for which very small hardening was observed. The strain at rupture was equal to 0.47. Much smaller strain (about 0.17) was obtained for sample A10.1, which had some 82.9% of martensite on the surface. Even smaller strain at rupture (0.045) was found for sample 62 with 100% of martensite content after tensile test.

A clear proof for the increased strength is provided in Fig. 11.52. The yield strength of sample A9.1, with 6.7% of martensite on the surface, was about 600MPa, whereas, for sample A10.1, with 82.9% of martensite on the surface, it was more than twice as large, i.e. about 1250Mpa. At the same time, the ductility decreased, which was indicated by decrease of the strain at rupture from 47% to 17%.
The stresses and the strains are summarized in Tab. 11.3. The character of the fracture is indicated. For two samples only it is brittle, i.e. for sample 1 and 62. The Young modulus and the yield stress are not indicated, as the measurement was not precise enough (Fig. 11.54). Smooth increase of stress for very small strains (samples: A9.1, A10.1), and additional variations (sample 62) were not expected. They were possibly caused by the type of grips, which had the possibility of sliding.

Sample number	Maximum stress	Strain at max. stress	Stress at rupture	Strain at rupture	Character of the fracture
[-]	[MPa]	[%]	[MPa]	[%]	[-]
1	1196	-	391	-	Brittle
2	1214	-	247	-	Ductile
3	858	-	394	-	Ductile
41	1234	-	820	-	Ductile
42	1266	-	277	-	Ductile
A9.1	750	27.10	459	47.0	Ductile
A9.2	769	-	483	-	Ductile
A10.1	1290	4.95	989	16.5	Ductile
A10.2	1262	-	919	-	Ductile
62	1357	3.87	1018	4.49	Brittle
Raw	732	-	456	-	Ductile

Table 11.3. Maximum stress, stress at rupture and the corresponding strain for all tested samples

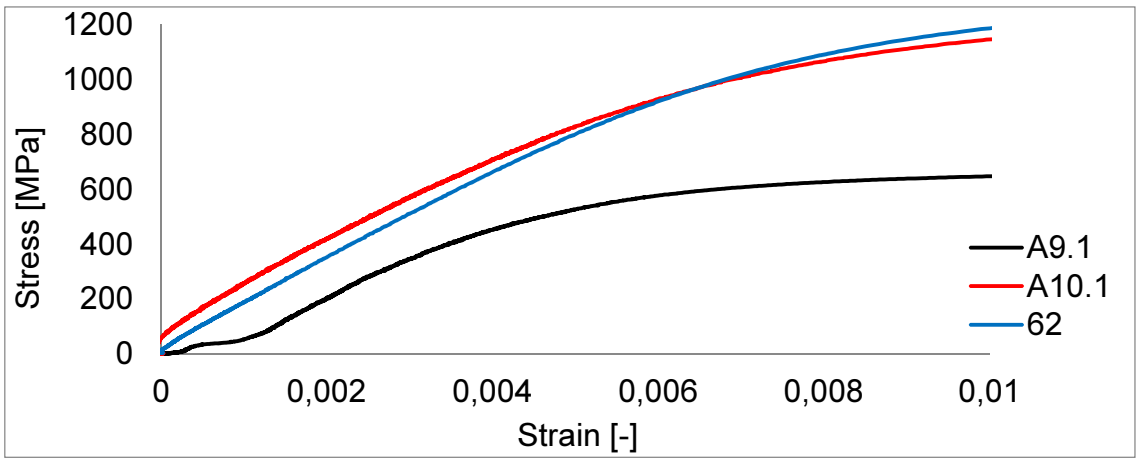

Figure 11.54. Stress versus strain in the range of strains smaller than 1%

11.7. Summary and conclusions

Several samples with various martensite content were subjected to tensile test. Some samples were pre-loaded by applying “monotonic” torsion (cycles with increasing amplitude – see Chapter 5), and the other by using cyclic torsion. As a result, they showed axisymmetric martensite distribution within their cross-sections (section 6.3). For samples 1, 2, 3, the martensite distribution within the cross-section was measured (sections 6.3.6 and 6.3.7). For samples 4, A9, A10 and raw, the martensite content on the surface was measured only. For sample 62, no measurement was done (the Feritscope was not yet available at that time).

The most important conclusions are as follows:

- Confirmation of increased mechanical properties of the samples with induced martensite was obtained. The maximum stress increases from 730MPa for the raw sample, to some 1357MPa for sample 62 (almost twice as large).
- The sample with high martensite content (sample 62) failed at 4.5% of strain, keeping some ductility and did not become brittle. Such a value of strain, exceeds typical engineering strains, which are usually limited to fractions of a percent.

12. Buckling of FGSMs - experiments

The so-called „Functionally Graded Structural Members" are created by torsion in cryogenic or at room temperature conditions. Both monotonic and cyclic torsion can be used. The mechanical response, expressed in terms of the torque versus the angle of twist, was measured for several samples made of different stainless steel grades. Also, the evolution of martensite content on the surface of the samples was measured during the tests. In addition, the martensite content was traced within the cross-sections of several samples, to reveal the distribution of α' martensite.
The newly created structural members have better mechanical properties, as shown during the torsion and the tension tests. Another positive characteristics of these structures, as foreseen in Chapter 2, is more stable behavior in the post-buckling range. Better stability is achieved because of higher mechanical properties of the martensitic phase, especially in terms of the yield strength and the hardening modulus.
In the present chapter, the results of the axial compression test are shown. The most important goal of this test was investigation of the real properties and the behavior of cylindrical bars under axial compression. The test was designed to allow high compression ranges. This experiment was at the same time a good test for the performance of FGSMs under bending, including large strains.
In total 9 samples were tested, all of them with different distribution of martensitic phase. All tested samples were made of grade 304 austenitic stainless steel. One sample in the raw state was tested for direct comparison.
It has been decided to perform all tests with double clamped boundary conditions. This was motivated by relatively easier and cheaper technical solution for this type of fixing conditions (compared to free or pinned type).

12.1. Description of the experiment

The samples selected for this test were pre-loaded by applying cyclic torsion. Detailed information about loading conditions and the measured martensite content are presented in Tab. 12.1 (see section 9.3.1 for detailed results). The martensite content measured on the surface is presented in Fig. 12.1.

Lp	Symbol	Material	Temp. [K]	Number of cycles	Loading control		ξ_{max}
					M [Nm]	φ [°]	[%]
1	A1	304	77	10	± 70 Nm	-	17.8
2	A2	304	77	10	± 80 Nm	-	26.7
3	A3	304	77	10	± 60 Nm	-	3.7
4	A4	304	77	10	± 100 Nm	-	67.1
5	A5	304	77	3	-	± 180°	84.9
6	A6	304	77	10	-	± 60°	49.7
7	A7	304	293	10	-	± 180°	31.0
8	A8	304	293	10	± 60 Nm	-	42.3

Table 12.1. Loading conditions for samples subjected to buckling test

According to the photographs of the samples after cyclic torsion tests, many samples became deformed. It means that the imperfections were introduced before the axial compression test. The samples were not straight anymore.
It is commonly known, that the post buckling path changes strongly as a function of imperfection size. In order to take into account this fact, the imperfect geometry of the samples was measured.

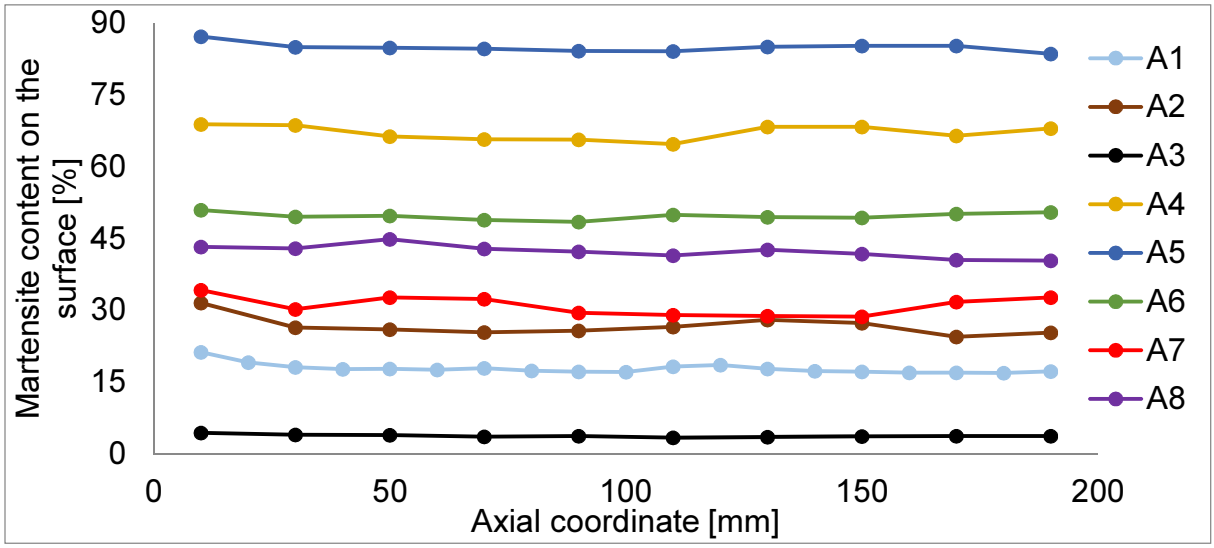

Figure 12.1. Martensite content on the surface of the samples before the axial compression test

A coordinate measuring machine was used to make a mapping of the shape of all samples. The shape was measured axially every 10 millimeters, starting from the distance of 5mm and finishing at 195mm (Fig. 12.2). At each axial location, the position of 16 points on the circumference of the bar was measured. In total, some 320 coordinates were collected for each sample.

Having gathered the position of 320 points on the surface of each sample, one is able to reconstruct the geometry of imperfect bars. Such models can be used in simulations that are close to experimental conditions. However, such simulations were not performed in the present Thesis. Simulating the behavior of imperfect samples under axial compression, with variable microstructure, is a subject of separate and rather complex study.

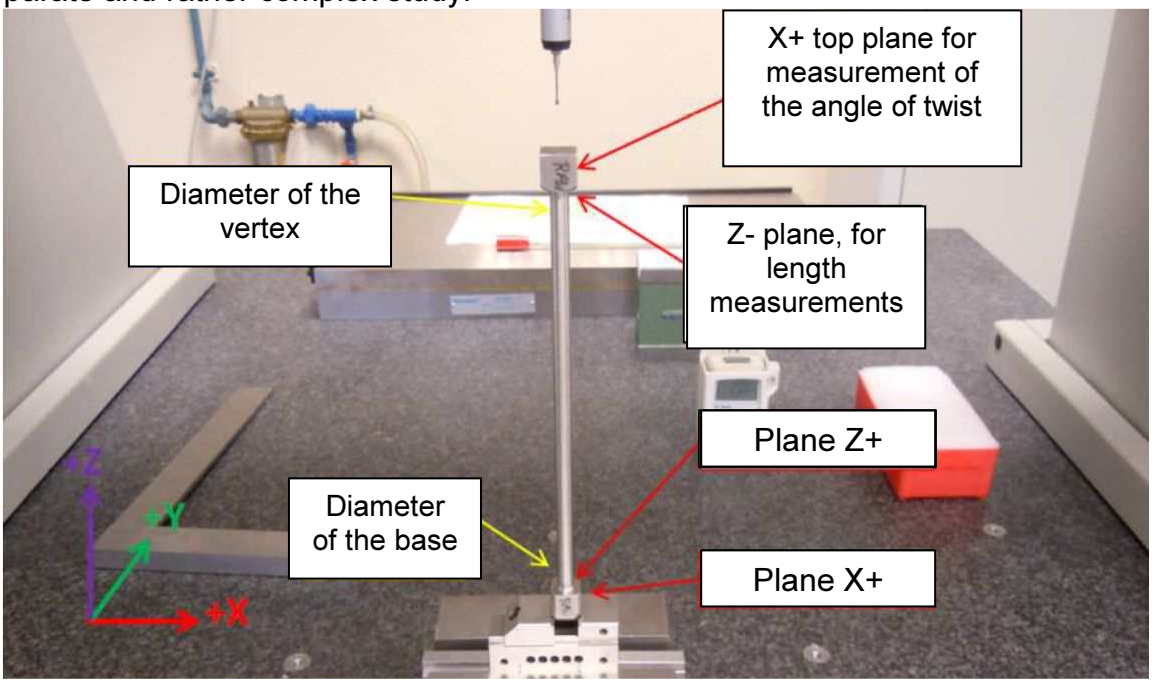

Figure 12.2. The principle of the measurements on the coordinate measuring machine, precision ±3μm

The angle of twist and the length, measured on the coordinate measuring machine, are listed in Table. 12.2. The highest residual angle of twist was equal to 56.5° for sample A6. The highest axial elongation of 2.76mm was measured for sample A5.

Lp	Sample	Angle of twist [º]	Length [mm]
1	A1	-24.289	200.642
2	A2	3.819	201.314
3	A3	3.486	200.308
4	A4	12.142	202.449
5	A5	22.415	202.756
6	A6	56.504	201.936
7	A7	35.467	200.949
8	A8	27.295	202.096
9	Raw	0.294	199.950

Table 12.2. Angle of twist and length of samples before the buckling test

The imperfections of samples after the cyclic torsion and before the buckling test are shown in Fig. 12.3a. The samples were cut at the top to obtain symmetric shapes. The length of end fittings of square cross-section was equal to 15mm. The placement of the cut is marked in Fig. 12.3a.

a b

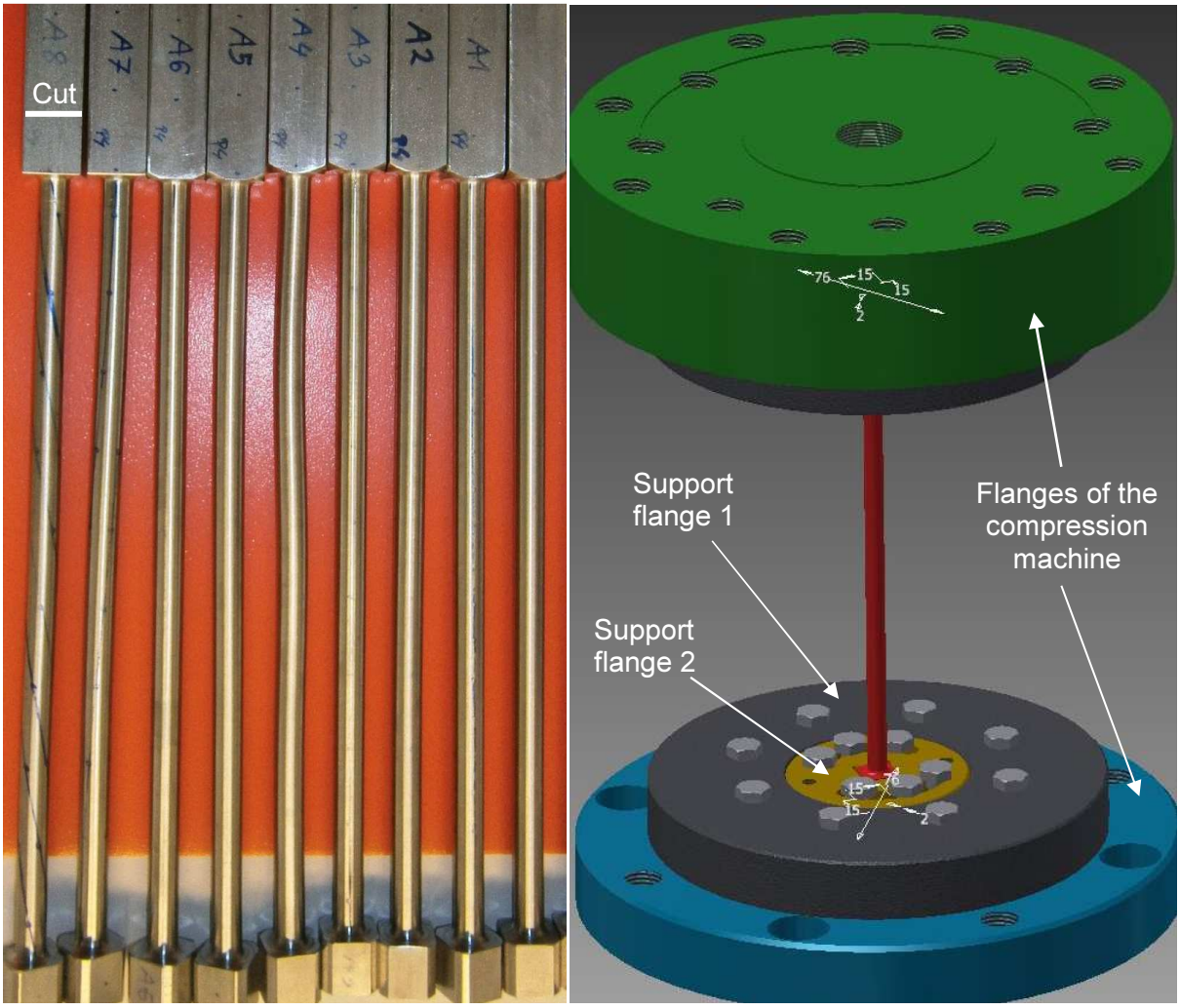

Figure 12.3. a) Samples before the buckling test, b) 3D layout of assembly with the supporting flanges and the sample

The maps containing the points, collected with the coordinate measuring machine, are shown in Fig. 12.4 for all samples.

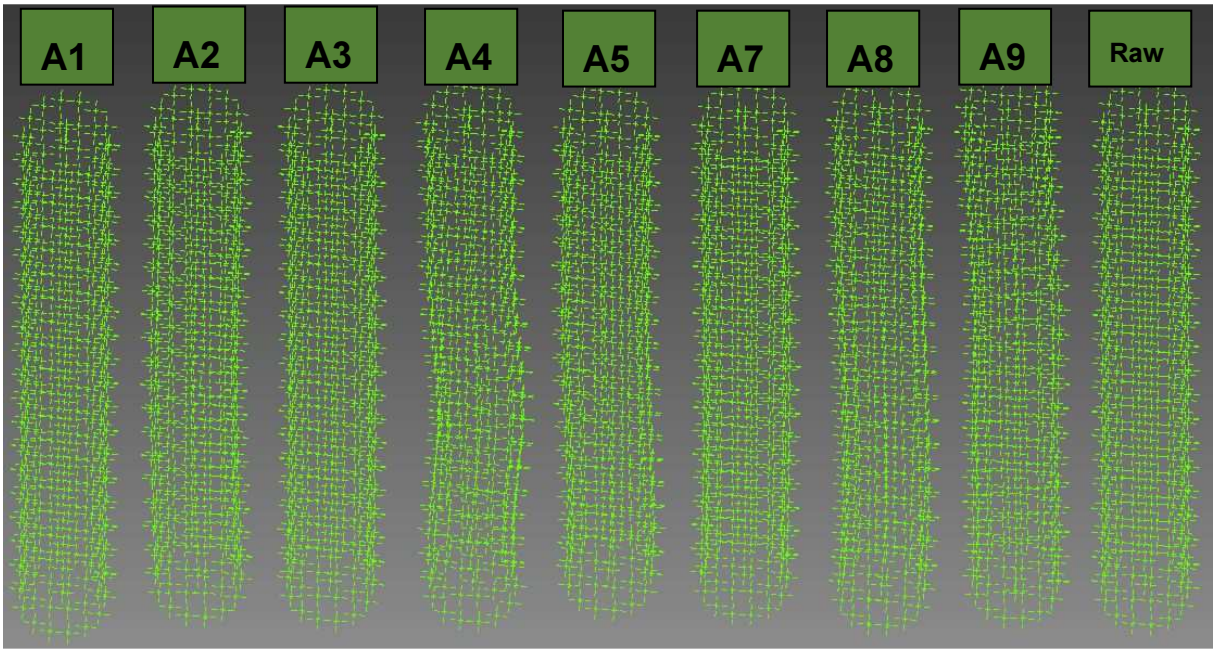

Figure 12.4. Imperfect surfaces of the samples before the buckling test

Four flanges were designed as an interface between the sample extremities and the compression machine. The system had to fulfill the following requirements:

- the bottom support of sample had to fit with the flange of the compression machine,
- the top support of sample had to fit with the top flange of the compression machine,
- the system provides clamping of both ends of sample, with enough rigidity against any translation and rotation,
- the system allowed clamping samples that had their square ends rotated with respect to each other.

A solution that satisfied all the above requirements was created. Four support flanges were used to clamp the sample. Two flanges were used to fix the sample to the compression machine at each side. They allowed rotation around the axis of the sample. The same geometry was used for both pairs of flanges to minimize machining cost. The assembly of the supporting flanges together with the sample is shown in Fig. 12.3b.

The bigger flange (denoted as “flange 1”) was connected to the compression machine by eight M8 screws. Detailed technical drawing is shown in Fig. 12.5.

The smaller flange (denoted as “flange 2”) was connected to the first flange by using 6 screws. Its technical drawing is shown in Fig. 12.6. In order to allow rotations of this flange, two circumferential “through” holes of ϕ60, spanned at 100° angle, were created. This solution allowed rotation of this flange by ± 45°. The angle of 100° allowed fitting at least 4 screws into the corresponding holes in the 1st flange.

The samples were inserted into the square holes in the second flange, without any additional mounting. There was no possibility of sliding back, as the sample was compressed from the top continuously.

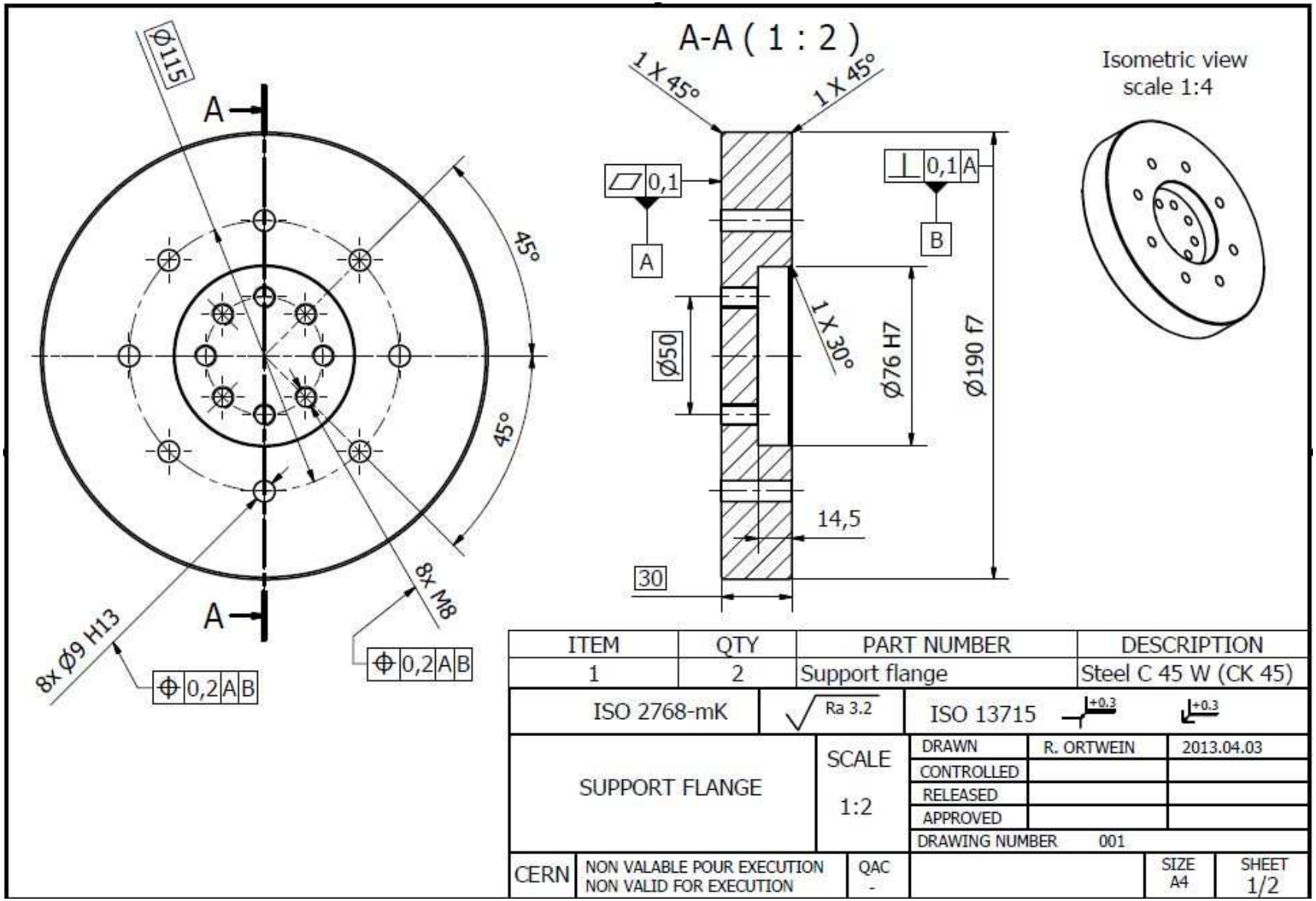

Figure 12.5. Technical drawing of the support flange 1

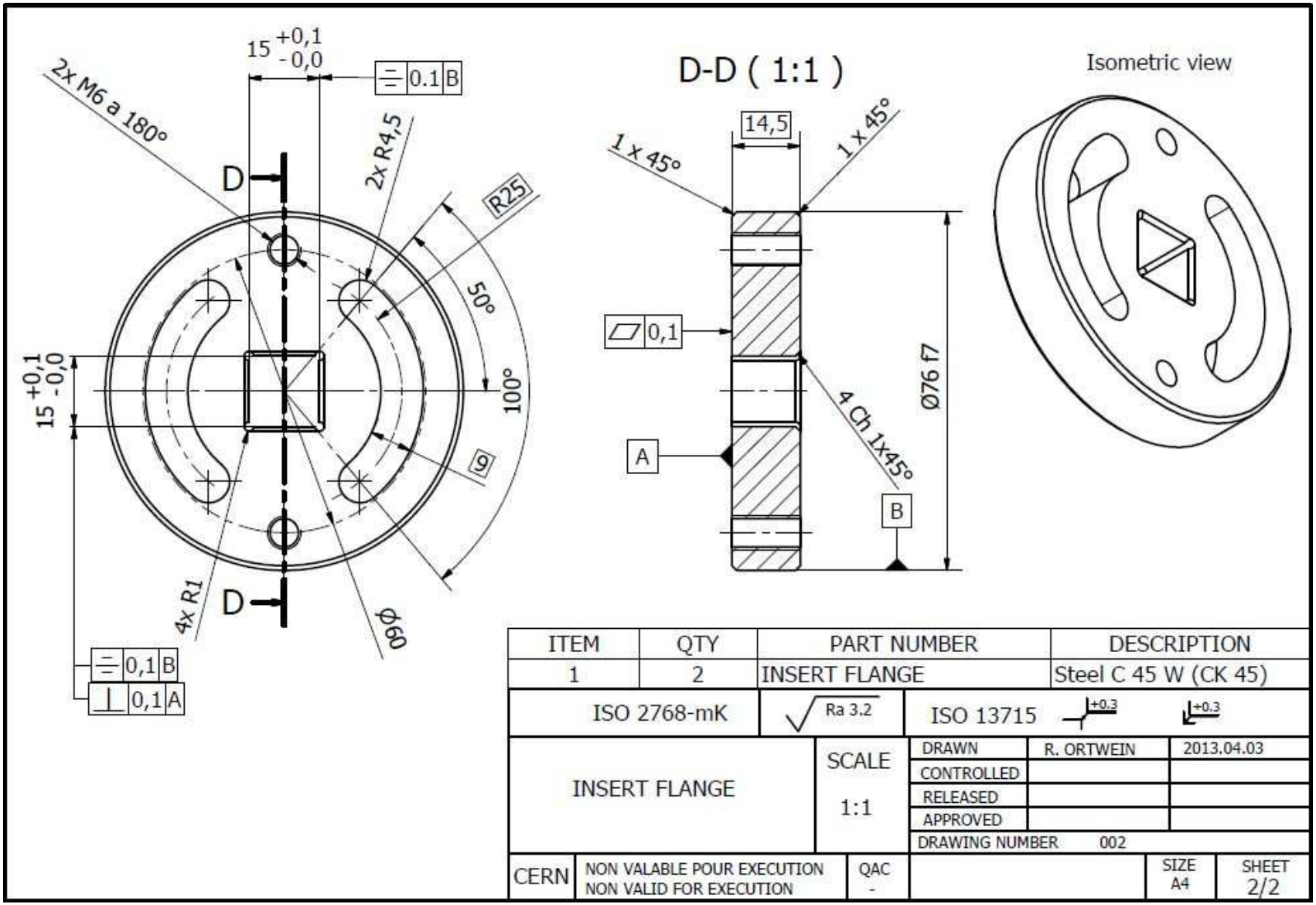

Figure 12.6. Technical drawing of the supporting flange 2

The set-up with a sample which has already buckled was is presented in Fig. 12.7. The camera was recording the deformation during the whole test. The videos were used later to measure the transverse deflection.

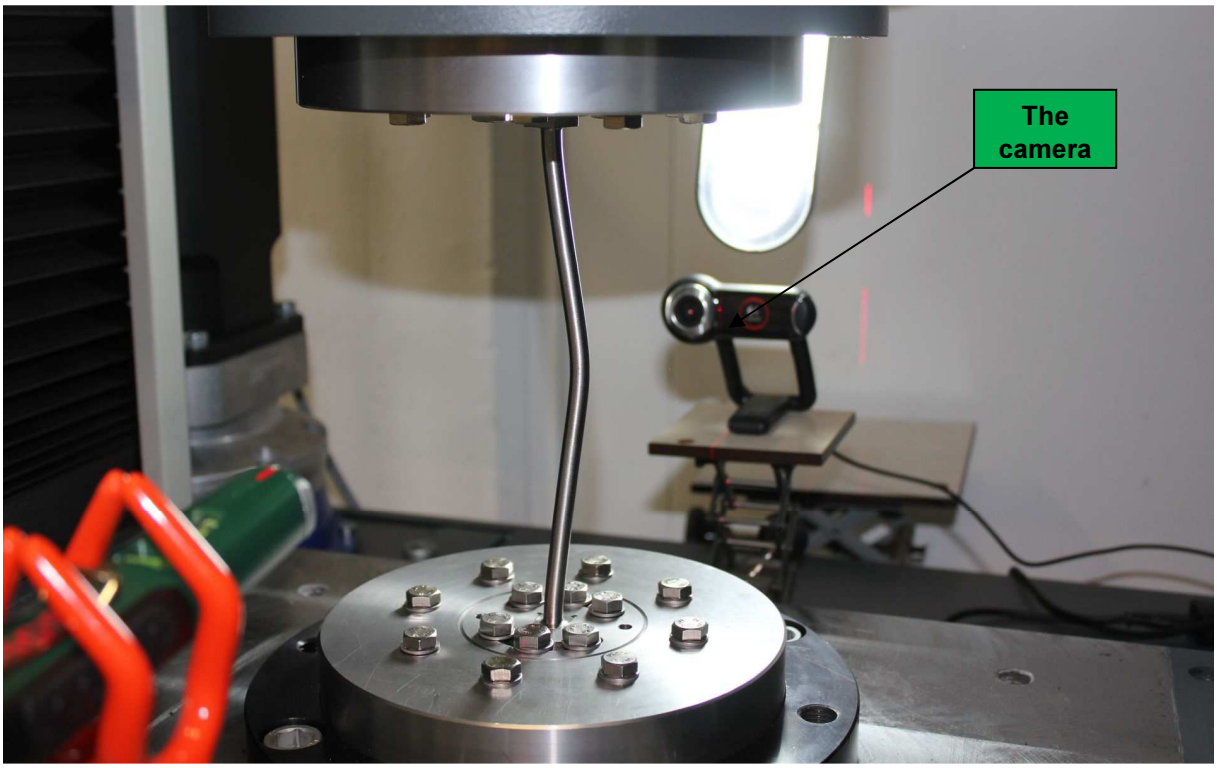

Fig. 12.7. The set up with buckled FGSM sample

The set-up was equipped with a scale, placed near the central part of the sample. The scale had lines drawn with known offset. They provided the calibration reference for the measurements of transverse deflection based on recorded videos (Fig. 12.8).

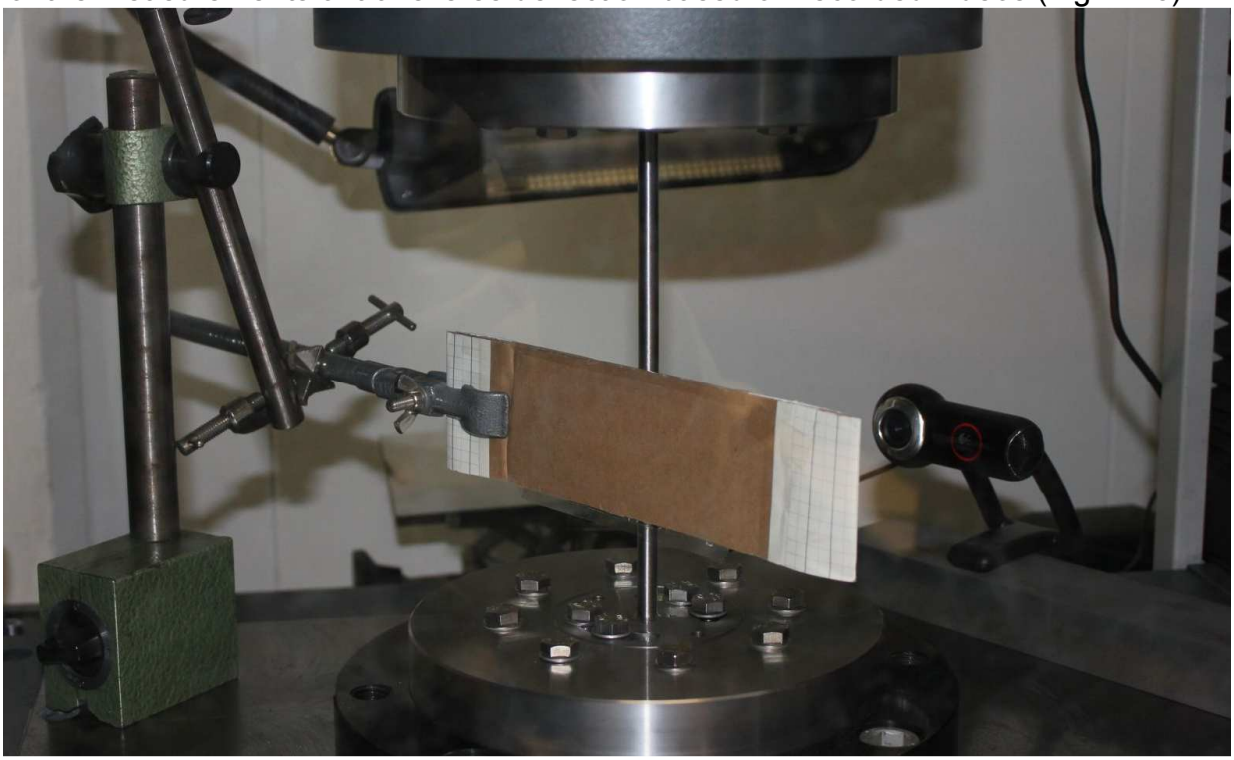

Fig. 12.8. The set-up to measure transverse deflection of the sample

12.2. The procedure of test

The following procedure was implemented for full axial compression test:

1. Fixing the sample in the compression machine Zwick Roell Z400.
2. Placing the scale behind the sample.
3. Setting the speed of the compression.
The speed of the compression was not constant. Three loading stages were pre-set. During the first 5mm the speed was $1\frac{mm}{min}$, then up to 50mm of the axial shortening the speed was set to $10\frac{mm}{min}$, and further up to 100mm the speed was equal to $20\frac{mm}{min}$. This sequence has been selected in order to minimize the time of the test, since the availability of the machine was very limited. The influence of the compression speed on the results was very small (smooth force versus axial compression response).
4. Starting the loading sequence.
The buckling plane was undetermined because of circular cross-section of the sample (the same moment of inertia in every plane). The obvious problem in the measurement of transverse deflection was positioning of the scale, which had to lie in the buckling plane. As the plane was unknown, the test had to be stopped several times for repositioning of the scale. As soon as the buckling direction was visible, the compression was stopped and the scale repositioned. The camera was directed perpendicularly to the scale, behind the sample.
The photograph of sample A6, just at the beginning of buckling, is shown in Fig. 12.9.

Fig. 12.9. Beginning of buckling for sample A6

5. After repositioning of the scale, continuation of loading sequence.
After about 20-30 mm of transverse deflection, second correction of placement of the scale was usually necessary. Both the scale and the camera were repositioned. A photograph of sample A6 at about 10mm of transverse deflection is shown in Fig. 12.10.

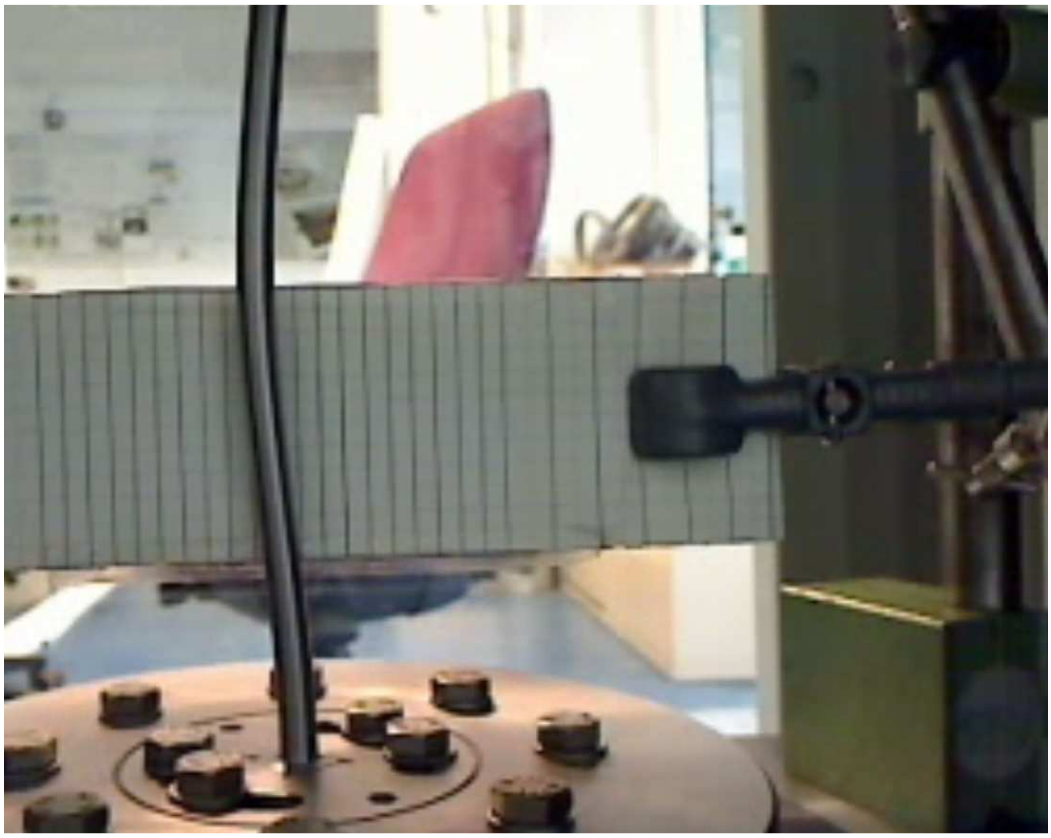

Fig. 12.10. Sample A6 after 10mm of transverse deflection

After about 80mm of the movement of the head, the scale started touching the top flange (Fig. 12.11). Again, repositioning of scale was needed. Discrepancy between the buckling plane and the plane of the scale is clearly visible in Fig. 12.11.

6. Continuation of test until the end of loading sequence.

The test was continued until 100mm of axial shortening was reached.

Fig. 12.11. The scale before final repositioning (sample A6)

12.3. Measuring transverse deflection of sample by using recorded videos

In order to measure maximum deflection of the samples, the deformation was recorded with a camera connected to the compression machine. As the samples were cylindrical, the buckling plane was random. In fact, most of the samples had imperfections (Fig. 12.3a), still there was no certainty in which plane they would buckle.

The principle of measurement of deflection is presented in Fig. 12.12. Deflection was measured in pixels, from the most deflected point of the sample to the reference axis, which coincided with the initial axis of the sample. The pixels were then recalculated into millimeters based on the calibration, which was made by using known distance between the lines in the scale and the corresponding number of pixels, according to simple formula:

$$u[mm] = C\left[\frac{mm}{pixel}\right] \cdot v\,[pixel] \tag{12.1}$$

where:

$v\,[pixel]$ – is the measured number of pixels from the video (see Fig. 12.12),

$C\left[\frac{mm}{pixel}\right]$ – is a calibration constant, obtained by dividing the distance by the number of pixels.

It is important to stress, that the scale repositioning was recorded on the video. After repositioning of the scale, an offset was created between the current and the previous positions. This was taken into account when the displacement was calculated. Still, the error of measurement was increased. Another problem was the contrast in the video, which was not perfect. All these factors made it difficult to measure precisely the maximum transverse deflection. Especially, in the initial phase of the buckling when the deflection was very small. For transverse deflections higher than 10-20mm, the reading of the results was much easier and more accurate.

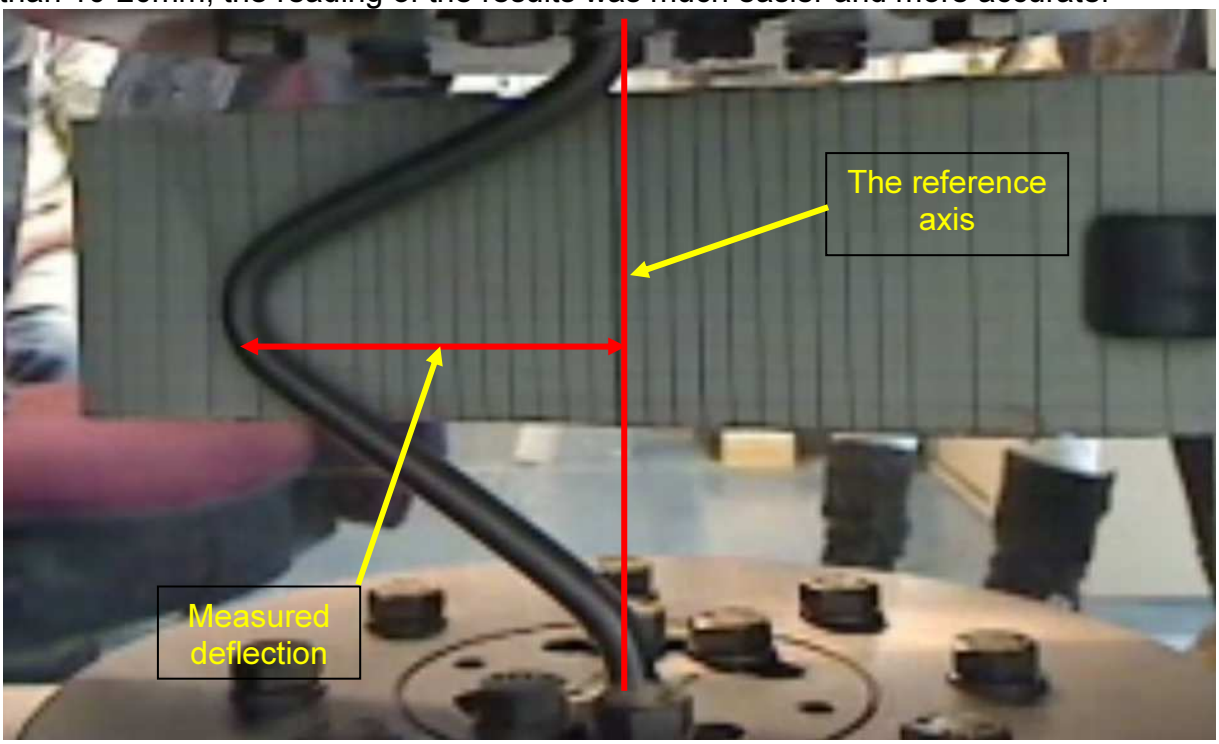

Figure 12.12. The reference system to measure transverse deflection

12.4. Experimental results

For each sample the compression force and the axial displacement were registered as functions of time. For all samples, plots of force versus time and force versus axial displacement were made. In addition, the speed of the compressive motion was calculated from displacements based on well-known foreword finite difference scheme:

$$\dot{u} = \left(\frac{u_{i+1} - u_i}{t_{i+1} - t_i}\right) \cdot 60 \left[\frac{mm}{min}\right] \tag{12.2}$$

where:

- u_i, u_{i+1} [mm] are axial displacements in the i and i+1 time moments,
- t_{i+1}, t_i [s] are time moments corresponding to displacements u_{i+1} and u_i.

Compression speed, calculated from equation 12.2, is plotted for all samples as well. It allows very clear identification of time moments at which the compression was stopped.

In the subsequent sections, the results are presented in the following order: Raw, A1, A2, A3, A4, A5, A6, A7. The results of force versus time and force versus axial displacement, were taken directly from the tensile machine. The results of compression speed versus time were calculated from Eq. 12.2. The results of force versus maximum deflection were obtained from the videos, according to the procedure described in section 12.3.

12.4.1. Results for the raw sample

The results of force versus time and the compression speed versus time are shown in Fig. 12.13. The peaks indicate the time moments when the test was stopped for scale repositioning. The results of force versus axial shortening are shown in Fig. 12.14, and the results of force versus maximum deflection are illustrated in Fig. 12.15.

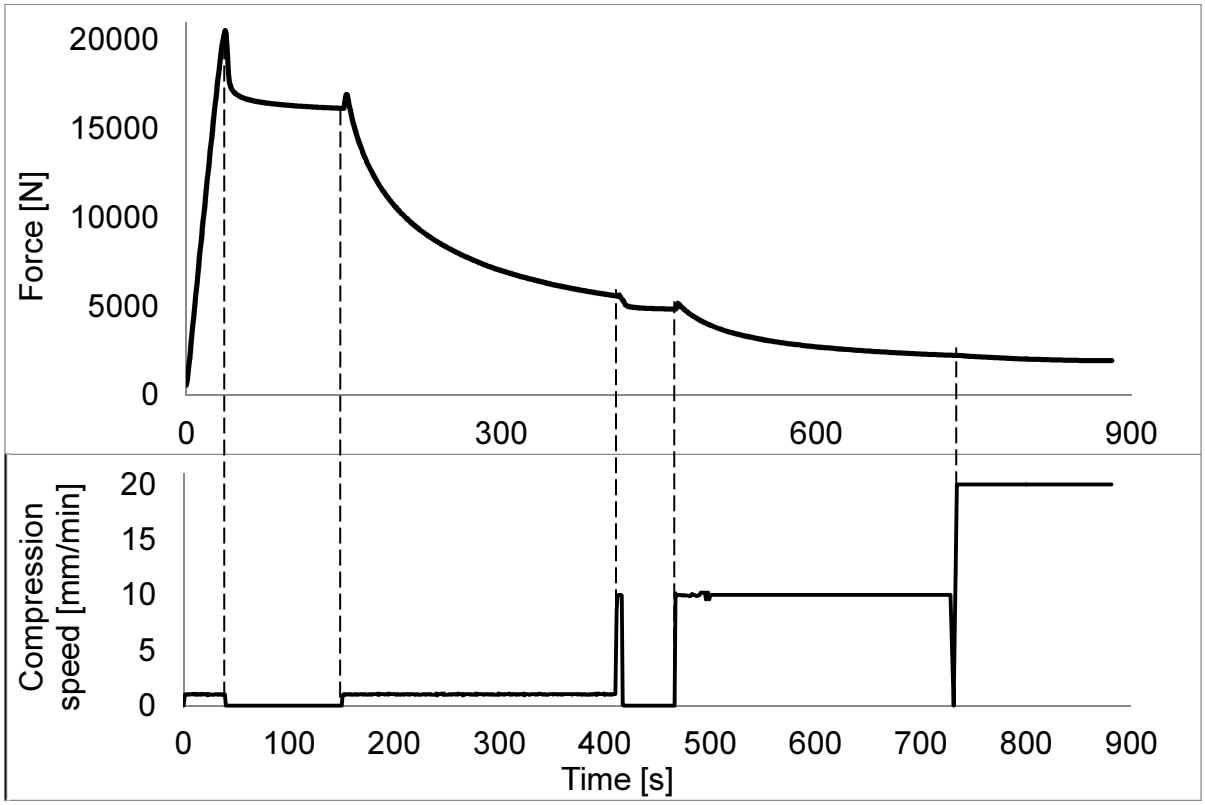

Figure 12.13. Force and compression speed versus time for “Raw” sample

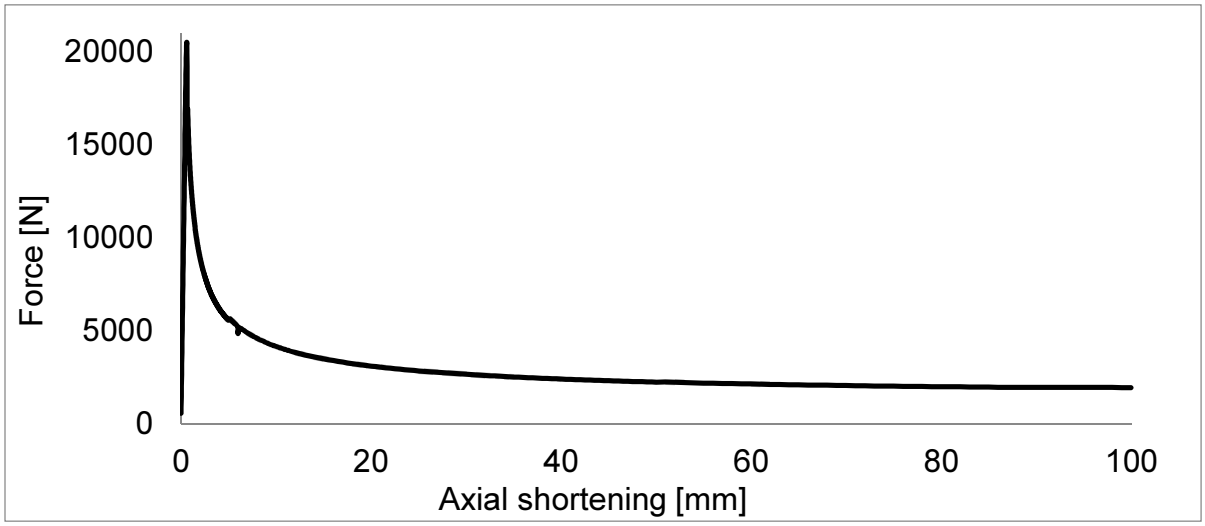

Figure 12.14. Force versus axial shortening for “Raw” sample

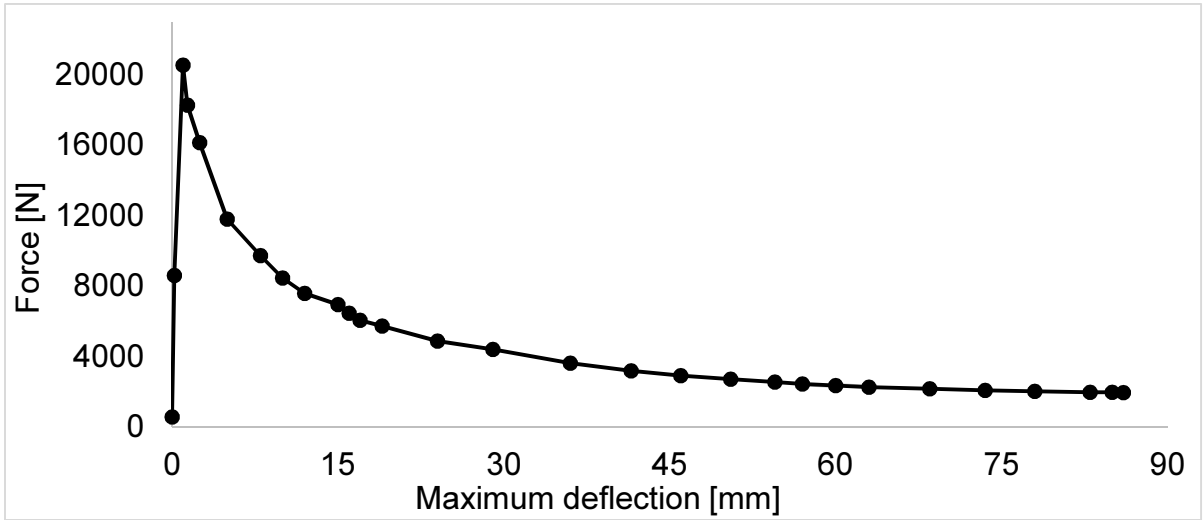

Figure 12.15. Force versus maximum displacement for “Raw” sample

12.4.2. Results for sample A1

The results of force versus axial shortening for sample A1 are shown in Fig. 12.16. The force and the compression speed are plotted against time in Fig. 12.17. The results of force versus maximum deflection are shown in Fig. 12.18.

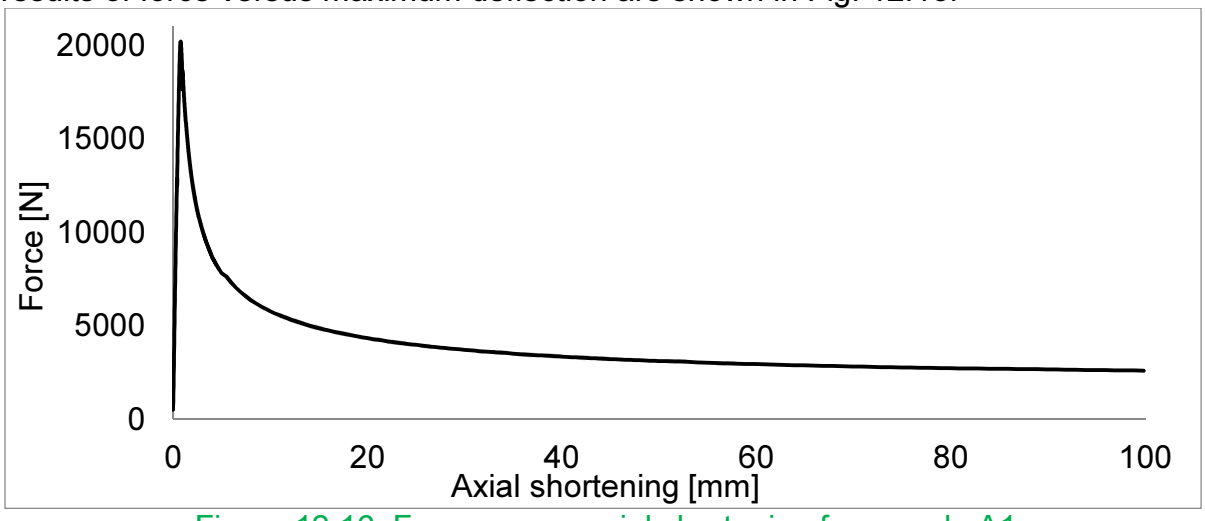

Figure 12.16. Force versus axial shortening for sample A1

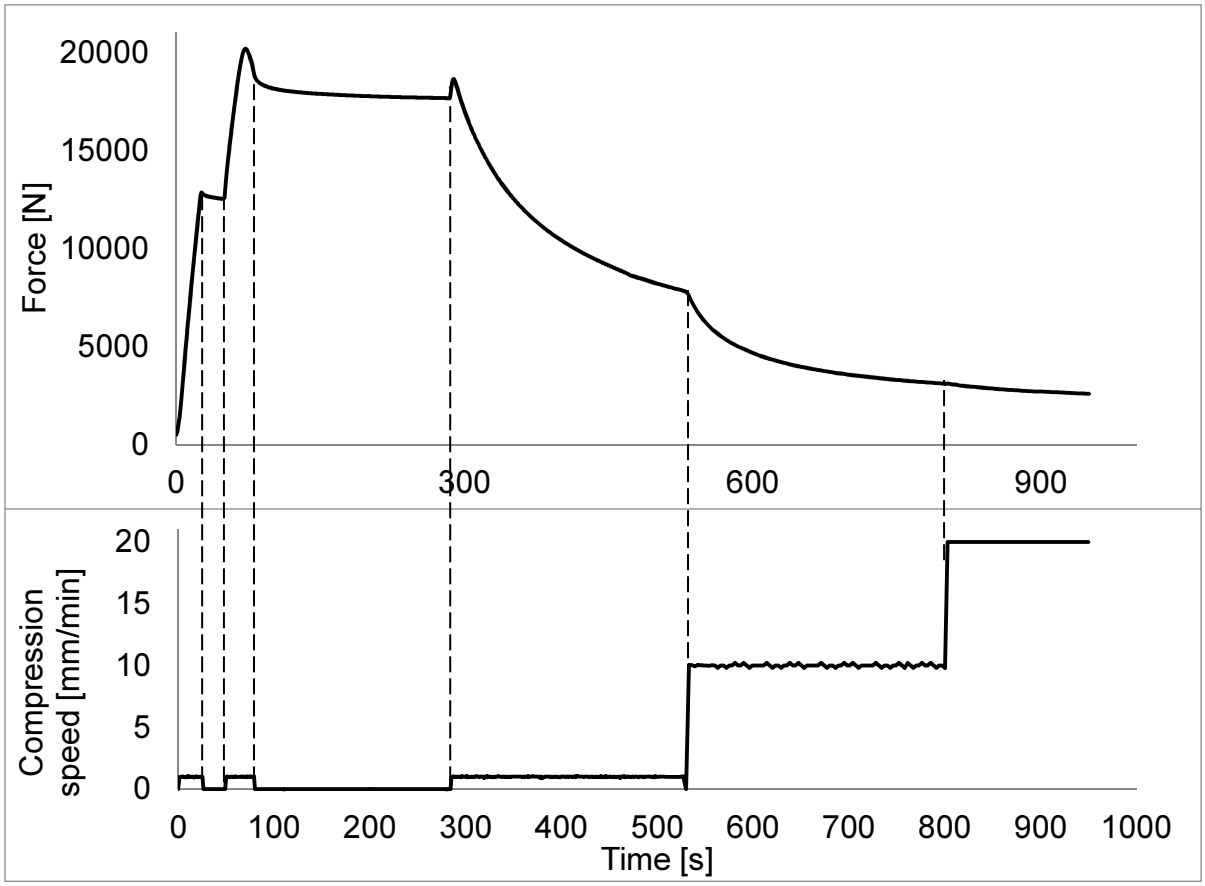

Figure 12.17. Force and compression speed versus time for sample A1

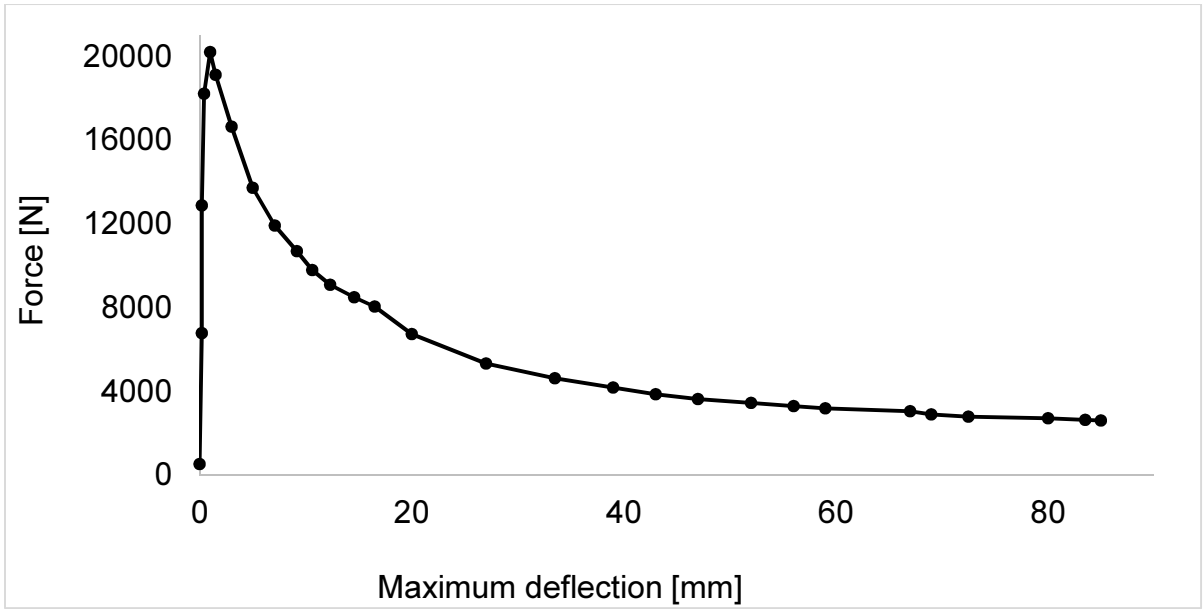

Figure 12.18. Force versus maximum displacement for sample A1

12.4.3. Results for sample A2

The force and the compression speed for sample A2 are plotted against time in Fig. 12.19. The results of force versus axial shortening are shown in Fig. 12.20. The results of force versus maximum deflection are shown in Fig. 12.21.

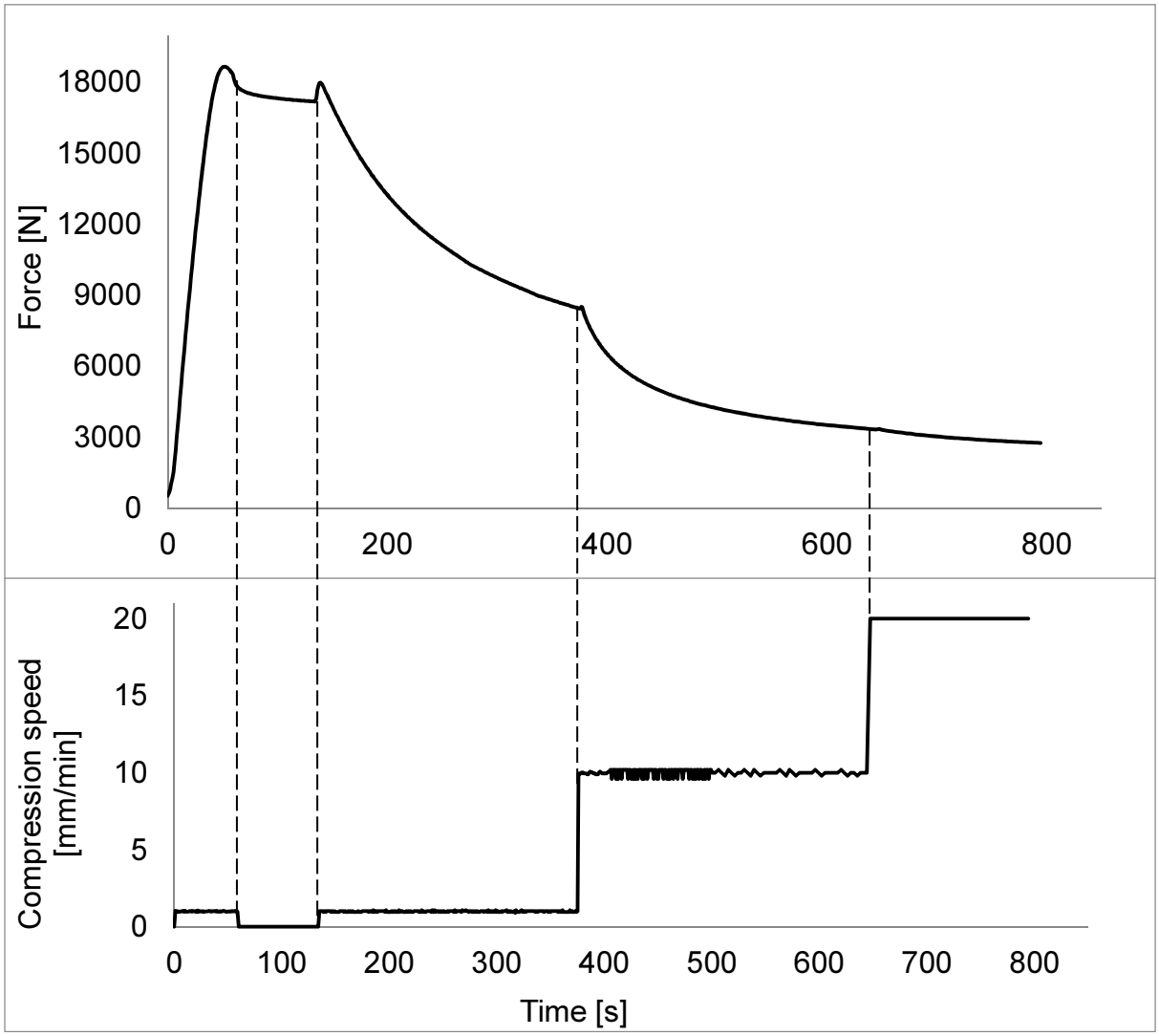

Figure 12.19. Force and compression speed versus time for sample A2

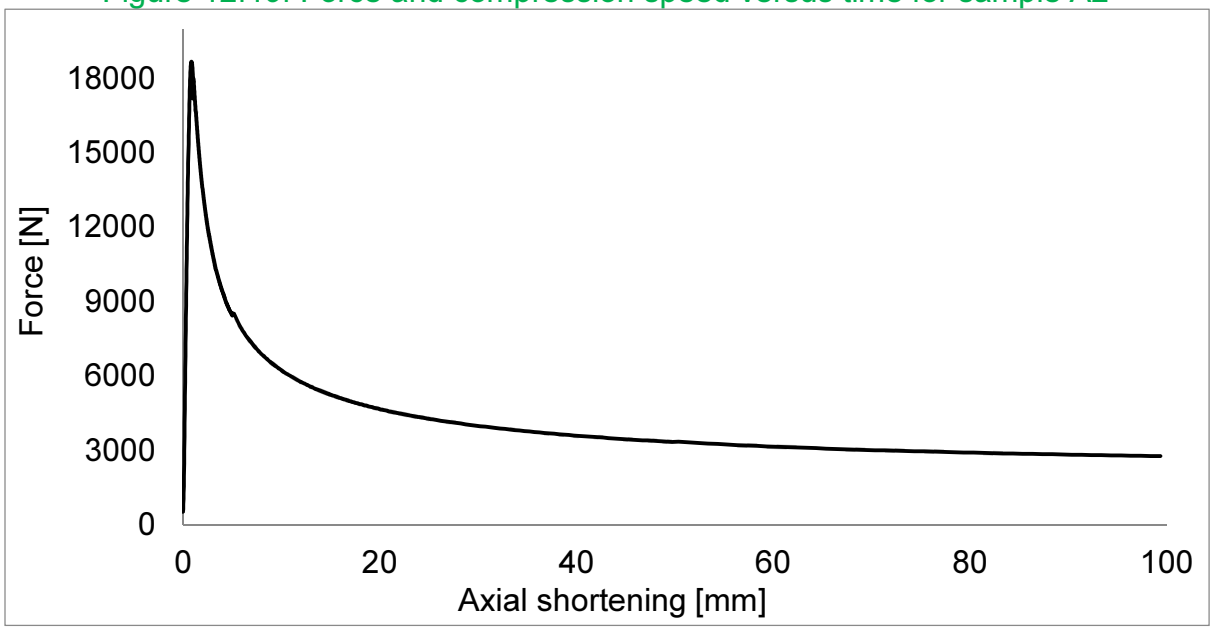

Figure 12.20. Force versus axial shortening for sample A2

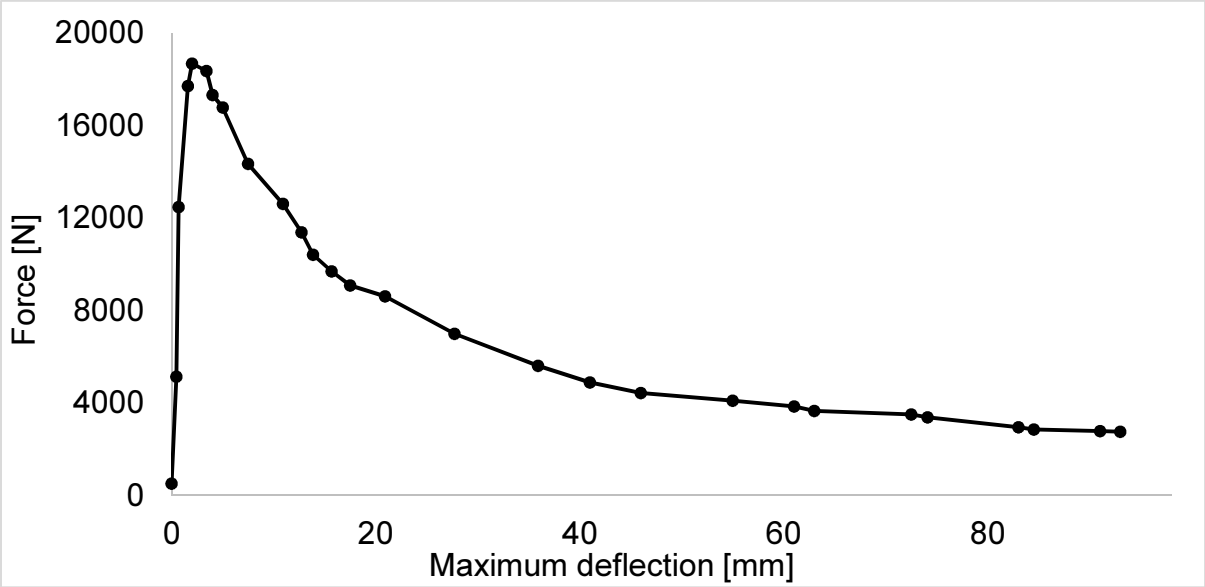

Figure 12.21. Force versus maximum displacement for sample A2

12.4.4. Results for sample A3

The force and the compression speed for sample A3 are plotted against time in Fig. 12.22. The results of force versus axial shortening are shown in Fig. 12.23. The results of force versus maximum deflection are shown in Fig. 12.24.

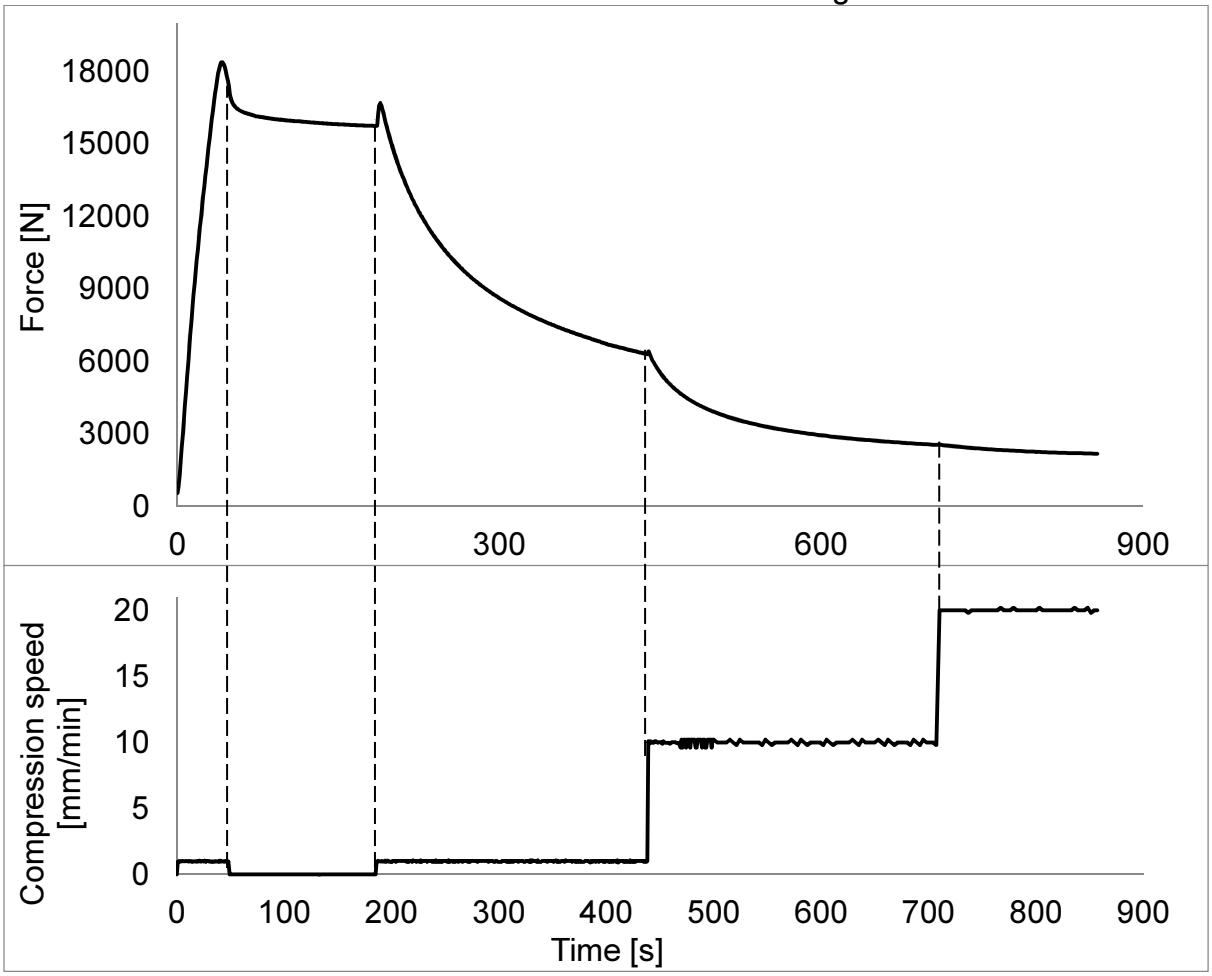

Figure 12.22. Force and compression speed versus time for sample A3

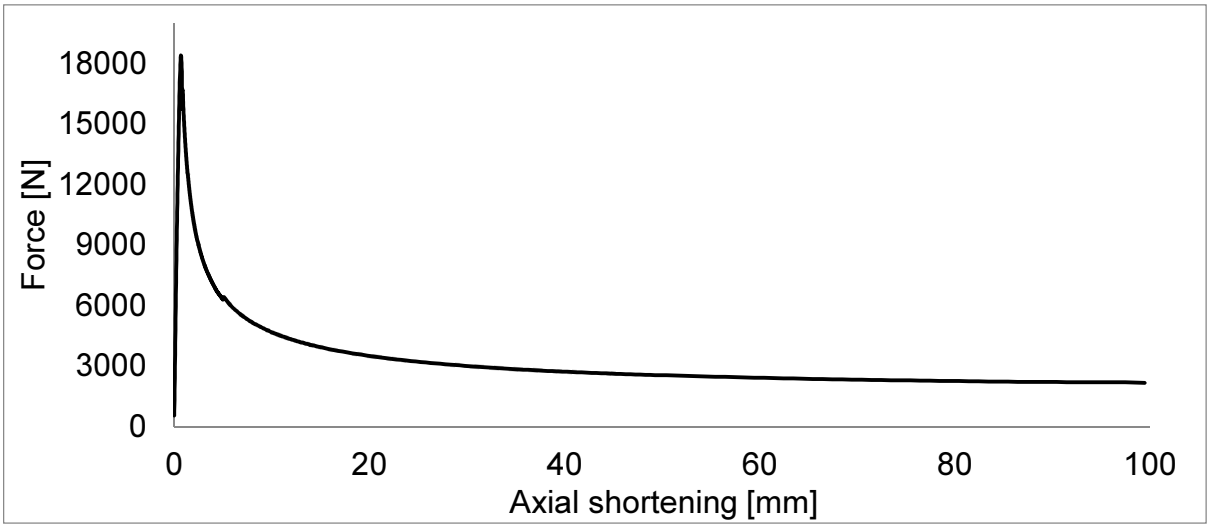

Figure 12.23. Force versus axial shortening for sample A3

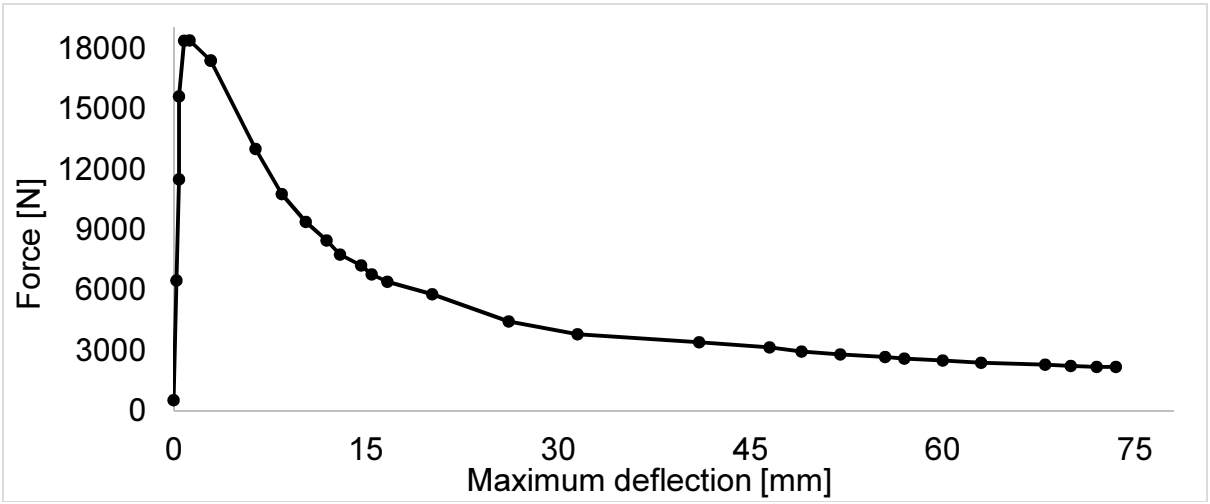

Figure 12.24. Force versus maximum deflection for sample A3

12.4.5. Results for sample A4

The force and the compression speed for sample A3 are plotted against time in Fig. 12.22. The results of force versus axial shortening are shown in Fig. 12.23. The results of force versus maximum deflection are shown in Fig. 12.24.

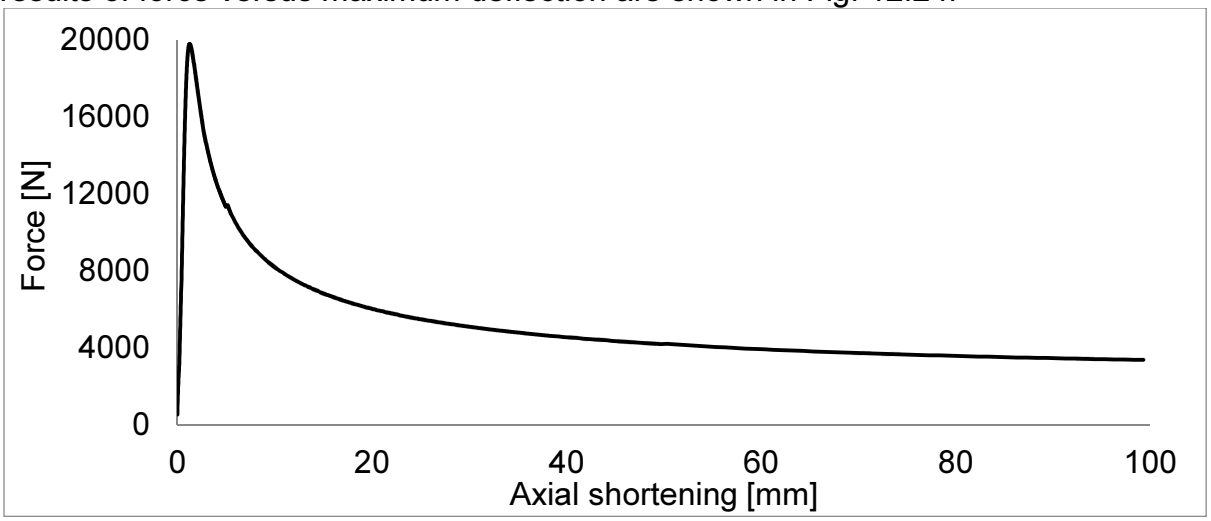

Figure 12.25. Force versus axial shortening for sample A4

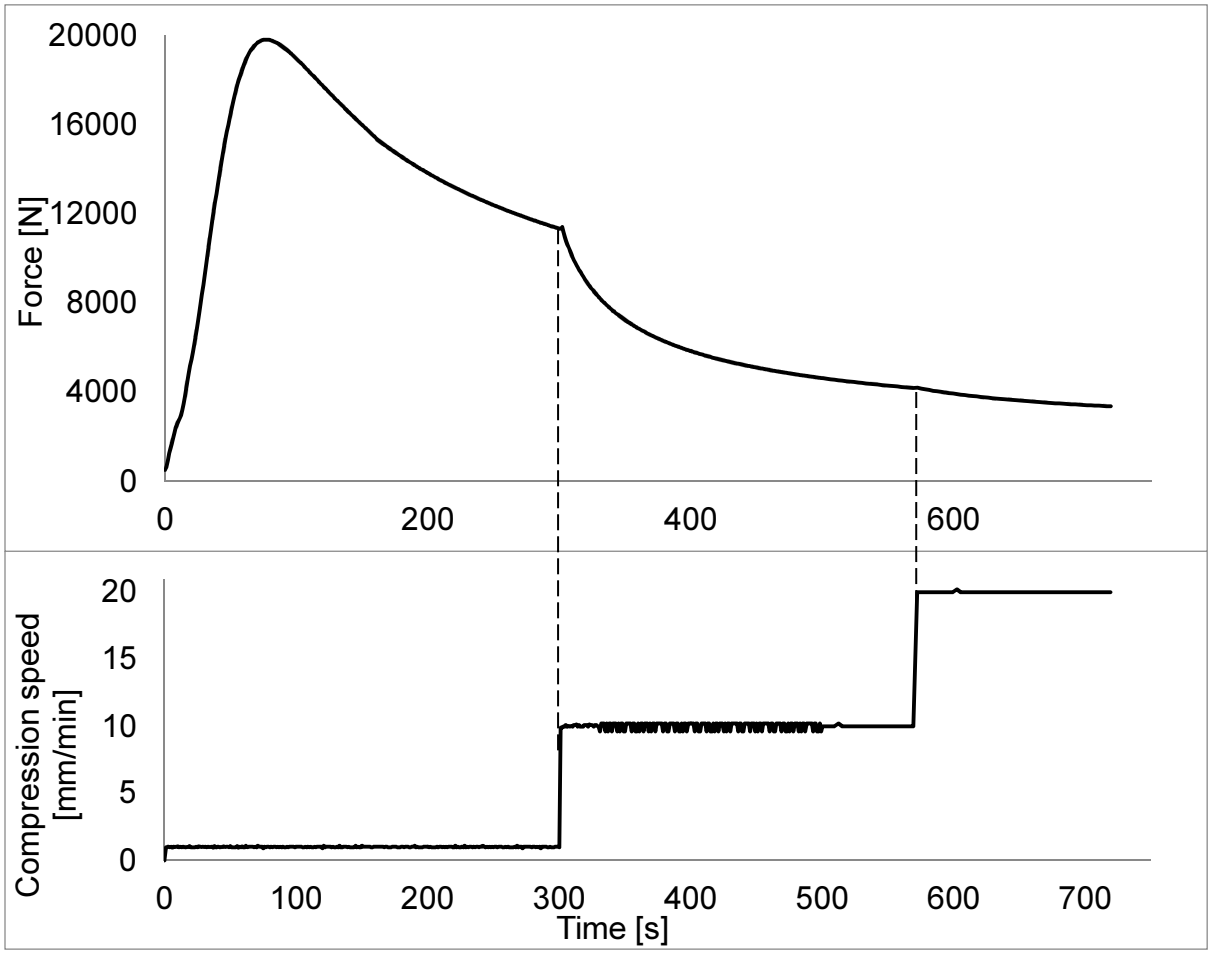

Figure 12.26. Force and compression speed versus time for sample A4

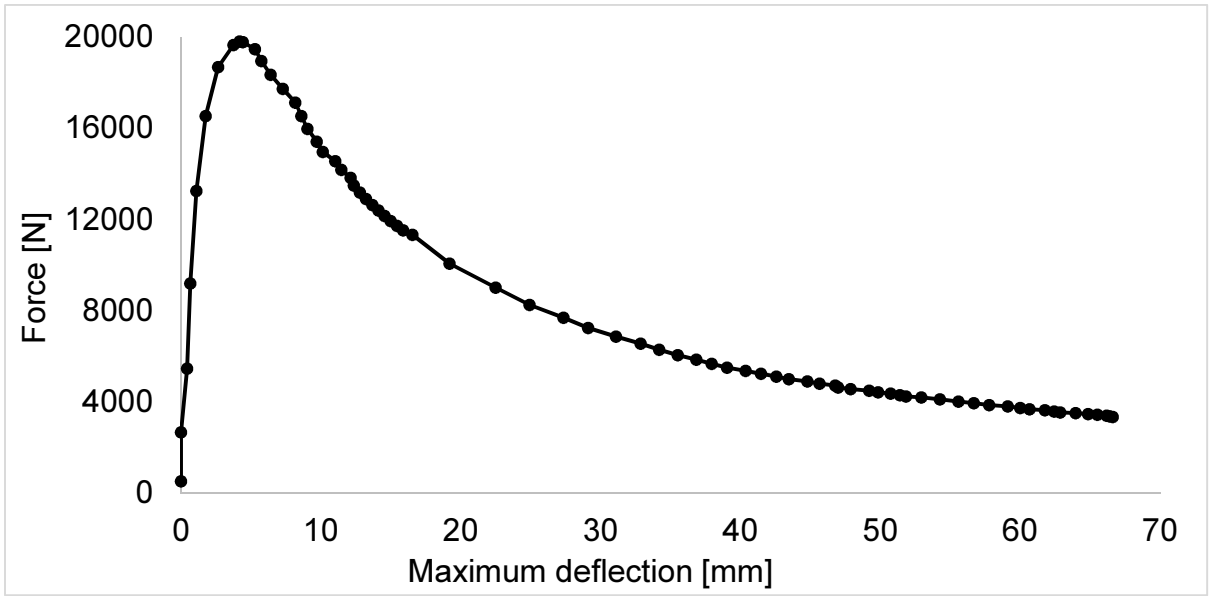

Figure 12.27. Force versus maximum deflection for sample A4

12.4.6. Results for sample A5

The force and the compression speed for sample A5 are plotted against time in Fig. 12.28. The results of force versus axial shortening are shown in Fig. 12.29. The results of force versus maximum deflection are shown in Fig. 12.30.

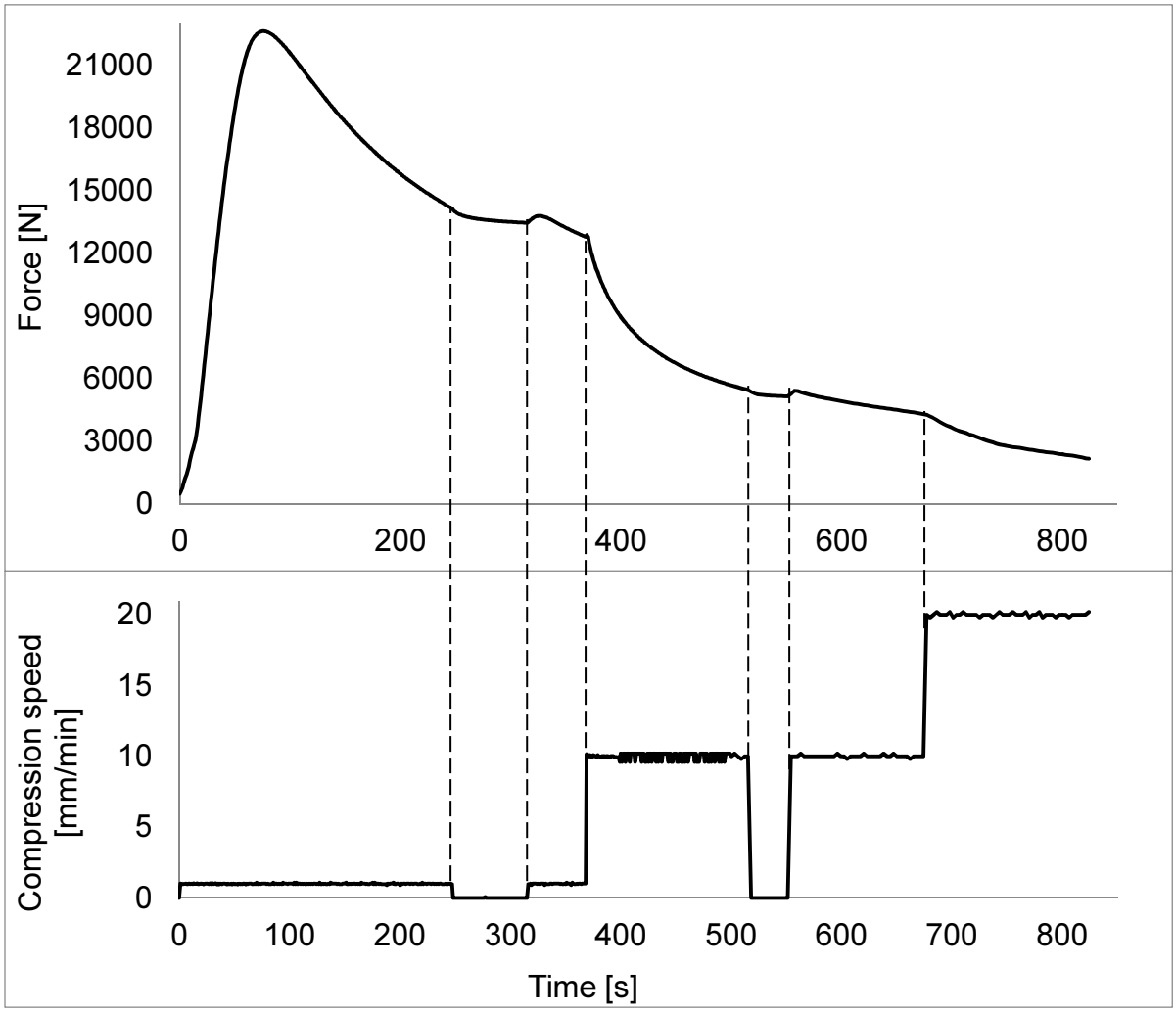

Figure 12.28. Force and compression speed versus time for sample A5

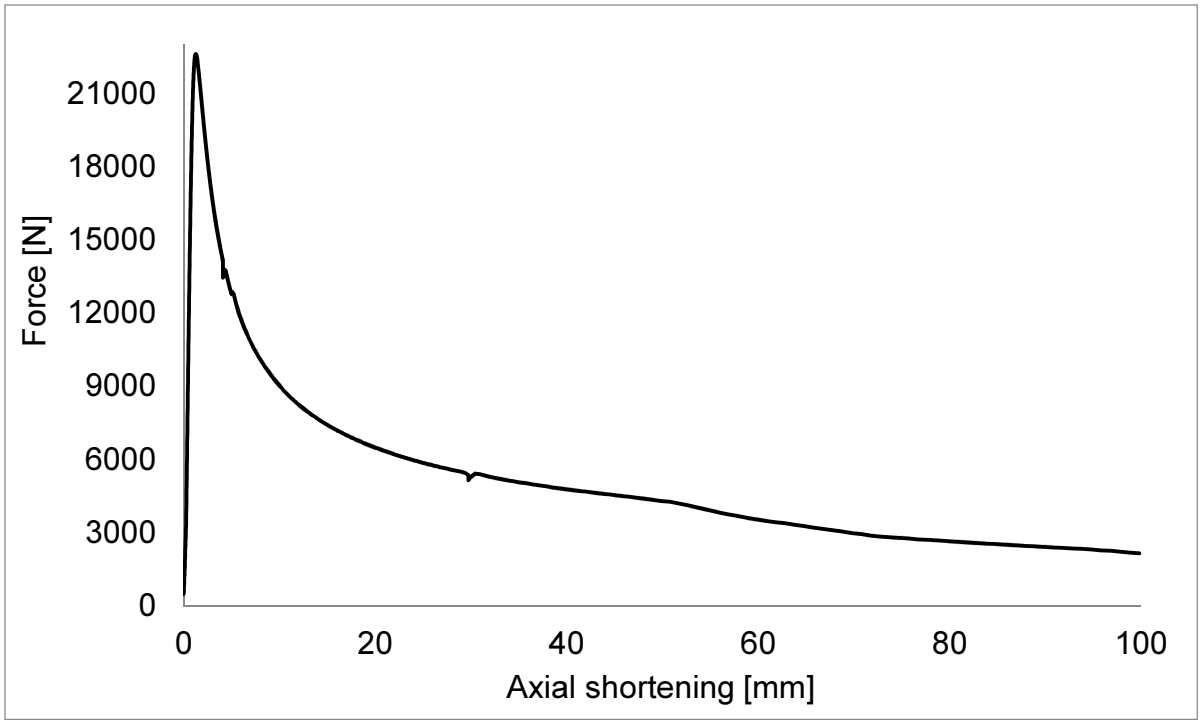

Figure 12.29. Force versus axial shortening for sample A5

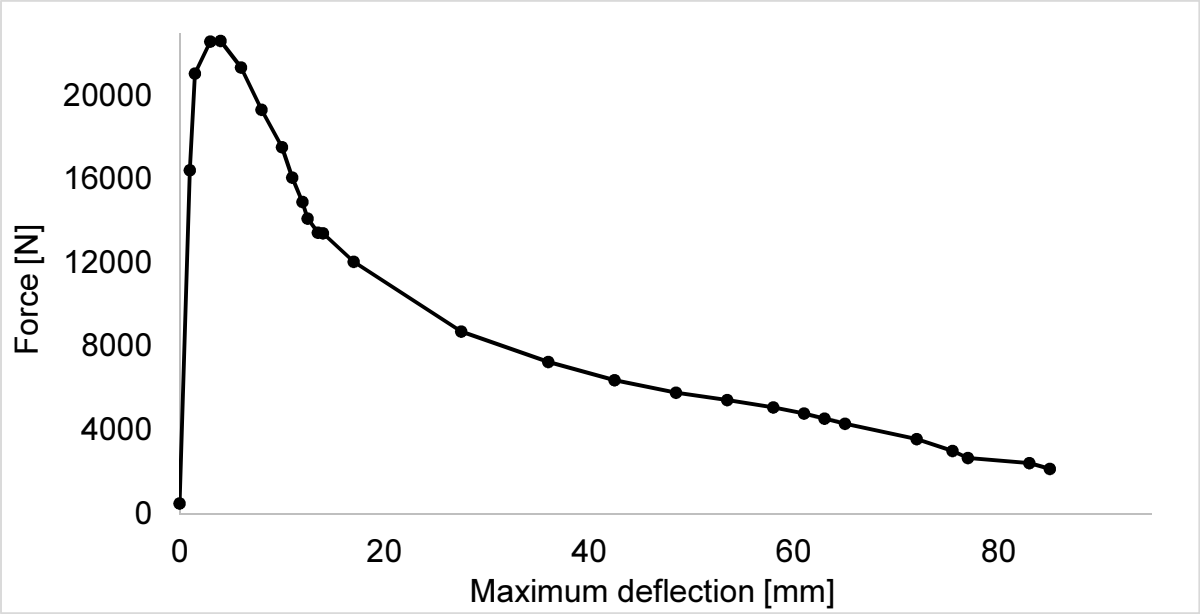

Figure 12.30. Force versus maximum deflection for sample A5

12.4.7. Results for sample A6

The force and the compression speed for sample A6 are plotted against time in Fig. 12.31. The results of force versus axial shortening are shown in Fig. 12.32. The results of force versus maximum deflection are shown in Fig. 12.33.

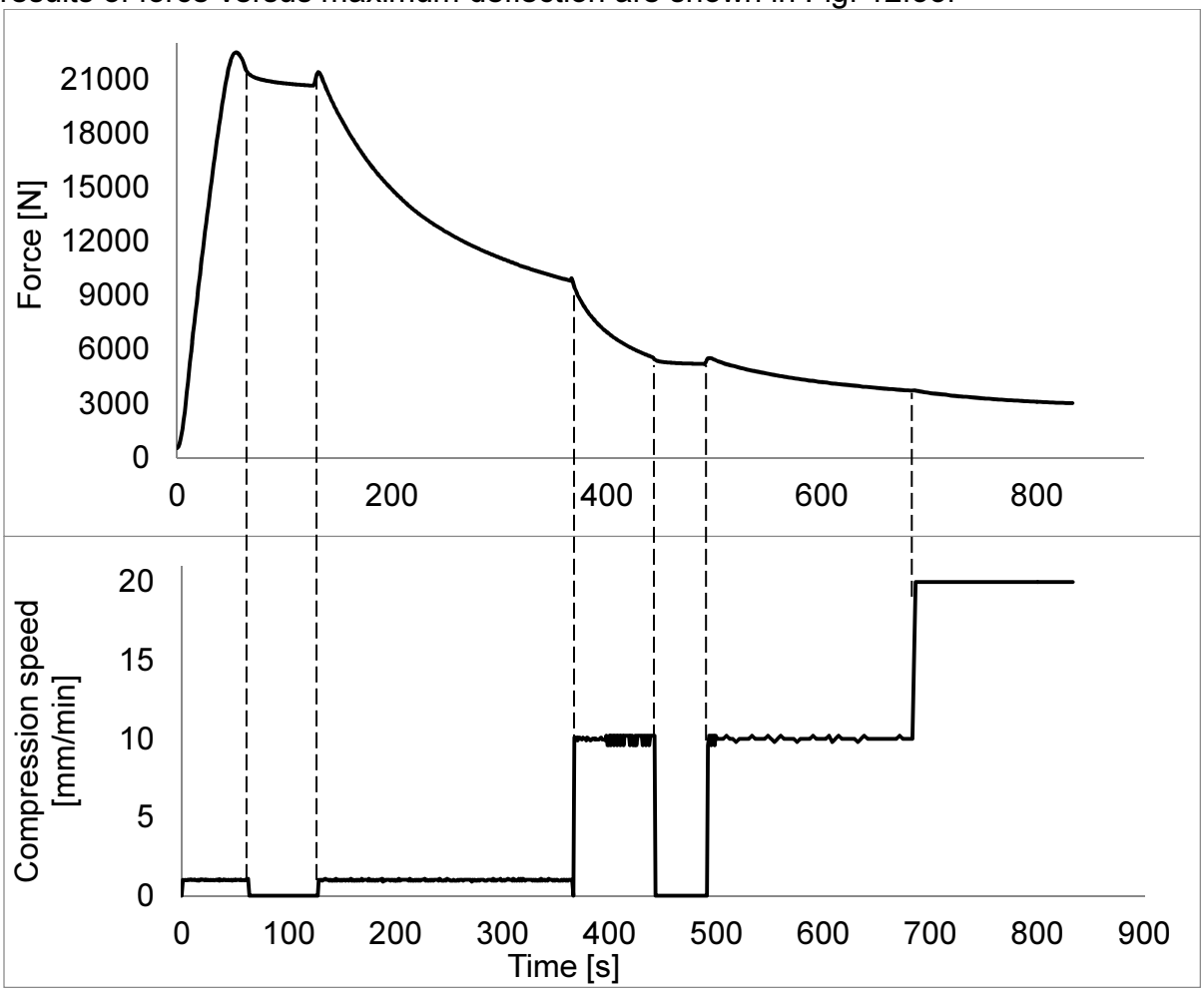

Figure 12.31. Force and compression speed versus time for sample A5

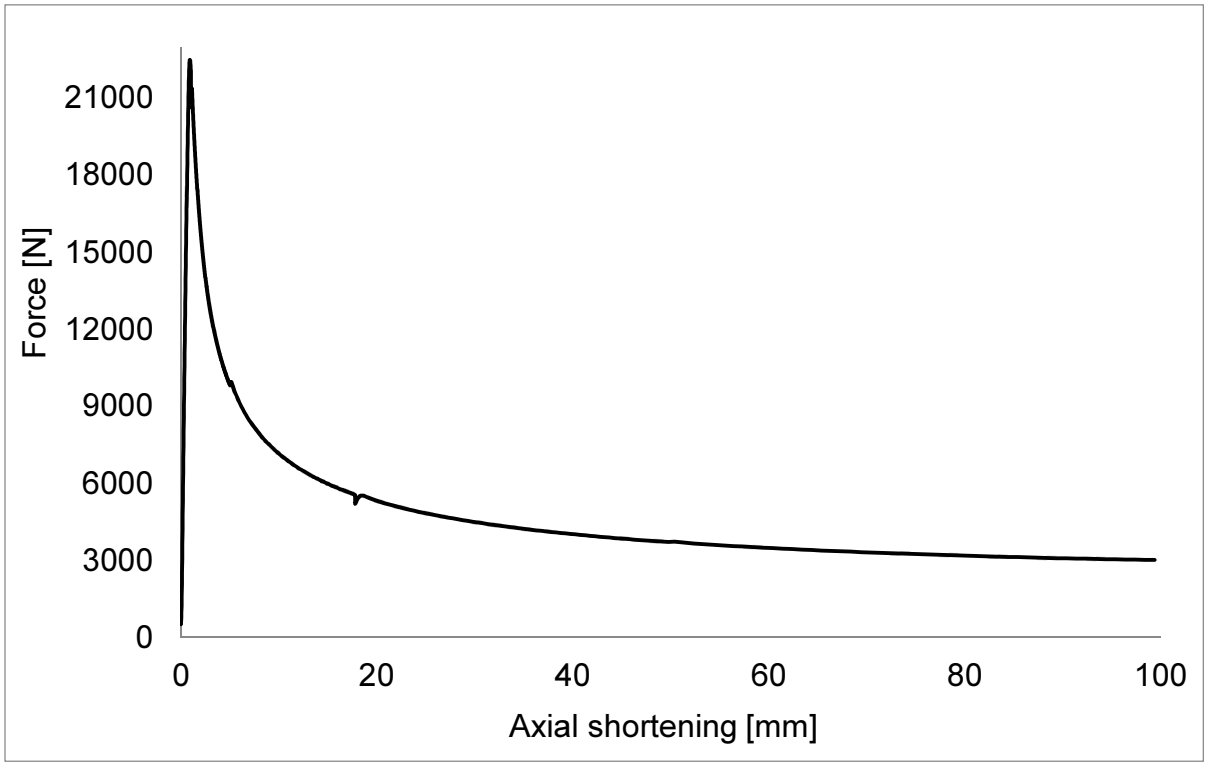

Figure 12.32. Force versus axial shortening for sample A6

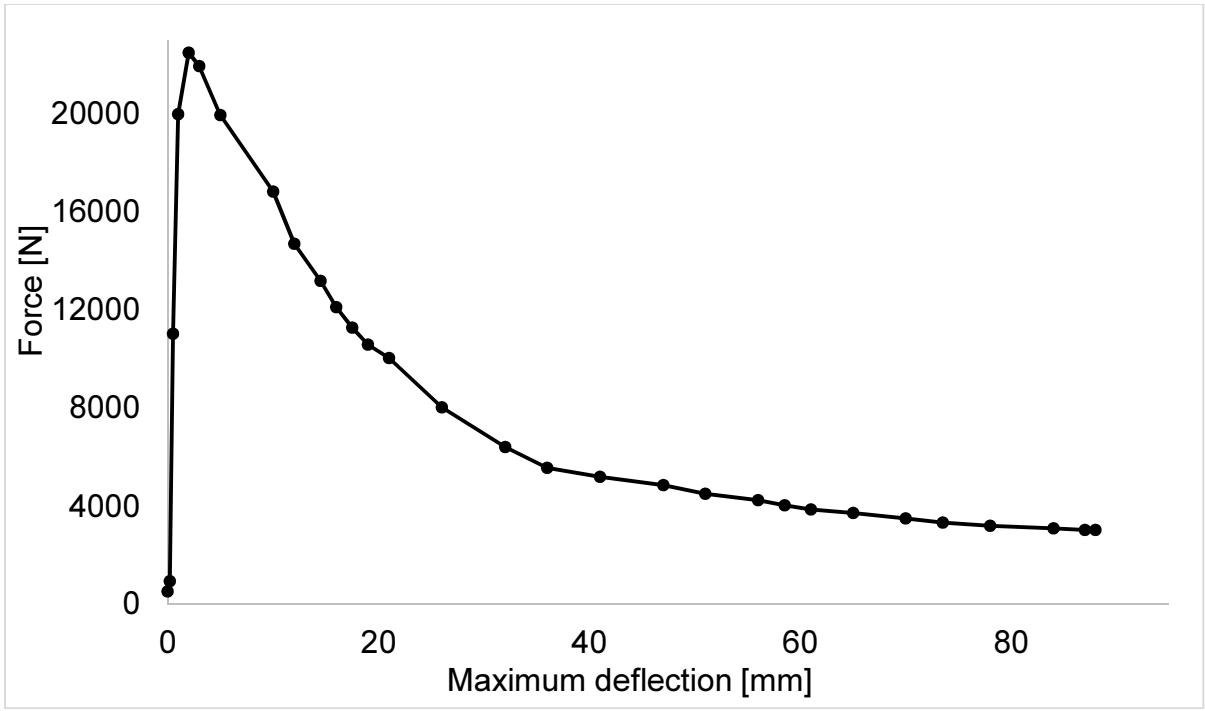

Figure 12.33. Force versus maximum deflection for sample A6

12.4.8. Results for sample A7

The force as a function of time for sample A7 is plotted in Fig. 12.34. The results of force versus axial shortening are shown in Fig. 12.35. This experiment was performed without scale to measure the transverse deflection. Thus, force versus maximum deflection was not measured.

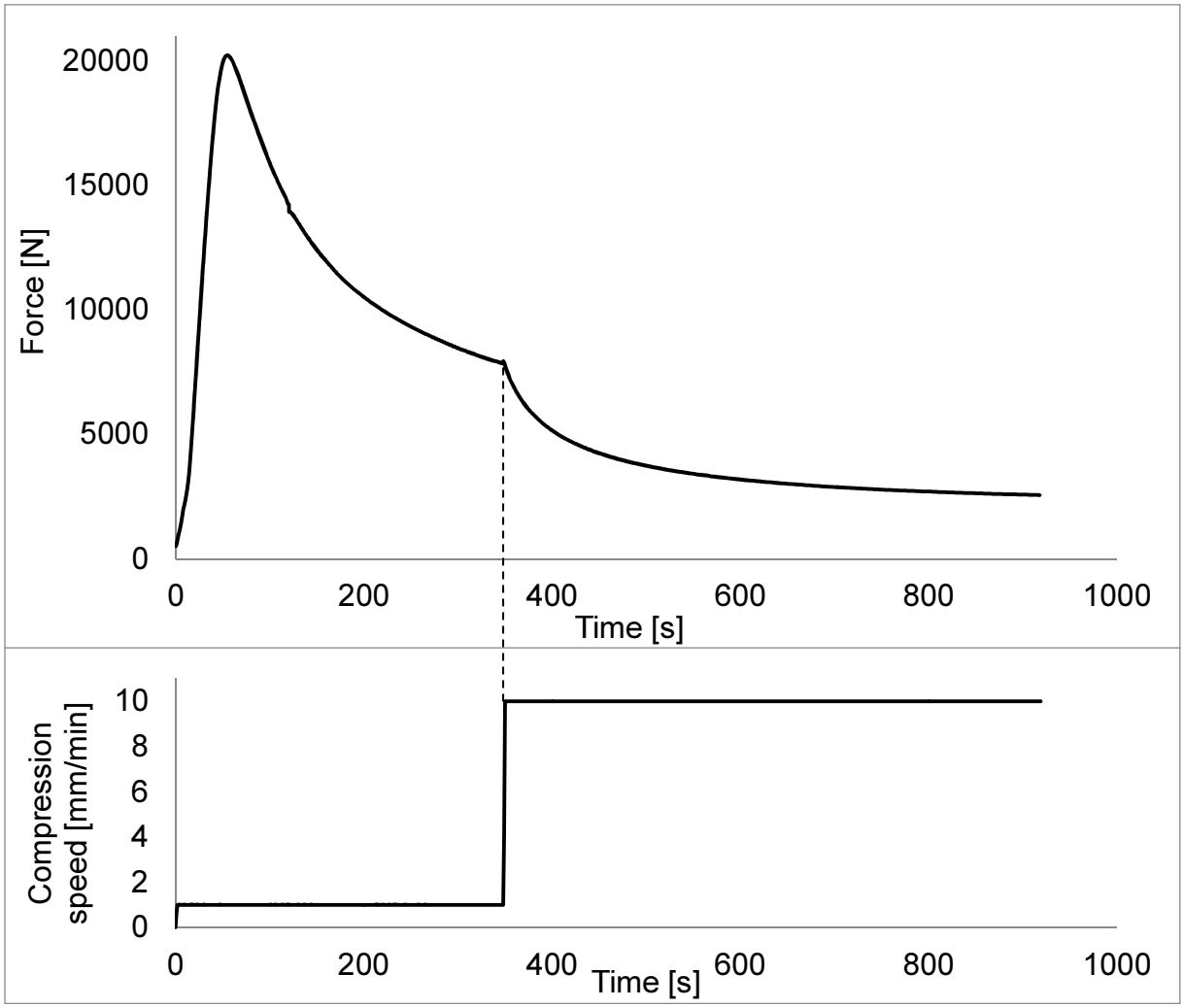

Figure 12.34. Force versus time for sample A7

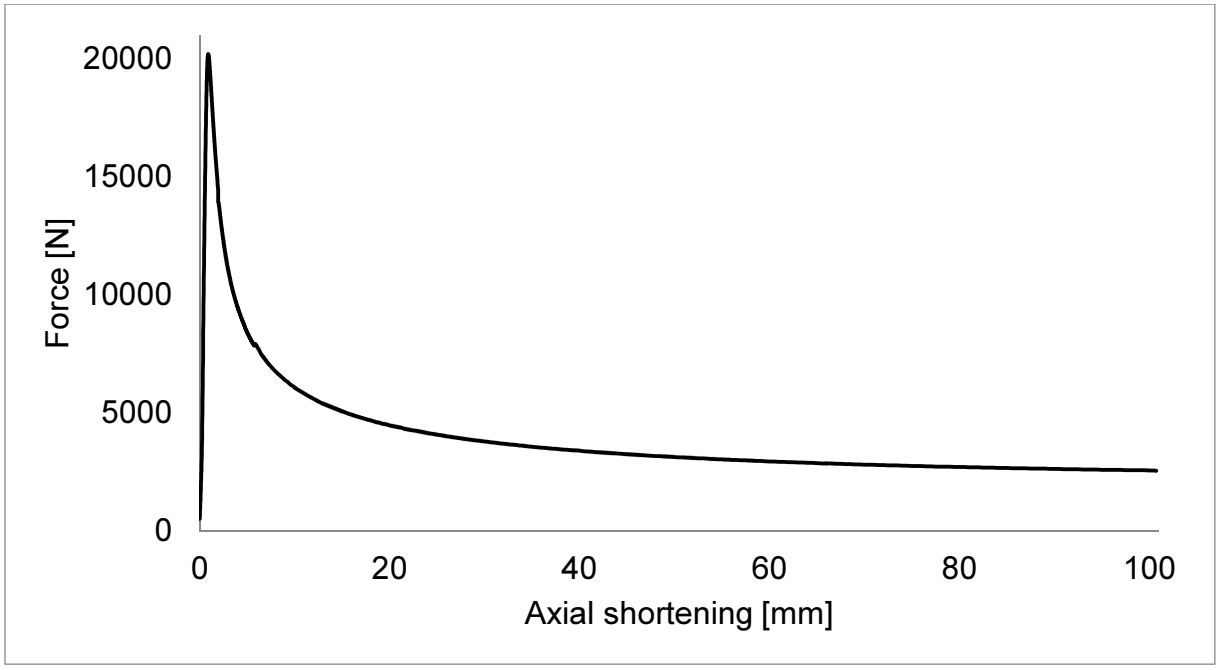

Figure 12.35. Force versus axial shortening for sample A7

12.4.9. Results for sample A8

Sample A8 was used as a trial sample in the experiment. It was dedicated to define the correct settings of tensile machine in the course of observation of the behavior of sample during buckling (to check if the support was correct etc.).

12.4.10. Comparison of the results

The results of force versus time for all samples are shown in Fig. 12.36. Similarly, the results of force versus time are illustrated in Fig. 12.37, and of force versus maximum deflection are shown in Fig. 12.38.

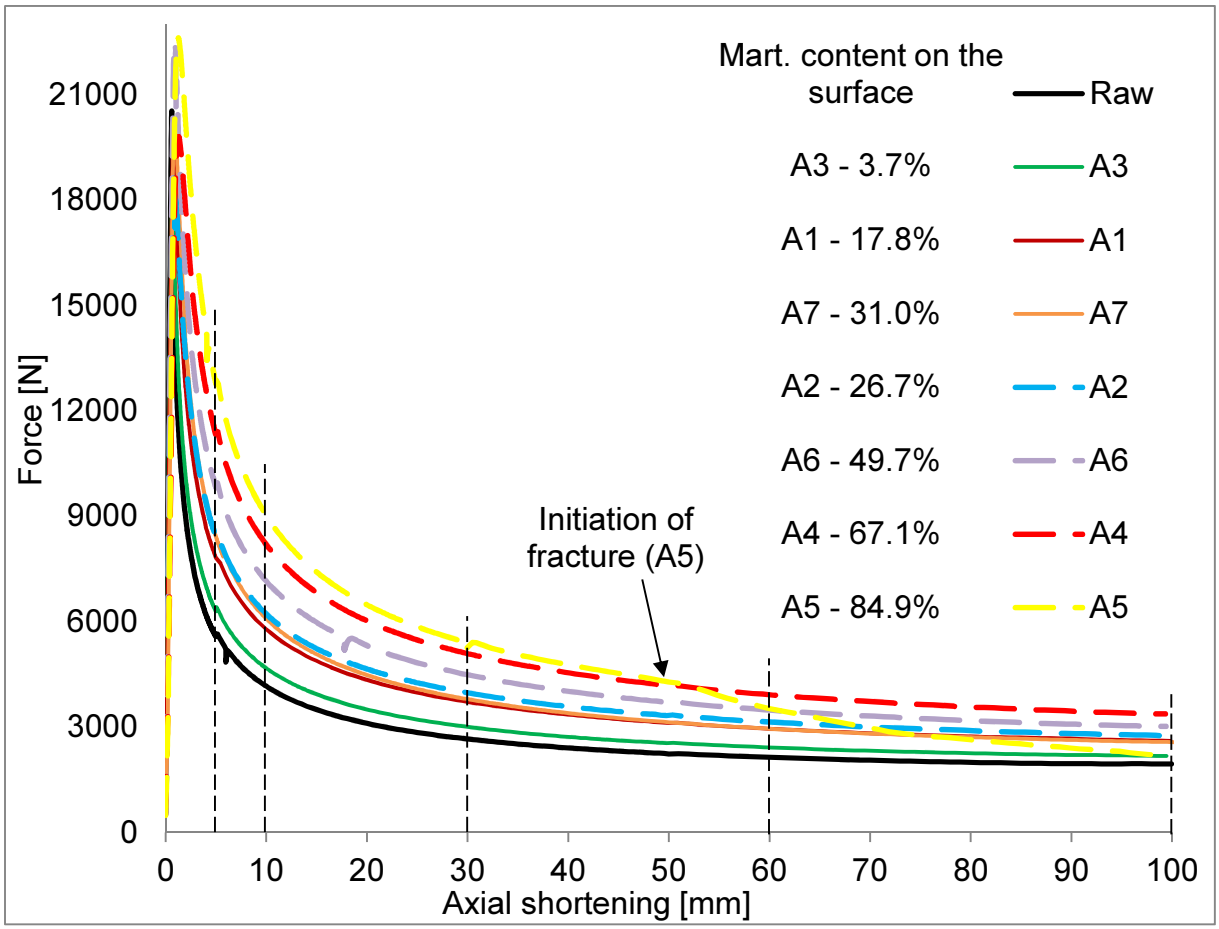

Figure 12.36. Force versus axial shortening for all samples

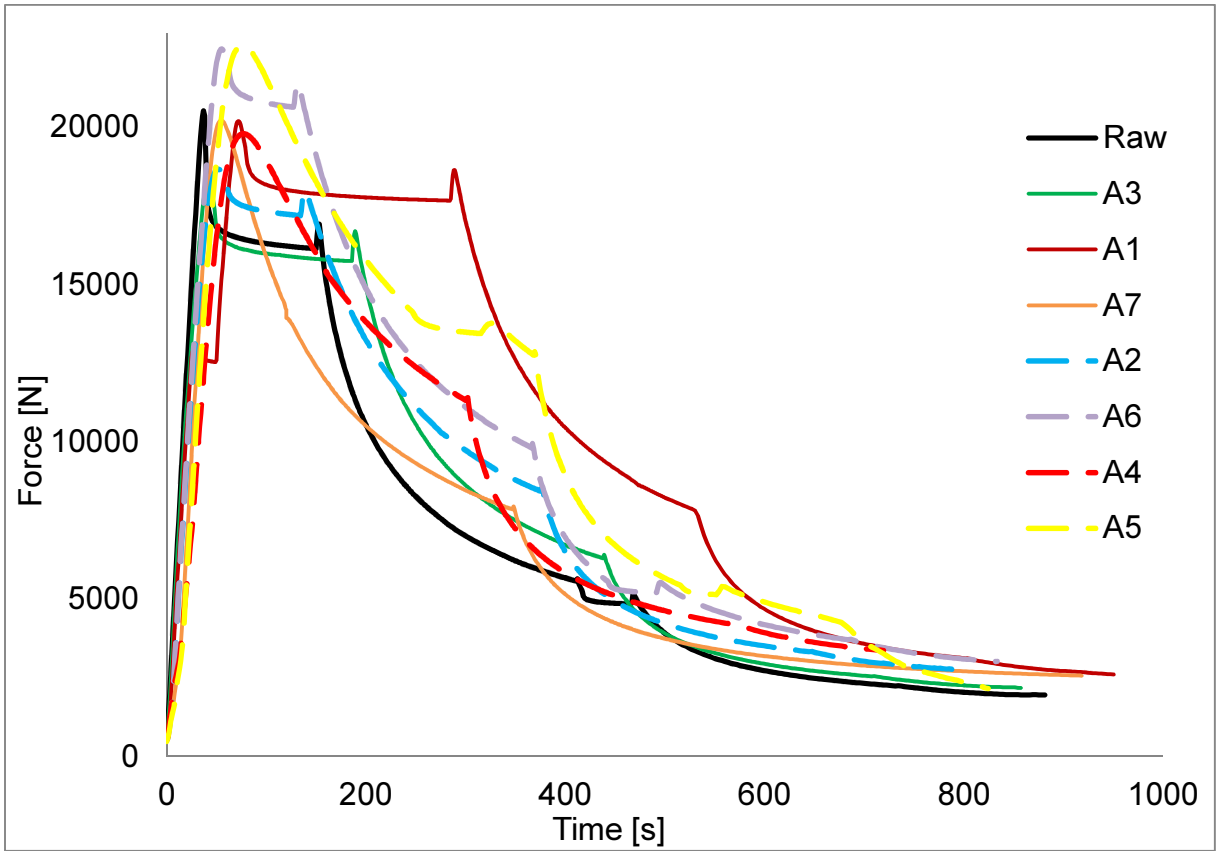

Figure 12.37. Force versus time for all samples

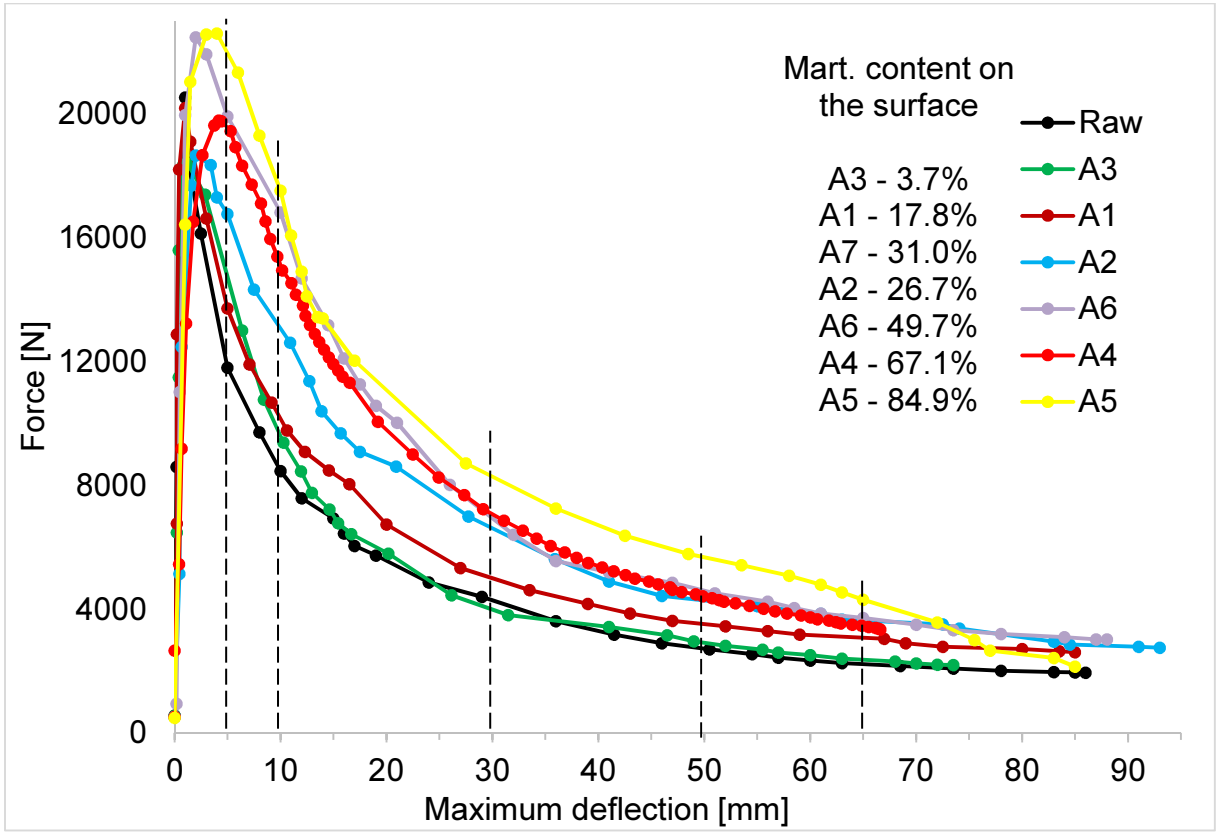

Figure 12.38. Force versus maximum deflection for all samples

The smallest values of force in Fig. 12.36 were found for the “raw” sample. All the other results are characterized by higher values of the force. The sequence of these relationships was dictated by increasing content of the martensitic phase on the surface of these samples. Small inconsistency was found for samples A7 and A2 only. Sample A7 showed 31.0% of martensite on the surface, whereas, in sample A2 26.7% was found, thus, some 4.3% less. The resulting force versus the axial shortening was almost the same for these two samples. Yet, slightly higher values were found for sample A2 with 26.7%, than for sample A7 with 31.0%. However, this difference was very small and did not undermine the evident fact, that with higher martensite content the post-buckling values of the force were higher.
The values of the force were compared at 5 axial stages: 5, 10, 30, 60 and 100 millimeters compression for all the samples. The results are listed in Tabs 12.3 and 12.4. For all values, the difference was calculated with respect to the “raw” sample according to the formula:

$$Diff(u) = \frac{F_{Sample}(u) - F_{Raw}(u)}{F_{Raw}(u)} \cdot 100\% \qquad (12.3)$$

where:

- u is the value of axial compression.

It turned out, that all the differences were positive. An increase of force was observed for all samples. For sample A1 the increase of force was of 34% at minimum. For sample A2 the increase of force reached 42% at minimum. For sample A3 the minimum increase of force was equal to 11%. For sample A4 the increase of force was in the range from 73% to 103%. For sample A5, at the beginning the increase was even higher – 129%, but at the end of the test (for 100mm) it was only 10%. This radical decrease was caused by fracture, that appeared near one of the ends of the sample (Fig. 12.41). The fracture started to develop at almost 50mm of axial compression (the point is marked in Fig. 12.36). This was clearly the reason of this radical drop of the force.
For sample A6 the increase in comparison to “raw” sample was 55% at minimum, and for sample A7 it was 31% at minimum.

Axial shortening	Raw	A1	Diff.	A2	Diff.	A3	Diff.
[mm]	Force [N]	Force [N]	[%]	Force [N]	[%]	Force [N]	[%]
5	5570.1	7813.7	40	8434	51	6296	13
10	4157.6	5788.7	39	6208	49	4657	12
30	2660.3	3716.7	40	3966	49	2994	13
60	2139.7	2953.7	38	3136	47	2415	13
100	1949.1	2605.1	34	2759	42	2173	11

Table 12.3. Force at several values of axial compression and difference in % compared to the raw sample, for samples A1, A2, A3

Axial shortening	A4	Diff.	A5	Diff.	A6	Diff.	A7	Diff.
[mm]	Force [N]	[%]	Force [N]	[%]	Force [N]	[%]	Force [N]	[%]
5	11320	103	12765	129	9814	76	8410	51
10	8183	97	8985	116	7162	72	6088	46
30	5090	91	5255	98	4505	69	3795	43
60	3914	83	3536	65	3477	62	2950	38
100	3371	73	2153	10	3021	55	2555	31

Table 12.4. Force at several values of axial compression and difference in % compared to the raw sample, for samples A4, A5, A6, A7

Similar comparison of force values was made by using force versus maximum deflection plots (Fig. 12.38). The values are listed in Tabs 12.5 and 12.6. Again, the difference was calculated according to Eq. 12.3.

Axial shortening	Raw	A1	Diff.	A2	Diff.	A3	Diff.
[mm]	Force [N]	Force [N]	[%]	Force [N]	[%]	Force [N]	[%]
5	11803	13718	16	16777	42	14736	25
10	8460	10164	20	13073	55	9607	14
30	4285	5000	17	6607	54	3984	-7
50	2720	3515	29	4281	57	2910	7
65	2223	3078	38	3627	63	2360	6

Table 12.5. Force at several values of maximum deflection and difference in % compared to the raw sample, for samples A1, A2, A3

Axial shortening	A4	Diff.	A5	Diff.	A6	Diff.
[mm]	Force [N]	[%]	Force [N]	[%]	Force [N]	[%]
5	19562	66	21976	86	19935	76
10	15095	78	17531	107	16821	72
30	7062	65	8282	93	6946	69
50	4406	62	5674	109	4594	62
65	3452	55	4300	93	3712	55

Table 12.6. Force at several values of maximum deflection and difference in % compared to the raw sample, for samples A4, A5, A6

For all calculated values of difference compared to the “raw” sample, the results were positive. However, one exception was found for sample A3, where at 30mm of deflection some -7% difference was obtained. Thus, the force was smaller than for raw sample. For all other cases, the samples with induced martensite content showed higher values of force. For sample A1, the minimum increase was of 16%, for the samples: A2, A4, A5 and A6 it reached 42%, 55%, 86% and 55%, respectively.

These results proved that the presence of martensite was beneficial for the behavior under axial compression, and higher values of force were obtained up to 100mm of axial compression.

Only one sample fractured before reaching 100mm of axial compression. Sample A5 with 84.9% martensite content on the surface developed a macro-crack near one of its ends, at about 50mm of axial compression.

These results suggest rather negative influence of very high martensite contents at large deformations. Sample A4 with 67.1% of martensite on the surface did not fracture. Thus, somewhere between 67.1% and 84.9% of martensite fraction on the surface, a limit to sustain 100mm of axial compression of a bar of 200mm in length might exist.
The values of maximum force are listed in Tab. 12.7. The results from Fig. 12.36 are replotted in Fig. 12.39 for axial compression smaller than 2mm.

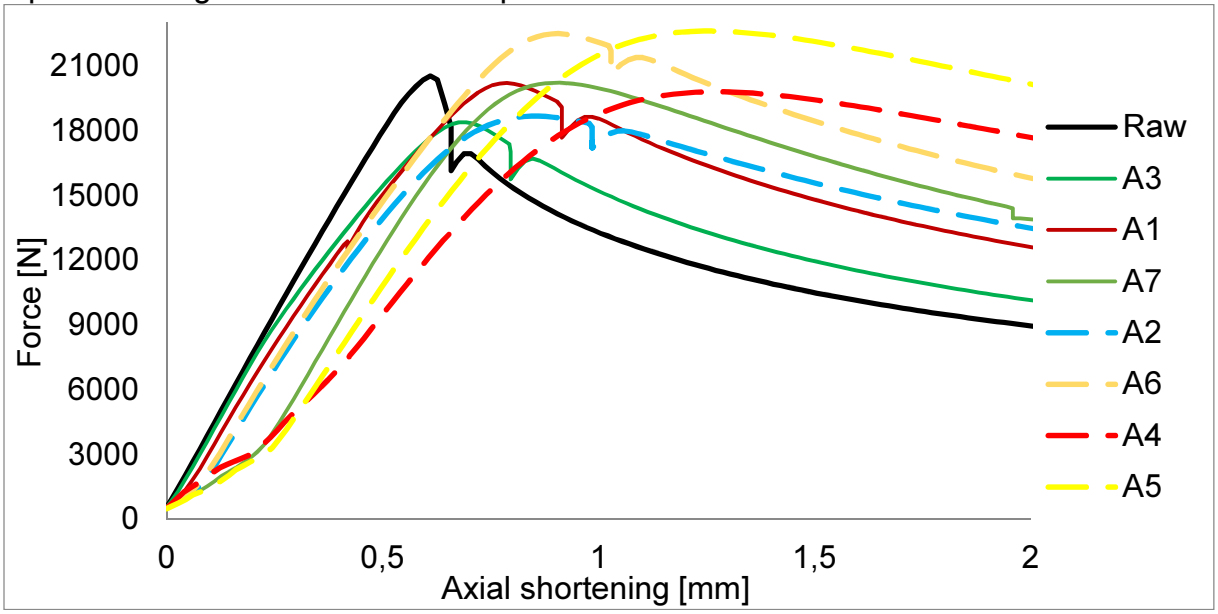

Figure 12.39. Force versus axial compression in the range 0÷2mm, for all samples

Sample	$F_{max}[N]$	Difference [%]
Raw	20526	-
A1	20195	-1.6
A2	18668	-9.0
A3	18383	-10.4
A4	19794	-3.6
A5	22606	10.1
A6	22486	9.6
A7	20210	-1.5

Table 12.7. Maximum force and the relative difference (compared to the “raw” sample)

For two samples A5 and A6, the maximum force exceeded by about 10% the “raw” sample. For the remaining ones, it was smaller (by 10.4% at minimum for sample A3). Thus, the presence of martensite did not cause much change in the maximum force. Yet, it is very important to stress, that the “raw” sample was almost perfectly straight, whereas, the samples A1÷A7 carried imperfections (Fig. 12.3a). It is known, that the imperfections substantially decrease the buckling force. Taking into account this fact one can say, that the imperfect samples with induced martensite performed comparably well to the “raw” sample, in terms of the buckling force.

12.5. Deformation of the samples

The shape of the samples after axial compression test is shown in Fig. 12.40. “Triangle” like shape was obtained for all of them. The flexural deformation was concentrated in the center and near the ends.

Figure 12.40. Deformed samples after buckling test (A1, A2, A3, A4, A7, A8)

Sample A5 is showed in Fig. 12.41. Macro crack appeared in both sides of the sample. Much bigger one appeared in the side which was fixed at the bottom in the compression machine.

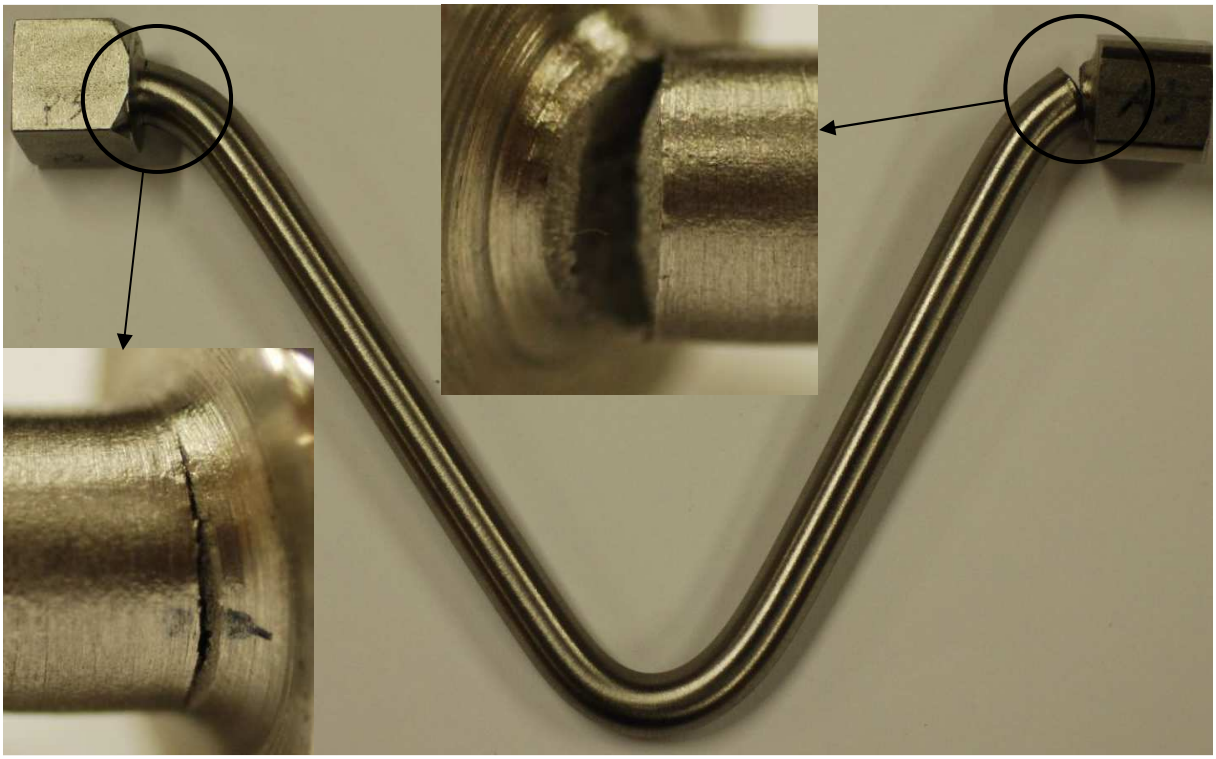

Figure 12.41. Sample A5 after compression test with magnified crack zones

12.6. Summary and conclusions

Experimental results of the axial compression tests were presented in details in this chapter. In total, 9 samples were tested: one “raw” purely austenitic sample, and 8 samples with induced martensite during cyclic torsion at 77K or 293K.
The force versus the axial compression was registered in the tensile testing machine. Deformation of the samples was recorded. The videos were analyzed and the deflections of the centers of the samples were calculated. The results in terms of force versus maximum deflection were finally plotted for all samples in Fig. 12.38.

The following conclusions are drawn from this chapter:

- The maximum force was comparable for all samples, the dispersion was of around ±10%. The samples A1÷A8 carried some imperfections, and the “raw” sample was almost perfectly straight. Thus, one can conclude that the presence of martensite did not drastically change the maximum force.
- In the post-buckling range, the samples A1÷A7 performed better than the “raw” sample. The values of the force were increasing with the increasing martensite content.
- Apart from sample A5, all the samples deformed without fracture to 100mm of axial compression. Thus, severe plastic strains remain without any negative influence on the performance of FGSM.

13. Stability of functionally graded bars - modeling

It is known that the post-buckling behavior of purely elastic columns is stable. In such a case, the force is increasing with respect to transverse deflection. As already presented in Chapter 12 (Fig. 12.36), the post-buckling behavior of FGSMs was highly unstable. The force decreased smoothly and reached at the end of test around 10% of its maximal value. This behavior indicated that substantial plastic deformation occurred, which led to softening and unstable post-buckling path.
Two modeling methods are proposed. Both of them are based on FEM simulation techniques. Two three-dimensional models were created. In the first one, the material behavior was assumed elastic-plastic with linear hardening. The parameters were identified based on the experimental results.
The second model of the column was modified, and 3 layers with different stress-strain curves was used. The layers represent different microstructures with varying martensite content (thus properties). The parameters of the layers were identified based on the results from tensile tests.
First, the FE model with one material behavior, and secondly the FE model with layers is developed.

13.1. Finite element model of functionally graded column based on bilinear elastic-plastic material

The finite element method allows detailed simulation as it encompasses various general elasto-plastic constitutive models. For example, a 3D model of a column can take into account the evolution of plastic zones at any point of the cross-section and along the axis of the column.
A 3D model made of solid elements has been built. The large displacements analysis has been carried out. The same axial compression was prescribed like in the experimental conditions.
It is well known, that it is difficult to simulate the perfectly plastic material, because it leads to indefinite strain at constant stress. Thus, one has to introduce a small hardening. This approach has been adopted in the present chapter.

13.1.1. Parameters of the material model

As already mentioned in the introduction, small hardening has been added to the model. In order to choose the correct material behavior, the results from the tensile test have been taken into account. For 3 samples the stress-strain relationships were measured. These 3 samples had different martensite distributions. Sample 62 (Tab. 11.1) reached almost 100% of martensite content on the surface after the tensile test. The value before tensile test was not measured. As the sample was twisted at 77K, and then again at 293K until rupture, one expected very high martensite fraction. Sample number A9.1 had 6.7% of martensite on the surface before tensile test. Sample number A10.1 had 82.9% of martensite on the surface before tensile test.. From the stress versus strain results (Fig. 13.12), one would expect higher martensite content for sample 62, as the curve was above the curve for sample A10.1.
In order to evaluate the hardening parameter, the experimental results were approximated with bilinear elastic-plastic model.

This bilinear approximation holds only for limited strain values, namely until necking which causes softening (decreasing stress). In order not to introduce nonlinear stress-strain relationships in the model, softening was ignored and bilinear behavior was adopted. Constant hardening modulus C_ε was used. The stress-strain relationships for samples A9.1, A10.1, 62 with their bilinear approximations are presented in Fig. 13.1. The parameters of the approximation are listed in Tab. 13.1. The first linear part is described by the Young's modulus ($\sigma = E\varepsilon$), and the second one by the hardening modulus ($\sigma = \sigma_0 + C_\varepsilon(\varepsilon - \varepsilon_0)$).

Parameter	A9.1	A10.1	62
E [Pa]	1.95e11	1.95e11	1.95e11
σ_0 [MPa]	690	1280	1350
C_ε [MPa]	300	300	300

Table 13.1. Parameters of bilinear approximation of the stress-strain curve, for samples A9.1, A10.1, 62

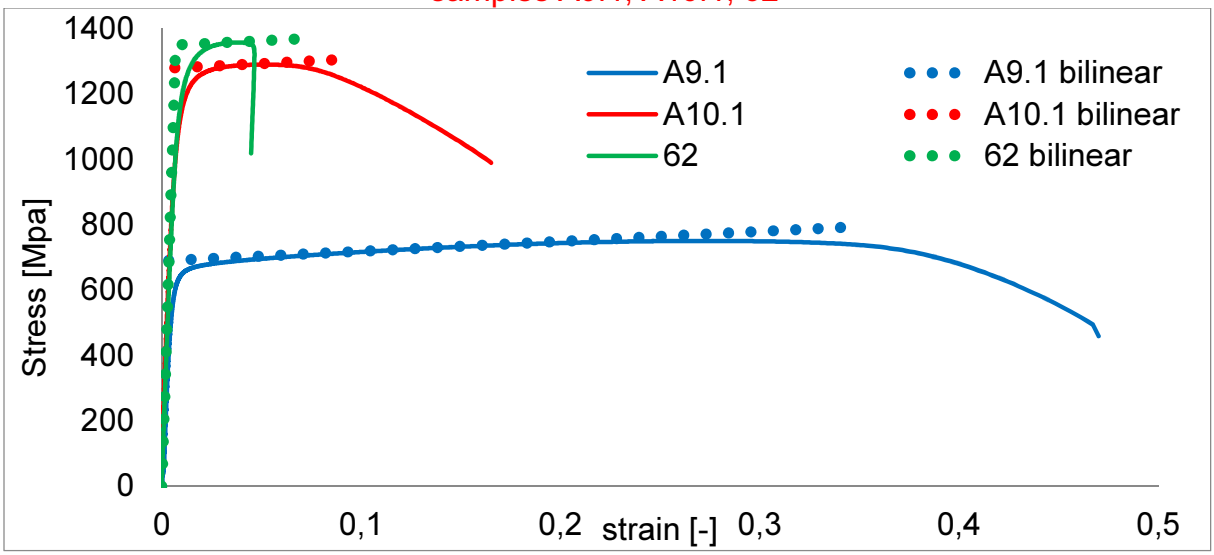

Figure 13.1. Stress versus strain - experimental and approximate results for samples A9.1, A10.1, 62

For all three experimental curves from Fig. 13.1, the hardening modulus of 300MPa fits very well. Thus, for small (close to 0) and high (close to 100%) martensite contents, the hardening modulus is constant and equal to $C_\varepsilon = 300MPa$.

13.1.2. Building the finite element model

A 3D model of the column was prepared by using the ANSYS software. The length of the column was of 200mm, and the radius of the cross-section was equal to 4mm. Clamped boundary conditions were used to match the experimental conditions.
The following steps of the analysis were carried out:
1. Solving the model in the static mode. Setting the pre-stress option on (pstres, on) for the subsequent buckling analysis.
2. Solving the model in the buckling mode (antype, buckle), in order to obtain the buckling load and the shape of the buckled column.
3. Updating the geometry of the column by means of the first buckling mode. This was carried out by updating initially straight geometry of the column by using the first buckling mode, multiplied by the imperfection amplitude. Applying the same kinematical loading, like in the experiment (100 millimeters). Performing a nonlinear analysis with large static displacements.

In order to obtain the buckling force and the corresponding mode, the column was loaded by the unit force. Such a force was applied at each node from the top surface in the “z” direction (Fig. 13.2a). The value of the force was equal to “-1”, because of direction of the z-axis.
The result of the buckling analysis is the load multiplier. In order to obtain the final buckling force, the applied load (-1) is multiplied by the result of the analysis and by the number of the nodes in the cross-section.
It is worth pointing out, that for different meshes the number of nodes is changing, and it is necessary to take this into account.
In the third step, the geometry of the column has been updated taking into account the first buckling mode. In the first analysis the multiplier was set to 0.001 [m], as the sample had imperfections of such a size approximately (Fig. 12.3a). The loading was realized by applying displacement on the top surface of the column. In particular, 100mm was applied like in the experimental conditions.
The column was clamped at each extremity. No displacements and rotations were allowed at the bottom end (6 degrees of freedom removed). At the top extremity, translation in the z direction was allowed only (5 degrees of freedom removed).
The boundary conditions in the finite element model are shown in Fig. 13.3.
All displacements of the nodes of the bottom cross-section of the column were set to 0 $(ux = uy = uz = 0)$. Apart from the end cross-section, the transverse displacements were set to zero also in the adjacent cross-sections in order to eliminate rotation (Fig. 13.3). Similar technique was applied at the top section of the column. Two displacements were blocked on the surface and in the adjacent cross-sections $(ux = uy = 0)$. The displacement uz was of course free, as this was the direction of loading.
In the post-buckling analysis the relationship between the compressive force and the axial displacement was looked for. The force was obtained by summing the reactions in all the nodes at the bottom cross-section (Fig. 13.2b), according to the formula:

$$F = \sum_{i} F_{i\,node} \tag{13.1}$$

The bilinear isotropic hardening model was used. The Young modulus was set to 195 [GPa], which was obtained from the relevant approximation (Tab. 13.1). The hardening modulus C_ε was set to 300 [MPa] in the first analysis (like in the experimental results - Tab. 13.1).
The yield stress was the only free variable. It was optimized to best fit the experimental results. The last parameter of the model, the Poisson ratio, was set close to 0.5 (for incompressible plastic material). In practice, it was set to $\nu = 0.499$ since the value 0.5 is not allowed in the FEM program (it leads to division by zero).

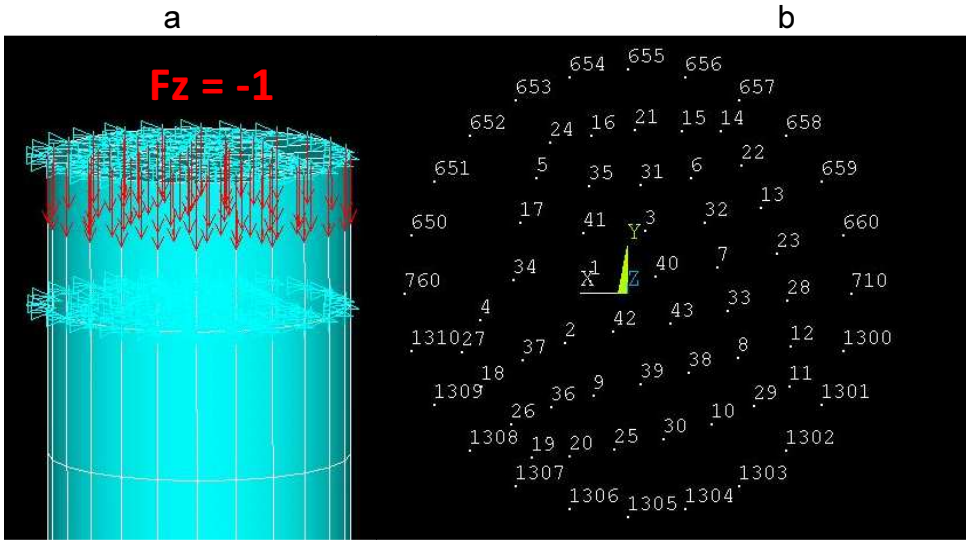

Figure 13.2. a) The load applied in the buckling analysis; b) nodes within the bottom cross-section where the reaction forces are identified

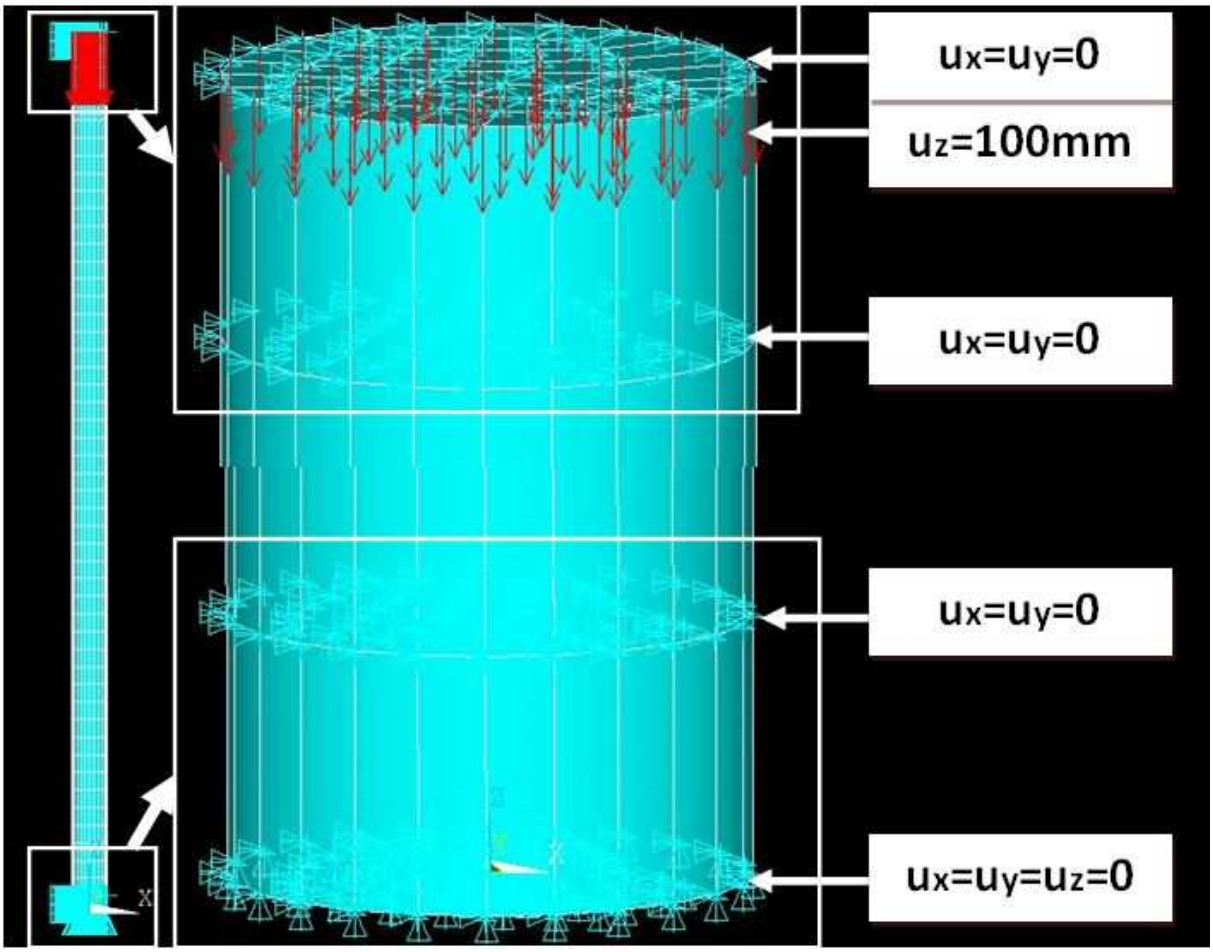

Figure 13.3. The mesh and the boundary conditions for the column

The buckling mode after the second step of the analysis is presented in Fig. 13.4a. Updated geometry (multiplied by 0.001) due to the nonlinear analysis is presented in Fig. 13.4b.

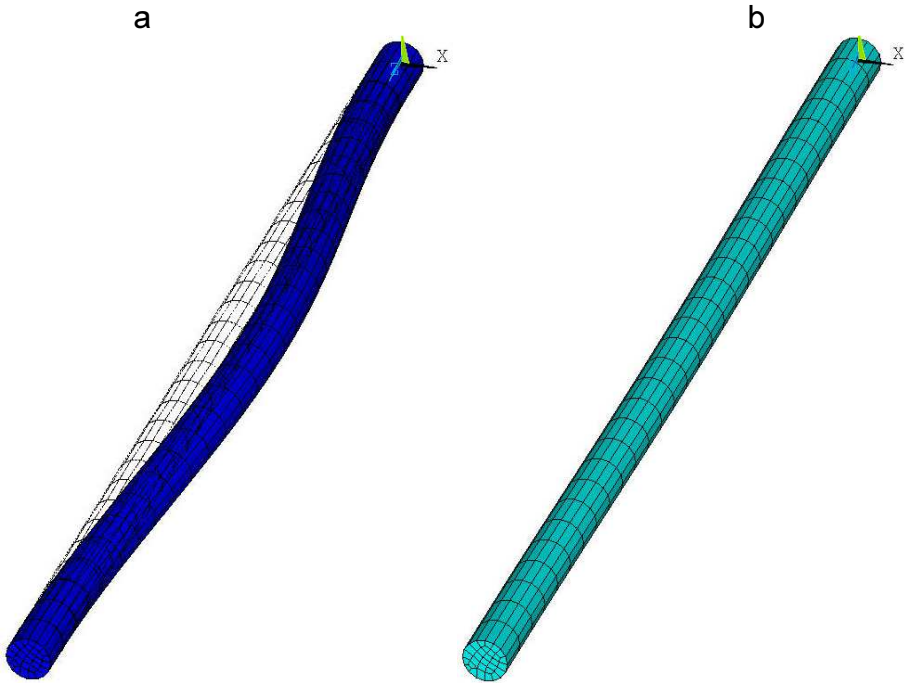

Figure 13.4. a) 1st buckling mode; b) updated geometry by the factor 0.001 (imperfection amplitude of 1mm)

A 3D model of the column has been prepared by using Ansys software. Both 8 node and 20 node elements have been used. The cylinder has been meshed with brick elements to increase the precision of the calculations.

In order to choose correct size of elements, several tests have been performed with different element and mesh types. As the analysis was nonlinear with respect to the geometry (large deformations) and with respect to the material (elasto-plastic behavior), the mesh size was very important to reduce time of computations. The optimal mesh size was chosen to optimize the ratio between the precision and the time of computations.

The parameters of the mesh (the number of elements per length and per the cross-section circumference, total number of elements and nodes) are presented in Tab. 13.2. For all meshes the same material behavior was used. Some additional parameters are listed in Tab. 13.3.

Meshing of the cross-section is presented in Fig. 13.5, whereas, a 3D view of the mesh is shown in Fig. 13.6.

The reaction force in “z” direction as a function of end displacement was adopted as a criterion of comparison between the meshes. Better convergence was expected with the increasing number of elements.

	Solid 185 (8 nodes)				Solid 186 (20 nodes)		
	Mesh1	Mesh2	Mesh3	Mesh4	Mesh5	Mesh6	Mesh7
Elements by length	30	50	70	100	30	50	70
Element on the circumference	16	24	40	60	16	24	40
Number of elements	870	2700	11550	36500	870	2700	11550
Number of nodes	1178	3417	13206	39996	4364	12887	51076
Buckling force [N]	54487	44139	41116	38758	40257	38899	38246

Table 13.2. Parameters of the mesh based on solid 185 and solid 186 elements

$\sigma_0\ [MPa]$	$C_\varepsilon\ [MPa]$	u_{max} [mm]	Num. of substeps	Imperfection multiplier [m]
600	300	100	50	0.001

Table 13.3. Parameters of numerical analysis

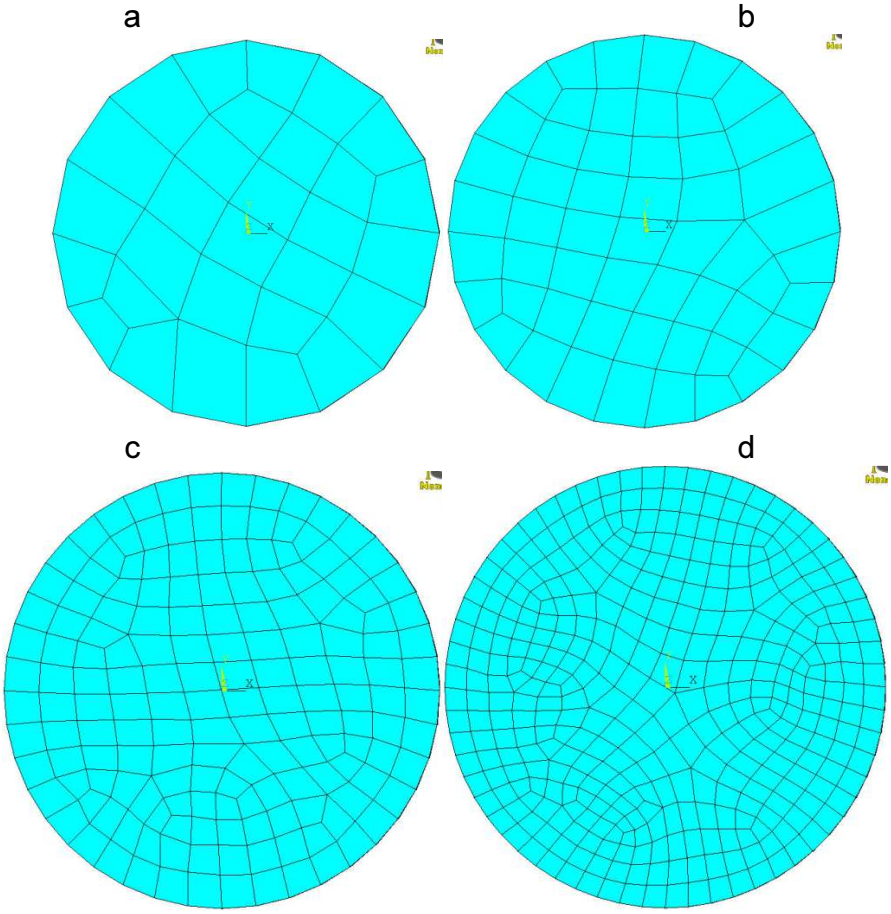

Figure 13.5. Meshed cross-section a) mesh 1 and mesh 5; b) mesh 2 and mesh 6; c) mesh 3 and mesh 7; d) mesh 4

Figure 13.6. Column mesh, from left to right: mesh 1 & 5, mesh 2 & 6, mesh 3 & 7, mesh 4

Based on 7 mesh types, the results in terms of force versus end displacement are presented in Figs 13.7, and 13.8.

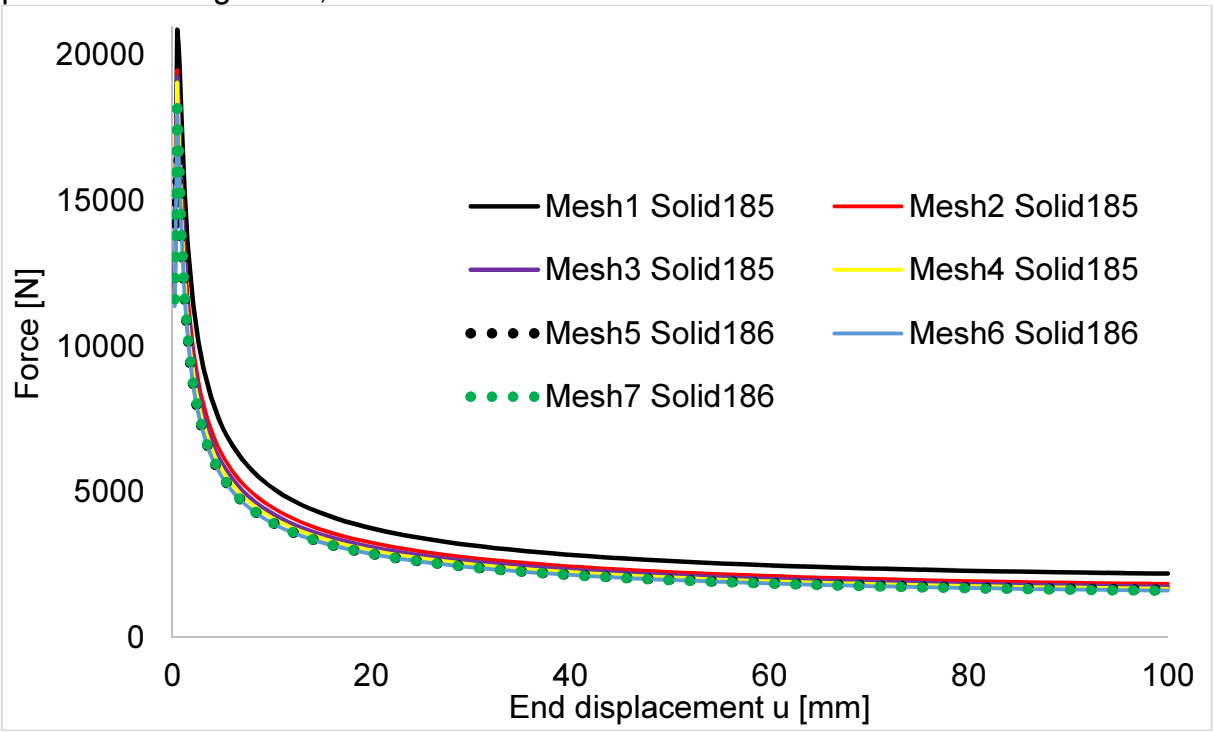

Figure 13.7. Force versus end displacement for 7 mesh types

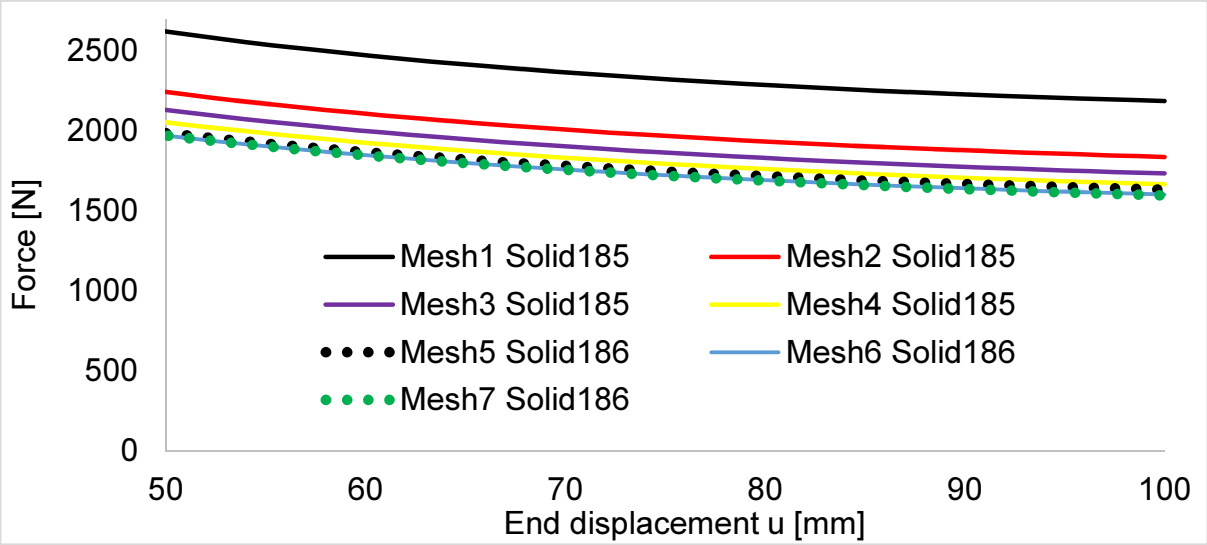

Figure 13.8. Force versus end displacement for 7 mesh types (limited range)

The results for all mesh types are similar. The only exception is the result obtained with the 1st mesh, that is clearly different from the others. This is reasonable, because the 1st mesh is coarse thanks to less precise Solid 185 elements.
The curve for 2nd mesh is placed below the curve for 1st mesh. Similarly, the result for 3rd mesh is located below the result for 2nd mesh. From all results for the first four mesh types based on Solid 185 elements, the best one is the 4th mesh, since the number of elements was the highest.
Comparing the results for 5th, 6th and 7th mesh type, built by means of Solid 186 elements (20 nodes per element), one can notice that they are almost the same. There is very little difference between them (Fig. 13.8). All three curves are located below the result for 4th mesh (the best, obtained with Solid 185 elements).
Taking into account these results (Fig. 13.8), the 6th mesh was selected as the optimal one in terms of the precision and the computational time (less than 30 minutes on server). The calculation for 7th mesh took much longer – some 4 hours.
Another important parameter is the number of sub-steps during the nonlinear analysis. In the previous calculations, 50 sub-steps were used always. To exclude possible source of error, several runs with the same mesh size and different number of sub-steps were carried out. Similarly to the previous case, the results in terms of force versus end displacement are compared in Fig. 13.9. The results are exactly the same. Thus, 50 sub-steps were used in all types of analysis.

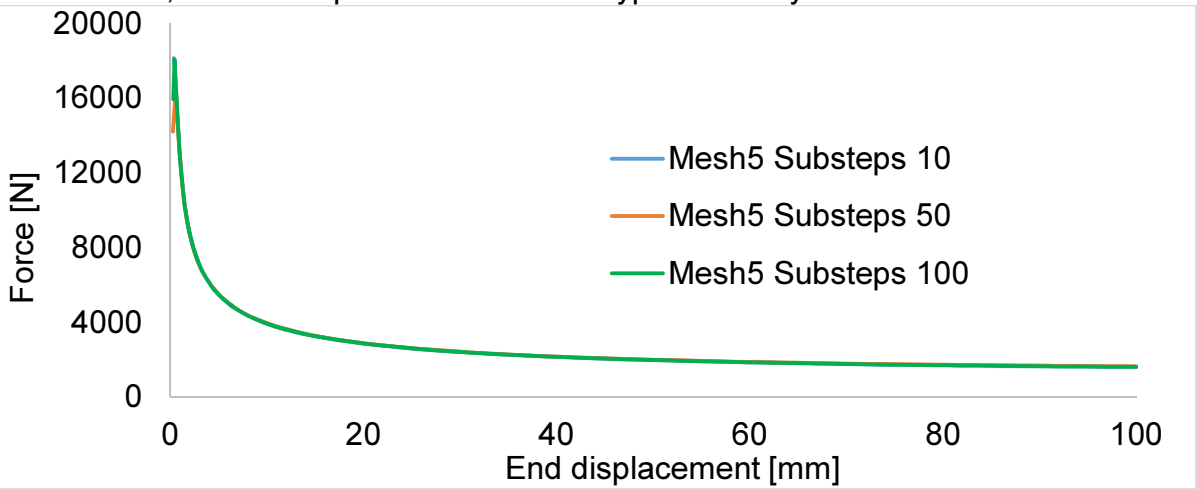

Figure 13.9. Force versus end displacement for different number of sub-steps

The last important parameter of the finite element analysis was the size of imperfection. All previous computations were run with the amplitude of imperfection of 1mm. Several different amplitudes were tested by using Mesh6. The results are presented in Figs 13.10 and 13.11. The whole range is shown in Fig. 13.10, whereas, a limited range to 15mm of end displacement is illustrated in Fig. 13.11.

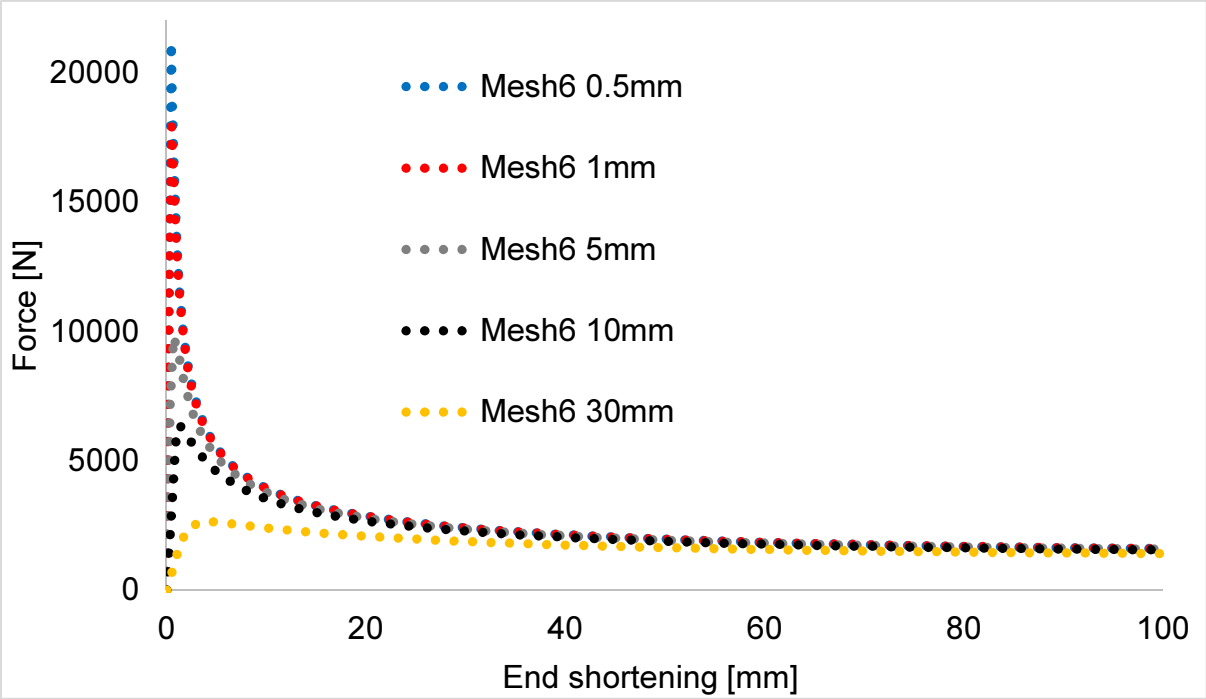

Figure 13.10. Force versus end displacement for various imperfection amplitudes

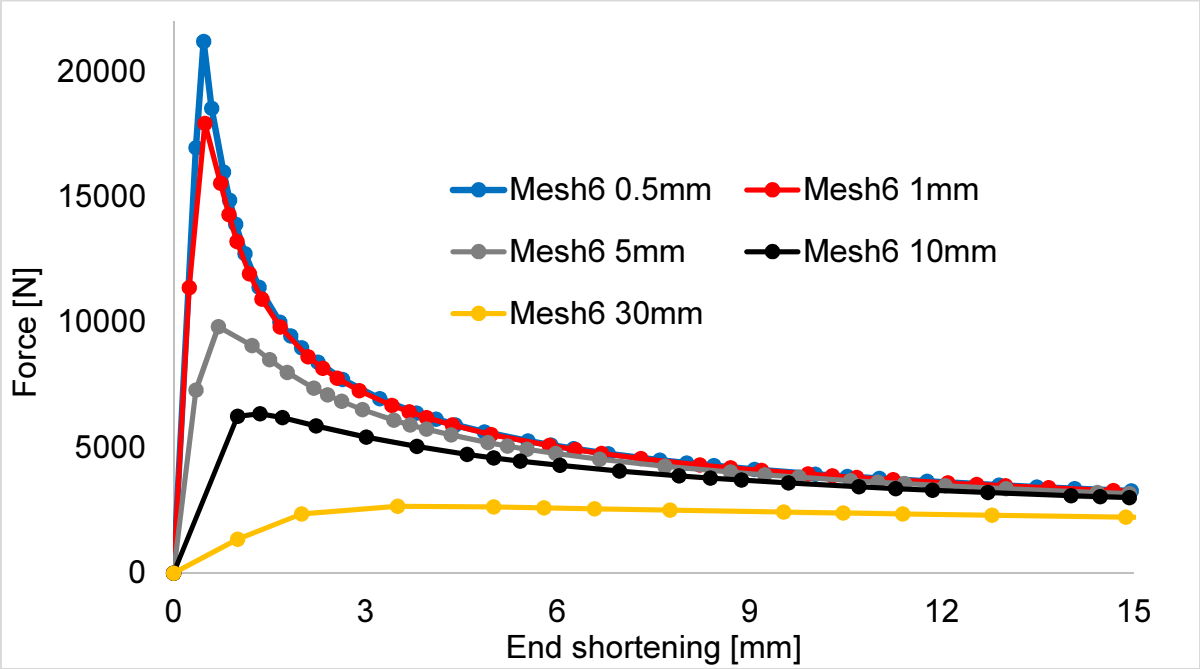

Figure 13.11. Force versus end displacement for various imperfection amplitudes, for end displacement lower than 15mm

There is very strong influence of the imperfection amplitude on the results (Figs 13.10, 13.11). Generally, the smaller amplitude the higher maximum force.
For imperfection amplitude of 30mm (Fig. 13.10), the force is almost constant with the end displacement.

This result is completely different, when compared to the other ones. In theory, near zero imperfection would lead to the best approximation of the bifurcation force.
Finally, the amplitude of imperfection was chosen to be equal to 0.5mm. This value implied the best approximation of the maximum force detected in the experiment (Fig. 12.36). Also, the imperfection was reasonable with respect to the initial geometry of the sample (Fig. 12.3a). In the subsequent analysis, 0.5 mm amplitude of imperfection was consequently used.
Another important parameter that affects the results in terms of force versus end displacement, is the hardening modulus C_ε. It has been set to 300 MPa in the previous analysis, according to the approximation based on the experimental stress-strain curves (Tab. 13.1). In the compression test however, this modulus was not measured. On the other hand, the modulus was assumed to be the same like in the tensile tests. Taking into account all the previously set parameters of the finite element analysis, the influence of the hardening modulus was numerically tested. The tests were performed by means of Mesh5 (Tab. 13.2) with $\sigma_0 = 600MPa$ and the imperfection multiplier equal to 0.0005 [m]. Several different values of parameter C_ε were used. The results are shown in Figs 13.12 and 13.13.
The difference of results for the modulus $C_\varepsilon = 1200MPa$ and $C_\varepsilon = 300MPa$ is quite small (Fig 13.13). There is a monotonic relationship between the increase of hardening modulus and the increase of the force values for the same end displacement. Yet, the total influence of the hardening modulus C_ε is small (Fig. 13.12).

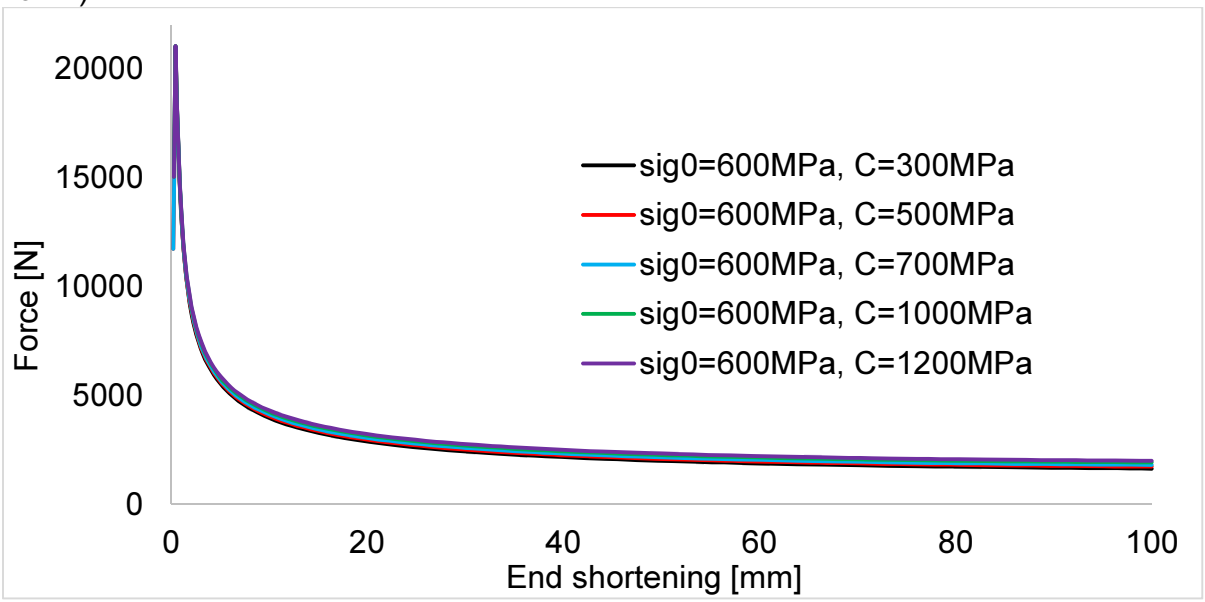

Figure 13.12. The influence of hardening modulus C_ε on the F(u) results (full range)

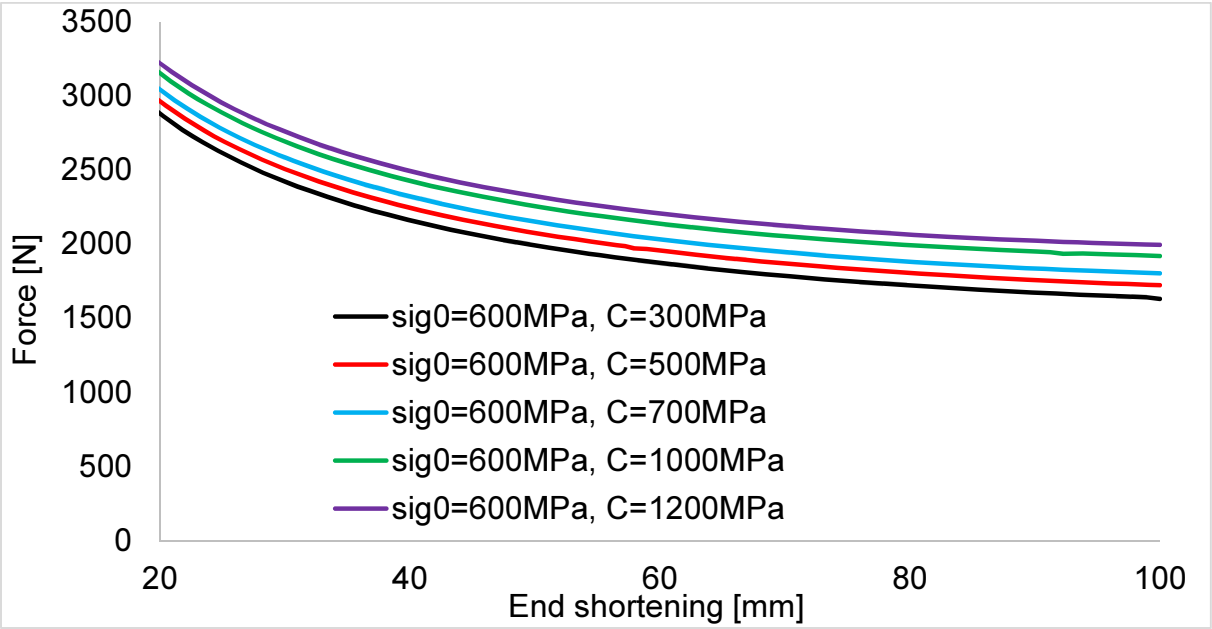

Figure 13.13. The influence of hardening modulus C_ε on the F(u) results, for end displacement greater than 20mm

The last parameter in the analysis is the yield stress σ_0. Several values have been selected to picture how the F(u) is related to increasing yield stress. The analysis has been done by using Mesh5 (Tab. 13.2), with the imperfection amplitude of 0.0005 [m] and the hardening modulus $C_\varepsilon = 300MPa$. The results are presented in Fig. 13.14. The influence of the yield stress was rather strong, much stronger than of the hardening modulus. This parameter was the most significant one in the modeling.

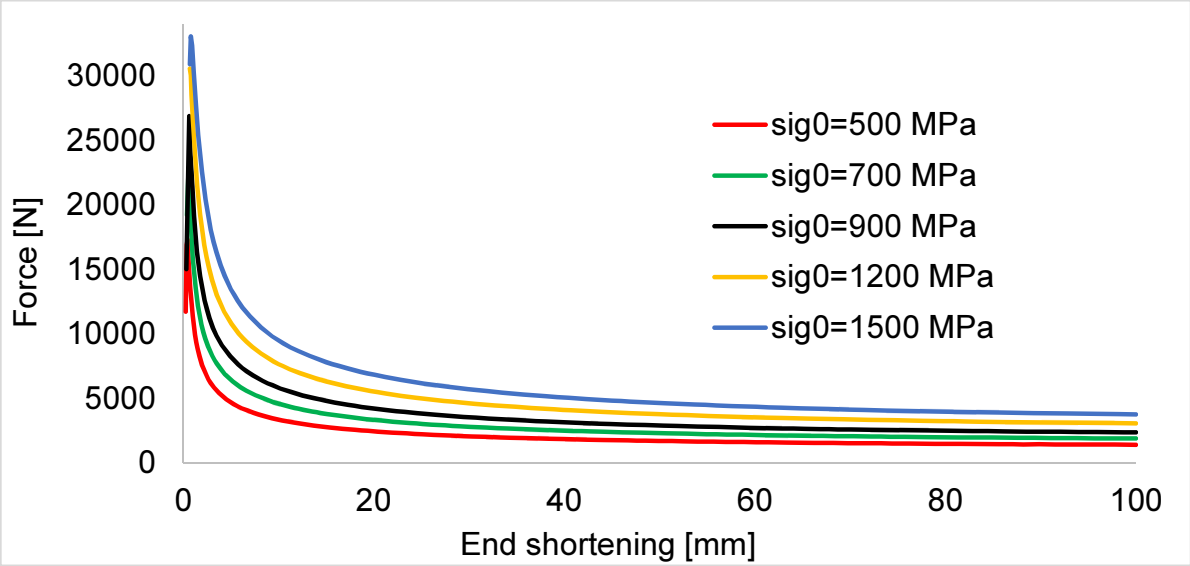

Figure 13.14. The influence of yield stress σ_0 on the force versus end displacement results

13.1.3. FEM model versus experimental results

After testing the influence of all parameters: C_ε, σ_0, number of sub-steps, amplitude of imperfection, size of the mesh, the best parameters were selected and listed in Tab. 13.5. Apart from the parameters shown in Tab. 13.5, two free parameters are left: the yield stress σ_0 and the hardening modulus C_ε. These two parameters were chosen to best fit the experimental results in terms of force versus axial displacement.

u_{max} [mm]	Number of sub-steps	Imperfection multiplier [m]	Mesh type
100	50	0.0005	Mesh6

Table 13.5. Parameters of the finite element model

Optimum parameters σ_0, C_ε were found and are listed in Tab. 13.6.

	A1	A2	A3	A4	A5	A6	Raw
σ_0 $[MPa]$,	950	1000	720	1300	1400	1100	650
C_ε $[MPa]$	300	600	700	300	300	700	500

Table 13.6. The yield stress σ_0 and the hardening modulus C_ε chosen to best fit the experimental data

Results of the finite element simulations, compared to the experimental data are presented in Figs 13.15 and 13.16.

Good correlation was obtained between the experimental and the numerical results within the whole axial compression range. This proves that this type of model can reasonably well describe the conditions of the axial compression experiment.

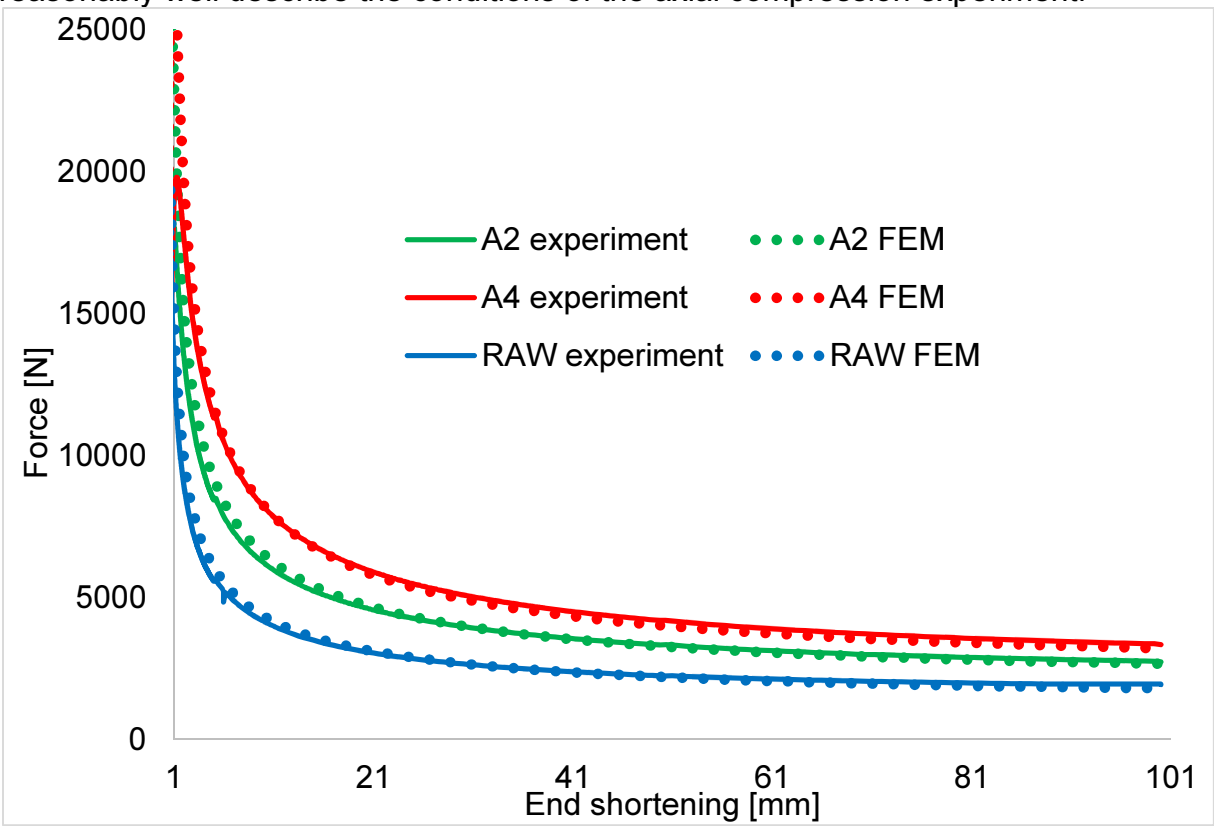

Figure 13.15. Force versus end displacement, experimental and FEM results, samples: A2, A4 and "raw"

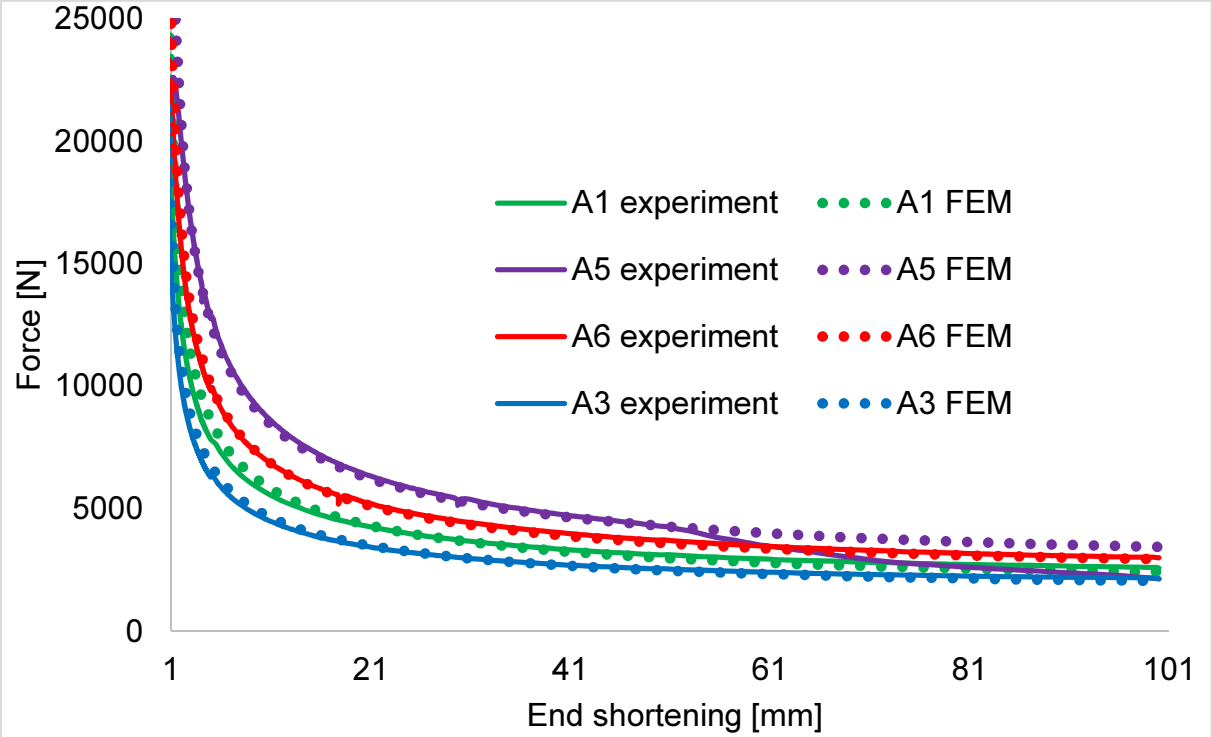

Figure 13.16. Force versus end displacement, experimental and FEM results, samples: A1, A3, A5, A6

13.1.4. Detailed results of numerical simulations for sample A2

FEM simulations provide much more advanced information when compared to the analytical model, which essentially describes force versus axial displacement only. The simulations offer extensive information: displacements, distribution of stresses and strains, etc.

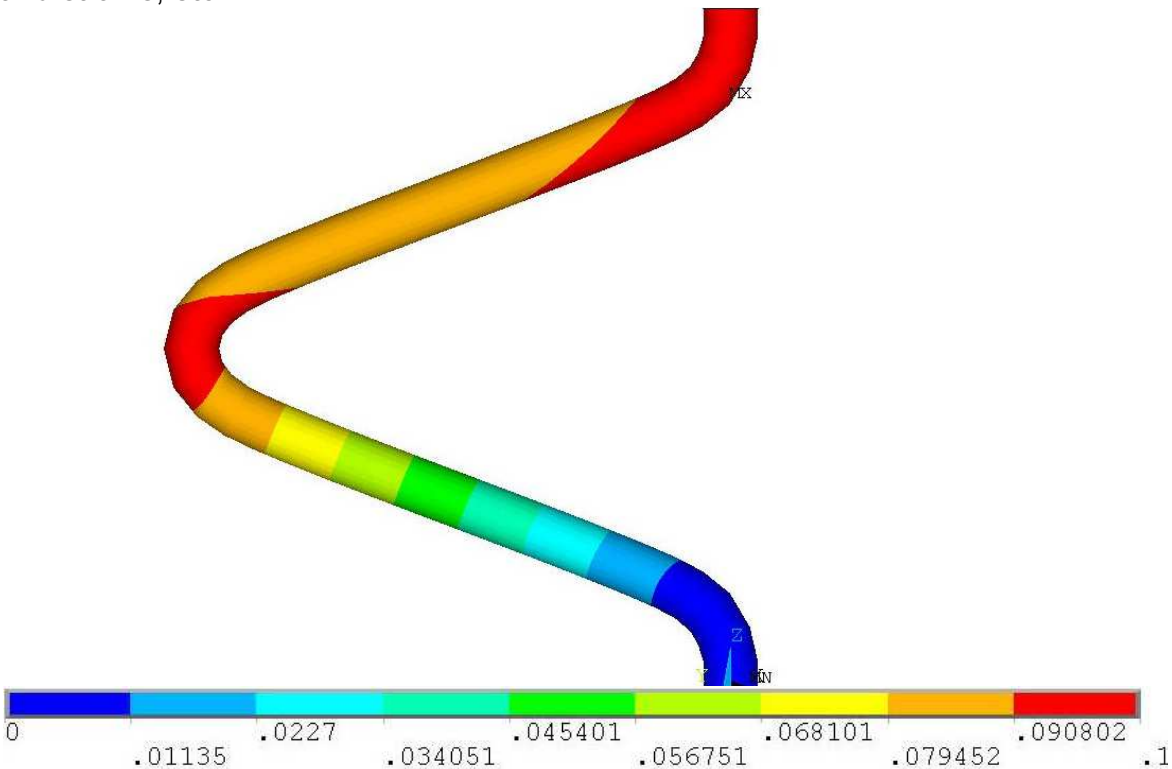

Figure 13.17. Displacement vector sum for sample A2

Firstly, the displacement vector sum is plotted at the end of the loading sequence (Fig. 13.17). The maximum displacement is of course equal to 100 mm. The second important result is the equivalent (von Mises) stress (Fig. 13.18a). The maximum stress was detected at the center of the concave side, and it was equal to 1370 MPa, much higher than the initial yield stress of 1000 MPa (Tab. 13.6). Increased stresses occurred near the boundary and at the center.
The straight sections of the column showed much smaller stress (11.7 ÷ 163 MPa - blue color). Thus, they remained elastic until the end of loading. The stress was concentrated mainly in the plastic hinges, at the center and near the ends.
The equivalent total strain is presented in Fig. 13.18b. Regions of concentrated strains are clearly visible in the zones near the boundaries, both in the convex and in the concave parts, as well as in the central zone on both sides.
Elastic component of the total strain is presented in Fig. 13.18c. The elastic strains are smaller than 0.007.
The plastic part of the total strain is shown in Fig. 13.18d. Its maximum value is almost equal to the total (elastic + plastic) strain.

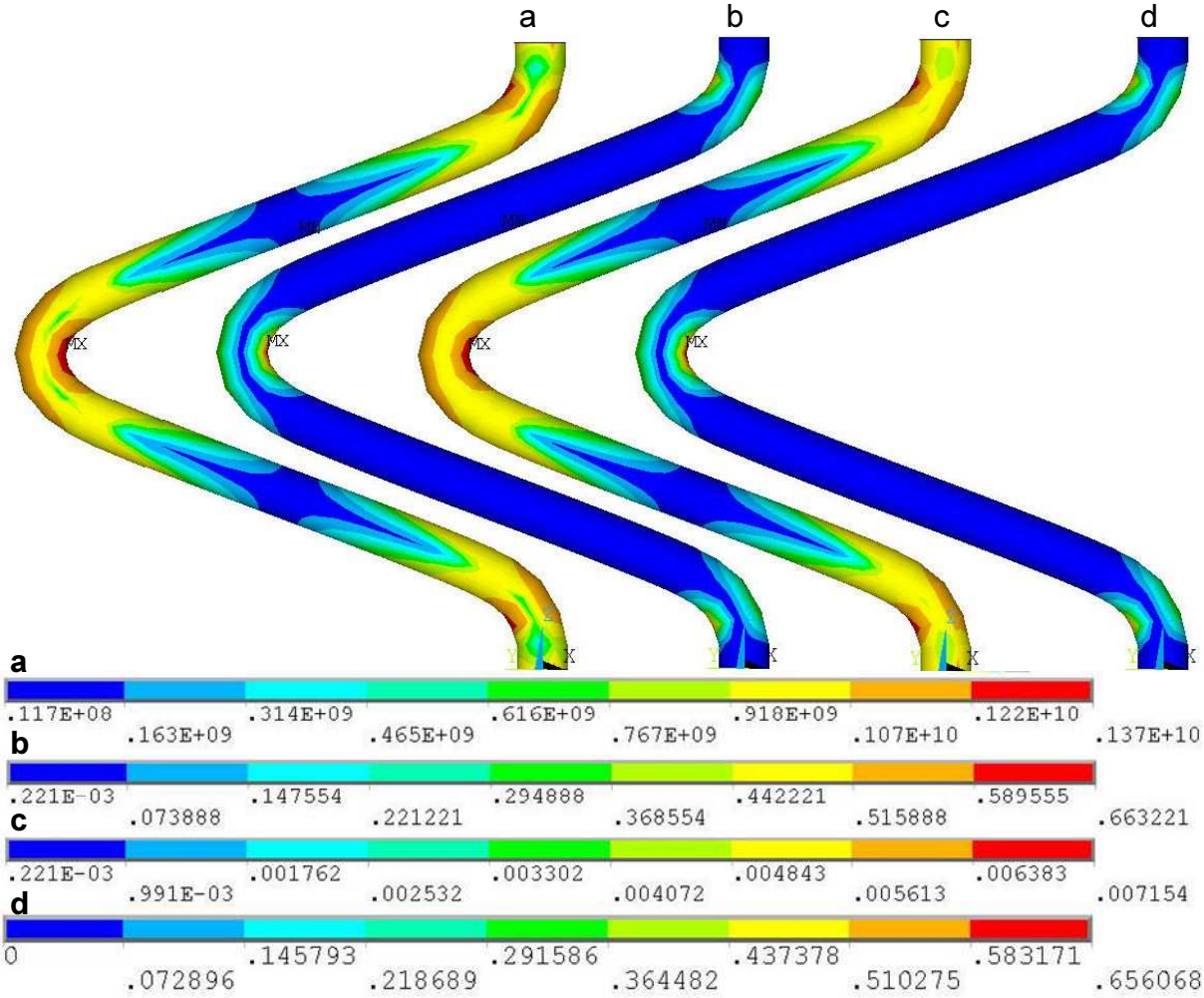

Figure 13.18. The results for sample A2 a) equivalent (von Mises) stress; b) total strain; c) elastic strain; d) plastic strain

13.1.5. Numerical simulations versus experiment for sample A2

Sample A2 was selected for more detailed analysis, because the deformation was recorded with good precision.
First of all, the form of the column was compared: the one recorded during the experiment and the one obtained in the course of simulation.
Five different stages of deformation were chosen. In the first stage, the column just started to bend (Fig. 13.19a). The results of simulations are placed on the right-hand side with the von Mises stresses. The blue color indicates the stress smaller than 163 MPa over almost the whole sample (elastic behavior).

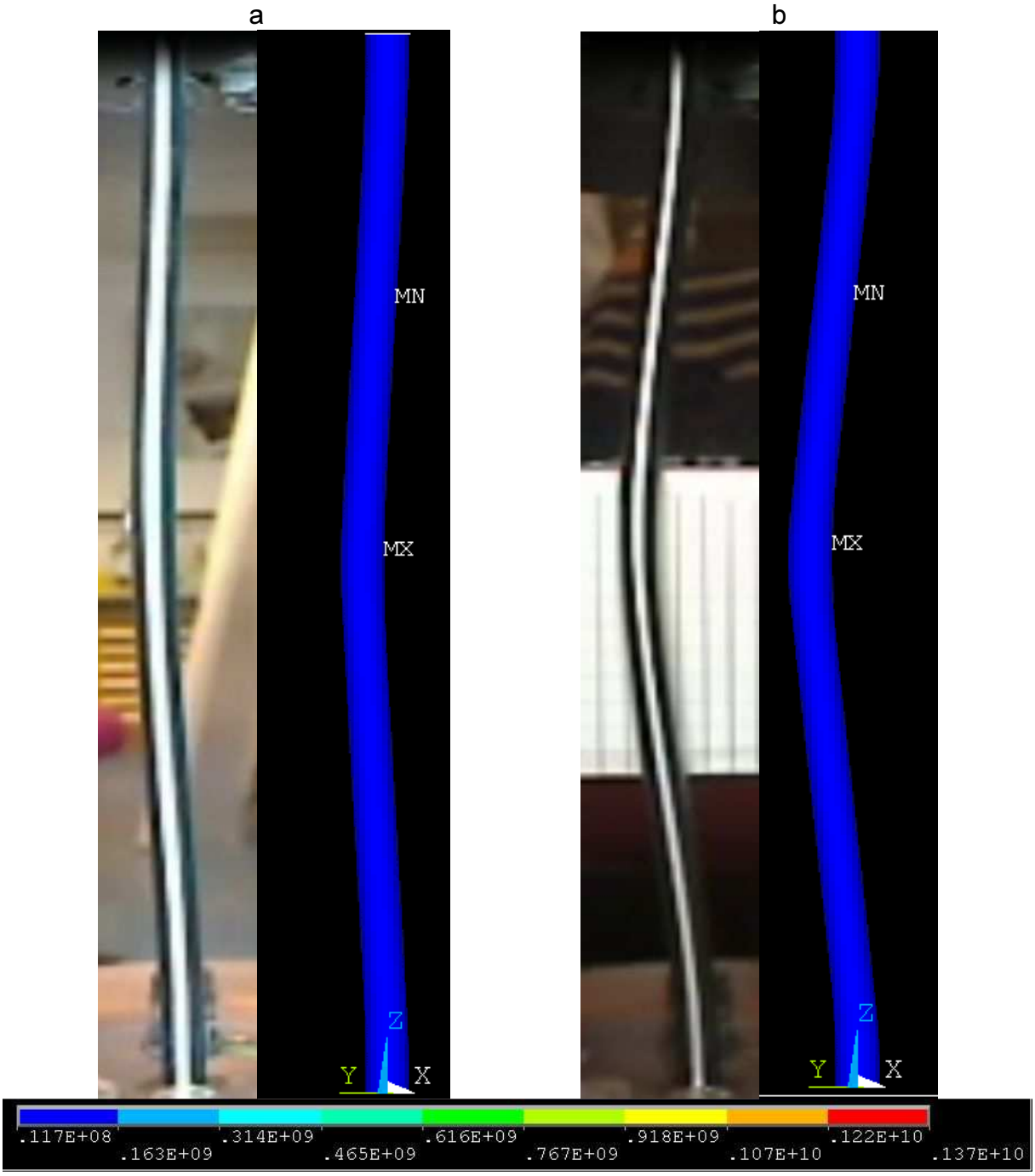

Figure 13.19. Deformed column A2 and the finite element results, with the von Mises stress, a) after few milimeters of deflection; b) after around 10 mm

The same situation was observed during the next deformation stage (Fig. 13.19b). The maximum deflection of the column reached about 10 mm. Still, the stress was small, and mostly elastic strains occurred. The simulated and the experimental forms of the column are very similar.
The next stage, with the maximum deflection equal to about 15mm, is shown in Fig. 13.20a. The finite element results agree very well in terms of the deformation. The stress level was smaller than 314 MPa, so most of the strains were elastic.
In Fig. 13.20b, the deflection is equal to about 35 mm, and the stress is smaller than 616 MPa.

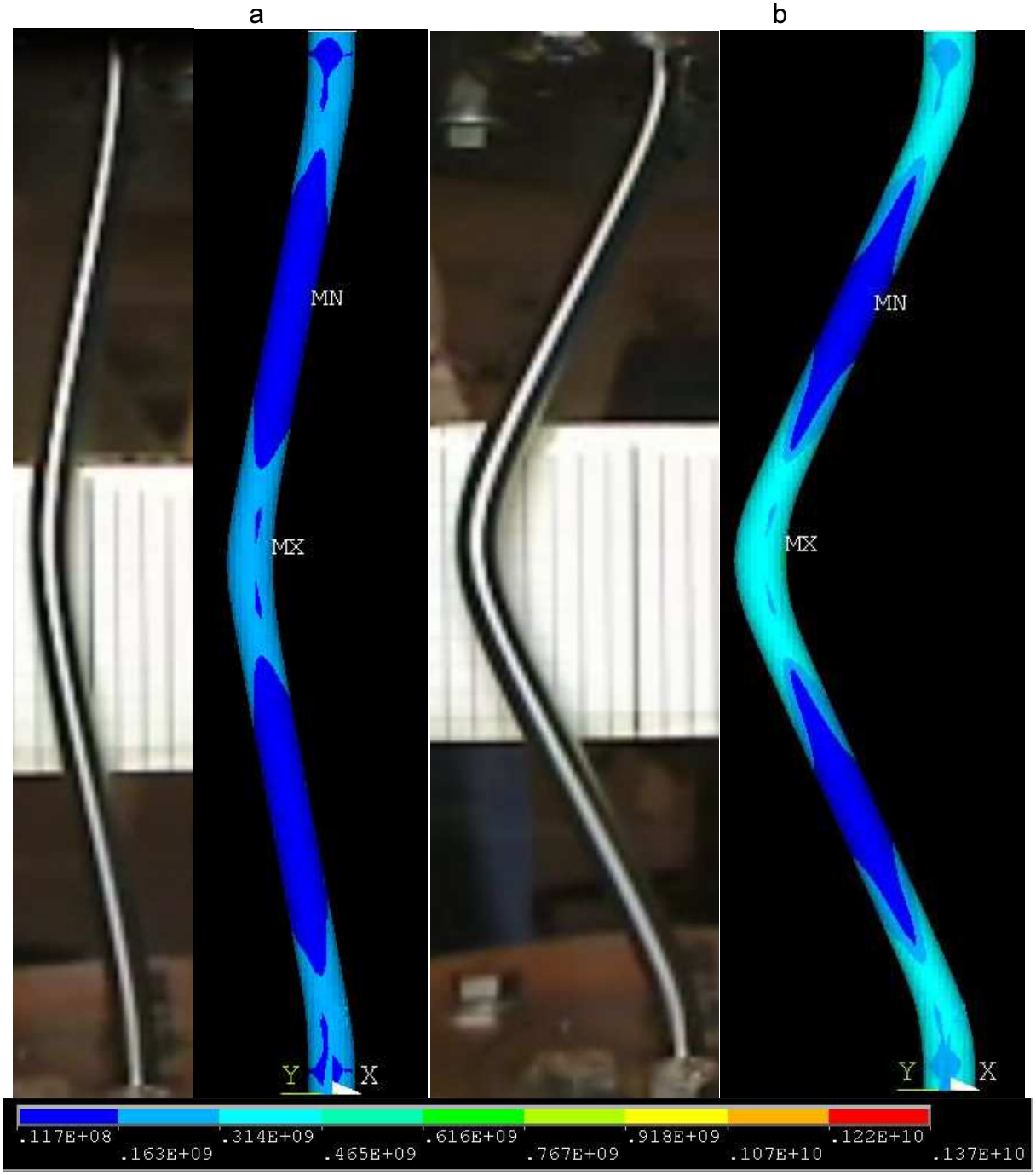

Figure 13.20. Deformed column A2 and the finite element results, with the von Mises stress, a) after about 15mm of deflection; b) after around 35 mm

The final stage of deformation is presented in Fig. 13.21a. The finite element simulation corresponds well to the experiment in terms of the deformed shape. The stresses increased to some 1370 MPa and exceeded the yield stress (Tab.13.6, 1000 MPa). The plastic yielding including hardening occurred. The regions of stress concentration are located at the center and at the ends of the column. No fracture was observed in sample A2. In sample A5, the fracture occurred after about 50mm of axial compression.

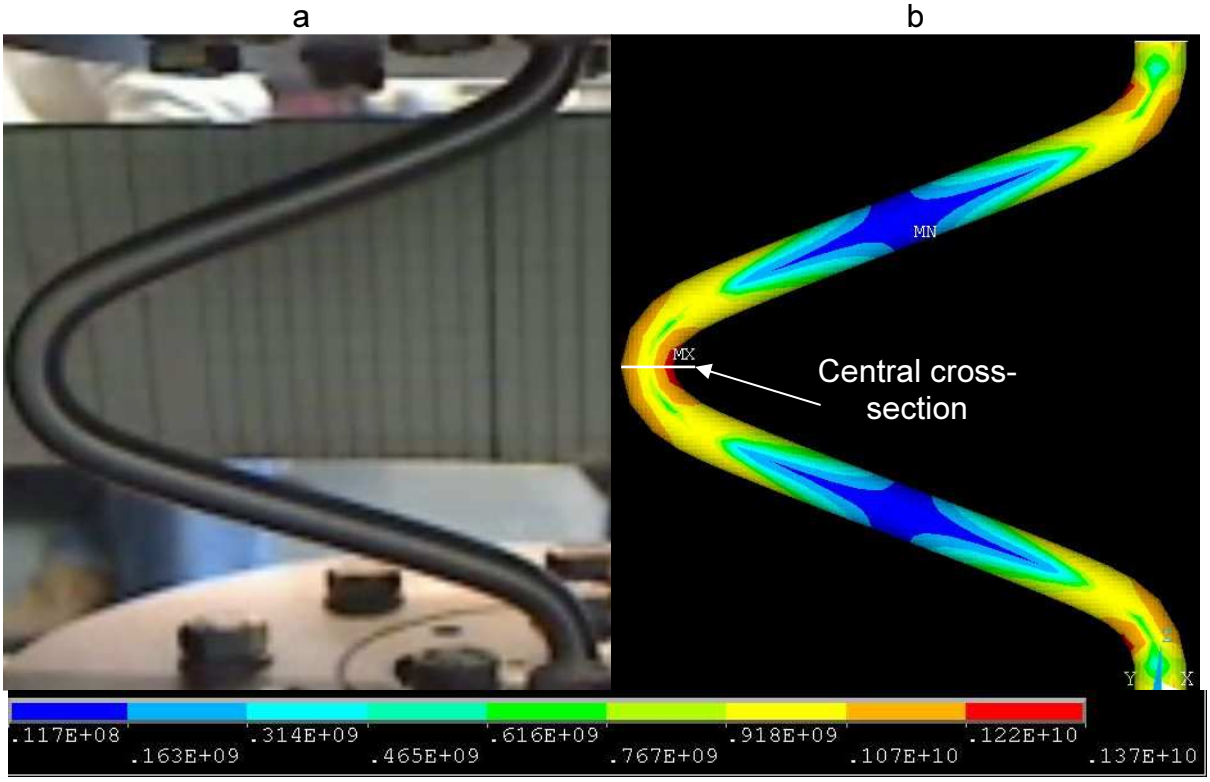

Figure 13.21. Results after compression by 10mm for sample A2 a) experimentally recorded, b) FEM results

The stress distribution in the central cross-section (illustrated in Fig. 13.21b) is presented in Fig. 13.22. Almost whole cross-section became plastified, with the stress in the range from 677 MPa to 1390 MPa.

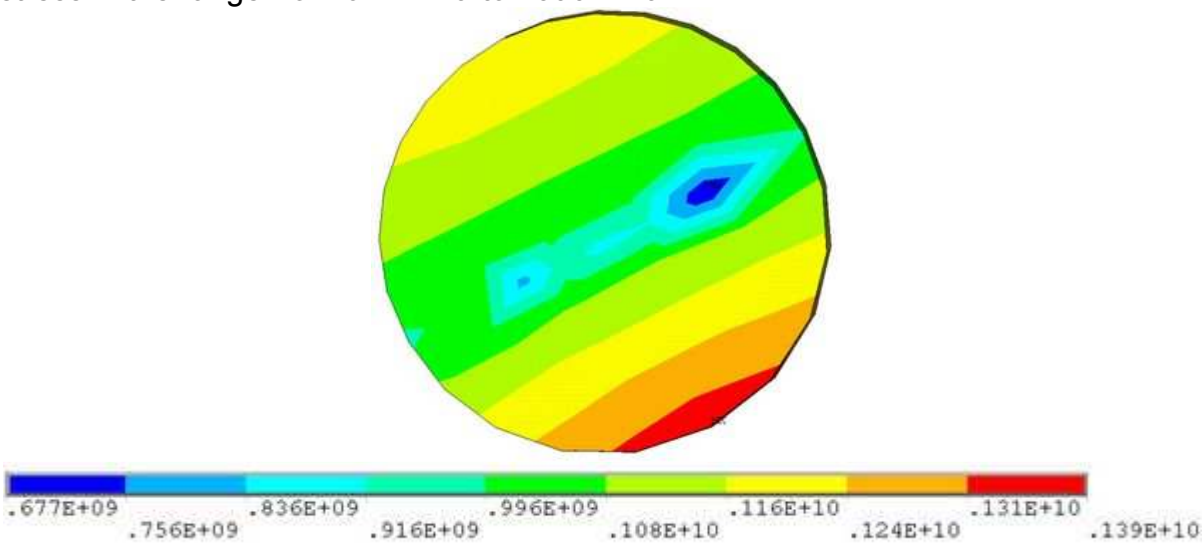

Figure 13.22. Equivalent stress distribution in the central cross-section at the end of loading

13.2. Finite element model with microstructure

The finite element approach presented in the previous section involved several simplifications. In particular:

- The model did not take into account distribution of the martensite content within the cross-section of the sample. Thus, it did not take into account specific material response corresponding to these layers.
- The model didn't capture the evolution of microstructure (increasing martensite content proportional to plastic strain) during compression. The martensite content was measured by using Feritscope on the surface of the most curved regions (center and the ends). It turned out, that the martensite content raised substantially up to around 50%, whereas, in the straight parts of the column it remained similar like before the test.

In order to better model the reality, another approach based on the finite element method was proposed. The approach is based on representing the variable martensite content by several layers with different material properties. This way, one can capture the influence of the microstructure and its properties on the response of the column under compression. All steps necessary to formulate such a model are described in the subsequent sections.

13.2.1. Description of the problem

The concept of the model is based on modeling separate layers of the material, with their specific behavior. This type of model does not need any fitting of material parameters, whereas, in the previous sections two free variables σ_0, C_ε were used to best fit the experimental results.

This model needs the tensile properties of several samples, characterized by different martensite content (constant within its volume). Having such material properties, one expects a response that matches the experimental results well.

This approach shows clear advantage compared to the previous purely phenomenological case, where actually one had to make the compression experiment in order to match the parameters of the finite element analysis (otherwise such parameters wouldn't be known).

With the approach based on modeling several layers of the column, one does not necessarily need compression experiment for parameter tuning. However, knowledge of martensite distribution within the cross-section, and then stress-strain results from tensile tests are necessary. Therefore, this approach still requires other experimental results. Yet, tensile tests are more common, when compared to the axial compression tests. Having these two approaches, one may decide which type of modeling is better for a particular case.

13.2.2. Tensile properties of samples with variable martensite content

All samples used in the buckling experiments were subjected to torsion in order to trigger the phase transformation. The resulting martensite content was characterized by nearly paraboloidal distribution within the cross-section. The experimental results were presented in section 6.3.6. For example, in Fig. 6.92 the results for a bar twisted to 870° at 77K were shown. Similar martensite content distributions were expected in the samples loaded by cyclic torsion which were subjected to axial compression.

In order to model such structures, one needs several stress strain curves measured for various martensite contents.

Many such curves are required in order to obtain smooth approximation. Such information was not available.
In order to solve this problem, the whole approach was simplified. The model accounted only for the known stress-strain curves, thus, based on three measurements (Fig. 13.1). For this reason, only a triple-layer model was possible to realize, because of lack of more experimental data. One has to remember, that these stress-strain results were obtained from samples that were twisted beforehand, and had approximately parabolic martensite content along the radius. Yet, the results that one needs are stress-strain functions corresponding to constant martensite content within the volume of the sample. In order to use the obtained results, the concept of average value was used. It means, that one expects the same overall behavior of sample with constant ξ_{av} martensite content in its volume, and of sample for which the average of distributed martensite content in the volume is equal to ξ_{av} (Fig. 13.23).

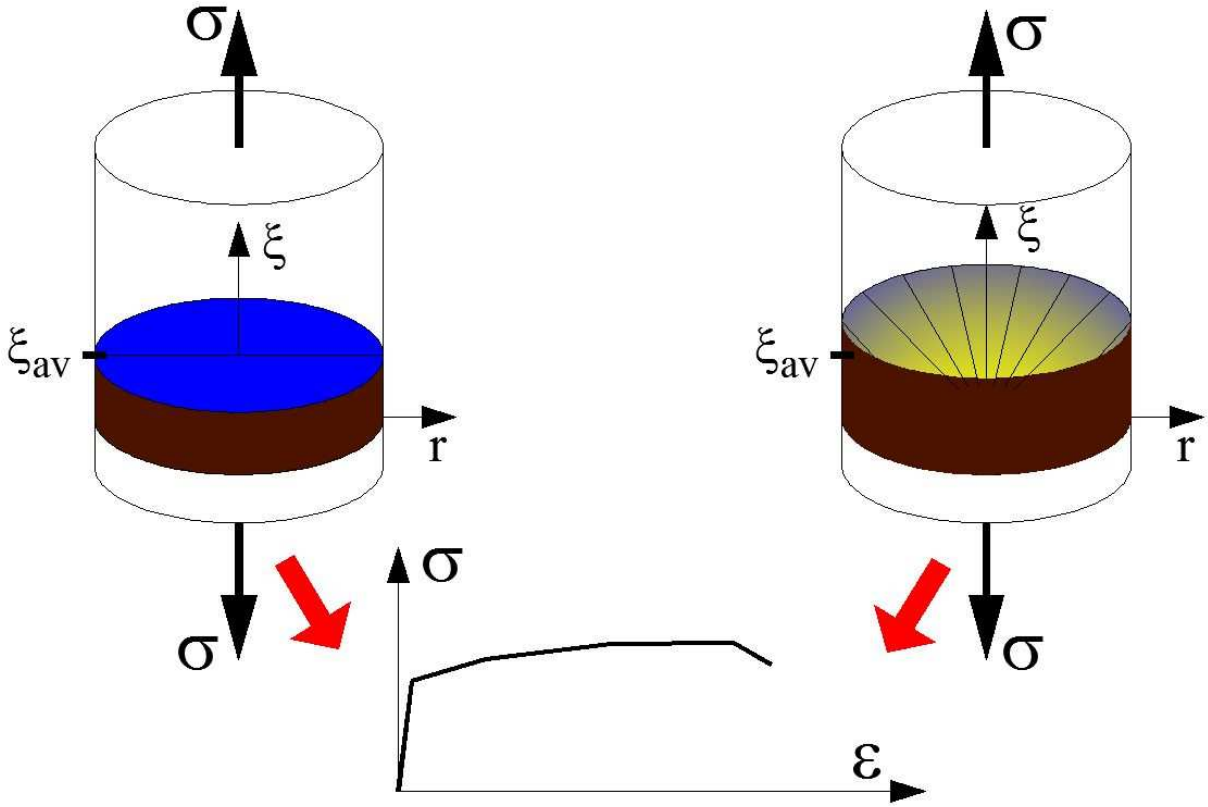

Figure 13.23. Equality of the stress-strain response for constant and variable martensite content distributions

For the samples for which the stress-strain results were obtained (Fig. 13.1), i.e.A9.1, A10.1, 62, the values of martensite content were known on the surface only. In order to calculate the average martensite content within the cross-section of these samples an approximation was proposed. It was based on the known results measured within the cross-sections (section 6.3.6), together with the results from the surface.
Detailed steps to obtain the function describing the martensite content, and how to calculate the average value, are described in the subsequent sections.

13.2.3. Approximation of the martensite content distribution

The function of the volume fraction of martensite along the radius was known only for 4 samples (1, 2, 3, raw, from Tab. 5.2, plotted in Fig. 6.111). For other samples the martensite content was measured on the surface only, and the distribution within the cross-section was not known.

A function that can describe distribution of martensite, and can be calculated based on single measurement made on the surface, has been postulated. Thus, it is assumed, that the distribution of martensite can be described with a parabolic function of the following form:

$$\xi = D \cdot r^2 + E \tag{13.2}$$

where ξ is the martensite content in [%], r is the radius in [mm], and D, E are parameters to be identified.

The only known condition from the experiment, is the following equation (from the measurement on the surface of the sample):

$$\xi(R) = \xi_{max} \tag{13.3}$$

Eq. 13.3 provides one condition only, whereas, two unknowns D, E have to be identified. It is proposed to introduce a material dependent parameter, that would provide the second condition. It is assumed namely, that the ratio of ξ_{max}/ξ_{min} is a constant parameter. Here, ξ_{min} is the minimum martensite content at the center of the cross-section, and ξ_{max} denotes the maximum martensite content on the surface. The values of ξ_{max}, ξ_{min} and their ratio are presented in Tab. 13.7.

Sample number	ξ_{max} [%]	ξ_{min} [%]	ξ_{max}/ξ_{min} [-]
1	49.5	9.55	5.18
2	58.4	10.02	5.83
3	5.9	0.90	6.61

Table 13.7. Maximum and minimum martensite contents measured via Feritscope

It turns out, that the ratios ξ_{max}/ξ_{min} are quite similar. Thus, it is assumed that the average of these 3 values is constant for all samples. Namely:

$$\frac{\xi_{max}}{\xi_{min}} = const = c = \frac{5.18 + 5.83 + 6.61}{3} = 5.856 \tag{13.4}$$

Thus, the following conditions for the parameters *D, E* are formulated:

$$\begin{cases} \xi(R) = \xi_{max} = D \cdot R^2 + E \\ \xi(0) = \xi_{min} = \dfrac{\xi_{max}}{c} = E \end{cases} \tag{13.5}$$

and

$$\begin{cases} D = \xi_{max} \dfrac{c-1}{c \cdot R^2} \\ E = \dfrac{\xi_{max}}{c} \end{cases} \tag{13.6}$$

After inserting parameters D, E from Eq. 13.6 into Eq. 13.2, the function $\xi(r)$ takes the form:

$$\xi(r) = \frac{\xi_{max}}{c}\left(\frac{c-1}{R^2} r^2 + 1\right) \tag{13.7}$$

which depends exclusively upon ξ_{max} obtained from the experiments, and the constant “c”.
Based on the experimental results from samples number 1, 2, 3, and the results obtained from Eq. 13.7, a comparison has been made (Figs 13.24, 13.25).

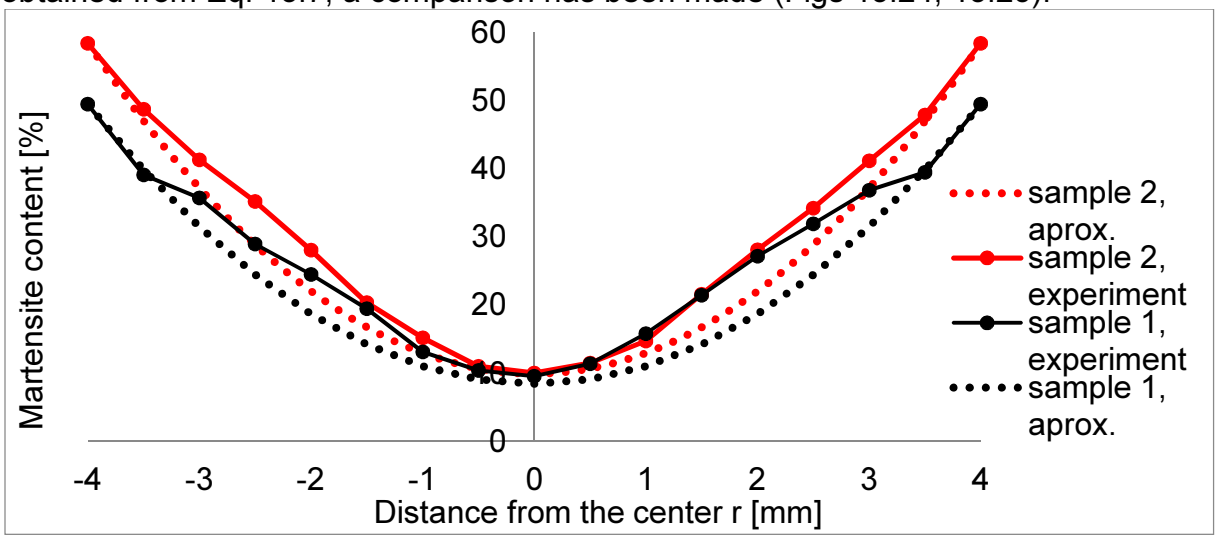

Figure 13.24. Martensite content along the radius and the approximation for samples 1 and 2

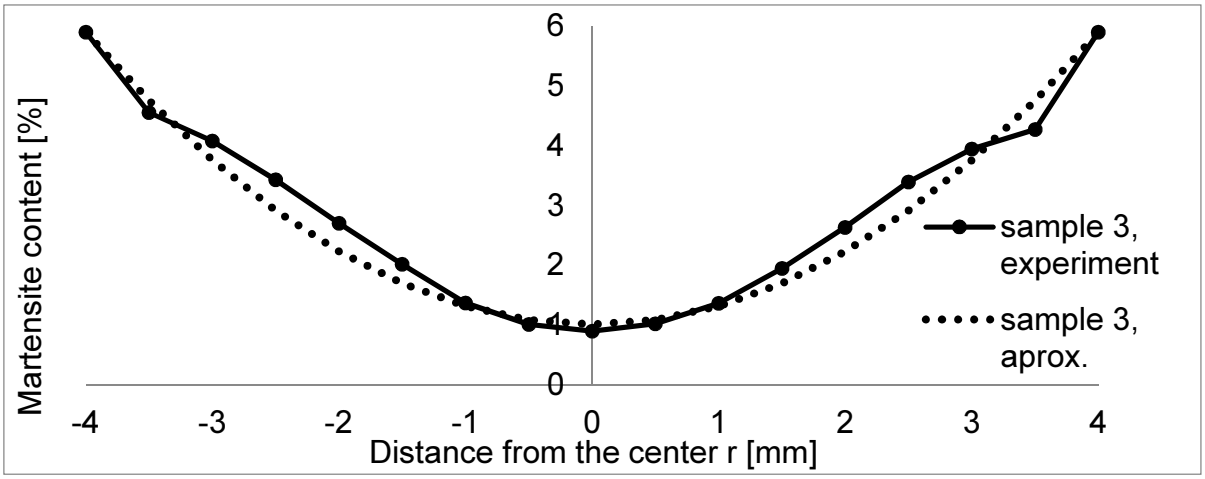

Figure 13.25. Martensite content along the radius, and the parabolic approximation for sample 3

The convergence between the proposed approximation and the experimental data is quite good (Figs 13.24, 13.25). Thus, this approach has been validated.
The distribution of martensite along the radius for twisted samples can be calculated based on Eq. 13.7. This approximation was derived for samples made of grade 304 austenitic stainless steels. For samples made of the other types of austenitic stainless steel, one would need additional experimental data.
Having defined the approximation (Eq. 13.7), the martensite distribution for samples A9, A10 and 62 (Tab. 11.1) can be computed, knowing that the martensite content was measured on the surface. The results along the axis of each sample are shown in Fig. 11.14.

Sample number	ξ_{max} [%]
A9	6.71
A10	82.9
62	99.9

Table 13.8. Martensite content measured on the surface of samples A9, A10, 62

Based on the values of ξ_{max} from Tab. 13.8, with the parameter c defined by Eq. 13.4 and the radius $R = 4mm$, the following expression was obtained for sample A9:

$$\xi(r) = 1.15(0.3034 \cdot r^2 + 1) \tag{13.8}$$

where the current radius r is expressed in [mm].
Similarly, for sample A10 one obtains:

$$\xi(r) = 14.16(0.3034 \cdot r^2 + 1) \tag{13.9}$$

and for sample 62:

$$\xi(r) = 17.06(0.3034 \cdot r^2 + 1) \tag{13.10}$$

The plots of the above formulas are presented in Fig. 13.26.

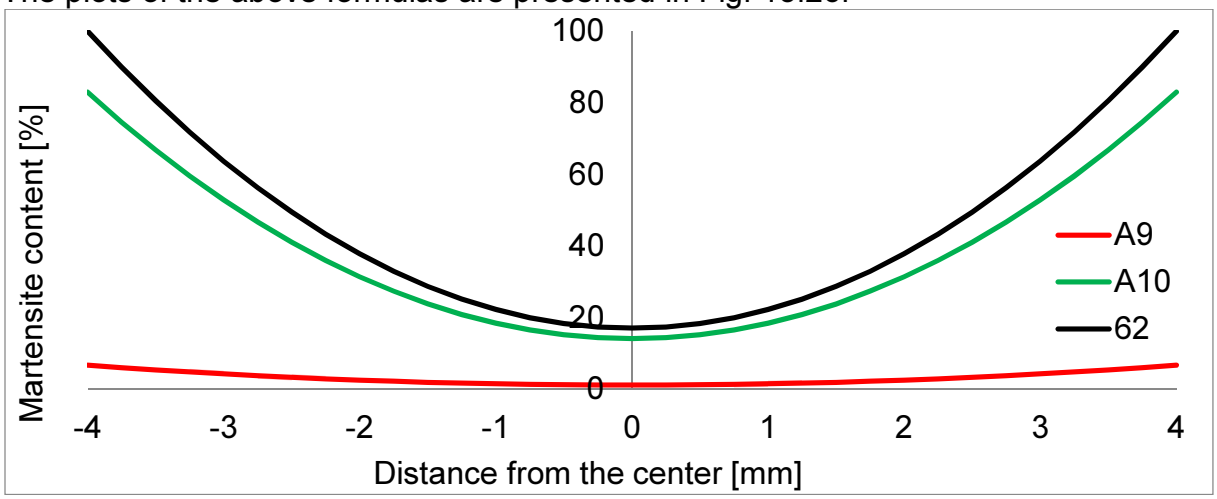

Figure 13.26. Calculated martensite content along the radius for samples A9, A10, 62

The distribution of martensite along the radius was calculated for samples A9, A10 and 62, for which the stress-strain curves were experimentally obtained. The last step consisted in calculation of the average value, based on the proposed functions (Eqs 13.8÷13.10), which is described in the next section.

13.2.4. Calculating the average martensite content

In order to characterize the martensite distribution for all 3 samples (1, 2, 3), one needs to calculate the average martensite content. To do so, one can use the following formula, which refers to the known scheme of integration:

$$\xi_{av} = \frac{1}{n}\left(\sum_{i=1}^{n-1} \xi_i + \frac{\xi_0 + \xi_n}{2}\right) \tag{13.11}$$

where n is the number of sections (equal to the number of points minus 1). In this particular case $n = 16$, ξ_0 and ξ_n are the first and the last values (see Fig. 13.27).

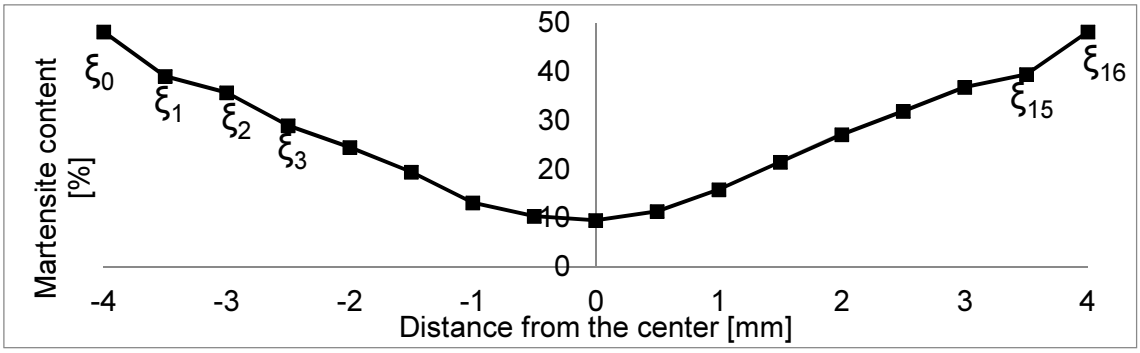

Figure 13.27. Depicted martensite content values for sample 1

Calculated average values, based on Eq. 13.11, are presented in Tab. 13.9.
For samples A9, A10 and 62, the martensite content was obtained from the approximate formulas 13.8÷13.10. To calculate the average of a continuous function, one can use the well-known formula:

$$\xi_{av} = \frac{1}{2R}\int_{-R}^{R} \xi(r)dr \tag{13.12}$$

Inserting Eq. 13.7 one obtains:

$$\xi_{av} = \frac{1}{2R}\int_{-R}^{R} \frac{\xi_{max}}{c}\left(\frac{c-1}{R^2}r^2 + 1\right)dr \tag{13.13}$$

and after calculating the integral:

$$\xi_{av} = \xi_{max} \cdot \frac{2+c}{3c} \tag{13.14}$$

The average values from Eq. 13.14 are presented in Tab. 13.9.

Sample number	*n [-]*	ξ_{av} *[%]*
1	16	25.8
2	16	29.2
3	16	2.8
A9	-	3.0
A10	-	37.1
62	-	44.8

Table 13.9. Average martensite content values

Thus, the average martensite content characterizing sample 62 was equal to 44.8%, 37.1 % for sample A10 and 3% for sample A9. These three material responses are used to model the column.
The FEM model is described in details in the next section.

13.2.5. Finite element model in Ansys

Sample A6, with 50% of martensite content on the surface (Fig. 12.1), was selected for modeling. Based on the approximation formula 13.7, the distribution of martensitic phase was calculated and plotted in Fig. 13.28. This distribution has been divided into three regions, representing three different average martensite contents and three distinct stress-strain relationships.

A simplified model was drawn, with a continuous martensite content distribution with $\xi_{max} = 50\%$. Three layers were not enough to describe the continuous function. For

this reason, the results were expected to differ from the experimental ones for sample A6. The choice of thickness of the layers was 1 mm for two outside layers. The core was modeled with the diameter of 4 mm.
According to these dimensions, a column made of three cylinders has been built by using Ansys program. The stress-strain curves from samples A9, A10 and 62 were assigned to these volumes (Fig. 13.29).

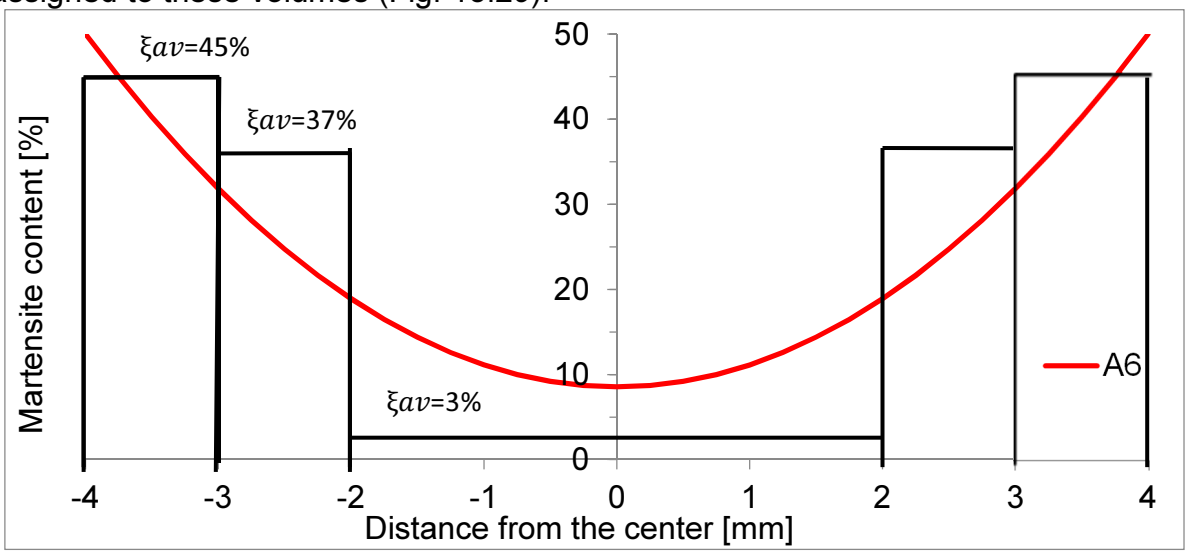

Figure 13.28. Calculated martensite content distribution and the simplified model with 3 layers

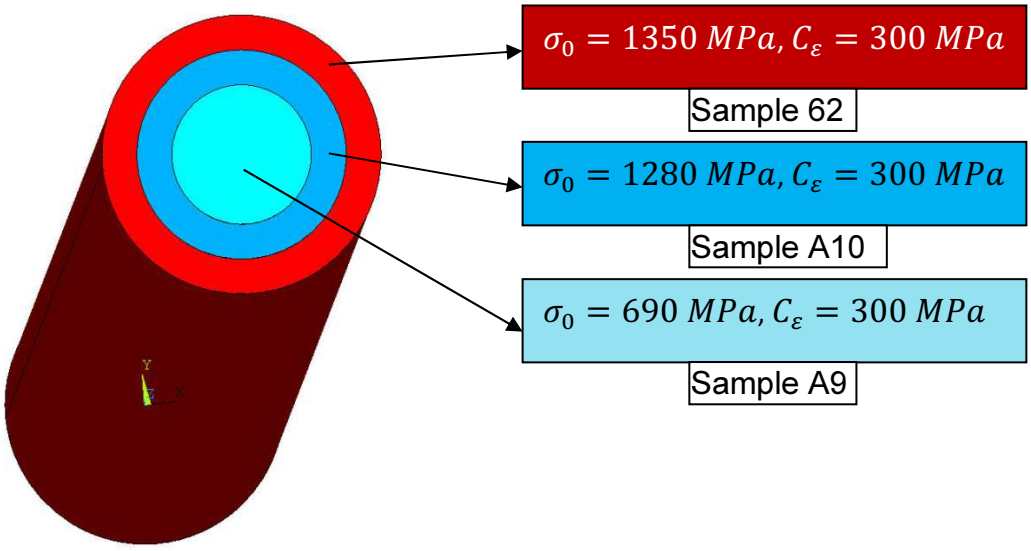

Figure 13.29. Three volumes in the finite element model and their material properties

Meshing of the column was similar to the mesh accepted in the previous chapter. The elements Solid 186, with 50 divisions along the length and 24 divisions along the circumference of the cross-section (Fig. 13.30), were used.

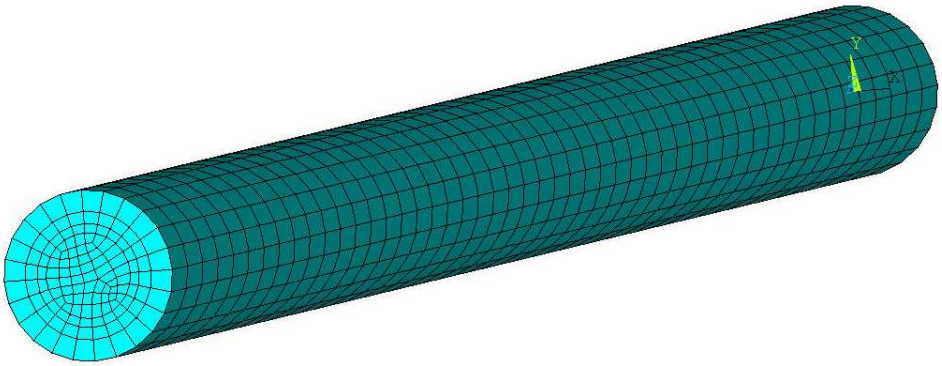

Figure 13.30. The mesh of the column with 3 layers

The buckling mode (Fig 13.31) is similar to the one obtained in the previous sections (Fig. 13.6a).

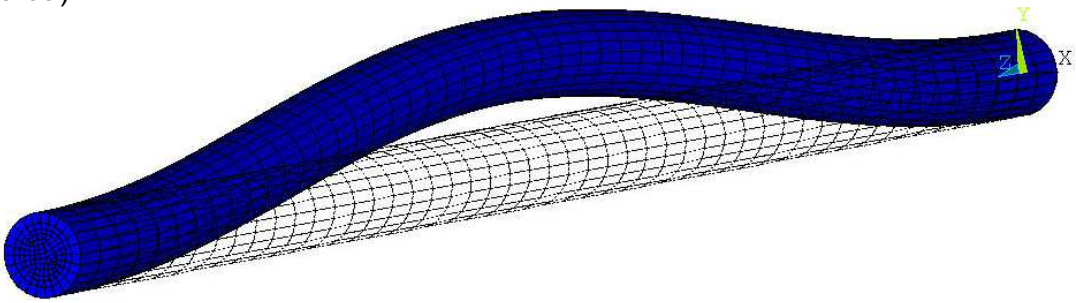

Figure 13.31. The first buckling mode, buckling force of 39887 [N]

a b

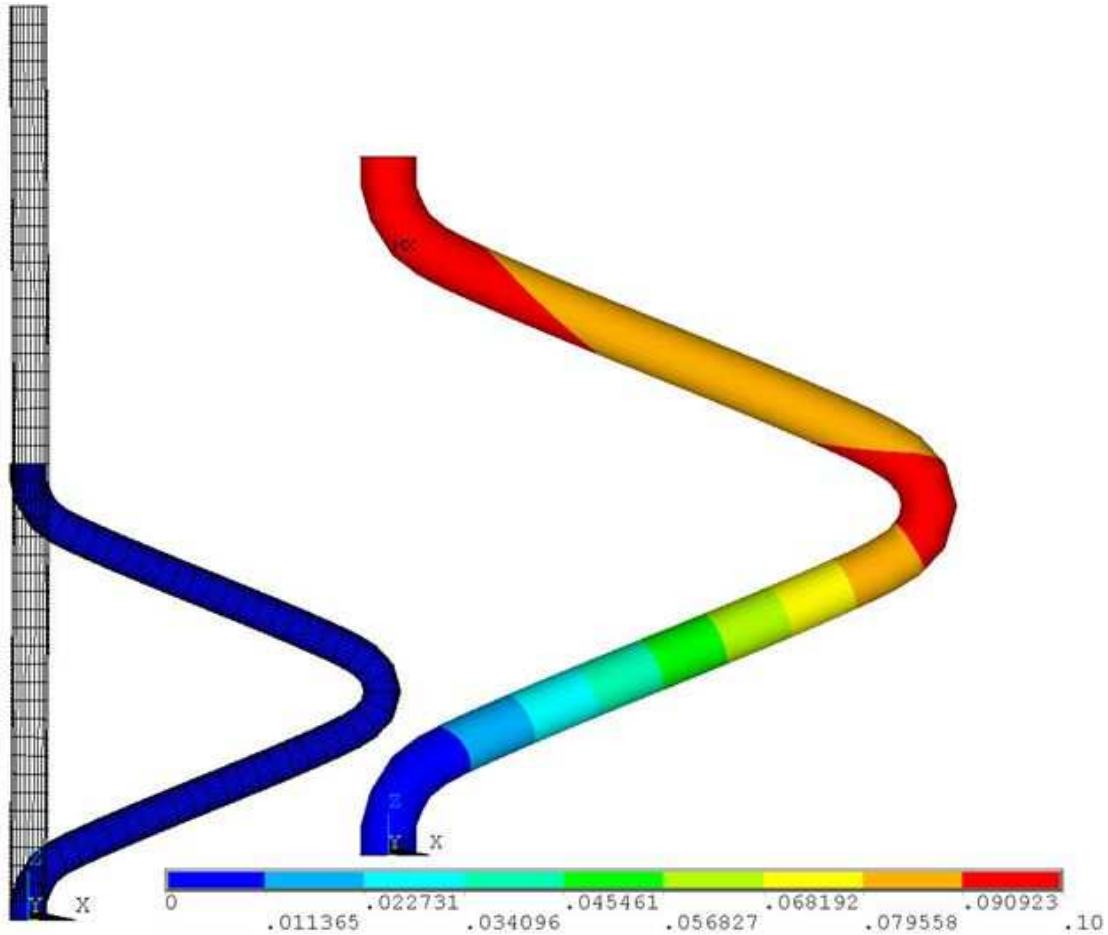

Figure 13.32. a) Deformed and undeformed shapes; b) displacement vector

The geometry has been modified to account for the imperfection according to the first buckling mode, with 0.0005 multiplier. Then, the model was constrained and loaded in the same way like in the previous sections (Fig. 13.3). In particular, 100 mm displacement has been applied at the top of the column. The results are presented in Fig. 13.32.
The results in terms of the equivalent (von Mises) stress, total strain, elastic and plastic strains, are presented in Fig. 13.33.

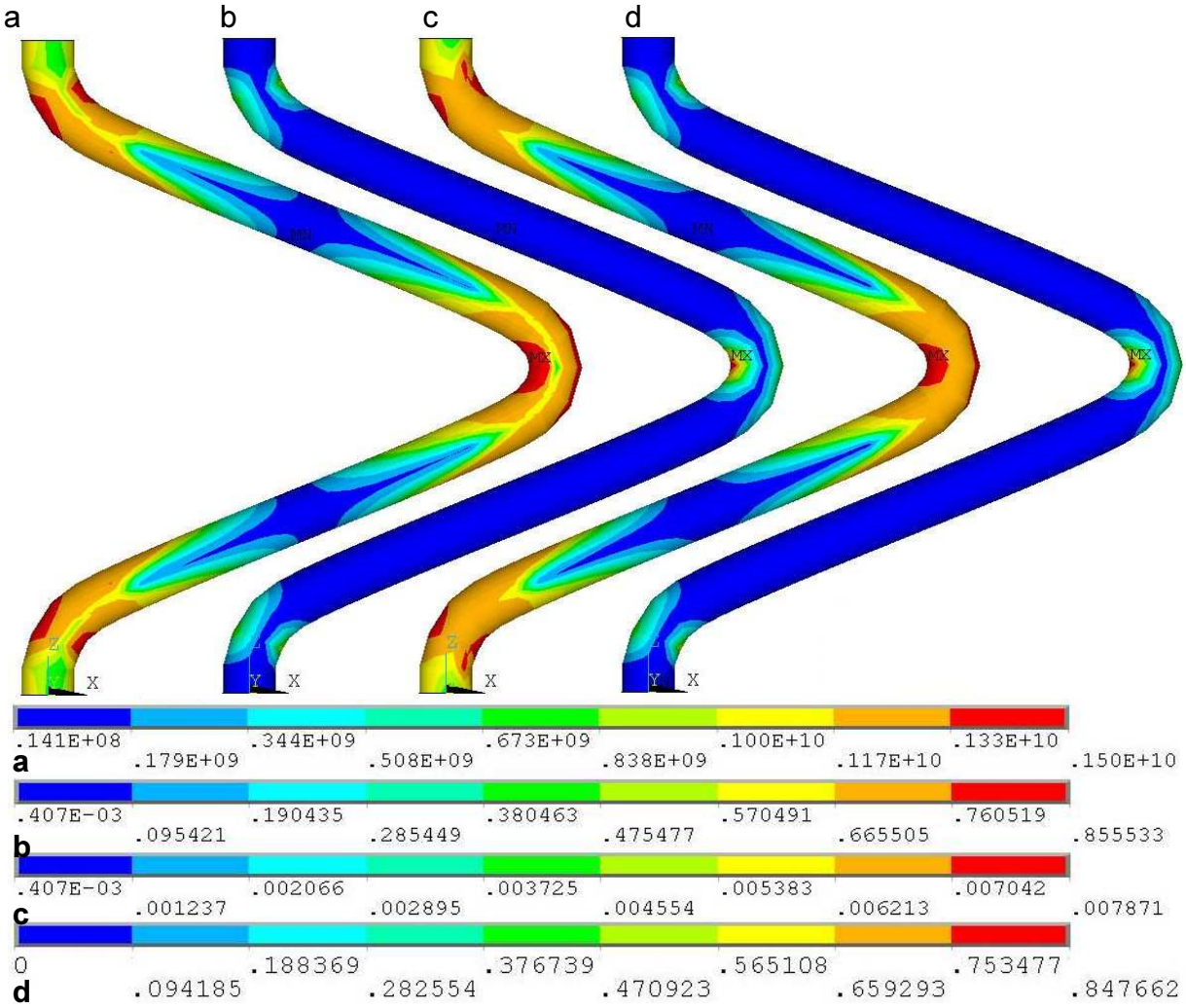

Figure 13.33 a) equivalent (von Mises) stress; b) total strain; c) elastic strain; d) plastic strain

The maximum equivalent (von Mises) stress from Fig. 13.33a is equal to 1500 MPa, and it has its maxima at the center of the column and near the clamped ends. At the center of straight sections, the stress remains in the elastic range. These results are very similar to the results obtained for a column with isotropic material (Fig. 13.18). The total strain has its extremes at the center and near the ends, as well. The maximum total strain reaches some 0.86 locally at the center. The elastic strain (Fig. 13.33c) is small, with the maximum of 0.0078. The biggest part in the total strain makes the plastic strain. Maximum plastic strain intensity reaches some 84.7% at the center, and it is highly localized near the regions of the plastic hinges.
The force versus end displacement has been obtained by summing the reaction forces in all the nodes of the bottom cross section (Fig 13.2b). The result is presented in Fig. 13.34, together with the experimental results for sample A6.

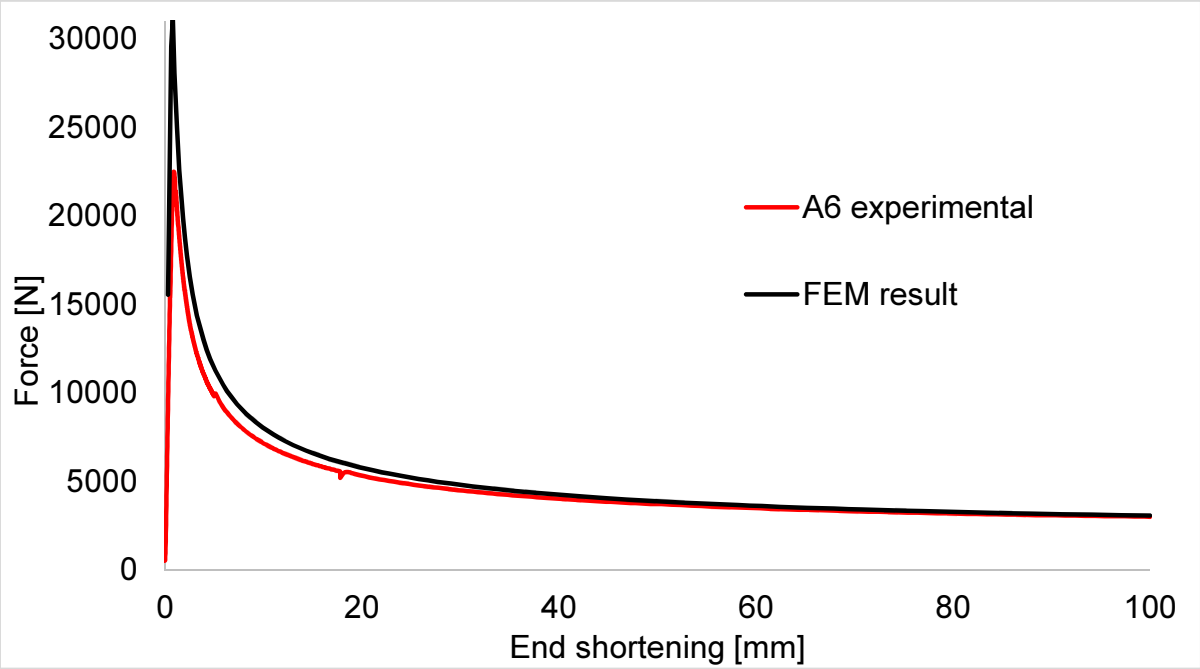

Figure 12.34. Force versus end displacement for sample A6, and the finite element model with 3 layers

It turns out, that the numerical simulation fits quite well to the experimental results, even though only three layers were used to build the finite element model.

13.2.6. Discussion and conclusions

The conclusions from section 13.2 are as follows:

- it is possible to account for different material properties of a column with variable microstructure,
- a model with three layers was built and solved by using Ansys program (the number of layers can be increased),
- quite good correlation with the experimental results was obtained.

Good correlation of numerical simulations with the experimental data confirms that the approach is correct. Knowing the stress-strain response of several samples, and the martensite content distribution of given sample, one can reproduce with reasonably good precision the compression force versus the end displacement of the column.

13.3. Conclusions

The following conclusions are drawn from this chapter:

- FEM approach based on elasto-plastic material showed good results, two parameters were used to calibrate this model (the yield stress and the hardening modulus),
- FEM approach based on modeling several layers with different martensite content performs well; a model with 3 layers only showed quite similar results as the experiment.

14. Summary and conclusions of the Thesis

Summary

The present Thesis addresses the topic of Functionally Graded Structural Members (FGSMs), the microstructure of which was created in a controllable, predefined way, in order to optimize their performance under prescribed loading.

First of all, a 3D constitutive model of elastic-plastic continuum undergoing plastic strain induced phase transformation was presented (Chapter 3). Later on, based on the multi-axial model, one-dimensional case of a bar subjected to torsion was analyzed. Stress – strain curve and torque – angle of twist response were derived, as well as distribution of secondary (α') phase within the cross-section. Cylindrical samples were manufactured and loaded by torsion in order to create FGSMs. Torque – angle of twist response was measured at two temperatures: 77K and 293K. Several grades of austenitic stainless steel were tested. Firstly, grade 304 stainless steel (Chapter 5), and then grades: 316L, 304L, 316LN (Chapter 7) were investigated.

Microscopic observations, micro-hardness measurements and martensite content measurements were performed within the cross-sections of samples made of 304 ss. The results were shown in Chapter 6. Microscopic photographs revealed the presence of martensite and its increasing content near the surface of the sample. Micro-hardness measurements confirmed increasing values of martensite fraction from the center towards the surface. Quantitative measurements revealed true distribution of martensitic phase within the cross-section. It resembles paraboloidal function with a minimum at the center and a maximum on the surface.

The results for grades: 304L, 316L, 316LN were presented in terms of torque versus angle of twist in Chapter 7. In the same chapter, evolution of martensitic phase measured on the surface of samples in the course of torsional loading at 77K, was presented.

Based on the experimental results, presented in Chapters 5 and 7, the parameters of the constitutive model were identified. Comparison between the model and the tests was presented in Chapter 8 for all tested grades (304, 304L, 316L, 316LN). Good agreement was obtained for all samples and the angle of twist up to 992.4° (Tab. 8.6), related to small strains framework with $\varepsilon_{max} = 0.2$. Distributions of martensite obtained by means of the constitutive model and from experiments converged in a satisfactory way. For grade 304 ss, distribution of martensite within the cross-section was predicted, whereas for grades: 316L, 304L, 316LN only the evolution of α' phase on the surface (Chapter 8). The results from Chapters 5 and 7 clearly proved possibility of creating FGSMs by means of torsion at cryogenic and at room temperatures. Martensite content was observed in all tested austenitic stainless steel grades: 304, 304L, 316L, 316LN. On the other hand, in grade 316LN ss large angles of twist were necessary, which is justified by the chemical composition of this grade. Similarly, at 293K much smaller martensite fractions were observed and large angles of twist were necessary to induce the phase transformation.

In Chapter 9, cyclic torsion tests performed at 77K and at 293K were reported. Evolution of martensite content on the surface of samples was measured during the tests. The results proved almost constant martensite content along the axis of twisted bars, confirming the same theoretical expectation. Functionally Graded Structural Members were obtained by means of cyclic torsion as well. Much smaller angles of twist were necessary, compared to monotonic torsion.

Yet, both due to “monotonic” (cycles of increasing amplitude, see Fig. 5.9) and cyclic torsion the bars became distorted, which was possibly caused by imperfect loading conditions and imperfect geometry of the samples.
Based on the results from Chapter 9, relating torque to the residual angle of twist, dissipated energy was calculated and the results were presented in Chapter 10. For grades 304, 304L, 316L, decreasing dissipation was observed for all samples loaded by the force-control. For grade 316LN, in two cases of loads equal to ±70Nm and ±80Nm, an increasing dissipation was observed without presence of martensitic transformation (the plastic strain threshold was not exceeded).
Tensile tests were performed at 293K for several samples with various martensite contents. The results were shown in Chapter 11. Theoretical expectations were confirmed: the higher martensite content, the higher yield and ultimate strength, and the smaller maximum strain.
Axial compression tests were performed on samples loaded by cyclic torsion, and characterized by various martensite contents. The results were presented in Chapter 12, in terms of compressive force versus axial displacement. Deformation was recorded by using camera, that allowed measurements of transverse deflection. It has been concluded, that the samples with higher martensite content (all samples were characterized by paraboloidal shape of martensite distribution) showed higher values of force in the post-buckling range (plastic buckling). Analytical model of a column with one plastic hinge was developed. One material dependent parameter was sufficient to fit the experimental results for all samples, with reasonably good accuracy (Chapter 13). In addition, a FEM model was prepared and the elastic-plastic material model with linear hardening was used. The results were reasonably well correlated with the experimental data. Finally, third model was developed, based on 3 layers of different properties, related to different martensite contents. The results of tensile tests were used in order to obtain necessary material parameters. Fully satisfactory correlation was obtained.

Conclusions

1. The possibility of creation of FGSMs by means of torsion was demonstrated.
2. Analyzing the performance of FGSMs, created by twisting stainless steel bars at 77K and at 293K, showed increased elastic and maximum torques. For the sample twisted at 77K, and later on again at 293K, the elastic torque increased by 89%, and the maximum torque by 36%. For the sample twisted at 77K, and later on again at 77K, the elastic torque increased by 100%, and the maximum torque by 7%. Thus, higher loads can be carried by FGSMs, compared to classical austenitic structures.
3. Optical microscopic analysis revealed increasing martensite content in twisted samples, from the center towards the surface.
4. The micro-hardness values, increasing along the radius of the sample, were obtained for all samples loaded by means of torque.
5. Quantitative martensite content measurements were performed by using Feritscope. Almost axisymmetric results were obtained for all samples. With the paraboloidal shape of the function, minimum (not zero) martensite content was obtained at the center, and increasing values were obtained towards the surface (where it reached its maximum).
6. Functionally Graded Structural Members were created from austenitic stainless steel grades: 304, 304L, 316L, 316LN.

7. Good agreement was obtained between the experimental results and the constitutive model, both in terms of torque – angle of twist and with respect to the martensite distribution.
8. Martensite content measured on the surface of the samples during cyclic torsion, proved almost constant distribution along the length. The evolution of martensite content on the surface followed well known sigmoidal kinetics. Thus, predicting distribution of martensite content is fully possible.
9. Cyclic torsion loading allowed applying smaller angle of twist per cycle, which resulted in less distorted samples.
10. Plastic shakedown was found for a number of samples loaded by cyclic torsion. Thanks to the plastic strain induced phase transformation, considerable portion of dissipative austenitic structure changed into elastic martensite.
11. Tensile tests proved increased strength of FGSMs obtained by torsion at 77K and at 293K. Maximum stress increased from 730MPa for the raw sample (austenitic structure, grade 304ss), to some 1357MPa for sample 62. Thus, almost twice as large. At the same time, maximum strain decreased from about 30% to some 4.5%. Still, some ductility reserve remained, even for martensite contents close to 100%.
12. Axial compression tests constitute direct proof that FGSMs perform well under bending. Even for very high martensite contents (67% on the surface, for sample A4), no fracture was observed up to 100mm of axial compression.
13. The maximum compressive force was comparable for all samples (±10%). All FGSM samples outperformed the raw 304ss sample in terms of force in the post-buckling range. The values of force were increasing with the increasing martensite content.
14. Very high martensite content (some 85% on the surface for sample A5) caused fracture during axial-compression test. Yet, only after about 55mm of axial compression (Fig. 12.36) the macro-crack occurred. Thus, for applications where large plastic deformations are expected, the martensite content should be limited to safe levels.
15. Three different models were proposed to describe force versus axial compression relationship, obtained during the buckling test. The analytical model contained one free parameter. The FEM model with elastic-plastic material behavior, contained two parameters. Finally, the FEM model incorporating layers of different material properties was also developed.

The objectives of the Thesis, presented in Chapter 2, were realized. The Functionally Graded Structural Members were created by means of “monotonic” and cyclic torsion. Their performance was tested under torsion, tension and axial compression. Their properties were analyzed by means of optical microscopy. Micro-hardness and martensite content were measured within the cross-sections of FGSM samples. In addition, evolution of martensite content was measured during cyclic loading at 77K and at 293K.
In Chapter 2, the positive characteristics of FGSMs was predicted. After performing campaign of tests, this characteristics was verified. The results of verification are as follows:
1. FGSMs have higher carrying capacity, which was shown in the course of tensile tests (Fig. 11.52).
2. Performance of FGSMs under torsion proved that much higher loads can be carried by the samples with martensite induced by means of phase transformation (Fig. 5.14).

2. Better wear-resistance of the outside layer was confirmed during micro-hardness measurements that indicated an increasing hardness from the center to the surface. Micro-hardness results were summarized in Fig. 6.64. Its values were almost twice as large as for purely austenitic structure.
3. Higher critical load (maximum force) was obtained for samples A5 and A6 by some 10%, compared to the raw sample (Fig. 12.39). For other samples, the maximum force was slightly lower (by not more than 10.4%). Yet, all preloaded samples carried imperfections, which was not the case for the raw sample. It is known, that the maximum force is inversely proportional to the size of imperfection. In terms of the force in the post-buckling range, for all FGSMs higher values were obtained compared to the raw sample (Figs 12.36, 12.38). The difference reached some 129% in the early post-buckling range (Tab. 12.4).
4. The axial compression tests showed that FGSMs with martensite contents up to 67% on the surface (sample A4, Fig. 12.38), withstood large plastic deformations during bending (Fig. 12.40) with no sign of fracture.
5 In terms of fatigue strength, no tests were made. One has to load the sample with millions of cycles and compare the performance of FGSMs with the classical stainless steel structures.

Future work

The following subjects are proposed for further work:

1. Experimental study:

1.1. Impact toughness as a function of temperature and martensite content should be investigated, in order to correlate decreasing values of this parameter with the increasing martensite content.
1.2. Performing martensite content measurements within the cross-sections of samples made of grades 304, 304L, 316L, 316LN, after cyclic torsion at 77K and at 293K. It is worth testing, if the martensite content is constant along the length of sample, and if its distribution has paraboloidal shape.
1.3. Performing tensile tests at 77K and at 293K on the FGSMs created by means of cyclic torsion (grades: 304, 304L, 316L, 316LN). To this point, only tensile tests at 293K of FGSMs created from grade 304 ss have been done.
1.4. Performing axial-compression tests of FGSMs made of grades: 304, 304L, 316L, 316LN at 293K, with in-situ measurements of martensite content evolution during deformation.
1.5. Creating FGSMs from bars of different than circular cross-sections. Measuring martensite content distributions and comparing their performance with untransformed structures.
1.6. Performing fatigue strength test of FGSMs.

2. Theoretical:

2.1. Developing a constitutive model incorporating large strains framework, in order to model the complete behavior of bars under torsion up to fracture (shear strain of the order 1.5).
2.2. Incorporating the Swift effect into the kinetics of plastic strain induced phase transformation. Thus, allowing predicting non-zero martensite content at the center of twisted samples (transformation is driven by non-zero axial strain, which accompanies torsional deformation).
2.3. Incorporating damage evolution in the constitutive model. Thus, allowing to describe decreasing unloading modulus that was observed during tests.
2.4. Developing a constitutive model for cyclic torsion, in order to describe the results presented in Chapter 9.

Politechnika Krakowska

Model struktury gradientowej otrzymanej w wyniku przemiany fazowej sterowanej odkształceniem

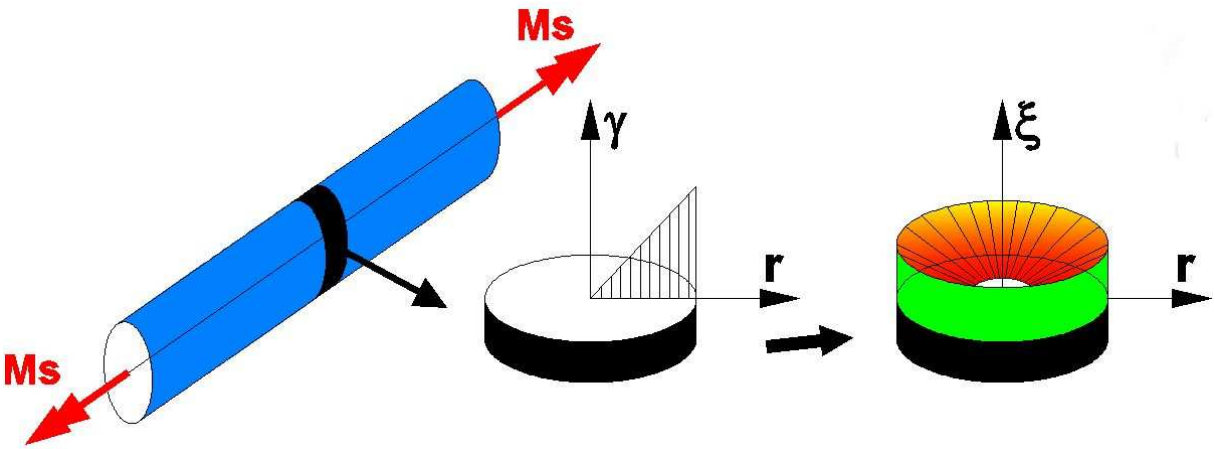

Rafał Ortwein

Promotor: Prof. dr hab. inż. Błażej Skoczeń

Kraków
Styczeń 2015

1. Przegląd literatury

Przegląd literatury został szczegółowo przedstawiony na stronach 11÷26. Najważniejszymi pracami na których oparty jest wielkoskalowy model konstytutywny są prace: Ortwein et. al. (2014), Sitko and Skoczeń (2012), Sitko et al. (2010), Skoczeń (2007), Garion et al. (2006).

2. Cel i zakres pracy

Zjawisko przemiany fazowej indukowanej odkształceniem plastycznym jest przedmiotem badań naukowych od dekad. Występuje ono m.in. w stalach nierdzewnych o strukturze austenitycznej, które są szeroko stosowane w konstrukcjach pracujących zarówno w temperaturach podwyższonych jak i temperaturach sięgających absolutnego zera (np. nadprzewodzące elektromagnesy w akceleratorze LHC w CERNie).
Pod wpływem odkształceń plastycznych faza austenityczna transformuje się stopniowo w fazę martenzytyczną. Przemiana ta może zachodzić wyłącznie w temperaturach niższych od temperatury M_d (stała materiałowa, rzędu 400°C).
W temperaturach poniżej M_s (rzędu kilkudziesięciu kelwinów) przemiana fazowa zachodzi spontanicznie w nieobciążonej próbce. W zakresie temperatur $M_s \div M_s^\sigma$ aby przemiana zaszła konieczne jest pewne naprężenie (odkształcenie), nie przekraczające granicy plastyczności. W temperaturach $M_s^\sigma \div M_d$ konieczne jest odkształcenie plastyczne, w tym zakresie temperatur mówi się o przemianie fazowej indukowanej odkształceniem plastycznym. Ten typ przemiany fazowej stanowi rdzeń niniejszej pracy.
Zjawisko przemiany fazowej prowadzi do zmiany struktury austenitycznej w martenzytyczną. Ponieważ martenzyt jest fazą znacznie twardszą i wytrzymalszą od fazy austenitycznej, przemiana fazowa ma korzystny wpływ na własności mechaniczne struktury. Element strukturalny otrzymany w wyniku takiej przemiany fazowej może przenosić wyższe obciążenia, przy tych samych wymiarach geometrycznych.
Element strukturalny otrzymany w wyniku przemiany fazowej nazywamy „Elementem o Strukturze Gradientowej" (z ang. Funcionally Graded Structural Member – FGSM). Koncepcja ta jest szerzej pokazana na Rys. 1. Przemiana fazowa indukowana jest odkształceniem plastycznym. Aby ją wywołać, konieczna jest kontrolowana deformacja (np. rozciąganie, skręcanie, zginanie, itp.) oraz przekroczenie granicy plastyczności. Po przekroczeniu pewnej progowej wartości odkształcenia plastycznego, proces przemiany martenzytycznej rozpoczyna się. Lokalna zawartość objętościowa martenzytu jest proporcjonalna do lokalnego odkształcenia plastycznego. Końcowa dystrybucja fazy martenzytycznej w objętości danego elementu (struktury) decyduje o jej właściwościach mechanicznych, polepszonych w stosunku do elementu o strukturze wyłącznie austenitycznej.

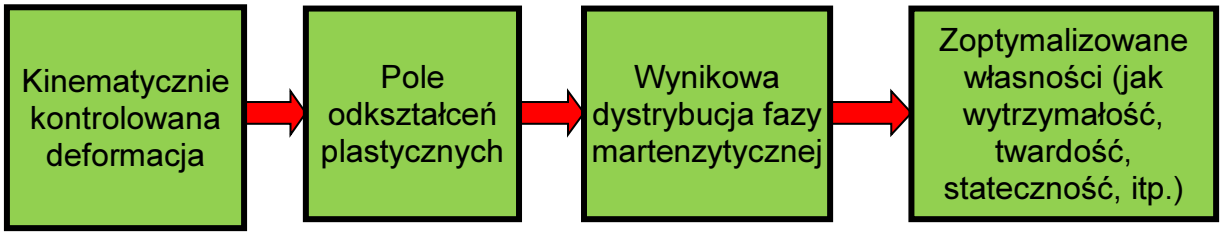

Rysunek 1.1. Koncepcja optymalizacji strukturalnej, wykorzystującej zjawisko przemiany fazowej indukowanej dokształceniem plastycznym

Dla zobrazowania koncepcji pokazanej na Rys. 1.1, przedstawiono przykład uzyskania elementu o strukturze gradientowej w wyniku skręcania (Rys. 1.2). Deformacja kontrolowana jest poprzez kąt skręcenia. Wynikowy rozkład odkształceń postaciowych w przekroju jest liniowy, co implikuje wynikowy rozkład fazy martenzytycznej, ponieważ jest on proporcjonalny do pola odkształceń plastycznych. Ze względu na występowanie progowej wartości odkształcenia, w środku przekroju zawartość fazy wtórnej jest teoretycznie zerowa.

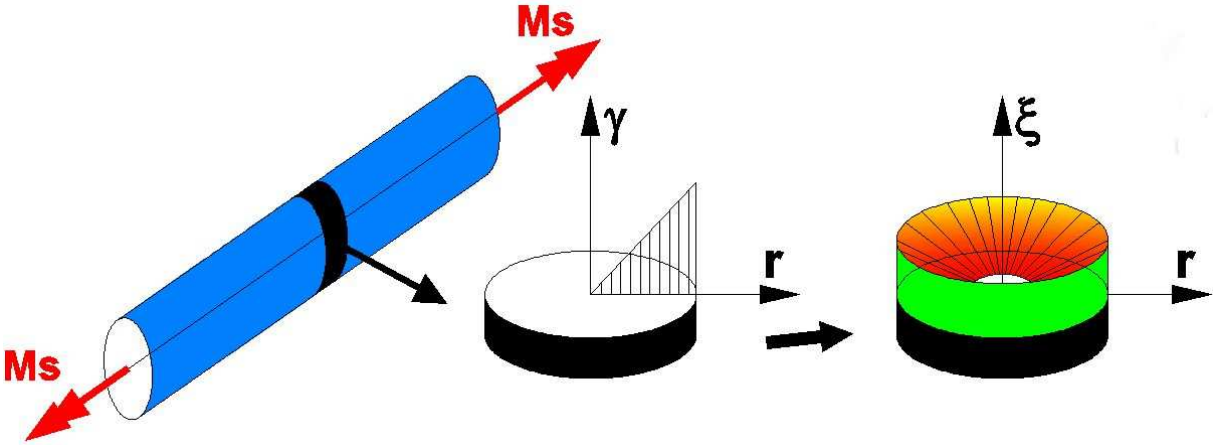

Rysunek 1.2. Element strukturalny o strukturze gradientowej, otrzymany w wyniku skręcania pręta o przekroju kołowym

Przedstawiony na Rys. 1.2 element strukturalny, charakteryzuje się wieloma pozytywnymi cechami w porównaniu z elementem o strukturze czysto austenitycznej. Mianowicie:

1. Posiada wyższą granicę plastyczności i wytrzymałości, które wynikają z wyższych własności mechanicznych fazy martenzytycznej w porównaniu z austenityczną. Brak martenzytu w środku próbki powoduje natomiast zachowanie wysokiej ciągliwości jej rdzenia.
2. Może przenosić wyższe obciążenia (momenty skręcające, siły rozciągające), dzięki obecności martenzytu.
3. Posiada lepszą odporność na zużycie warstwy zewnętrznej. Zawartość martenzytu jest tam najwyższa (Rys. 1.2). Twardość martenzytu jest około 3 krotnie wyższa od twardości austenitu.
4. Cechuje się wyższą siłą krytyczną oraz wyższą siłą w zakresie pokrytycznym. Wynikają one z przemiany fazowej zachodzącej w trakcie ściskania osiowego w zakresie plastycznym. Przemiana fazowa powoduje znaczne umocnienie materiału a zatem podwyższenie przenoszonego obciążenia.
5. Posiada lepszą wytrzymałość zmęczeniową, ponieważ inkluzje martenzytu hamują rozwój mikro-pęknięć.

Przedstawione powyżej pozytywne cechy stanowią motywację dla niniejszej pracy. Eksperymentalna weryfikacja tych cech została przeprowadzona, zaś wyniki zostały przedstawione w kolejnych rozdziałach pracy.

Zakres pracy:

1. Badania eksperymentalne:

1.1. Wytworzenie Elementu o Strukturze Gradientowej (FGSM) przy użyciu skręcania w temperaturach kriogenicznych (77K) oraz pokojowej (293K).

1.2. Porównanie zależności momentu skręcającego od kąta skręcenia dla elementu FGSM i elementu o strukturze austenitycznej.

1.3. Przeprowadzenie szeregu testów materiałowych na nowo wytworzonych elementach FGSM, takich jak: obserwacji mikroskopowych, badań mikrotwardości, pomiarów zawartości martenzytu na powierzchni przekroju.

1.4. Wytworzenie elementów FGSM w wyniku cyklicznego skręcania w temperaturach 77K oraz 293K. Pomiar momentu skręcającego w funkcji kąta skręcenia oraz pomiar ewolucji zawartości martenzytu w trakcie obciążania.

1.5. Przeprowadzenie szeregu testów cyklicznego skręcania w celu zbadania zjawiska przystosowania plastycznego.

1.6. Przeprowadzenie testów rozciągania nowo wytworzonych elementów FGSM, cechujących się zmiennym rozkładem fazy martenzytycznej.

1.7. Przeprowadzenie testów osiowego ściskania elementów FGSM oraz porównanie ich zachowania z odpowiedzią elementu klasycznego o strukturze austenitycznej.

2. Badania teoretyczne:

2.1. Zbudowanie i kalibracja wieloskalowego i wieloosiowego modelu konstytutywnego kontinuum, podlegającego przemianie fazowej typu RSC-RPC indukowanej odkształceniem plastycznym.

2.2. Wyprowadzenie zamkniętych rozwiązań analitycznych dla przypadku jednowymiarowego skręcania pręta, w którym zachodzi przemiana fazowa.

2.3. Zbudowanie modelu opisującego zależność siły od skrócenia pręta podlegającego osiowemu ściskaniu, w którym występuje przemiana fazowa.

3. Wieloosiowy model konstytutywny kontinuum podlegającego przemianie fazowej w temperaturach kriogenicznych

W niniejszym streszczeniu przedstawione zostały wyłącznie końcowe wzory opisujące pełny model trójwymiarowy.

Model konstytutywny składa się z następujących równań:

1. Związku pomiędzy naprężeniem a odkształceniem, przy czym odkształcenie termiczne zostało pominięte $\underline{\underline{\varepsilon}}^{th} = \underline{\underline{0}}$, zatem:

$$\underline{\underline{\sigma}} = \underline{\underline{\underline{\underline{E}}}} : \left(\underline{\underline{\varepsilon}} - \underline{\underline{\varepsilon}}^{p} - \underline{\underline{\varepsilon}}^{bs}\right) \tag{3.1}$$

2. Definicja tensora odkształcenia przemiany fazowej (tzw. “Bain-strain”):

$$\underline{\underline{\varepsilon}}^{bs} = \xi \cdot \frac{1}{3}\Delta v \underline{\underline{I}} \tag{3.2}$$

3. Równania opisującego kinetykę przemiany fazowej, indukowanej odkształceniem plastycznym:

$$\dot{\xi} = A(T) \cdot \dot{p} \cdot H\left[\left(\mathrm{p} - \mathrm{p}_{\xi}\right)(\xi_L - \xi)\right] \tag{3.3}$$

4. Definicję tensora prędkości odkształceń plastycznych (Eq. 3.144):

$$\underline{\underline{\dot{\varepsilon}}}^{p} = \dot{\lambda}\frac{3}{2}\frac{\left(\underline{\underline{s}}-\underline{\underline{X}}\right)}{\sqrt{\frac{3}{2}\left(\underline{\underline{s}}-\underline{\underline{X}}\right):\left(\underline{\underline{s}}-\underline{\underline{X}}\right)}} \tag{3.4}$$

5. Wzór na mnożnik plastyczności w stowarzyszonym prawie płynięcia (Eq. 3.165):

$$\dot{\lambda} = \frac{\frac{\frac{3}{2}\left(\underline{\underline{s}}-\underline{\underline{X}}\right)}{\sqrt{\frac{3}{2}\left(\underline{\underline{s}}-\underline{\underline{X}}\right):\left(\underline{\underline{s}}-\underline{\underline{X}}\right)}}:\left[\underline{\underline{\underline{\underline{E}}}}:\left(\underline{\underline{\dot{\varepsilon}}}-\frac{\dot{\xi}\Delta v\underline{\underline{I}}}{3}\right)\right]}{\left[\frac{\frac{3}{2}\left(\underline{\underline{s}}-\underline{\underline{X}}\right)}{\sqrt{\frac{3}{2}\left(\underline{\underline{s}}-\underline{\underline{X}}\right):\left(\underline{\underline{s}}-\underline{\underline{X}}\right)}}:\underline{\underline{\underline{\underline{E}}}}:\frac{\frac{3}{2}\left(\underline{\underline{s}}-\underline{\underline{X}}\right)}{\sqrt{\frac{3}{2}\left(\underline{\underline{s}}-\underline{\underline{X}}\right):\left(\underline{\underline{s}}-\underline{\underline{X}}\right)}}-C_X(\xi)-(1-\beta)\mathrm{C}_{a+m}\right]} \tag{3.5}$$

6. Równanie opisujące ewolucję zmiennej wzmocnienia kinematycznego $\underline{\underline{\dot{X}}}$ (Eq. 3.122):

$$\underline{\underline{\dot{X}}} = \frac{2}{3}[C_{a0}+C_{a0}h\xi+(1-\beta)\mathrm{C}_{a+m}]\underline{\underline{\dot{\varepsilon}}}^{p} = \frac{2}{3}C_X(\xi)\underline{\underline{\dot{\varepsilon}}}^{p} \tag{3.6}$$

7. Równanie ewolucji zmiennej wzmocnienia izotropowego $\dot{R}$ (Eq. 3.130):

$$\dot{R} = (1-\beta)\mathrm{C}_{a+m}\dot{p} \tag{3.7}$$

8. Definicję prędkości kumulowanego odkształcenia plastycznego $\dot{p}$:

$$\dot{p} = \sqrt{\frac{2}{3}\underline{\underline{\dot{\varepsilon}}}^{p}:\underline{\underline{\dot{\varepsilon}}}^{p}} \tag{3.8}$$

9. Wyrażenie na moduł styczny otrzymany w wyniku homogenizacji C_{a+m} (Eq. 3.120):

$$\mathrm{C}_{a+m} = \frac{E_a\cdot C_{a0}(1+h\xi)}{[E_a+C_{a0}(1+h\xi)]}\frac{\xi\frac{15}{2}\frac{(1-\nu_\mathrm{a})}{(4-5\nu_\mathrm{a})(1+\nu_\mathrm{a})}\left[\frac{\mathrm{E_m}}{(1+\nu_\mathrm{m})}-\frac{E_a\cdot C_{a0}(1+h\xi)}{[E_a+C_{a0}(1+h\xi)](1+\nu_\mathrm{a})}\right]}{\left[\frac{\mathrm{E_m}(1-\xi)}{(1+\nu_\mathrm{m})}+\frac{E_a\cdot C_{a0}(1+h\xi)}{[E_a+C_{a0}(1+h\xi)](1+\nu_\mathrm{a})}\left(\xi+\frac{(7-5\nu_\mathrm{a})}{2(4-5\nu_\mathrm{a})}\right)\right]} \tag{3.9}$$

10. Wyrażenie na moduł wzmocnienia $C_X(\xi)$ (Eq. 3.135):

$$C_X(\xi) = C_{a0}(1+h\xi)+\frac{(1-\beta)E_aC_{a0}(1+h\xi)}{2[E_a+C_{a0}(1+h\xi)]}\frac{\frac{15\xi\cdot(1-\nu_\mathrm{a})}{(4-5\nu_\mathrm{a})(1+\nu_\mathrm{a})}\left[\frac{\mathrm{E_m}}{(1+\nu_\mathrm{m})}-\frac{E_a\cdot C_{a0}(1+h\xi)}{[E_a+C_{a0}(1+h\xi)](1+\nu_\mathrm{a})}\right]}{\left[\frac{\mathrm{E_m}(1-\xi)}{(1+\nu_\mathrm{m})}+\frac{E_a\cdot C_{a0}(1+h\xi)}{[E_a+C_{a0}(1+h\xi)](1+\nu_\mathrm{a})}\left(\xi+\frac{(7-5\nu_\mathrm{a})}{2(4-5\nu_\mathrm{a})}\right)\right]} \tag{3.10}$$

Przedstawiony powyżej model konstytutywny posiada 12 parametrów materiałowych:

1. Parametry związane z przemianą fazową

$A(T)$	ε_ξ^p	ξ_L	Δv

2. Parametry związane z kontinuum dwufazowym:

E_a	C_{a0}	ν_a	$\mathrm{E_m}$	ν_m	h	β	ε_0

4. Jednoosiowy model konstytutywny kontinuum podlegającego przemianie fazowej indukowanej odkształceniem plastycznym

Dla przypadku skręcania, równanie kinetyki przemiany fazowej określa związek pomiędzy prędkością przyrostu zawartości martenzytu a prędkością przyrostu plastycznego odkształcenia postaciowego. Ponieważ zależność ta jest liniowa, można ją scałkować i otrzymać zawartość martenzytu w funkcji odkształcenia postaciowego:

$$\xi = \begin{cases} 0, & \gamma^p \le \gamma_\xi^p \\ A(T)\cdot\left(\gamma^p - \gamma_\xi^p\right) & \gamma_\xi^p < \gamma^p \le \gamma_L^p \\ \xi_L & \gamma^p > \gamma_L^p \end{cases} \tag{4.1}$$

Tak więc, jeśli odkształcenie γ^p nie przekracza wartości progowej γ_ξ^p przemiana nie zachodzi. W zakresie odkształceń $\gamma_\xi^p \div \gamma_L^p$ zawartość martenzytu jest proporcjonalna do okształcenia, zaś dla $\gamma^p > \gamma_L^p$ zawartość fazy wtórnej osiągnęła próg nasycenia (Rys. 4.1).

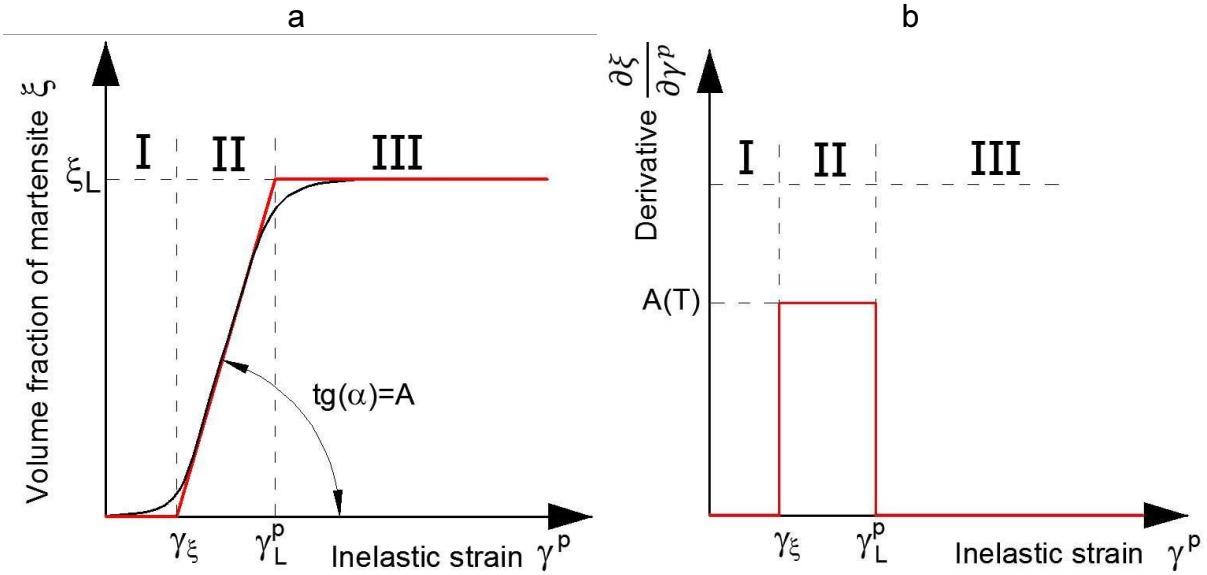

Rysunek 4.1 a) Objętościowa zawartość martenzytu w funkcji plastycznego odkształcenia postaciowego, b) pochodna $\partial\xi/\partial\gamma^p$

Dla jednowymiarowego przypadku skręcania, model konstytutywny sprowadza się do jednej zależności funkcyjnej naprężenia stycznego τ od odkształcenia postaciowego γ (Rys. 4.2).

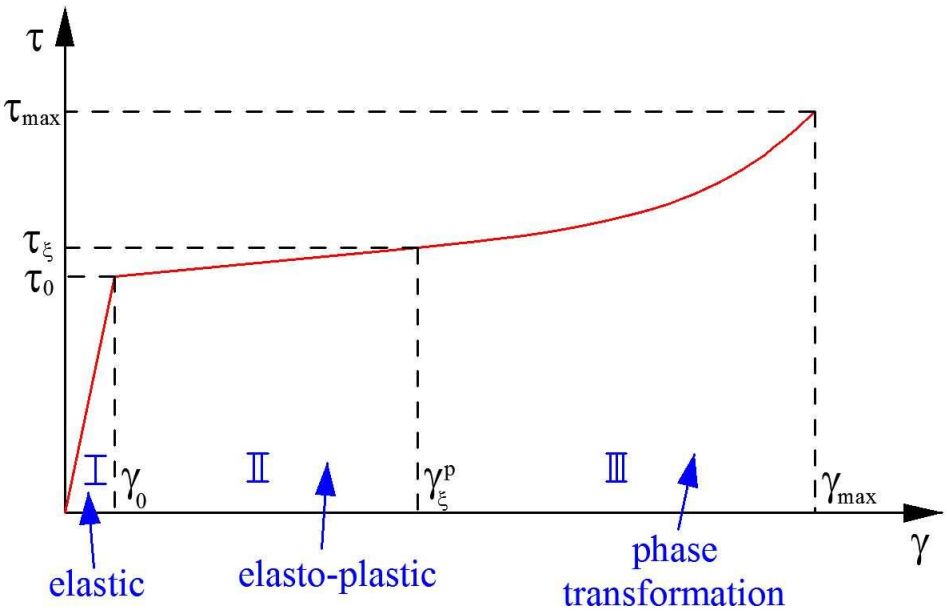

Rysunek 4.2. Jednowymiarowy model konstytutywny przemiany fazowej indukowanej odkształceniem postaciowym

Wyprowadzenia wzorów zostały szczegółowo przedstawione w Rozdziale 4. W tym miejscu przytoczone zostały jedynie wzory końcowe, zgodnie z Rys. 4.2:

$$\tau_I = G \cdot \gamma \qquad \boldsymbol{\gamma < \gamma_0} \tag{4.2}$$

$$\tau_{II} = \tau_0 + C_{a0} \cdot (\gamma - \gamma_0) \qquad \boldsymbol{\gamma_0 < \gamma < \gamma_\xi^p} \tag{4.3}$$

$$\tau_{III} = \tau_\xi + \frac{1}{2} C_{a0}\left(\gamma - \gamma_\xi^p\right)\left[2 + Ah\left(\gamma - \gamma_\xi^p\right)\right] + \\ + \frac{15 C_{a0}(1-\nu_a)}{8A(-4+\nu_a+5\nu_a^2)}\left[A\left(\gamma - \gamma_\xi^p\right)\left(2 + \left(2 + A\left(\gamma - \gamma_\xi^p\right)\right)h\right) + 2(1+h) ln\left(1 - A\left(\gamma - \gamma_\xi^p\right)\right)\right]$$

$$\boldsymbol{\gamma_\xi^p < \gamma < \gamma_{max}} \tag{4.4}$$

Podobnie zostały przedstawione końcowe wzory opisujące zależność momentu skręcającego od jednostkowego kąta skręcenia (Rozdział 4):

$$M_I(\theta) = \frac{\pi R^4 G}{2}\theta \tag{4.5}$$

$$M_{II}(\theta) = A_1 + A_2 \cdot \theta + A_3 \cdot \frac{1}{\theta^3} \tag{4.6}$$

$$M_{III}(\theta) = B_1\theta^{-3} + B_2\theta^{-2} + B_3\theta^{-1} + B_4 + B_5\theta + B_6\theta^2 + B_7\theta^{-3} ln\left[1 - A\left(\theta R - \gamma_\xi^p\right)\right] \\ + B_8 ln\left[1 - A\left(\theta R - \gamma_\xi^p\right)\right] \tag{4.7}$$

Stałe A_1, A_2, A_3 oraz $B_1 \div B_8$ zostały podane w Rozdziale 4.

5. Zestaw eksperymentalny do testów skręcania w temperaturach 77K i 293K

Model zestawu eksperymentalnego pokazano na Rys. 5.1, zaś gotową próbkę ze stali 304 na Rys. 5.2.

W trakcie wykonywania testów w temperaturze 77K kriostat był wypełniony ciekłym azotem. Pomiar kąta skręcenia wykonywany był na wydrukowanej podziałce, zaś momentu skręcającego przy pomocy klucza dynamometrycznego.

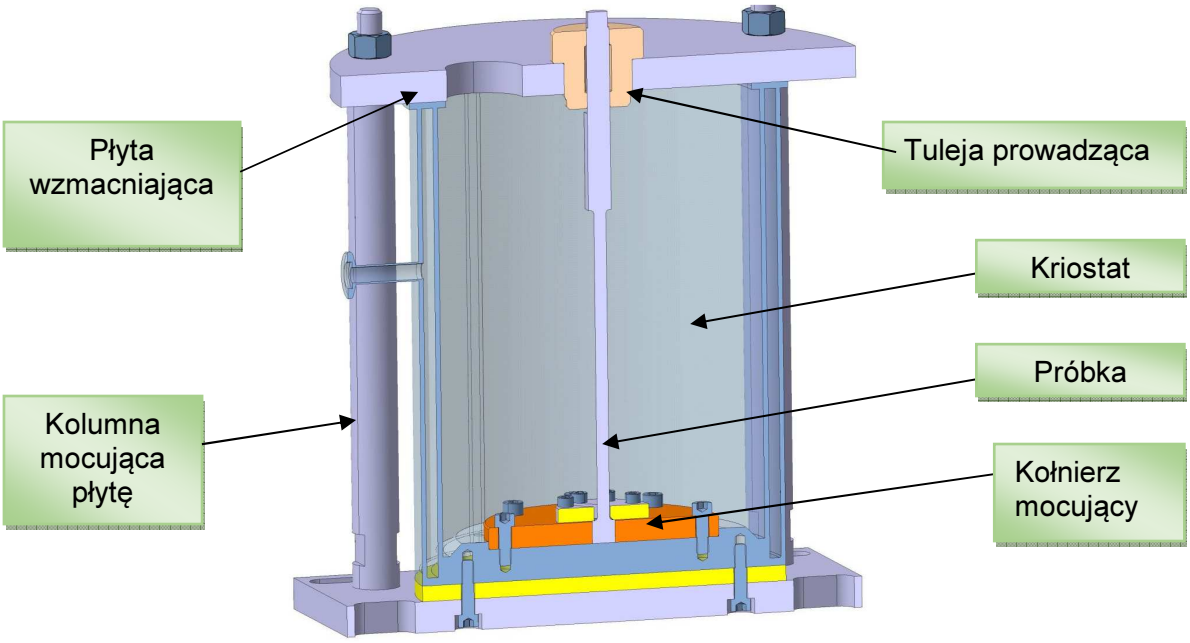

Rysunek 5.1. Model układu eksperymentalnego do testów skręcania

Rysunek 5.2. Geometria próbki, stal austenityczna 304

6.1. Analiza mikroskopowa elementów FGSM

Wykonano szereg zdjęć mikroskopowych na przekrojach poprzecznych prętów o strukturze gradientowej. Dwa przykładowe zdjęcia zostały pokazane na Rys. 6.1 a, b. Późniejsza analiza wykazała nieznacznie większą zawartość martenzytu w próbce 2 (Rys. 6.1a) niż w próbce 1 (Rys. 6.1b). Maksymalna zawartość na powierzchni próbki wynosiła ok. 50%.

a b

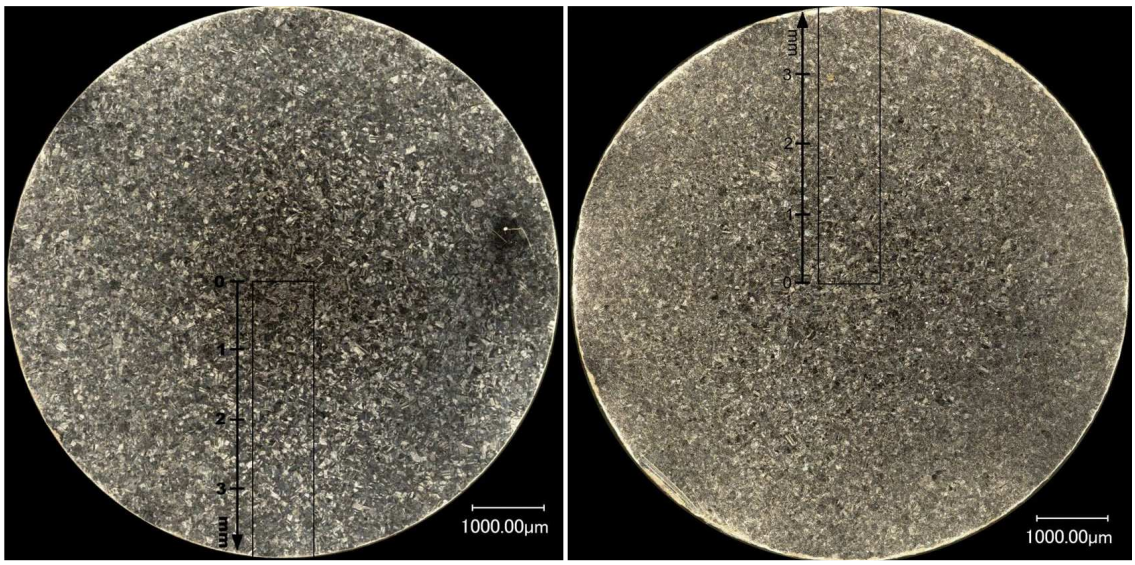

Rysunek 6.1 a) Mikrostruktura próbki 2 skręconej w temp. 77K do 870°, b) próbka 1 skręcona w temp. 293K do zniszczenia

6.2. Badania mikrotwardości

Pomiary mikrotwardości zostały wykonane dla 5 próbek. Dla każdej z nich dokonano pomiarów w 3 przekrojach poprzecznych, a na każdym z przekrojów wzdłuż 4 promieni. Średnie wyniki dla wszystkich próbek zostały pokazane na Rys. 6.2.
Dla próbek surowych ze stali 304L i 304 mikrotwardość jest stała wzdłuż promienia, zgodnie z oczekiwaniami. Dla pozostałych próbek o niezerowym rozkładzie martenzytu. mikrotwardość rośnie osiągając maksimum na powierzchni zewnętrznej, potwierdzając tym samym rosnącą zawartość martenzytu wzdłuż promienia przekroju.

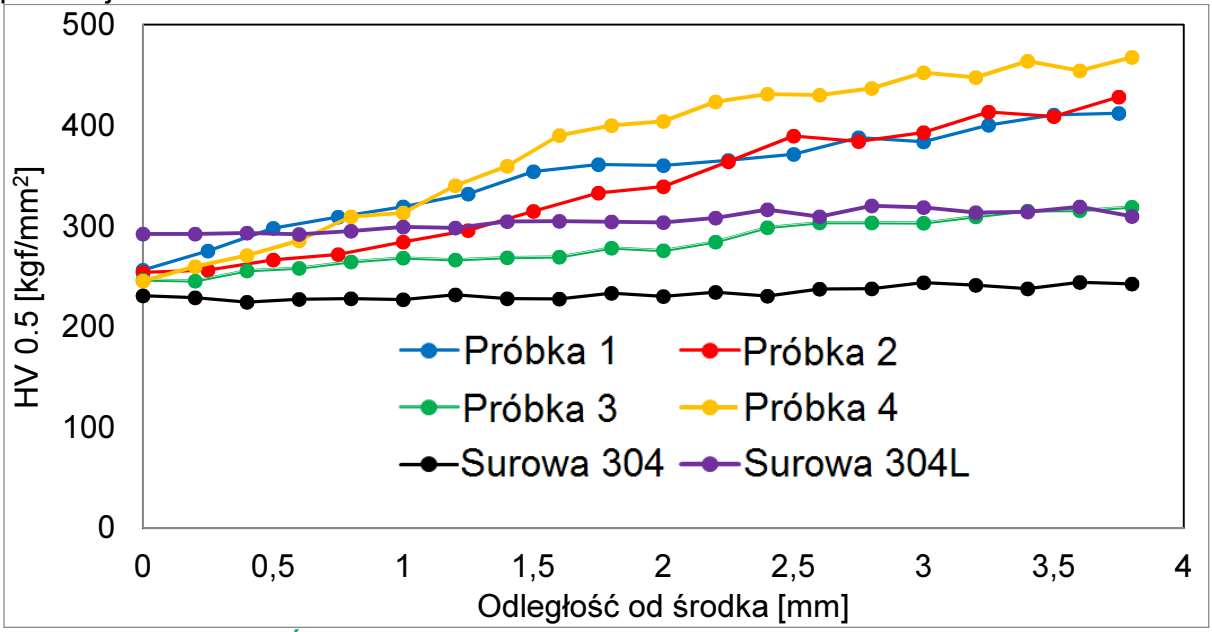

Rysunek 6.2. Średnie wartości mikrotwardości dla wszystkich przekrojów poprzecznych, jedna próbka ze stali 304L, pozostałe ze stali 304

6.3. Pomiary zawartości martenzytu

Pomiary zawartości martenzytu zostały wykonane dla 4 próbek i 3 przekrojów poprzecznych w każdej z nich. Przykładowy wynik dla próbki 2, skręconej w temp. 77K do kąta 870°, został pokazany na Rys. 6.3. Jak widać, maksymalna zawartość na powierzchni próbki wynosi ok. 50%, zaś w środku próbki ok. 10%.

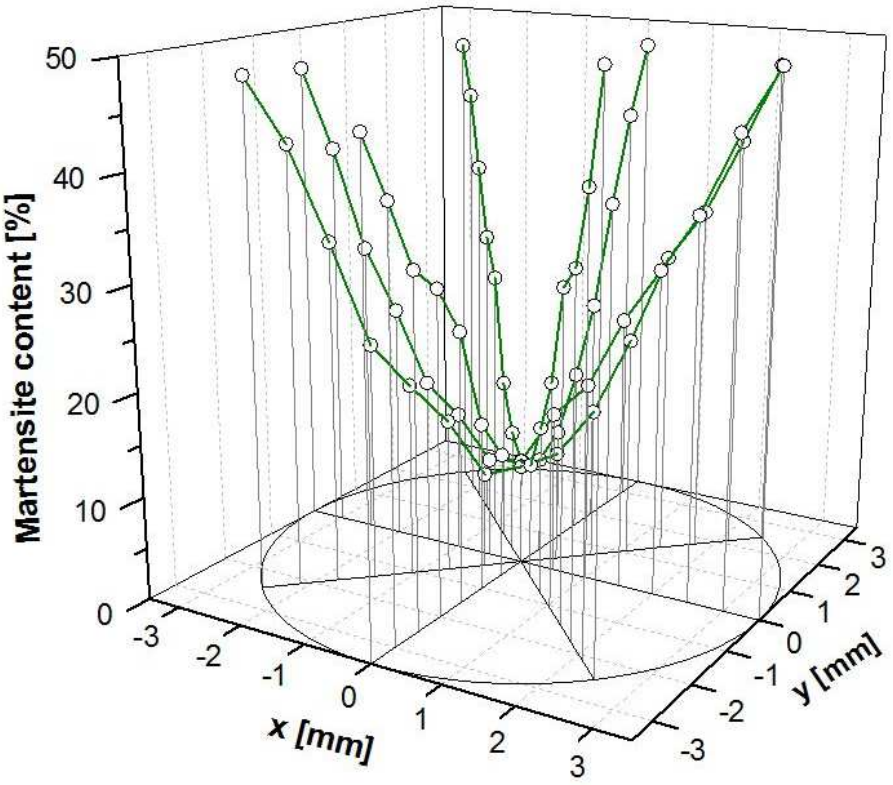

Rysunek 6.3. Zawartość martenzytu w przekroju próbki 2 (skręconej w temp. 77K do 870°), przekrój numer 1

7. Testy skręcania: pręty o przekroju kołowym ze stali austenitycznych 304L, 316L and 316LN

Podsumowanie wyników testów skręcania przedstawiono na Rys. 7.1. Jak widać maksymalne wartości momentu skręcającego są podobne dla wszystkich próbek. Jednak charakter krzywych oraz maksymalna wartość kąta skręcenia różnią się znacznie.

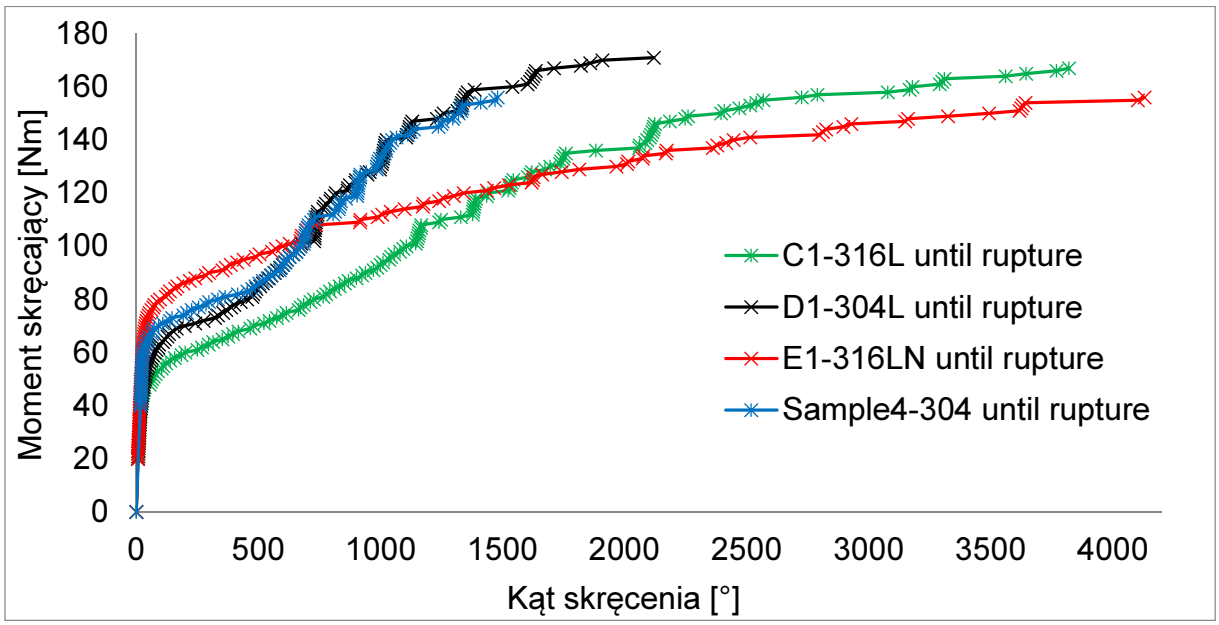

Rysunek 7.1. Moment skręcający w funkcji kąta skręcenia, test skręcania do zniszczenia w temp. 77K, próbki C1, D1, E1, Sample4.

8. Porównanie wyników eksperymentalnych i teoretycznych

Na Rys. 8.1 przedstawiono zestawienie wyników eksperymentalnych oraz teoretycznych na podstawie równań modelu konstytutywnego dla próbek skręcanych w temperaturze 293K. Zgodność wyników jest bardzo dobra dla kątów poniżej 992° (granica modelu wynikająca z teorii małych odkształceń).
Na Rys. 8.2 przedstawiono wyniki testów w temperaturze ciekłego azotu (77K) dla 4 różnych próbek oraz wynik teoretyczny. Otrzymane wyniki pokazują rozbieżność zachowania pomiędzy poszczególnymi próbkami. Wraz z nimi zestawiono wynik teoretyczny, który z wystarczającą dokładnością pokrywa się wynikami testów.

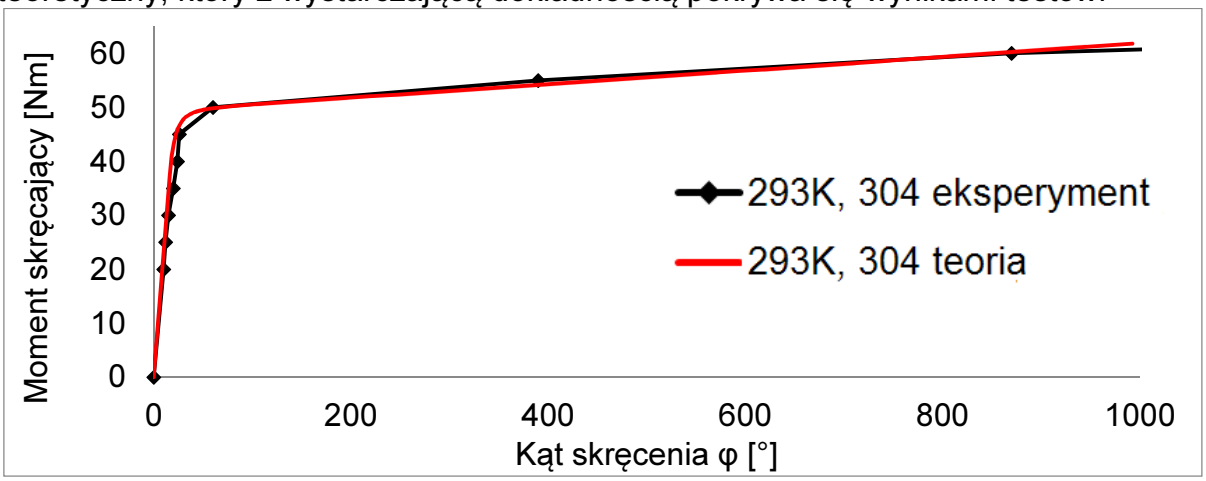

Rysunek 8.1. Teoretyczne i eksperymentalne zależności pomiędzy momentem skręcającym a kątem skręcenia dla stali 304, temperatura 293K

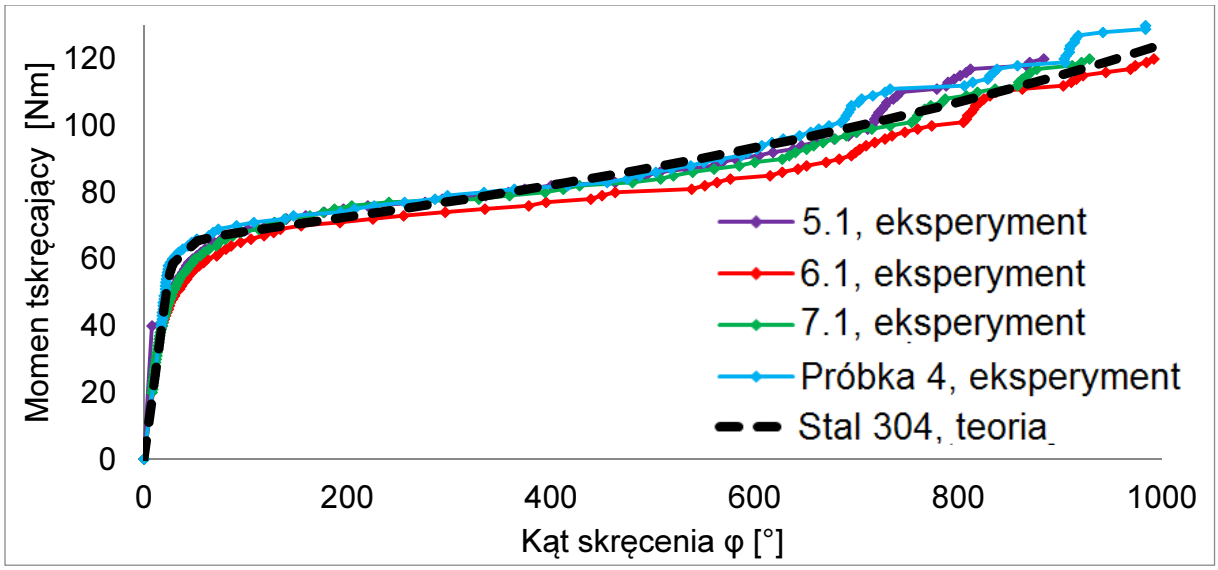

Rysunek 8.2. Wyniki eksperymentalne i teoretyczne dla próbek ze stali 304 skręconych w temperaturze 77K

9. Cykliczne skręcanie prętów w temperaturach 77K i 293K

W ramach niniejszej pracy wykonano szereg testów cyklicznego skręcania w temp. 77K oraz 293K, zarówno przy sterowaniu momentem skręcającym jak i kątem skręcenia. Dokonano również pomiarów zawartości martenzytu na powierzchni pręta, oraz wzdłuż jego długości po każdym półcyklu obciążenia.
Przykładowy wynik dla próbki oznaczonej A2 ze stali 304 przedstawiono na Rys. 9.1.

Próbka ta została poddana cyklicznemu skręcaniu w temp. 77K, przy sterowaniu momentem skręcającym ±80Nm. Wykonano 10 pełnych cykli. Wyniki ewolucji zawartości martenzytu zostały przedstawione na Rys. 9.2, gdzie „hf" oznacza półcykl obciążenia.
Jak widać zawartość martenzytu przed testem jest bliska zeru. W trakcie testu zawartość wtórnej fazy narasta osiągając wartość 27% po 10 cyklach. Należy pamiętać, że wynik ten oznacza, iż maksymalna zawartość na powierzchni próbki wynosi 27%, zaś rozkład jest podobny do paraboloidy, tak jak dla próbki 2 (Rys. 6.3).

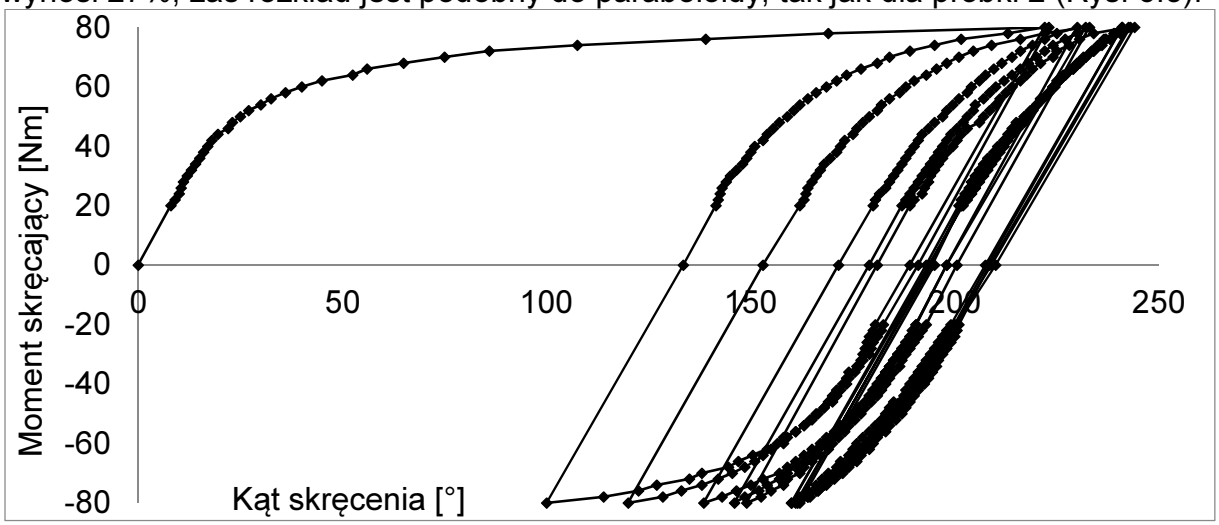

Rysunek 9.1. Moment skręcający w funkcji kąta skręcenia, próbka A2, ±80Nm, 10 cykli w temp. 77K

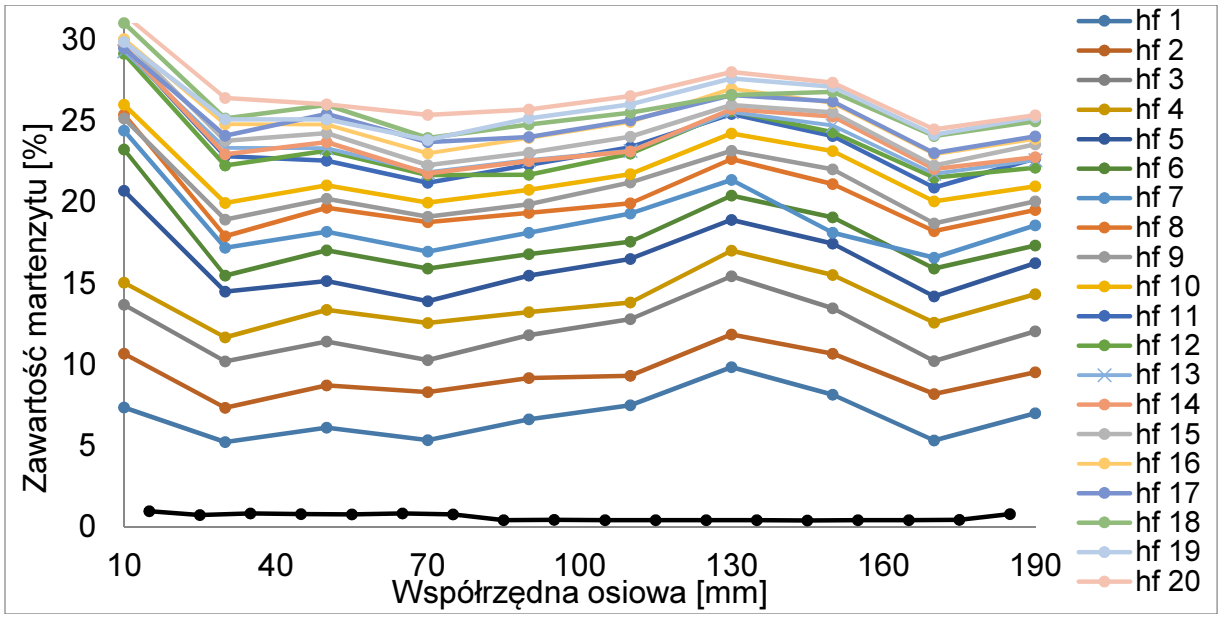

Rysunek 9.2. Zawartość martenzytu na powierzchni próbki po każdym półcyklu obciążenia, próbka A2, ±80Nm, 10 cykli w temp. 77K

10. Przystosowanie plastyczne do obciążeń cyklicznych

Wzmocnienie plastyczne powoduje zwiększenie granicy plastyczności. Przy obciążeniach cyklicznych sterowanych siłowo, następuje proces cyklicznego umacniania. Jeśli szerokość pętli histerezy zmaleje do zera oznacza to, że nie występuje już rozpraszanie energii. Gdy jednak pozostaje jeszcze jakaś niewielka stała dyssypacja w kolejnych cyklach, mówimy o przystosowaniu plastycznym.

Energia dyssypowana została wyliczona na podstawie testów cyklicznego skręcania. Wyniki zostały przedstawiona na Rys. 10.1. Wszystkie próbki były wykonane ze stali austenitycznej 304. Jak widać w temp. pokojowej (próbka A8), dyssypacja jest znacznie większa, gdyż umocnienie postępuje znacznie wolniej. W temperaturze 77K, już po dwóch cyklach dyssypacja osiąga znacznie mniejsze wartości.

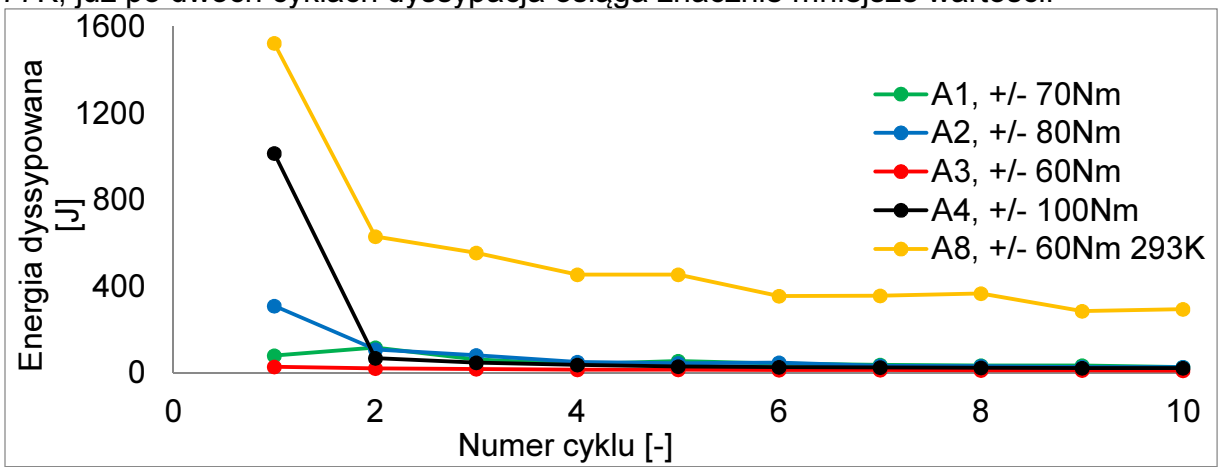

Rysunek 10.1. Energia dyssypowana podczas cyklicznego skręcania w temp. 77K. próbki wykonane ze stali 304

W pracy wykazano, że w przypadku przemiany fazowej typu RSC-RPC zachodzi zjawisko przyspieszonego przystosowania plastycznego do obciążeń cyklicznych, które wynika ze zmian mikrostrukturalnych polegających na zastąpieniu plastycznej matrycy austenitycznej sprężystymi inkluzjami nowej fazy.

11. Test rozciągania w temperaturze pokojowej

Podsumowanie wyników testów rozciągania przedstawiono na Rys. 11.1. W porównaniu do próbki surowej („raw") naprężenie maksymalne wzrosło dwukrotnie dla próbek 41, 1, A10.1 zawierających pow. 50% martenzytu na powierzchni.

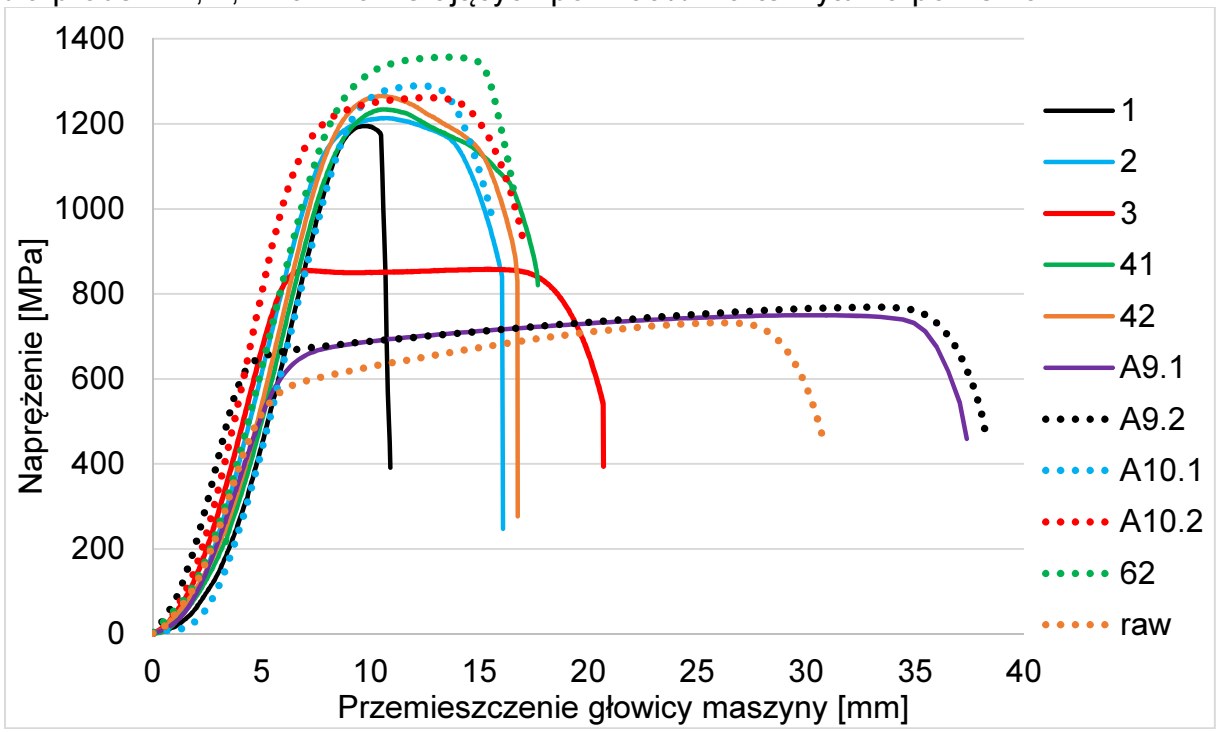

Rysunek 11.1. Naprężenie w funkcji przemieszczenia głowicy maszyny wytrzymałościowej

12. Wyboczenie kolumn o strukturze gradientowej - eksperyment

Wyniki testów osiowego ściskania dla zestawu próbek ze stali 304 zostały pokazane na Rys. 12.1.

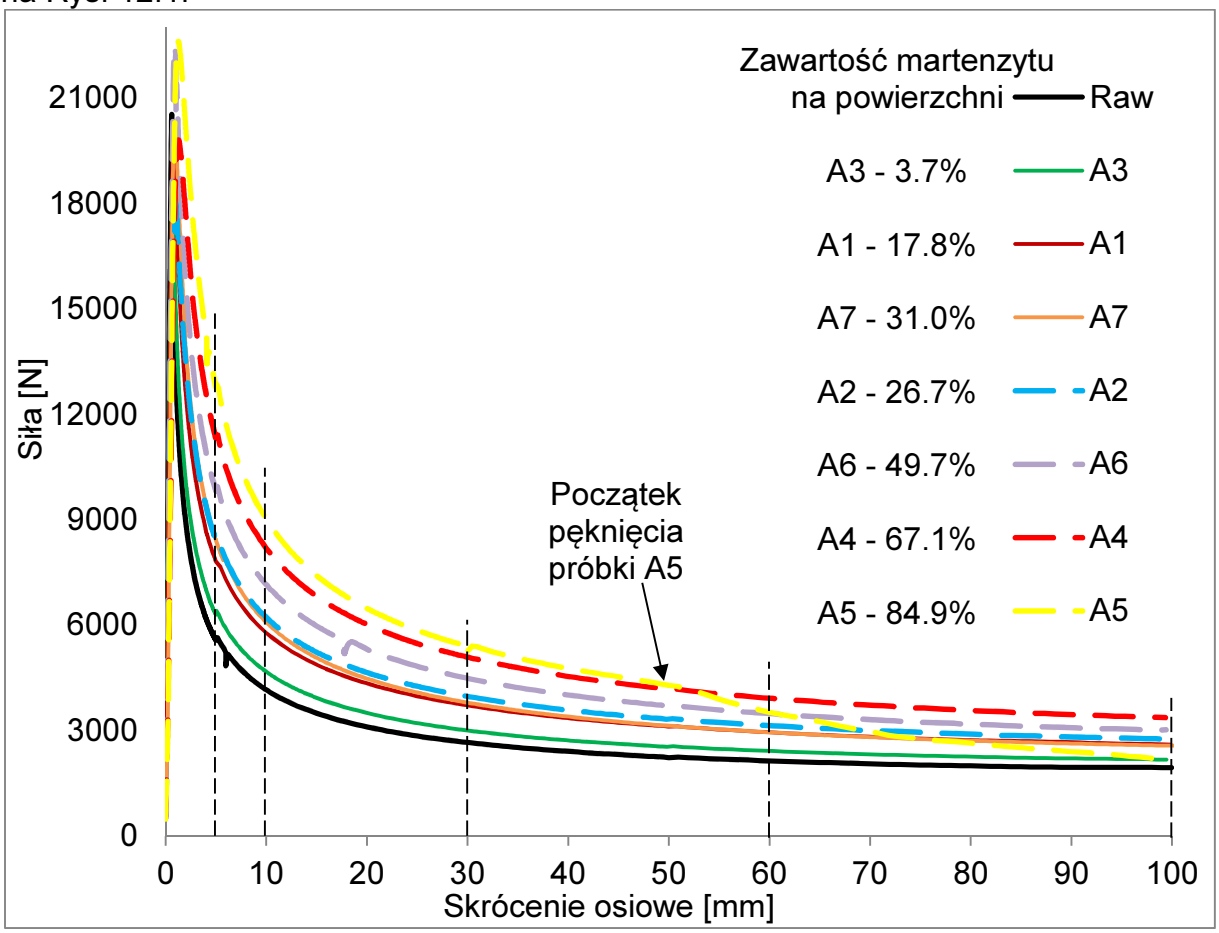

Rysunek 12.1 Siła w funkcji skrócenia osiowego dla wszystkich testowanych próbek

W porównaniu z próbką surową (Raw), przenoszona siła okazała się większa dla wszystkich próbek FGSM. Im większa zawartość martenzytu tym większe obciążenie może przenieść próbka.

13. Wyboczenie kolumn o strukturze gradientowej - modelowanie

Wyniki doświadczalne zostały skorelowane z analizą utraty stateczności kolumny za pomocą dwóch modeli: modelu jednorodnego oraz modelu warstwowego. Obydwa modele zostały zbudowane w programie ANSYS, a obliczenia wykonano metodą elementów skończonych. W modelu jednorodnym przyjęto identyczny opis konstytutywny materiału w całej objętości kolumny. W modelu warstwowym przyjęto natomiast inne zależności naprężenia od odkształcenia w poszczególnych warstwach, w funkcji zawartości fazy wtórnej (martenzytu). Model warstwowy o budowie koncentrycznej, okazał się szczególnie wartościowy z punktu widzenia uwzględnienia ewolucji mikrostruktury w analizie stateczności kolumny typu FGSM (Rys. 13.1).

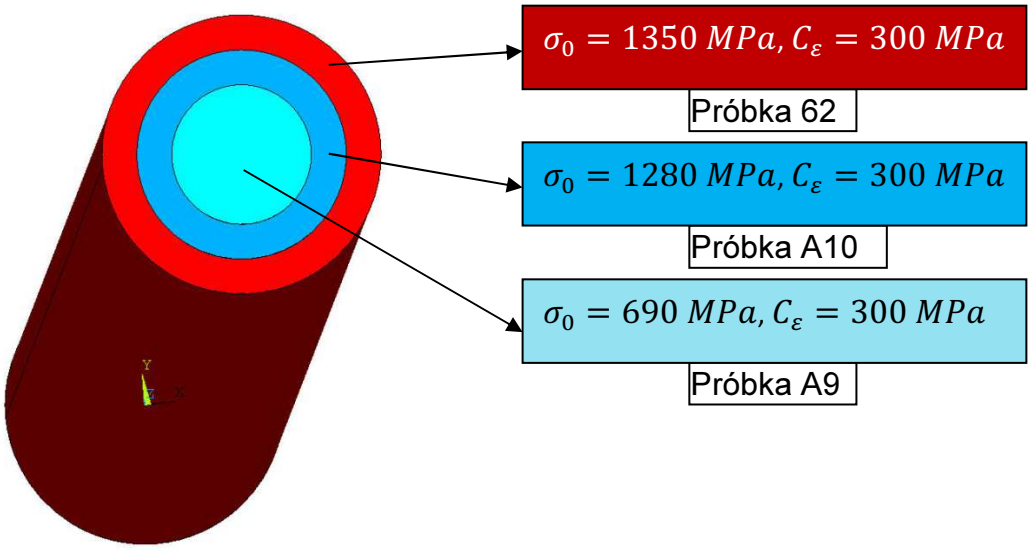

Rysunek 13.1 Model warstwowy kolumny FGSM, analizowany metodą elementów skończonych

14. Podsumowanie i wnioski

Najważniejszymi wnioskami z niniejszej pracy są:

1. Zademonstrowanie możliwości sterowania mikrostrukturą przy pomocy kąta skręcenia, zarówno przy skręcaniu monotonicznym jak i cyklicznym.
2. Potwierdzone ulepszone właściwości mechaniczne Elementów o Strukturze Gradientowej (FGSM) pod kątem wyższej granicy plastyczności, wytrzymałości, możliwości przenoszenia wyższych obciążeń (nawet do 100%), wyższej siły krytycznej, lepszego zachowania w zakresie pokrytycznym oraz lepszej odporności na zużycie ze względu na wyższą twardość powierzchni.
3. Wieloskalowy model konstytutywny, uwzględniający ewolucję fazy wtórnej w trakcie procesu obciążania, z wystarczającą dokładnością opisał wyniki skręcania prętów o przekroju kołowym w temperaturach: ciekłego azotu (77K) i pokojowej (293K).
4. Istotnym osiągnięciem jest znalezienie zamkniętego rozwiązania analitycznego problemu skręcania prętów o przekroju kołowym, które podlegają ciągłej bezdyfuzyjnej przemianie fazowej. W szczególności otrzymano zamkniętą zależność momentu skręcającego od kąta skręcenia.

4. W pracy wykazano ponadto efekt przyspieszonego przystosowania plastycznego elementów strukturalnych, które podlegają przemianie fazowej od struktury austenitycznej do struktury martenzytycznej. Efekt ten nazwano plastycznym przystosowaniem mikrostrukturalnym.
4. Model numeryczny (MES) o strukturze koncentrycznej, warstwowej, z dobrą dokładnością opisuje zależność siły od skrócenia osiowego (ugięcia) dla próbek o różnej dystrybucji martenzytu.

15. References

1. Angel, T.J. 1954. Formation of martensite in austenitic stainless steels. Journal of the Iron and Steel Institute 177, 165-174.
2. Backer, F.D., Schoss, V., Maussner, G. 2001. Investigations on the evaluation of the residual fatigue life-time in austenitic stainless steels. Nuclear Engineering and Design 206, 201–219.
3. Beese, A.M., Mohr, D. 2011. Effect of stress triaxiality and Lode angle on the kinetics of strain-induced austenite-to-martensite transformation. Acta Materialia 59, 2589–2600.
4. Beese, A.M., Mohr, D. 2012. Anisotropic plasticity model coupled with Lode angle dependent strain-induced transformation kinetics law. Journal of the Mechanics and Physics of Solids 60, 1922–1940.
5. Bhattacharyya, A., Weng, G.J. 1994. An energy criterion for the stress-induced martensitic transformation in a ductile system. J. Mech. Phys. Solids 42, 1699-1724.
6. Boers, S.H.A., Geers, M.G.D., Kouznetsova, V.G., 2010. Exp. Mech. 50, 683-693.
7. Cakmak, E., Choo, H., An, K., Ren, Y. 2012. A synchrotron X-ray diffraction study on the phase transformation kinetics and texture evolution of a TRIP steel subjected to torsional loading. Acta Materialia, Volume 60, Issue 19. 6703-6713.
8. Cherkaoui, M., Berveiller, M., Lemoine, X., 1998. Micromechanical modeling of martensitic transformation induced placidity (TRIP) in austenitic single crystals. Int. J. Plasticity 14 (7), 597-626.
9. Cherkaoui, M., Berveiller, M., Lemoine, X., 2000. Couplings between plasticity and martensitic phase transformation: overall behavior of polycrystalline TRIP steels. Int. J. Plasticity 16 (10-11), 1215-1241.
10. Choi, K.S., Liu, W.N., Sun, X., Khaleel, M.A. 2009. Microstructure-based constitutive modeling of TRIP steel: Prediction of ductility and failure modes under different loading conditions. Acta Materialia, Volume 57, Issue 8, 2592-2604.
11. Colak, O.U., Krempl, E. 2005. Modeling of the monotonic and cyclic Swift effects using an isotropic, finite viscoplasticity theory based on overstress (FVBO). International Journal of Plasticity 21, 573-588.
12. Curtze, S., Kuokkala, V.T., Hokka, M., Peura, P., 2009. Deformation behavior of TRIP and DP steels in tension at different temperatures over a wide range of strain rates. Materials Science and Engineering A 507, 124–131.
13. Dan, W.J., Li, S.H., Zhang, W.G., Lin, Z.Q. 2008. The effect of strain-induced martensitic transformation on mechanical properties of TRIP steel. Materials and Design 29, 604-612.
14. Dan, W.J., Zhang, W.G., Li, S.H., Lin, Z.Q. 2007. A model for strain-induced martensitic transformation of TRIP still with strain rate. 2007. Computational Materials Science 40, 101-107.
15. Das, A., Tarafder, S. 2009. Experimental investigation on martensitic transformation and fracture morphologies of austenitic stainless steel. International Journal of Plasticity, Voume 25, Issue 11, 2222-2247.
16. de Souza Neto, E.A., Perić, D., Owen, D.R.J. 2008. Computational Methods for Plasticity: Theory and Applications. United Kingdom: John Wiley & Sons.
17. De, A.K., Murdock, D.C., Mataya, M.C., Speer, J.G., Matlock, D.K. 2004. Quantitative measurements of deformation-induced martensite in 304 stainless steel by X-ray diffraction. Scripta Materialia. 50, 1445-1449.

18. Delannay, L., Jacques, P., Pardoen, T., 2008. Modelling of the plastic flow of trip-aided multiphase steel based on an incremental mean field approach. Int. J. Solids Struct. 45, 1825–1843.
19. Diani, J.M., Berveller, M., Sabar, H. 1996. Incremental micromechanical modelling of the transformation induced plasticity, J. Phys. 6, C1, 419–427.
20. Diani, J.M., Sabar, H., Berveiller, M. 1995a. Micromechanical modelling of the transformation induced plasticity (TRIP) phenomenon in steels. Int. J. Engng Sci. Vol. 33, 1921-1934.
21. Diani, J.M., Soler, M., Berveller, M., Sabar, H. 1995b. Elasto-plastic micro–macro modelling of solid–solid phase transformation: application to transformation induced plasticity, J. Phys. 5, C2, 507-512.
22. Doghri, I., Ouaar, A., 2003. Homogenisation of two-phase elasto-plastic composite materials and structures: study of tangent operators, cyclic plasticity and numerical algorithms. International Journal of Solids and Structures 40 (7), 1681–1712.
23. Doghri, I., Tinel, L., 2005. Micromechanical modelling and computational of elasto-plastic materials reinforced with distributed-orientation fibers. International Journal of Plasticity 21, 1919-1940.
24. Eshelby JD. The determination of the elastic field of an ellipsoidal inclusion and related problems. Proceedings of the Royal Society of London, Series A 1957, 241, 376-396.
25. Fischer, F.D. 1990. A micromechanical model for transformation plasticity in steels, Acta Metall. Mater. 38, 1535–1546.
26. Fischer, F.D. 1992. Transformation induced plasticity in triaxially loaded steel specimens subjected to a martensitic transformation, Eur. J. Mech. A/Solids 11, 233–244.
27. Fischer, F.D., Oberaigner, E.R., Tanaka, K., Nishimura, F. 1998. Transformation induced plasticity revised an updated formulation, Int. J. Solids Struct. 35, 2209–2227.
28. Fischer, F.D., Schlögl, S.M., 1995. The infuence of material anisotropy on transformation induced plasticity in steel subject to martensitic transformation. Mech. Mater. 21, 1-23.
29. Fischer, F.D., Sun, Q.P., Tanaka, K. 1996. Transformation-induced plasticity (TRIP), Appl. Mech. Rev. 49, 317–364.
30. Fischlschweiger, M., Cailletaud, G., Antretter, T. 2012. A mean-filed model for transformation induced plasticity including backstress effects for non-proportional loadings. International Journal of Plasticity 37, 53-71.
31. Fisher, F.D., Reisner, G., Werner, E., Tanaka, K., Cailletaud, G., Antretter, T., 2000. A new view on transformation induced plasticity (TRIP). Int. J. Plast. 16, 723–748.
32. Garion, C., Skoczeń, B., Sgobba, S. 2006. Constitutive modelling and identification of parameters of the plastic strain-induced martensitic transformation in 316L stainless steel at cryogenic temperatures. International Journal of Plasticity, Volume 22, Issue 7, 1234-1264.
33. Glage, A., Weider, M., Hasterok, M., Weidner, A., Eigenfeld, K., Aneziris, C.G., Biermann, H. 2011. Mechanical properties of metal matrix composites based on TRIP steel and ZrO_2 ceramic foams. Procedia Engineering 10, 548–555.
34. Glage, A., Weidner, A., Biermann, H. 2009. Effect of austenite stability on the low cycle fatigue behavior and microstructure of high alloyed metastable austenitic cast TRIP steels. Procedia Engineering 2, 2085-2094.

35. Greenwood, G.W., Johnson, R.H., 1965. The deformation of metals under small stresses during phase transformation. Proc. Roy. Soc. A 283, 403.
36. Gussev, M.N., Busby, J.T., Byun, T.S., Parish, C.M. 2013. Twinning and martensitic transformations in nickel-enriched 304 austenitic steel during tensile and indentation deformations. Materials Science & Engineering A 588, 299–307.
37. Hallberg, H., Hakansso, P., Ristinmaa, M. 2007. A constitutive model for the formulaton of martensite in austenitic steels under large strain plasticity. International Journal of Plasticity, 23 (7), 1213-1239.
38. Han, H.N., Lee, C.G., Oh, C.-S., Lee, T.-H., Kim, S.-J., 2004. A model for deformation behavior and mechanically induced martensitic transformation of metastable austenitic steel. Acta Mater. 52, 5203–5214.
39. Hong Chul Shin, Tae Kwon Ha, Young Won Chang, 2001. Kinetics of deformation induced martensitic transformation in a 304 stainless steel. Scripta Materialia 45, 823-829.
40. Idesman, A.V., Levitas, V.I., Preston, D.L., Cho, J.-Y. 2005. Finite element simulations of martensitic phase transitions and microstructures based on a strain softening model. Journal of the Mechanics and Physics of solids, 53, 495-523.
41. Iwamoto, T., Tsuta, T., Tomita, Y. 1998. Investigation on deformation mode dependence of strain-induced martensitic transformation in trip steels and modelling of transformation kinetics. International Journal of Mechanical Sciences, Volume 40, Issues 2-3, 173-182.
42. Jacques, P., Furnémont, Q., Pardoen, T., Delannay, F. 2001. On the role of martensitic transformation on damage and cracking resistance in TRIP-assisted multiphase steels. Acta Materialia, Volume 49, Issue 1, 139-152.
43. Kisko, A., Misra, R.D.K., Talonen, J., Karjalainen, L.P. 2013. The influence of grain size on the strain-induced martensite formation in tensile straining of an austenitic 15Cr–9Mn–Ni–Cu stainless steel. Materials Science & Engineering A 578, 408–416.
44. Koistinen, D.P., Marburger, R.E. 1959. A general equation prescribing the extent of the austenite-martensite transformation in pure iron-carbon alloys and plain carbon steels. Acta Metallurgica 7, 59-60.
45. Krajewski, S., Nowacki, J. 2014. Dual-phase steels microstructure and properties consideration based on artificial intelligence techniques. Archives of civil and mechanical engineering 14, 278-286.
46. Kubler, R.F., Berveiller, M., Buessler, P. 2011. Semi phenomenological modelling of the behavior of TRIP steels. International Journal of Plasticity Volume 27, Issue 3, 299-327.
47. Lacroix, G., Pardoen, T., Jacques, P.J. 2008. The fracture toughness of TRIP-assisted multiphase steels. Acta Materialia, Volume 56, Issue 15, 3900-3913.
48. Larbalestier, D.C., King, H.W. 1973. Austenitic stainless steels at cryogenic temperatures 1 – Structureal stability and magnetic properties. Cryogenics 13 (3), 160-168.
49. Leal, R. 1984. Ph.D. Thesis, MIT, Cambridge, MA, USA.
50. Lebedev, A.A., Kosarchuk, V.V. 2000. A tensorial description of the transformation kinetics of the martensitic phase transformation. International Journal of Plasticity, Volume 16, Issue 7-8, 749-767.
51. Leblond, J. B. (1989b). Mathematical modelling of transformation plasticity in steels II: Coupling with strain hardening phenomena. International Journal of Plasticity, 5, 573–591.

52. Leblond, J. B., Devaux, J., and Devaux, J. C. (1989a). Mathematical modelling of transformation plasticity in steels I: Case of ideal-plastic phases. International Journal of Plasticity, 5, 551–572.
53. Leblond, J. B., Mottet, G., and Devaux, J. C. (1986a). A theoretical and numerical approach to the plastic behaviour of steels during phase transformations - i. Derivation of general relations. Journal of the Mechanics and Physics of Solids, 34(4), 395–409.
54. Leblond, J. B., Mottet, G., and Devaux, J. C. (1986b). A theoretical and numerical approach to the plastic behaviour of steels during phase transformations - ii. study of classical plasticity for ideal-plastic phases. Journal of the Mechanics and Physics of Solids, 34(4), 411–432.
55. Lee, M.G., Kim, S.J., Han, H.N. 2010. Crystal plasticity finite element modeling of mechanically induced martensitic transformation (MIMT) in metastable austenite. International Journal of Plasticity 26, 688-710.
56. Levitas, V.I., 1998. Thermomechanical theory of martensitic phase transformations in inelastic materials. Int. J. Solids Structures 35, 889-940.
57. Levitas, V.I., Idesman, A.V., Stein, E., 1998. Finite element simulation of martensitic phase transitions in elastoplastic materials. Int. J. Solids Structures 35, 889-940.
58. Lichtenfeld, J.A., Mataya, M., Tyne, C.J.V., 2006. Effect of strain rate on stress–strain behavior of alloy 309 and 304L austenitic stainless steel. Metallurgical and Materials Transactions A 37A, 147–161.
59. Ma, A., Harmaier, A. 2015. A study of deformation and phase transformation coupling for TRIP-assisted steels. International Journal of Plasticity 64, 40-55.
60. Magee, C.L. 1966. Transformation Kinetics, Microplasticity and Aging of Martensite in Fe-31Ni. Ph.D. Thesis, Carnegie Institute of Technology, Pittsburg, PA.
61. Mahnken, R., Schneidt, A., Antretter, T. 2009. Macro modelling and homogenization for transformation induced plasticity of a low-alloy steel. International Journal of Plasticity 25, 183-204.
62. Mahnken, R., Wolff, M., Schneidt, A., Bohm, M. 2012. Multi-Phase Transformations at Large Strains – Thermodynamic Framework and Simulation. Inernational Journal of Plasticity 39, 1-26.
63. Malik, A., Amber, G., Borgenstam, A., Agren, J. 2013. Effect of external loading on the martensitic transformation – A phase field study. Acta Materialia, Volume 61, Issue 20, 7868-7880.
64. Man, J., Obrtlík, K., Petrenec, M., Beran, P., Smaga, M., Weidner, A., Dluhoš, J., Kruml, T., Biermann, H., Eifler, D., Polák, J. 2011. Stability of austenitic 316L steel against martensite formation during cyclic straining. Procedia Engineering 10, 1279-1284.
65. McGuire, M. 2008. Stainless steel for design engineers. ASM International. USA.
66. Meftah, S., Barbe, F., Taleb, L., Sidoroff, F., 2007. Parametric numerical simulations of TRIP and its interaction with classical plasticity in martensitic transformation. Eur. J. Mech. A/Solids 26, 688–700.
67. Meyer, D., Brinksmeier, E., Hoffmann, F. 2011. Surface hardening by cryogenic deep rolling. Procedia Engineering 19, 258-263.
68. Mori, T., Tanaka, K., 1973. Average stress in matrix and average energy of materials with misfitting inclusions. Acta Metall. 21, 571–574.
69. Mróz, Z., Ziętek, G. 2007. Modeling of cyclic hardening of metals coupled with martensitic transformation. Arch. Mech. 59 (1), 3-20.

70. Müller-Bollenhagen, C., Zimmermann, M., Christ H.J. 2010. Adjusting the very high cycle fatigue properties of a metastable austenitic stainless steel by means of the martensite content. Procedia Engineering 2, 1663-1672.
71. Müller-Bollenhagen, C., Zimmermann, M., Christ. H.-J. 2009. Adjusting the very high cycle fatigue properties of a metastable austenitic stainless steel by means of the martensite content. Procedia Engineering 2, 1663-1672.
72. Nagayama, K., Terasaki, T., Goto, S., Tanaka, K., Antretter, T., Fischer, F.D., Cailletaud, G., Azzouz, F., 2002. Back stress evolution and iso-volume fraction lines in a Cr–Ni–Mo–Al–Ti maraging steel in the process of martensitic transformation. Mater. Sci. Eng. A—Struct. 336, 30–38.
73. Nagayama, K., Terasaki, T., Goto, S., Tanaka, K., Fischer, F., Antretter, T., Cailletaud, G., Azzouz, F., 2001. Mechanical properties of a Cr–Ni–Mo–Al–Ti maraging steel in the process of martensitic transformation. Mater. Sci. Eng. A—Struct. 308, 25–37.
74. Nakada, N., Ito, H., Matsuoka, Y., Tsuchiyama, T., Takaki, S. 2010. Deformation-induced martensitic transformation behavior in cold-rolled and cold-drawn type 316 stainless steels. Acta Materiaia, Volume 58, Issue 3, 895-903.
75. Nakajima, M., Uematsu, Y., Kakiuchi, T., Akita, M., Tokaji, K. 2011. Effect of quantity of martensitic transformation on fatigue behavior in type 304 stainless steel. Procedia Engineering 10, 299-304.
76. Naraghi, R., 2009. Martensitic transformation in austenitic stainless steels (Master's thesis). Retrieved from http://kth.diva-portal.org/smash/search.jsf.
77. Oberste-Brandenburg, C., Bruhns, O.T. 2004. A tensorial description of the transformation kinetics of the martensitic phase transformation. International Journal of Plasticity, Volume 20, Issue 12, 2083-2109.
78. Olson, G.B. 1996. Transformation plasticity and toughening. Jorunal de physique. IV, Colloque C1, Volume 6 (1), 407-418.
79. Olson, G.B., Azrin, M. 1978. Transformation behavior of TRIP steels. Metall. Trans. 9A, 713-721.
80. Olson, G.B., Cohen, M. 1975. Kinetics of strain-Induced martensitic nucleation. Metall. Trans. A 6A, 791-795.
81. Ortwein, R., Skoczeń, B., Tock, J.Ph. 2014. Micromechanics based constitutive modeling of martensitic transformation in metastable materials subjected to torsion at cryogenic temperatures. International Journal of Plasticity, 59, 152-179.
82. Papatriantafillou, I., Agoras, M., Aravas, N., Haidemenopoulos, G., 2006. Constitutive modeling and finite element methods for TRIP steels. Computer Methods in Applied Mechanics and Engineering, Volume 195, Issues 37-40, 5094-5114.
83. Papatriantafillou, I., Aravas, N., Haidemenopoulos, G., 2004. Finite element modelling of trip steels. Steel Research International 75, 732–738.
84. Perdahcıoğlu, E.S., Geijselaers, H.J.M. 2012. A macroscopic model to simulate the mechanically induced martensitic transformation in metastable austenitic stainless steels. Acta Materialia, Volume 60, Issue 11, 4409-4419.
85. Perdahcioglu, E.S., Geijselaers, H.J.M., Groen, M. 2008. Influence of plastic strain on deformation-induced martensitic transformations, Scripta Materialia 58, 947-950.
86. Petit, B., Gey, N., Cherkaoui, M., Bolle, B., Humbert, M. 2007. Deformation behavior and microstructure/texture evolution of an annealed 304 AISI stainless steel sheet. Experimental and micromechanical modeling. International Journal of Plasticity 23. 323-341.

87. Pierman, A.P., Bouaziz, O., Pardoen, T., Jacques, P.J. 2014. The influence of microstructure and composition on the plastic behaviour of dual-phase steels. Acta Materialia 73, 298-311.
88. Pruger, S., Seupel, A., Kuna, M. 2014. A thermomechanically coupled material model for TRIP-steel. International Journal of Plasticity 55, 182-197.
89. Prüger, S., Seupel, A., Kuna, M. 2014. A thermomechanically coupled material model for TRIP-steel. International Journal of Plasticity, Volume 55, 182-197.
90. Shen, Y.F., Li, X.X., Sun, X., Wang, Y.D., Zuo, L. 2012. Twinning and martensite in a 304 austenitic stainless steel. Materials Science and Engineering A 552, 514-522.
91. Shin, H.C., Ha, T.K., Chang, Y.W. 2001. Kinetics of deformation induced martensitic transformation in a 304 stainless steel. Scripta Materialia 45, 823-829.
92. Sitko, M., Skoczeń, B. 2012. Effect of γ − α′ phase transformation on plastic adaptation to cyclic loads at cryogenic temperatures. International Journal of Solids and Structures, Volume 49, Issue 3-4, 613–634.
93. Sitko, M., Skoczeń, B., Wróblewski, A. 2010. FCC–BCC phase transformation in rectangular beams subjected to plastic straining at cryogenic temperatures. International Journal of Mechanical Sciences, Volume 52, Issue 7, 993-1007.
94. Skoczeń, B. 2007. Functionally graded structural members obtained via the low temperature strain induced phase transformation. International Journal of Solids and Structures, Volume 44, Issue 16, 5182–5207.
95. Solomon, N., Solomon, I., 2010. Deformation induced martensite in AISI 316 stainless steel. Revista de Metalurgia, 46 (2), 121-128.
96. Somani, M.C., Juntunen, P., Karjalainen, L.P., Misra, R.D.K., Kyröläinen, A. 2009. Enhanced mechanical properties through reversion in metastable austenitic stainless steels. Metallurgical and Materials Transactions A 40 (3), 729-744.
97. Stavehaug, F., 1990. Ph.D. Thesis, MIT, Cambridge, MA, USA.
98. Stevehaug, F. 1990. Ph.D. Thesis, MIT, Cambridge, MA, USA.
99. Stringfellow, R.G., Parks, D.M. 1991. Strain-induced transformation plasticity in metastable austenitic steels. Anisotropy and Localization of Plastic Deformation, 516-519.
100. Stringfellow, R.G., Parks, D.M., Olson, G.B., 1992. A constitutive model for transformation plasticity accompanying strain-induced martensitic transformation in metastable austenitic steels. Acta Metall. Mater. 40, 1703-1716.
101. Swift, H., 1947. Length changes in metals under torsional overstrain. Engineering 163, 253–257.
102. Taleb, L, Sidoroff, F. 2003. A micromechanical modeling of the Greenwood–Johnson mechanism in transformation induced plasticity. International Journal of Plasticity, Volume 19, Issue 10, 1821-1842.
103. Taleb, L., Cavallo, N., Waeckel, F., 2001. Experimental analysis of transformation plasticity. Int. J. Plasticity 17, 1–20.
104. Talonen, J. 2007. Effect of strain-induced α’ martensite transformation on mechanical properties of metastable austenitic stainless steels. (Doctoral dissertation). Retrieved from http://lib.aalto.fi/fi/.
105. Talonen, J., Aspegren, P., Hanninen, H. 2004. Comparison of different methods for measuring strain induced α'-martensite content in austenitic steels. Materials science and technology 20 (12), 1506-1512.

106. Tanaka, K., Terasaki, T., Goto, S., Antretter, T., Fischer, F.D., Cailletaud, G., 2003. Effect of back stress evolution due to martensitic transformation on isovolume fraction lines in a Cr–Ni–Mo–Al–Ti maraging steel. Mater. Sci. Eng. A—Struct. 341, 189–196.
107. Tjahjanto, D.D., Rosters, F., Eisenlohr, P., 2007b. Iso-work-rate weighted-Taylor homogenization scheme for multiphase steels assisted by transformation induced plasticity effect. Steel Res. Int. 78, 777–783.
108. Tjahjanto, D.D., Suiker, A.S.J., Turteltaub, S., Rivera Diaz del Castillo, P.E.J., van der Zwaag, S., 2007a. Micromechanical predictions of TRIP steel behavior as a function of microstructural parameters. Comp. Mater. Sci. 41, 107–116.
109. Tjahjanto, D.D., Turteltaub, S., Suiker, A.S.J., 2008. Crystallographically based model for transformation-induced plasticity in multiphase carbon steels. Continuum Mech. Therm. 19, 399–422.
110. Tjahjanto, D.D., Turteltaub, S., Suiker, A.S.J., van der Zwaag, S., 2006. Modelling of the effects of grain orientation on transformation-induced plasticity in multi-phase steels. Model. Simul. Mater. Sci. Eng. 14, 617–636.
111. Tomita, Y., Iwamoto, T., 1995. Constitutive modeling of TRIP steel and its application to the improvement of mechanical properties. Int. J. Mech. Sci. 37, 1295–1305.
112. Tomita, Y., Shibutani, Y. 2000. Estimation of deformation behavior of TRIP steels — smooth/ringed-notched specimens under monotonic and cyclic loading. International Journal of Plasticity, Volume 16, Issue 7-8, 769-789.
113. Tsipouridis, P. 2006. Mechanical properties of Dual-Phase steels. PhD thesis.
114. Turteltaub, S., Suiker, A.S.J., 2005. Transformation-induced plasticity in ferrous alloys. J. Mech. Phys. Solids 53, 1747–1788.
115. Turteltaub, S., Suiker, A.S.J., 2006. A multi-scale thermomechanical model for cubic to tetragonal martensitic phase transformations. Int. J. Solids Struct. 43, 4509–4545.
116. van Beeck, J., Kouznetsowa, V.G., van Maris, M.P.F.H.L. 2011. The mechanical behaviour of metastable austenitic steels in pure bending. Materials Science and Engineering A 528, 7207– 7213.
117. Wang, C., Ding, H., Cai, M., Rolfe, B. 2014. Characterization of microstructures and tensile properties of TRIP-aided steels with different matrix microstructure. Materials Science & Engineering A 610, 65-75.
118. Wechsler, M.S., Lieberman, D.S., Read, T.A., 1953. On the theory of the formation of martensite. AIME Transactions on Journal of Metals 197, 1503–1515.
119. Weidner, A., Glage, A., Biermann, H. 2010. In-situ characterization of the microstructure evolution during cyclic deformation of novel cast TRIP steel. Procedia Engineering 2, 1961-1971.
120. Weidner, A., Muller, A., Weiss, A., Biermann, H. 2013. Ultrafine grained high-alloyed austenitic TRIP steel. Materials Science & Engineering A 571, 68-76.
121. Yan, Y.H., Kai, G.Y., Jian, M.D. 2006. Transformation behavior of retained austenite under different deformation modes for low alloy TRIP-assisted steels. Materials Science and Engineering A 441, 331-335.
122. Zaera, R., Rodríguez-Martínez, J.A., Casado, A., Fernandez-Saez, J., Rusinek, A., Pesci, R., 2012. A constitutive model for analyzing martensite formation in austenitic steels deforming at high strain rates. International Journal of Plasticity 29, 77–101.
123. Zyczkowski, M. Combined loadings in the theory of plasticity. Warsaw, Poland: PWN;1981.

124. http://www.outokumpu.com/SiteCollectionDocuments/Outokumpu-stainless-steel-handbook.pdf, 2014
125. http://www.industrycortex.com/datasheets/profile/750983975/stainless-stainless-steels-and-their-properties-by-bla-leffle, 2014
126. http://www.keytometals.com/page.aspx?ID=CheckArticle&site=kts&LN=PL&NM=270, 2014
127. http://www.nickelinstitute.org/~/media/files/technicalliterature/materialsforcryogenicservice_engineeringpropertiesofausteniticstainlesssteel_4368_.pdf, 2014
128. http://www.worldautosteel.org/steel-basics/steel-types/transformation-induced-plasticity-trip-steel/, 2014
129. http://www.uz.zgora.pl/~mkuczma/07.pdf, 2015
130. http://www.radiatronics.com/assets/pdf-files/R-FT-FCM.pdf, 2015
131. http://www.asams.co.uk/download/feritscope_manual.pdf, 2015